

University of Alberta

Elemental Speciation Using Electrospray Ionization - Mass Spectrometry and
Electrospray Ionization - High-Field Asymmetric Waveform Ion Mobility Spectrometry -
Mass Spectrometry

by

Russell Patrick Handy



A thesis submitted to the Faculty of Graduate Studies and Research in partial fulfillment
of the requirements for the degree of Doctor of Philosophy

Department of Chemistry

Edmonton, Alberta
Fall 2002



National Library
of Canada

Acquisitions and
Bibliographic Services

395 Wellington Street
Ottawa ON K1A 0N4
Canada

Bibliothèque nationale
du Canada

Acquisitions et
services bibliographiques

395, rue Wellington
Ottawa ON K1A 0N4
Canada

Your file Votre référence

Our file Notre référence

The author has granted a non-exclusive licence allowing the National Library of Canada to reproduce, loan, distribute or sell copies of this thesis in microform, paper or electronic formats.

The author retains ownership of the copyright in this thesis. Neither the thesis nor substantial extracts from it may be printed or otherwise reproduced without the author's permission.

L'auteur a accordé une licence non exclusive permettant à la Bibliothèque nationale du Canada de reproduire, prêter, distribuer ou vendre des copies de cette thèse sous la forme de microfiche/film, de reproduction sur papier ou sur format électronique.

L'auteur conserve la propriété du droit d'auteur qui protège cette thèse. Ni la thèse ni des extraits substantiels de celle-ci ne doivent être imprimés ou autrement reproduits sans son autorisation.

0-612-81198-0

Canada

University of Alberta

Library Release Form

Name of Author: Russell Patrick Handy

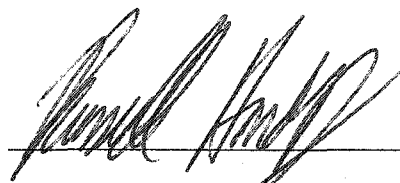
Title of Thesis: Elemental Speciation Using Electrospray Ionization - Mass Spectrometry and Electrospray Ionization - High-Field Asymmetric Waveform Ion Mobility Spectrometry - Mass Spectrometry

Degree: Doctor of Philosophy

Year this Degree Granted: 2002

Permission is hereby granted to the University of Alberta Library to reproduce single copies of this thesis and to lend or sell such copies for private, scholarly or scientific research purposes only.

The author reserves all other publication and other rights in association with the copyright in the thesis, and except as herein before provided, neither the thesis nor any substantial portion thereof may be printed or otherwise reproduced in any material form whatever without the author's prior written permission.



Russell Patrick Handy
124 Carlson Close
Edmonton, Alberta
T6R 2J7

Date: August 26, 2002

August 26, 2002

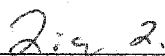
University of Alberta

Faculty of Graduate Studies and Research

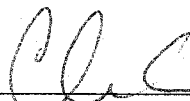
The undersigned certify that they have read, and recommend to the Faculty of Graduate Studies and Research for acceptance, a thesis entitled Elemental Speciation Using Electrospray Ionization - Mass Spectrometry and Electrospray Ionization - High-Field Asymmetric Waveform Ion Mobility Spectrometry - Mass Spectrometry submitted by Russell Patrick Handy in partial fulfillment of the requirements for the degree of Doctor of Philosophy.



Dr. Gary Horlick



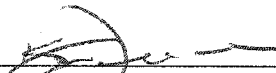
Dr. Liang Li



Dr. Charles A. Lucy



Dr. John S. Klassen



Dr. Kenneth L. Froese



Dr. Gary M. Hieftje

Date:

July 30, 2002

Abstract

A new interface for the electrospray ionization (ESI) of ions in purely aqueous matrices is described. Combined with mass spectrometry (MS), the performance of the aqueous ESI interface was evaluated in both positive and negative modes using small inorganic ions in both aqueous and methanolic matrix. Several demonstrations of using purely aqueous solvent to preserve the original species information in the resultant ESI-MS spectrum are presented for selenite and hypochlorite, among others. This aqueous ESI source was also used for the direct speciation of the lanthanides. The combination of this ESI source with high-energy collision-induced dissociation (CID) in the MS interface region demonstrates a significant improvement to the elemental determination of these species by ESI-MS.

A detailed introduction to the theory of operation of a relatively new technique, called high-field asymmetric waveform ion mobility spectrometry (FAIMS) is presented. Due to the ability of FAIMS to separate different gas-phase ions and dramatically reduce the spectral background, ESI-FAIMS-MS was used to detect perchlorate at low nanomolar levels, even in the presence of matrix ions known to severely interfere with perchlorate analysis by ESI-MS alone. An experimental description of a more recent FAIMS prototype is presented using simple inorganic ions. Included in this description is a detailed discussion of the relative importance of tuning several of the FAIMS operating parameters. Using the aqueous ESI source, ESI-FAIMS-MS was used for a detailed speciation analysis of some Arsenic and Selenium species in a purely aqueous solvent,

and comparisons to the species observed in methanolic solvent are presented. The separation of the major species in the FAIMS from other ions representing isobaric interferences allowed for their detection at low nanomolar levels. Also, the FAIMS facilitated a more detailed examination of the gas-phase species produced by ESI, allowing for the detection of some very low intensity Se species, not previously observed by ESI-MS alone. Finally, the ion filtering mechanism of FAIMS permitted the use of very mild MS interface sampling conditions, which resulted in the observation of ion adducts, especially with carbon dioxide in the drift gas.

Acknowledgements

I would like to thank my supervisor, Dr. Gary Horlick for his guidance and support. Thanks to Dr. Youbin Shao, for his friendship and technical help, especially in the machine shop.

Special thanks to Dr. Tiebang Wang, who convinced me to get my Ph. D., instead of continuing to work as a B. Sc. level scientist for a private company.

Thanks to the people who let me work with FAIMS. Thanks to Dr. Roger Guevremont, Dr. Randy Purves, Dr. David Barnett, Dr. Kenneth Froese, and Dr. Wojceich Gabryelski.

Financial support provided by the Department of Chemistry at the University of Alberta, and the National Science and Engineering Research Council (NSERC) is greatly appreciated.

I have also been fortunate to have a few beers with some other students, all of who have helped me deal with the often frustrating and uncertain process of being a graduate student. Thanks to Dr. Bernd Keller, Dr. Rob Polakowski, and Darren Lewis for their friendship.

Finally, thanks to my constant companion, Pam, for all her understanding and love over the past few years.

Table of Contents

Chapter 1	Introduction	1
1.1	Objective	2
1.2	Electrospray	4
1.2.1	The Electrospray Phenomenon	5
1.2.2	Electrospray as an Electrolysis Cell	11
1.3	Electrospray Ionization – Mass Spectrometry (ESI-MS)	17
1.3.1	ESI Interfaces	17
1.3.2	MS Interface for ESI	20
1.3.3	Collision Induced Dissociation (CID)	20
1.3.4	Relative Signal Intensity with ESI-MS	23
1.4	Instrumentation	23
1.4.1	ESI Interfaces	24
1.4.2	Mass Spectrometers	24
1.4.3	FAIMS Interfaces	26
1.5	References	27
Chapter 2	Evaluation of an Electrospray Source for Purely Aqueous Solvents with ESI-MS	34
2.1	Introduction	35
2.2	Experimental	38
2.2.1	Aqueous Electrospray Interface	38
2.2.2	Mass Spectrometry	40
2.2.3	Reagents and Sample Preparation	40
2.3	Results and Discussion	42
2.3.1	Optimization of ESI Voltages in Positive Mode	42

2.3.2	Influence of Solution Flow Rate in Positive Mode	44
2.3.3	Comment on the Bath Gas	47
2.3.4	Comparison of Methanol and Water Solvent Performance	50
2.3.5	Selenite in Methanol and Water Solvents	54
2.3.6	Sulfite in Methanolic and Water Solvents	57
2.3.7	Hypochlorite in Methanol and Water Solvents	57
2.4	Conclusions	60
2.5	References	61

**Chapter 3 ESI-MS of Lanthanides in Aqueous Solution - Investigations
Using High-Energy Collision-Induced Dissociation 63**

3.1	Introduction	64
3.2	Experimental	65
3.2.1	Aqueous Electrospray Interface	65
3.2.2	Mass Spectrometry	67
3.2.3	Reagents and Sample Preparation	69
3.3	Results and Discussion	69
3.3.1	Methanolic Solvent	69
3.3.2	Aqueous Solvent	75
3.3.3	Comparison of Species Generation with Aqueous and Methanol Solvent	80
3.3.4	Aqueous ESI Reproducibility	82
3.3.5	High CID Sampling	85
3.3.6	Ln Spectra Using a Commercial Interface	89
3.3.7	Implications for Speciation and Quantitation	89
3.3.8	Oxygen Curtain Gas	94
3.4	Conclusions	96
3.5	References	99

Chapter 4	An Introduction to High-Field Asymmetric Waveform Ion Mobility Spectrometry (FAIMS)	101
4.1	Objective	102
4.2	Introduction	102
4.3	What is IMS	103
4.4	Development of IMS	105
4.5	IMS at High Fields	106
4.6	Origins of High-Field Asymmetric Field Ion Mobility Spectrometry (FAIMS)	108
4.7	Fundamental Discussion of Ion Motion in a Gas	114
	4.7.1 Basic IMS Considerations	114
	4.7.2 Dependence of Mobility on E / N	115
	4.7.3 Considerations Towards a More Refined Theory	117
	4.7.4 Comments on Diffusion and Space-Charge Repulsion	118
4.8	IMS Theory as it Relates to FAIMS	119
	4.8.1 Ion Mobility Determination	119
	4.8.2 Ion – Neutral Collisions and Variation of Observed Mobility with Field Strength	121
	4.8.3 Comments on Diffusion and Space-Charge Repulsion	122
4.9	FAIMS Voltage and Field Expressions	123
	4.9.1 Relations of Voltage and Field for Three Simple Geometries	123
	4.9.2 Dependence of Voltage and Field with Position Between Parallel Plates	127
	4.9.3 Radial Dependence of Voltage Between Cylinders	129
	4.9.4 Radial Dependence of Field Between Cylinders	131
	4.9.5 Radial Dependence of Voltage Between Spheres	132
	4.9.6 Radial Dependence of Field Between Spheres	134
4.10	Ion Motion Along Force Lines in a FAIMS Analyzer	135
	4.10.1 Ion Motion Within a Parallel Plate FAIMS Analyzer	135

4.10.2	Ion Motion Within a Concentric Cylinder	
	FAIMS Analyzer	140
4.11	Introduction to Ion Modeling	142
4.12	Modeling Limitations	143
4.13	High Field Mobilities	144
4.14	Calculation of Ion Trajectories	144
4.15	Modeling Examples	147
	4.15.1 Parallel Plate FAIMS	147
	4.15.2 Concentric Cylinder FAIMS	150
	4.15.3 Concentric Cylinders that Terminate in a Spherical Dome	157
4.16	Waveform Generation	162
4.17	Waveforms for Various K_h/K Behaviors	163
4.18	References	166

Chapter 5	Determination of Nanomolar Levels of Perchlorate in Water by ESI-FAIMS-MS	172
5.1	Introduction	173
	5.1.1 Concentric Cylinder FAIMS Prototype	173
	5.1.2 Analysis of Perchlorate	175
5.2	Experimental	176
5.3	Results and Discussion	178
	5.3.1 ESI-MS	178
	5.3.2 ESI-FAIMS-MS	180
5.4	Conclusions	191
5.5	References	192

Chapter 6	Experimental Characterization of a Dome FAIMS Prototype Using Small Anions	194
6.1	Introduction	195
6.2	Experimental	200
6.2.1	FAIMS Dome Interface	200
6.2.2	Waveform Generator	204
6.2.3	Mass Spectrometry	206
6.2.4	ESI Source	208
6.2.5	ESI-FAIMS-MS Coupling	208
6.2.6	Reagents	213
6.3	Results and Discussion	213
6.3.1	Effects of Curtain Gas Flow Rate	214
6.3.2	Effects of Waveform Symmetry	218
6.3.3	Effect of Dome Spacing on CV	223
6.3.4	Effects of DV and Dome Spacing on Mass-Selected CV Peak Width and Intensity	224
6.4	Conclusions	238
6.5	References	241
Chapter 7	FAIMS Dome Prototype: Investigations with Aqueous Sampling	245
7.1	Introduction	246
7.2	Experimental	255
7.2.1	ESI-FAIMS-MS	255
7.2.2	Asymmetric Waveform	258
7.2.3	ESI Sources	260
7.2.4	Reagents	263
7.3	Results and Discussion	263

7.3.1	Performance Characteristics of the Aqueous ESI Source	264
7.3.2	Speciation of Selenite in Methanol Solvent	267
7.3.3	Speciation of Selenite in Purely Aqueous Solvent	280
7.3.4	Speciation of Selenite in a Solvent Mixture	283
7.3.5	Speciation of Arsenate	288
7.3.6	Speciation of Arsenite - Preliminary Results	288
7.3.7	Sensitivity and Detection Limits of the Technique	298
7.3.8	Comment on ESI-FAIMS-MS as a Tool for Speciation	307
7.4	Conclusions	308
7.5	References	310

Chapter 8 Low CID Sampling Conditions in the MS Interface Using ESI-FAIMS-MS 315

8.1	Introduction	316
8.2	Experimental	319
8.2.1	ESI-FAIMS-MS	319
8.2.2	ESI Sources	323
8.2.3	Reagents	326
8.3	Results and Discussion	327
8.3.1	Low CID Sampling for Simple Anions and Cations	327
8.3.2	Solvent and Gas Adducts Observed with CO ₂ in the Drift Gas	332
8.3.3	Collision-Induced Dissociation (CID) with CO ₂	340
8.3.4	Arsenite in Water Solvent using CO ₂ in the Drift Gas	342
8.3.5	Speciation of Hypochlorite in Water Solvent Using CO ₂ in the Drift Gas	343
8.4	Conclusions	347
8.5	References	348

Chapter 9	Conclusions and Future Work	351
9.1	Summary	352
9.2	Future Work	356
9.2.1	Negative Mode ES with Aqueous Solvents	356
9.2.2	Matrix Effects in ESI-FAIMS-MS	356
9.2.3	Multiply Charged Cations	358
9.2.4	Modifications to the FAIMS Interface	361
9.2.5	FAIMS – Drift Tube IMS Coupling	362
9.2.6	Alternate Ion Sources with FAIMS-MS	362
9.3	References	363

List of Figures

- Figure 1.01** Taylor cone morphology with electrospray. (a) Photograph of an operational ES source with a metal capillary (reproduced with permission from reference 47); (b) illustration of (a).....6
- Figure 1.02** Illustration of a metal capillary electrospray tip with an applied high voltage of positive polarity..... 7
- Figure 1.03** Schematic illustration of repeated droplet fissions responsible for generation of gas-phase species from electrosprayed droplets..... 10
- Figure 1.04** Schematic illustration of theoretical models for gas-phase ion generation from electrosprayed droplets; Charged Residue Model (CRM) and Ion Evaporation Model (IEM).....12
- Figure 1.05** Illustration of a CE-ES-MS interface to balance the high current of CE with the lower current of ES. Variable resistor adjusted to allow current flow..... 16
- Figure 1.06** A typical ESI interface with a metal capillary..... 18
- Figure 1.07** Schematic diagram of the modified ELAN 250 ICP-MS interface..... 21
- Figure 1.08** Illustration of ESI interfaces based on using fused silica emitters. Both involve a continuous piece of fused silica from the pump to the tip. (a) high-voltage solution contact made at tip by back-wetting of solution to the metal capillary; (b) dual voltage system, where the only high voltage solution contact is made at the syringe needle.....25
- Figure 2.01** Illustration of a metal capillary electrospray tip with an applied high voltage of positive polarity..... 36
- Figure 2.02** Illustration of an interface for electrospraying purely aqueous solvents (not to scale)..... 39
- Figure 2.03** Schematic diagram of the modified ELAN 250 ICP-MS interface..... 41
- Figure 2.04** Effect of capillary voltage on (a) average intensity at m/z 85, and (b) on signal stability (as %RSD). M/z 85 for Rb^+ was monitored for 5 minute measurement interval; dwell time = 0.1 sec, 300 measurements. Solution was 0.5 mM KI with 0.01 mM $RbCl$ in 100% water solvent. Solution flow rate = 20 $\mu L/hr$, tip voltage = 1.0 kV..... 43

Figure 2.05	Effect of applied capillary voltage on the current at the syringe needle. Tip support voltage = 1.0 kV, solution flow rate = 20 $\mu\text{L/hr}$. Sample was 0.5 mM KI with 0.01 mM RbCl in 100% water solvent.....	45
Figure 2.06	Effects of flow rate on Rb^+ signal (monitored at m/z 85) on (a) average intensity and (b) signal stability (as %RSD) with 100% water solvent using the dual voltage ESI source. Sample was 0.5 mM KI with 0.01 mM RbCl. Capillary voltage = 4.7 kV, tip voltage = 1.0 kV.....	46
Figure 2.07	Effect of solution flow rate on the observed current at the syringe needle with the dual voltage ESI source. Capillary voltage = 4.7 kV, tip support voltage = 1.0 kV. Sample was 0.5 mM KI with 0.01 mM RbCl in 100% water solvent.....	48
Figure 2.08	Balance of flow rate and capillary voltage using the dual voltage ESI source with 100% water solvent. Selected ion monitoring at m/z 85 and 87 for the Rb^+ ion. (a) 20 $\mu\text{L/hr}$ solution flow, 4.6 kV capillary voltage; (b) 24 $\mu\text{L/hr}$ solution flow, 4.6 kV capillary voltage; (c) 24 $\mu\text{L/hr}$ solution flow, 5.0 kV capillary voltage. Tip voltage = 1.0 kV.....	49
Figure 2.09	ESI-MS spectra of a mixture of LiCl, RbCl, and BaCl_2 each at a concentration of 0.01 mM, with 0.5 mM KI. $\Delta V = 90$ V. (a) 92% methanol solvent (8% water), (b) 100% water solvent.....	51
Figure 2.10	ESI-MS spectra of a sample containing 0.5 mM Na_2SeO_3 in 95% methanol (5% water). (a) $\Delta V = -34$ V (b) $\Delta V = -50$ V.....	55
Figure 2.11	ESI-MS spectra of a sample containing 0.5 mM Na_2SeO_3 in 100% water solvent. (a) $\Delta V = -50$ V (b) expanded view of the spectrum in (a).....	56
Figure 2.12	ESI-MS spectrum of 0.5 mM Na_2SO_3 in (a) 95% methanol, 5% water and (b) 100% water solvent.....	58
Figure 2.13	ESI-MS spectrum of a commercial bleach solution diluted to give approx. 0.1 mM NaOCl. (a) 95% methanol, 5% water and (b) 100% water solvent.....	59
Figure 3.01	Interface for electrospraying purely aqueous solvents in positive mode (not to scale).....	66
Figure 3.02	Schematic diagram of the modified ELAN 250 ICP-MS interface.....	68
Figure 3.03	ESI-MS spectrum of solutions containing 0.1 mM Ln salt and 0.4 mM LiCl in 95% methanol, 5% water matrix. Spectra acquired at a SPV of 200 V; (a) LaCl_3 , (b) $\text{Eu}(\text{NO}_3)_3$, (c) LuCl_3	70

Figure 3.04	ESI-MS spectrum of solutions containing 0.1 mM Ln salt and 0.4 mM LiCl in 100% aqueous solvent. Spectra were acquired at a sampling plate voltage of 200 V; (a) LaCl ₃ , (b) Eu(NO ₃) ₃ , (c) LuCl ₃	76
Figure 3.05	ESI-MS spectrum of a solution containing 0.1 mM LaCl ₃ with 0.4 mM LiCl in 100% aqueous solvent. Spectra acquired at SPV = 100 V with N ₂ curtain gas.....	77
Figure 3.06	Low mass regions of the ESI-MS spectra of a solution containing 0.1 mM LaCl ₃ with 0.4 mM LiCl in 100% aqueous solvent. Spectra acquired at (a) SPV = 100 V and (b) SPV = 200 V with N ₂ curtain gas.....	79
Figure 3.07	Signal intensity as a function of sampling plate voltage with N ₂ curtain gas for a sample containing 0.1 mM Ln salt and 0.4 mM LiCl in 95% methanol, 5% water or 100% aqueous solvent; (a) LaCl ₃ , (b) Eu(NO ₃) ₃ , (c) LuCl ₃	81
Figure 3.08	ESI-MS spectra from 2 different days, acquired under identical MS interface conditions (N ₂ curtain @ 300 mL/min, SPV = 100 V). Differences in clusters likely reflect differences in ESI performance and / or solution differences. Solution contained 0.1 mM LaCl ₃ with 0.4 mM LiCl in 100% aqueous solvent; (a) day 1, (b) day 2.....	83
Figure 3.09	ESI-MS spectra of solutions containing 0.1 mM LaCl ₃ with 0.4 mM LiCl in 100% aqueous solvent at different N ₂ curtain gas flow rates. SPV = 100 V. Curtain gas flow rates: a) 175 mL/min, b) 300 mL/min, c) 450 mL/min.....	84
Figure 3.10	ESI-MS spectra of solutions containing 0.1 mM Ln salt and 0.4 mM LiCl in 95% methanol, 5% water matrix. Spectra acquired at a SPV = 350 V; (a) LaCl ₃ , (b) Eu(NO ₃) ₃ , (c) LuCl ₃	86
Figure 3.11	ESI-MS spectrum of solutions containing 0.1 mM Ln salt and 0.4 mM LiCl in purely aqueous solvent. Spectra were acquired at a sampling plate voltage of 350 V; (a) LaCl ₃ , (b) Eu(NO ₃) ₃ , (c) LuCl ₃	87
Figure 3.12	(a) Low mass region of the spectrum in Figure 3.10 (a); (b) same spectrum as in Figure 3.10 (a), but with wider mass range and expanded intensity axis to show the baseline species.....	88
Figure 3.13	Ln salts in 95% methanol (5% water) acquired on a HP1100 Series LC/MSD. (a) 0.1 mM LaCl ₃ with 0.4 mM LiCl; (b) 0.1 mM Eu(NO ₃) ₃ with 0.1 mM LiCl.....	90

Figure 3.14	ESI-MS spectra of a solution containing 0.1 mM Pr(NO ₃) ₃ , 0.1 mM LuCl ₃ , and 0.2 mM GdCl ₃ in 100% water solvent using N ₂ curtain gas; (a) SPV = 200 V, (b) SPV = 350 V.....	92
Figure 3.15	High resolution quadrupole (R ~0.6 amu) ESI-MS spectra of a solution containing 0.1 mM Pr(NO ₃) ₃ , 0.1 mM LuCl ₃ , and 0.2 mM GdCl ₃ in 100% water solvent using N ₂ curtain gas and SPV = 350V; (a) full spectrum, (b) doubly-charged region, (c) same as in (b) with expanded intensity axis to show the baseline species.....	93
Figure 3.16	0.1 mM Lanthanide salt and 0.4 mM LiCl in 100% water matrix, using O ₂ curtain gas, SPV = 350 V. (a) LaCl ₃ , (b) Eu(NO ₃) ₃ , (c) LuCl ₃	95
Figure 3.17	0.1 mM Lanthanide salt and 0.4 mM LiCl in 100% water matrix, using O ₂ curtain gas, SPV = 350 V. Same spectra as Figure 3.15, with intensity axis expanded to show the baseline species. (a) LaCl ₃ , (b) Eu(NO ₃) ₃ , (c) LuCl ₃	97
Figure 4.01	Schematic illustration of a drift tube ion mobility spectrometer.....	104
Figure 4.02	Types of ion mobility behavior (K _h /K) in response to increasing applied electric field. K _h = high field mobility. K = low field mobility. A = increasing mobility with increasing applied field. B = complex mobility dependence with applied field; initially increasing, then decreasing with higher applied field. C = decreasing mobility with increasing applied field.....	107
Figure 4.03	Schematic illustration of a parallel plate FAIMS device.....	109
Figure 4.04	Examples of waveforms used with FAIMS. (a) Two composite sine waves that are combined to form (b) an asymmetric waveform with a negative high voltage peak.....	110
Figure 4.05	Timeline outlining the development of the FAIMS interface.....	112
Figure 4.06	FAIMS electrode geometries. (a) parallel plates, (b) concentric cylinders, (c) concentric cylinders terminating as a spherical dome.....	124
Figure 4.07	Parallel flat plates separated at a uniform distance r _{total} , with test charge at a distance r _{test} from lower plate. Plates biased to voltages V ₁ and V ₂ , where V ₂ > V ₁	128
Figure 4.08	Radius definitions for concentric cylinders or concentric spheres.....	130

- Figure 4.09** Basics of parallel plate FAIMS operation. (a) Schematic of a parallel plate FAIMS apparatus with the dc potential (i.e., the compensation voltage, CV) set to transmit the A_2 ion. (b) Theoretical example of two different ions, A_1 and A_2 , with different K_h/K ratios in response to increasing applied electric field..... 136
- Figure 4.10** Hypothetical CV spectrum of negative ions A_1 and A_2 using the N1-P2 waveform, with hypothetical K_h/K mobility as illustrated in Figure 4.09 (b).....139
- Figure 4.11** Schematic illustration of a longitudinal cross section concentric cylinder FAIMS instrument with electrometer detection..... 141
- Figure 4.12** Measured dependence of ion mobility (expressed as K_h/K) in air for perchlorate as a function of electric field strength within the FAIMS analyzer (expressed as E/N , where N represents the gas number density).....145
- Figure 4.13** Calculated ion trajectory in a parallel plate FAIMS for type A ion. Ion mobility as defined in Equation 4.63. Plate spacing = 0.2 cm. Square wave approximation, $f = 210$ kHz, 2:1 $t_{low}:t_{high}$. Initial ion position at 0.90 cm. X-axis (time) represents residence time in the analyzer region. Limits of the y-axis represent the surface of the plates. (a) $DV = -3300$ V, $CV = 0$ V, (b) $DV = -3300$ V, $CV = 32.5$ V.....148
- Figure 4.14** Calculated ion trajectory in a parallel plate FAIMS for type A ion with balanced DV and CV for different initial ion positions. Ion mobility as defined in Equation 4.63. $DV = -3300$ V, $CV = 32.5$ V. Plate spacing = 0.20 cm. Square wave approximation, $f = 210$ kHz, 2:1 $t_{low}:t_{high}$. X-axis (time) represents residence time in the analyzer region. Limits of the y-axis represent the surface of the plates. a) $r_{initial} = 0.90$ cm, b) $r_{initial} = 0.95$ cm, c) $r_{initial} = 0.81$ cm.....149
- Figure 4.15** Calculated trajectory of a type A ion in a concentric cylinder FAIMS with $a = 0.8$ cm, $b = 1.0$ cm with the low-field portion of the waveform applied first. Ion mobility as defined in Equation 4.63. Square wave approximation, 2:1 $t_{low}:t_{high}$, $f=210$ kHz, $DV = -3300$ V, $CV = 35.0$ V, $r_{initial} = 0.95$ cm. X-axis (time) represents residence time in the analyzer region. Limits of the y-axis represent the surface of the cylinders..... 151

- Figure 4.16** Calculated ion trajectory in a parallel plate FAIMS for a type A ion with a short residence time in the analyzer. Ion mobility as defined in Equation 4.63. Plate spacing = 0.2 cm, $r_{\text{initial}} = 0.90$ cm. Square wave approximation, $f = 210$ kHz, 2:1 $t_{\text{low}}:t_{\text{high}}$. X-axis (time) represents residence time in the analyzer region (2 msec total). Limits of the y-axis represent the surface of the plates. (a) $DV = -3300$ V, $CV = 29.8$ V, (b) $DV = -3300$ V, $CV = 37.0$ V..... 152
- Figure 4.17** Calculated trajectory of a type A ion in a concentric cylinder FAIMS with $a = 0.8$ cm, $b = 1.0$ cm. Ion mobility as defined in Equation 4.63. Square wave approximation, $f = 210$ kHz, 2:1 $t_{\text{low}}:t_{\text{high}}$, $DV = -3300$ V, $CV = 35.0$ V. X-axis (time) represents residence time in the analyzer region. Limits of the y-axis represent the surface of the cylinders. (a) $r_{\text{initial}} = 0.90$ cm, (b) $r_{\text{initial}} = 0.95$ cm, (c) $r_{\text{initial}} = 0.81$ cm..... 153
- Figure 4.18** Calculated trajectory of a type A ion in a concentric cylinder FAIMS with $a = 0.8$ cm, $b = 1.0$ cm at a frequency of 750 kHz. Ion mobility as defined in Equation 4.63. Square wave approximation, 2:1 $t_{\text{low}}:t_{\text{high}}$, $DV = -3300$ V, $CV = 35.0$ V, $r_{\text{initial}} = 0.95$ cm. X-axis (time) represents residence time in the analyzer region. Limits of the y-axis represent the surface of the cylinders..... 155
- Figure 4.19** Calculated ion trajectory path width as a function of waveform frequency. Symmetry ($t_{\text{low}}:t_{\text{high}}$) of applied waveform as indicated. Type A ion in a concentric cylinder FAIMS with $a = 0.8$ cm, $b = 1.0$ cm. Ion mobility as defined in Equation 4.63. Square wave approximation, $DV = -3300$ V, $CV = 35.0$ V, $r_{\text{initial}} = 0.95$ cm..... 156
- Figure 4.20** Calculated fields at various radial positions within parallel plates, concentric cylinders and concentric spheres. Electrode geometries as indicated. Field values calculated as the field at peak $DV = -3300$ V.... 158
- Figure 4.21** Calculated trajectory of a type A ion in a FAIMS with both concentric cylinder and concentric dome geometry. Cylinder and dome regions have dimensions $a = 0.8$ cm, $b = 1.0$ cm. Ion mobility as defined in Equation 4.63. Square wave approximation, $f = 210$ kHz, 2:1 $t_{\text{low}}:t_{\text{high}}$, $DV = -3300$ V, $CV = 35.0$ V. X-axis (time) represents residence time in the analyzer region. Limits of the y-axis represent the surface of the electrodes. First half of modeling for concentric cylinder geometry, second half for concentric sphere geometry. (a) $r_{\text{initial}} = 0.90$ cm, (b) $r_{\text{initial}} = 0.95$ cm, (c) $r_{\text{initial}} = 0.81$ cm..... 160

Figure 4.22	Calculated trajectory of a type A ion in a FAIMS with both concentric cylinder and concentric dome geometry. Cylinder region has dimensions $a = 0.8$ cm, $b = 1.0$ cm. Ion mobility as defined in Equation 4.63. Square wave approximation, $f = 210$ kHz, 2:1 $t_{low}:t_{high}$, $DV = -3300$ V, $CV = 35.0$ V. X-axis (time) represents residence time in the analyzer region. Limits of the y-axis represent the surface of the electrodes. First half of modeling for concentric cylinder geometry, second half for concentric sphere geometry. (a) dome dimensions $a = 1.0$ cm, $b = 0.8$ cm, (b) dome dimensions $a = 1.0$ cm, $b = 0.79$ cm, (c) dome dimensions $a = 1.0$ cm, $b = 0.81$ cm.....	161
Figure 4.23	Waveforms used in FAIMS; (a) the N1-P2 waveform; (b) the P1-N2 waveform.....	165
Figure 5.01	An illustration of ion motion between the concentric cylinders of the FAIMS analyzer during the application of an asymmetric waveform shown as $V(t)$; the ion is transported horizontally by a gas flow (distance not to scale).....	174
Figure 5.02	Schematic of the ESI-FAIMS-MS instrument.....	177
Figure 5.03	(a) Mass spectrum of $10 \mu\text{M}$ sulphate in 0.2 mM ammonium acetate (9:1 methanol/water (v/v)) acquired by conventional ESI-MS on an API 300 triple-quadrupole mass spectrometer; (b) expanded view of the spectrum shown in (a).....	179
Figure 5.04	(a) Mass spectrum of $1 \mu\text{M}$ perchlorate and $10 \mu\text{M}$ sulphate in 0.2 mM ammonium acetate (9:1 methanol/water (v/v)) acquired by conventional ESI-MS on an API 300 triple-quadrupole mass spectrometer; (b) expanded view of the spectrum shown in (a).....	181
Figure 5.05	Measured dependence of ion mobility (expressed as K_h/K) in air for (a) perchlorate and bisulphate and (b) dihydrogen orthophosphate and bisulphate as a function of electric field strength within the FAIMS analyser (expressed as E/N , where N represents the gas number density).....	182
Figure 5.06	Variation of observed ion compensation voltage scan peak as a function of pressure within the FAIMS analyzer for bisulphate and dihydrogen orthophosphate in air drift gas at $DV = -3300$ V.....	184
Figure 5.07	Mass-selected CV spectra (m/z -97, -99, and -101; $CV = -1$ V to 29 V; $DV = -3300$ V) of $1 \mu\text{M}$ perchlorate and $10 \mu\text{M}$ sulphate in 0.2 mM ammonium acetate (9:1 methanol/water (v/v)). (i) $DV = 0$ V, shown magnified 10x for clarity; (ii) $DV = -1600$ V; (iii) $DV = -2100$ V; (iv) $DV = -2700$ V; (v) $DV = -3300$ V.....	186

Figure 5.08	(a) Mass spectrum of 1 μ M perchlorate 10 μ M sulphate in 0.2 mM ammonium acetate (9:1 methanol/water (v/v)) at DV = -3300 V and CV = 23.6 V; (b) expanded view of the spectra in (a).....	187
Figure 5.09	(a) Mass-selected CV spectra (m/z -97, -99, and -101; CV = 15 to 29 V; DV = -3300 V) of 0.1 μ M perchlorate, 50 μ M sulphate, and 50 μ M phosphate in 0.2 mM ammonium acetate (9:1 methanol/water (v/v)); (b) expanded view of (a) with m/z -97 shown as a dashed line for clarity; (c) mass spectrum of the same solution at CV = 24.2 V.....	189
Figure 5.10	Signal intensity at m/z -99 (DV = -3300 V, CV = 24.2 V) as a function of perchlorate concentration (with 10 μ M sulphate and 0.2 mM ammonium acetate in 9:1 methanol/water).....	190
Figure 6.01	A hypothetical mass-selected compensation voltage (CV) spectrum of ions A ₁ and A ₂ . Signal intensity at a single mass/charge is plotted as a function of the applied compensation voltage (CV).....	196
Figure 6.02	FAIMS electrode geometries. (a) parallel plates, (b) concentric cylinders, (c) concentric cylinders terminating as a spherical dome.....	197
Figure 6.03	Longitudinal cross-sections of a FAIMS dome interface prototype.....	199
Figure 6.04	Radial cross section at the sampling inlet of the dome FAIMS prototype.....	201
Figure 6.05	External side view of the dome FAIMS prototype.....	202
Figure 6.06	External side view of the dome FAIMS prototype.....	203
Figure 6.07	(a) Two composite sine waves that are combined to form (b) the asymmetric waveform for FAIMS operation.....	205
Figure 6.08	Ion optics schematic of the PE-Sciex API-150EX mass spectrometer with the collision-induced dissociation (CID) region highlighted. OR = orifice plate, RNG = ring electrode, SK = skimmer, Q0 = RF-only focusing quadrupole, IQ1 = intermediate quadrupole 1, ST = stubbies (quadrupole), Q1 = mass selection quadrupole, DF = deflector, CEM = channel electron multiplier detector.....	207
Figure 6.09	Face of API-150EX MS sampling orifice with mounting ring attached.....	209
Figure 6.10	Electrical connections for the FAIMS-MS interface.....	210

Figure 6.11	Ion sampling during an ESI-FAIMS-MS experiment.....	212
Figure 6.12	Superimposed mass-selected CV spectra of bisulfate and perchlorate from an ESI-FAIMS-MS experiment, monitored at m/z 97, 99, and 101. Sample solution was 0.1 mM $KClO_4$, with 0.4 mM ammonium acetate in 95% methanol (5% water). Sulphate is present as a solution contaminant. Curtain gas = 2.0 L/min, DV = -3300 V. Dome spacing = 0.232 cm.....	215
Figure 6.13	Effect of N_2 curtain gas flow rate on (a) normalized signal intensity, (b) peak CV, and (c) peak width for the ions perchlorate (ClO_4^-) and bisulfate (HSO_4^-).....	216
Figure 6.14	Effect of altering the theoretical composite sine wave amplitudes (high/low) on (a) normalized signal intensity, (b) peak CV, and (c) peak width for the ions perchlorate (ClO_4^-) and bisulfate (HSO_4^-).....	219
Figure 6.15	Examples of waveform symmetry for phases angles of (a) 90° and (b) 120° . V_{p1} and V_{p2} refer to the peak voltages of the composite sine waves.....	221
Figure 6.16	Effect of altering the phase of the composite sine waves on (a) normalized signal intensity, (b) peak CV, and (c) peak width for the ions perchlorate (ClO_4^-) and bisulfate (HSO_4^-). The symmetry of the resulting asymmetric waveform is represented as the ratio of the negative (A) and positive peak (B) voltage, expressed as $ A/B $	222
Figure 6.17	Observed peak CV as a function of the dome spacing. (a) DV = -2300 V; (b) DV = -3300 V.....	225
Figure 6.18	Variation of peak width and normalized intensity with dome spacing for the chloride ion (Cl^-) at DV = -2300 V and -3300 V.....	226
Figure 6.19	Variation of peak width and normalized intensity with dome spacing for the bromide ion (Br^-) at DV = -2300 V and -3300 V.....	227
Figure 6.20	Variation of peak width and normalized intensity with dome spacing for the iodide ion (I^-) at DV = -2300 V and -3300 V.....	228
Figure 6.21	Variation of peak width and normalized intensity with dome spacing for the biselenate ion ($HSeO_4^-$) at DV = -2300 V and -3300 V.....	229
Figure 6.22	Variation of peak width and normalized intensity with dome spacing for the perchlorate ion (ClO_4^-) at DV = -2300 V and -3300 V.....	230

Figure 6.23	Calculated trajectory of a type A “perchlorate-like” ion in a FAIMS with both concentric cylinder and concentric dome geometry. Cylinder and dome regions have dimensions $a = 0.8$ cm, $b = 1.0$ cm. Square wave approximation, $f = 210$ kHz, 2:1 $t_{low}:t_{high}$, $DV = -3300$ V. X-axis (time) represents residence time in the analyzer region. Limits of the y-axis represent the surface of the electrodes. First half of modeling for concentric cylinder geometry, second half for concentric sphere geometry. (a) $CV = 31.0$ V, (b) $CV = 35.0$ V, (c) $CV = 44.5$ V.....	233
Figure 6.24	Observed ion CV at the dome position required for maximum signal intensity. (a) $DV = -2300$ V; (b) $DV = -3300$ V.....	237
Figure 6.25	Observed variations in mass-selected CV spectra of bisulfate and perchlorate with the annular spacing at the dome region. Dome spacing of (a) 0.199 cm, (b) 0.219 cm, and (c) 0.232 cm. Solution and sampling conditions as in Figure 6.12, with noted exceptions.....	239
Figure 7.01	Ion mobility behavior (K_h/K) in response to increasing applied electric field strength. $K_h =$ high field mobility. $K =$ low field mobility. (a) General mobility behaviors; type A = increasing mobility with increasing applied field. Type B = complex mobility dependence with applied field; initially increasing, then decreasing with higher applied field. Type C = decreasing mobility with increasing applied field; (b) Two different hypothetical ions with type A mobility, A_1 and A_2	249
Figure 7.02	Schematic diagram of a parallel plate FAIMS analyzer region, with the application of an asymmetric waveform to the lower plate. DC potential (i.e., the compensation voltage, CV) set to transmit the A_2 ion.....	250
Figure 7.03	Hypothetical CV spectrum of negative ions A_1 and A_2 using the N1-P2 waveform, with hypothetical K_h/K mobility as illustrated in Figure 7.01 (b).....	253
Figure 7.04	Theoretical variation of ion mobility in response to increasing electric field strength. The same ion, A_1 , in three different drift gas compositions, X, Y and Z.....	254
Figure 7.05	Electrical connections for the FAIMS-MS interface.....	257
Figure 7.06	Cross-section of an ESI-FAIMS-MS interface.....	259
Figure 7.07	(a) Two composite sine waves that are combined to form (b) the N1-P2 asymmetric waveform for FAIMS operation.....	261
Figure 7.08	Two ESI interfaces; (a) typical interface for methanolic solvents, (b) interface for ESI of purely aqueous solvents.....	262

- Figure 7.09** (a) Superimposed mass-selected CV spectra (m/z 59, 143, and 145) in N_2 drift gas of a solution containing Na_2SeO_4 at $1 \mu M$ with 0.4 mM ammonium acetate in 100% water solvent. $DV = -3.5 \text{ kV}$, $F_{OR} = 0 \text{ V}$; (b) Mass spectrum of the same solution at $CV = 21.6 \text{ V}$ 265
- Figure 7.10** Superimposed mass-selected CV spectra in N_2 drift gas of a solution containing $1 \mu M$ Na_2SeO_3 with 0.4 mM ammonium acetate in 95% methanol, 5% water. (a) m/z 143 and 147; (b) m/z 128, 129, 158, and 171. Se species at m/z 201 and 225 identified (traces not shown)..... 271
- Figure 7.11** Mass spectra of selenium species found in the mass-selected CV spectra in Figure 7.10. $DV = -3.5 \text{ kV}$, $F_{OR} = 0 \text{ V}$, N_2 drift gas. Test solution was $1 \mu M$ Na_2SeO_3 with 0.4 mM ammonium acetate in 95% methanol, 5% water. (a) CV set to the m/z 143 peak in the CV spectrum, $CV = 22.6$; (b) CV set to transmit the high CV side of the same peak, $CV = 24.2 \text{ V}$272
- Figure 7.12** Mass spectra of selenium species found in the mass-selected CV spectra in Figure 7.10. $DV = -3.5 \text{ kV}$, $F_{OR} = 0 \text{ V}$, N_2 drift gas. Test solution was $1 \mu M$ Na_2SeO_3 with 0.4 mM ammonium acetate in 95% methanol, 5% water. (a) $CV = 25.8 \text{ V}$; (b) $CV = 29.4 \text{ V}$ 273
- Figure 7.13** Mass spectra of selenium species found in the mass-selected CV spectra in Figure 7.10. $DV = -3.5 \text{ kV}$, $F_{OR} = 0 \text{ V}$, N_2 drift gas. Test solution was $1 \mu M$ Na_2SeO_3 with 0.4 mM ammonium acetate in 95% methanol, 5% water. (a) $CV = 14.0 \text{ V}$; (b) $CV = 18.6 \text{ V}$ 274
- Figure 7.14** Mass spectra of selenium species found in the mass-selected CV spectra in Figure 7.10. $DV = -3.5 \text{ kV}$, $F_{OR} = 0 \text{ V}$, N_2 drift gas. Test solution was $1 \mu M$ Na_2SeO_3 with 0.4 mM ammonium acetate in 95% methanol, 5% water. (a) $CV = 8.8 \text{ V}$; (b) $CV = 6.4 \text{ V}$ 275
- Figure 7.15** Mass-selected CV spectrum in $\sim 10\%$ CO_2 , 90% N_2 drift gas of a solution containing $1 \mu M$ Na_2SeO_3 with 0.4 mM ammonium acetate in 95% methanol, 5% water. (a) m/z 143 and 147; (b) m/z 128, 129, 158, and 171. Se species at m/z 225 identified (trace not shown).....277
- Figure 7.16** Mass spectra of the unknown m/z 147 mass-selected CV peak for $1 \mu M$ Na_2SeO_3 in 95% methanol solvent with 0.4 mM NH_4OAc . (a) $\sim 10\%$ CO_2 drift gas; (b) N_2 drift gas. The N_2 drift gas spectrum has been reconstructed by subtraction of spectra in Figure 7.11..... 278
- Figure 7.17** Superimposed mass-selected CV spectra in N_2 drift gas of a solution containing Na_2SeO_3 at $1 \mu M$ with 0.4 mM ammonium acetate in 100% water solvent. $DV = -3.5 \text{ kV}$, $F_{OR} = 0 \text{ V}$. (a) m/z 128, 129, 143, 147; (b) m/z 158, 171, 201..... 281

- Figure 7.18** Mass spectra of from the CV spectrum in Figure 7.17 of a solution of 1 μM Na_2SeO_3 with 0.4 mM ammonium acetate in 100% water solvent. DV = -3.5 kV, $F_{\text{OR}} = 0$ V, N_2 drift gas. (a) CV = 14.4 V; (b) CV = 9.0 V.... 282
- Figure 7.19** Superimposed mass-selected CV spectra in $\sim 10\%$ CO_2 , 90% N_2 drift gas of a solution containing Na_2SeO_3 at 1 μM with 0.4 mM ammonium acetate in 100% water solvent. DV = -3.5 kV, $F_{\text{OR}} = 0$ V. (a) m/z 128, 129, 143, 147; (b) m/z 158, 171, 201.....284
- Figure 7.20** Superimposed mass-selected CV spectra (m/z 129 and 143) for a solution of Na_2SeO_3 diluted in a solvent mixture of 1:1 methanol:water, with 0.4 mM KOH. Drift gas $\sim 10\%$ Ar, 90% N_2 , DV = -3.5 kV, $F_{\text{OR}} = 0$ V. (a) original $[\text{Na}_2\text{SeO}_3] = 10 \mu\text{M}$; (b) original $[\text{Na}_2\text{SeO}_3] = 1 \mu\text{M}$ 286
- Figure 7.21** Superimposed mass-selected CV spectra (m/z 129 and 143) for the same solution of Na_2SeO_3 from Figure 7.17 after 1 day at room temperature. The Na_2SeO_3 was diluted in a solvent mixture of 1:1 methanol:water, with 0.4 mM KOH. Drift gas $\sim 10\%$ Ar, 90% N_2 , DV = -3.5 kV, $F_{\text{OR}} = 0$ V. (a) original $[\text{Na}_2\text{SeO}_3] = 10 \mu\text{M}$; (b) original $[\text{Na}_2\text{SeO}_3] = 1 \mu\text{M}$ 287
- Figure 7.22** (a) Mass-selected CV spectrum (m/z 141) in $\sim 10\%$ CO_2 , 90% N_2 drift gas of a sample containing 1 μM NaH_2AsO_4 and 0.4 mM KOH in 100% water solvent. DV = -3.5 kV, $F_{\text{OR}} = 0$ V; (b) Mass spectrum at CV = 31.2 V.....289
- Figure 7.23** Mass spectra of the unknown m/z 141 peak in a blank solution of 0.4 mM KOH in 100% aqueous solvent. (a) N_2 drift gas, (b) $\sim 10\%$ CO_2 , 90% N_2 drift gas. DV = -3.3 kV, $F_{\text{OR}} = 0$ V..... 290
- Figure 7.24** Superimposed mass-selected CV spectra (m/z 125, 139, and 153) of 0.1 mM NaAsO_2 with 0.4 mM KOH in 95% methanol, 5% water. Drift gas $\sim 10\%$ Ar, 90% N_2 . DV = -3.1 kV, $F_{\text{OR}} = 0$ V..... 292
- Figure 7.25** (a) Mass spectra at CV = 22.8 V with 0.1 mM NaAsO_2 with 0.4 mM KOH in 95% methanol, 5% water. Drift gas $\sim 10\%$ Ar, 90% N_2 . DV = -3.1 kV, $F_{\text{OR}} = 0$ V; (b) expanded view of the spectrum in (a)..... 293
- Figure 7.26** Mass spectra for 0.1 mM NaAsO_2 with 0.4 mM KOH in 95% methanol, 5% water. Drift gas $\sim 10\%$ Ar, 90% N_2 . DV = -3.1 kV, $F_{\text{OR}} = 0$ V; (a) CV = 18.2 V; (b) CV = 26.4 V..... 294
- Figure 7.27** Superimposed mass-selected CV spectra (m/z 75, 91, 107, 123, 125, 139, and 153) in $\sim 10\%$ CO_2 , 90% N_2 drift gas of a sample containing 0.1 mM NaAsO_2 and 0.4 mM KOH in 100% water solvent. DV = -3.3 kV; (a) $F_{\text{OR}} = -70$ V; (b) $F_{\text{OR}} = -120$ V..... 296

Figure 7.28	(a) Superimposed mass-selected CV spectra (m/z 125 and 141) in ~10% CO ₂ , 90% N ₂ drift gas of a sample containing 0.1 mM NaAsO ₂ and 0.4 mM KOH in 100% water solvent. DV = -3.3 kV, F _{OR} = 0 V; (b) Mass spectrum at CV = 17.0 V.....	299
Figure 7.29	Superimposed mass-selected CV spectra (m/z 129, 141, 145, and 196) in ~5% CO ₂ , 95% N ₂ drift gas of a mixture of Na ₂ SeO ₄ , Na ₂ SeO ₃ , NaH ₂ AsO ₄ , and selenomethionine each at a concentration of 0.1 μM in 100% water solvent with 0.4 mM KOH as an electrospray stabilizer. DV = -3.5 kV, F _{OR} = -10 V.....	301
Figure 7.30	Mass spectra from a solution containing Na ₂ SeO ₃ , Na ₂ SeO ₄ , NaH ₂ AsO ₄ , and selenomethionine, each at 0.1 μM, with 0.4 mM KOH in 100% water solvent. Conditions as in Figure 7.29; DV = -3.5 kV, F _{OR} = -10 V, drift gas ~5% CO ₂ , 90% N ₂ . (a) CV = 24.8 V; (b) CV = 40.8 V.....	302
Figure 7.31	Mass spectra from a solution containing Na ₂ SeO ₃ , Na ₂ SeO ₄ , NaH ₂ AsO ₄ , and selenomethionine, each at 0.1 μM, with 0.4 mM KOH in 100% water solvent. Conditions as in Figure 7.29; DV = -3.5 kV, F _{OR} = -10 V, drift gas ~5% CO ₂ , 90% N ₂ . (a) CV = 32.0 V; (b) CV = 6.8 V.....	303
Figure 7.32	Linear range of HSeO ₄ ⁻ at m/z 145. Intensity (cps) / concentration (μM) as a function of log(concentration). R _c is the line of constant response. Linear range of response is within 0.95 and 1.05 R _c	306
Figure 8.01	Ion mobility behavior (K _h /K) in response to increasing applied electric field strength. K _h = high field mobility. K = low field mobility. (a) General mobility behaviors; type A = increasing mobility with increasing applied field. Type B = complex mobility dependence with applied field; initially increasing, then decreasing with higher applied field. Type C = decreasing mobility with increasing applied field; (b) Two different hypothetical ions with type A mobility, A ₁ and A ₂	317
Figure 8.02	Theoretical variation of ion mobility in response to increasing electric field strength. The same ion, A ₁ , in three different drift gas compositions, X, Y and Z.....	318
Figure 8.03	Electrical connections for the FAIMS-MS interface.....	320
Figure 8.04	The asymmetric waveforms used in FAIMS; (a) the P1-N2 waveform, (b) the N1-P2 asymmetric waveform.....	322
Figure 8.05	Cross-section of an ESI-FAIMS-MS interface.....	324

- Figure 8.06** Two ESI interfaces; (a) typical interface for methanolic solvents, (b) interface for ESI of purely aqueous solvents..... 325
- Figure 8.07** Superimposed mass-selected CV spectra. (a) (m/z 39, 41, 59, 85, 87, and 133) in N_2 drift gas of a mixture of KCl, RbCl, and CsCl at 10 μ M in methanol with 0.4 mM ammonium acetate. $DV = 3.5$ kV, $F_{OR} = 0$ V; (b) (m/z 35, 37, 79, 81, and 127) in N_2 drift gas of a mixture of KCl, KBr, and KI at 10 μ M in methanol with 0.4 mM ammonium acetate. $DV = -3.5$ kV, $F_{OR} = 0$ V..... 328
- Figure 8.08** Mass spectra of (a) Cs^+ , (b) Rb^+ , and (c) K^+ in N_2 drift gas. Conditions as in Figure 8.07 (a). CVs set as indicated in Figures..... 330
- Figure 8.09** Mass spectra of (a) I^- , (b) Br^- , and (c) Cl^- in N_2 drift gas. Conditions as in Figure 8.07 (b). CVs set as indicated in Figures..... 331
- Figure 8.10** Superimposed mass-selected CV spectra. (a) (m/z 39, 41, 59, 85, 87, and 133) in $\sim 15\%$ CO_2 , 85% N_2 drift gas of a mixture of KCl, RbCl, and CsCl at 10 μ M in methanol with 0.4 mM ammonium acetate. $DV = 3.5$ kV, $F_{OR} = 0$ V; (b) (m/z 35, 37, 79, 81, and 127) in $\sim 10\%$ CO_2 , 90% N_2 drift gas of a mixture of KCl, KBr, and KI at 10 μ M in methanol with 0.4 mM ammonium acetate. $DV = -3.5$ kV, $F_{OR} = 0$ V..... 333
- Figure 8.11** Mass spectra of the unknown m/z 85 mass-selected CV peak with (a) N_2 drift gas and (b) $\sim 15\%$ CO_2 , 85% N_2 drift gas..... 335
- Figure 8.12** Mass spectra of (a) Cs^+ , (b) Rb^+ , and (c) K^+ in $\sim 15\%$ CO_2 , 85% N_2 drift gas. Conditions as in Figure 8.11 (b). CVs set as indicated in Figures..... 336
- Figure 8.13** Expanded view of the mass spectra in Figure 8.12. Mass spectra of (a) Cs^+ , (b) Rb^+ , and (c) K^+ in $\sim 15\%$ CO_2 , 85% N_2 drift gas..... 338
- Figure 8.14** Mass spectra of (a) I^- , (b) Br^- , and (c) Cl^- in $\sim 10\%$ CO_2 , 90% N_2 drift gas. Conditions as in Figure 8.11 (b). CVs set as indicated in Figures..... 339
- Figure 8.15** Mass spectra of a solution containing selenomethionine at 10 μ M and 0.4 mM KOH in methanol using (a) N_2 drift gas and (b) $\sim 10\%$ CO_2 , 90% N_2 drift gas. $DV = -3.5$ kV, $F_{OR} = 0$ V, $CV = 5.4$ V, $RNG = -100$ V..... 341
- Figure 8.16** (a) Superimposed mass-selected CV spectra (m/z 125 and 141) in $\sim 10\%$ CO_2 , 90% N_2 drift gas of a sample containing 0.1 mM $NaAsO_2$ and 0.4 mM KOH in 100% water solvent. $DV = -3.3$ kV, $F_{OR} = 0$ V; (b) Mass spectrum at $CV = 17.0$ V..... 344

- Figure 8.17** Superimposed mass-selected CV spectra (m/z 51, 67, 83, 95, and 99) in (a) N_2 drift gas and (b) $\sim 10\%$ CO_2 , 90% N_2 drift gas for the same solution containing $1 \mu M$ $KClO_4$, $10 \mu M$ $KClO_2$, and ~ 0.1 mM $NaOCl$ in 100% water solvent with 0.4 mM KOH . $DV = -3.3$ kV, $F_{OR} = 0$ V. Trace for m/z 51 present but not visible..... 345
- Figure 8.18** Mass spectra of a hypochlorite species observed when using $\sim 10\%$ CO_2 , 90% N_2 drift gas at different orifice voltages, (a) $F_{OR} = -20$ V, (b) $F_{OR} = -80$ V. $DV = -3.5$ kV. Solution used was a commercial bleach sample diluted to give a $[ClO^-]$ of ~ 0.1 mM in 100% water solvent with 0.4 mM KOH 346
- Figure 9.01** Observed signal intensity of $Na^+(H_2O)$ at m/z 41 and Cs^+ at m/z 133 as a function of applied DV. Second axis represents the difference in CV of $Na^+(H_2O)$ and Cs^+ as a function of DV. Sample was 0.01 mM $CsCl$, $RbCl$, and KCl with 0.4 mM ammonium acetate in 100% water matrix. Drift gas $\sim 15\%$ CO_2 , 85% N_2 . $F_{OR} = 0$ V..... 357
- Figure 9.02** Superimposed mass-selected CV spectra in N_2 drift gas of (a) 0.1 mM $BaCl_2$ with 0.4 mM ammonium acetate in water matrix and (b) 0.1 mM $LaCl_3$ with 0.4 mM ammonium chloride in water matrix. $DV = 3.5$ kV, $F_{OR} = 65$ V..... 359
- Figure 9.03** Mass spectra in N_2 drift gas of 0.1 mM $LaCl_3$ with 0.4 mM ammonium chloride in water matrix. $DV = 3.5$ kV, $F_{OR} = 65$ V. (a) $CV = -19.1$ V; (b) $CV = -22.4$ V..... 360

List of Tables

Table 2.01	Positive ion mode solvent comparison data from 300 replicates.....	53
Table 3.01	Physical data for the Lanthanide series.....	73
Table 3.02	Ionization potentials for selected molecules.....	74
Table 7.01	Observed CV (at DV = -3.5 kV) for the HSeO ₄ ⁻ ion in various drift gases with different sample solvents.....	266
Table 7.02	Average signal intensity and stability for the HSeO ₄ ⁻ ion in ESI-FAIMS-MS. DV = -3.5 kV, F _{OR} = 0V, N ₂ drift gas.....	268
Table 7.03	Figures of merit for the measurement of selected ions by ESI-FAIMS-MS in 100% water solution.....	305

Chapter 1

Introduction

1.1 Objective

Elemental analysis techniques, such as those based on inductively coupled plasma (ICP) and flame ionization sources, have made trace level determinations of many of the elements possible in a variety of sample matrices. Today, trace elemental analysis has reached a relative degree of maturity, and atomic absorption, ICP-atomic emission spectroscopy (AES), and ICP-mass spectrometry (MS) instrumentation is common in a wide variety of commercial laboratories. However, as the evidence for distribution of the elements in a system (e.g., the environment) accumulated, it became apparent that simply understanding the elemental composition does not provide the complete picture. In other words, the chemical form of the element is very important. For example, inorganic forms of arsenic are highly toxic, whereas many of the organic forms exhibit very low toxicity [1, 2].

With the need for determining the chemical form or chemical species of an element, a variety of analytical techniques have been developed to achieve this goal. These analyses have been termed “elemental speciation” [3], and are generally some combination of chromatography and an elemental analysis technique. In most methodologies, the different chemical species are separated by chromatographic means, such as ion chromatography (IC), high-pressure liquid chromatography (HPLC), or capillary electrophoresis (CE). These separations are usually combined with element-specific detection, such as atomic absorption, ICP-AES, or ICP-MS. These “hard” atomization and ionization sources break the chemical species down into its constituent atoms, allowing for element-specific detection. The information provided by these hyphenated systems is a chromatogram, where the response due to each element monitored is plotted as a function of elution time. By comparing this information to the retention time of known standards, the identity and quantity of these chemical species in a sample can be determined. While using elemental analysis techniques generally provide low detection limits, the disadvantage is that information regarding the actual chemical form is lost. As a result, when peaks in the chromatogram are observed at a

retention time other than those of the available standards, the species must be identified by other means.

An alternative approach is to employ techniques that preserve the molecular information of the analytes. One such technique is the use of electrospray ionization (ESI) in combination with mass spectrometry (MS). Electrospray ionization is a relatively "soft" means of ionization, where the chemical form of an ion in solution is preserved during its promotion to the gas-phase. In 1968, Dole and co-workers [4] attempted to characterize the electrosprayed ions using ion mobility spectrometry (IMS). Later, in 1983, in a short communication by Alexandrov *et al* [5], an electrohydrodynamic ion source (i.e., electrospray) was coupled with a mass spectrometer. In this work, the electrospray was apparently operated at reduced pressure, and stable ion signals could only be observed in a corona discharge mode. At about the same time, a paper coupling ESI with MS by Yamashita and Fenn was submitted, although not published until the following year [6]. This work marked the first coupling of an atmospheric pressure ESI source with a mass spectrometer. Now almost 20 years since the first ESI-MS reports, this technique has become common in the literature. In a recent review by Stewart [7], he notes an exponential increase in the number of publications using ESI and MS since 1990, based on a Chemical Abstracts search. This publication explosion is no doubt related to the first reported analysis of oligonucleotides and proteins by ESI-MS in 1989 by Fenn *et al* [8]. As such, the majority of publications involve the analysis of large biomolecules. The speciation of smaller ions (especially organometallic compounds) has also received significant attention, as demonstrated by several recent reviews in the field [7, 9-12].

By coupling electrospray to a mass spectrometer, ESI-MS can be used as a direct speciation technique, providing both elemental and molecular information about the ionic species of interest. In our lab, ESI-MS has been used in an attempt to directly determine the species of simple cations and anions in solution [7, 13-22]. Unfortunately, this information can come at the expense of higher detection limits as compared to other analysis methods. One of the major factors for the higher detection limits is the intense

chemical background that may be present in an ESI-MS spectrum. Another disadvantage is the difficulty associated with electrospraying purely aqueous matrices, due to the high surface tension of water [23-29]. As a result, the sample is generally diluted with a volatile solvent to make the ESI process more reliable and easier to use.

One objective of this study was to attempt to develop an ESI interface capable of reliably electrospraying purely aqueous matrices and to investigate the differences in the observed spectra when aqueous solvent is used. The other main objective of this study was to investigate a new technique known as high-field asymmetric waveform ion mobility spectrometry (FAIMS) [30-43] for the analysis of low m/z inorganic ions. A more detailed introduction to this technique is the subject of Chapter 4, but, in short, it provides a front end separation step which can significantly reduce "chemical noise". By developing a reliable ESI interface for aqueous matrices and the application of FAIMS, it was hoped that the speciation analysis of small inorganic ions could be enhanced, avoiding some of the typical limitations with ESI-MS.

1.2 Electrospray

The term "ionization" is a bit of a misnomer in regards to the electrospray process. While the electrospray process may generate ions through electrolysis or by gas-phase charge transfer, generally, the ions of analytical interest are pre-existing in solution. The electrospray mechanism then serves to promote these pre-existing solution ions to the gas phase. This likely accounts for the terms electrospray (ES) and electrospray mass spectrometry (ES-MS) becoming more popular in the literature than ESI and ESI-MS. As such, ES and ESI will be used interchangeably in this work. This section will discuss some of the theoretical and empirical considerations for the electrospray process. Also, some types of ES interfaces will be discussed, especially in regards to electrospraying difficult matrices (e.g., aqueous solvents).

1.2.1 The Electrospray Phenomenon

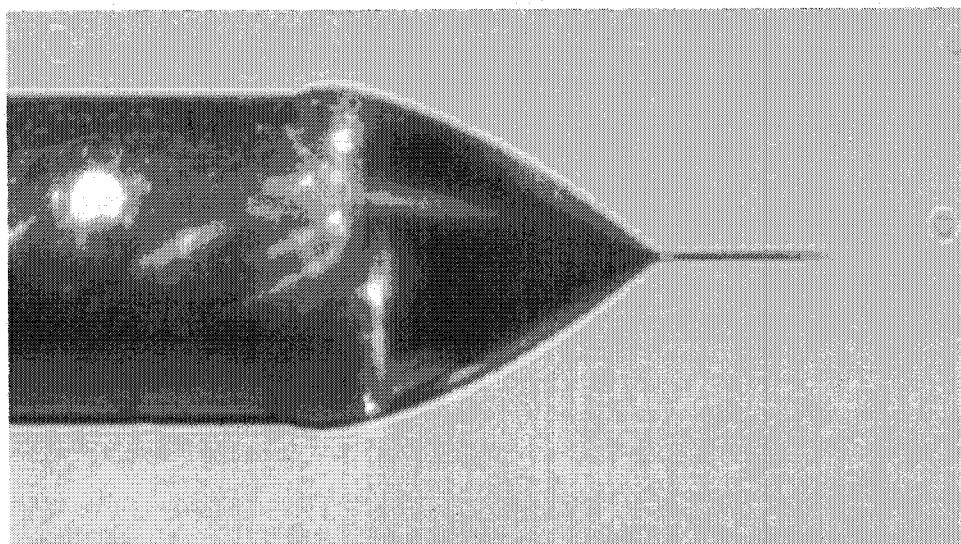
The earliest reported observation of the electrospray phenomenon was in the early 1900s by Zeleny [44-46]. It wasn't until many years later in 1969 when Taylor described the conditions necessary for a charged liquid to form a cone morphology at the tip of a metal capillary in the absence of solution flow [27]. This morphology is also observed with typical electrospray sources, which continuously pump solution to the ES tip [26]. This cone morphology with ES systems later became known as the "Taylor cone", in reference to his work. An example of this morphology is presented in Figure 1.01, which shows a photograph taken by Stewart [47] of an operational ES source, with the liquid exhibiting the Taylor cone morphology.

Typical ES interfaces involve pumping a solution of ions in a polar organic solvent through a metal capillary, to which a high-voltage is applied. If the applied voltage is positive, an excess of positive ions is generated via electrolysis, as illustrated in Figure 1.02. The anions migrate towards the positively charged metal capillary, and the cations move away into the liquid drop extending from the tip of the capillary. In this process, termed electrophoretic charging [48], the liquid surface acquires a net positive charge. If the fields are high enough, the liquid surface may be distorted into a Taylor cone [26, 27].

The generation of a stable Taylor cone is highly dependent on the experimental conditions, and this distortion of the solution surface represents a balance between the surface tension of the solution and the applied electric field forces that "pull" ions towards lower potentials. The field E_{on} (V/m) that must be generated at the electrospray tip to form a Taylor cone [26] is given by Equation 1.01,

$$E_{on} = \left(\frac{2\gamma \cos 49^\circ}{\epsilon_o r_c} \right)^{1/2} \quad 1.01$$

(a)



(b)

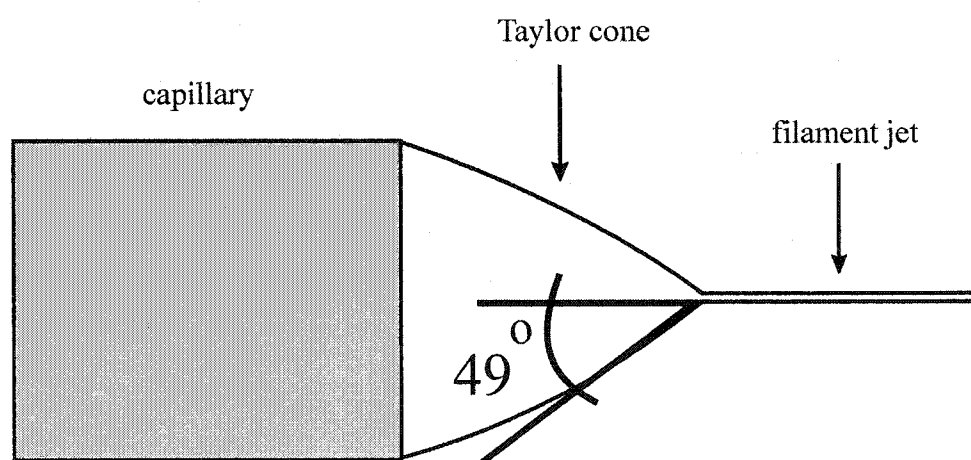


Figure 1.01 Taylor cone morphology with electrostatic spray. (a) Photograph of an operational ES source with a metal capillary (reproduced with permission from reference 47); (b) illustration of (a).

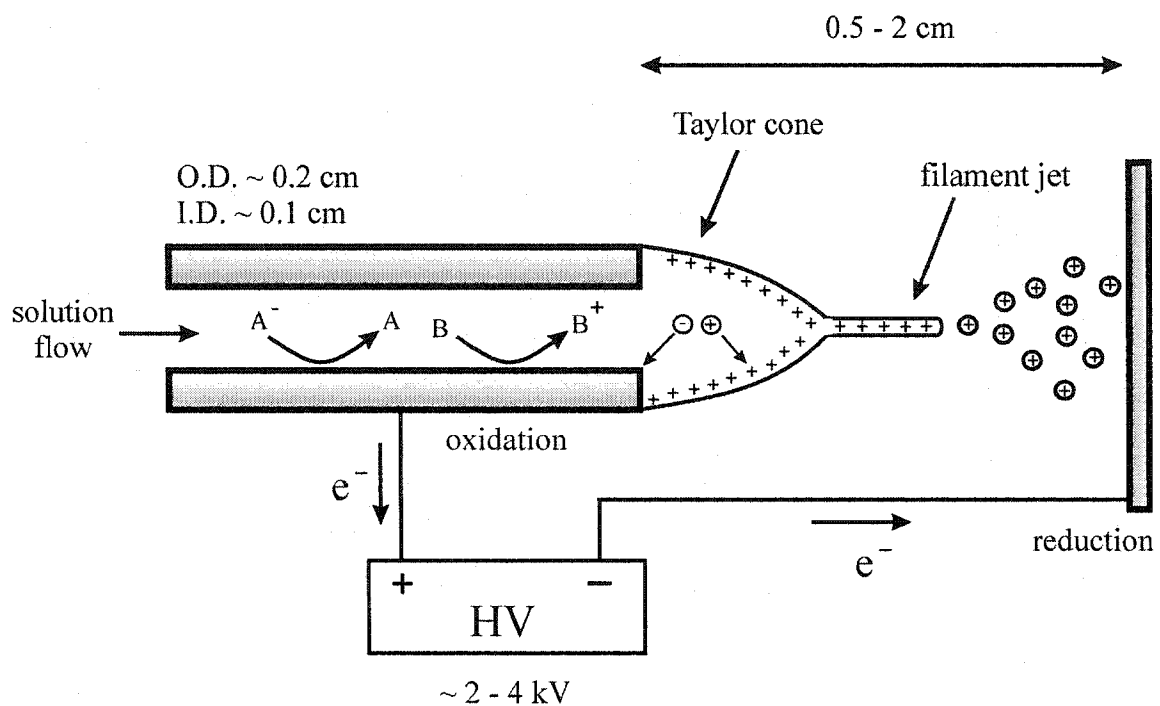


Figure 1.02 Illustration of a metal capillary electro spray tip with an applied high voltage of positive polarity.

where γ is the surface tension (N/m) of the liquid, $\cos 49^\circ$ is the half-angle of the Taylor cone (as shown in Figure 1.01), ϵ_0 is the permittivity of free space ($\epsilon_0 = 8.8 \times 10^{-12} \text{ C}^2/\text{Jm}$) and r_c is the radius (m) of the capillary. Similarly, the voltage (V_{on}) required to generate a Taylor cone [26] is given by Equation 1.02,

$$V_{on} = -\left(\frac{\gamma r_c \cos 49^\circ}{2\epsilon_0}\right)^{1/2} \ln\left(\frac{4d}{r_c}\right) \quad 1.02$$

where d is the distance of the capillary from the counter electrode in meters. Due to the dependence on the surface tension of the liquid, liquids with high surface tension, such as water, require fields higher than the fields required to generate a corona discharge [23-29]. As a result, electrospraying purely aqueous solutions can be difficult. To avoid this problem, dilutions are usually done with a polar organic solvent (e.g., methanol) to reduce the surface tension.

In Figure 1.01 (a), a filament jet can be observed to emanate from the tip of the cone, and this is illustrated in Figure 1.01 (b) and 1.02. The filament jet is the result of the charge repulsion of the ions exceeding the surface tension of the liquid, with charged droplets emitting from the cone surface. This process of charge and liquid ejection has been likened to pulling off the charged skin of the Taylor cone [49]. As the charged droplets collide with the ambient gas, solvent may evaporate from the droplet. As the solvent evaporates from a charged droplet, the droplet may begin a cycle of repeated droplet fissions to produce ions suitable for MS sampling. Lord Rayleigh first described this droplet fission process in 1882 [50]. In this work, Rayleigh described a condition where the forces of ion repulsion in the droplet would reach the limit that the surface tension of the droplet could handle. If the charge density exceeded this value, the droplet would eject ions via a Coulombic asymmetric fission event to alleviate this imbalance. This condition, now known as the ‘‘Rayleigh limit’’, is described as Equation 1.03 [50],

$$q_r^2 = 64\pi^2 \epsilon_0 \gamma r^3 \quad 1.03$$

where q_r is the maximum stable droplet charge (C), γ is the surface tension (N/m) of the liquid, ϵ_0 is the permittivity of free space ($\epsilon_0 = 8.8 \times 10^{-12} \text{ C}^2/\text{Jm}$) and r_r is the radius (m) of the droplet. Equation 1.03 states that the maximum charge stable in a droplet is a function of the surface tension of the liquid and the volume of the droplet, expressed as the cube of the radius. This asymmetric fission process is illustrated in Figure 1.03. Small charged droplets generated from the ES tip lose solvent through collisions with the ambient gas (e.g., N_2). The charge of the droplet remains constant, but the volume (and surface area) is reduced. This leads to an increase in the charge density within the droplet. When the charge reaches the Rayleigh limit, asymmetric fission occurs to relieve the charge repulsion. More recent studies by Gomez and Tang [51] suggest that the droplet fission actually occurs at $\sim 80\%$ of the Rayleigh limit. So, as the solvent evaporates from a charged droplet to reduce the radius to $\sim 80\%$ of the Rayleigh limit, it was found experimentally that about 20 offspring droplets were produced via droplet fission. The fission was observed to occur at right angles to the electric field lines, and the charged offspring droplets were estimated to contain about 15% of the total charge, but only 2% of the mass of the parent droplet. Both the offspring droplets and the parent droplet may then continue to lose solvent by evaporation, and undergo further asymmetric fission events. Note, however, that the work of Gomez and Tang was done using heptane as the solvent and with relatively large droplets, so it has been suggested that these data are only of qualitative validity [51, 52]. Early in the development of electrospray as an ion source, Dole *et al.* [4] noted that the addition of a flow of N_2 gas counter current to the electrospray was beneficial. This was likely to offset the effects of evaporative cooling of the droplet as the solvent was lost [53]. Tang and Kebarle [54] estimated the time required for solvent to evaporate from a charged droplet to a radius suitable for Rayleigh fission. Their calculations demonstrated that the time between fission events was inversely proportional to the droplet temperature. So, if the droplet temperature was low, the time between fission events was greater. Since the drift of charged droplets from the electrospray tip to the counter electrode occurs in a finite time period, a higher droplet temperature will allow for more fission events to occur during the

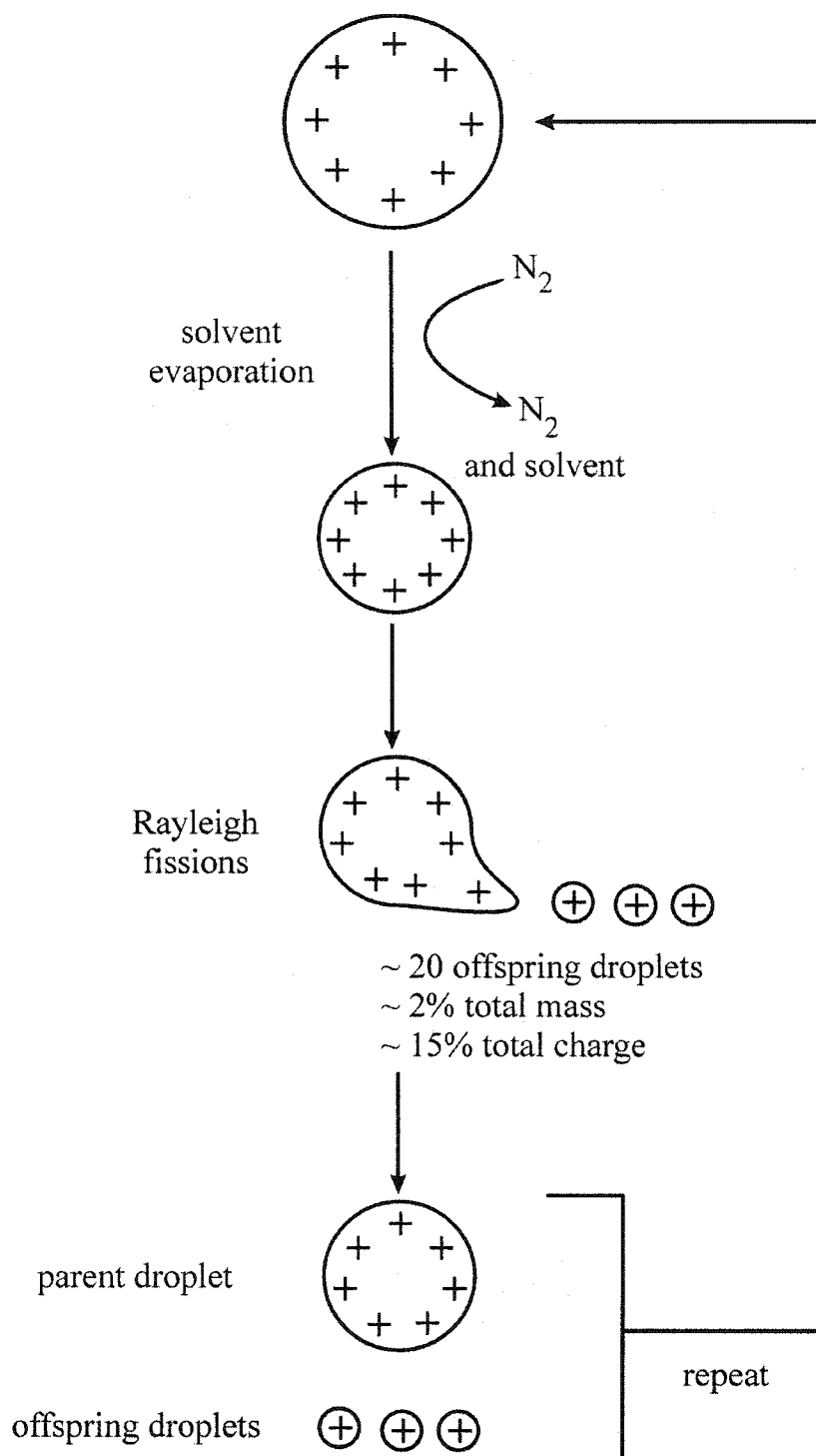


Figure 1.03 Schematic illustration of repeated droplet fissions responsible for generation of gas-phase species from electrospayed droplets.

drift. This could lead to the generation of more gas-phase ions suitable for sampling into a mass spectrometer.

While the process of repeated droplet fissions to produce small charged droplets is considered accurate, the actual process for the final generation of a small ion-solvent cluster suitable for sampling into a mass spectrometer remains the subject of debate [52, 55-58]. Two subtly different mechanisms describing how ions may be liberated from small charged droplets have been proposed. These mechanisms are illustrated in Figure 1.04. Dole *et al.* [4] proposed a “charged residue model” (CRM), which is now also known as the “single ion droplet theory” (SIDT) [4, 54]. In this model, repeated droplet fissions eventually generate single solvated ions. Another theory named the “ion evaporation model” (IEM), was proposed by Irbane and Thomson [59, 60]. In this model, after the droplet reaches a certain radius (~10 nm), direct emission or “evaporation” of ions to the gas phase occurs. In a recent commentary by Kebarle [52], he notes that the existing data seem to support the IEM for small ions, whereas larger ions seem to be generated via the CRM. In any case, the empirical result of the ES process is the same: the promotion of pre-existing solution ions to the gas phase at atmospheric pressure as solvated single ions.

1.2.2 Electrospray as an Electrolysis Cell

The operation of a typical electrospray source has been described as an electrolysis cell of a special kind [48]. Referring to the illustration in Figure 1.02, when a positive voltage is applied to the metal capillary, species are oxidized and electrons flow to the positive input of the power supply. In order to maintain the charge balance, positive ions ejected from the tip are collected at the counter-electrode, where they are reduced. The electrons for this reduction are supplied from the negative input of the power supply (i.e., ground). The magnitude of the current that flows in an ES system has been characterized by Fernandez de la Mora *et al.* [61, 62], and is described by Equation 1.04,

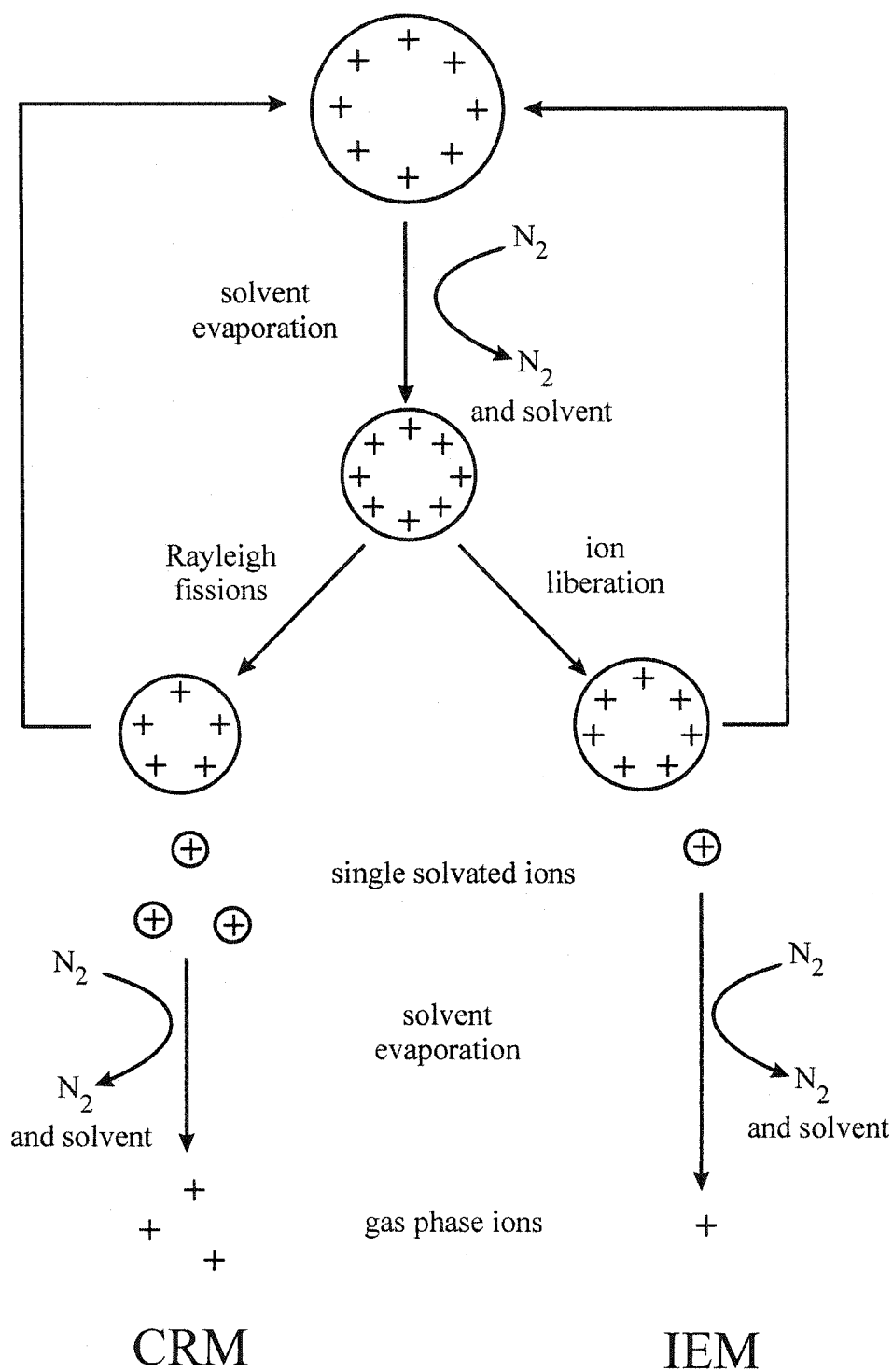


Figure 1.04 Schematic illustration of theoretical models for gas-phase ion generation from electro sprayed droplets; Charged Residue Model (CRM) and Ion Evaporation Model (IEM).

$$I \approx f\left(\frac{\varepsilon}{\varepsilon_0}\right) \left[\gamma Q K \frac{\varepsilon}{\varepsilon_0} \right]^{1/2} \quad 1.04$$

where the current, I (A), is a complex function of the dielectric constant or permittivity of the liquid, ε ($C^2/J\cdot m$), and the permittivity of vacuum, ε_0 . The current is directly proportional to the square root of the liquid surface tension, γ (N/m), the liquid flow rate, Q (m^3/sec), and the solution conductivity, K (S/m). The term $f(\varepsilon/\varepsilon_0)$ is a complex term, which varies with the experimental conditions. Relations describing the approximate radius of the droplets, R (m), and the resultant charge on the droplet, q (C) have been derived, and are presented here as Equations 1.05 and 1.06 [52, 62].

$$R \approx \left(\frac{Q\varepsilon}{K} \right)^{1/3} \quad 1.05$$

$$q \approx 0.7 \left[8\pi (\varepsilon_0 R^3 \gamma)^{1/2} \right] \quad 1.06$$

These relationships predict that ES sources operating at lower flow rates, Q , or with solutions with higher conductivity, K , will produce droplets with a smaller initial radius, R . Also, a solvent with a higher dielectric constant, ε , should also produce smaller initial droplets. This is important, since smaller initial droplets should lead to more efficient desolvation, and a more efficient promotion of ions to the gas phase. Furthermore, if the volume of a droplet is approximated as the volume of a sphere ($V = \frac{4}{3} \pi R^3$), then comparison with Equation 1.05 suggests that the volume of the droplet varies directly with the flow rate, Q , and inversely with the conductivity, K . If Equations 1.05 and 1.06 are combined, Equation 1.07 can be derived.

$$q \approx 0.7 \left[8\pi \left(\frac{\varepsilon \varepsilon_0 \gamma Q}{K} \right)^{1/2} \right] \quad 1.07$$

This relationship suggests that the charge of the droplet varies with the square root of the flow rate. Since the droplet charge only reduces as $Q^{1/2}$ and radius decreases with Q , the charge density in the droplet should increase with decreasing flow rate. The combination of higher charge density and more efficient desolvation should increase the rate at which ions (or small ion-solvent clusters) are liberated into the gas phase. In other words, lower flow rates with ES should be more efficient at promoting ions to the gas phase.

The effects of electrolysis in the ES system have been studied by Van Berkel and his colleagues [58, 63, 64], who note that the solution pH can be altered by about 4 pH units due to solvent electrolysis. Also, corrosion of the electrospray emitter may occur. In the case when a stainless ES tip is used, iron may be observed in the resultant mass spectrum as the result of corrosion.

Another very interesting description of the ES system is that of Jackson and Enke [65]. Their analysis of an ES source is an extension of the previous work by Kebarle *et al* [48]. They describe the ES system as a closed circuit, with all components acting in series. The ES circuit is composed of a power supply, an electrochemical contact to the solution, solution resistance, a constant current regulator, and charge neutralization at the counter electrode. The constant current regulator represents the process of charge separation and charge transport in the air gap between the tip and the counter electrode. By placing a large resistance ($\sim 50 \text{ G}\Omega$) in series with the power supply and the solution contact, a much wider range of operating currents (10 – 70 nA) was possible over the voltages tested, and made the metal capillary behave more like a non-conducting one. Since this was a series circuit, Equation 1.08 applies,

$$V_{\text{applied}} = V_{\text{gap}} + IR_{\text{series}} + IR_{\text{solution}} \quad 1.08$$

where the applied voltage equals the sum of the voltage drops across each resistance, the air gap (V_{gap}), the added series resistor (IR_{series}), and the resistance from the solution (IR_{solution}). With such a large resistor, the solution resistance was negligible for a metal capillary, and Equation 1.09 applies.

$$V_{\text{applied}} \approx V_{\text{gap}} + IR_{\text{series}} \quad 1.09$$

In fact, the voltage drop across the air gap was calculated to be relatively constant at about 2000 V, which likely represents the voltage required for the onset of the Taylor cone under their test conditions. Applied voltages in excess of V_{gap} were demonstrated to draw currents, with a magnitude that satisfies Equation 1.10.

$$I = (V_{\text{applied}} - V_{\text{gap}}) / R_{\text{series}} \quad 1.10$$

Also, since the series resistance was large compared to the solution resistance, the current performance of their ES system was apparently the same regardless of analyte concentration [66].

These types of voltage-current considerations are very important, especially when attempting to couple ES with a high current interface, such as capillary electrophoresis (CE). A stable ES typically only emits enough charged particles to generate a current of < 200 nA during stable operation, and CE typically operates with currents in the μA range. This imbalance in the currents of these two systems creates a condition where the ES may be destabilized. Adding a path to ground to the solution contact (at the ES tip) and generating a current divider (i.e., parallel resistances) can rectify the charge imbalance. This kind of setup is illustrated in Figure 1.05. In positive mode operation, the charge can either flow through the air gap in the form of positively charged droplets, or electrons may flow from ground through a resistor to neutralize some of the excess charge. In this kind of configuration, the magnitude of the resistance to ground is tuned to give stable ES operation. This type of configuration has been reported previously for CE-ES-MS systems [67].

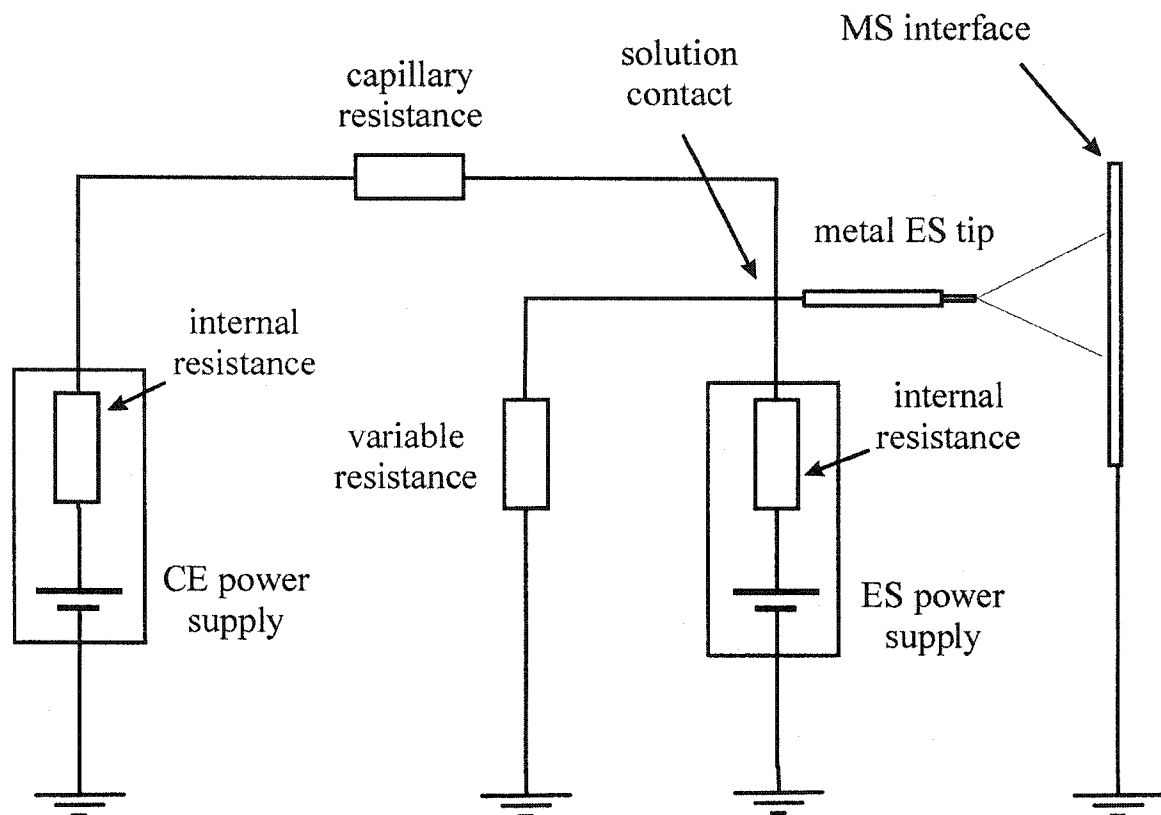


Figure 1.05 Illustration of a CE-ES-MS interface to balance the high current of CE with the lower current of ES. Variable resistor adjusted to allow current flow.

1.3 Electrospray Ionization – Mass Spectrometry (ESI-MS)

1.3.1 ESI Interfaces

The classic ES interface is based on the use of a metal capillary, and is illustrated in Figure 1.06. In this setup, a small piece of stainless steel capillary (O.D. $\sim 200\ \mu\text{m}$, I.D. $\sim 100\ \mu\text{m}$) is inserted into a larger stainless steel HPLC tubing (I.D. 0.010" μm , O.D. 1/16"), and is soldered at the tip to keep the capillary secure. Solution is pumped between 1-10 $\mu\text{L}/\text{min}$ into the metal capillary to which a high voltage is applied. The tip to counter electrode separation is typically 0.5 - 2 cm, and the voltage difference between the tip and the counter electrode is in the range of 2-4 kV, depending on the spacing, as indicated in Equation 1.02. This type of configuration allows for purely electrostatic ES operation.

The low flow rate required with pure ES presents a limitation to the coupling of ES to liquid chromatography systems, since these systems typically operate at much higher flow rates ($\sim 1.0\ \text{mL}/\text{min}$). To accommodate these higher flow rates, a modified ES interface, called "ion spray", was developed [68]. Ion spray (IS) uses a turbulent stream of gas (usually N_2) introduced coaxially to the main capillary to generate an aerosol mist as the solution exits. The metal capillary is the same as with the pure ES system just described, however, the role of the capillary is more to provide an electrical contact for the generation of excess charge, as opposed to the electrohydrodynamic generation of the initial droplets. Since the initial nebulization is largely pneumatic, a wider range of initial droplet sizes is generated, and the tip must be oriented away from the MS orifice to prevent sampling of the larger droplets. Heated variations of this interface also exist, which heat the capillary and introduce a heated stream of N_2 to the spray to enhance desolvation. These IS configurations are reported to be more robust than pure ES systems, due to their ability to nebulize without the formation of a Taylor cone. Sensitivities with these types of interfaces are reported to be just as good as ES with methanol solutions [28]. These IS interfaces can also handle pure water solvents, although at the sacrifice of signal intensity ($\sim 5\times$ lower) and stability, as compared to

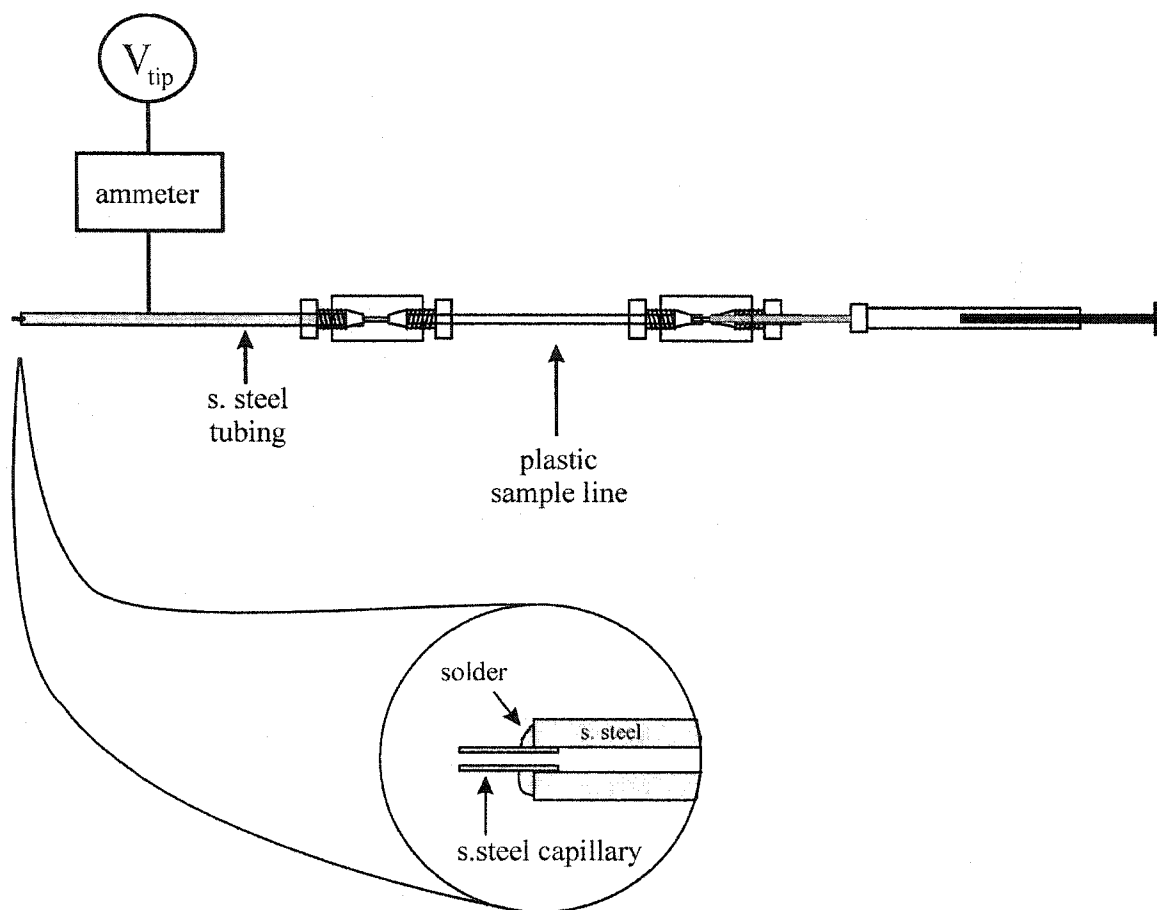


Figure 1.06 A typical ESI interface with a metal capillary.

methanol [28]. Due to the success of interfacing IS with LC, the IS interface is a common interface for commercially available electrospray mass spectrometers.

Another option for electrospraying purely aqueous solvents is that of changing the ambient gas near the tip. The principle here is that by replacing the ambient air with a gas with a greater breakdown potential (i.e., SF₆), higher applied fields may be used, which may allow aqueous solutions to be electrosprayed [23, 26, 29]. Another interesting variation of this is the use of a CO₂ atmosphere for electrospraying aqueous solutions in positive mode [24, 25]. In this case, it was suggested that the CO₂ was ionized to generate a steady corona discharge. The ionized CO₂ then removes electrons from the liquid surface to enhance the charge density on the aqueous droplets and induce the necessary droplet fissions [24, 25]. The discharge was essential to the performance of the interface, since replacement of the CO₂ with SF₆, a gas with higher breakdown threshold, destabilized the spray [25].

Another popular variation on the ES interface is what Wilm and Mann initially described in 1994 as a “micro electrospray” [69], but is now known as nanospray. In these systems, a small glass capillary has been pulled to a very fine tip, with an outer diameter of ~2 μm [69, 70]. About 1 μL of sample is loaded into the capillary, and the nanospray source operates without the need to pump solution to the tip. This type of setup can sustain stable signals for relatively long testing intervals (~20 minutes). Electrical contact to the solution may be made either by coating the capillary with metal, or by inserting a metal electrode into the back end of the capillary. Although these sources do not emit a large volume of solution, their efficiency is very high, likely due to the small initial droplet sizes and efficient desolvation that accompanies these interfaces. As a result, the signal intensities are reported to be comparable to regular ES interfaces. Also, nanospray exhibits a tolerance to ionic concentration superior to normal ES [70]. The rising popularity of the nanospray interface is related to the low sample volumes required. This can be very advantageous when the sample volume is limited, such as for the determination of proteins and other biomolecules. However, with such small tip dimensions, clogging can be a problem, as can the electrolytic removal of the thin metal

coating. With these concerns, and to prevent cross-contamination between samples, these tips are generally only used for a single sample analysis. Since these tips must be manufactured with reproducible dimensions, and are usually coated with a metal (e.g., Au), these tips are expensive to produce and purchase, making them a relatively expensive consumable item (~\$10 US each). More recent developments in the design of these tips promise a longer operational lifetime, for up to two weeks [71]. As mentioned, since many labs use a new capillary for each sample, the actual utility of this new type of tip may be limited, unless production costs are less. Another alternative may be to use a plastic pipette tip as the ES tip [72]. In this configuration, a pipette tip is filled with solution (similar to a nanospray capillary), and a Pt wire is inserted into the back end of the tip to provide electrical contact to the solution and generate the high field required for ES. No performance characteristics have yet been provided, and a means to clean the Pt wire between samples has not been suggested.

1.3.2 MS Interface for ESI

The interface of the mass spectrometer must be able to sample ions from atmospheric pressure. Different instrument manufactures use different schemes for sampling ions. Instruments made by PE-Sciex use what is known as a curtain gas interface. This interface is similar to the interface illustrated in Figure 1.07. In the interface shown in Figure 1.07, the curtain gas is introduced between the sampling plate and the front plate. Some of this dry curtain gas is sampled into the mass spectrometer, but the majority of the gas exits the hole in the front plate. This gas flows counter-current to the electrosprayed droplets, enhancing desolvation and minimizing the solvent that is sampled into the mass spectrometer.

1.3.3 Collision - Induced Dissociation (CID)

An important part of sampling ions from atmospheric pressure is the role of the MS interface in causing declustering and fragmentation of the electrosprayed ions as they are sampled into the low pressure region of the MS. In Figure 1.07, the region between

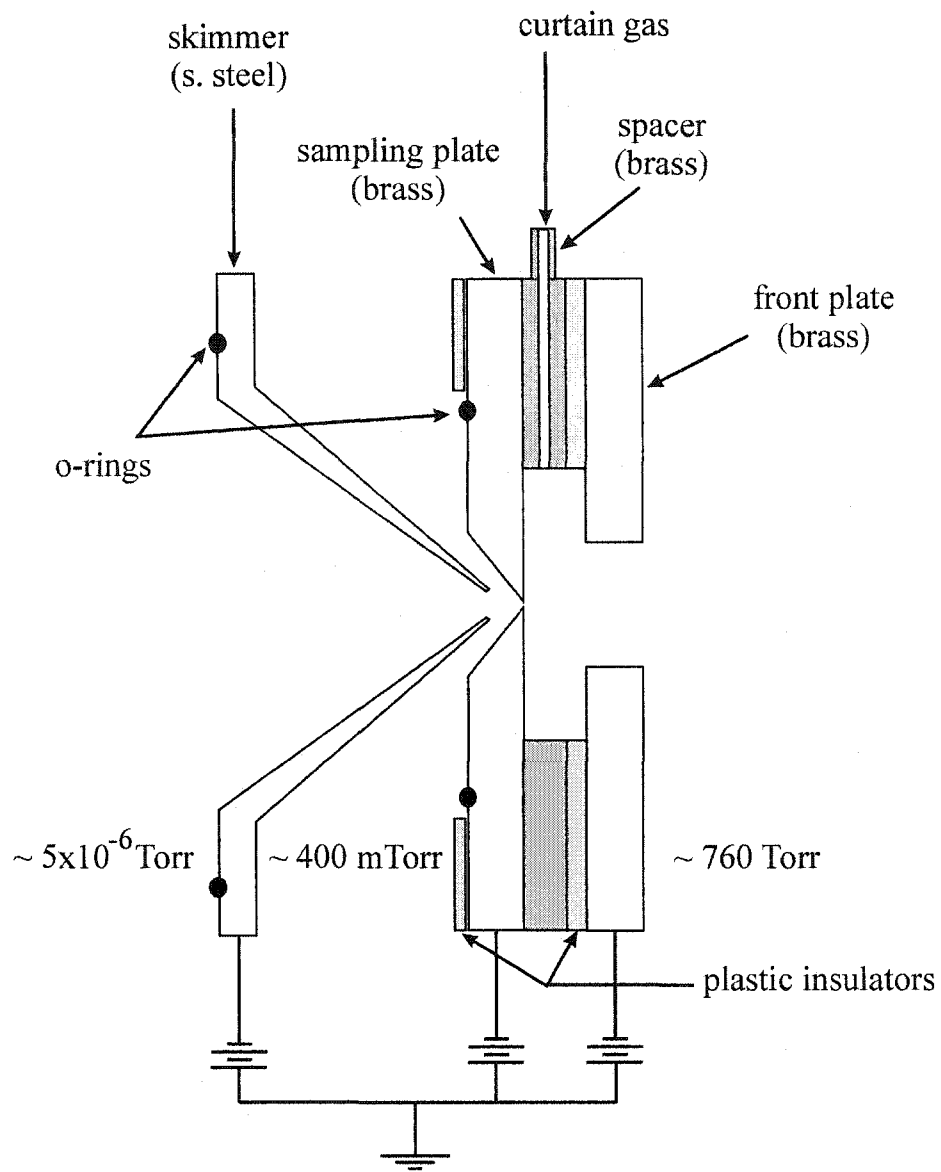
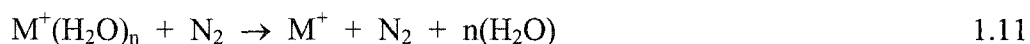
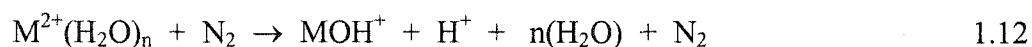


Figure 1.07 Schematic diagram of the modified ELAN 250 ICP-MS interface.

the sampling plate and the skimmer is very important. In the region behind the sampling plate, the pressure is about 400 mTorr, whereas on the other side of the skimmer, the pressure is about 5×10^{-6} Torr during operation. The differential pressure between each region generates a “free jet expansion” zone behind the sampling plate and skimmer. In this region, both neutral and charged molecules and atoms are rapidly accelerated as they are sampled into the vacuum chamber. This causes ions and solvated clusters to collide with the drift gas. The collisions can be made even more energetic if a potential difference is applied between the sampling plate and the skimmer. In this case, the ions will experience an additional “pull” and will be further accelerated relative to the neutral drift gas. The greater the potential difference, the greater the acceleration, and the more energetic the collisions between ions and neutrals will be. By increasing the collision energy, ions may be more efficiently desolvated, as hypothetically described by Equation 1.11, where M^+ represents a simple cation.



Under conditions of low potential difference (e.g., 5 - 30 V), it has been reported that simple cations and anions will exhibit a mixture of solvated and unsolvated species in the mass spectrum [7, 13-22, 47, 73-78]. With higher potential differences and more vigorous collision conditions, reactions involving the transfer of electrons and the breaking of bonds can be induced. In the hypothetical example in Equation 1.12, a divalent metal M^{2+} reacts with a molecule of solvent to reduce its effective charge. In Equation 1.13, the hypothetical ion $ABCD^+$ fragments upon energetic collision with N_2 .



By changing the potential difference between the sampling plate and the skimmer, the relative degree of declustering and fragmentation can be controlled. By manipulating

these voltages, the ES-MS can be tuned to provide both elemental and molecular information from the same sample [14, 16, 18-21, 47, 78].

1.3.4 Relative Signal Intensity with ESI-MS

While the interface conditions and the CID process can have a significant effect on the observed signal intensity, other factors, including the surface activity and gas-phase proton affinity of the analyte are also very important. As described earlier, the generation of droplets from an ES tip has been compared to the removing of the charged skin from the Taylor cone. This is a good description, since analytes with greater surface activity tend to exhibit greater relative signals in an ESI-MS spectrum [79-81]. It has been suggested that when using polar solvents, analytes with significant non-polar character will tend to dominate at the surface of the charged droplets. These analytes tend to dominate in the ESI-MS spectrum, since the promotion of these surface-active species to the gas phase is more efficient. Another factor for the relative ESI response are the reactions that take place in the gas phase during the electrospray process [82]. For example, protons may be transferred between different molecules in the gas phase. It has been suggested that as the result of proton transfer in the gas phase, the solvent with the highest proton affinity will suppress the response of all other solvents and analytes present in positive mode operation [66]. This also suggests that the selection of the solvent is important, since the gas-phase proton affinity of the solvent should be less than that of the analyte in order to maintain optimal ESI response of the analyte.

1.4 Instrumentation

In this work, several different types of ES interfaces, mass spectrometers, and FAIMS interfaces were used. As such, detailed discussions of these interfaces will be introduced in the appropriate chapter, as required.

1.4.1 ESI Interfaces

The two main types of ES interfaces used in this study were based on fused silica emitters, and both were in-house designed. One system, as illustrated in Figure 1.08 (a), consists of a piece of fused silica, with dimensions O.D. $\sim 180\ \mu\text{m}$, I.D. $\sim 50\ \mu\text{m}$, and a length of $\sim 45\ \text{cm}$. Solution was pumped into one end of the capillary using a Hamilton 250 μL gas-tight syringe and a syringe pump. A zero dead volume fitting was used to couple the syringe to the fused silica. The other end of the capillary was inserted into a metal capillary with dimensions of 0.009" I.D., 0.018" O.D. The metal capillary was housed in a larger piece of stainless steel HPLC tubing (0.020" I.D., 1/16" O.D.) for support. The high voltage was applied to the metal capillary, and the end of the fused silica was adjusted to extend $\sim 1\ \text{mm}$ from the tip of the metal capillary. The extension of the capillary was critical to stable spray operation. An in-house built ammeter with nanoampere sensitivity was placed in series with the high voltage, and the magnitude and stability of the current was used to determine if a stable spray was established.

The other type of ES interface used is illustrated in Figure 1.08 (b). This system also uses a continuous piece of fused silica, but utilizes a second high voltage, as well as a bath gas introduced coaxially to the ES tip. A more detailed discussion of this interface can be found in Chapter 2.

1.4.2 Mass Spectrometers

In Chapters 2 and 3, a modified PE-Sciex ELAN 250 was used. This instrument was formerly an ICP-MS, which has been modified for ESI. The ICP components have been removed, and the interface has been modified for room-temperature atmospheric pressure sampling. It is a single quadrupole instrument with a sampler-skimmer interface (as in Figure 1.07) and utilizes Einzel lenses for ion optics. In Chapters 3, 5, 6, 7, and 8, a PE-Sciex API 150EX was used. This is a single quadrupole instrument with a sampler-skimmer interface, similar to that in Figure 1.07, but with a RF-only quadrupole for ion optics. In Chapter 4, a PE-Sciex API 3000 was used. This instrument has the same ion

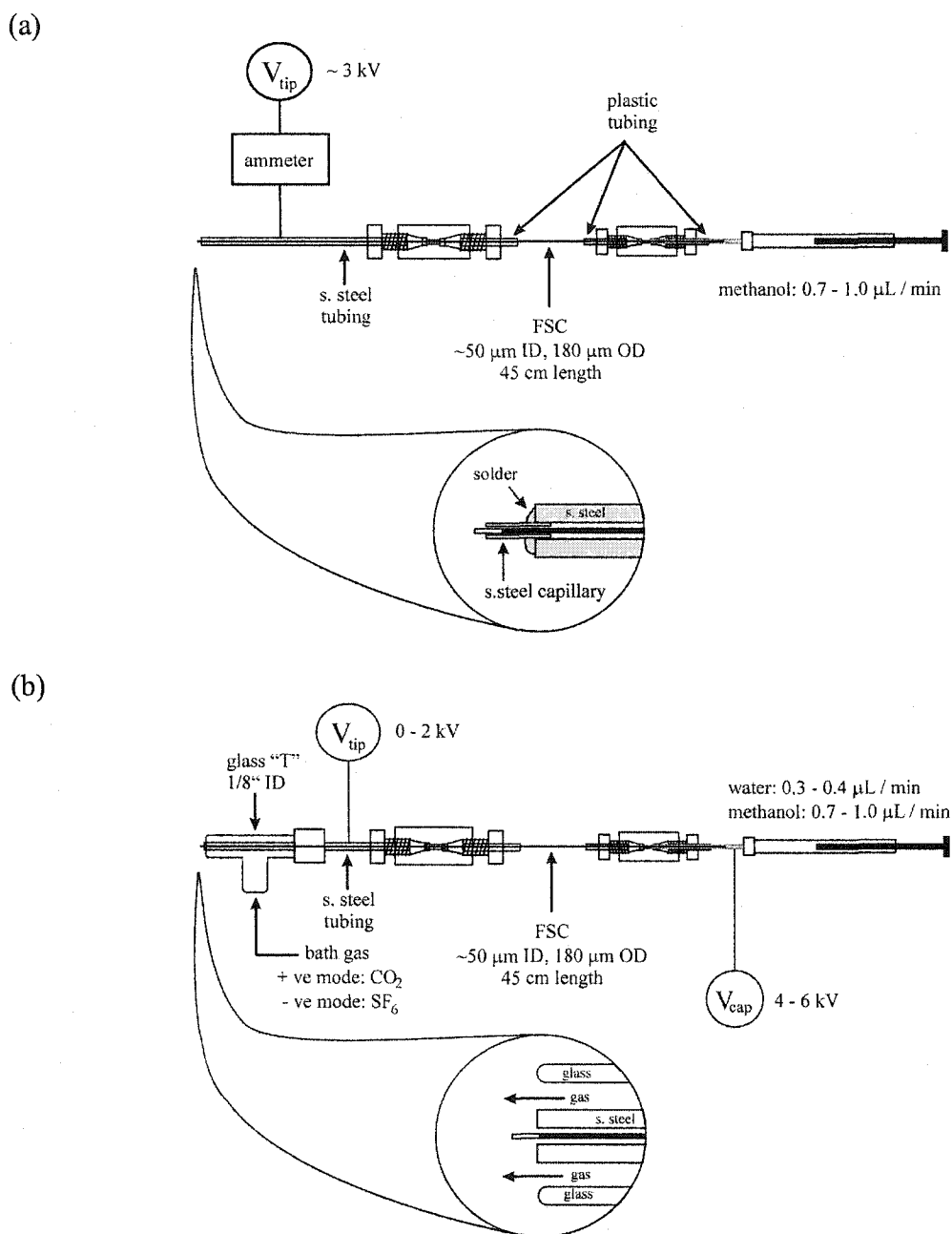


Figure 1.08 Illustration of ESI interfaces based on using fused silica emitters. Both involve a continuous piece of fused silica from the pump to the tip. (a) high-voltage solution contact made at tip by back-wetting of solution to the metal capillary; (b) dual voltage system, where the only high voltage solution contact is made at the syringe needle.

sampling interface as the API 150EX, but is a triple quadrupole instrument, capable of tandem mass spectrometry (MS / MS).

1.4.3 FAIMS Interfaces

Two different FAIMS prototypes were used. Both of these interfaces will be discussed in detail in upcoming chapters. In Chapter 5, the first reported ESI-FAIMS-MS prototype was used [42, 43]. This system incorporated a concentric cylinder design, with the ESI source internal to the FAIMS unit. In Chapters 6 to 8, a dome FAIMS prototype was used. The ESI source was external, and the FAIMS used a combination of concentric cylinders and spherical geometry.

1.5 References

1. NRC "Arsenic in Drinking Water"; National Research Council, National Academy Press. **1999**.
2. ATSDR "Toxicological profile for arsenic"; Agency for Toxic Substances and Disease Registry, U.S. Department of Health and Human Services. **2000**.
3. Caruso, J.; Sutton, K.; Ackley, K. *Elemental Speciation: New Approaches for Trace Element Analysis*; Elsevier: New York, 2000.
4. Dole, M.; Mack, L. L.; Hines, R. L.; Mobley, R. C.; Ferguson, L. D.; Alice, M. B. "Molecular beams of macroions"; *J. Chem. Phys.* **1968**, 49, 2240-2249.
5. Alexandrov, M. L.; Gall, L. N.; Krasnov, N. V.; Nikolaev, V. I.; Pavlenko, V. A.; Shukurov, V. A. "On the working characteristics of an ion source with electrohydrodynamic introduction of liquids into the mass spectrometer"; *Int. J. Mass Spectrom. Ion Processes* **1983**, 54, 231-235.
6. Yamashita, M.; Fenn, J. B. "Electrospray ion source. Another variation on the free-jet theme"; *J. Phys. Chem.* **1984**, 88, 4451-4459.
7. Stewart, I. I. "Electrospray mass spectrometry: A tool for elemental speciation"; *Spectrochim. Acta B* **1999**, 54, 1649-1695.
8. Fenn, J. B.; Mann, M.; Meng, C. I.; Wong, S. F.; Whitehouse, C. M. "Electrospray ionization for mass spectrometry of large biomolecules"; *Science* **1989**, 246, 64-71.
9. Traeger, J. C. "Electrospray mass spectrometry of organometallic compounds"; *Int. J. Mass Spectrom.* **2000**, 200, 387-401.
10. Henderson, W.; Nicholson, B. K.; McCaffrey, L. J. "Applications of electrospray mass spectrometry in organometallic chemistry"; *Polyhedron* **1998**, 17, 4291-4313.
11. Hop, C. E. C. A.; Bakhtiar, R. "Electrospray ionization mass spectrometry. 3. Applications in inorganic chemistry and synthetic polymer chemistry"; *J. Chem. Educ.* **1996**, 73, A162-A169.

12. Colton, R.; D'Agostino, A.; Traeger, J. C. "Electrospray mass spectrometry applied to inorganic and organometallic chemistry"; *Mass Spectrom. Rev.* **1995**, *14*, 79-106.
13. Agnes, G. R.; Horlick, G. "Electrospray mass spectrometry as a technique for elemental analysis: Preliminary results"; *Appl. Spectrosc.* **1992**, *46*, 401-406.
14. Agnes, G. R.; Stewart, I. I.; Horlick, G. "Elemental speciation measurements with electrospray mass spectrometry: An assessment"; *Appl. Spectrosc.* **1994**, *11*, 1347-1359.
15. Agnes, G. R.; Horlick, G. "Electrospray mass spectrometry as a technique for elemental analysis: Quantitative aspects"; *Appl. Spectrosc.* **1994**, *48*, 649-654.
16. Agnes, G. R.; Horlick, G. "Determination of solution ions by electrospray mass spectrometry"; *Appl. Spectrosc.* **1994**, *48*, 655-661.
17. Agnes, G. R.; Horlick, G. "Effect of operating parameters on analyte signals in elemental electrospray mass spectrometry"; *Appl. Spectrosc.* **1995**, *49*, 324-334.
18. Barnett, D. A.; Horlick, G. "Quantitative electrospray mass spectrometry of halides and halogenic anions"; *J. Anal. At. Spectrom.* **1997**, *12*, 497-501.
19. Stewart, I. I.; Horlick, G. "Electrospray mass spectra of lanthanides"; *Anal. Chem.* **1994**, *66*, 3983-3993.
20. Stewart, I. I.; Barnett, D. A.; Horlick, G. "Investigations into sulfur speciation by electrospray mass spectrometry"; *J. Anal. Atom. Spec.* **1996**, *11*, 877-886.
21. Stewart, I. I.; Horlick, G. "Investigations into chromium speciation by electrospray mass spectrometry"; *J. Anal. Atom. Spectrom.* **1996**, *11*, 1203-1214.
22. Stewart, I. I.; Horlick, G. "Developments in the electrospray mass spectrometry of inorganic species"; *Trends Anal. Chem.* **1996**, *15*, 80-90.
23. Wampler, F. M.; Blades, A. T.; Kebarle, P. "Negative ion electrospray mass spectrometry of nucleotides: Ionization from water solution with SF₆ discharge suppression"; *J. Am. Soc. Mass Spectrom.* **1993**, *4*, 289-295.
24. Tang, K.; Smith, R. D. "Sensitivity enhancement of electrospray ionization-MS for aqueous solutions in the corona-assisted cone-jet mode"; *Int. J. Mass Spectrom. Ion. Proc.* **1997**, *162*, 69-76.

25. Tang, K.; Gomez, A. "Generation of monodisperse water droplets from electrosprays in a corona-assisted cone-jet mode"; *J. Colloid Interface Sci.* **1995**, 175, 326-332.
26. Smith, D. P. H. "The electrohydrodynamic atomization of liquids"; *IEEE Trans. Int. Appl.* **1986**, IA-22, 527-535.
27. Taylor, G. I. "Disintegration of water drops in an electric field"; *Proc. R. Soc. London, Sec. A.* **1964**, 280, 383-397.
28. Ikonou, M. G.; Blades, A. T.; Kebarle, P. "Electrospray - ion spray: A comparison of mechanisms and performance"; *Anal. Chem.* **1991**, 63, 1989-1998.
29. Ikonou, M. G.; Blades, A. T.; Kebarle, P. "Electrospray mass spectrometry of methanol and water solutions suppression of electric discharge with SF₆ gas"; *J. Am. Soc. Mass Spectrom.* **1991**, 2, 497-505.
30. Guevremont, R.; Purves, R.; Barnett, D. A. "Method for separation of isomers and different conformations of ions in gaseous phase"; *Canadian Intellectual Property Office* **1999**. Canada. Canadian Patent No. 2,339,553.
31. Guevremont, R.; Purves, R. "Apparatus and method for desolvating and focussing ions for introduction into a mass spectrometer"; *Canadian Intellectual Property Office* **1999**. Canada. Canadian Patent No. 2,273,322.
32. Guevremont, R.; Purves, R.; Barnett, D. A. "Method for separation and enrichment of isotopes in gaseous phase"; *Canadian Intellectual Property Office* **1999**. Canada. Canadian Patent No. 2,339,549.
33. Guevremont, R.; Purves, R. "Apparatus and method for atmospheric pressure 3-dimensional ion trapping"; *Canadian Intellectual Property Office* **1999**. Canada. Canadian Patent No. 2,339,548.
34. Guevremont, R.; Purves, R. W.; Barnett, D. A.; Ding, L. "Ion trapping at atmospheric pressure (760 Torr) and room temperature with a high-field asymmetric waveform ion mobility spectrometer"; *Int. J. Mass Spectrom.* **1999**, 193, 45-56.
35. Gorshkov, M. P. "Inventors Certificate (USSR) No. 966583"; *Byull. Izobret.* **1982**. USSR. No. 966583.

36. Guevremont, R.; Purves, R. W. "Atmospheric pressure ion focusing in a high-field asymmetric waveform ion mobility spectrometer"; *Rev. Sci. Instrum.* **1999**, *70*, 1370-1383.
37. Carnahan, B. L.; Tarassov, A. S. "Ion Mobility Spectrometer"; **1995**, Mine Safety Appliances Company, Pittsburgh, Pa. United States. Patent No. 5 420 424.
38. Buryakov, I. A.; Krylov, E. V.; Soldatov, V. P. "Inventor's Certificate (USSR) No. 1485808 [in Russian], G01 No. 27/62"; *Byull. Izobret.* **1989**. USSR. No. 1485808.
39. Buryakov, I. A.; Krylov, E. V.; Makas', A. L.; Nazarov, E. G.; Pervukhin, V. V.; Rasulev, U. K. "Separation of ions according to mobility in a strong AC electric field"; *Sov. Tech. Phys. Lett.* **1991**, *17*, 446-447.
40. Buryakov, I. A.; Krylov, E. V.; Nazarov, E. G.; Rasulev, U. K. "A new method of separation of multi-atomic ions by mobility at atmospheric pressure using a high-frequency amplitude-asymmetric strong electric field"; *Int. J. Mass Spectrom. Ion Proc.* **1993**, *128*, 143-148.
41. Avakov, A. S.; Buryakov, I. A.; Krylov, E. V.; Nazarov, E. G.; Rasulev, U. K.; Soldatov, V. P. "Proceedings of the Eighth All-Union Conference"; *Physics of Low-Temperature Plasmas.*, .
42. Purves, R. W.; Day, S.; Pipich, C. W.; Matyjaszczyk, M. S.; Guevremont, R. "Mass spectrometric characterization of a high-field asymmetric waveform ion mobility spectrometer"; *Rev. Sci. Instrum.* **1998**, *69*, 4094-4105.
43. Purves, R. W.; Guevremont, R. "Electrospray ionization high-field asymmetric waveform ion mobility spectrometry-mass spectrometry"; *Anal. Chem.* **1999**, *71*, 2346-2357.
44. Zeleny, J. "The electrical discharge from liquid points and a hydrostatic method of measuring the electric intensity at their surfaces."; *Phys. Rev.* **1914**, *3*, 69-91.
45. Zeleny, J. "Instability of electrified surfaces"; *Phys. Rev.* **1917**, *10*, 1-6.
46. Zeleny, J. "On the conditions of instability of electrified drops with applications to the electrical discharge from liquid points."; *Proc. Cambridge Philos. Soc.* **1915**, *18*, 71-83.
47. Stewart, I. I. Ph.D. Thesis, University of Alberta, Edmonton, Alberta, 1996.

48. Blades, A. T.; Ikononou, M. G.; Kebarle, P. "Mechanism of electrospray mass spectrometry. Electrospray as an electrolysis cell"; *Anal. Chem.* **1991**, 63, 2109-2114.
49. Hayati, I.; Bailey, A. I.; Tadros, T. H. F. "Investigations into the mechanisms of electrohydrodynamic spraying of liquids"; *J. Colloid Interface Sci.* **1987**, 117, 205-221.
50. Rayleigh "On the equilibrium of liquid conducting masses charged with electricity"; *Philos. Mag.* **1882**, 14, 184-186.
51. Gomez, A.; Tang, K. "Charge and fission of droplets in electrostatic sprays"; *Phys. Fluids* **1994**, 6, 404-414.
52. Kebarle, P. "A brief overview of the present status of the mechanisms involved in electrospray mass spectrometry"; *J. Mass Spectrom.* **2000**, 35, 804-817.
53. Davies, C. N. In *Fundamentals of Aerosol Science*; Shaw, D. T., Ed.; John Wiley and Sons: New York, 1978, pp 154.
54. Kebarle, P.; Tang, L. "From ions in solution to ions in the gas phase"; *Anal. Chem.* **1993**, 65, 972A-986A.
55. Cole, R. B. "Some tenets pertaining to electrospray ionization mass spectrometry"; *J. Mass Spectrom.* **2000**, 35, 763-772.
56. Fernandez de la Mora, J.; van Berkel, G. J.; Enke, C. G.; Cole, R. B.; Martinez-Sanchez, M.; Fenn, J. B. "Electrochemical processes in electrospray ionization mass spectrometry"; *J. Mass Spectrom.* **2000**, 35, 939-952.
57. Gamero-Castano, M.; Mora, J. F. d. l. "Kinetics of small ion evaporation from the charge and mass distribution of multiply charged clusters in electrosprays"; *J. Mass Spectrom.* **2000**, 35, 790-803.
58. Van Berkel, G. J. "Electrolytic deposition of metals on to the high-voltage contact in an electrospray emitter: Implications for gas-phase ion formation"; *J. Mass Spectrom.* **2000**, 35, 773-783.
59. Thomson, B. A.; Irbane, J. V. "Field-induced ion evaporation from liquid surfaces at atmospheric pressure"; *J. Chem. Phys.* **1979**, 71, 4451-4463.
60. Irbane, J. V.; Thomson, B. A. "On the evaporation of small ions from charged droplets"; *J. Chem. Phys.* **1976**, 64, 2287-2294.

61. Fernandez de la Mora, J.; Loscertales, I. G. "The current emitted by highly conducting Taylor cones"; *J. Fluid Mech.* **1994**, 260, 155-184.
62. de Juan, L.; Fernandez de la Mora, J. "Charge and size distributions of electrospray drops"; *J. Colloid Interface Sci.* **1997**, 186, 280-293.
63. Van Berkel, G. J.; Zhou, F.; Aronson, J. T. "Changes in bulk solution pH caused by the inherent controlled-current electrolytic process of an electrospray ion source"; *Int. J. Mass Spectrom. Ion Proc.* **1997**, 162, 55-67.
64. Van Berkel, G. J. "Electrolytic corrosion of a stainless - steel electrospray emitter monitored using an electrospray - photodiode array system"; *J. Anal. Atom. Spectros.* **1998**, 13, 603-607.
65. Jackson, G. S.; Enke, C. G. "Electrical equivalence of electrospray ionization with conducting and nonconducting needles"; *Anal. Chem.* **1999**, 71, 3777-3784.
66. Amad, M. H.; Cech, N. B.; Jackson, G. S.; Enke, C. G. "Importance of gas-phase proton affinities in determining the electrospray ionization response for analytes and solvents"; *J. Mass Spectrom.* **2000**, 35, 784-789.
67. Hau, J.; Roberts, M. "Advantages of pressurization in capillary electrophoresis / electrospray ionization mass spectrometry"; *Anal. Chem.* **1999**, 71, 3977-3984.
68. Bruins, A. P.; Covey, T. R.; Henion, J. D. "Ion spray interface for combined liquid chromatography / atmospheric pressure ionization mass spectrometry"; *Anal. Chem.* **1987**, 59, 2642-2646.
69. Wilm, M. S.; Mann, M. "Electrospray and Taylor-cone theory, Dole's beam of macromolecules at last?"; *Int. J. Mass Spectrom. Ion Processes* **1994**, 135, 167-186.
70. Wilm, M.; Mann, M. "Analytical properties of the nanoelectrospray ion source"; *Anal. Chem.* **1996**, 68, 1-8.
71. Nilsson, S.; Wetterhall, M.; Bergquist, J.; Nyholm, L.; Markides, K. E. "A simple and robust conductive graphite coating for sheathless electrospray emitters used in capillary electrophoresis / mass spectrometry"; *Rapid Comm. Mass Spectrom.* **2001**, 15, 1997-2000.
72. Aksyonov, S.; Williams, P. "Electrospray ionization using disposable plastic pipette tips"; *Rapid Comm. Mass Spectrom.* **2001**, 15, 1890-1891.

73. Schramel, O.; Michalke, B.; Kettrup, A. "Analysis of metal species by using electrospray ionization mass spectrometry and capillary electrophoresis - electrospray ionization mass spectrometry"; *J. Chromatogr. A* **1998**, 819, 231-242.
74. Mollah, S.; Pris, A. D.; Johnson, S. K.; Gwizdala, A. B.; Houk, R. S. "Identification of metal cations, metal complexes, and anions by electrospray mass spectrometry in the negative ion mode"; *Anal. Chem.* **2000**, 72, 985-991.
75. Blades, A. T.; Jayaweera, P.; Ikonomou, M. G.; Kebarle, P. "Studies of alkaline earth and transition metal M^{++} gas phase ion chemistry"; *J. Chem. Phys.* **1990**, 92, 5900-5906.
76. Blades, A. T.; Jayaweera, P.; Ikonomou, M. G.; Kebarle, P. "Ion-molecule clusters involving doubly charged metal ions (M^{2+})"; *Int. J. Mass Spectrom. Ion Proc.* **1990**, 102, 251-267.
77. Blades, A. T.; Jayaweera, P.; Ikonomou, M. G.; Kebarle, P. "First studies of the gas phase ion chemistry of M^{3+} metal ion ligands"; *Int. J. Mass. Spectrom. Ion Proc.* **1990**, 101, 325-336.
78. Barnett, D. A. Ph. D. Thesis, University of Alberta, Edmonton, Alberta, 1999.
79. Tang, K.; Smith, R. D. "Physical / chemical separations in the break-up of highly charged droplets from electrosprays"; *J. Am. Soc. Mass Spectrom.* **2001**, 12, 343-347.
80. Rundlett, K. L.; Armstrong, D. W. "Mechanism of signal suppression by anionic surfactants in capillary electrophoresis-electrospray ionization mass spectrometry"; *Anal. Chem.* **1996**, 68, 3493-3497.
81. Cech, N. B.; Enke, C. G. "Relating electrospray ionization response to nonpolar character of small peptides"; *Anal. Chem.* **2000**, 72, 2717-2723.
82. Kebarle, P.; Peschke, M. "On the mechanisms by which the charged droplets produced by electrospray lead to gas phase ions"; *Anal. Chim. Acta* **2000**, 406, 11-35.

Chapter 2

Evaluation of an Electrospray Source for Purely Aqueous Solvents with ESI-MS

2.1 Introduction

Since some of the earliest couplings of electrospray ionization (ESI) with mass spectrometry (MS) by Yamashita and Fenn in 1984 [1, 2], interest in both the fundamental aspects of ESI and the application of ESI to specific problems has been progressively improving. Part of these improvements involves modifications of the electrospray source itself to fit the demands of the analytical scenario. Typical ESI sources generally involve pumping a solution of ions in a polar organic solvent through a metal capillary, to which a high voltage is applied. The applied voltage serves two major roles. One major role is the generation of excess charge in the capillary through electrolysis. The other major role is the generation of a high electric field at the tip of the capillary. As illustrated in Figure 2.01, a metal capillary is biased to a high positive voltage, and the solution becomes positively charged. Charge repulsion causes the positive ions to move away from the metal capillary, and towards a lower potential at the liquid surface that extends from the capillary. If the fields are high enough, the liquid surface may be distorted into a conical shape, referred to as a Taylor cone [3]. From the tip of this cone, small, positively charged droplets may be emitted from the bulk solution. These droplets may then undergo repeated droplet fissions to produce ions suitable for MS sampling. While the actual process of ion generation in the electrospray process is still the subject of debate [4-9], the empirical result of the ESI process is the same: the promotion of pre-existing solution ions to the gas phase at atmospheric pressure.

The generation of a stable Taylor cone is highly dependent on the experimental conditions, and this distortion of the solution surface represents a balance between the surface tension of the solution and the applied electric field forces that “pull” ions towards lower potentials. The field E_{on} (V/m) that must be generated at the electrospray tip to form a Taylor cone is given by [10]

$$E_{on} = \left(\frac{2\gamma \cos 49^\circ}{\epsilon_o r_c} \right)^{1/2} \quad 2.01$$

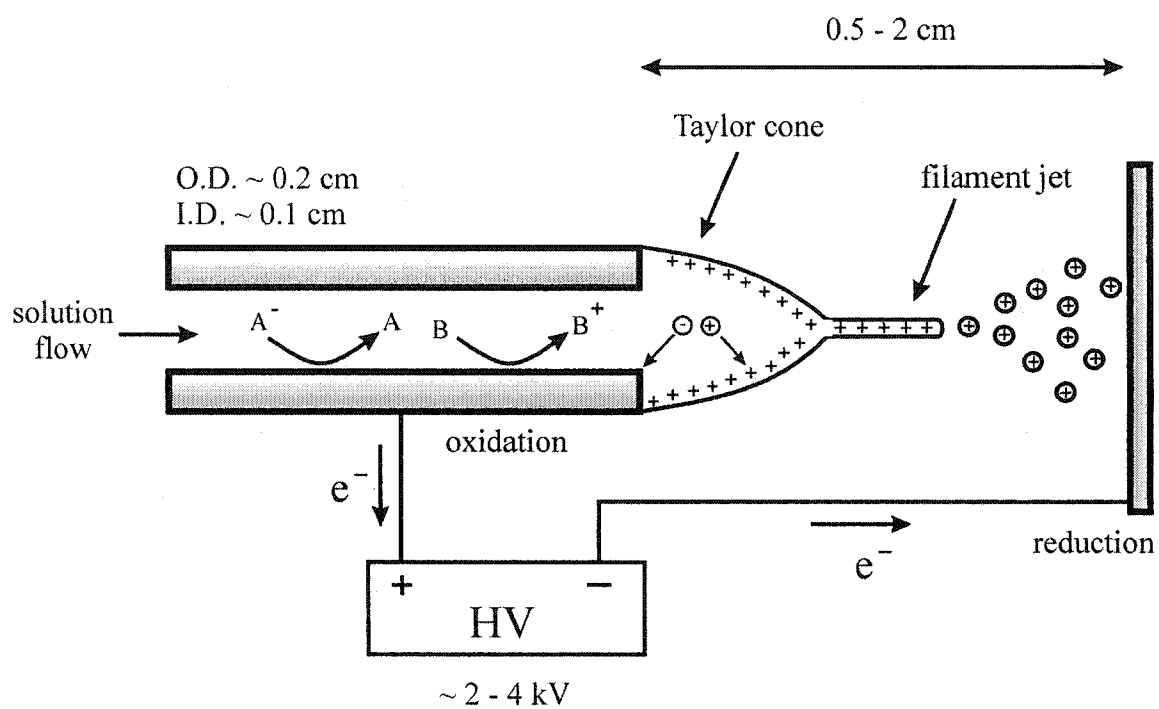


Figure 2.01 Illustration of a metal capillary electrospray tip with an applied high voltage of positive polarity.

where γ is the surface tension (N/m) of the liquid, $\cos 49^\circ$ is the half-angle of the Taylor cone, ϵ_0 is the permittivity of free space ($\epsilon_0 = 8.8 \times 10^{-12} \text{ C}^2/\text{Jm}$) and r_c is the radius (m) of the capillary. Due to the dependence on the surface tension of the liquid, liquids such as water require fields higher than the fields required to generate a corona discharge [11, 12]. As a result, the electrospraying of purely aqueous solutions can be difficult. To avoid these kinds of difficulties, dilutions are usually done with a polar organic solvent (i.e., methanol) to reduce the surface tension.

Modifications to the typical ESI source to improve the performance with aqueous solvents include pneumatically assisted ESI (i.e., ionspray, and heated variations) and nanospray interfaces. Most of the ESI-MS literature still focuses on the use of an organic solvent to reduce the surface tension. Presumably, this is due to the difficulty or compromise that accompanies using purely aqueous solvent. Another option for electrospraying purely aqueous solvents is changing the ambient gas near the tip. The principle here is that by replacing the ambient air with a gas with a greater breakdown potential (i.e., SF_6), higher applied fields may be used, which may allow aqueous solutions to be electrosprayed [11, 12]. Another interesting variation of this is the use of a CO_2 atmosphere for electrospraying aqueous solutions in positive mode [13, 14]. In this case, it was suggested that the CO_2 was ionized to generate a steady corona discharge, which then removed electrons from the liquid surface to enhance the charge density on the aqueous droplets and induce the necessary droplet fissions [13, 14]. The discharge was essential to the performance of the interface, since replacement of the CO_2 with SF_6 , a gas with higher breakdown threshold, destabilized the spray [14].

Based on a combination of ESI sources previously described [13-16], an in-house designed ESI source capable of electrospraying purely aqueous solutions was developed. The ESI-MS signal intensity and stability for some simple inorganic ions were evaluated in both purely aqueous and methanolic solutions. Also, in negative mode, demonstrations of how the solvent selection may dramatically alter the observed ion in the mass spectrum are presented for selenite (SeO_3^{-2}), sulfite (SO_3^{-2}), and hypochlorite (ClO^-).

2.2 Experimental

2.2.1 Aqueous Electrospray Interface

The electrospray (ES) interface used for this study is an in-house design, and is based on the use of a fused silica capillary as the electrospray tip. A schematic diagram of the interface used in this study is presented in Figure 2.02. A syringe pump (Cole-Parmer 74900 Series) and a Hamilton 250 μL syringe with a stainless steel needle were used to deliver solution through a fused silica capillary with approximate dimensions of 50 μm I.D., 150 μm O.D., and 45 cm in length. The fused silica capillary was a continuous piece that began from inside the syringe needle and terminated as the ES tip. The polyimide coating was removed from the tip to remove any rough edges due to the coating, and the fused silica capillary was positioned to extend about 2 mm from the stainless steel support tubing. The only electrical contact with the solution was made at the syringe needle. This voltage will be referred to as the “capillary voltage”. To monitor the current, an in-house built ammeter with nanoampere sensitivity was placed in series with the high voltage power supply and the syringe needle. A second high voltage could be applied to the stainless steel support tubing near the tip, and will be referred to as the “tip support voltage”. This voltage does not have any direct electrical contact to the solution as it exits the fused silica capillary. Glass tubing (1/8" ID) surrounded the stainless steel support and delivered gas to enshroud the ES tip in a controlled atmosphere. This non-nebulizing flow of gas is referred to as the bath gas. In positive mode, CO_2 was used as the bath gas, whereas in negative mode, SF_6 was used. For aqueous ES, typical parameters were about 0.3 $\mu\text{L}/\text{min}$ solution flow rate, 4-6 kV at the syringe needle, 1 kV at the tip support, and ~ 0.3 to 0.8 L/min bath gas flow rate. The fused silica tip was positioned directly on axis to the mass spectrometer interface, at an offset of ~ 3 mm. This setup was also used for methanolic solution studies, but with solution flow rates of about 0.8 $\mu\text{L}/\text{min}$.

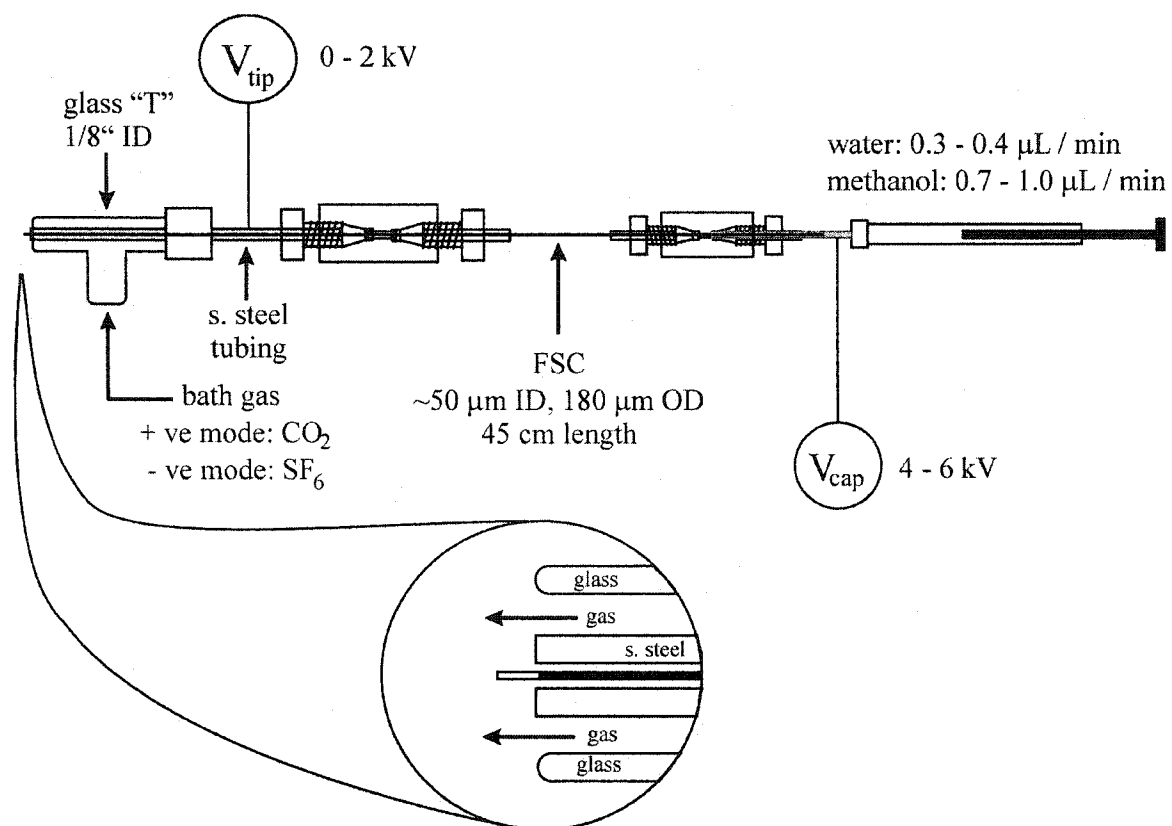


Figure 2.02 Illustration of an interface for electrospaying purely aqueous solvents (not to scale).

2.2.2 Mass Spectrometry

The mass spectrometer used was an ELAN 250 ICP-MS, modified for an electrospray ion source. All components associated with the ICP were removed, and the interface was re-designed, as discussed in detail in Chapter 1. The sampling plate used for ICP was replaced with another sampling plate with a smaller orifice ($\sim 100 \mu\text{m}$) and a front plate, which allowed addition of a curtain gas, as illustrated in Figure 2.03. The front plate (FP), the sampling plate (SP) and the skimmer (SK) were insulated from each other, and were independently biased to different voltages. The N_2 curtain gas flowed at 0.3 mL/min between the sampling plate and front plate and flowed counter-current to the movement of electrosprayed ions. The roles of the curtain gas are the same as with other ES systems, which are to augment evaporation of solvent from the droplets during the ESI process, preventing solvent from entering the MS, and to act as an "inert" gas for collision-induced dissociation (CID). The front plate voltage was set to a constant 900 V, the skimmer voltage was set at a constant 6 V, and the sampling plate voltage (SPV) was varied. The difference in the skimmer and the sampling plate voltage allowed control of the amount of energy imparted to the ions relative to the uncharged curtain gas (i.e., control the amount of CID imparted to the ESI-generated ions).

2.2.3 Reagents and Sample Preparation

Stock solutions at a concentration of 10 mM were prepared from the appropriate reagent grade salt dissolved in 18 M Ω de-ionized water. Further dilutions were done using either reagent grade methanol or 18 M Ω de-ionized water. For the methanolic solutions, between 5-8% water was present. A commercial bleach solution ($\sim 6\%$ NaOCl) was used as a source of sodium hypochlorite, NaOCl, and was diluted in the appropriate solvent just prior to use to provide a sample with an approximate concentration of 0.1 mM NaOCl.

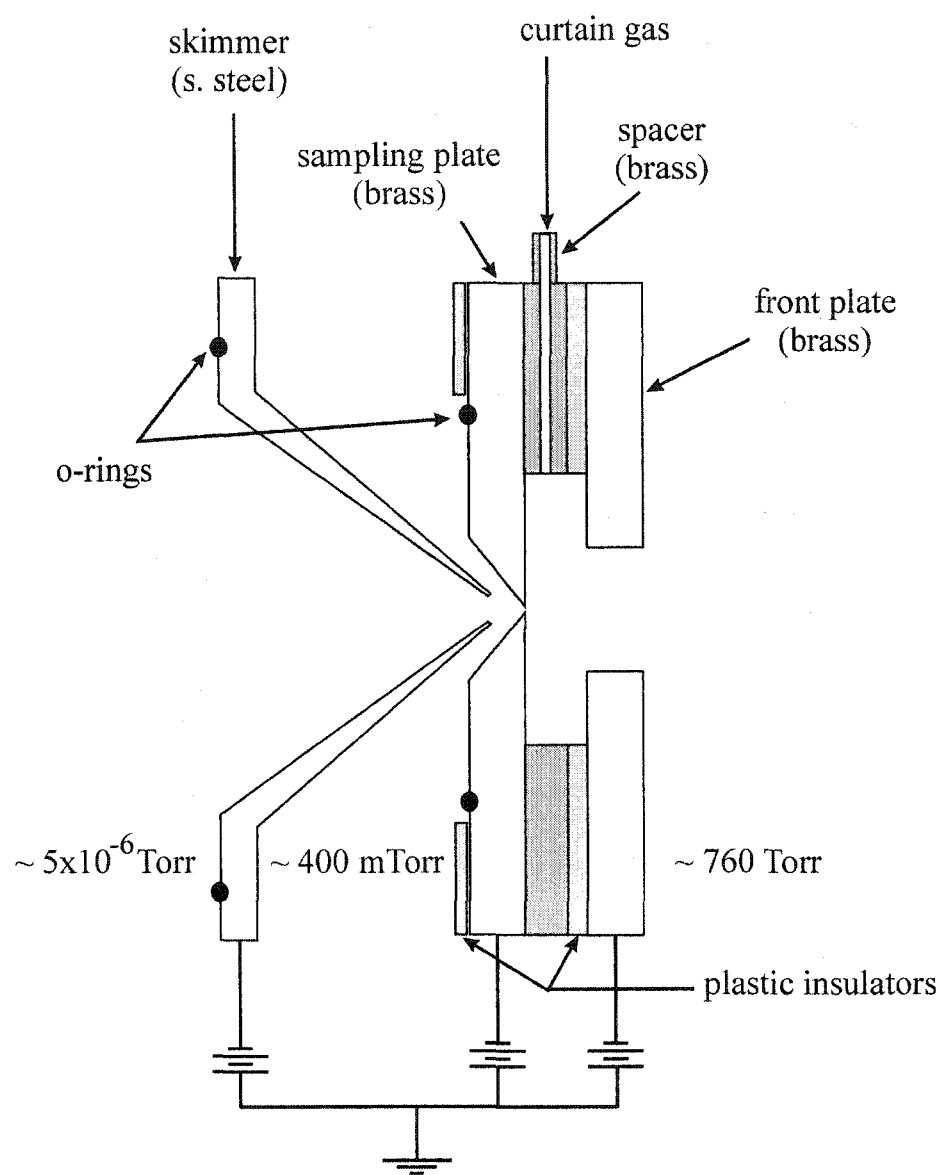


Figure 2.03 Schematic diagram of the modified ELAN 250 ICP-MS interface.

2.3 Results and Discussion

Some basic parameter studies were performed in positive mode. Similar studies could not be performed in negative mode due to limitations imposed by the instrument software (i.e., this former ICP-MS cannot perform selected ion monitoring in negative mode). As most people who have operated an ESI source realize, an ESI source generally needs to be tuned to optimize the performance, and a set of conditions may not produce the exact same performance on a day-to-day basis. As such, these parameter studies were intended to provide some indication of which factors were the most important in tuning the aqueous ESI source, as opposed to trying to elucidate a detailed mechanism of the process involved.

2.3.1 Optimization of ESI Voltages in Positive Mode

Using the dual voltage ESI source described, a purely aqueous solution containing 0.01 mM RbCl with 0.5 mM KI was electrosprayed into the mass spectrometer. The sampling plate voltage (SPV) was set at 60 V, which provided a high degree of declustering via collision-induced dissociation (CID). The solution flow rate was set to 20 $\mu\text{L/hr}$, and the tip support voltage was set to 1 kV. The capillary voltage was varied, and the Rb^+ signal intensity at m/z 85 and 87 was monitored for 300 replicates, each with a dwell time of 0.1 seconds. This was the minimum dwell time that this instrument would allow, and due to the slow scanning speeds, one set of replicates was measured per second, and 5 minutes were required to collect 300 measurements. The average signal intensity and the standard deviation for 300 replicate readings were determined. A plot of the average signal intensity at m/z 85 as a function of the applied capillary voltage is presented in Figure 2.04 (a). While signal intensities ranging from $\sim 10,000$ cps to $\sim 50,000$ cps were produced at all the voltages tested (3-8 kV), the stability of this signal varied significantly. Figure 2.04 (b) is a plot of the percent relative standard deviation (%RSD) as a function of the applied capillary voltage. In the range of 4.5 to 5.0 kV, the %RSD was optimal at $< 3.5\%$ RSD, with a signal intensity of $\sim 40,000$ cps. The data suggests that the ESI is only stable within a fairly narrow window of applied

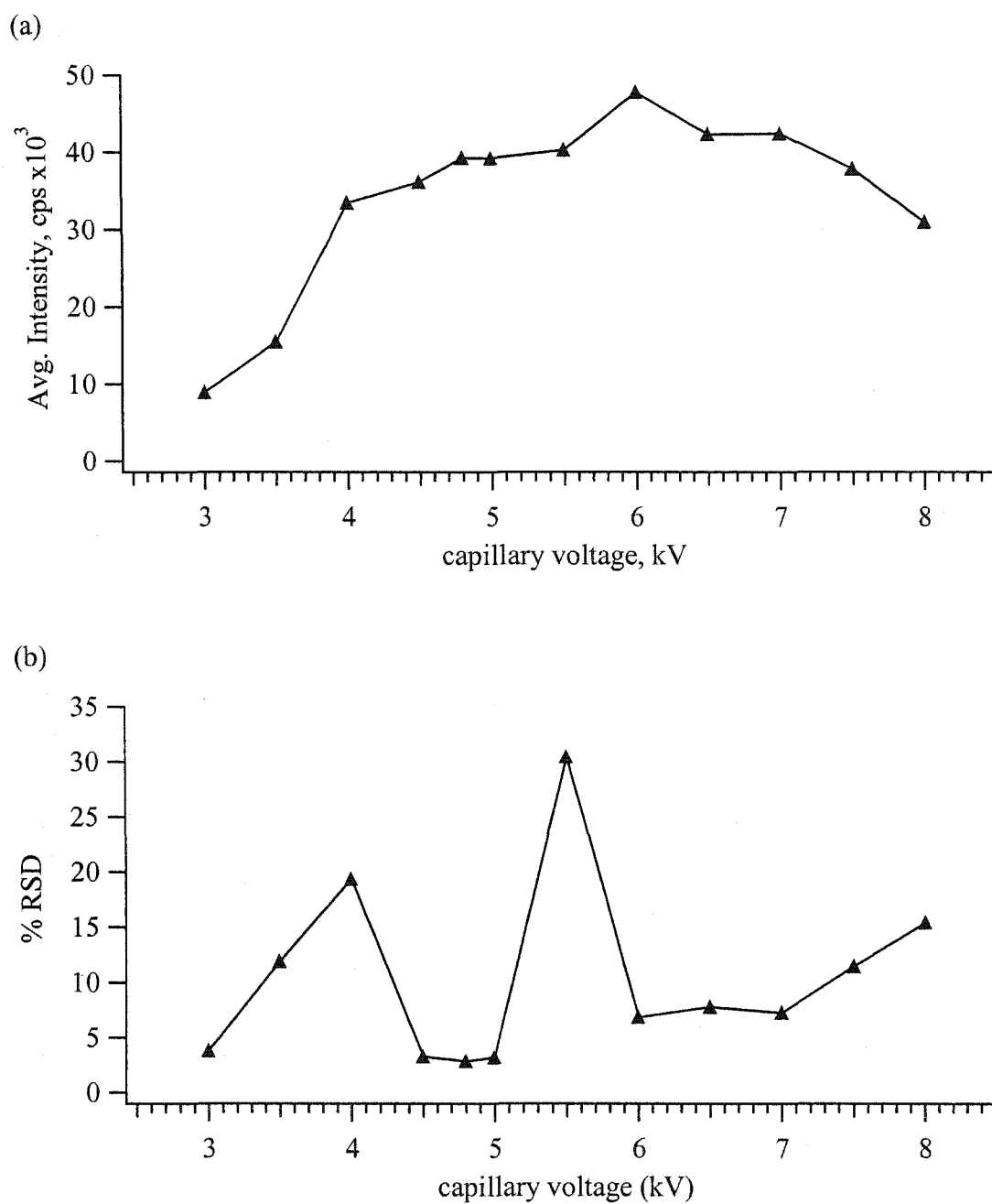


Figure 2.04 Effect of capillary voltage on (a) average intensity at m/z 85, and (b) on signal stability (as %RSD). M/z 85 for Rb^+ was monitored for 5 minute measurement interval; dwell time = 0.1 sec, 300 measurements. Solution was 0.5 mM KI with 0.01 mM $RbCl$ in 100% water solvent. Solution flow rate = 20 $\mu L/hr$, tip voltage = 1.0 kV.

voltages. Figure 2.05 is a plot of the observed current at the syringe needle as a function of the applied capillary voltage. Between 3 to 4.5 kV, the current increases with the applied voltage, then seems to plateau between 4.5 and about 5.5 kV (~70 nA), then continues to climb with applied capillary voltage from 5.5 – 8 kV. This type of current-voltage relationship is similar to those observed with other ESI systems, where the stable ESI voltage-current region is in the plateau [17]. Also, it has been suggested that ESI systems that use CO₂ as a nebulizer gas involve a mixed electrospray and chemical ionization process that begins at the breakpoints in the spray current – potential curves [18]. With this system, the onset of the stable ESI operation began at ~4.5 kV, where the current plateau seems to begin. The capillary voltage is considerably greater than normally applied to metal capillary systems. With the application of the high voltage remote from the ESI tip, any current must flow through the high resistance of the capillary. The resistance of systems with similar capillary dimensions and solution conditions has been estimated in excess of 40 GΩ [19]. Also, the lack of a good conductor of electrons at the ESI tip reduces the risk of generating a strong corona discharge (i.e., a spark).

In most cases, the tip support voltage was not necessary for a stable signal to be generated in positive mode. However, this voltage appears to provide some enhancements in signal intensity and stability.

2.3.2 Influence of Solution Flow Rate in Positive Mode

As previous, the average signal intensity and the standard deviation for 300 replicate readings were determined as the flow rate was varied. The voltage applied to the capillary was 4.7 kV, and 1.0 kV was applied to the tip support. A plot of the average signal intensity at *m/z* 85 as a function of flow rate is presented in Figure 2.06 (a). The data indicate that under these conditions, the signal maximum is at a flow rate between 18 and 20 μL/hr. If the percent relative standard deviation (%RSD) is plotted as a function of the flow rate (Figure 2.06 (b)), the resultant curve illustrates that the signal at *m/z* 85 is only stable (RSD < 3.5%) at flow rates between 18 and 20 μL/hr. This data indicates that

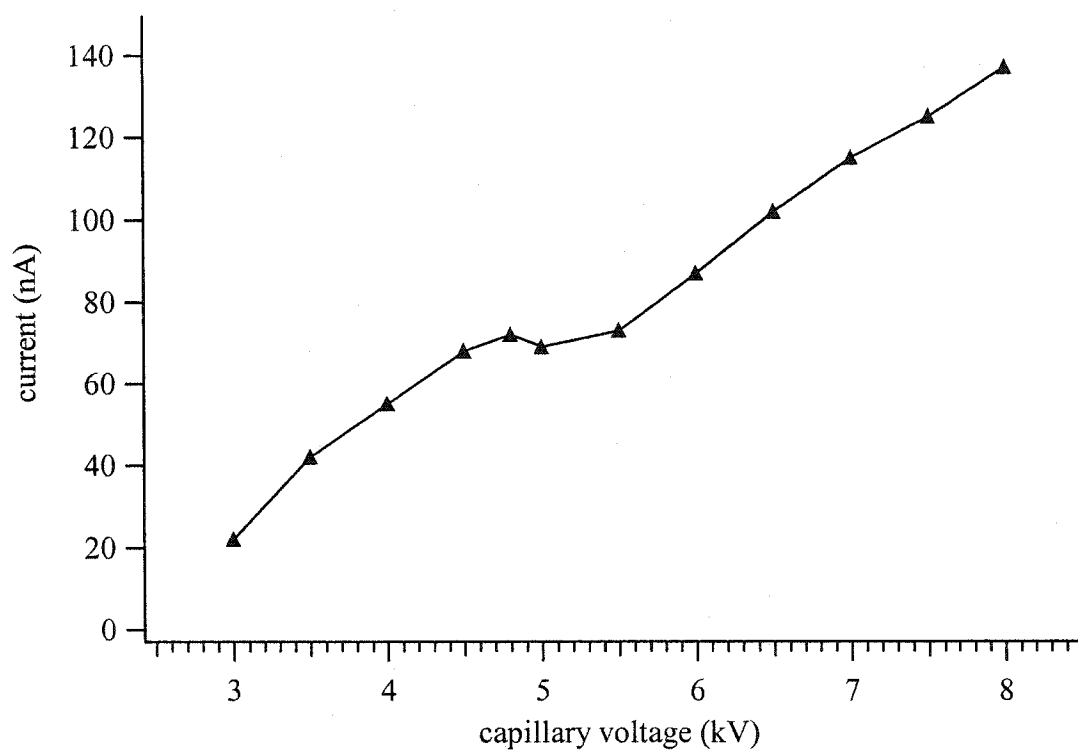


Figure 2.05 Effect of applied capillary voltage on the current at the syringe needle. Tip support voltage = 1.0 kV, solution flow rate = 20 $\mu\text{L/hr}$. Sample was 0.5 mM KI with 0.01 mM RbCl in 100% water solvent.

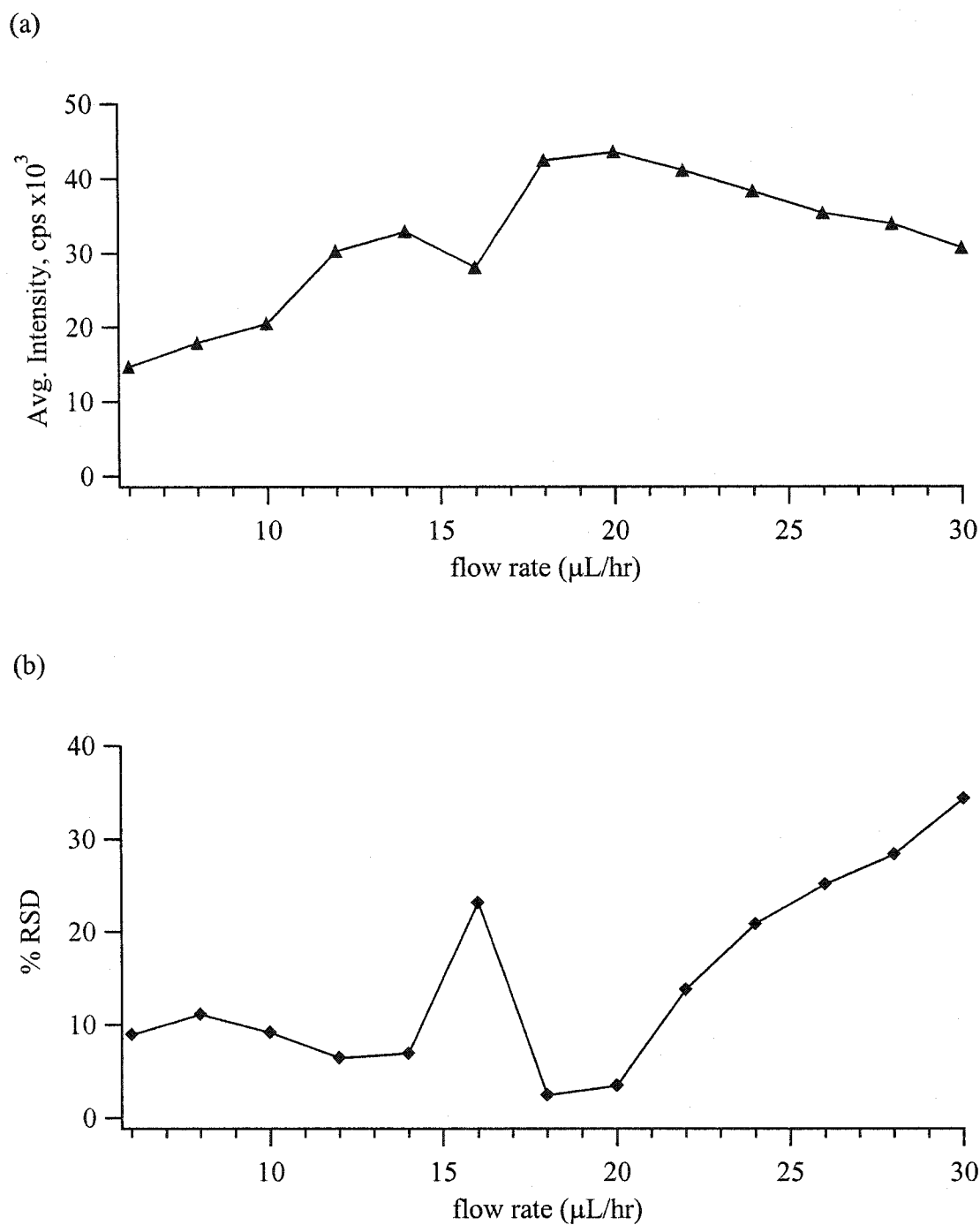


Figure 2.06 Effects of flow rate on Rb^+ signal (monitored at m/z 85) on (a) average intensity and (b) signal stability (as %RSD) with 100% water solvent using the dual voltage ESI source. Sample was 0.5 mM KI with 0.01 mM RbCl . Capillary voltage = 4.7 kV, tip voltage = 1.0 kV.

the operation of this source is only stable within a relatively narrow window of flow rates under a set of voltage conditions.

The cause of the high RSD at 16 $\mu\text{L/hr}$ is unclear. Perhaps this flow rate represents a transition point from different operational modes of the ESI source. Figure 2.07 is a plot of the observed current as a function of the solution flow rate. At flow rates less than 16 $\mu\text{L/hr}$, the current is about 40 nA, which then climbs to about 60 nA at 20 $\mu\text{L/hr}$. These current data suggest that the ESI performance changes near 16 $\mu\text{L/hr}$, which may account for the high % RSD observed at this flow rate. Previous work where the ESI cone morphology was visually monitored indicates that just prior to stable ESI operation, a rapid pulsed droplet mode of operation occurs [17], which may generate large fluctuations in the observed signal.

As with regular ESI interfaces, the system could be tuned for variations in flow rate and applied voltage. Figure 2.08 is the selected ion monitoring (SIM) of the Rb^+ signal at m/z 85 and 87 for different settings of flow rate and applied voltage. With the flow rate at 20 $\mu\text{L/hr}$, and the applied capillary voltage at 4.6 kV, the observed signals are stable and the system draws about 59 nA from the power supply (Figure 2.08 (a)). However, if the flow rate is increased to 24 $\mu\text{L/hr}$, the signals become unstable (Figure 2.08 (b)). By increasing the applied voltage to 5.0 kV, the signal stability returns, with about the same signal intensity, but now a higher current of ~ 80 nA is observed (Figure 2.08 (c)). So, while under certain voltage conditions the acceptable flow rate needs to be tuned to within a few $\mu\text{L/hr}$, the applied capillary voltage influences which flow rate is optimal.

2.3.3 Comment on the Bath Gas

In positive mode, the use of a CO_2 bath gas for aqueous samples was critical to stable operation. Other types of gas were investigated, including O_2 , Ar, N_2O , and SF_6 , and only CO_2 was found to generate stable signals, consistent with Tang *et al* [14] in their description of an aqueous ESI source using CO_2 . In the absence of an applied voltage,

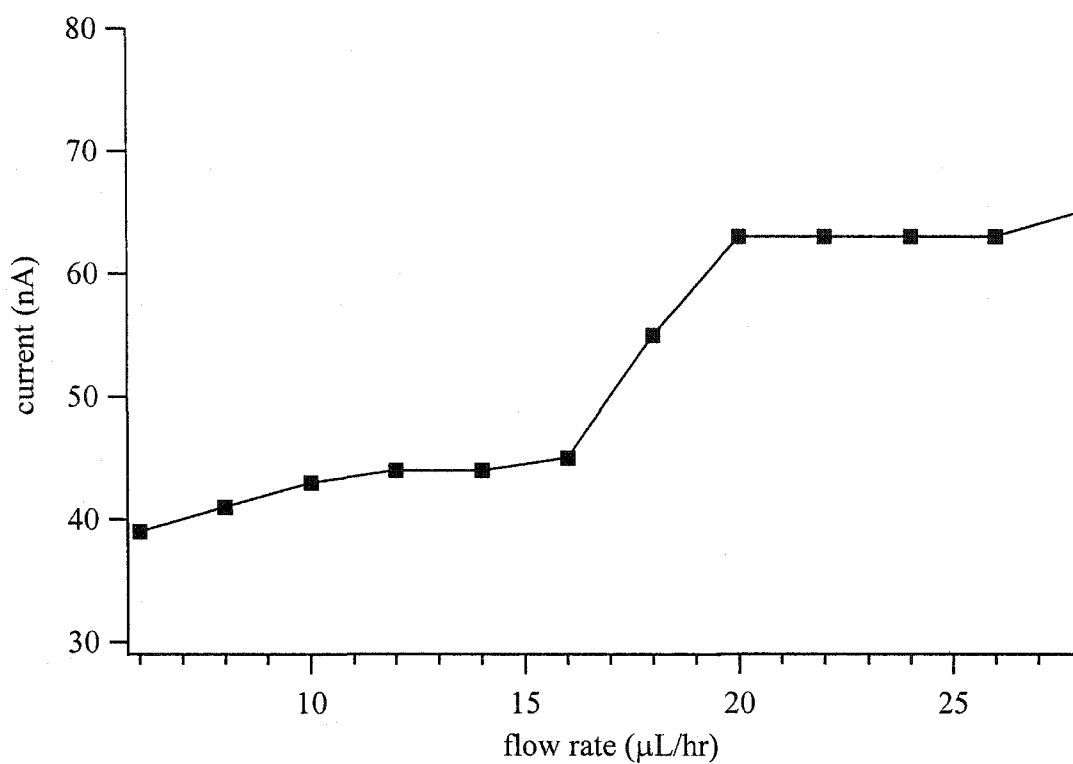


Figure 2.07 Effect of solution flow rate on the observed current at the syringe needle with the dual voltage ESI source. Capillary voltage = 4.7 kV, tip support voltage = 1.0 kV. Sample was 0.5 mM KI with 0.01 mM RbCl in 100% water solvent.

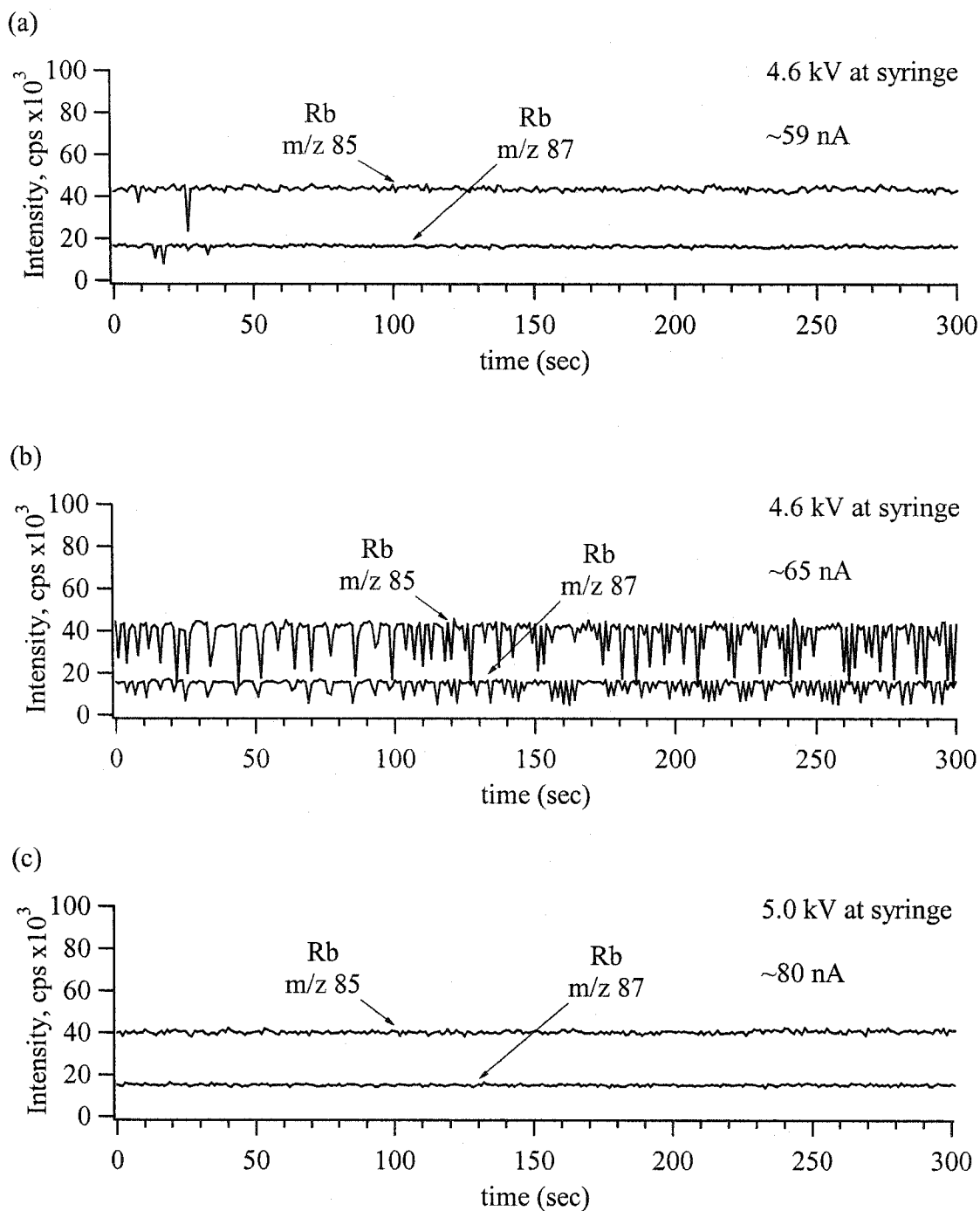


Figure 2.08 Balance of flow rate and capillary voltage using the dual voltage ESI source with 100% water solvent. Selected ion monitoring at m/z 85 and 87 for the Rb^+ ion. (a) 20 $\mu\text{L/hr}$ solution flow, 4.6 kV capillary voltage; (b) 24 $\mu\text{L/hr}$ solution flow, 4.6 kV capillary voltage; (c) 24 $\mu\text{L/hr}$ solution flow, 5.0 kV capillary voltage. Tip voltage = 1.0 kV.

large droplets visible to the naked eye formed at the tip when the bath gas was flowing, indicating that nebulization is not occurring to any significant extent.

In negative mode, only SF₆ was successful at generating stable ESI signals. The use of SF₆, however, comes at a significant cost. Sulfur hexafluoride is one of the most potent greenhouse gases, where SF₆ has been evaluated as 23,900 times more potent as a greenhouse gas than an equivalent amount of CO₂ in the atmosphere [20]. As such, recent regulations have resulted in a reduction in SF₆ production, and the costs of this gas has increased significantly. In our lab, the purchase of 35 pounds of SF₆ cost \$1195 in Canadian dollars. Assuming ideal gas behavior, at 25 °C and 1 atm, this corresponds to a volume of about 2660 L. At a consumption of ~0.8 L/min as the bath gas, this tank will theoretically allow ESI operation for about 55 hrs, at a cost of \$22/hr. Tests with narrower bath gas delivery systems indicate that the flow of SF₆ could be significantly reduced to alleviate the high cost, however, the effects in the earth's atmosphere make long-term use of this gas undesirable.

2.3.4 Comparison of Methanol and Water Solvent Performance

The ESI-MS spectra of a mixture of LiCl, RbCl and BaCl₂ (each at 0.01 mM) in purely aqueous solvent and 92% methanol (8% water) solvent with 0.5 mM KI were acquired under similar sampling conditions. The capillary voltage was 4.6 kV, the tip support voltage was 1.0 kV, the sampling plate voltage was 96 V, producing a $\Delta V = 90$ V. The mass spectrum of the sample with methanolic solvent (Figure 2.09 (a)) produces a mass spectrum very similar to that for purely aqueous solvent (Figure 2.09 (b)). Note that the CO₂ bath gas was applied for both samples. The signal intensity of Li⁺, Rb⁺, and Ba²⁺ are similar with both solvents, and the ions observed in the spectral background are relatively low with both systems. The observed intensity of these species was similar to previous work using this instrument with a typical ESI source (i.e., a metal capillary) [21].

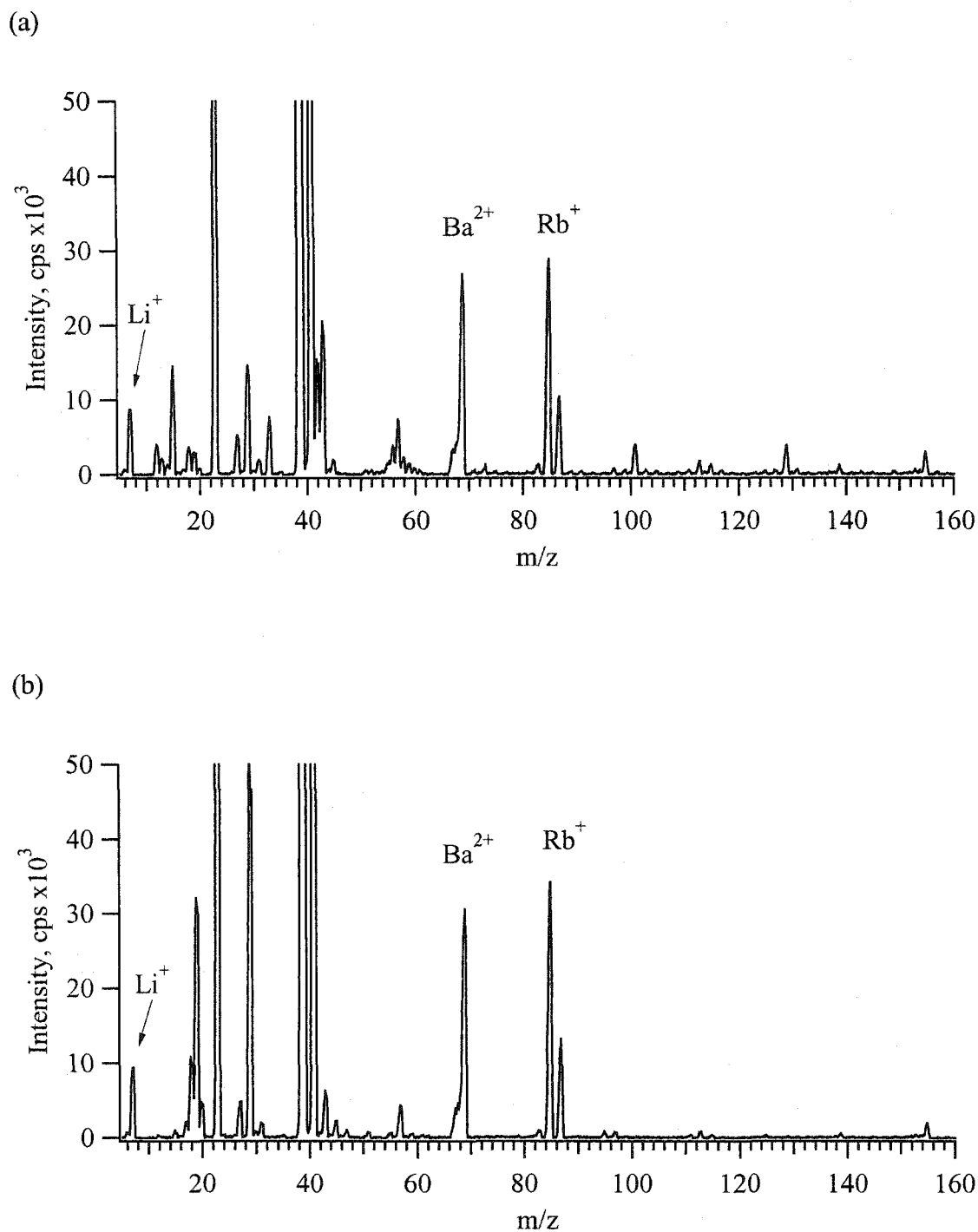


Figure 2.09 ESI-MS spectra of a mixture of LiCl, RbCl, and BaCl₂ each at a concentration of 0.01 mM, with 0.5 mM KI. $\Delta V = 90$ V. (a) 92% methanol solvent (8% water), (b) 100% water solvent.

The initial design of this ESI interface [22] involved a similar setup as to that shown in Figure 2.02, with a few significant differences. Bath gas was not added to the operation of the ESI, and the concentration of ions in solution needed to be at least 1mM for a stable ESI to be achieved. Also, while voltages were applied to the tip support and the capillary, the magnitudes of these voltages were equal. This configuration was reported to give stable signals in positive mode only. Also, the signal intensity produced by this system was lower than the results with the system described here, by over 2 orders of magnitude. The observation of significant levels of O_2^+ in the mass spectrum when using the previous setup suggests that ionization of the ambient gas was occurring, and this may account for the lower observed ion intensities. So, the modifications to the system represent very significant improvements.

Selected ion monitoring at m/z 7, 69, and 85, corresponding to the major isotopes of Li^+ , Ba^{2+} , and Rb^+ was performed under the same conditions, however, the methanol sample was also run without the CO_2 bath gas. The intensity of these signals was measured for 300 replicates, and the average signals and percent relative standard deviations (%RSDs) are presented as Table 2.01. The signal intensity for all the ions was slightly higher for the methanol solvent (no CO_2), however, the signal stability over the 5 minute testing intervals was comparable (i.e., about 3% RSD). In fact, the water signal %RSDs were equal to or less than the signal %RSDs with methanol, and the signal intensity with the water was better than methanol with CO_2 bath gas applied. This data demonstrates that for these simple ions, the performance of the aqueous ESI system is comparable to that of methanol in positive mode in terms of signal intensity and stability. The previous example comparing the mass spectra (Figure 2.09) indicate that the spectral background is also very similar. The signal stability in negative mode could not be evaluated using this instrument, due to limitations imposed by the ICP-MS acquisition software. The spectral quality in negative mode can be further examined in the context of speciation of anions with both solvent systems.

Sample solvent	Average signal intensity (cps)	RSD
H ₂ O	⁷ Li = 8470 ⁶⁹ Ba = 29500 ⁸⁵ Rb = 32400	⁷ Li = 3.79 % ⁶⁹ Ba = 2.38 % ⁸⁵ Rb = 2.14 %
Methanol*	⁷ Li = 7830 ⁶⁹ Ba = 27000 ⁸⁵ Rb = 26600	⁷ Li = 3.79 % ⁶⁹ Ba = 5.26 % ⁸⁵ Rb = 2.58 %
Methanol	⁷ Li = 12100 ⁶⁹ Ba = 36500 ⁸⁵ Rb = 38400	⁷ Li = 4.08 % ⁶⁹ Ba = 3.88 % ⁸⁵ Rb = 2.48 %

* with CO₂ bath gas

Table 2.01 Positive ion mode solvent comparison data from 300 replicates.

2.3.5 Selenite in Methanol and Water Solvents

The ESI-MS spectra of 0.5 mM Na_2SeO_3 in methanolic solvent under two different MS sampling conditions are shown in Figure 2.10. Under relatively mild sampling conditions ($\Delta V = -34$ V), the major selenium species observed is the seleno-ester $\text{CH}_3\text{OSeO}_2^-$. The observation of the seleno-ester is consistent with previous work [22]. As the potential difference is increased to $\Delta V = -50$ V, several additional Se species are observed, including SeO_2^- , HSeO_2^- , and SeO_3^- . Presumably, these species were generated via CID of the seleno-ester species.

If sodium selenite is diluted to the same concentration (0.5 mM) in purely aqueous solution, the major species observed in the ESI-MS spectrum is HSeO_3^- , as shown in the mass spectrum in Figure 2.11 (a). In this figure, a higher potential difference of $\Delta V = -50$ V could be used without fragmentation of the major species. Another Se species, $\text{NaSeO}_3^-(\text{H}_2\text{O})_x$, was observed at low intensity with water solvent (Figure 2.11 (b)). Sodium adducts were not observed at this ΔV with methanol solvent. Similar species have been previously observed for dilutions of sodium selenite in methanol, although under much more vigorous CID conditions [22]. As with the cation studies, the signal intensity of the major selenium species is comparable to that with methanol. In addition to altering the observed Se species, the methanol also seems to have altered the species observed for carbonate, CO_3^{2-} . With the water solvent, HCO_3^- was observed, whereas with the methanol, $\text{CH}_3\text{OCO}_2^-$ was observed, similar to the selenite species. Again, these observed ion intensities are comparable in both solvents. This data demonstrates how the aqueous ESI interface can be applied to prevent significant alteration in the species observed in the mass spectrum, without severe compromise in signal intensity.

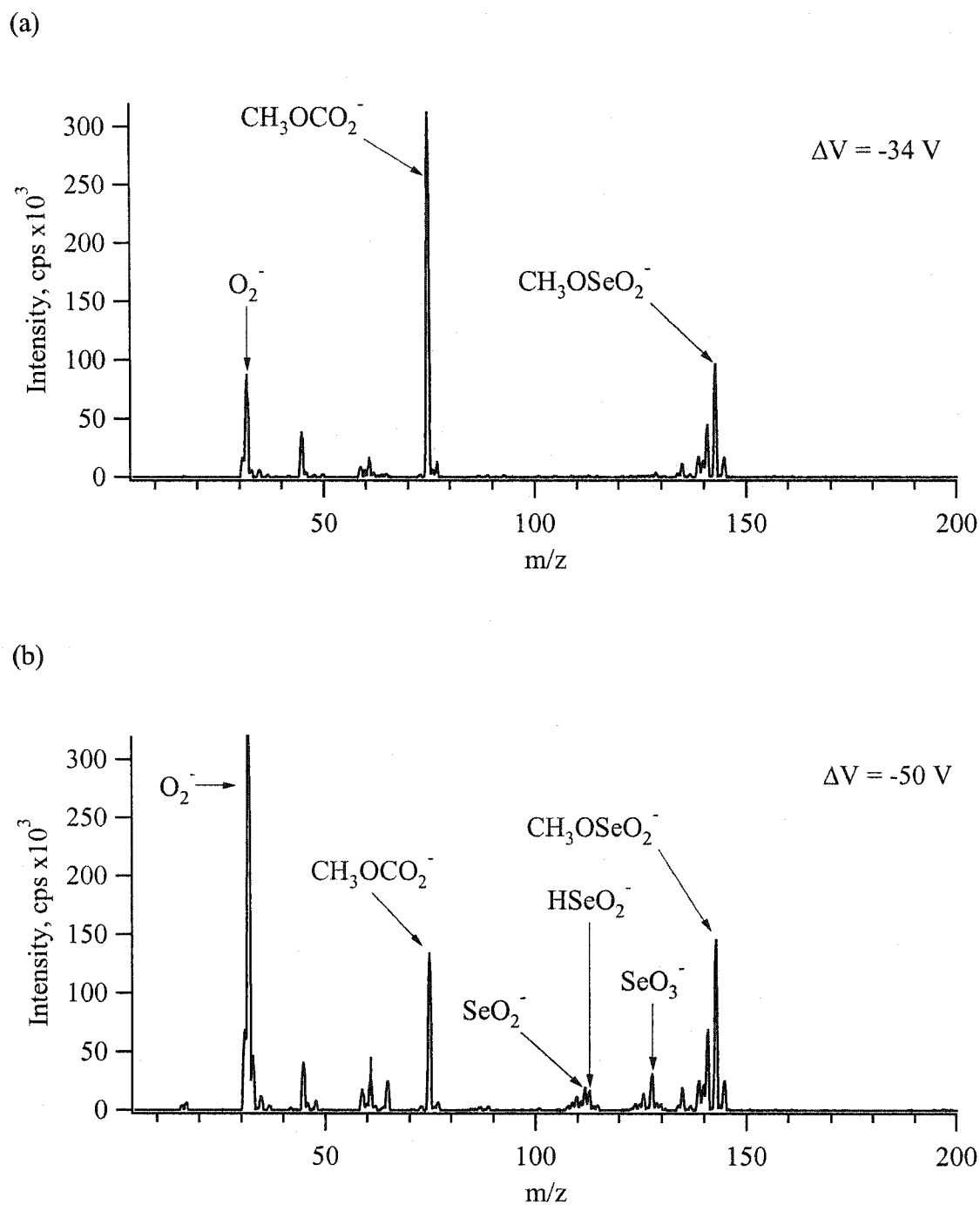


Figure 2.10 ESI-MS spectra of a sample containing 0.5 mM Na_2SeO_3 in 95% methanol (5% water). (a) $\Delta V = -34 \text{ V}$ (b) $\Delta V = -50 \text{ V}$.

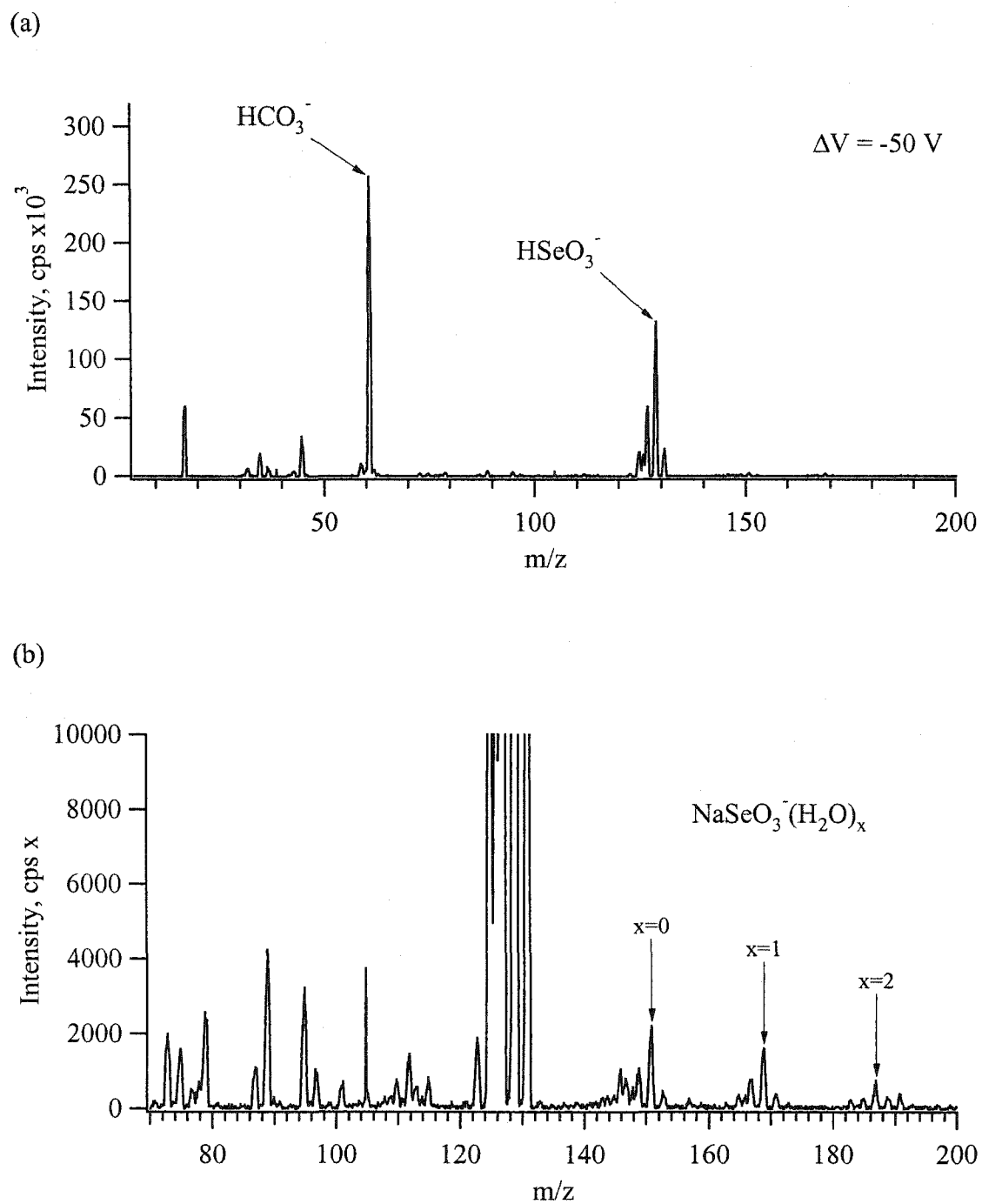


Figure 2.11 ESI-MS spectra of a sample containing 0.5 mM Na_2SeO_3 in 100% water solvent. (a) $\Delta V = -50 \text{ V}$ (b) expanded view of the spectrum in (a).

2.3.6 Sulfite in Methanolic and Water Solvents

Analogous to the selenite, sulfite also forms a species with the methanol solvent. Samples containing 0.5 mM Na_2SO_3 in 95% methanol (5% water) and 100% water solvents were run on the ESI-MS system, and the spectra are presented in Figures 2.12 (a) and (b), respectively. With methanol, the sulfite is observed as CH_3SO_2^- , whereas with water it is observed as HSO_3^- . The maximum potential difference that could be applied without fragmenting the species CH_3SO_2^- was $\Delta V = -34$ V, however, a $\Delta V = -44$ V could be tolerated using water solvent without fragmenting HSO_3^- . Being able to use a higher ΔV to analyze the target species is advantageous, since this creates a greater degree of declustering, and generally reduces the intensity of cluster species that can complicate the background of the ESI-MS spectrum, especially at low masses.

2.3.7 Hypochlorite in Methanol and Water Solvents

A commercial bleach sample was diluted to produce a final solution of ~ 0.1 mM NaOCl in both methanolic and aqueous solvents. In the methanolic sample, no species corresponding to the original hypochlorite, ClO^- , were observed, as the spectrum in Figure 2.13 (a) indicates. A spectrum of the same solution was also acquired under conditions of lower potential difference to look for fragile species that may have formed, however, none were observed. The only major chlorine-containing species observed were an intense Cl^- signal as well as chlorate, ClO_3^- . Chlorate is a known by-product of bleach production, and is also present as a decomposition product of ClO^- [23]. In this case, it seems that the presence of methanol has resulted in the reaction of the hypochlorite with the methanol to produce a species that cannot be observed with ESI-MS. When the aqueous sample was analyzed, an intense signal due to ClO^- was observed. Previous tests were done to confirm that neither ClO_2^- , ClO_3^- , nor ClO_4^- were significantly fragmented under these testing conditions, which indicates that the observation of ClO^- was not due to the fragmentation of any of these species.

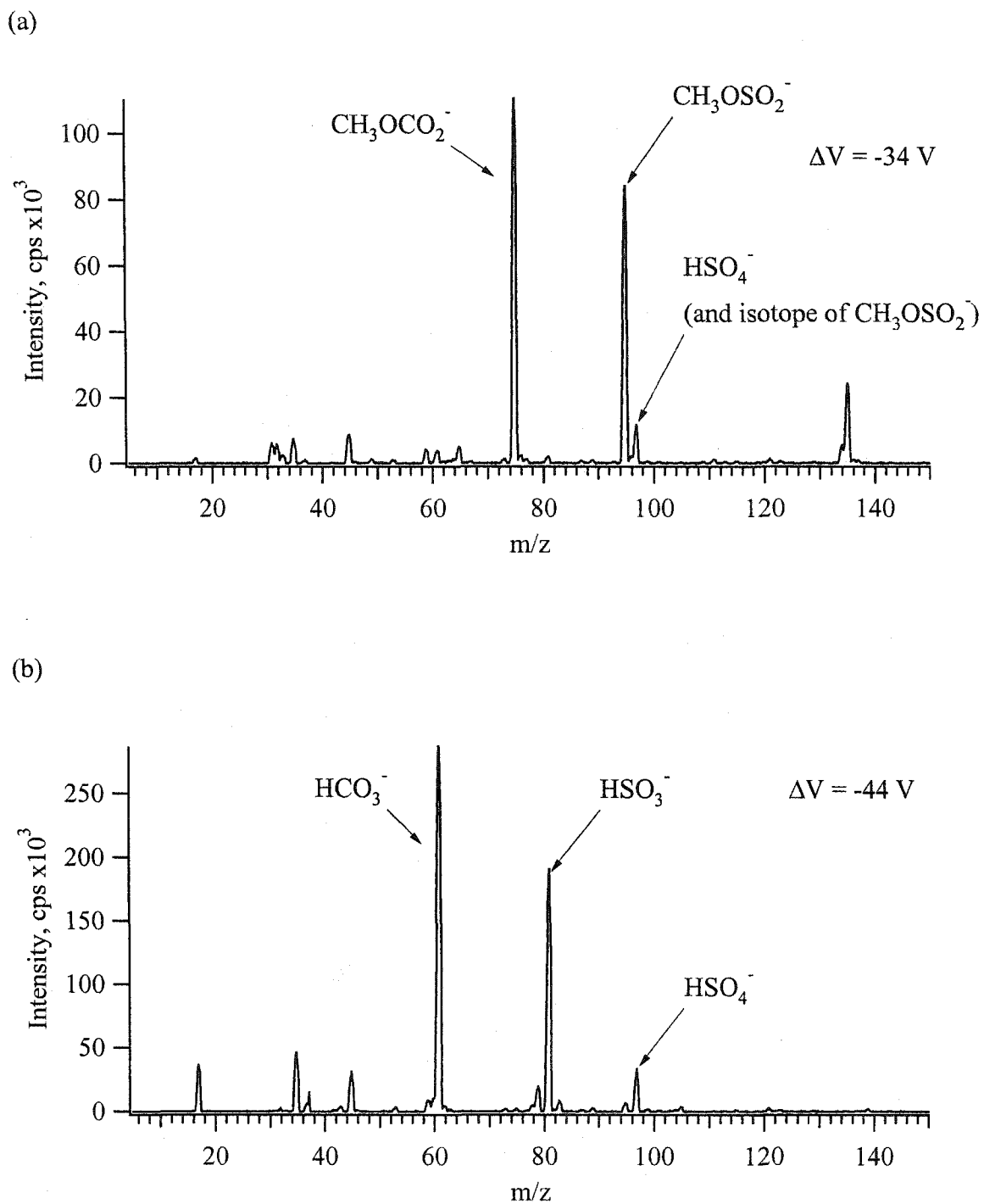


Figure 2.12 ESI-MS spectrum of 0.5 mM Na_2SO_3 in (a) 95% methanol, 5% water and (b) 100% water solvent.

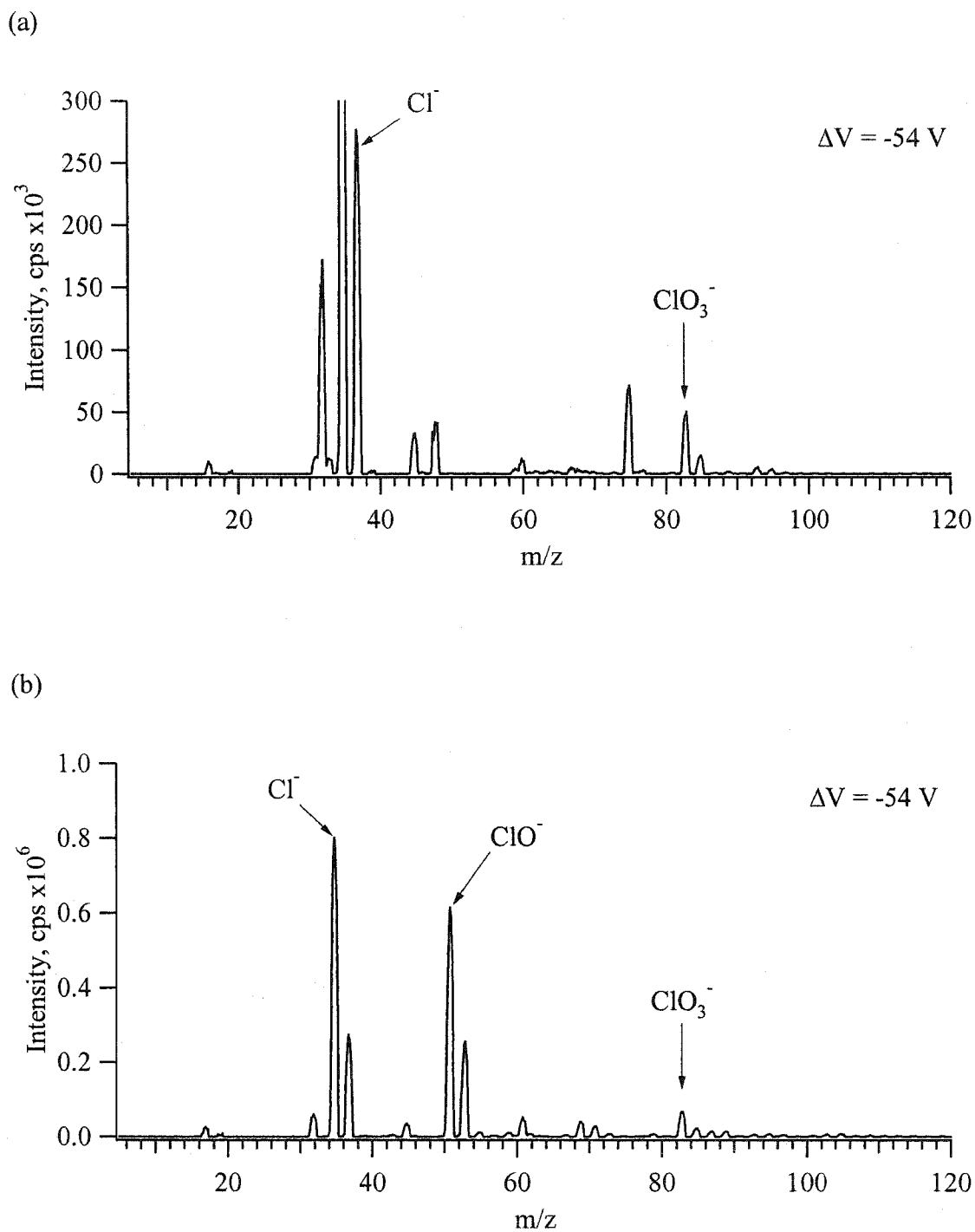


Figure 2.13 ESI-MS spectrum of a commercial bleach solution diluted to give approx. 0.1 mM NaOCl. (a) 95% methanol, 5% water and (b) 100% water solvent.

2.4 Conclusions

The data with the simple cations demonstrated that the aqueous ESI interface exhibited signal intensity and stability comparable to when methanol was the solvent. Aqueous ESI was demonstrated to operate at much lower flows than methanol for the same ESI configuration, and the tuning of the flow rate and the applied voltage were critical to generating stable signals. While the signal stability could not be evaluated in negative mode due to instrumental limitations, the signal intensities of both the analyte ion and ions in the spectral background were comparable when using either solvent. Examples of how the sample solvent can alter the species observed in the ESI-MS spectrum highlights testing scenarios where dilution of an original sample with methanol can complicate the speciation of ions in the original sample. While the addition of CO₂ bath gas in the positive mode is easy and inexpensive, the use of SF₆ in the negative mode is not as attractive an option, due to the high cost of SF₆ and due to its action in the environment as a greenhouse gas [20].

2.5 References

1. Yamashita, M.; Fenn, J. B. "Negative ion production with the electrospray ion source"; *J. Phys. Chem.* **1984**, 88, 4671-4675.
2. Yamashita, M.; Fenn, J. B. "Electrospray ion source. Another variation on the free-jet theme"; *J. Phys. Chem.* **1984**, 88, 4451-4459.
3. Taylor, G. I. "Disintegration of water drops in an electric field"; *Proc. R. Soc. London, Sec. A.* **1964**, 280, 383-397.
4. Van Berkel, G. J. "Electrolytic deposition of metals on to the high-voltage contact in an electrospray emitter: Implications for gas-phase ion formation"; *J. Mass Spectrom.* **2000**, 35, 773-783.
5. Amad, M. H.; Cech, N. B.; Jackson, G. S.; Enke, C. G. "Importance of gas-phase proton affinities in determining the electrospray ionization response for analytes and solvents"; *J. Mass Spectrom.* **2000**, 35, 784-789.
6. Fernandez de la Mora, J.; van Berkel, G. J.; Enke, C. G.; Cole, R. B.; Martinez-Sanchez, M.; Fenn, J. B. "Electrochemical processes in electrospray ionization mass spectrometry"; *J. Mass Spectrom.* **2000**, 35, 939-952.
7. Gamero-Castano, M.; Mora, J. F. d. l. "Kinetics of small ion evaporation from the charge and mass distribution of multiply charged clusters in electrosprays"; *J. Mass Spectrom.* **2000**, 35, 790-803.
8. Kebarle, P. "A brief overview of the present status of the mechanisms involved in electrospray mass spectrometry"; *J. Mass Spectrom.* **2000**, 35, 804-817.
9. Cole, R. B. "Some tenets pertaining to electrospray ionization mass spectrometry"; *J. Mass Spectrom.* **2000**, 35, 763-772.
10. Smith, D. P. H. "The electrohydrodynamic atomization of liquids"; *IEEE Trans. Int. Appl.* **1986**, IA-22, 527-535.
11. Wampler, F. M.; Blades, A. T.; Kebarle, P. "Negative ion electrospray mass spectrometry of nucleotides: Ionization from water solution with SF₆ discharge suppression"; *J. Am. Soc. Mass Spectrom.* **1993**, 4, 289-295.

12. Ikonomou, M. G.; Blades, A. T.; Kebarle, P. "Electrospray mass spectrometry of methanol and water solutions suppression of electric discharge with SF₆ gas"; *J. Am. Soc. Mass Spectrom.* **1991**, *2*, 497-505.
13. Tang, K.; Smith, R. D. "Sensitivity enhancement of electrospray ionization-MS for aqueous solutions in the corona-assisted cone-jet mode"; *Int. J. Mass Spectrom. Ion. Proc.* **1997**, *162*, 69-76.
14. Tang, K.; Gomez, A. "Generation of monodisperse water droplets from electrosprays in a corona-assisted cone-jet mode"; *J. Colloid Interface Sci.* **1995**, *175*, 326-332.
15. Wilm, M.; Mann, M. "Analytical properties of the nanoelectrospray ion source"; *Anal. Chem.* **1996**, *68*, 1-8.
16. Konig, S.; Fales, H. M.; Haegele, K. D. "Comment on the cylindrical capacitor electrospray interface"; *Anal. Chem.* **1998**, *70*, 4453-4455.
17. Stewart, I. I. Ph.D. Thesis, University of Alberta, Edmonton, Alberta, 1996.
18. Sjoberg, P. J. R.; Nyholm, L.; Markides, K. E. "Characterization of the atmospheric pressure ionization mass spectrometric process obtained using a fused-silica emitter with the high voltage applied upstream"; *J. Mass Spectrom.* **2000**, *35*, 330-336.
19. Jackson, G. S.; Enke, C. G. "Electrical equivalence of electrospray ionization with conducting and nonconducting needles"; *Anal. Chem.* **1999**, *71*, 3777-3784.
20. "'Radiative forcing of climate change", The 1994 Report of the Scientific Assessment Working Group of IPCC"; Intergovernmental Panel on Climate Change (IPCC). **1994**.
21. Agnes, G. R.; Horlick, G. "Effect of operating parameters on analyte signals in elemental electrospray mass spectrometry"; *Appl. Spectrosc.* **1995**, *49*, 324-334.
22. Barnett, D. A. Ph. D. Thesis, University of Alberta, Edmonton, Alberta, 1999.
23. U.S.E.P.A. In *EPA Guidance Manual: Alternative Disinfectants and Oxidants*, 1999, pp 1-54.

Chapter 3

ESI-MS of Lanthanides in Aqueous Solution - Investigations Using High-Energy Collision-Induced Dissociation

3.1 Introduction

In the previous chapter, the performance of an aqueous ESI interface was demonstrated. In positive mode, the aqueous solvent was demonstrated to not have any significant compromise in signal intensity or stability as compared to utilizing a methanolic solvent, for the simple ions tested. As demonstrated in Chapter 2, aqueous sampling may be used to detect highly reactive species that are not stable in other common solvent systems, such as methanol. Aqueous sampling might also be used when solubility of the analyte is a concern, and dilution in a non-aqueous solvent is not an option. In general, however, applications in which an organic solvent cannot be used will be relatively few.

One concern with using an organic solvent, such as methanol, is how this introduced solvent may be changing the observed species in the mass spectrum. Early work in the field of inorganic ESI-MS by Kebarle and co-workers demonstrated that multiply-charged cations undergo gas-phase charge reduction reactions, which can result in several different species observed in the resultant mass spectrum [1-3]. Previous work in our lab (and many others) has demonstrated that the types of species observed in the mass spectrum are highly dependent on the amount of declustering imparted to the ions being sampled [4-8]. In regards to simple, multiply charged cations, low energy declustering generally provides a mixture of species, whereas higher energy declustering provides spectra with far fewer species. This high declustering condition has been referred to as the “metal ion mode”, since the spectra generally look like the singly-charged metal, without any accompanying ligands [5]. Some multiply-charged metals, such as the lanthanides, still show several species in the mass spectrum under “metal ion mode” sampling conditions [8]. While the formation of several of the basic species has been related to the chemistry of the lanthanides, the MS sampling is still not vigorous enough to break the bonds between the ligand and the metal. Furthermore, when high-energy declustering interface conditions were used, the resultant ion signals suffered from low sensitivity, making this mode of operation very limited in scope.

As part of an evaluation of the performance of the aqueous ESI interface for inorganic analytes, it was decided that the lanthanides would provide a good example of how a multiply-charged species may behave in these different solvents. These ions have been investigated previously using methanolic solvents and have been shown to exhibit several different species in the mass spectrum [1, 8]. As will be demonstrated, the use of aqueous solvent can have a significant impact on the observed spectra of these elements. Minor modifications to our in-house designed mass spectrometer interface allowed for use of higher voltage differences between the sampling plate and the skimmer. This allowed higher energy declustering, which was used in an attempt to improve the “metal ion mode” of operation.

3.2 Experimental

3.2.1 Aqueous Electrospray Interface

The electrospray (ES) interface used for this study is an in-house design, and is similar to electrospray interfaces reported previously for methanolic solvents [9, 10]. A schematic diagram of the interface used in this study is presented in Figure 3.01. A syringe pump (Cole-Parmer 74900 Series) and a Hamilton 250 μL syringe with a stainless steel needle were used to deliver solution through a fused silica capillary with approximate dimensions of 50 μm I.D., 150 μm O.D., and 45 cm in length. The fused silica capillary was a continuous piece that began from inside the syringe needle and terminated as the ES tip. The polyimide coating was removed from the tip to improve the tip appearance, and the fused silica capillary was positioned to extend about 2 mm from the stainless steel support tubing. The only electrical contact with the solution was at the syringe needle. A second voltage was applied to the stainless steel support tubing near the tip to moderately enhance sensitivity and stability. Glass tubing (1/8" ID) surrounded the stainless steel support and delivered CO_2 bath gas to enshroud the ES tip in an atmosphere of CO_2 . Using this system, purely aqueous matrices could be reliably electrosprayed in positive mode, without the help of pneumatic nebulization. A more

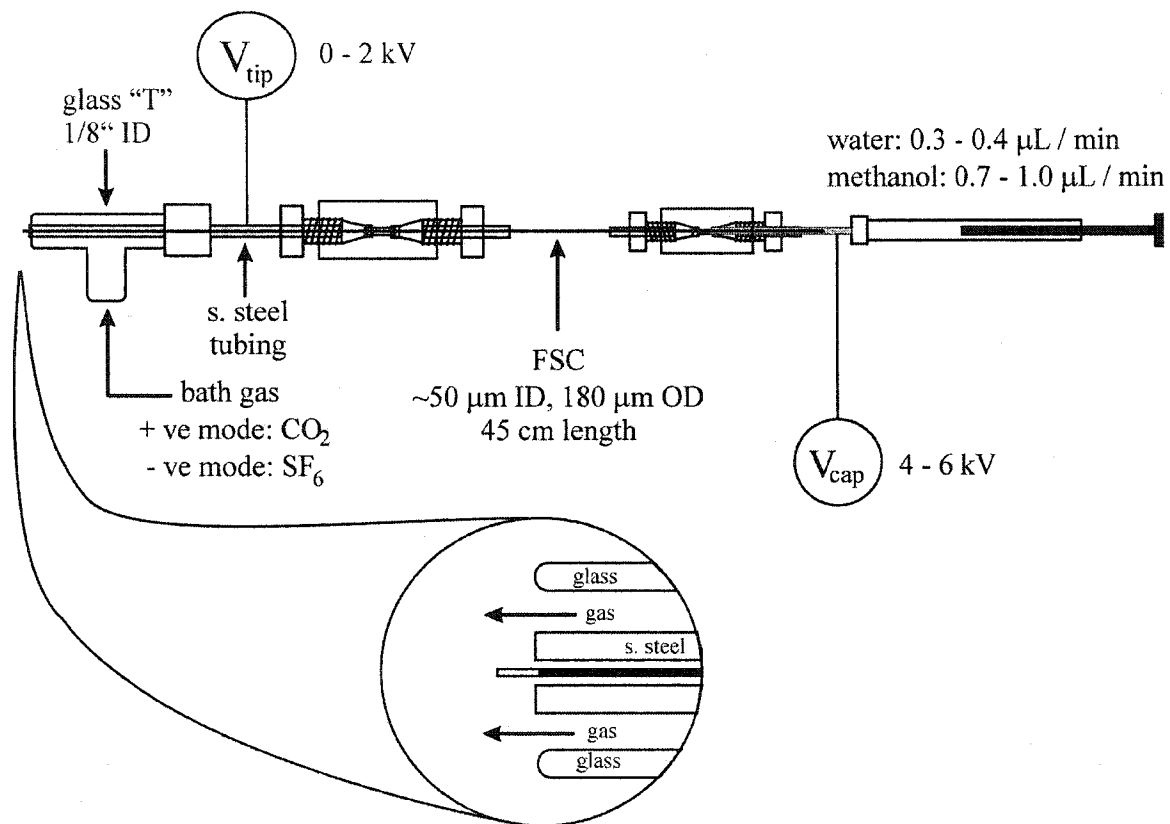


Figure 3.01 Interface for electrospaying purely aqueous solvents in positive mode (not to scale).

detailed description of this system can be found in Chapter 2. For aqueous ES, typical parameters were about 0.3 $\mu\text{L}/\text{min}$ solution flow rate, 5-6 kV at the syringe needle, 1 kV at the tip support, and ~ 0.8 L/min CO_2 flow rate. The fused silica tip was positioned directly on axis to the mass spectrometer interface, at an offset of 3 mm. This setup was also used for methanolic solution studies, but with solution flow rates of about 0.8 $\mu\text{L}/\text{min}$.

3.2.2 Mass Spectrometry

The mass spectrometer used was an ELAN 250 ICP-MS, modified for an electrospray ion source. All components associated with the ICP were removed, and the interface was re-designed, as discussed in detail in Chapter 1. The sampling plate used for ICP was replaced with another sampling plate with a smaller orifice (~ 100 μm) and a front plate, which allowed addition of a curtain gas, as illustrated in Figure 3.02. The front plate (FP), the sampling plate (SP) and the skimmer (SK) were insulated from each other, and were independently biased to different voltages. The N_2 curtain gas flowed at 0.3 mL/min between the sampling plate and front plate and flowed counter-current to the movement of electrosprayed ions. The roles of the curtain gas are the same as with other ES systems, which are to cause evaporation of solvent from the droplets during the ESI process, preventing solvent from entering the MS, and to act as an "inert" gas for collision-induced dissociation (CID). The front plate voltage was set to a constant 900 V, the skimmer voltage was set at a constant 6 V, and the sampling plate voltage (SPV) was varied. The difference in the skimmer and the sampling plate voltage allowed control of the amount of energy imparted to the ions relative to the uncharged curtain gas (i.e. control the amount of CID imparted to the ESI-generated ions). For this study, the SPV ranged from 70 V to 400 V, providing a range of relatively harsh sampling conditions. The high voltages applied to the sampling plate were made possible by improving the insulation of the sampling plate from the other components, allowing for a potential difference between the sampling plate and the skimmer of up to 500 V in positive mode.

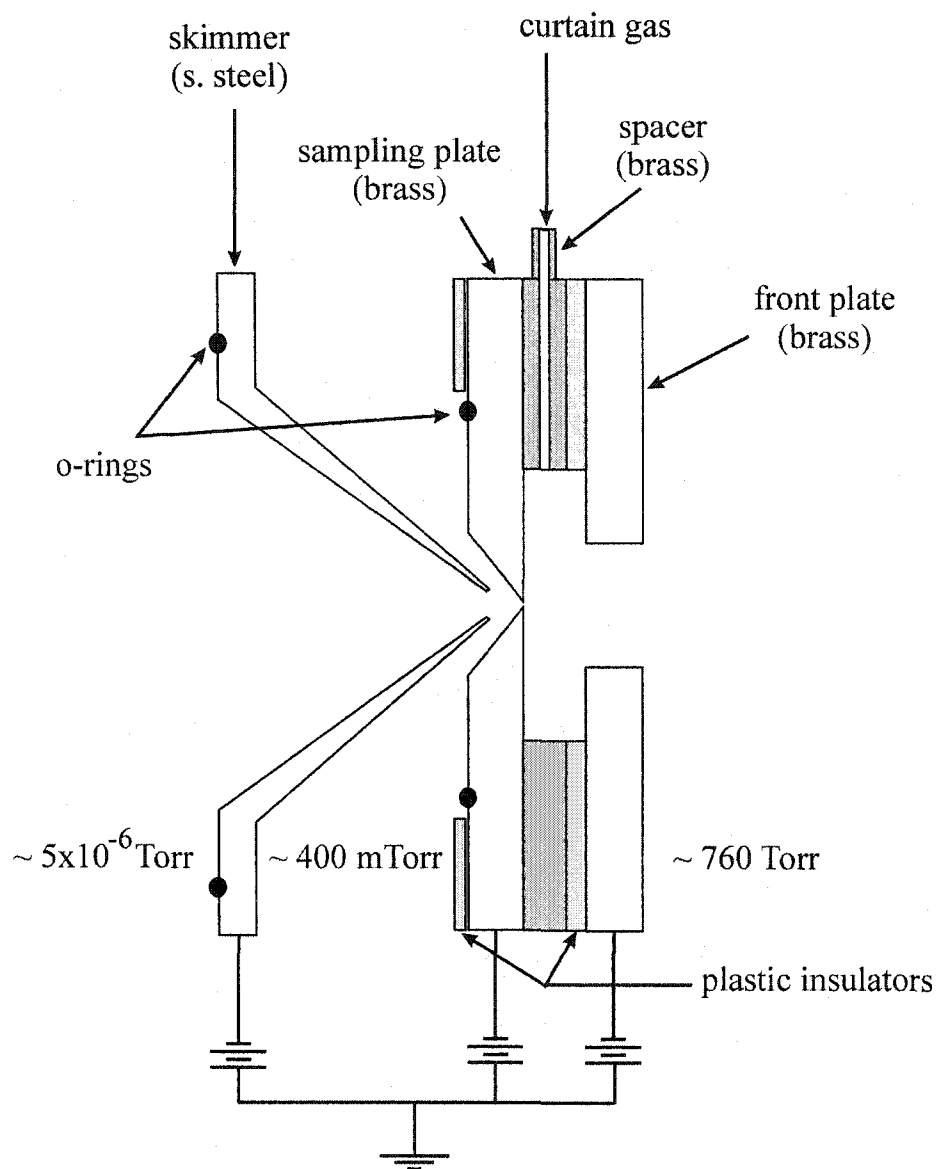


Figure 3.02 Schematic diagram of the modified ELAN 250 ICP-MS interface.

3.2.3 Reagents and Sample Preparation

The metal salts used were commercially available from Sigma-Aldrich and from Nuclear Corp. of America. Due to the variable amount of hydration that can occur with these salts, the percent metal in the salts was determined using a Sciex ELAN 5000 ICP-MS. Although care was taken to keep the oxide levels low (< 2%), the salts were analyzed in 3 separate groupings in order to avoid any potential interference due to oxides. The results from this were used to accurately make lanthanide stock solutions by dissolving the lanthanide salt in 18 M Ω de-ionized water and diluting to 10 mM. Further dilutions were done using either reagent grade methanol or 18 M Ω de-ionized water. For the methanolic solutions, 5% water was present. All dilutions contained 0.4 mM LiCl as an electrospray stabilizer.

3.3 Results and Discussion

3.3.1 Methanolic Solvent

Although all of the lanthanide salts were examined (except Pm), only selected elements are shown in detail, since they exhibit spectra that seem to be representative of the entire series. The spectra presented in Figure 3.03 are for La, Eu, and Lu salts in methanolic solvent (95% methanol, 5% water), using nitrogen curtain gas and a SPV = 200 V. In previous work in our lab, a relatively harsh sampling condition (SPV \approx 200 V) that stripped solvent and most ligands off the central metal ion to yield simplified spectra was termed the "metal ion mode" of ESI-MS operation [5]. In Figure 3.03, the spectra look very similar to the previous studies, with the dominant species being M^+ and MO^+ . Other major species, such as M^{2+} , MCl^+ , MOH^+ , and even MH^+ are evident for Eu.

In solution, these metals generally exist in the form $Ln^{3+}(\text{solvent})_n$ [11]. When using methanolic solvent, only species with a formal 3+ charge (i.e., LnO^+ , $LnOH^{2+}$) were observed under relatively low CID conditions [1, 8, 12]. As the solvated 3+ metal

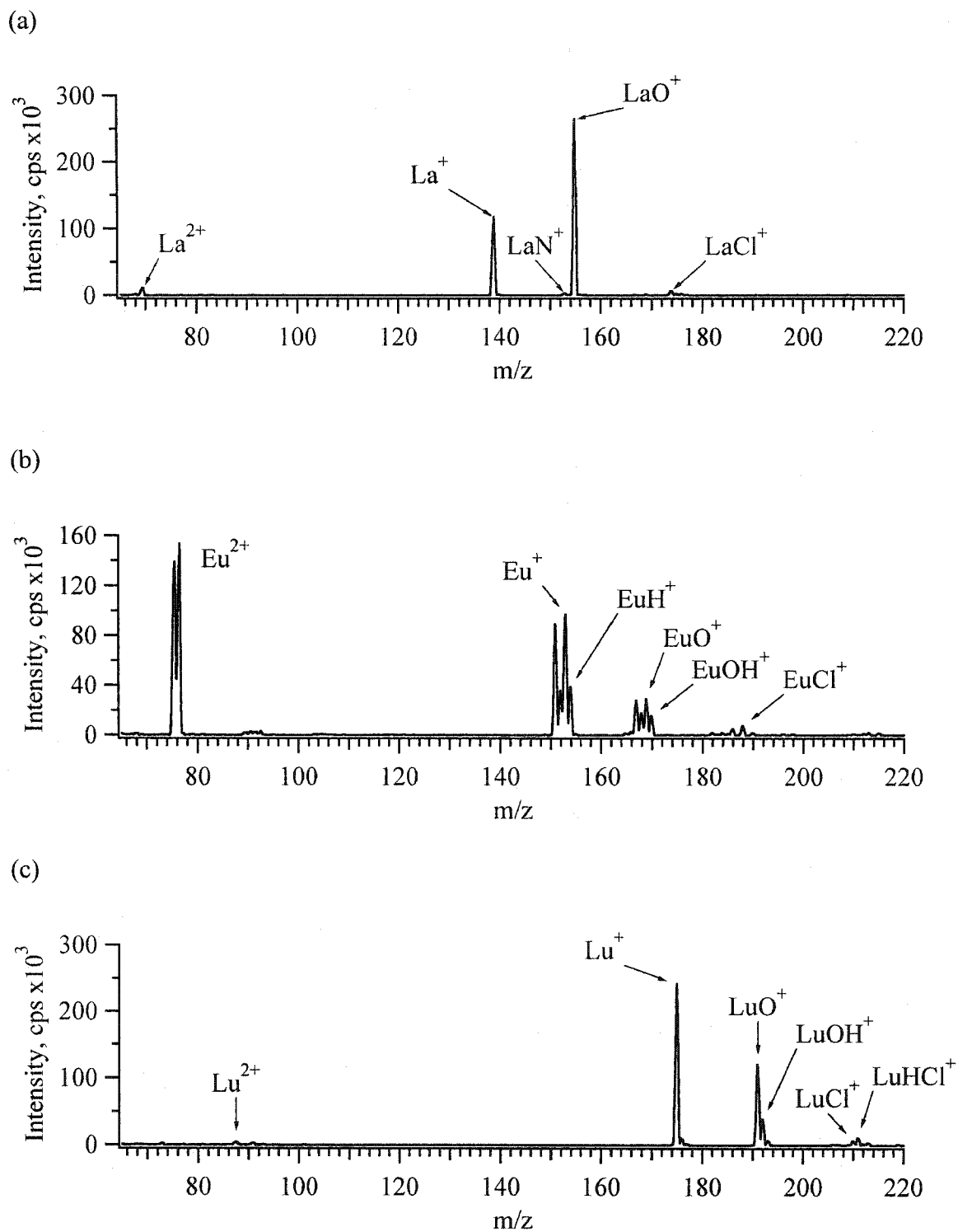
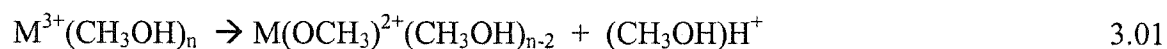


Figure 3.03 ESI-MS spectrum of solutions containing 0.1 mM Ln salt and 0.4 mM LiCl in 95% methanol, 5% water matrix. Spectra acquired at a SPV of 200 V; (a) LaCl_3 , (b) $\text{Eu}(\text{NO}_3)_3$, (c) LuCl_3 .

ion loses stabilizing solvent through evaporation and collisions with the curtain gas, the metal ion must charge reduce or form a stable adduct in order to reduce its effective charge [1-3]. In other words, a competition between ligand loss and charge reduction exists. These spectra are very similar to those observed earlier under similar sampling conditions, with a few notable exceptions. First, these spectra do not exhibit significant solvent-derived species, such as $M(\text{OCH}_3)_2^+$ and $M(\text{OCH}_3)^{2+}$. Second, the spectral signals here are about 30 times more intense for the same concentration of analyte when using the same mass spectrometer. These differences must be partly related to the different type of electrospray source used in each study. For the earlier study, a metal capillary ($\sim 200 \mu\text{m}$ OD, $\sim 100 \mu\text{m}$ ID) was used, as compared to the fused silica tip used here ($< 150 \mu\text{m}$ OD, $50 \mu\text{m}$ ID). The enhanced sensitivity that was observed with the fused silica capillary interface was likely due to more efficient ion generation through the forming of smaller initial droplets. Signal enhancements and the ability to use lower curtain gas flow rates have been observed previously for nanospray fused silica interfaces, and are believed to be related to the smaller initial droplets that these fused silica systems can provide [13]. It has been proposed that as the solvent surrounding the ion is lost, the ion reacts with a molecule of solvent to reduce its effective charge, as proposed in Equation 3.01.



Perhaps with small initial droplets, desolvation and CID are more efficient, which may explain the absence of species such as $M(\text{OCH}_3)_2^+$ at this SPV, as compared to previous studies. A more detailed rationale has been proposed for the reactions leading to the formation of these products when using methanol solvent and will not be repeated here [1, 8]. Under these vigorous sampling conditions, sequential CID reactions of the product in Equation 3.01 generate the observed major species [8]. The relative abundance of M^+ , MO^+ , and M^{2+} under these sampling conditions has been related to the relative strengths of the MO^+ bond and the relative magnitude of the ionization potential, IP [1, 2, 8]. The data for the M^+ -O bond dissociation energies and the ionization potentials for the lanthanides are presented in Table 3.01 [14, 15]. As the data show, the M^+ -O bond

dissociation energy of La (8.89 eV) is the highest, and this species was observed to have one of the highest relative oxide species signals at SPV = 200 V, as the spectra in Figure 3.03 demonstrate. Lu exhibited the next most oxides (M^+-O dissociation energy = 5.51 eV), followed by Eu (M^+-O dissociation energy = 4.03 eV). These results seem in agreement with previous studies and the relative M^+-O bond dissociation energies [8].

Most of the lanthanides exhibit a very low signal for M^{2+} , except Eu and Yb. Both Eu and Yb have a relatively stable M^{2+} oxidation state, due to the exchange energy derived from the resulting electron configuration. In the case of Eu^{2+} , the resulting valence electron configuration would be $4f^76s^0$, producing a half-filled subshell. Similarly, for Yb^{2+} , the electron configuration would be $4f^{14}6s^0$, with a full 4f subshell. In both cases, the extra stability gained from these electron configurations makes Eu^{2+} and Yb^{2+} the most stable dipositive lanthanides [16]. This is reflected in the high 3rd ionization potentials for Eu and Yb, with values near 25 eV, the highest of the lanthanide series (Table 3.01). It has been suggested that the product, $M(OCH_3)^{2+}(CH_3OH)_{n-2}$ undergoes CID reactions to form either M^{2+} or MO^+ , depending on the MO^+ bond strength, the IP of the lanthanide, and the IP of the solvent (i.e., methanol) [8]. In the case of Eu and Yb, perhaps these ions are more likely to form a M^{2+} species, rather than form MO^+ , which has a formal 3+ charge on the metal. Similar reasoning may also account for the low oxides (and low oxide bond strength) observed for these species. The preferred M^{2+} state may also account for the higher levels of species with a formal 2+ metal charge, such as EuH^+ , $EuOH^+$, and $EuCl^+$. The presence of methanol is likely prohibitive to the observation of the M^{2+} species for the other lanthanides. The ionization potential of several molecules, including methanol, is shown in Table 3.02 [14]. The IP(methanol) is 10.8 eV, which is less than most of the lanthanide IP(II), with Pr and Nd being just less at 10.55 and 10.73 eV, respectively. This may explain the low M^{2+} observed for the lanthanides other than Eu and Yb, since the M^{2+} lanthanide may be able to remove an electron from a methanol ligand to reduce its charge. For Eu and Yb, perhaps the M^{2+} species forms without any methanol ligands remaining, in which case it cannot further charge reduce to M^+ .

Element	Dissociation energies ^a (eV)	Ionization potentials ^b (eV)		
	M ⁺ -O	I	II	III
La	8.89	5.58	11.06	19.18
Ce	8.80	5.47	10.85	20.20
Pr	8.20	5.42	10.55	21.62
Nd	7.76	5.49	10.73	22.10
Sm	5.98	5.63	11.07	23.40
Eu	4.03	5.67	11.24	24.92
Gd	7.80	6.14	12.09	20.63
Tb	7.67	5.84	11.52	21.91
Dy	6.29	5.93	11.67	22.80
Ho	6.11	6.02	11.80	22.84
Er	6.07	6.10	11.93	22.74
Tm	5.03	6.18	12.05	23.68
Yb	3.82	6.25	12.18	25.03
Lu	5.51	5.43	13.90	20.96

^a Murad, E; Hilderbrand, D. L. *J. Chem. Phys.* **1980**, *73*, 4005-4011.

^b CRC Handbook of Chemistry and Physics; CRC Press: Boca Raton, FL, 1993.

Table 3.01 Physical data for the Lanthanide series.

Molecule	Ionization potential ^a (eV)
O ₂	12.1
N ₂	15.6
CO ₂	13.4
CH ₃ OH	10.8
H ₂ O	12.6
CH ₃ CN	12.2

^a CRC Handbook of Chemistry and Physics;
CRC Press: Boca Raton, FL, 1993.

Table 3.02 Ionization potentials for selected molecules.

3.3.2 Aqueous Solvent

The same salts were run using 100% water solvent under similar conditions as with the methanol studies. The spectra of La, Eu, and Lu acquired at a SPV = 200 V can be found in Figure 3.04. The observed signal intensities are similar in both solvent systems, suggesting that the efficiency of ion generation when using water solvent is comparable to that for methanol. As with methanol, a M^{3+} species was not observed under the range of sampling conditions tested. Similar to Equation 3.01, Equation 3.02 has been proposed to account as a general step for the first charge reduction for M^{3+} ions in the presence of water ligands [1].



The spectrum in Figure 3.05 is for an aqueous $LaCl_3$ solution acquired under milder CID conditions (SPV = 100 V), and shows several $M(OH)^{2+}$ species, which seems consistent with the proposed reactions for aqueous solvent. Like with the methanolic solvent, intense M^+ and MO^+ peaks were observed (Figure 3.04), although the aqueous spectra were found to (generally) exhibit fewer oxides under the same MS interface conditions.

The most significant difference with the aqueous solvent is that all the lanthanides exhibited intense M^{2+} signals (Figure 3.04). This is in sharp contrast to the methanolic solvent, where only Eu and Yb were found to have significant M^{2+} species in the mass spectrum. Previous work has suggested that charge-reduced species tend to form when the IP(II) of the metal was greater than the IP(ligand) [1-3, 8]. In the case of the water solvent ($IP_{H_2O} = 12.6$ eV), only Lu has a greater IP_{II} (13.9 eV). So, for most of the lanthanides, it should be less likely that the doubly charged metal ion would be able to remove an electron from a water ligand. The large difference in energy for $IP_{II, Lu}$ and for the IP_{H_2O} suggests that the water ligands should not be good at protecting the Lu^{2+} charge. The observation of a significant amount of Lu^{2+} suggests that ionization potentials are not the only factors determining charge reduction for these metals in

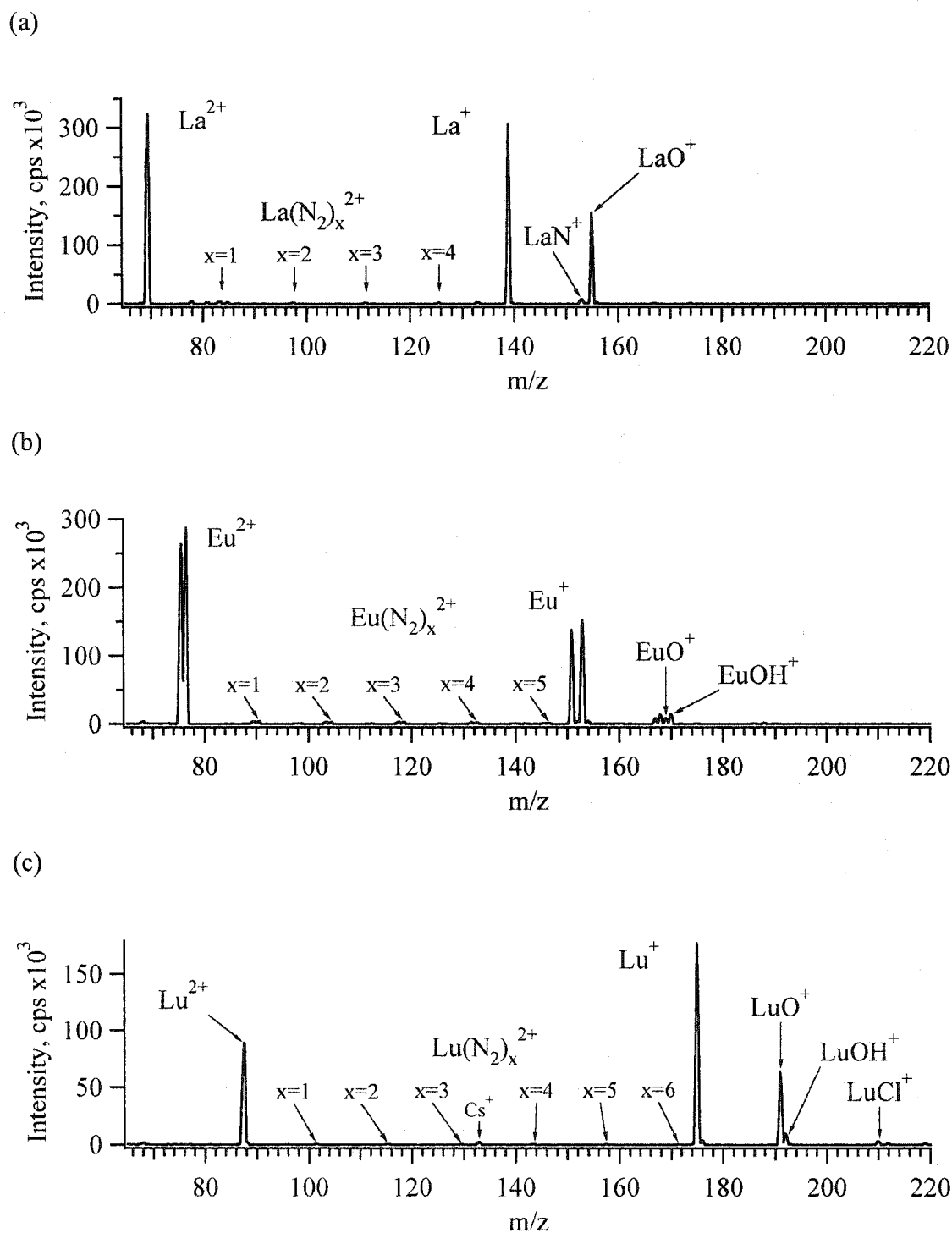


Figure 3.04 ESI-MS spectrum of solutions containing 0.1 mM Ln salt and 0.4 mM LiCl in 100% aqueous solvent. Spectra were acquired at a sampling plate voltage of 200 V; (a) LaCl_3 , (b) $\text{Eu}(\text{NO}_3)_3$, (c) LuCl_3 .

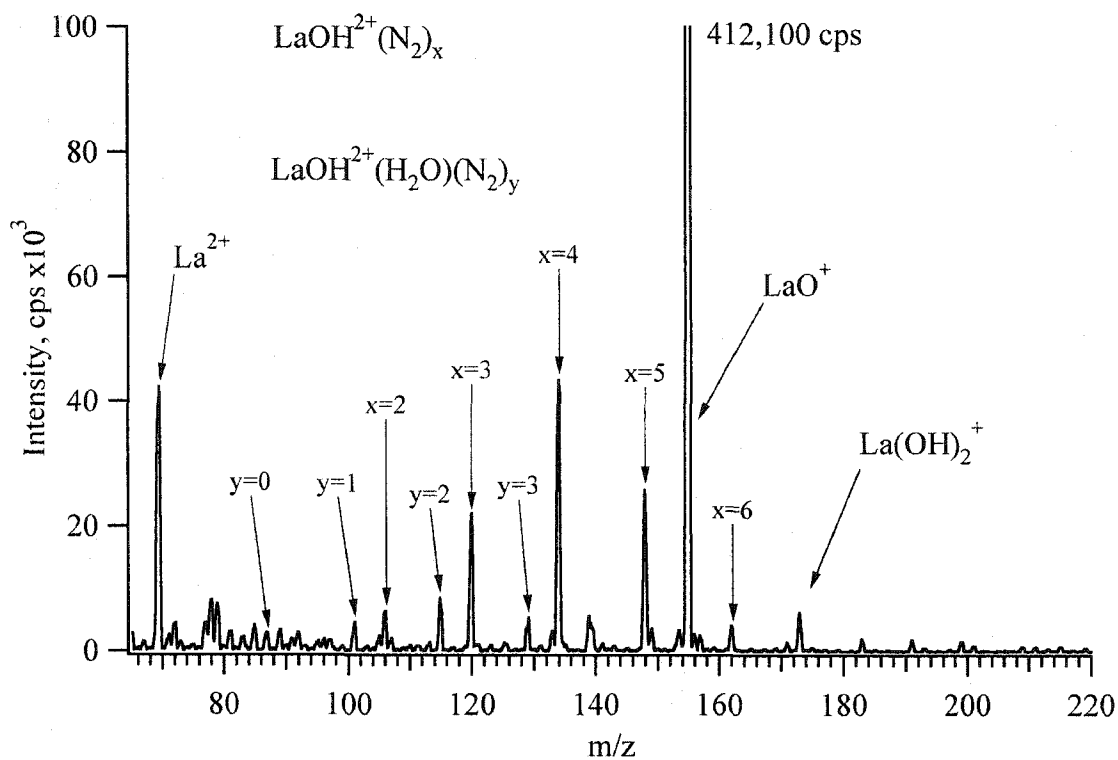


Figure 3.05 ESI-MS spectrum of a solution containing 0.1 mM LaCl_3 with 0.4 mM LiCl in 100% aqueous solvent. Spectra acquired at SPV = 100 V with N_2 curtain gas.

aqueous solvent. Perhaps these values do not take into account the activation energy required for the charge transfer to occur, or ignore the possible reaction pathways that may be needed to produce a bare M^{2+} ion. However, the general trend suggested by the second ionization potentials is correct in that the relative amount of M^{2+} observed is the lowest for Lu, relative to all the other lanthanides tested. The presence of low intensity signals for La^{2+} and Lu^{2+} in the methanolic solvent spectra may be due to the presence of water (5%) in the matrix. As has been observed previously with other cations, water is often observed in cation-solvent clusters when spraying methanolic solutions [1-4, 6]. This is likely due to the greater dielectric constant of water (78.5 @ 25 °C), and thus better charge insulating properties as compared to methanol (32.6 @ 25 °C) [14]. As the solvent is removed from the gas-phase ion cluster, perhaps a small percentage of the cations will have only water solvent ligands remaining (i.e., the same species as with water solvent).

The presence of another class of species was evident, as can be seen in Figure 3.04. All lanthanides tested exhibit various amounts of what appear to be $M^{2+}(N_2)_x$ gas adducts, with the number of nitrogen ligands ranging from $x = 1$ to 6. Similar adducts were also observed under milder sampling conditions, as shown in Figure 3.05 (SPV = 100 V), where species attributed as $LaOH^{2+}(N_2)_x(H_2O)_y$ were observed. Since N_2 does not have a permanent dipole, it makes a poor ligand, and the observation of N_2 adducts was unexpected. As this mass spectrometer was formerly an ICP-MS, this instrument can scan to lower masses. When the low mass regions of the spectra were examined, several species corresponding to a corona discharge were evident, as illustrated in Figure 3.06. Under both sampling conditions, Nitrogen species dominate the low mass region of the spectrum. Under milder sampling conditions N_2H^+ dominates, whereas at higher declustering (SPV = 200 V) other species such as N_2^+ and $(N_2)_2^+$ are observed at significant levels. Since this was not observed with methanol, the operation of the aqueous sprayer interface is likely responsible. When using CO_2 as a bath gas for aqueous ESI, it has been suggested that a corona is required for successful operation [17, 18]. With a CO_2 corona, it is possible to form CO [19], which also has a mass of 28 Da. Since CO has a permanent dipole, it would be expected to readily form adducts with ions.

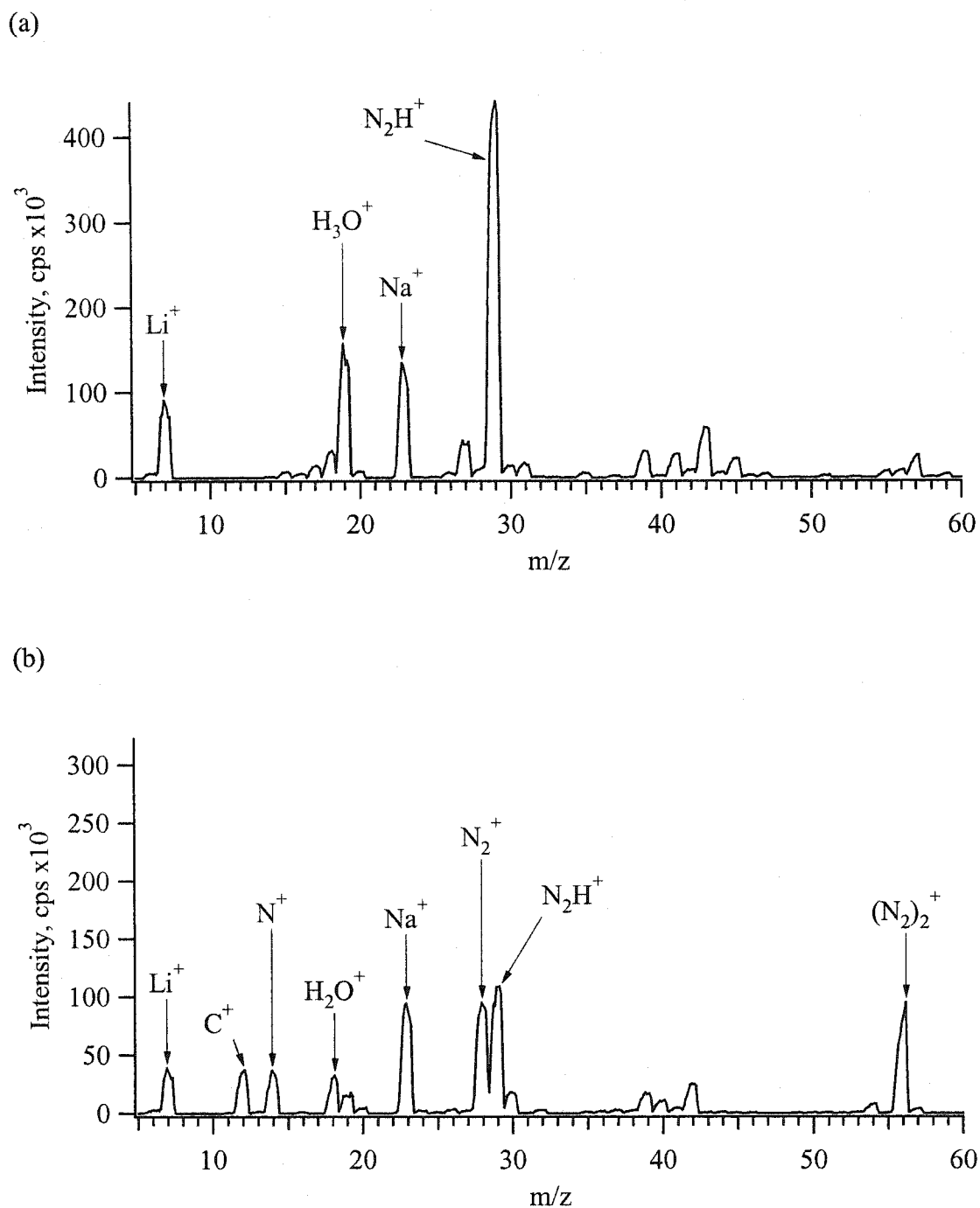
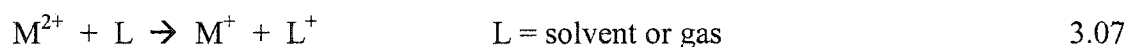
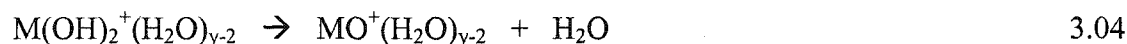
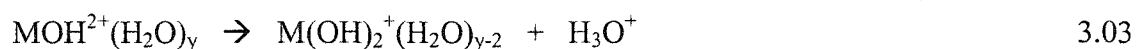


Figure 3.06 Low mass regions of the ESI-MS spectra of a solution containing 0.1 mM LaCl_3 with 0.4 mM LiCl in 100% aqueous solvent. Spectra acquired at (a) $\text{SPV} = 100 \text{ V}$ and (b) $\text{SPV} = 200 \text{ V}$ with N_2 curtain gas.

However, when O₂ was used as the curtain gas, M²⁺ lanthanides were observed as adducts with ligands of a nominal mass of 32 Da, suggesting that O₂ was the ligand. As such, the M²⁺ adducts observed with N₂ curtain gas are assigned as N₂ adducts, although the ligand identity was not confirmed.

3.3.3 Comparison of Species Generation with Aqueous and Methanol Solvent

The signal intensity of major metal species as a function of the sampling plate voltage used for La, Eu, and Lu in both methanolic and aqueous solvents can be found as Figure 3.07. Most elements tend to show curves similar to La and Lu, with Eu and Yb being two notable exceptions. For most lanthanides, MO⁺ was the first major species to be observed under the high energy CID conditions. As the SPV was increased, the intensity of the MO⁺ species decreased, presumably due to the CID breakup of the M⁺-O bond. For most lanthanides in the aqueous matrix, the next species observed was M²⁺, closely followed by M⁺ as the SPV was increased. At lower voltages, oxides dominated, whereas at high voltages (> 350 V), oxides were very low. At intermediate voltages (150 - 250 V) a mixture of MO⁺, M²⁺, and M⁺ was observed. Equations 3.03 to 3.07 propose some of the possible reaction pathways, which may generate the observed species when using water solvent.



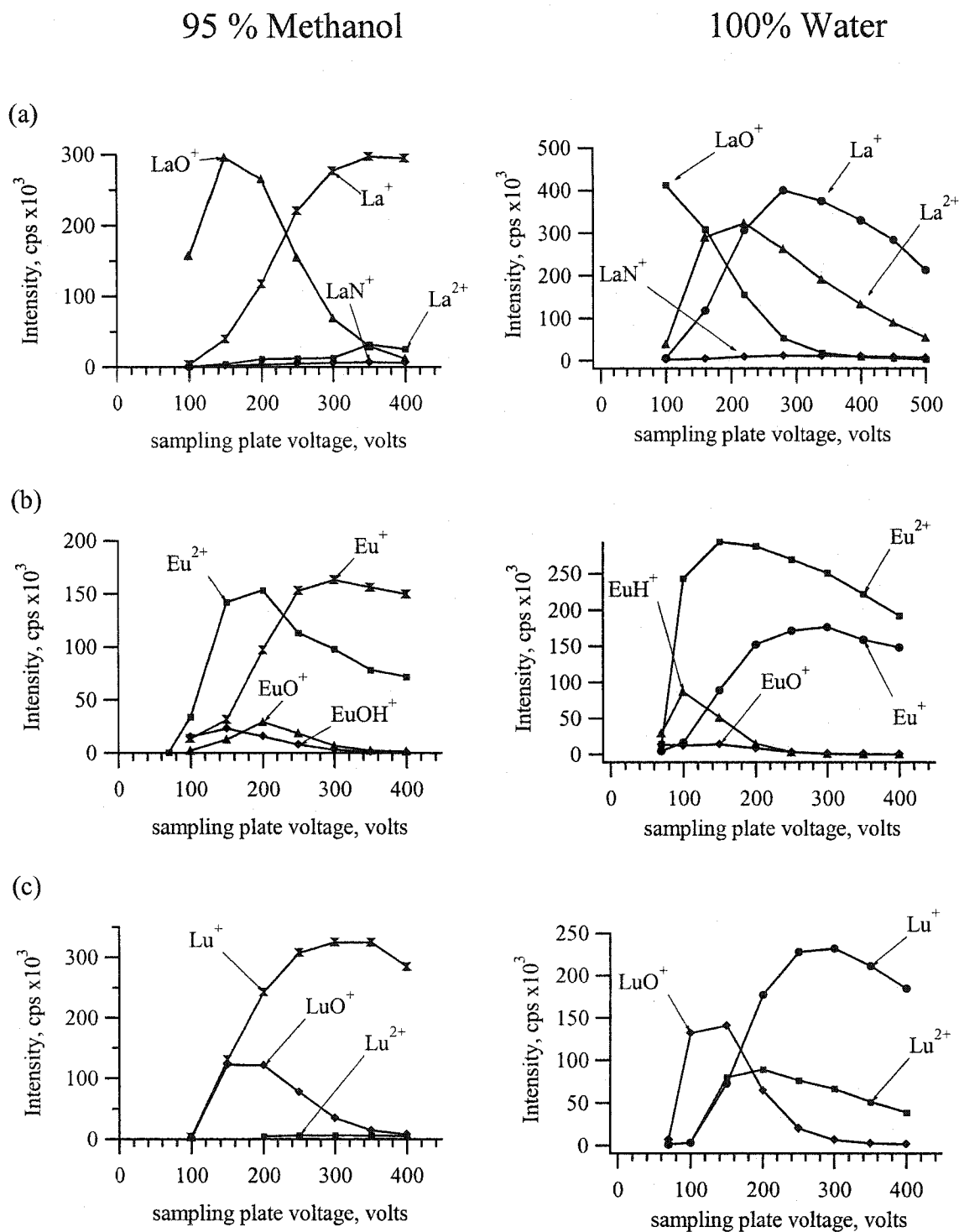
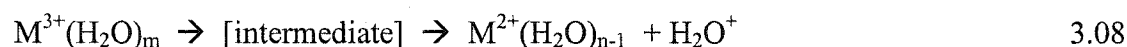


Figure 3.07 Signal intensity as a function of sampling plate voltage with N_2 curtain gas for a sample containing 0.1 mM Ln salt and 0.4 mM LiCl in 95% methanol, 5% water or 100% aqueous solvent; (a) $LaCl_3$, (b) $Eu(NO_3)_3$, (c) $LuCl_3$.

These equations suggest that M^{2+} may form directly from MO^+ . Due to the presence of a corona discharge, it is conceivable that M^{2+} forms via positively charged gas removing an electron from M^+ . The ionization potentials of N_2 (15.6 eV), O_2 (12.1 eV) and CO_2 (13.4 eV) are greater than most of the IP_{II} of the lanthanides (Table 3.01), so removal of an electron from M^+ to form M^{2+} may be favored in the presence of a corona discharge.

The SPV curves in Figure 3.07 show that Eu behaves differently than La and Lu. For Eu, the oxides are low at all SPV tested, in both methanol and water. This seems to suggest that Eu^{2+} and Eu^+ do not form through a stable EuO^+ intermediate, as the other lanthanides seem to do. For Eu, perhaps the M^{3+} species is able to remove an electron from the solvent (either methanol or water) without needing to form a M-O bond, as proposed in Equation 3.08.



3.3.4 Aqueous ESI Reproducibility

One issue with ESI is the reproducibility. Figure 3.08 shows spectra for a $LaCl_3$ solution acquired on different days under, presumably, the same sampling conditions. The relative abundance and type of clusters observed has slightly changed under these CID conditions (SPV = 100 V), but the relative intensity of the LaO^+ species was similar for both days. To further investigate the cause of this, the curtain flow rates were varied (175, 300, and 450 mL/min), and the resultant spectra are presented in Figure 3.09. As the curtain gas flow was increased to higher values, it was found that the gas adduct species were shifted to a higher number of N_2 molecules, and the La^{2+} species becomes evident. Since the MS interface voltages were the same, and the electrospray conditions were constant, it seems that the observed differences were the result of enhanced desolvation due to higher curtain gas flow. Note that at low curtain gas flows, a gas adduct with CO_2 is present. The CO_2 was likely from the bath gas used at the ESI tip that has entered the CID region at low curtain gas flow rates. These results also indicate a possible reason for the day-to-day variation as demonstrated in Figure 3.08. However,

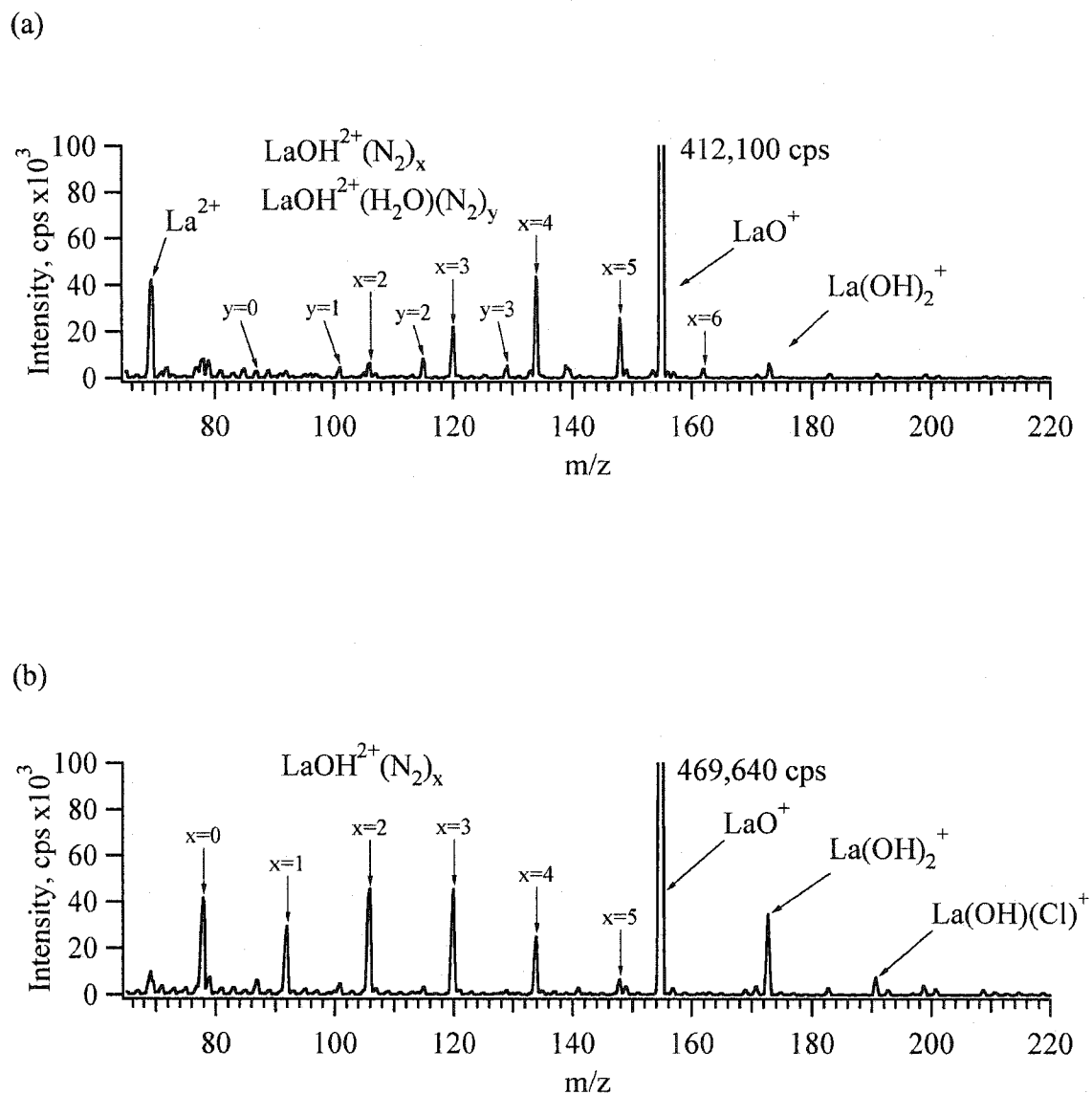


Figure 3.08 ESI-MS spectra from 2 different days, acquired under identical MS interface conditions (N_2 curtain @ 300 mL/min, SPV = 100 V). Differences in clusters likely reflect differences in ESI performance and / or solution differences. Solution contained 0.1 mM LaCl_3 with 0.4 mM LiCl in 100% aqueous solvent; (a) day 1, (b) day 2.

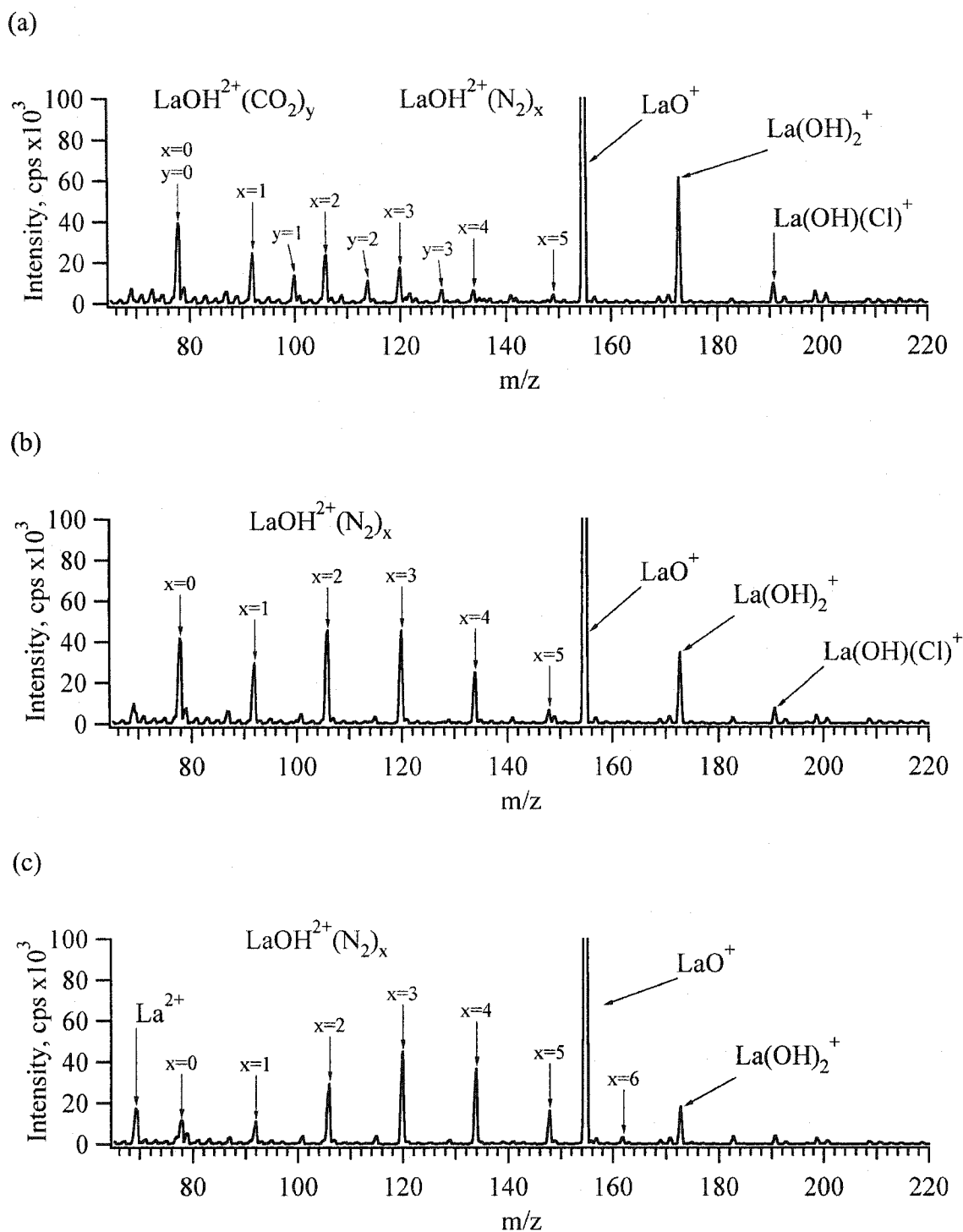


Figure 3.09 ESI-MS spectra of solutions containing 0.1 mM LaCl_3 with 0.4 mM LiCl in 100% aqueous solvent at different N_2 curtain gas flow rates. SPV = 100 V. Curtain gas flow rates: a) 175 mL/min, b) 300 mL/min, c) 450 mL/min.

the performance is arguably similar, and can be tuned to provide the required performance. The similar intensities of the LaO^+ species each day suggests that the ion yield was similar, with only minor differences in desolvation efficiency.

3.3.5 High CID Sampling

Since the MS interface region was an in-house design, the insulation of the sampling plate was easily modified. By improving the insulation of each component, higher voltages were possible here than could be previously utilized. While the design was similar to a Sciex API interface, a commercial ESI-MS instrument (such as the Sciex API) can only be set for a voltage difference between the sampling plate and the skimmer of 200 V. In contrast, our interface could be set to voltage differences of over 500 V in positive polarity. The spectra at $\text{SPV} = 350$ V of the same solutions with methanol and 100% water solvents are shown in Figure 3.10 and 3.11, respectively. At this higher CID potential, it is evident that fewer species were observable for these elements and that the methanolic and aqueous spectra are very similar. Using the higher CID potential, it seems that the energy is sufficient to break the majority of $\text{M}^+\text{-O}$ bonds for all of the lanthanides. With the methanol solvent, the dominant species here is the M^+ ion, with minor contributions from M^{2+} , MO^+ and MN^+ . With aqueous solvent, significant M^{2+} is still present, even for Lu. These "bare metal ion mode" spectra were much more similar to ICP-MS than with previous work. Further increases in the SPV (up to 500 V) were examined, but it was decided that the losses in M^{2+} and M^+ signal intensity were too much relative to the reduction in MO^+ peak intensity to be advantageous.

Under these very vigorous sampling conditions, several different ions can be observed at the low mass end, as the spectrum in Figure 3.12(a) demonstrates. As discussed earlier, different ions due to ionization and fragmentation of the nitrogen curtain gas are evident, including N^+ , N_2^+ , N_3^+ , and $(\text{N}_2)_2^+$. Also, peaks due to Li^+ , Na^+ , and H_2O^+ are also evident. If the baseline of this spectrum is examined (Figure 3.12 (b)), the low mass region of the spectrum is still not free from the chemical noise background observed at lower SPV settings. However, at m/z greater than 60, the spectral

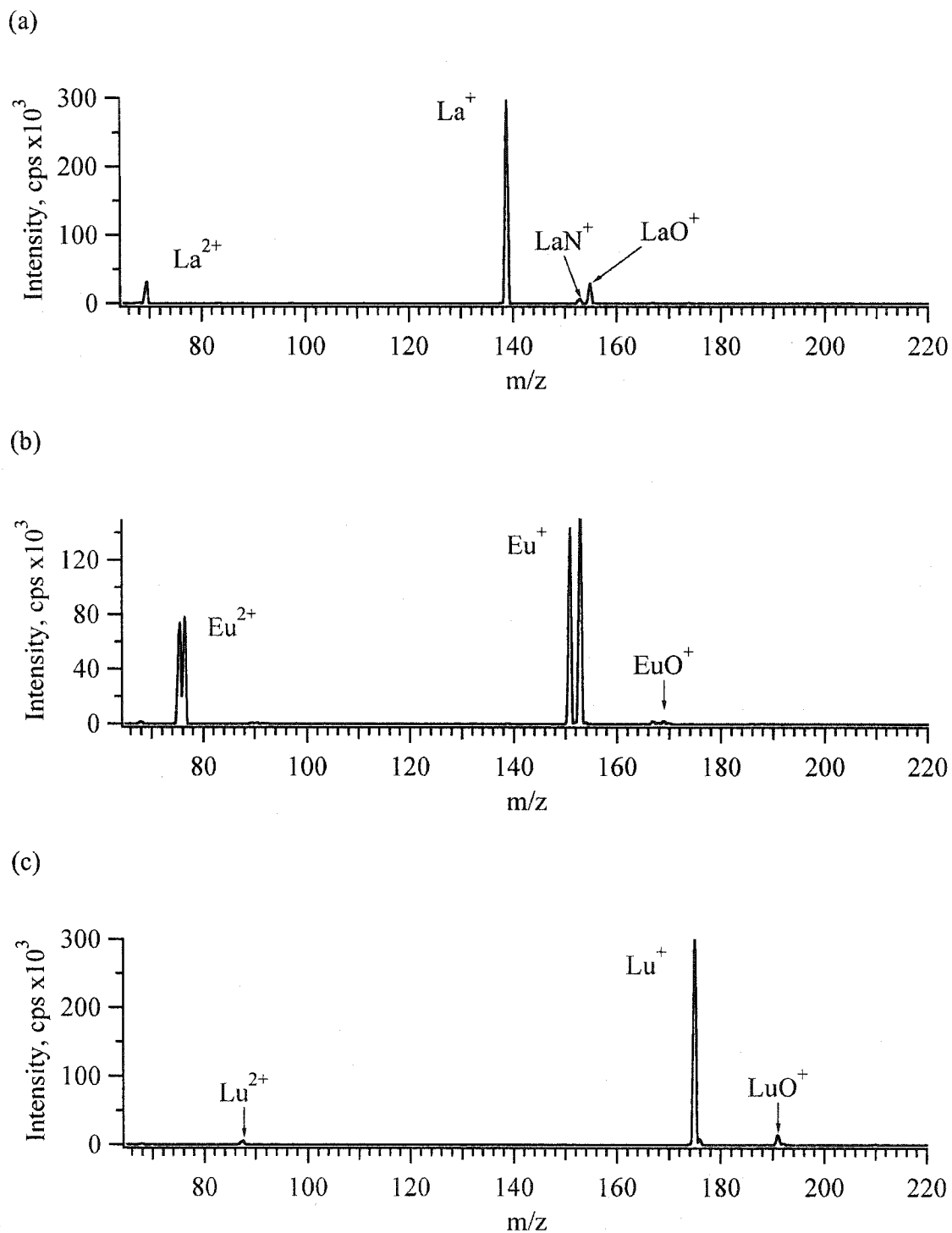


Figure 3.10 ESI-MS spectra of solutions containing 0.1 mM Ln salt and 0.4 mM LiCl in 95% methanol, 5% water matrix. Spectra acquired at a SPV = 350 V; (a) LaCl_3 , (b) $\text{Eu}(\text{NO}_3)_3$, (c) LuCl_3 .

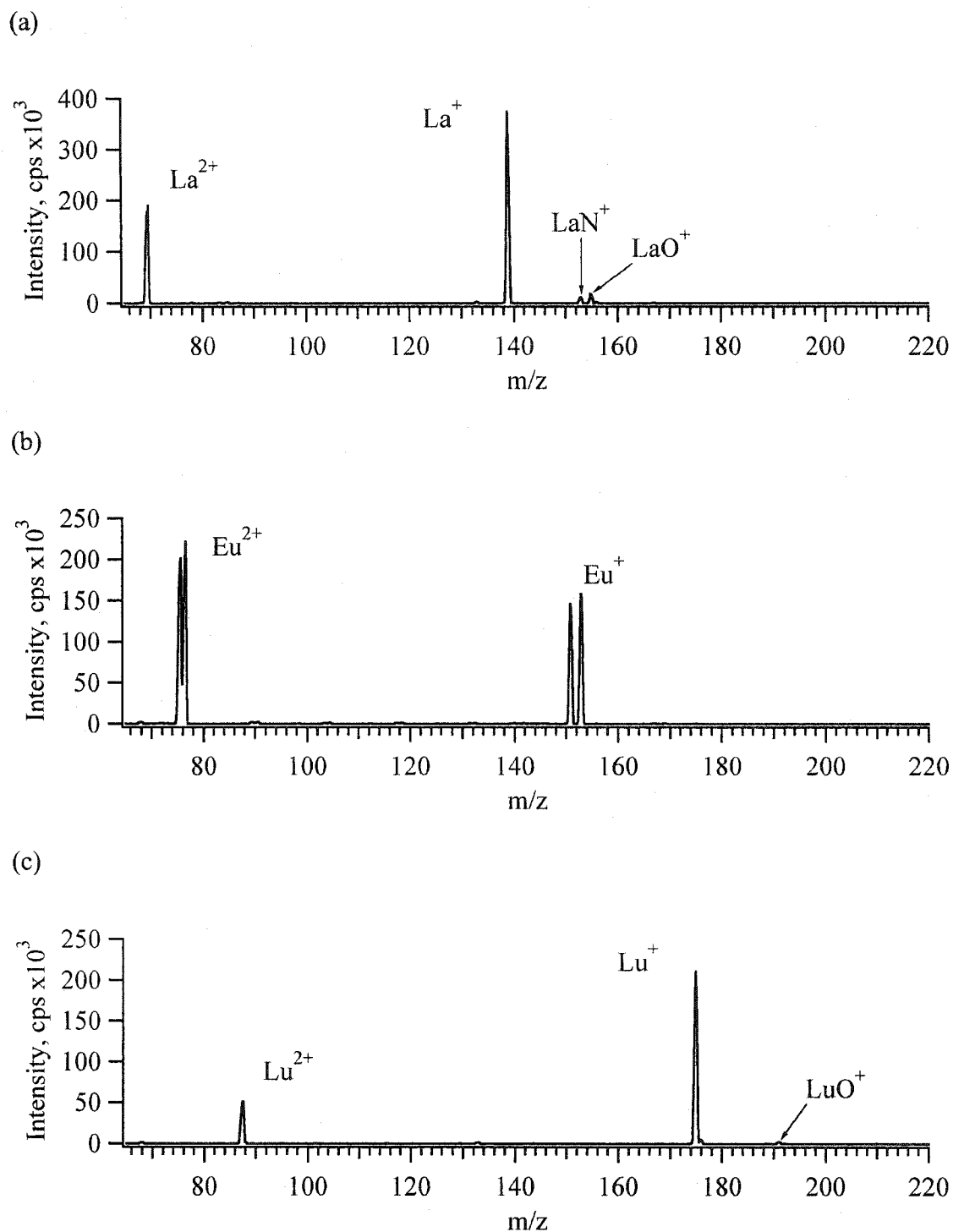


Figure 3.11 ESI-MS spectrum of solutions containing 0.1 mM Ln salt and 0.4 mM LiCl in purely aqueous solvent. Spectra were acquired at a sampling plate voltage of 350 V; (a) LaCl_3 , (b) $\text{Eu}(\text{NO}_3)_3$, (c) LuCl_3 .

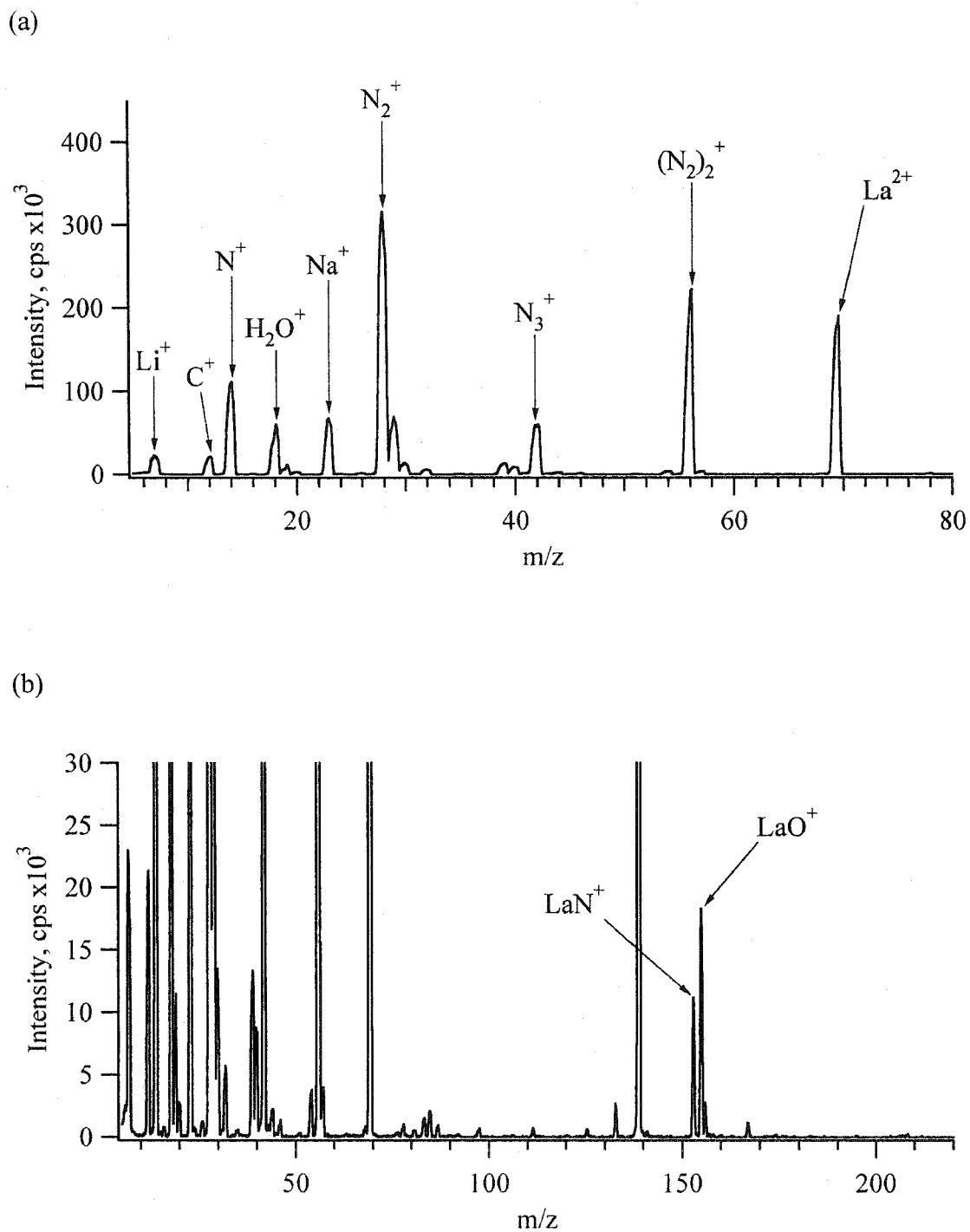


Figure 3.12 (a) Low mass region of the spectrum in Figure 3.11 (a); (b) same spectrum as in Figure 3.11 (a), but with wider mass range and expanded intensity axis to show the baseline species.

background is much better, since the high CID conditions serve to break up these molecules and clusters normally observed at these masses at lower SPV.

3.3.6 Ln Spectra Using a Commercial Interface

For the purpose for comparison, La and Eu salts were run using 95% methanol, 5% water solvent, on a HP 1100 Series LC/MSD. The commercial electrospray source for this instrument was used, and spectra at several different declustering settings were acquired. This instrument has dual skimmers to which a potential difference can be applied to induce CID. Figure 3.13 shows the mass spectra acquired at a $\Delta V = 200$ V for (a) 0.1 mM LaCl_3 with 0.4 mM LiCl in 95% methanol, and (b) 0.1 mM $\text{Eu}(\text{NO}_3)_3$ with 0.4 mM LiCl in 95% methanol. While these spectra are similar to those in Figure 3.03, some obvious differences exist. With the HP, the doubly-charged species were not observed for either La or Eu. For La, only LaO^+ was observed on the HP instrument, and further increases to the voltage difference (up to 400 V) did not produce any significant levels of La^+ . For Eu, no evidence of Eu^{2+} or EuH^+ was observed on the HP.

3.3.7 Implications for Speciation and Quantification

Thus far, the study of the lanthanide series has demonstrated that aqueous sampling does not suffer signal losses relative to methanolic solutions. So, provided that the concentration of ions in a given sample can be electrosprayed, dilution with a volatile organic solvent is not required. Also, by using water solvent, higher charge states may be observed for these elements, with fewer anion adducts to complicate the observed spectrum. Both the ability to analyze an aqueous sample and the fewer adducts observed provide an improved system for the analysis of these species. Insight into the solution valence state can be obtained using relatively mild sampling conditions, and the elemental composition may be more clearly determined using more vigorous CID conditions. It is evident that the CID conditions selected can have a significant impact on the observed species, and the species observed in an aqueous matrix mass spectrum can

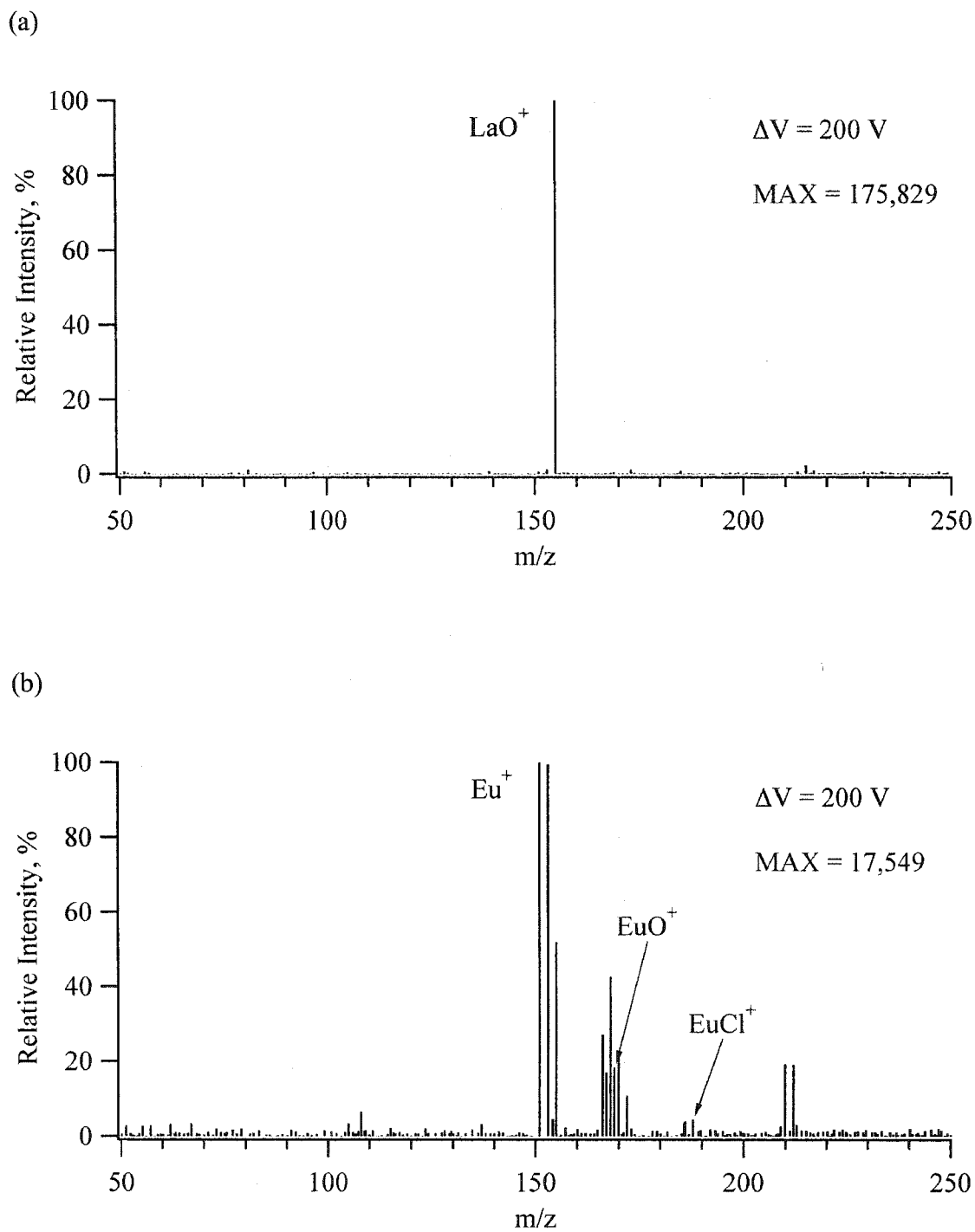


Figure 3.13 Ln salts in 95% methanol (5% water) acquired on a HP1100 Series LC/MSD. (a) 0.1 mM LaCl_3 with 0.4 mM LiCl ; (b) 0.1 mM $\text{Eu}(\text{NO}_3)_3$ with 0.1 mM LiCl .

be very different as compared to a methanolic one. The obvious concerns here are the sensitivity and interferences of the method.

Although the different sampling conditions used represent an improvement in the spectral quality as compared to previous studies, the oxides interference was not totally removed, as illustrated in Figure 3.14. Figure 3.14 shows mass spectra of a mixture of Pr, Gd, and Lu acquired at two different sampling plate voltages using 100% water solvent. The spectrum at 200 V (Figure 3.14 (a)) looks very similar to previous work in methanolic solvent [8], except that these data have a more intense signal and fewer anion adducts (as described earlier). Obviously, the oxides dominate at this SPV. The mass spectrum in Figure 3.14 (b) is for the same solution acquired with a SPV = 350 V. The oxides were much lower, and the spectra more closely approximate correct isotopic ratios. All of the lanthanides were examined under these sampling conditions, and Gadolinium was found to have the highest ratio of oxides. For the spectrum in Figure 3.14 (b), the relative amount of $\text{GdO}^+ / \text{Gd}^+$ was 4.7%. As a comparison, $\text{LuO}^+ / \text{Lu}^+$ was 1.2%. So, under these harsh sampling conditions, the spectra exhibit oxide levels comparable to typical ICP-MS determinations. This Elan 250 ICP-MS instrument, when new, produced a signal of about 286,000 cps for a $[\text{La}] = 0.02 \text{ mM}$ [20]. For the purposes of comparison, the ICP-MS would, hypothetically, produce a signal of about 1.4 million cps for a $[\text{La}] = 0.1 \text{ mM}$. In this study, a $[\text{La}] = 0.1 \text{ mM}$ produced about 400,000 cps at M^+ and 200,000 cps at M^{2+} . So, the analytical signals produced with our ES-MS system are roughly one-fourth of the intensity of signals produced by a similar ICP-MS.

With aqueous sampling, M^{2+} could be used to get isotopic peaks without interference from oxides, as shown in Figure 3.15. This is the same solution as in Figure 3.14, but the instrument resolution has been changed to $\sim 0.6 \text{ amu}$ (at 10% peak height). The M^{2+} species isotopes are well-resolved, and the ratios appear correct. The obvious absence of MO^{2+} species make these isotopes free from the oxide interferences observed earlier. The potential of gas adducts is still a problem, as demonstrated by the $\text{Gd}(\text{N}_2)^{2+}$ species observed. However, the potential interferences have changed. For the singly charged case, GdO^+ interferes with Lu^+ analysis, but the $\text{Gd}(\text{N}_2)^{2+}$ adduct does not

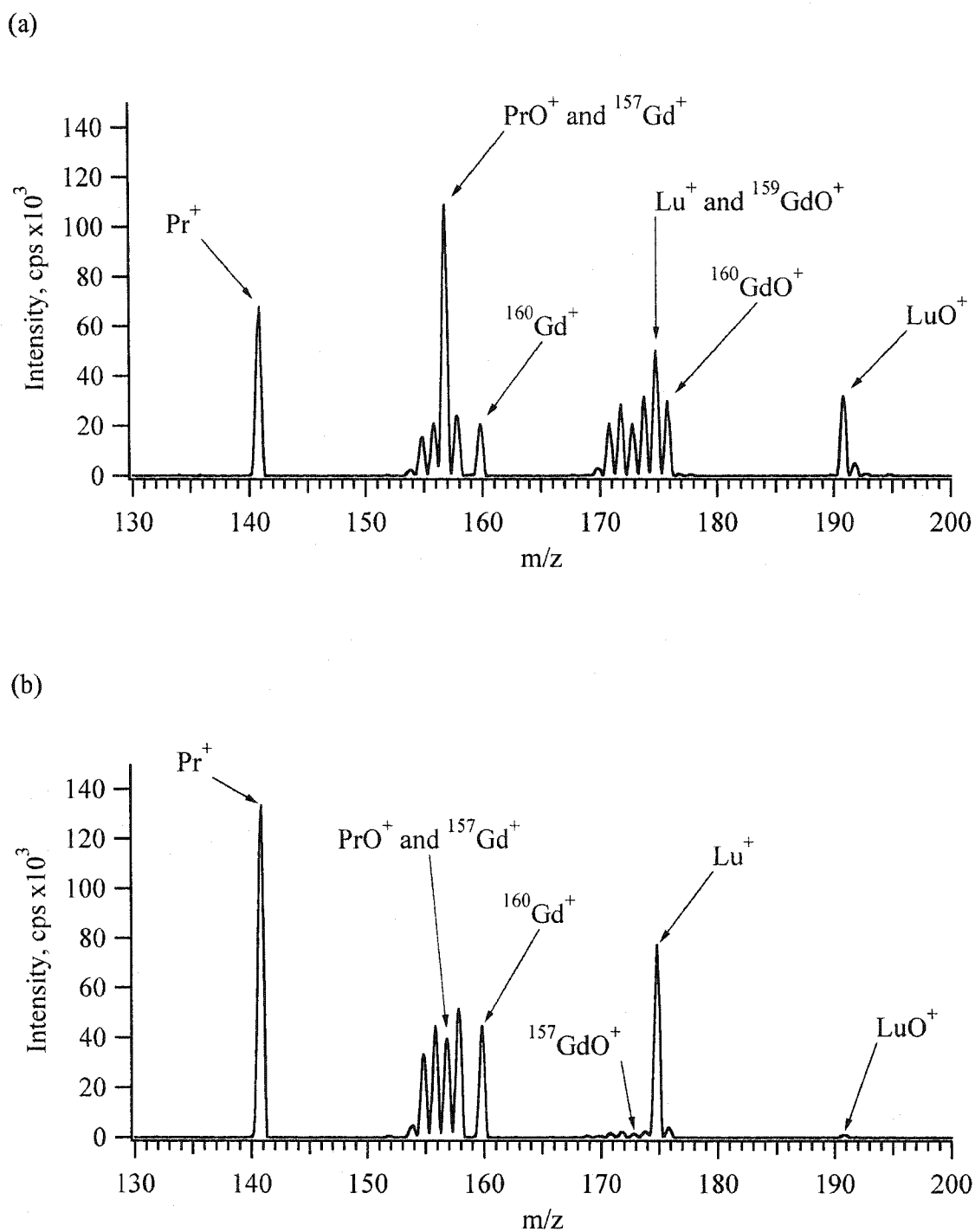


Figure 3.14 ESI-MS spectra of a solution containing 0.1 mM $\text{Pr}(\text{NO}_3)_3$, 0.1 mM LuCl_3 , and 0.2 mM GdCl_3 in 100% water solvent using N_2 curtain gas; (a) SPV = 200 V, (b) SPV = 350 V.

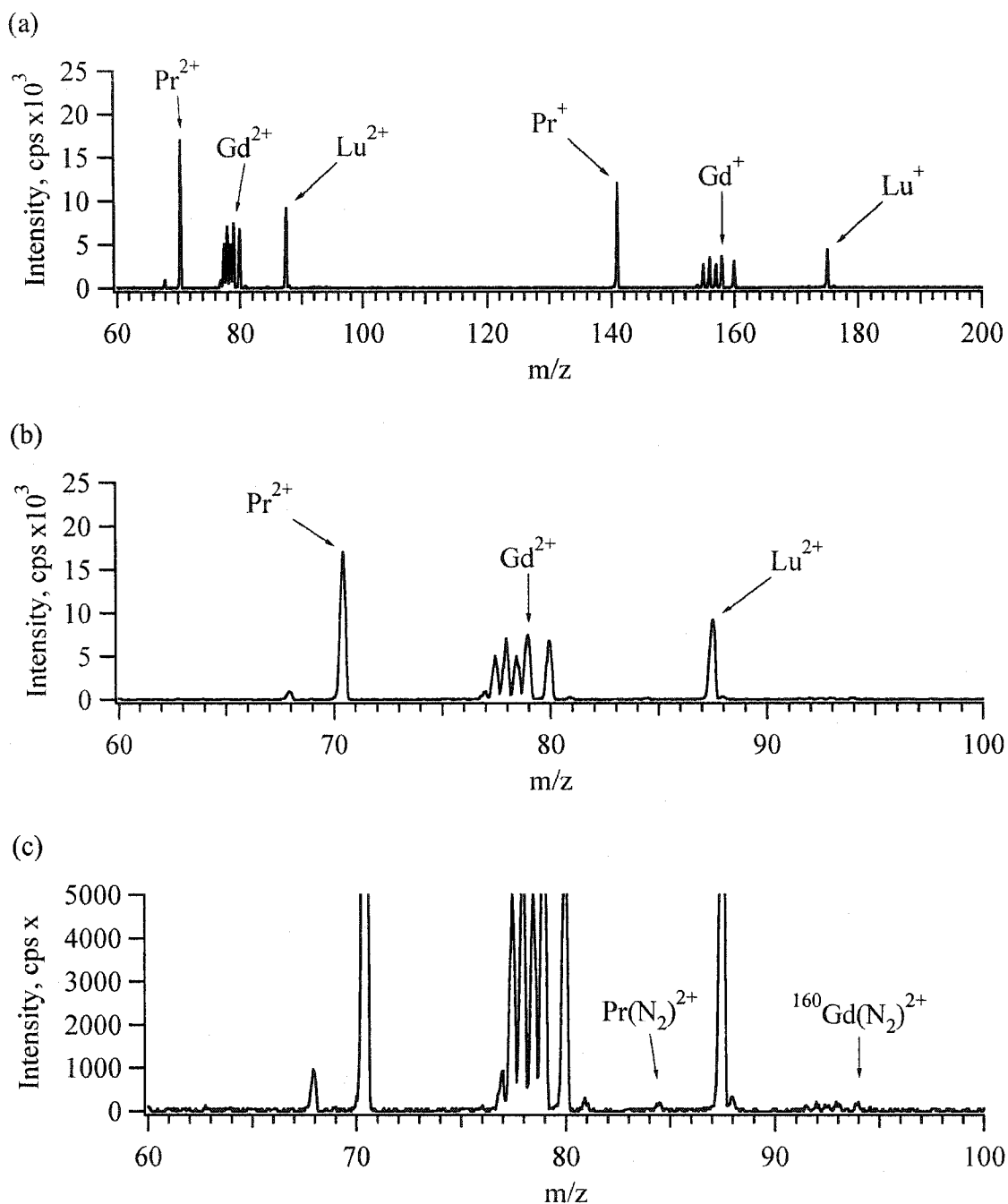


Figure 3.15 High resolution quadrupole ($R \sim 0.6$ amu) ESI-MS spectra of a solution containing 0.1 mM $\text{Pr}(\text{NO}_3)_3$, 0.1 mM LuCl_3 , and 0.2 mM GdCl_3 in 100% water solvent using N_2 curtain gas and $\text{SPV} = 350\text{V}$; (a) full spectrum, (b) doubly-charged region, (c) same as in (b) with expanded intensity axis to show the baseline species.

interfere with the Lu^{2+} spectrum. Similarly, LaO^+ would interfere with Gd^+ analysis, but the $\text{La}(\text{N}_2)^{2+}$ peak would interfere with Er^{2+} determination. Using the M^{2+} peaks, only elements with isotopes of 147 or less (i.e., La, Ce, Pr, Nd, and Sm) will potentially cause gas adduct interferences with heavier lanthanides. However, this region of the spectrum (m/z 69 - 90) is not free from peaks in positive mode. Under "bare metal ion mode" conditions, the species that we might expect here would be elements such as Rb, Sr, Y, and Zr. Other elements, such as As and Se may also interfere, provided the chemical species was a cation in solution. So, this is not a strong analytical option for these species without some form of species separation prior to ES sampling (i.e., chromatography). One benefit, however, is that the detection of the lanthanides could be done independent of chromatographic separation of the lanthanides themselves, since the combination of M^{2+} and M^+ spectra could provide relatively interference-free detection, provided that these species were successfully separated from the other mentioned cations. One obvious disadvantage with this mode of detection is the reduction in signal intensity to about one-tenth described earlier due to the compromise in ion throughput with operating the quadrupole at higher resolution.

3.3.8 Oxygen Curtain Gas

Another possibility for resolving potential oxide interference is to induce the formation of oxides. Using a dynamic reaction cell (DRC) with ICP-MS, reports using oxygen to promote oxidation of interfering species to higher oxides to resolve isobaric overlap has been reported [21]. To examine if this could be applied here, oxygen was used as the curtain gas in ESI-MS experiments. As with nitrogen, spectra for all of the lanthanides were acquired at a range of declustering potentials. As before, La, Eu, and Lu were representative of the entire lanthanide series. Mass spectra of La, Eu, and Lu using oxygen curtain gas and a $\text{SPV} = 350$ V are presented in Figure 3.16. As with nitrogen, most of the lanthanides were similar to La and Lu. The major species observed was LnO^+ , with some signal for M^{2+} . Although sufficient energy is supplied to break the oxides, since the target gas is oxygen, any intermediate likely quickly re-forms the oxide. Eu (and Yb) exhibited a mixture of species under these conditions, including intense

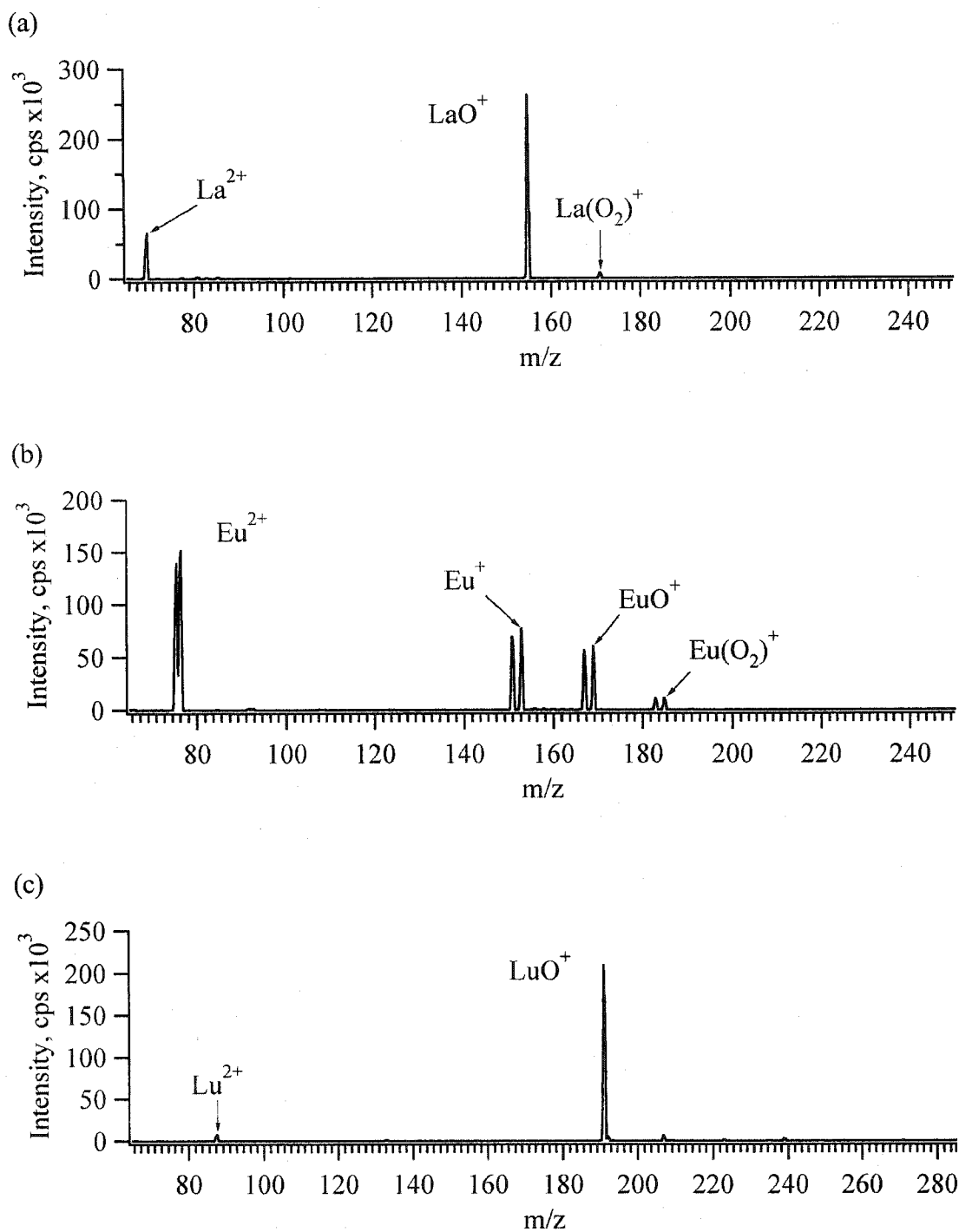


Figure 3.16 0.1 mM Lanthanide salt and 0.4 mM LiCl in 100% water matrix, using O_2 curtain gas, SPV = 350 V. (a) LaCl_3 , (b) $\text{Eu}(\text{NO}_3)_3$, (c) LuCl_3 .

signals for M^{2+} , M^+ , MO^+ , and even $M(O_2)^+$. For these two species, full conversion to the oxides was not possible. This is likely due to the relatively low second ionization potentials of these elements, and the relatively weak MO^+ bonds that may form. With a tendency to form M^{2+} , these elements can then readily undergo charge reduction to form M^+ , similar to that proposed in Equation 3.05.

While all of the lanthanides were also examined at lower CID potentials, the high voltage condition provided the lowest levels of the gas adducts. Figure 3.17 shows the same mass spectra as shown in Figure 3.16, with the intensity scale expanded to better show the baseline species. Under these conditions, gas adducts of both the M^{2+} and the MO^+ species were observed, similar to the results using nitrogen. Also, even under these conditions, the higher lanthanides produced low levels of M^+ , as illustrated by the Lu spectrum in Figure 3.17 (c). The presence of these intense gas adducts and the persistence of M^+ for the higher lanthanides make this approach less advantageous as compared to using only nitrogen.

3.4 Conclusions

In terms of signal intensity, the aqueous ESI interface was demonstrated to provide signals similar to using methanol. However, using a purely aqueous solvent can result in some significant differences in the mass spectra of the lanthanides, as compared to methanol solvent. Most significant was that the aqueous solvent tended to preserve a higher charge on the metal, likely due to the higher ionization potential of the water ligands, as compared to methanol. The presence of nitrogen gas adducts across a range of CID conditions was observed, although the origins and significance of these species need to be further investigated.

The MS interface used was shown to provide sampling conditions vigorous enough to reduce the observed oxides for all of the lanthanides to less than 5%, without much compromise in signal intensity. These operating conditions provide an improved

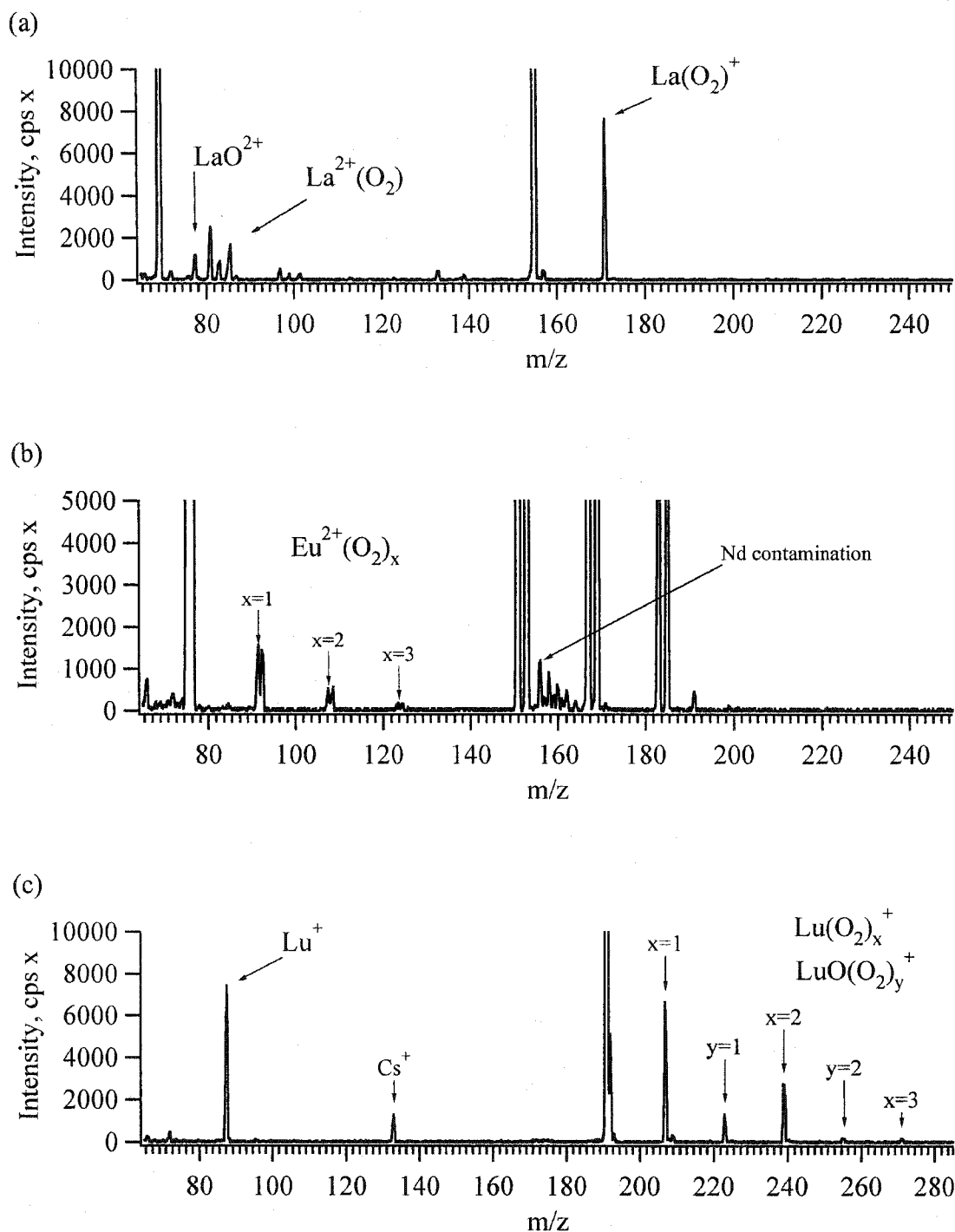


Figure 3.17 0.1 mM Lanthanide salt and 0.4 mM LiCl in 100% water matrix, using O_2 curtain gas, SPV = 350 V. Same spectra as Figure 3.16, with intensity axis expanded to show the baseline species. (a) LaCl_3 , (b) $\text{Eu}(\text{NO}_3)_3$, (c) LuCl_3 .

“metal ion mode” of operation for electrospray, as compared to previous studies. The combination of aqueous sampling and vigorous CID conditions presents an analytical option for these analytes, where elemental information of the solution species is desired.

3.5 References

1. Blades, A. T.; Jayaweera, P.; Ikonomou, M. G.; Kebarle, P. "First studies of the gas phase ion chemistry of M^{3+} metal ion ligands"; *Int. J. Mass. Spectrom. Ion Proc.* **1990**, 101, 325-336.
2. Blades, A. T.; Jayaweera, P.; Ikonomou, M. G.; Kebarle, P. "Ion-molecule clusters involving doubly charged metal ions (M^{2+})"; *Int. J. Mass Spectrom. Ion Proc.* **1990**, 102, 251-267.
3. Blades, A. T.; Jayaweera, P.; Ikonomou, M. G.; Kebarle, P. "Studies of alkaline earth and transition metal M^{++} gas phase ion chemistry"; *J. Chem. Phys.* **1990**, 92, 5900-5906.
4. Agnes, G. R.; Horlick, G. "Effect of operating parameters on analyte signals in elemental electrospray mass spectrometry"; *Appl. Spectros.* **1995**, 49, 324-334.
5. Agnes, G. R.; Horlick, G. "Determination of solution ions by electrospray mass spectrometry"; *Appl. Spectros.* **1994**, 48, 655-661.
6. Agnes, G. R.; Stewart, I. I.; Horlick, G. "Elemental speciation measurements with electrospray mass spectrometry: An assessment"; *Appl. Spectros.* **1994**, 11, 1347-1359.
7. Stewart, I. I.; Horlick, G. "Investigations into chromium speciation by electrospray mass spectrometry"; *J. Anal. Atom. Spectrom.* **1996**, 11, 1203-1214.
8. Stewart, I. I.; Horlick, G. "Electrospray mass spectra of lanthanides"; *Anal. Chem.* **1994**, 66, 3983-3993.
9. Konig, S.; Fales, H. M.; Haegele, K. D. "Comment on the cylindrical capacitor electrospray interface"; *Anal. Chem.* **1998**, 70, 4453-4455.
10. Wang, H.; Hackett, M. "Ionization within a cylindrical capacitor: Electrospray without an externally applied high voltage"; *Anal. Chem.* **1998**, 70, 205-212.
11. Meyer, G. "Reduced halides of the rare-earth elements"; *Chem. Rev.* **1988**, 88, 93-107.
12. Cheng, Z. L.; Siu, K. W. M.; Guevremont, R.; Berman, S. S. "Solvent-derived metal oxides in electrospray mass spectrometry of metal salt solutions"; *Org. Mass Spectrom.* **1992**, 27, 1370-1376.

13. Wilm, M.; Mann, M. "Analytical properties of the nanoelectrospray ion source"; *Anal. Chem.* **1996**, 68, 1-8.
14. *CRC Handbook of Chemistry and Physics*; CRC Press: Boca Raton, FL, 1993.
15. Murad, E.; Hilderbrand, D. L. "Dissociation energies of GdO, HoO, ErO, TmO, and LuO; correlation of results for the lanthanide monoxide species."; *J. Chem. Phys.* **1980**, 73, 4005-4011.
16. Huheey, J. E.; Keiter, E. A.; Keiter, R. L. *Inorganic Chemistry: Principles of Structure and Reactivity*, 4th ed.; Harper Collins College Publishers: New York, 1993.
17. Tang, K.; Gomez, A. "Generation of monodisperse water droplets from electrosprays in a corona-assisted cone-jet mode"; *J. Colloid Interface Sci.* **1995**, 175, 326-332.
18. Tang, K.; Smith, R. D. "Sensitivity enhancement of electrospray ionization-MS for aqueous solutions in the corona-assisted cone-jet mode"; *Int. J. Mass Spectrom. Ion. Proc.* **1997**, 162, 69-76.
19. Morvova, M. "Dc corona discharges in CO₂-air and CO-air mixtures for various electrode materials"; *J. Phys. D: Appl. Phys.* **1998**, 31, 1865-1874.
20. Tan, S. Ph. D. Thesis, University of Alberta, Edmonton, Alberta, 1987.
21. Simpson, L. A.; Thomsen, M.; Alloway, B. J.; Parker, A. "A dynamic reaction cell (DRC) solution to oxide-based interferences in inductively coupled plasma mass spectrometry (ICP-MS) analysis of the noble metals"; *J. Anal. At. Spectros.* **2001**, 16, 1375-1380.

Chapter 4

An Introduction to High-Field Asymmetric Waveform Ion Mobility Spectrometry (FAIMS)

4.1 Objective

In the following sections, a relatively new type of ion mobility spectrometry (IMS) called high-field asymmetric waveform ion mobility spectrometry (FAIMS) is introduced and described. A brief history of the development of the technology will be presented, including comparisons to typical drift tube IMS. Basic theoretical concepts of operation will be presented and will be compared to an experimental description where possible. In order to better describe the operation of a FAIMS interface, basic concepts of how voltage and field vary with electrode geometry will be derived, and numerical modeling will be used for illustrative purposes to describe ion motion along field lines within the analyzer region. Hopefully, this section will serve as a good initial resource for information regarding current FAIMS theory and will facilitate the discussion of experimental data in the following chapters.

4.2 Introduction

Ion mobility spectrometry (IMS) was introduced as an analytical tool in the 1960s, and although this research field is over 40 years old, the elementary concepts are still unrefined [1]. Several different models for describing the motion of ions in a gas exist, and all are relatively complex and include several assumptions and approximations [2]. Discussion of the mathematical models is beyond the scope of this thesis; however, this section will introduce some basic concepts to highlight some of the variables that determine an ion's observed mobility. The book "Transport Properties of Ions in Gases" by Mason and McDaniel serves as the authoritative source of information regarding these theories and is referred to throughout the IMS literature in general [2].

4.3 What is IMS?

As a first step in the discussion of a new form of ion mobility spectrometry (IMS), basic concepts of classic IMS should be first introduced. In modern IMS, ion mobilities in the gas phase are determined by measuring their velocity as a result of a low applied field. A cartoon schematic of an IMS instrument is shown in Figure 4.01. The instrument consists of a sample inlet, an ionization region, an ion gate, a constant field drift tube, and an electrometer with associated electronics for signal handling. The system may be at atmospheric or reduced pressure, and the drift region is filled with a gas, which flows from the electrometer end towards the sample inlet. Classic IMS uses ion sources such as a corona needle or a radioactive source to generate sample ions from gas-phase sample molecules. The ions are then gated into the drift region as a pulse or packet of ions. As the ions are exposed to a force due to a constant field, E (~ 200 V/cm), the ions very rapidly accelerate to a terminal velocity and migrate against the flow of gas towards the lower field intensity at the end of the drift tube. When the ions strike the electrometer, a current proportional to the number of ions is generated. By monitoring the current as a function of time, a drift spectrum is recorded. Since the length (L) of the drift region is known and the ion arrival time (t) has been measured, the velocity of the ion can be determined (i.e., $v = L/t$). Ideally, different ions will have different velocity due to the applied field and arrive at the detector at different times. Using the ion's measured velocity, often referred to as the drift velocity, v_{drift} , the ion mobility, K , can be determined using Equation 4.01.

$$v_{\text{drift}} = KE \quad 4.01$$

The assumption is that at any low applied field, the ion mobility is a constant value, so the observed ion velocity varies linearly with the magnitude of the applied field. If more than one ion is generated from a sample vapor, hopefully the mobility of each ion (i.e., K) will differ enough that their time of arrival at the electrometer will be different, and a time-resolved spectrum will result. Overall, detection and identification of ions is based

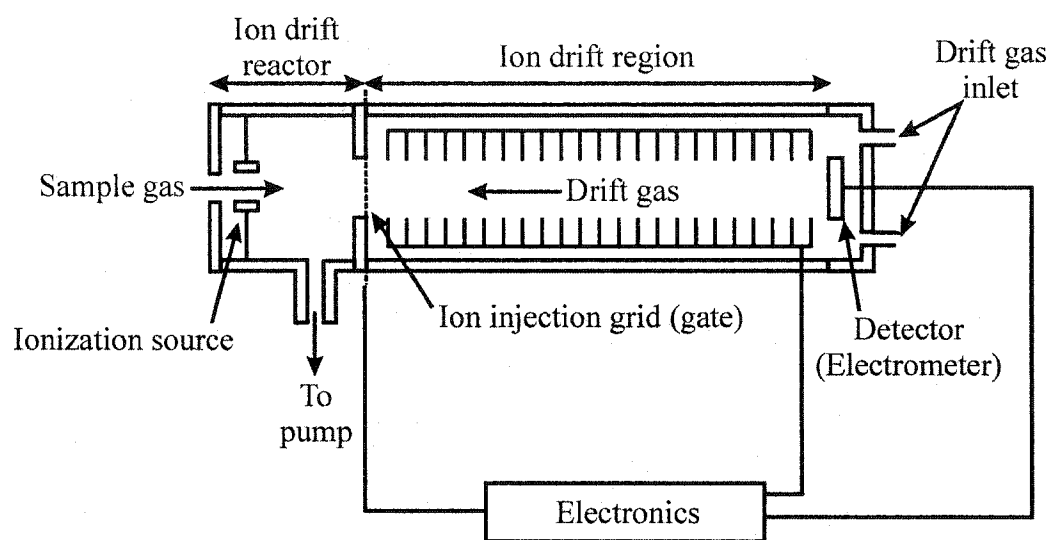


Figure 4.01 Schematic illustration of a drift tube ion mobility spectrometer.

on the assumption that ions exhibit a unique mobility and will have a constant, reproducible drift time under a constant applied low field.

Expanding on this concept is the use of IMS for the detection of a target compound in a mixture of ions. With the target compound exhibiting a drift time that is different from the others in the mixture, the presence or absence of that compound can be determined. The success of this method makes several assumptions: 1) the ion rapidly reaches terminal velocity so as to be insignificant to the assumption of a constant velocity, 2) the field in the drift region is constant, 3) the ion mobility is constant at the field applied, and that the mobility of each different ion is unique, and 4) adequate resolution of ions can be achieved.

4.4 Development of IMS

The development and implementation of IMS as an analytical tool has fundamental roots over 100 years old. In 1896, Röntgen observed that X-rays could cause gases to become electrically conducting [1]. Soon after, in 1897, Thompson and Rutherford observed that the product of the X-ray - gas interaction (i.e., ions) had a speed proportional to the field strength [1]. Arguably, these initial observations were the origins of gas phase ion chemistry. A few years later, the first real developments towards today's IMS were developed by Langevin in an effort to further characterize these gas-phase observations [1]. Langevin demonstrated that ionized air was a mixture of several chemical species, proposed a mathematical basis and chemical models for ion mobilities, and actually constructed a functional instrument [1]. Further development of IMS, by the research community was delayed due to interest in vacuum - based ion separations (i.e., mass spectrometry). A private company, Franklin GNO, developed an IMS spectrometer in the late 1960s. Soon after, a large amount of research the IMS field developed, largely due to the efforts of Karasek at the University of Waterloo in the late 1960s and early 1970s, using the instrument developed by Franklin GNO [1]. During this period, IMS was known as “plasma chromatography”, which likely led to some confusion for those

unfamiliar with the technique. Also, initial promises of low detection limits and simple operation were mired with difficulties related to the interpretation of the drift spectra of complex mixtures. As a result, interest in this field subsided until the 1980s, when military establishments realized the need for portable, sensitive means of detecting compounds such as chemical warfare agents [1]. For this class of analytes, IMS has found a niche application for which it has the best combination of detection ability and field portability. Other niche applications include screening passenger baggage for explosives and narcotics at airports. Still, relatively few IMS-only analyzers have reached common use. More recently, IMS-MS couplings have been re-investigated. One IMS-MS interface uses a segmented quadrupole for ion mobility separations, which operates at mTorr pressures and provides mobility-based separations with enhanced ion transmission efficiency [3]. From an applications standpoint, IMS has found renewed interest as a means for rapid separation of proteins prior to introduction to a MS [4-9]. So, while comprehensive models to describe the motion of ions in IMS are still under refinement, the applications of IMS are being investigated with renewed interest.

4.5 IMS at High Fields

Historically, drift tube IMS research has focused on the use of low fields ($E < \sim 200$ V/cm), since under these conditions, an ion's mobility is essentially constant [1, 2]. At higher applied fields, the mobility varies as a function of the field magnitude [2]. Expressing the change in mobility as a ratio of high-field mobility (K_h) to low-field mobility (K), K_h/K , an ion's experimental behavior can be classified into three general types, which are illustrated in Figure 4.02. As the applied field strength increases, an ion's mobility can either increase (type A), decrease (type C), or show a more complex behavior (type B). This adds another level of complexity to interpreting the drift spectrum and complicates ion modeling. It is likely due to these added complications that high-field IMS studies were never pursued to the same extent as the low-field studies [2]. The possible factors that dictate why these ions exhibit these behaviors will be discussed in later sections.

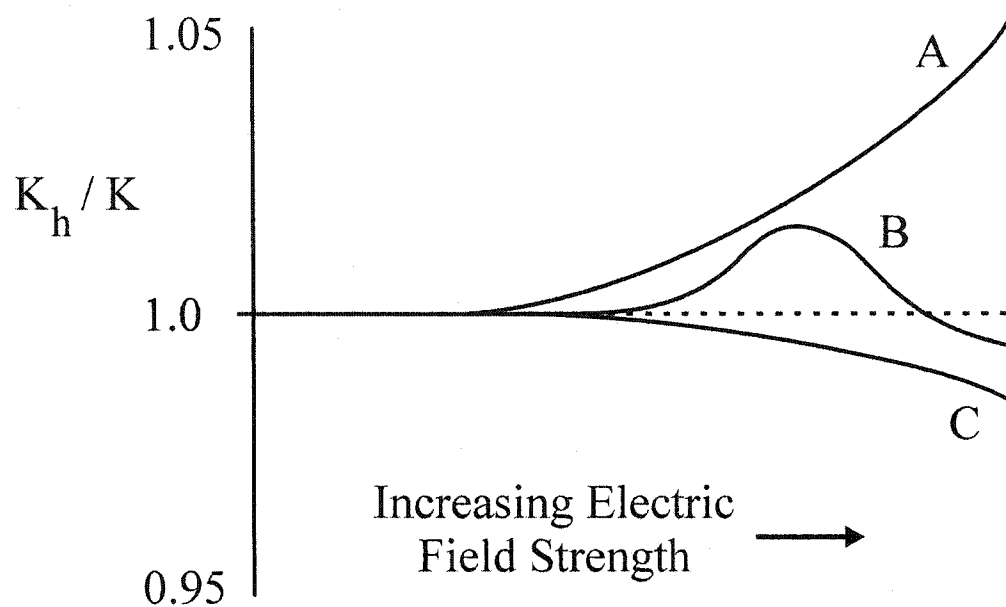


Figure 4.02 Types of ion mobility behavior (K_h/K) in response to increasing applied electric field. K_h = high field mobility. K = low field mobility. A = increasing mobility with increasing applied field. B = complex mobility dependence with applied field; initially increasing, then decreasing with higher applied field. C = decreasing mobility with increasing applied field.

4.6 Origins of High-Field Asymmetric Field Ion Mobility Spectrometry (FAIMS)

During the 1970s and 1980s, a considerable amount of research in the IMS field was directed to the development of field instruments for military use in the US and UK [1]. Not surprisingly, similar research was going on in the research labs of the former USSR. It is during this period when scientists in the USSR developed a new type of IMS. This new type of IMS was based on the field-dependence of ion mobilities at high applied fields, as described briefly in the previous section. Originally described as transverse field compensation IMS, it would later be known as high-field asymmetric waveform ion mobility spectrometry (FA-IMS or FAIMS), and even radio frequency IMS (RF-IMS).

The technology originated as a pair of closely spaced parallel plates, as shown in Figure 4.03 [10-13]. At one side of the plates, ions were generated using either a tritium β -source or a Mo wire coil for surface ionization. The ions were moved into the space between the parallel plates by means of a pumping system. At the other side of the plates, an electrometer was placed to detect ions that had successfully traversed the parallel plates. A radio-frequency (rf) asymmetric waveform was applied to one plate, which alternately generated high fields of one polarity and low fields of opposite polarity between these plates. An example of this waveform is illustrated in Figure 4.04. Two different sine waves (Figure 4.04 (a)) are combined to form the final waveform (Figure 4.04 (b)), where the amplitude of the high voltage peak is referred to as the dispersion voltage (DV). As briefly described earlier, an ion may exhibit a field-dependent velocity (mobility) at high applied field. As a result, an ion may have different velocities in opposite directions during each half cycle of the waveform, and an ion would experience a net displacement relative to its starting position between the plates. Different ions, with different field-dependent mobilities, would exhibit different net displacements. In order to prevent the ion from drifting into one of the plates, a direct current (dc) potential of suitable polarity was superimposed on the alternating current (ac) waveform. Since different ions have different mobilities (and hence, different displacements) in high and low field, different ions required different values of dc voltage to prevent them from

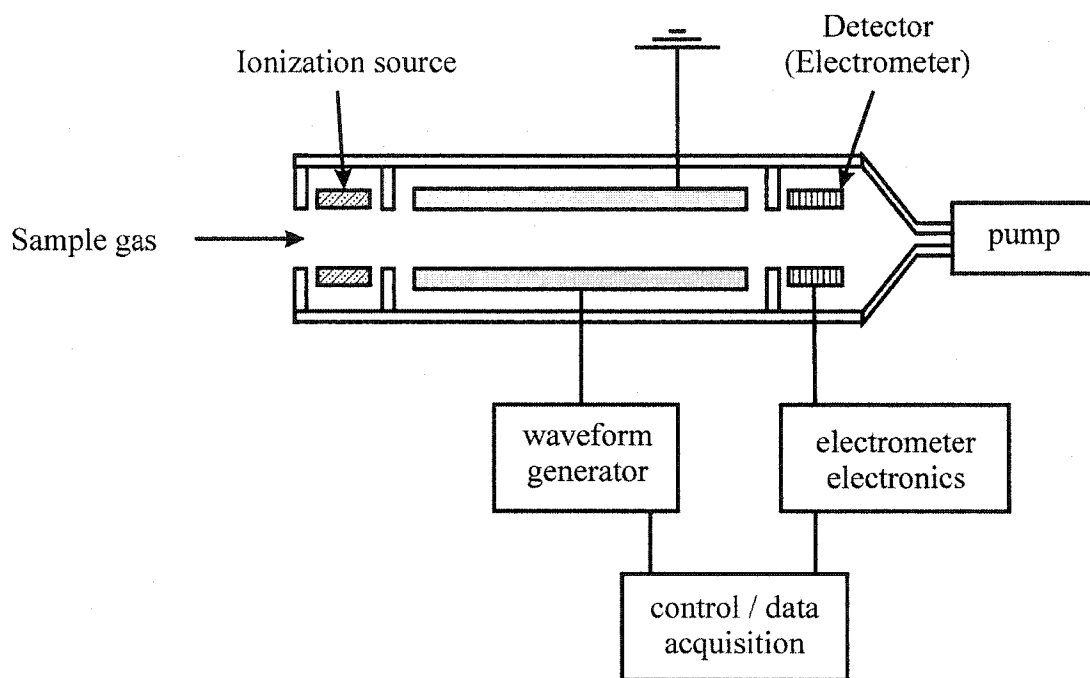


Figure 4.03 Schematic illustration of a parallel plate FAIMS device.

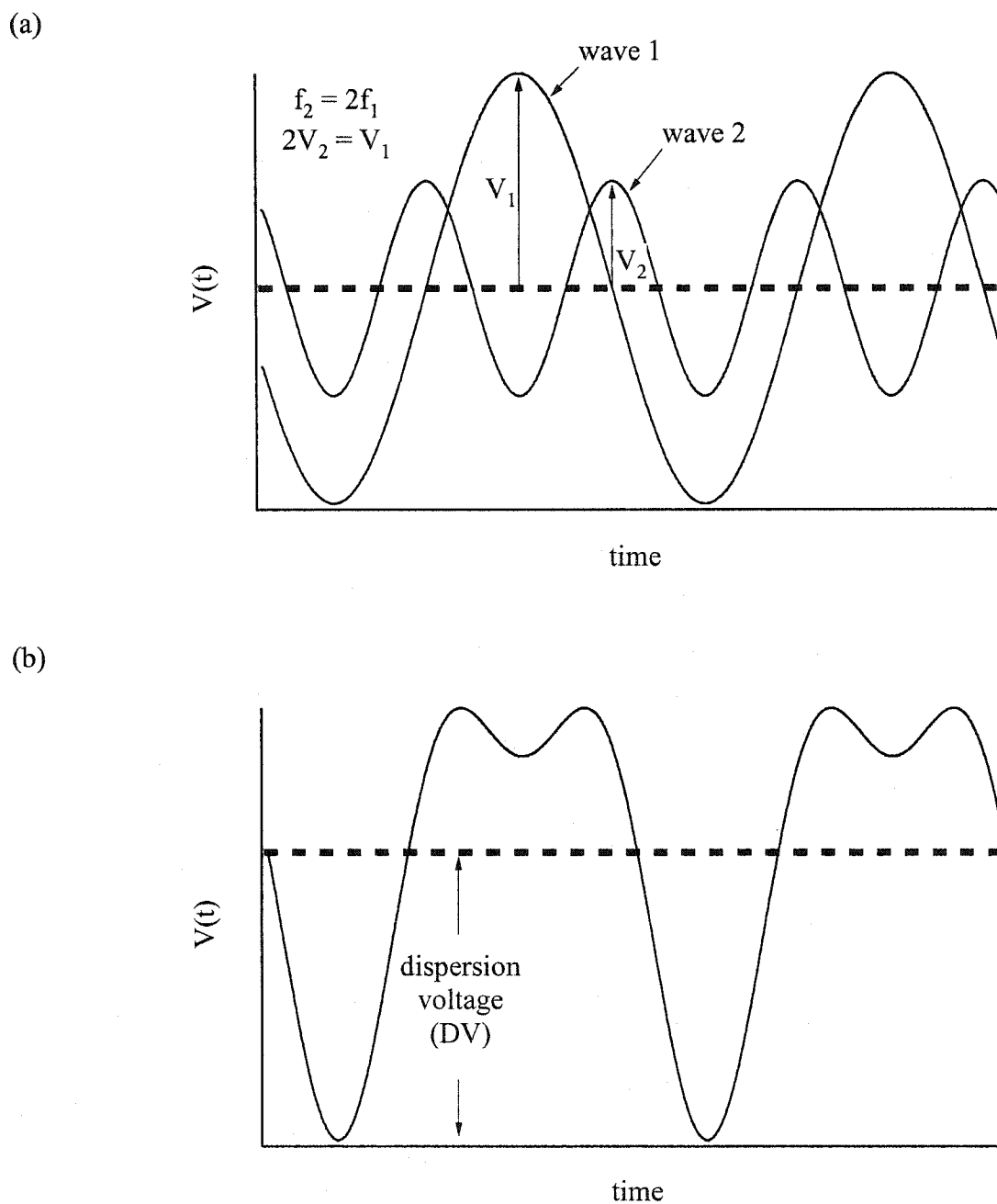
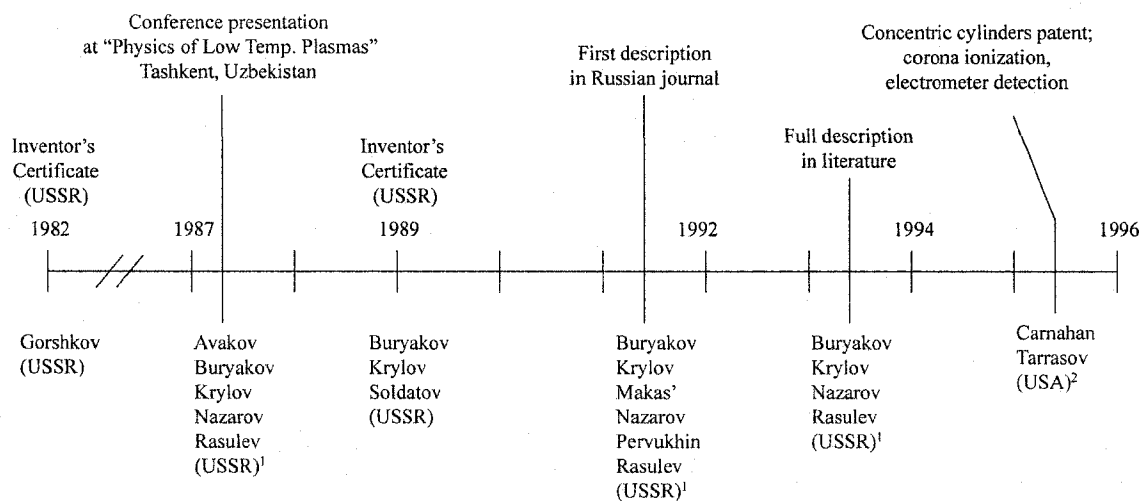


Figure 4.04 Examples of waveforms used with FAIMS. (a) Two composite sine waves that are combined to form (b) an asymmetric waveform with a negative high voltage peak.

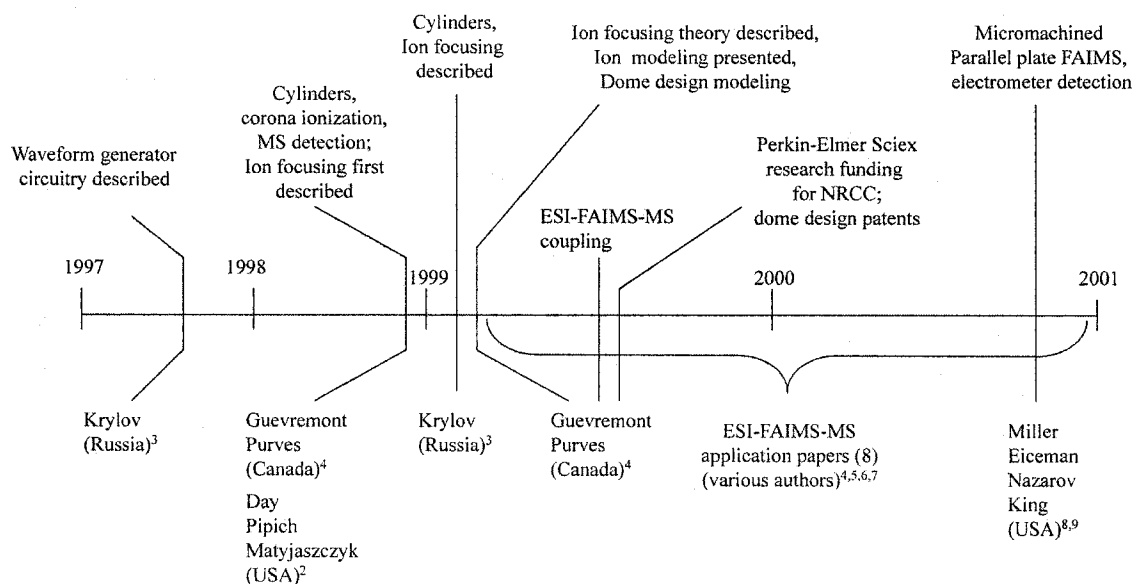
striking one of the plates. If the dc voltage was sufficient to create a balance condition for a particular ion, a flow of gas between the plates would successfully transport the ion to the electrometer detector and generate a current. As such, the dc potential could be scanned, sequentially passing a shifting bandpass of ions to the electrometer to produce a spectrum of current vs. applied dc voltage. This dc voltage will be referred to as the compensation voltage, CV.

A brief summary of the history of FAIMS is shown as a timeline in Figure 4.05. The first full disclosure of an experimental system appeared in 1993, although the origins of the technology trace back much earlier. The first known documentation of the FAIMS technology appeared as an USSR Inventor's Certificate in 1982, listing M.P. Gorshkov as the principal inventor, followed by another Inventor's Certificate in 1989, listing I.A. Buryakov, E.V. Krylov, and V.P. Soldatov as the inventors [12, 14]. It is unclear whether this documentation properly represents the actual development date, since it is conceivable that the development of this technology could have been classified military research. This first form of FAIMS used parallel plates spaced 0.5 mm apart, an asymmetric waveform with a frequency of 2 MHz and a high voltage peak of 925 V, a radioactive ion source, and an electrometer for detection. Some data were apparently presented at a conference in Tashkent, Uzbekistan in 1987, and a description of the experimental apparatus and data appeared in a Soviet journal in 1991 [11, 13]. It is conceivable that the drive to develop this new IMS technology was in response (or vice versa) to military research being conducted in the US and UK using drift tube IMS during the same period of time. It is interesting to note that the publication of much of this research coincides with Gorbachev's policy of Perestroika (1986), or the "warming" of relations with the Western world, and the beginning of the end of the Cold War (most estimates put the end of the Cold War at the end of 1991). In 1993 a more detailed description of this technology appeared in the literature [10]. Later, in 1995, Byron L. Carnahan and Alexander S. Tarrasov filed international patents on a modified version of this technology, replacing the parallel plates with concentric cylinders [15]. Using this patent, a private company called Mine Safety Appliances Company (MSA, Pittsburgh, PA, USA) developed a prototype of a portable FAIMS apparatus for detection of gas



1. Arifov Institute of Electronics, Uzbek Academy of Sciences, Tashkent, Uzbekistan

2. Mine Safety Appliances, Co., Pittsburgh, PA, USA



3. Technical Design Institute of Geophysical and Environmental Instrumentation, Siberian Branch of the Russian Academy of Sciences, Novosibirsk, Russia

4. Institute for National Measurement Standards, National Research Council of Canada (NRCC), Ottawa, ON, Canada

5. PE Sciex, Concord, ON, Canada

6. Department of Public Health Sciences, University of Alberta, Edmonton, AB, Canada

7. Department of Chemistry, University of Alberta, Edmonton, AB, Canada

8. The Charles Stark Draper Laboratory, Cambridge, MA, USA

9. Department of Chemistry and Biochemistry, New Mexico State University, Las Cruces, NM, USA

Figure 4.05 Timeline outlining the development of the FAIMS interface.

impurities. The name of their product was the Field Ion Spectrometer®, FIS®, which employed a corona discharge as the ion source and an electrometer for detection. As such, results using this system were presented at conferences in 1996 and 1997 [16, 17]. The development of the technology by MSA was not very successful. Using electrometer-based detection, gas phase species could not be reliably characterized, and the relatively low resolution of the instrument likely made mixture analysis difficult. Circa 1998, a prototype was given to Roger Guevremont at the National Research Council of Canada (NRCC) in Ottawa, ON, Canada for mass spectrometric characterization. By coupling FAIMS to a mass spectrometer, the identity of the ions detected with the electrometer version could be confirmed. Using a corona discharge ionization source, the researchers at NRCC confirmed that many of the ions observed were due to gas-discharge ions and clusters, which would forever complicate the interpretation of the electrometer drift spectra [18]. As a result of the complexity of the instrumentation, drift spectra interpretation, and the relatively large power requirements, the FIS® was slow to gain acceptance, and MSA eventually discontinued research and production of the Field Ion Spectrometer®. Following this initial FAIMS-MS work, Roger Guevremont and Randy Purves at the NRCC continued FAIMS-MS research. By incorporating an electrospray (ESI) ion source, many interesting and useful applications of this coupling were demonstrated, marking the onset of a number of publications from within this research group at the NRCC from 1999 to 2001 [18-42]. Based on computer modeling by Guevremont, another modification to the FAIMS itself was introduced and patented [29, 43-46]. This design was also based on a concentric cylinder configuration, but with one end terminating in a spherical dome. This led to improved ion sampling and MS coupling. Based on these patents, MDS - Sciex (formerly Perkin-Elmer Sciex) in Concord, ON, Canada investigated this prototype for potential as a commercial interface for ESI-MS. Apparently unsatisfied with the Sciex commitment to the project, the research group at the NRCC has established their own company, Ionalytics Corp. (late 2001), with the hopes of producing a commercial product.

4.7 Discussion of Ion Motion in a Gas

Before discussing the motion of ions in a FAIMS, some of the factors influencing the motion of an ion in a gas need to be discussed. This section will include a basic discussion of the effects of ion-gas collisions, ion-ion repulsion, diffusion, and the influence of an applied field.

4.7.1 Basic IMS Considerations

To introduce the concepts that determine the motion of an ion in a gas during an IMS experiment, we should first consider some of the forces acting on the ion. Let's assume that the sample ions have been generated and gated into the drift region of an IMS spectrometer. At this point, the ions are subjected to a constant electric field, E . This electric field exerts a constant force on the ion, pushing it towards the other end of the drift tube (i.e., the detector). Using Newton's Second Law of motion (force = mass * acceleration), and defining the electric field (E) as the force (F) per unit charge (q) (i.e., $E = F/q$), the expression $E = ma/q$ can be derived. So, for an ion experiencing a constant electric field, the acceleration that an ion will achieve is dependent on the ion's mass to charge ratio, with larger m/q ions accelerating less than smaller m/q ions. These considerations are the same as for mass spectrometry. The major difference between mass spectrometry and ion mobility spectrometry lies in the different pressures that the ion experiences. In mass spectrometry, an ion is moved by the electric field in a vacuum, so the ion is free to move without colliding with neutral gas molecules. In IMS, the pressure is much greater, typically 7.5×10^{-2} Torr [2], so the mean free path of the ion is much less, and an ion will travel a small distance before colliding with a molecule of the drift gas. Factors influencing the mean free path include the area swept out by the tumbling ion and gas molecule (i.e., their collision cross sections), as well as the gas number density, N . The gas number density is simply the number of gas molecules present in a given volume. By specifying the number density, both the pressure and temperature are accounted for. When the ion and the gas molecule collide, a transfer of momentum must occur. For simplicity, the collisions can be assumed to be elastic,

binary collisions, where momentum is conserved [2]. For example, collision of the ion moving along force lines with a stationary gas molecule results in a loss of momentum (and hence, velocity) for the ion, as momentum is transferred to the gas molecule. In addition to losing momentum, the ion may be scattered in a direction other than along the lines of force (i.e., other than towards the detector). Note that in an IMS experiment, the observed velocity is only due to the net motion of the ion along the lines of force (i.e., the z-axis of the drift tube). On the micro level, the ion accelerates between collisions, loses its momentum (and may have its path altered), and then begins to accelerate again along force lines, etc. On the macro level, the collisions cause the ion to reach a terminal velocity in response to a constant electric field. This steady-state velocity is a balance of accelerations due to the applied field and collisions with gas molecules, which cause deceleration. This velocity is assumed to be constant only in response to a low applied field. Furthermore, when the applied field is low enough, the drift velocity (v_d) is observed to vary linearly with the magnitude of the electric field [2]. This allows the relationship expressed in Equation 4.01, and the determination of an ion's mobility, K . From this simplified description of ion motion, it should be easy to understand that the mobility of an ion depends on several factors. These factors include the charge, mass, and collision cross-section of the ion, as well as the mass, collision cross section, and number density of the drift gas.

4.7.2 Dependence of Mobility on E/N

In IMS, collisions with the drift gas are of critical importance. In general, ion velocities are inversely dependent on the effective collisional cross section of an ion, and this makes drift tube IMS a type of molecular size analyzer [1]. Since the number of collisions an ion experiences will depend on the gas number density, N , the relationship between E and N is an intimate one. If E is doubled, the ion accelerates twice as much between collisions. If N is doubled, the mean free path and the time between collisions is reduced by half. So, if E and N are both doubled, the ion arrives at the next collision in half the time as the original, and with the same speed. Since the number of collision events is doubled, the total drift time is the same, with the net effect being zero change in

observed mobility [2]. This simple argument demonstrates that the ratio E/N is more descriptive than just considering E . This is why ion mobilities are generally reported as reduced mobilities, K_o , which extrapolates the experimental conditions used to those of a standard gas density at 760 Torr and 273 K. This standard gas density, N_o , termed the Loschmidt constant ($N_o = 2.686763 \times 10^{25} \text{ m}^{-3}$), represents a gas density that is about 4 orders of magnitude greater than the typical operating pressure for drift IMS experiments [2]. The calculation of a reduced mobility, K_o , assumes that the observed mobility can be extrapolated to standard conditions of temperature and pressure. Experimentally, this has been found to be a reasonable assumption [2].

The relationship between the applied field and the ion mobility has been expressed as Equation 4.02,

$$K_o(E) = K_o(0)[1 + \alpha(E/N)^2 + \beta(E/N)^4 + \dots] \quad 4.02$$

where α and β are complex constants, characteristic of the ion under specific test conditions [2]. The value, $K_o(E)$, is also known as the high-field mobility, K_h , or as the polarization mobility [21]. In the case of relatively low E/N , the α and β terms are very small, and the ion mobility shows little to no dependence on the applied field. In this case, $K_o(E) = K_o(0)$, and the terminal velocity achieved by the ion is directly proportional to the magnitude of the applied field, and Equation 4.01 applies. So, a linear extrapolation of low E/N over a limited range of test conditions is a reasonable assumption. At higher values of E/N , the α and β terms become significant, leading to a non-linear relationship between the applied field and the ion mobility. Due to the added complications for both modeling and instrumentation, it was believed (historically speaking) that high-field IMS showed little analytical utility, and thus was not an actively pursued research field [2].

4.7.3 Considerations Towards a More Refined Theory

Models that accurately describe the motion of ions in a gas have been under development for some time, with the origins dating back to Maxwell in 1860. It was Maxwell who developed momentum-transfer theory and mean free path theory to describe diffusion of ions in gases [1]. Later, in 1905, Langevin used similar theories to develop the first quantitatively accurate theory of low-field ion mobility [1]. Building on these initial theories, several kinetic theories have been developed in an attempt to describe the mobility and diffusion of ions in a gas [2]. Here, only the momentum transfer kinetic theory will be discussed, due to its relative simplicity as compared to the other models. In the derivation of this model, several assumptions are made. One is that the concentration of ions is sufficiently dilute so that the effects of space-charge can be ignored. Also, ion-ion interactions (i.e., interactions producing random mutual scattering) are also ignored, based on the assumption that the mean ion energy is much greater. When an ion is under the influence of a very weak field, the ion energy is assumed to be largely thermal, with only a small drift component in the direction of the applied field. In other words, the temperature of the gas is the predominant factor in determining the ion's energy, with the ion motion largely the random thermal motion produced by the heat energy of the gas. Under these conditions, the ion mobility is said to be defined by the Nernst - Townsend equation,

$$K = \frac{eD}{kT} \quad 4.03$$

where K is the ion mobility (cm²/V·sec), e is the ion charge (C), D is the ion diffusion coefficient (cm²/sec), k is the Boltzmann constant (1.38 x 10⁻²³ J/K), and T is the temperature (K). For normal IMS, the ion energy due to the applied field is significant and this field causes the motion of ions directed along the lines of force, superimposed on the much faster random motion of diffusion. However, in the presence of a non-zero field, the Nernst - Townsend relationship is no longer applicable, and additional refinements must be made to describe an ion's mobility that account for the applied field.

Momentum transfer theory suggests that the total energy of the ion is a combination of thermal energy and the energy gained from the applied field. The thermal energy is imparted to the ions by collisions with the gas, and is determined by the temperature and pressure of the gas. As described earlier, the applied field induces the acceleration of ions and causes collisions with the drift gas. The energy gained from the applied field can be described as having two components, one as the energy of the ion observable as drift motion (i.e., measurable kinetic energy), and another as random energy due to field-induced collisions with the drift gas. A term described as the effective temperature, T_{eff} , represents the total random energy of the ions, due to both thermal and field-induced random motions. So, in a very weak field, the $T_{\text{eff}} = T_{\text{thermal}}$. In a higher field, the $T_{\text{eff}} = T_{\text{thermal}} + T_{\text{field}}$. The presence of a high field effectively raises the energy of an ion proportional to the magnitude of the applied field. This is the basis for a commonly used model, known as the two-temperature theory of ion motion [2]. For further information on this and other models, "Transport Properties of Ions In Gases" by Mason and McDaniel should be consulted [2].

4.7.4 Comments on Diffusion and Space-Charge Repulsion

While the adverse effects of diffusion and space-charge repulsion will not be discussed in detail, it is necessary to point out that diffusion and space-charge repulsion are largely responsible for the observed width of peaks in a typical drift IMS spectrum. Most of the elementary considerations of ion motion assume that the ions under study are relatively dilute such that the effects of space-charge can be ignored, simplifying the modeling [2]. In any case, all of the field-induced motions are superimposed on the motions due to diffusion and space-charge repulsion. While the ions are gated into the drift tube as a relatively narrow packet, diffusion causes spreading of this ion cloud, with the rate of diffusion proportional to the magnitude of the gradient (Fick's first law of diffusion). For the purposes of simple modeling, the ion density is assumed to be Gaussian at all points of the drift time, with the curve flattening as time progresses [2]. Under the assumption of a Gaussian distribution, the average lifetime of an ion before

hitting a wall (due to diffusion) in a container can be approximated [2]. Using Equation 4.04, the average lifetime of an ion in an infinitely long cylinder can be estimated,

$$\tau = \frac{1}{D} \left(\frac{r_o}{2.405} \right)^2 \quad 4.04$$

where τ is the average lifetime of an ion (sec), D is the diffusion coefficient under the test conditions (cm^2/sec), and r_o is the radius of the cylinder (cm). Assuming STP and a $D = 0.2 \text{ cm}^2/\text{sec}$, the average lifetime of an ion in a cylinder of $r_o = 1 \text{ cm}$ is $\tau = \sim 0.86 \text{ sec}$. At lower pressures, say $P = 1 \text{ Torr}$, and using $D = 50 \text{ cm}^2/\text{sec}$, the lifetime is considerably shorter, $\tau = \sim 0.0035 \text{ sec}$. In an effort to maintain good resolution and high signals, the effects of diffusion must be minimized. Generally, the length of the drift tube and the applied field strength are set to keep the residence time of an ion in the analyzer as short as possible. As mentioned previously, drift IMS was (historically) performed at reduced pressures. Although the lifetime of an ion is theoretically less at lower pressures, tests were presumably done at reduced pressures to avoid ion sampling problems that can occur at higher pressures [2].

4.8 IMS Theory as it Relates to FAIMS

Having discussed some of the basic factors influencing the movement of an ion in an electric field, these factors need to be discussed in regards to FAIMS. Some of the current theoretical models about FAIMS will be briefly discussed, and this information will provide some theoretical basis for the experimental results that will be discussed in later chapters.

4.8.1 Ion Mobility Determination

Since the inception of FAIMS, the theoretical description of FAIMS operation has been progressively developing [13, 18, 21, 29, 30, 32-34, 47-49]. The field dependence

of K_h described earlier (Equation 4.02) has been used to describe the mobility of an ion in FAIMS [13, 21, 33, 35, 50]. Ion mobilities (K_h/K) have been calculated by multivariable analysis using FAIMS experimental data, and Equation 4.05,

$$CV + \alpha \left[\frac{(DV)^3}{9d^2} + \frac{15(CV)(DV)^2}{18d^2} + \frac{(CV)^3}{d^2} \right] + \beta \left[\frac{55(DV)^5}{486d^4} \right] = 0 \quad 4.05$$

where CV is the compensation voltage, DV is the dispersion voltage, d is the analyzer spacing, and α and β are complex constants characteristic of an ion under the specific test conditions [50]. The variables α and β are determined by using multiple values of CV and DV for a particular ion and determining values which best satisfy Equation 4.05 [50]. Experimental results demonstrate that truncating after the β term in Equation 4.02 does not lead to appreciable errors in calculating the K_h/K [50]. Also, it has been demonstrated that there is no correlation between the values of α and β and the molar mass of the ions tested (amino acid ions) [33, 50]. Furthermore, the high-field mobilities calculated using FAIMS have been shown to be in good agreement with drift tube IMS data up to about 50 Td (Td = Townsend = 10^{-17} Vcm²) [50].

One of the major differences between FAIMS and classic IMS is the application of a rapidly changing applied field. Since an ion must accelerate / decelerate rapidly for the presumption of a constant velocity to be valid, calculations for a “worst case” time for this to occur at atmospheric pressure have been done [50]. The “worst-case” time for acceleration to a terminal velocity was calculated as 4×10^{-11} s, which is much faster than the field reversals, which occur in $1-20 \times 10^{-6}$ s [50]. As a result, the ion should rapidly achieve terminal velocity during a FAIMS experiment, and the time to reach this terminal velocity can be ignored.

4.8.2 Ion – Neutral Collisions and Variation of Observed Mobility with Field Strength

There has been interest in using different gases or mixtures of gases to alter the selectivity of separation of ions within the FAIMS [21, 23, 25, 27]. In some cases, the behavior of the ion in a mixed gas could be described by Blanc's Law (Equation 4.06) [23].

$$\frac{1}{K_{mix}} = \sum_j \frac{X_j}{K_j} \quad 4.06$$

Blanc's Law states that the mobility of the ion in a gas mixture, K_{mix} , is the inverse sum of the mole fraction, X_j , divided by the mobility of the ion in the pure gas, K_j , for all gases present. However, it has been found that for some mixed gases, especially those containing CO_2 , that Blanc's Law is inadequate [23]. Further studies, combined with ion motion theory, have been used to try to explain these relationships [21]. Using the two-temperature theory of gaseous ion transport, the motion of an ion in the FAIMS has been described. Under weak-field conditions, the ion-neutral (gas) collision energy was described as a function of the temperature of the gas, and the energy was represented as $T_{thermal}$. At high-applied fields, the average collision energy was described as a function of the gas temperature and the velocity of the ion. Since this velocity is field-dependent, the magnitude of the field represents a significant contribution to the collision energy. Under influence of an applied field, the effective temperature, T_{eff} , is defined by Equation 4.07, and characterizes the relative kinetic energy of the ion-neutral.

$$T_{eff} = T_{thermal} + T_{field} \quad 4.07$$

In Equation 4.07, the effective temperature, T_{eff} , is the sum of the thermal energy, $T_{thermal}$ and the temperature due to the field-induced velocity of the ions, T_{field} . Under typical FAIMS test conditions of $E/N = 60 \text{ Td}$, it was estimated that the effective temperature of a Cs^+ ion in N_2 drift gas was increased 700 K (to 1000 K), as compared to no applied

field ($T_{\text{eff}} = 300 \text{ K}$) [21]. The collision interaction between an ion and the gas was described as being dominated by either long-range attractive forces or by short-range repulsive forces. The combination of the attractive and repulsive forces was described as the interaction potential well for the ion and the neutral gas. A shallow interaction well would describe a net interaction for the ion-gas that has a large contribution from short-range repulsive forces. A deep interaction potential well describes an interaction that is dominated by long-range attractive forces. Provided the interaction potential was substantially greater than the thermal energy (at zero field), the K_h/K should be independent of the gas type, provided that a large fraction of the collision energy was not lost to inelastic collisions [21]. So, the variations of increasing K_h/K for an ion in different gas types were partly attributed to differing degrees of inelasticity of the ion-gas collision [21]. Again, problems were encountered when attempting to correlate the observed results to CO_2 . The proposed reason for this discrepancy was that the ion might be forming complexes during the FAIMS experiment [21]. One factor influencing ion-neutral interactions is the polarizability of the drift gas. For example, if a dipole is easily induced in a neutral gas molecule, the attractive force between these two species may increase, potentially changing both the interaction potential and the elasticity of the collision.

With the introduction of the concept of field-induced temperature, a comment regarding the motion of ions due to the field should also be made. If the magnitude of the field is raised, two components of motion can become significant; one motion is along the field lines, and another motion is a random motion. This random motion is due to energy acquired from the drift field and converted into random form by collisions with molecules [2]. Both of these motions are superimposed on the motions due to diffusion and space-charge repulsion.

4.8.3 Comments on Diffusion and Space-Charge Repulsion

In relation to FAIMS, the effect of diffusion has been limited to hypothetical discussions, and leaves considerable room for refinement [29]. As with drift tube IMS,

ion signals in FAIMS are believed to be adversely affected by diffusion and space-charge repulsion. However, with some FAIMS prototypes, the field generated in the analyzer region helps to prevent diffusion losses to the walls of the analyzer, by a process termed “ion focusing” [29]. A more detailed discussion of this effect is the subject of later sections in this chapter.

4.9 FAIMS Voltage and Field Expressions

In order to develop the theoretical foundation for describing the basic motion of an ion along field lines in a FAIMS experiment, the equations of voltage and field are derived in this Section, and similar derivations can be found elsewhere [51]. To date, there are three main types of FAIMS geometries in the literature: flat plates, concentric cylinders, and the concentric cylinders that terminate with a spherical dome. These geometries are illustrated in Figure 4.06. The first FAIMS prototype to appear in the literature was composed of flat plates, and will be the first geometry to be considered.

4.9.1 Relations of Voltage and Field for Three Simple Geometries

In order to discuss how voltage can vary with respect to different geometries, we must first define a few simple relationships. The symmetry considerations and the derivation of these relationships can be found in many textbooks on classical physics [51]. For point charges, the electric field, E (V/cm), can be expressed by Equation 4.08,

$$E = \frac{F}{q_{\text{test}}} = \frac{kq q_{\text{test}}}{q_{\text{test}} r^2} = \frac{kq}{r^2} \quad 4.08$$

where F is the force (N) experienced by a test charge, q_{test} (C), as a result of charge q , $k = 1/4\pi\epsilon_0$ ($k = 8.99 \times 10^9 \text{ Nm}^2/\text{C}^2$), and r is the distance (m) between the test charge and charge q . For an infinite surface of charge, the field experienced by a test charge is constant at all points, and Equation 4.09 describes the magnitude of the field,

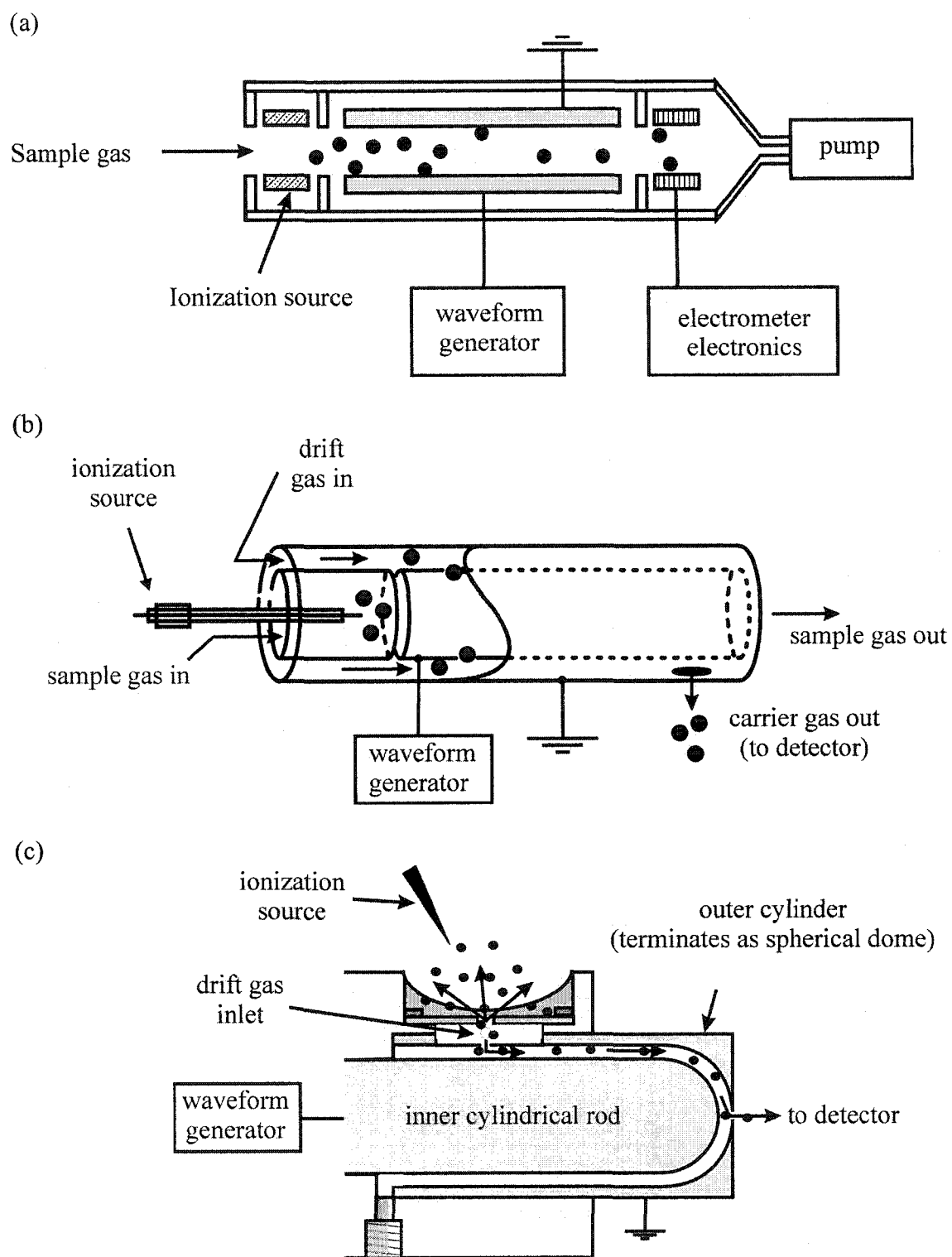


Figure 4.06 FAIMS electrode geometries. (a) parallel plates, (b) concentric cylinders, (c) concentric cylinders terminating as a spherical dome.

$$E = \frac{\sigma}{2\epsilon_0} \quad 4.09$$

where σ is the surface charge density (C/m^2), and ϵ_0 is the permittivity of free space ($\epsilon_0 = 8.85 \times 10^{-12} C^2/Jm$). The third geometry to be considered here is an infinitely long wire of charge. For this geometry, the electric field is proportional to $1/r$, and can be expressed as Equation 4.10, where λ is the linear charge density (C/m).

$$E = \frac{2k\lambda}{r} \quad 4.10$$

Again, considering our hypothetical test charge, we need to define an equation for the difference in the potential energy that occurs in moving the test charge closer to one of the charged surfaces just described. The work energy, W , required to move a test charge, q_{test} , some distance, dr , closer to charge q can be expressed by Equation 4.11.

$$W = \int_1^2 F \cdot dr \quad 4.11$$

The work can also be described as the change in potential energy, $U_2 - U_1$, as shown in Equation 4.12.

$$U_2 - U_1 = \int_1^2 F \cdot dr \quad 4.12$$

Dividing each term in Equation 4.12 by q_{test} gives Equation 4.13:

$$\frac{U_2}{q_{test}} - \frac{U_1}{q_{test}} = - \int_1^2 \frac{F_e}{q_{test}} \cdot dr \quad 4.13$$

Substituting known relationships ($V = U/q_{test}$, and $E = F_e/q_{test}$):

$$V_2 - V_1 = - \int_1^2 E \cdot dr \quad 4.14$$

Equation 4.14 describes the basic relationship of field and potential difference. Using the basic definitions of field for the geometries described earlier, equations describing the potential difference specific to each geometry can be defined.

Using Equations 4.08 and 4.14, the expression for the potential difference between two point charges (Equation 4.17) can be derived.

$$V_2 - V_1 = - \int_1^2 \frac{kq}{r^2} \cdot dr \quad 4.15$$

$$= -kq \int_1^2 \frac{1}{r^2} \cdot dr \quad 4.16$$

Using the relation $\int r^{-2} \cdot dr = -r^{-1}$,

$$V_2 - V_1 = kq \left(\frac{1}{r_2} - \frac{1}{r_1} \right) \quad \text{point charges} \quad 4.17$$

For a surface of charge, since E is constant (Equation 4.09), Equation 4.14 can be integrated to get Equation 4.21.

$$V_2 - V_1 = - \int_{r_1}^{r_2} E \cdot dr \quad 4.18$$

$$V_2 - V_1 = -E \int_{r_1}^{r_2} dr \quad 4.19$$

$$V_2 - V_1 = -E(r_2 - r_1) \quad 4.20$$

$$\Delta V = -E\Delta r \quad \text{surface of charge} \quad 4.21$$

For a line of charge geometry, using Equations 4.10 and 4.14 yields Equation 4.23.

$$V_2 - V_1 = -\int_{r_1}^{r_2} E \cdot dr \quad 4.14$$

$$V_2 - V_1 = -2k\lambda \int_{r_1}^{r_2} \frac{dr}{r} \quad 4.22$$

$$V_2 - V_1 = -2k\lambda \cdot \ln \frac{r_2}{r_1} \quad \text{line of charge} \quad 4.23$$

These three relationships between the potential difference and the relevant geometry will be used to describe the field and voltages experienced by an ion within a FAIMS analyzer. The surface of charge definition will be used for the parallel plate FAIMS, the line of charge definition will be used for the concentric cylinder FAIMS, and the point charge definition will be used to describe the spherical dome region of a dome FAIMS analyzer.

4.9.2 Dependence of Voltage and Field with Position Between Parallel Plates

Earlier, the field strength between two infinite surfaces of charge was defined to be a constant value. So, for parallel plates, the field strength is the same for all points between the plates (i.e., no dependence on position between the two plates). Figure 4.07 shows a set of parallel plates with a test charge at some distance r_{test} from the lower plate to which a voltage V_2 is applied. The field between these plates (E) can be calculated as the difference in voltage at which each plate is biased ($V_2 - V_1$, where $V_2 > V_1$), divided by the spacing between the plates (r_{total}).

$$E = \frac{V_2 - V_1}{r_{\text{total}}} \quad 4.24$$

$$V_2 - V_1 = Er_{\text{total}} \quad 4.25$$

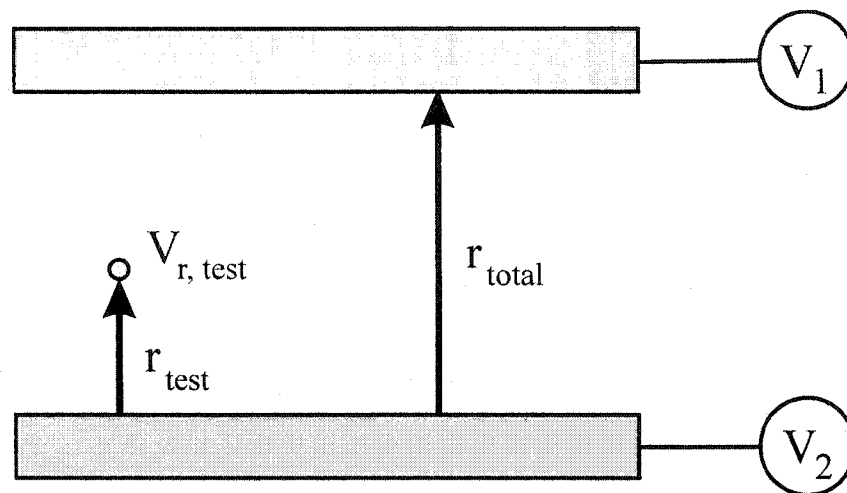


Figure 4.07 Parallel flat plates separated at a uniform distance r_{total} , with test charge at a distance r_{test} from lower plate. Plates biased to voltages V_1 and V_2 , where $V_2 > V_1$.

Since the field is constant between the plates, the voltage ($V_{r, \text{test}}$) at any point between these plates can be expressed as

$$V_2 - V_{r, \text{test}} = Er_{\text{test}} \quad 4.26$$

$$V_{r, \text{test}} = V_2 - Er_{\text{test}} \quad 4.27$$

$$V_{r, \text{test}} = V_2 - \left(\frac{V_2 - V_1}{r_{\text{total}}} \right) r_{\text{test}} \quad \text{parallel plates} \quad 4.28$$

In other words, the voltage at any point between the plates is a linear function of the voltage difference between said plates. This is consistent with a constant field at any distance, r_{test} .

4.9.3 Radial Dependence of Voltage Between Cylinders

The second FAIMS prototype to appear in the literature, as patented by Carnahan and Tarrasov, consisted of concentric cylinders [15, 16, 18]. Using the infinite line of charge expression to describe a cylinder, an expression for each concentric cylinder can be derived. Referring to Figure 4.08, let us define the radial dimensions of the two cylinders as follows: the smaller, inner cylinder has an outer radius = a , and the larger, outer cylinder has an inner radius = b . A radial position at some point between these two cylinders will be defined as r . Starting with the line of charge equation (Equation 4.23), we can express the voltage difference between point b and point r , defining $V_2 = V_b$ and $V_1 = V_r$,

$$V_b - V_r = -2k\lambda \ln \frac{b}{r} \quad 4.29$$

$$-2k\lambda = \frac{V_b - V_r}{\ln(b/r)} \quad 4.30$$

Similarly, the voltage difference between cylinders a and b can be expressed as:

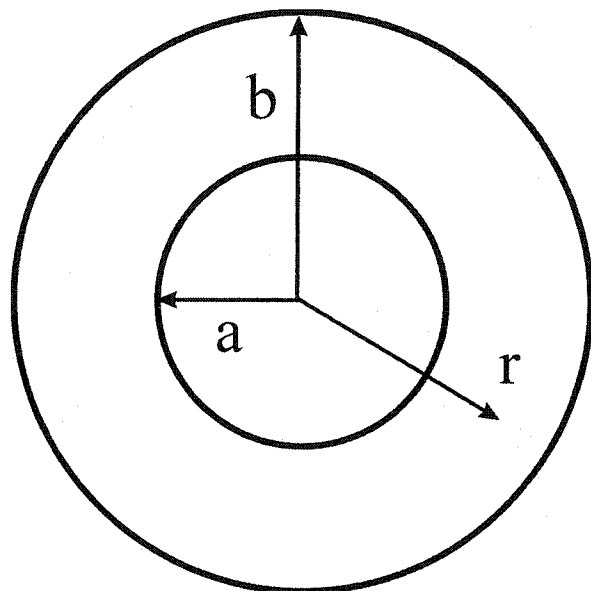


Figure 4.08 Radius definitions for concentric cylinders or concentric spheres.

$$V_b - V_a = -2k\lambda \ln \frac{b}{a} \quad 4.31$$

$$-2k\lambda = \frac{V_b - V_a}{\ln(b/a)} \quad 4.32$$

Combining the two equations leads to a new expression that describes the voltage at any point, r , between the two cylinders, expressed as a function of the voltages applied to each cylinder and the radial geometry (Equation 4.34).

$$\frac{V_b - V_r}{\ln(b/r)} = \frac{V_b - V_a}{\ln(b/a)} \quad 4.33$$

$$V_r = V_b - (V_b - V_a) \frac{\ln(b/r)}{\ln(b/a)} \quad \text{concentric cylinders} \quad 4.34$$

4.9.4 Radial Dependence of Field Between Cylinders

The field can be defined as the negative rate of change of voltage with respect to distance, or:

$$E = \frac{-dV}{dr} \quad 4.35$$

Taking the derivative of Equation 4.34:

$$\frac{dV_r}{dr} = D_r \left(V_b - (V_b - V_a) \frac{\ln(b/r)}{\ln(b/a)} \right) \quad 4.36$$

$$= 0 - D_r \left((V_b - V_a) \frac{\ln(b/r)}{\ln(b/a)} \right) \quad 4.37$$

Applying the constant multiple rule, $D_x c f(x) = c D_x f(x)$:

$$= -(V_b - V_a) \cdot D_r \frac{\ln(b/r)}{\ln(b/a)} \quad 4.38$$

$$= -\frac{(V_b - V_a)}{\ln(b/a)} \cdot D_r \left(\ln \frac{b}{r} \right) \quad 4.39$$

$$= -\frac{(V_b - V_a)}{\ln(b/a)} \cdot D_r (\ln b - \ln r) \quad 4.40$$

Using the sum rule ($D_x(f+g) = D_x f + D_x g$) and realizing that the rate of change of the constant, $\ln(b)$, is equal to zero:

$$\frac{dV_r}{dr} = -\frac{(V_b - V_a)}{\ln(b/a)} \cdot (0 - D_r(\ln r)) \quad 4.41$$

Using the identity $D_x \ln x = \frac{1}{x}$ and the expression $E_r = -\frac{dV_r}{dr}$, the final expression for the field/voltage relationship between cylinders can be determined:

$$\frac{dV_r}{dr} = \frac{V_b - V_a}{r \cdot \ln(b/a)} \quad 4.42$$

$$E_r = \frac{-(V_b - V_a)}{r \cdot \ln(b/a)} \quad \text{concentric cylinders} \quad 4.43a$$

or

$$E_r = \frac{(V_b - V_a)}{r \cdot \ln(a/b)} \quad 4.43b$$

4.9.5 Radial Dependence of Voltage Between Spheres

For the dome prototype described by Guevremont and Purves, the dome end has a geometry similar to that of concentric spheres [29]. Point charges have spherical

symmetry, so the same equations can apply when considering spheres. Again, referring to Figure 4.08, let us define the radial dimensions of the two spheres as follows: the smaller, inner sphere has an outer radius = a, and the larger, outer sphere has an inner radius = b. A radial position at some point between these two spheres will be defined as r. Starting with the point charge voltage equation used earlier (Equation 4.17), we can express the voltage difference between point b and point r, defining $V_2 = V_b$ and $V_1 = V_r$.

$$V_b - V_r = kq \left(\frac{1}{b} - \frac{1}{r} \right) \quad 4.44$$

$$kq = \frac{V_b - V_r}{\frac{1}{b} - \frac{1}{r}} \quad 4.45$$

Similarly, the voltage difference between spheres a and b can be expressed as:

$$V_b - V_a = kq \left(\frac{1}{b} - \frac{1}{a} \right) \quad 4.46$$

$$kq = \frac{V_b - V_a}{\frac{1}{b} - \frac{1}{a}} \quad 4.47$$

Combining the two equations leads to a new expression that describes the voltage at any point, r, between the two spheres, expressed as a function of the voltages applied to each sphere and the radial symmetry (Equation 4.49).

$$\frac{V_b - V_r}{\frac{1}{b} - \frac{1}{r}} = \frac{V_b - V_a}{\frac{1}{b} - \frac{1}{a}} \quad 4.48$$

$$V_r = V_b - (V_b - V_a) \frac{\frac{1}{b} - \frac{1}{r}}{\frac{1}{b} - \frac{1}{a}} \quad \text{concentric spheres} \quad 4.49$$

4.9.6 Radial Dependence of Field Between Spheres

Taking the derivative of the sphere voltage equation just derived (Equation 4.49):

$$\frac{dV_r}{dr} = D_r \left(V_b - (V_b - V_a) \frac{\frac{1}{b} - \frac{1}{r}}{\frac{1}{b} - \frac{1}{a}} \right) \quad 4.50$$

$$= 0 - D_r \left((V_b - V_a) \frac{\frac{1}{b} - \frac{1}{r}}{\frac{1}{b} - \frac{1}{a}} \right) \quad 4.51$$

$$= -(V_b - V_a) \cdot D_r \frac{\frac{1}{b} - \frac{1}{r}}{\frac{1}{b} - \frac{1}{a}} \quad 4.52$$

$$= -\frac{(V_b - V_a)}{\frac{1}{b} - \frac{1}{a}} \cdot D_r \left(\frac{1}{b} - \frac{1}{r} \right) \quad 4.53$$

$$\frac{dV_r}{dr} = -\frac{(V_b - V_a)}{\frac{1}{b} - \frac{1}{a}} \cdot \left(0 - D_r \left(\frac{1}{r} \right) \right) \quad 4.54$$

$$\frac{dV_r}{dr} = -\frac{(V_b - V_a)}{\frac{1}{b} - \frac{1}{a}} \cdot \left(\frac{1}{r^2} \right) \quad 4.55$$

Since $E_r = -\frac{dV_r}{dr}$, the final expression for the field/voltage relationship between spheres can be determined:

$$E = \frac{(V_b - V_a)}{\frac{1}{b} - \frac{1}{a}} \cdot \left(\frac{1}{r^2} \right) \quad \text{concentric spheres} \quad 4.56$$

As with the concentric cylinders, the radial dependence of the field is non-linear.

4.10 Ion Motion Along Force Lines in a FAIMS Analyzer

Using the field relationships for the 3 geometries as described in Section 4.9, the motion of ions in response to an electric field can be more accurately described.

4.10.1 Ion Motion Within a Parallel Plate FAIMS Analyzer

As mentioned in Section 4.6, the development of FAIMS in the 1980s was based on an ion's changing mobility with high-applied field. The basic FAIMS apparatus, as first described in the literature by Buryakov, *et al* [13], was composed of two parallel metal plates separated by 0.5 cm, similar to that schematically shown in Figure 4.09 (a). One plate was grounded, and to the other plate an asymmetric waveform was applied. As shown, the waveform was composed of a low voltage component of one polarity, and a high-voltage component of opposite polarity, with an approximate voltage magnitude of 2:1 high:low. The frequency of the waveform was 2 MHz, and the high voltage peak (the dispersion voltage, DV) was 925 V. For the purposes of clarity, the waveform is represented as a square wave approximation; however, the actual waveform is better represented as illustrated in Figure 4.04. When this waveform is applied to the lower plate, alternating high and low fields are generated within the plate gap. Also, the waveform has a negative polarity high voltage and a positive polarity low voltage. As a result, a high negative field of short duration follows a low positive field of longer duration. Due to the symmetry of the waveform, the voltage (V) * time (t) products of the positive and negative portions of each cycle are of equal magnitude and opposite sign.

$$V_{\text{low}}t_{\text{low}} = -V_{\text{high}}t_{\text{high}} \quad 4.57$$

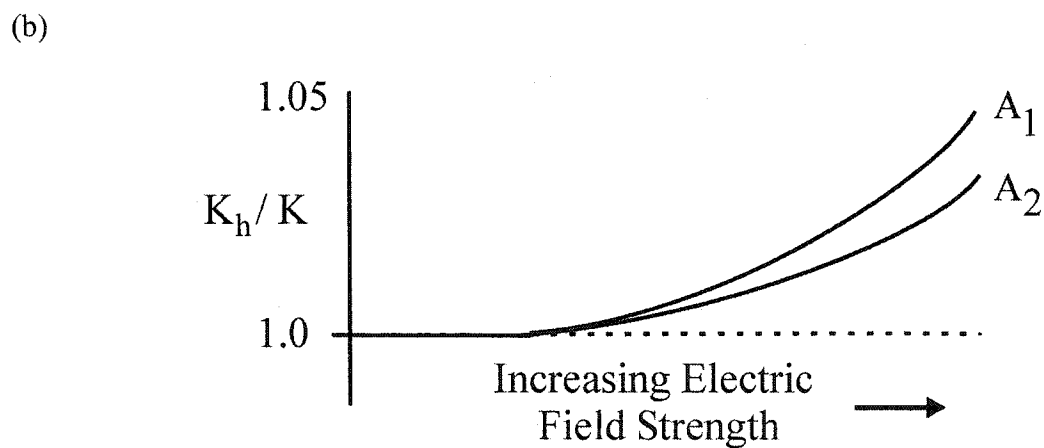
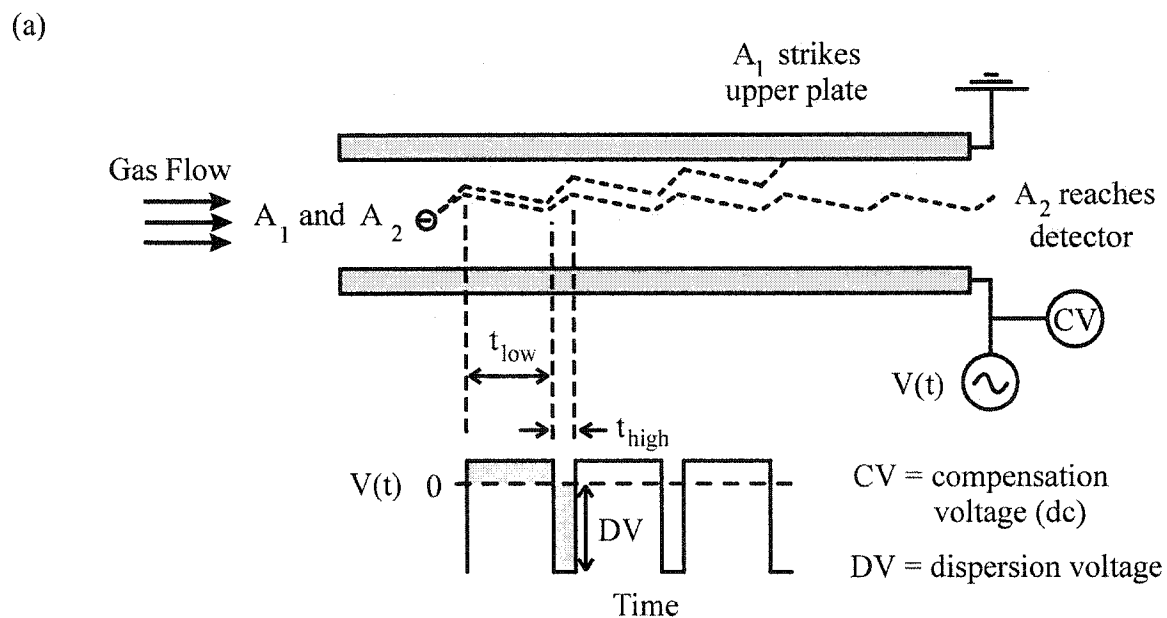


Figure 4.09 Basics of parallel plate FAIMS operation. (a) Schematic of a parallel plate FAIMS apparatus with the dc potential (i.e., the compensation voltage, CV) set to transmit the A_2 ion. (b) Theoretical example of two different ions, A_1 and A_2 , with different K_h/K ratios in response to increasing applied electric field.

As shown earlier, parallel plates are known to generate uniform fields within the space between them (i.e., for a constant applied voltage, the field that an ion experiences is a constant value, regardless of the ion position within the gap). As a result, the field-time products are also equal and opposite.

$$E_{\text{low}}t_{\text{low}} = -E_{\text{high}}t_{\text{high}} \quad 4.58$$

The velocity of an ion due to an applied field can be described combining Equations 4.01 and 4.02:

$$v_{\text{drift}} = K_o(E)E \quad 4.59$$

Also, using $d = vt$, the following relations can be derived:

$$d_{\text{low}} = KE_{\text{low}}t_{\text{low}} \quad 4.60$$

$$d_{\text{high}} = K_h E_{\text{high}}t_{\text{high}} \quad 4.61$$

Since the field-time products are equal, any differences in magnitude of the distance traveled will be proportional to the ion mobility ratio within the applied fields. This can be further expressed as:

$$d_{\text{high}}/d_{\text{low}} = K_h/K \quad 4.62$$

Note that the relation $d_{\text{high}}/d_{\text{low}}$ depends on the magnitude of the applied fields, since $K_h = f(E_{\text{high}})$. If the ion exhibits no change in mobility at high applied fields, the ion will have no net displacement toward either plate, and $d_{\text{high}}/d_{\text{low}}$ will be unity. In our hypothetical case (see Figure 4.09 (b)), the ion will exhibit an increase in mobility at high applied field, so both the mobility ratio and the distance ratio will be greater than unity for each cycle of the waveform. During the positive low-field portion of the waveform, the ion will very rapidly accelerate to a terminal velocity and migrate towards the bottom plate.

Likewise, during the negative high-field portion of the waveform, the ion rapidly accelerates to a terminal velocity and migrates toward the top plate. Overall, the ion will experience a net drift towards the top plate and eventually strike the surface. However, if a small dc potential of polarity opposite to the ion's net charge is applied (in this case a positive voltage will be applied for a negative ion), a balance condition may result, and the ion experiences no net drift towards either plate. This dc potential is called the compensation voltage (CV).

With the configuration described by Buryakov *et al* [10, 13], the ion source ionized the sample gas at one side of the plates and pumping transported a continuous flow of dry sample gas and sample ions into the plate gap, where the ions moved perpendicular to the plates due to the applied asymmetric voltage. If the applied CV created a balance condition, the ion passed through to the other side of the plates, striking an electrometer. Ion motions that were not balanced struck one of the plates before the gas flow could transport them to the electrometer. For demonstration purposes, let's assume that two different negative ions, A_1 and A_2 , are located between the two plates, and that these ions exhibit an increase in mobility when exposed to a high electric field, as shown in Figure 4.09 (b). In the example in Figure 4.09 (a), the DV and CV are set to balance the drift of the A_2 ion, so A_1 strikes the upper plate and A_2 reaches the detector. The applied CV could be scanned, sequentially transmitting ions with different K_h/K ratios, generating a spectrum (current vs. applied CV), where the applied CV determined the bandpass of K_h/K ions that reached the detector (at a given DV amplitude). A hypothetical illustration of a CV spectrum is presented in Figure 4.10. The lower K_h/K ion (i.e., A_2) is transmitted to the detector at a lower $CV = V_1$, and the higher K_h/K ion (i.e., A_1) is transmitted at the higher $CV = V_2$.

At this point, it is worth noting the obvious difference between the separation criteria and observed spectra here as compared to drift tube IMS. With drift tube IMS, ions are separated on the basis of their mobility (assumed constant) at constant applied field, and the observed spectra are a function of time. With FAIMS, ions are separated

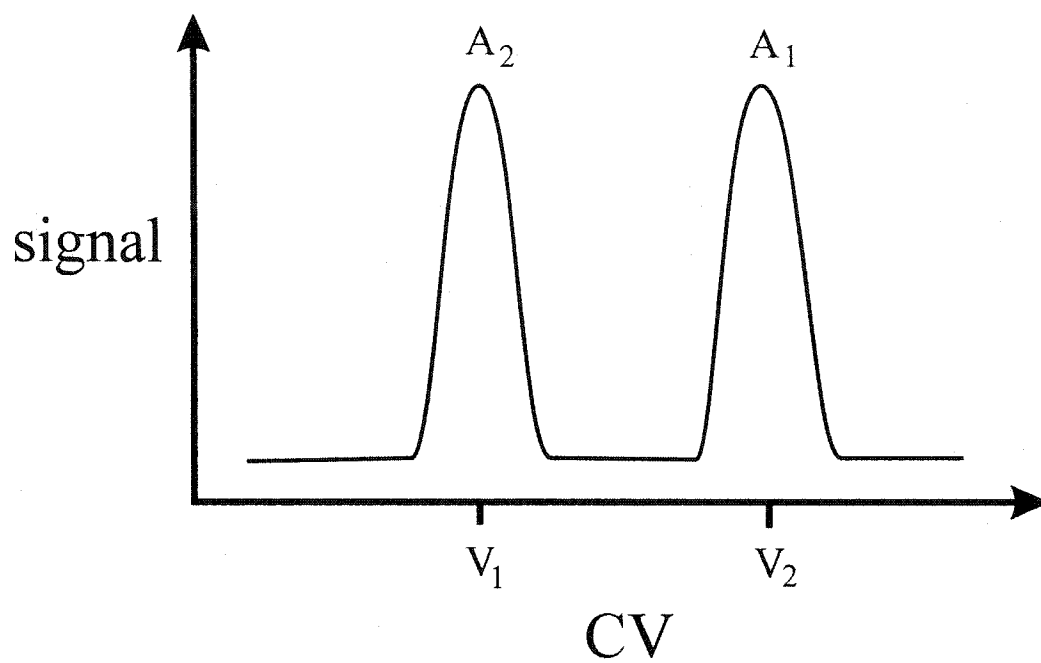


Figure 4.10 Hypothetical CV spectrum of negative ions A_1 and A_2 using a waveform similar to that depicted in Figure 4.04, with hypothetical K_{-}/K mobility as illustrated in Figure 4.09 (b).

on the basis of their K_b/K within a varying field of constant intensity ratio, and the spectra are a function of the applied dc voltage (which is, in turn, related to the applied ac peak voltage). Simply put, the observed spectra and modes of separation are very different.

4.10.2 Ion Motion Within a Concentric Cylinder FAIMS Analyzer

The concentric cylinder FAIMS analyzer was developed and patented by Carnahan and Tarassov [15]. The motion of ions within this configuration is very similar to that of a parallel plate geometry, however certain differences exist that make concentric cylinders advantageous over the parallel plate configuration. The main advantage of a concentric cylinder FAIMS analyzer is an ion focusing mechanism, which prevents diffusional losses and improves the ion throughput [29, 47].

A longitudinal cross section of the concentric cylinder FAIMS interface as patented by Carnahan and Tarassov is shown in Figure 4.11. The interface consists of two inner cylinders inside a single outer cylinder. As shown, an ionization source is positioned within the short inner cylinder. Using electrostatics, ions are extracted through the gap between the inner cylinders, into the annular space between the long inner cylinder and the outer cylinder. Ions are separated in this annular space in similar fashion to that described earlier for parallel plates by applying the asymmetric waveform to the long inner cylinder. At the end of the analyzer, the outer cylinder is designed with holes leading to a cylindrical electrometer, biased at a suitable voltage to extract the ions from the analyzer space.

To examine the critical differences between the parallel plate and the concentric cylinder geometries, the different voltage equations derived earlier for each geometry should be examined. For the parallel plate geometry, it was found (Equation 4.28) that the voltage at any point between the plates was a linear relationship between the voltages applied to each plate and the total plate separation. In other words, the rate of change in

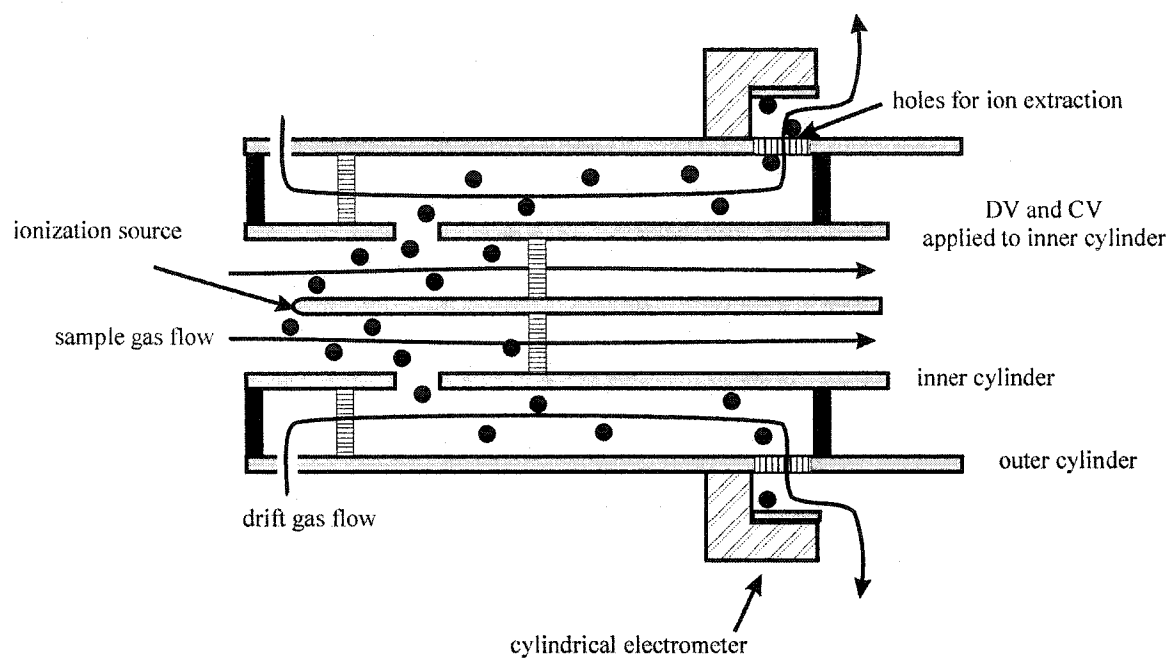


Figure 4.11 Schematic illustration of a longitudinal cross section concentric cylinder FAIMS instrument with electrometer detection.

voltage with position (i.e., the field) was constant for any point between the plates, and the magnitude was expressed by Equation 4.24.

In the case of a concentric cylinder geometry, the voltage at any point between the cylinders was shown (Equation 4.34) to have a logarithmic dependence with the radial position in the annular space. More importantly, the rate of change of the voltage with radial position was a function of the radial position (Equation 4.43a, b). As a result, the variation of the magnitude of the field with radial position is non-linear for concentric cylinders.

The effects of the concentric cylinders on the observed ion signals exiting the FAIMS apparatus was first described by Krylov in early 1999 [47]. Soon after this, Guevremont and Purves presented a more fundamental and detailed account of the effect, which they termed “ion focusing” [29]. In effect, the consequence of the radial dependence of the field is that ions are focused to an optimal radial position within the annular space, so fewer losses to the walls occur and higher ion currents are observed. It should be noted that in the same paper, Guevremont and Purves also presented a third geometry (i.e., the dome geometry) and presented ion modeling to demonstrate the effects of the ion focusing mechanism [29]. Such modeling is very instructive, and so modeling similar to that of Guevremont and Purves will be used to describe and compare the systems.

4.11 Introduction to Ion Modeling

This section will use ion modeling to demonstrate some of the differences between parallel plates, concentric cylinders, and concentric cylinders that incorporate a dome at one end. Also, the effects of several different parameters on an ion's motion within the analyzer will be demonstrated. Some of the modeling presented here is similar to that presented by Guevremont and Purves, and is repeated here due to its instructive value [29].

The modeling was done using a "digital" technique (using Microsoft ExcelTM), where each cycle of the waveform was broken down into discrete steps, and the ion's position in the analyzer was approximated at each step. The actual waveform used with FAIMS is a combination of two sine waves out of phase by 90° ; one wave with a peak amplitude = V and frequency = $2f$, combined with a second wave of peak amplitude = $2V$ and frequency = f , as illustrated in Figure 4.04. In order to digitize this waveform with enough points (so as to not introduce too much error in the approximation of ion position), it was estimated that at least 1000 points per cycle were needed. The possible error in the estimation arises due to the variation of field with radial position. Since K_h/K varies with the field, it also varies with radial position. So, it is very important to keep the time increments very small to keep the calculated change in radial position also very small. With the modeling requiring about 1000 waveform cycles to effectively demonstrate the ion's motion, and several separate calculations for each iteration, this would lead to about one million data points (each with several calculations) in the spreadsheet. It was decided that this many data points were too much for our computer to handle efficiently, so a square wave approximation was used. Using a square wave approximation, it was determined that as few as 30 data points per cycle could be used without severely affecting the ion position approximations. Most of the calculations presented in the following sections use a square waveform with a 2:1 $t_{low}:t_{high}$ ratio (and a 1:2 $V_{low}:V_{high}$ ratio), which approximates the voltages of the actual waveform.

4.12 Modeling Limitations

Since the actual waveform was not used, this modeling could not be used to predict the voltage for an ion's bandpass through the analyzer. Also, effects of diffusion and space-charge repulsion were ignored, so the actual motion of ions was not accurately represented. Furthermore, the time required for accelerating to a terminal velocity after a collision was ignored, as has been suggested by other work [50]. In spite of these limitations, these demonstrations effectively show the effects of several operating

parameters and the factors that must be considered in both the design and use of a FAIMS interface.

4.13 High Field Mobilities

A curve of K_h/K as a function of applied field for a perchlorate anion in air is shown in Figure 4.12 (Details regarding the acquisition of this data will appear in the following chapter). The field is expressed as E/N , where N is the gas number density. These data could also be expressed as E/P , where P is pressure, however, the gas number density accounts for variations in temperature between test systems. Assuming that the spacing between cylinders is 0.2 cm, Figure 4.12 shows the mobility for a range of applied DV with a maximum of about -3300 V at about room temperature and atmospheric pressure. Note that at the highest E/N shown, the K_h exceeds K only by about 6 %.

4.14 Calculation of Ion Trajectories

A square waveform was used with 2:1 high:low voltage and 1:2 high:low time, using 30 points per cycle (10 points at high voltage, 20 points at low voltage). For most calculations, the waveform frequency was 210 kHz. Most demos used the same total number of data points. As such, higher frequency demos had more total cycles, but less total time. For example, using 63,000 data points and a frequency of 210 kHz, 2100 cycles were modeled over a time of 10 milliseconds. If the same number of data points were used for a 750 kHz frequency, 2100 cycles were modeled over 2.8 milliseconds. For some demonstrations at higher frequencies, 126,000 data points were used in order to allow enough time for the ion motion to be effectively modeled.

To do the calculations, several parameters had to be defined, and some assumptions had to be made. In addition to all required voltages and frequencies, the

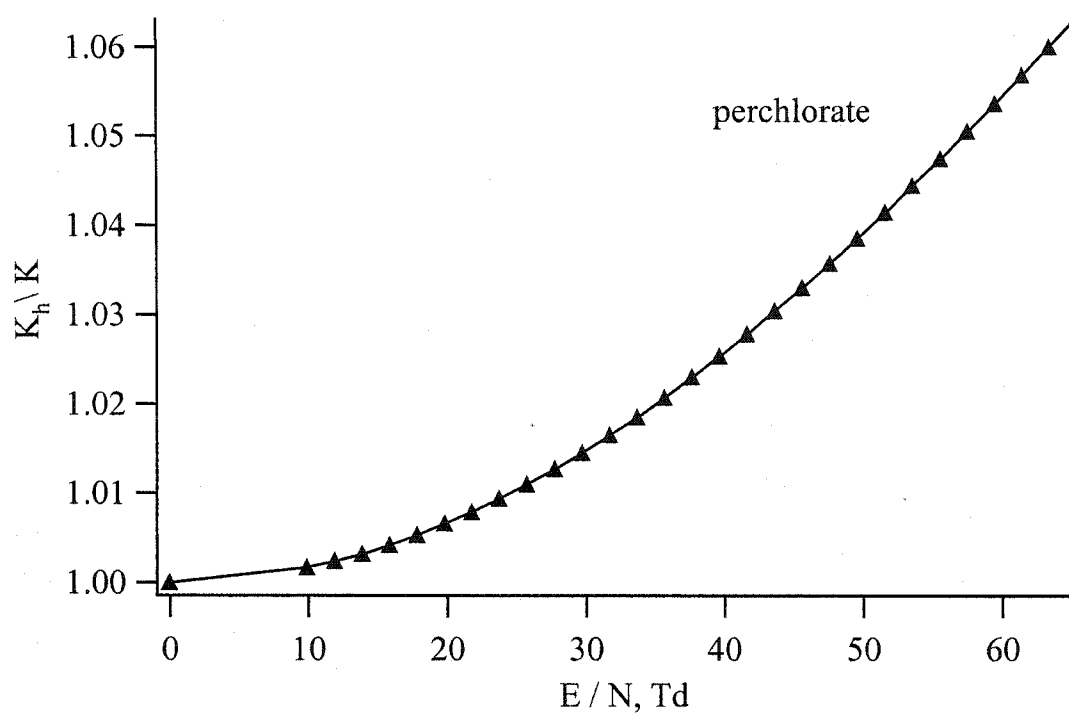


Figure 4.12 Measured dependence of ion mobility (expressed as K_h/K) in air for perchlorate as a function of electric field strength within the FAIMS analyzer (expressed as E/N , where N represents the gas number density).

ion's initial radial position within the analyzer had to be defined. The effects of this assumption will be examined in detail. Also, a function for the variation in ion mobility had to be defined; for this study, the experimentally determined K_h/K of the perchlorate ion in air as a function of applied E (at approximately atmospheric pressure) was used. Using the experimental data from Figure 4.12, the K_h/K data were re-plotted as a function of applied E , where E was determined at a radial position of 0.90 cm (i.e., the mid-point of the analyzer). At the mid-point, the field was calculated based on the value of the DV and an analyzer spacing of 0.20 cm. Using the experimental data and using a polynomial fit, the equation for perchlorate was determined as:

$$\frac{K_h}{K} = 2.25 \times 10^{-10} (E)^2 + 5.51 \times 10^{-7} (E) + 0.999 \quad 4.63$$

where E is the applied field in V/cm. This equation describes the mobility of a perchlorate ion in a FAIMS using the actual waveform. Since a square waveform is more efficient than the real waveform, this equation is not really accurate in the context of the modeling [50, 52]. Note in the above equation that at low values of E , the K_h/K becomes close to unity, as would be expected. In addition, an assumed low-field mobility had to be defined; for demonstration purposes, the ion mobility of a m/z 100 ion was estimated as $K_0 = 2.0 \text{ cm}^2/\text{V}\cdot\text{sec}$ [2, 53]. As such, the hypothetical ion will be a “perchlorate-like” ion.

The order of calculations was as follows: 1) based on the user-defined frequency of the waveform and 30 points per cycle, calculate the time increment (Δt) for each data point, 2) calculate the total time elapsed, and the applied voltage at each time, 3) calculate the field at the defined initial ion radial position, using the appropriate field equations, 4) determine an assumed ion mobility at the applied field (based on the K_h/K function and the assumed value of K), 5) calculate the distance traveled during the particular time increment ($d = KE\Delta t$), 6) calculate the ion's new radial position ($r = r_{\text{initial}} + d$) and plot this new r as a function of time elapsed, and 7) repeat calculations starting at step 2, for 63,000 iterations.

4.15 Modeling Examples

4.15.1 Parallel Plate FAIMS

Earlier, in Section 4.6, the basics of ion motion within a parallel plate FAIMS were introduced. The first example of ion motion between parallel plates is shown in Figure 4.13. In our hypothetical example, the waveform ($DV = -3300$ V) is applied to the lower plate. Arbitrarily, the lower plate is positioned at 0.80 cm, with the upper plate at 1.00 cm, and the limits of the y-axis represent the surface of each plate. In this example, the initial starting point (time = 0 μ sec) of the ion between the plates is mid-way between the plates, at 0.90 cm, and the waveform is assumed to start at the high-field, negative polarity portion of the waveform cycle. As the negative ion experiences the field created by the asymmetric waveform, it has a net displacement towards the upper plate as a result of the ion's field-dependent mobility at high-applied fields. In the absence of any CV to compensate for this drift, the ion path quickly moves towards the upper plate, eventually striking the upper plate, as shown in Figure 4.13 (a). In this case, the ion is lost to the wall in less than 50 cycles of the waveform. Figure 4.13 (b) shows the same conditions as before, but with a $CV = 32.5$ V applied to the lower plate. Under these conditions, the calculated ion trajectory is a balanced condition over the time period shown (250 μ sec), and the ion experiences no net drift. In Figure 4.14, the same ion under influence of the same applied fields as Figure 4.13 (b) is shown. Like Figure 4.13 (b), Figure 4.14 (a) has the ion starting with an initial position of 0.90 cm, and has a balanced trajectory over the time period demonstrated (~ 7.5 msec). Likewise, when the same DV and CV are applied to ions starting with different initial positions, these ion trajectories are balanced as well. Figure 4.14 (b) illustrates a starting position of 0.95 cm, and Figure 4.14 (c) illustrates a starting position of 0.81 cm. For all three of these initial starting positions, the ion experiences no net drift under the applied field conditions. So, under these hypothetical conditions, the ion would be transported by the drift gas through the analyzer region. In these examples, the waveform started at a high-field condition, so the

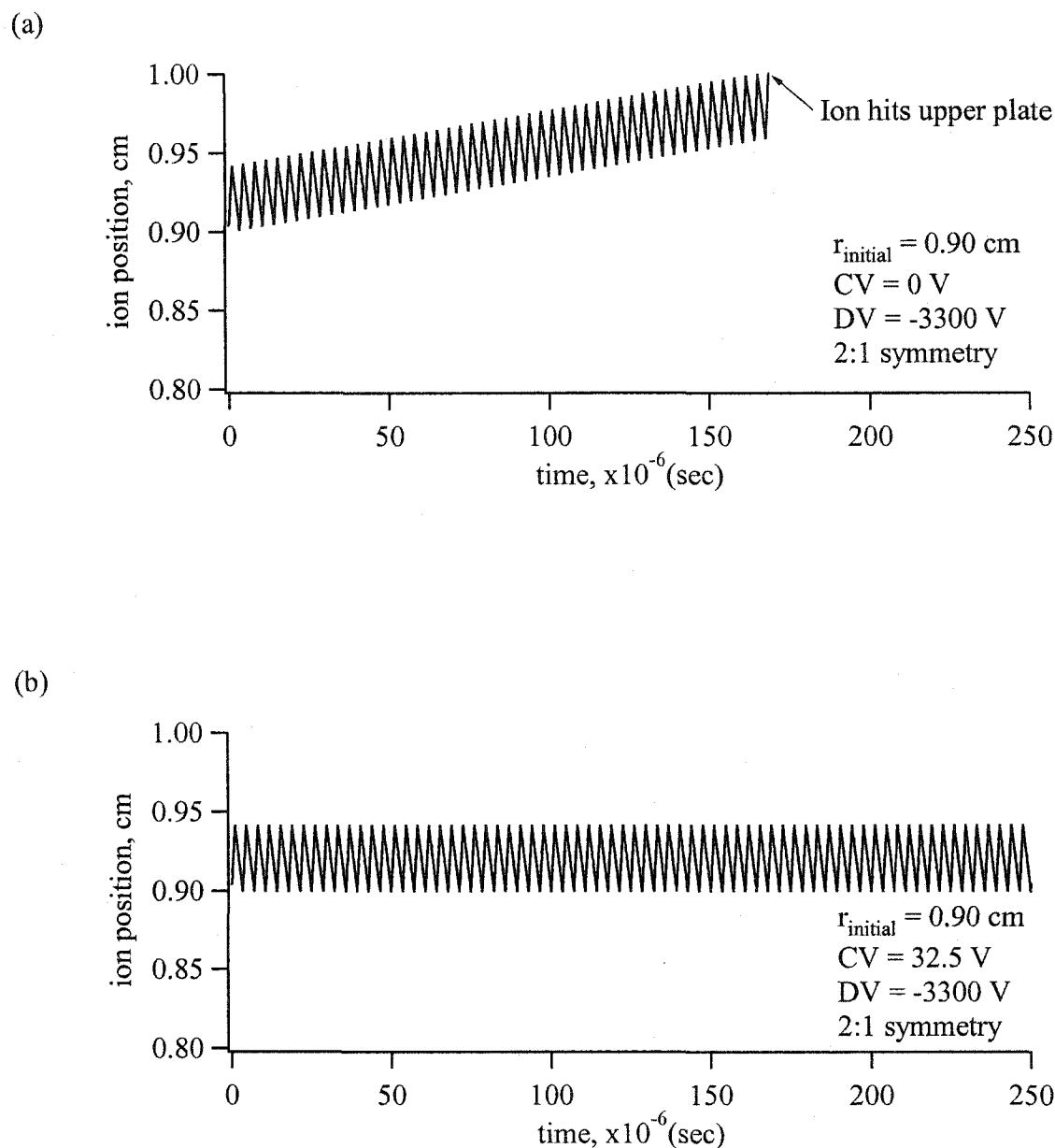


Figure 4.13 Calculated ion trajectory in a parallel plate FAIMS for type A ion. Ion mobility as defined in Equation 4.63. Plate spacing = 0.2 cm. Square wave approximation, $f = 210$ kHz, 2:1 $t_{\text{low}}:t_{\text{high}}$. Initial ion position at 0.90 cm. X-axis (time) represents residence time in the analyzer region. Limits of the y-axis represent the surface of the plates. (a) DV = -3300 V, CV = 0 V, (b) DV = -3300 V, CV = 32.5 V.

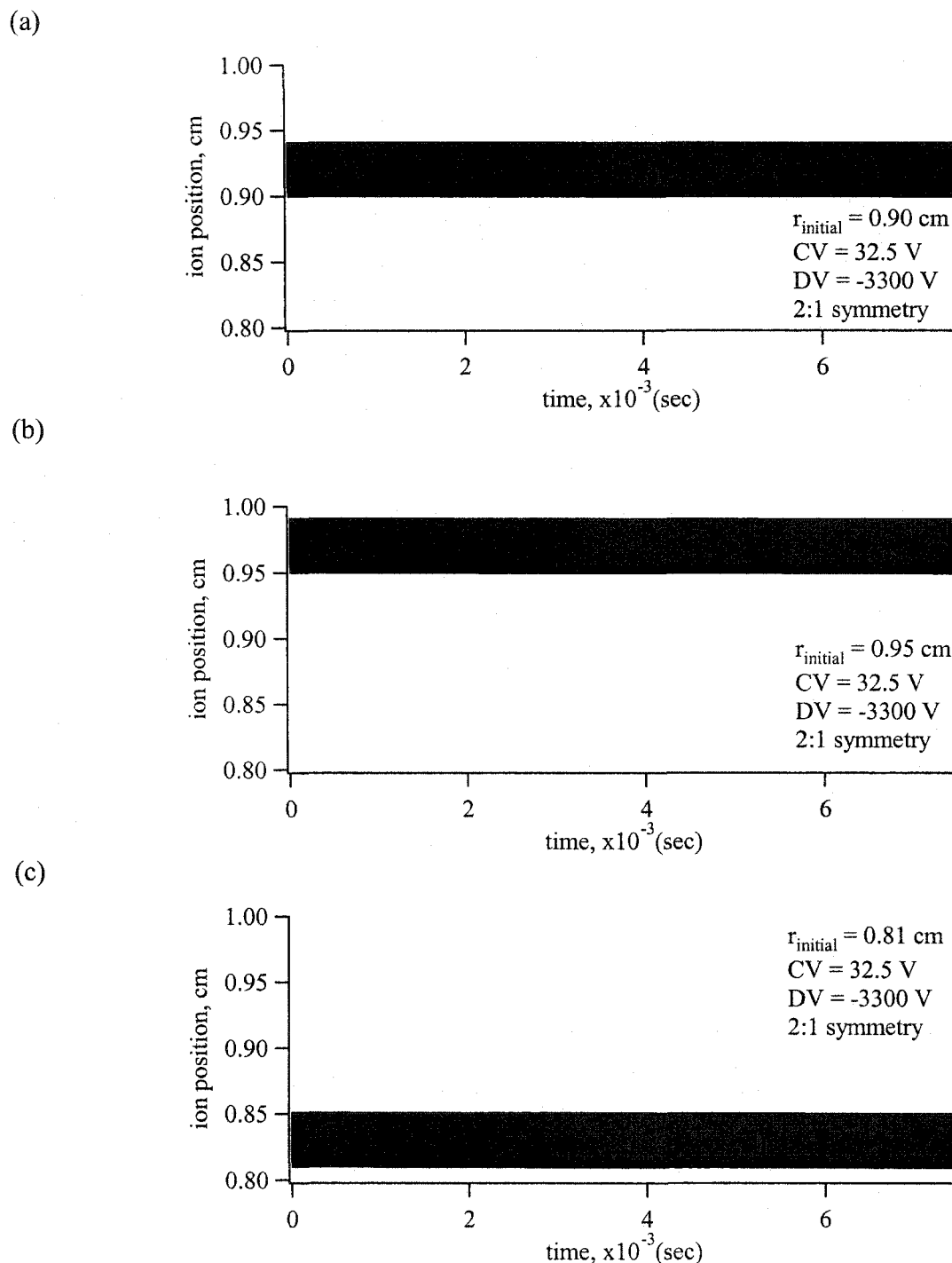


Figure 4.14 Calculated ion trajectory in a parallel plate FAIMS for type A ion with balanced DV and CV for different initial ion positions. Ion mobility as defined in Equation 4.63. DV = -3300 V, CV = 32.5 V. Plate spacing = 0.20 cm. Square wave approximation, $f = 210$ kHz, 2:1 $t_{\text{low}}:t_{\text{high}}$. X-axis (time) represents residence time in the analyzer region. Limits of the y-axis represent the surface of the plates. a) $r_{\text{initial}} = 0.90$ cm, b) $r_{\text{initial}} = 0.95$ cm, c) $r_{\text{initial}} = 0.81$ cm.

first motion was towards the upper plate. If the low-field condition was applied first, the ion would first move towards the lower plate, but with the same balance point after each cycle of the waveform, as shown in Figure 4.15. As a consequence of this, ions with initial positions near the walls will have a significant chance of having field-induced paths that will cause them to strike a wall and be lost. In this example, the width of the field-induced path is about 0.05 cm, so initial positions within 0.05 cm of either wall will tend to strike the wall and be lost. For simplicity, this alternative waveform possibility will be ignored in future modeling.

The CV window that will successfully transport ions is largely dependent on the residence time of the ion within the analyzer. While the true CV balance condition is achieved at $CV = 32.5$ V, under real use conditions, the ion will be transmitted over a range of values, as shown in Figure 4.16. For the parallel plate analyzer as described by Buryakov, *et al* [10, 13], the rate of gas flow through the analyzer suggests that the residence time of an ion in their parallel plate FAIMS apparatus was less than 2 msec [13]. Under this condition of residence time, this hypothetical ion can have a range of CVs that will allow it to be transported through the plates. Figures 4.16 (a) and (b) show the ion under conditions of $CV = 29.8$ V, and $CV = 37.0$ V, respectively, for a CV transmission window of 7.2 V. Obviously, a longer residence time would mean a narrower transmission window. However, the consequence of longer residence time is increased diffusional and collisional losses of ions to the walls, resulting in poor ion transmission, even for ions with the correct balance of DV and CV. So, while a parallel plate apparatus is theoretically capable of very narrow peak widths, in practice the peak widths are much wider, owing to the short residence times used to avoid excessive losses.

4.15.2 Concentric Cylinder FAIMS

The non-linear field dependence with radial position between concentric cylinders makes this FAIMS apparatus advantageous over the parallel plate version. These effects are highlighted by the ion trajectory calculations as illustrated in Figure 4.17. Using the same waveform as with the parallel plates (square wave, 2:1 $t_{low}:t_{high}$, $f = 210$ kHz, $DV =$

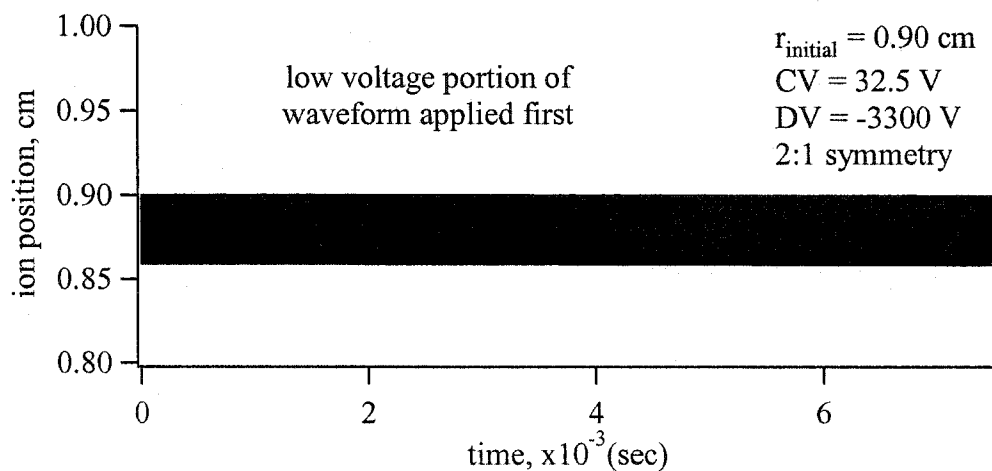
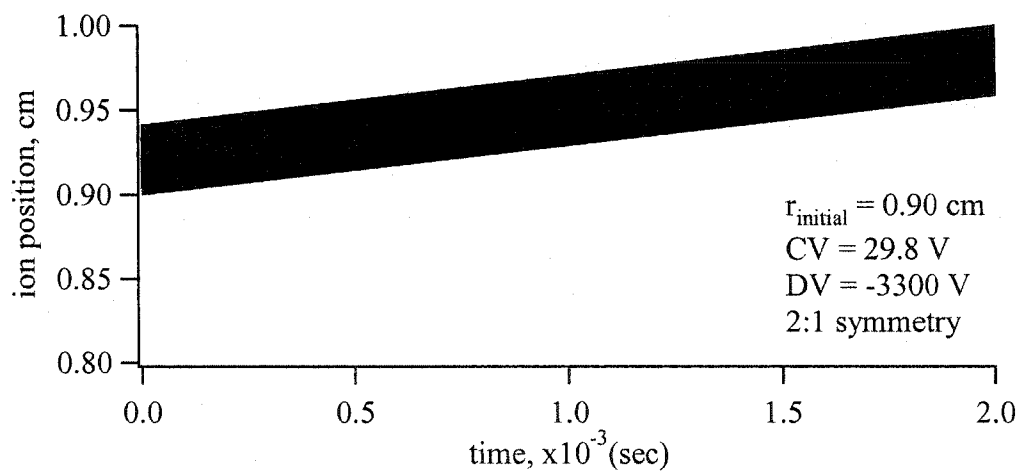


Figure 4.15 Calculated trajectory of a type A ion in a concentric cylinder FAIMS with $a = 0.8 \text{ cm}$, $b = 1.0 \text{ cm}$ with the low-field portion of the waveform applied first. Ion mobility as defined in Equation 4.63. Square wave approximation, 2:1 $t_{\text{low}}:t_{\text{high}}$, $f=210 \text{ kHz}$, $DV = -3300 \text{ V}$, $CV = 35.0 \text{ V}$, $r_{\text{initial}} = 0.95 \text{ cm}$. X-axis (time) represents residence time in the analyzer region. Limits of the y-axis represent the surface of the cylinders.

(a)



(b)

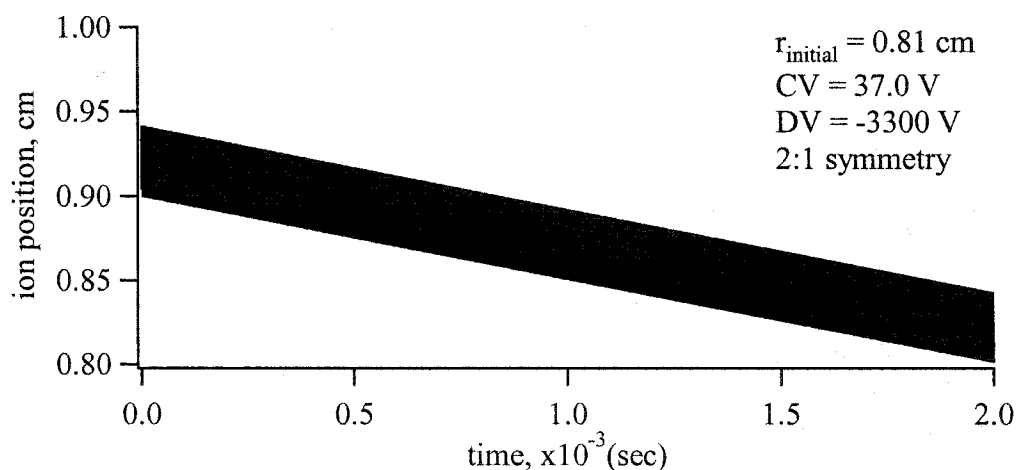


Figure 4.16 Calculated ion trajectory in a parallel plate FAIMS for a type A ion with a short residence time in the analyzer. Ion mobility as defined in Equation 4.63. Plate spacing = 0.2 cm, $r_{\text{initial}} = 0.90$ cm. Square wave approximation, $f = 210$ kHz, 2:1 $t_{\text{low}}:t_{\text{high}}$. X-axis (time) represents residence time in the analyzer region (2 msec total). Limits of the y-axis represent the surface of the plates. (a) DV = -3300 V, CV = 29.8 V, (b) DV = -3300 V, CV = 37.0 V.

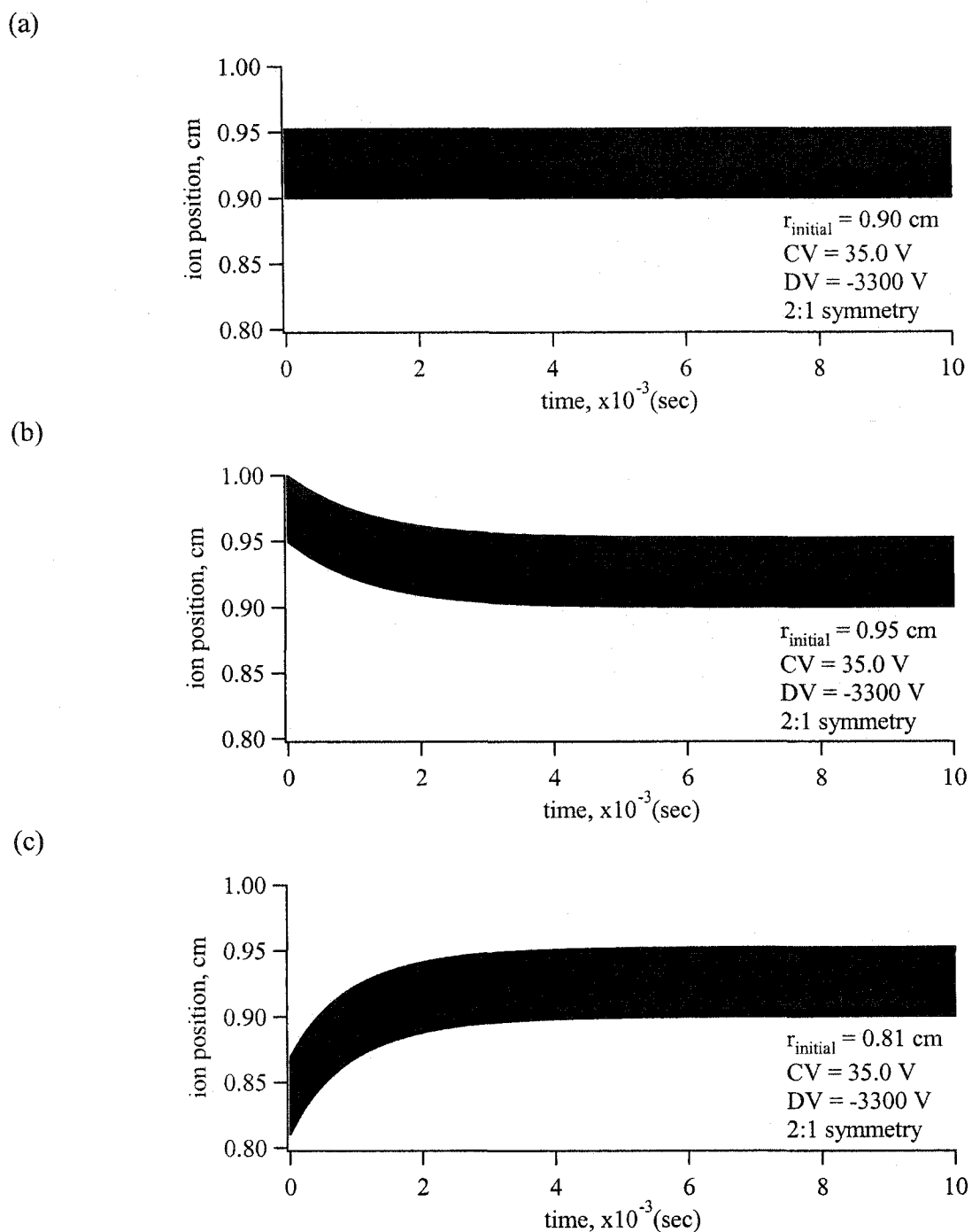


Figure 4.17 Calculated trajectory of a type A ion in a concentric cylinder FAIMS with $a = 0.8$ cm, $b = 1.0$ cm. Ion mobility as defined in Equation 4.63. Square wave approximation, $f = 210$ kHz, 2:1 $t_{\text{low}}:t_{\text{high}}$, $DV = -3300$ V, $CV = 35.0$ V. X-axis (time) represents residence time in the analyzer region. Limits of the y-axis represent the surface of the cylinders. (a) $r_{\text{initial}} = 0.90$ cm, (b) $r_{\text{initial}} = 0.95$ cm, (c) $r_{\text{initial}} = 0.81$ cm.

-3300 V), the motion of the same hypothetical ion was modeled for a concentric cylinder FAIMS with $a = 0.80$ cm, $b = 1.00$ cm. With the $r_{\text{initial}} = 0.90$ cm, the CV required to balance the ion's trajectory was found to be $CV = 35.0$ V (Figure 4.17 (a)). When only the ion's initial radial position was changed, the effects of the non-linear field dependence can be seen. In Figure 4.17 (b), when the initial position is near the outer cylinder ($r_{\text{initial}} = 0.95$ cm), the ion trajectory is moved to the center of the analyzer at $r = 0.90$ cm. Similar effects are observed with the initial position near the inner cylinder at $r_{\text{initial}} = 0.81$ cm (Figure 4.17 (c)). This effect has been termed "ion focusing", and is largely responsible for the success of this interface design [29]. For ions that have not reached the balance position (in this case, at $r = 0.90$ cm), the fields will direct the ion towards this position. As a result, ions that have been moved away from the balance point by diffusion or field-induced random motion will tend to be re-focused towards the balance point. So, by moving ions away from the walls, losses to the walls will be significantly reduced, as compared to a parallel plate apparatus. Furthermore, a longer residence time can be tolerated, since the adverse effects of diffusion have been reduced.

The calculations so far have used a waveform frequency of 210 kHz. Figure 4.18 shows the effect of operating at a frequency of 750 kHz under the same initial radial position, DV, and CV as in Figure 4.17 (b). In calculating the trajectory in Figure 4.18, 126,000 iterations were calculated in order to provide enough modeling time for the trajectory. The obvious effect is the reduction in the calculated ion path width, which has been reduced to ~ 0.0155 cm, as compared to ~ 0.0526 cm at 210 kHz. As discussed earlier, ions near the walls are more likely to strike a wall due to the width of the field-induced path. Obviously, the effect of a narrower path will be to (theoretically) have stable ion paths for a wider range of initial ion positions. So, fewer ions will be lost to diffusion, and ion sampling and transmission should be improved.

The theoretical path widths of the ion trajectories for the same theoretical ion were calculated for a range of frequencies at waveform symmetries of 2:1, 3:1, and 5:1, as shown in Figure 4.19. For all of the symmetries, significant reductions in the path width are achieved with 750 kHz as compared to 210 kHz, with the path widths reducing

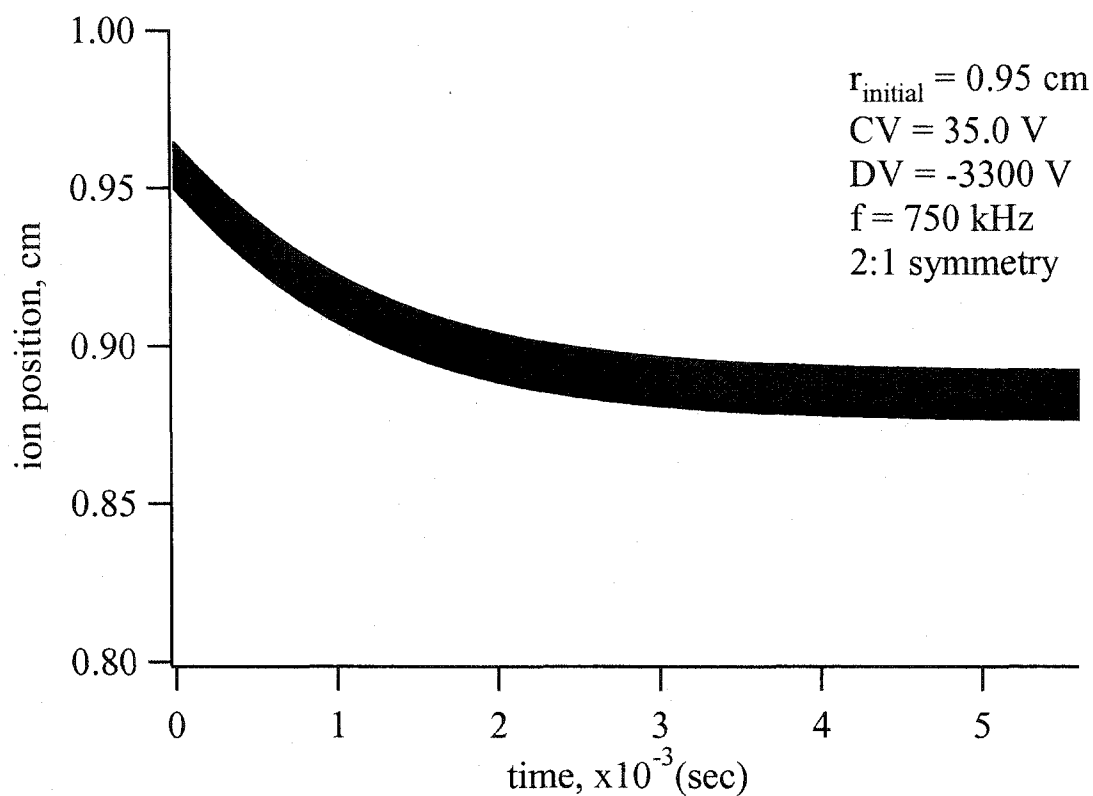


Figure 4.18 Calculated trajectory of a type A ion in a concentric cylinder FAIMS with $a = 0.8 \text{ cm}$, $b = 1.0 \text{ cm}$ at a frequency of 750 kHz . Ion mobility as defined in Equation 4.63. Square wave approximation, 2:1 $t_{\text{low}}:t_{\text{high}}$, $DV = -3300 \text{ V}$, $CV = 35.0 \text{ V}$, $r_{\text{initial}} = 0.95 \text{ cm}$. X-axis (time) represents residence time in the analyzer region. Limits of the y-axis represent the surface of the cylinders.

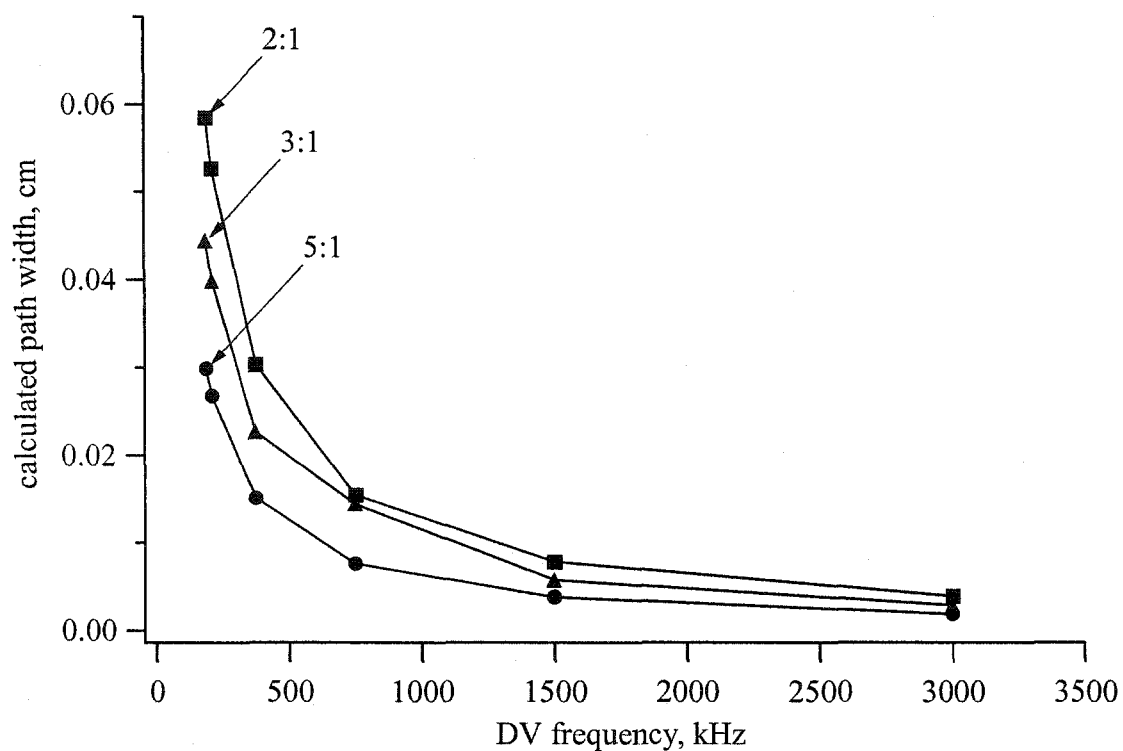


Figure 4.19 Calculated ion trajectory path width as a function of waveform frequency. Symmetry ($t_{\text{low}}:t_{\text{high}}$) of applied waveform as indicated. Type A ion in a concentric cylinder FAIMS with $a = 0.8$ cm, $b = 1.0$ cm. Ion mobility as defined in Equation 4.63. Square wave approximation, $DV = -3300$ V, $CV = 35.0$ V, $r_{\text{initial}} = 0.95$ cm.

about 70 %. Further increases in frequency also provide further reduction in path width, with the path width reducing by about 50% for each doubling in the frequency. While high frequencies are advantageous, building a waveform generator capable of providing both high voltage and high frequency is difficult [52]. For the initial work using parallel plates, a frequency of 2 MHz was used, but only provided a high voltage peak of 925 V [13]. Figure 4.19 also shows that using a symmetry with a greater $t_{\text{low}}:t_{\text{high}}$ ratio also provides narrower path widths. This suggests that using a waveform symmetry with a higher ratio of low:high should be advantageous. However, as will be discussed in Section 4.16, these simulations also show that using a higher ratio leads to a lower CV required to balance the trajectory.

At this point, a comment should be made on observed CV scan peak widths, as related to parallel plates. With parallel plates, the residence time in the analyzer was a major determinant in determining the CV window that would transmit a particular ion. In the case of concentric cylinders, the CV window is determined by the range of CVs that lead to a balanced condition. For our hypothetical ion, the modeling suggests that the range of CVs could be as large as ~ 9 V, for $DV = -3300$ V, $f = 210$ kHz.

4.15.3 Concentric Cylinders that Terminate in a Spherical Dome

The third type of FAIMS interface that appears in the literature is the one of concentric cylinders that terminates in a spherical dome at one end, as illustrated in Figure 4.06 (c). This geometry employs both the cylinder and the spherical expressions for field variation with radial position in the annular space. While the variation of field between both cylinders and spheres is non-linear, the degree of non-linearity differs. The variation of field with radial position for different geometries has been calculated, and is shown in Figure 4.20. The spacing between the electrodes is the same for all calculations at 0.20 cm. The equations for field at radial position discussed earlier were used to calculate the fields at a range of radial positions for parallel plates, concentric cylinders, and concentric spheres. The fields were calculated for 3 different sets of radial dimensions, including 1) $a = 1.2$ cm, $b = 1.4$ cm, 2) $a = 0.8$ cm, $b = 1.0$ cm, and 3) $a = 0.4$

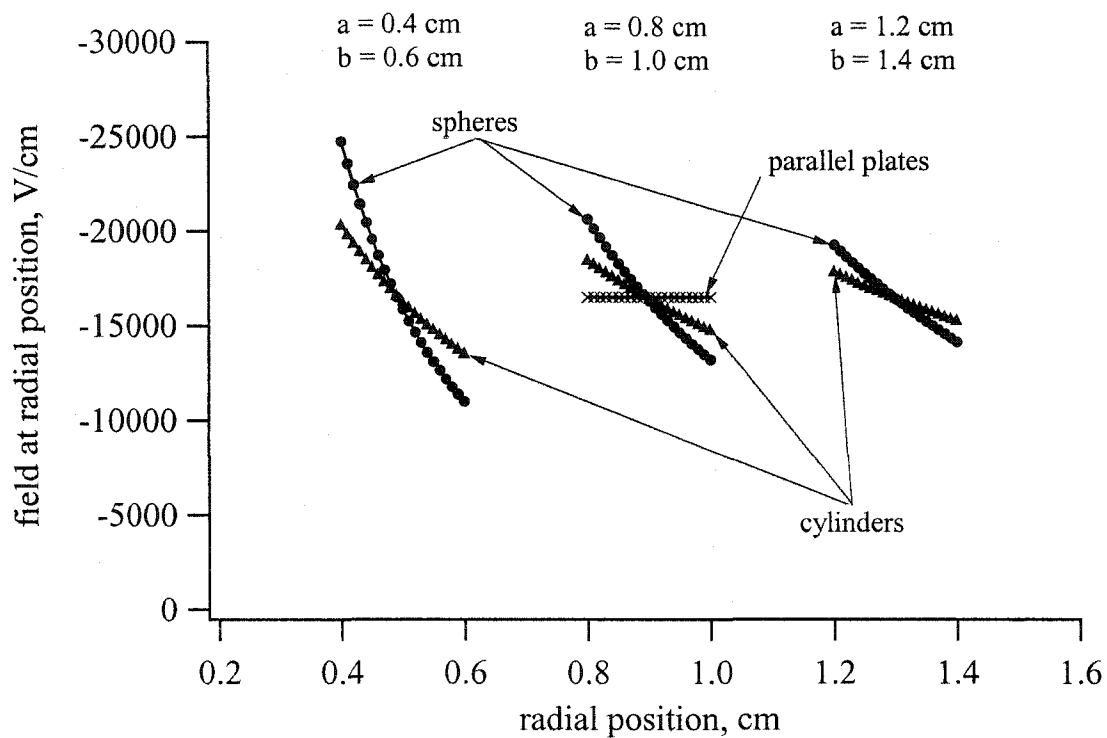


Figure 4.20 Calculated fields at various radial positions within parallel plates, concentric cylinders and concentric spheres. Electrode geometries as indicated. Field values calculated as the field at peak DV = -3300 V.

cm, $b = 0.6$ cm. At a constant voltage applied to the lower (inner) electrode of -3300 V, the field between parallel plates is constant at $-16,500$ V/cm (for all sets of radial dimensions). For concentric cylinders and concentric spheres, there is significant variation in the applied field with radial position. Also, as the electrode radii become smaller, the greater variations in the field strength at different positions results, although the field strength at the mid-point of the annular space remains constant at $-16,500$ V/cm. The slope of these curves is an indication of the relative ion focusing strength that can be achieved with these geometries. For parallel plates, the slope is zero, indicating no ion focusing. As can be seen from the curves, the concentric sphere geometry has a steeper slope than the concentric cylinders by almost a factor of two. So, the ion focusing ability of concentric spheres should be greater than concentric cylinders. Also, a FAIMS with smaller radii of the electrodes will provide increased focusing strength, even though the mid-point field has not been altered.

For determining ion trajectories in a dome FAIMS interface, the modeling was split into two sections. First, the modeling for the concentric cylinder region was done, followed by an abrupt change to a concentric sphere geometry, as shown in Figure 4.21. While in the actual interface the transition from cylinders to dome may be more gradual, the modeling does demonstrate the ion's final radial position at the top of the dome, provided the assumed geometry is correct. For the first set of trajectory calculations, the spherical geometry was maintained at the same radial dimensions as the concentric cylinders at $a = 0.8$ cm, $b = 1.0$ cm. Figure 4.21 (a) shows the calculated ion trajectory for conditions that balance the trajectory ($DV = -3300$ V, $CV = 35.0$ V) for $r_{\text{initial}} = 0.90$ cm while the ion is in the concentric cylinder region. When the ion shifts to the concentric sphere geometry, the ion balance point moves towards the outer cylinder to a radial balance point of 0.91 cm. The effect of different initial radial positions in the cylinder region is the same as in Figure 4.17; the ion is balanced to a radial position of 0.90 cm within the cylinders under these field conditions. Likewise, in Figure 4.21 (b) ($r_i = 0.95$ cm) and 4.21 (c) ($r_i = 0.81$ cm), the ion is balanced in the cylinder region at 0.90 cm. So, with the ion moving into the sphere region at 0.90 cm, the net effect of the fields within the spheres will be to move the ion towards the outer cylinder to a radial position

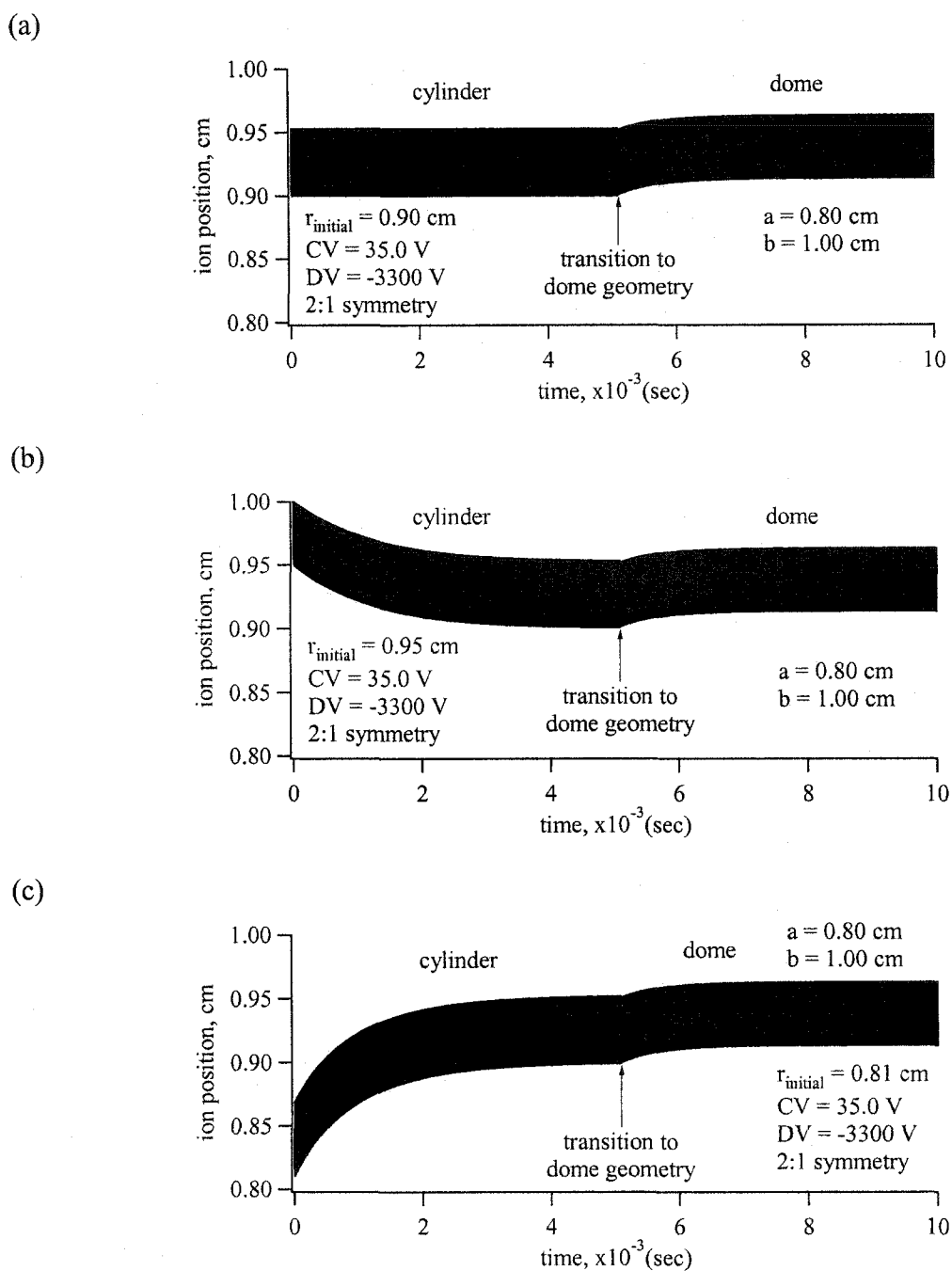


Figure 4.21 Calculated trajectory of a type A ion in a FAIMS with both concentric cylinder and concentric dome geometry. Cylinder and dome regions have dimensions $a = 0.8 \text{ cm}$, $b = 1.0 \text{ cm}$. Ion mobility as defined in Equation 4.63. Square wave approximation, $f = 210 \text{ kHz}$, 2:1 $t_{\text{low}}:t_{\text{high}}$, $DV = -3300 \text{ V}$, $CV = 35.0 \text{ V}$. X-axis (time) represents residence time in the analyzer region. Limits of the y-axis represent the surface of the electrodes. First half of modeling for concentric cylinder geometry, second half for concentric sphere geometry. (a) $r_{\text{initial}} = 0.90 \text{ cm}$, (b) $r_{\text{initial}} = 0.95 \text{ cm}$, (c) $r_{\text{initial}} = 0.81 \text{ cm}$.

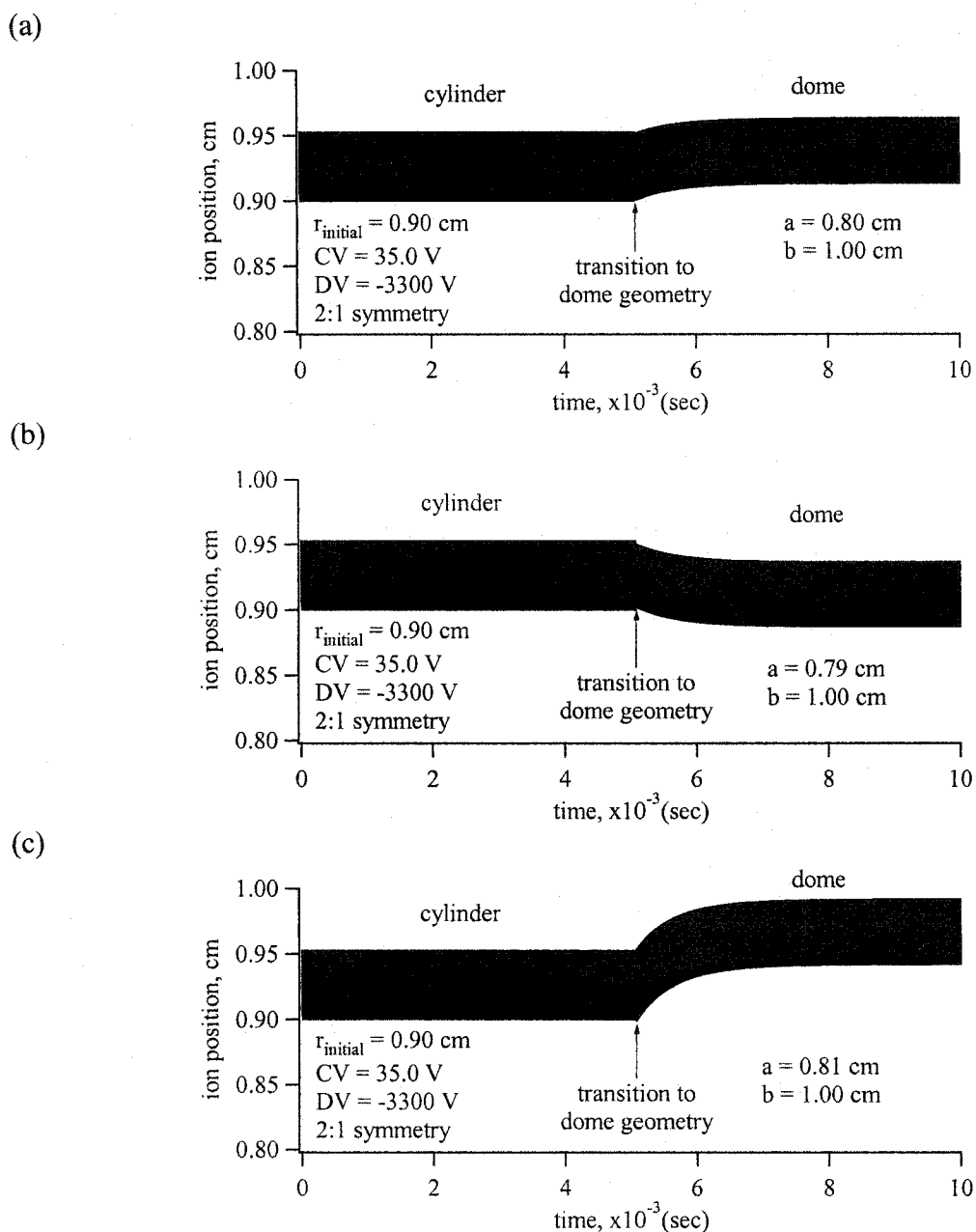


Figure 4.22 Calculated trajectory of a type A ion in a FAIMS with both concentric cylinder and concentric dome geometry. Cylinder region has dimensions $a = 0.8 \text{ cm}$, $b = 1.0 \text{ cm}$. Ion mobility as defined in Equation 4.63. Square wave approximation, $f = 210 \text{ kHz}$, 2:1 $t_{\text{low}}:t_{\text{high}}$, $DV = -3300 \text{ V}$, $CV = 35.0 \text{ V}$. X-axis (time) represents residence time in the analyzer region. Limits of the y-axis represent the surface of the electrodes. First half of modeling for concentric cylinder geometry, second half for concentric sphere geometry. (a) dome dimensions $a = 1.0 \text{ cm}$, $b = 0.8 \text{ cm}$, (b) dome dimensions $a = 1.0 \text{ cm}$, $b = 0.79 \text{ cm}$, (c) dome dimensions $a = 1.0 \text{ cm}$, $b = 0.81 \text{ cm}$.

of 0.91 cm. In the dome FAIMS, the spacing at the top of the dome can be adjusted, and this has significant effects on the fields. Figure 4.22 (a) shows the dome spacing equal to the cylinder region. In Figure 4.22 (b) and (c), the dome dimensions have been altered in order to approximate the effect of adjusting the dome spacing. In Figure 4.22 (b), the inner radius has been reduced to 0.79 cm. Under these conditions, the ion balance point has been moved to 0.89 cm, towards the inner electrode. Similarly, making the inner electrode radius $a = 0.81$ cm, the ion balance point has been moved to 0.94 cm, towards the outer electrode. The impact of these adjustments will be discussed in Chapter 6. Overall, the concentric sphere geometry allows for a greater degree of ion focusing than concentric cylinders, and variations in the sphere geometry relative to the cylinder geometry can have significant effects on the calculated ion trajectory.

4.16 Waveform Generation

One type of asymmetric waveform that can be used with FAIMS is illustrated in Figure 4.04. It is composed of two sine waves, with one sine wave at frequency = f and peak voltage = $2V$, and the other sine wave with frequency = $2f$ and a peak voltage = V . If these two sine waves are combined, such that their positive polarity peaks are out of phase by 90° (as illustrated in Figure 4.04 (a)), the resultant waveform is illustrated in Figure 4.04 (b)). This is the actual symmetry of the waveform used in most of the FAIMS literature, and in this work. However, as outlined in a paper by Krylov, several different waveform symmetries can be used for a FAIMS apparatus [52]. This paper provides the circuit diagrams for 4 different types of waveform generators, and evaluates their performance characteristics (peak amplitude, frequency, power consumption, and symmetry) for use with FAIMS, and provides an excellent first reference for those interested in building their own waveform generator.

As mentioned previously, the theoretical performance of square waveforms of differing voltage symmetry was evaluated. Using the same ion modeling conditions for concentric cylinders, the symmetries of 2:1, 3:1, and 5:1 were tested, and the CV required

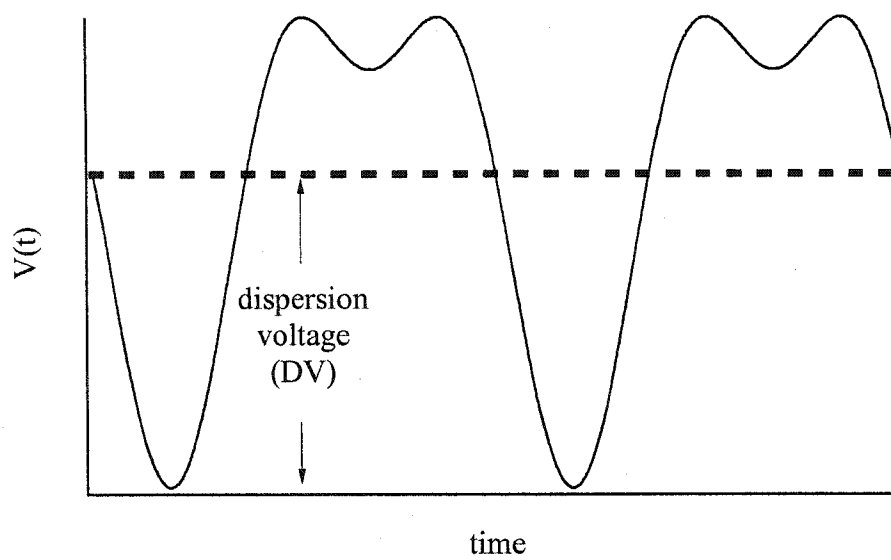
to balance an initial ion position of 0.90 cm was determined. Theoretically, the larger the CV required under a set of test conditions, the better the likelihood that 2 different ions may be separated as the result of inducing greater relative K_h/K differences. The symmetry of 2:1 was the best, with a CV = 35.0 V, closely followed by 3:1 with a CV = 33.6 V. The symmetry of 5:1 was found to need a CV = 25.4 V, significantly lower than the other symmetries. The basis for this is fairly straightforward. First, the magnitude of the applied CV is directly proportional to the magnitude of the net drift per cycle of the waveform. So, the net drift is maximized by allowing the time at high field to be as large as possible. For these symmetries tested, the 2:1 ratio symmetry provides the longest time at the DV, so should provide the greatest net drift per cycle, and hence, CV. It should be noted that a 3:1 ratio may be considered the superior symmetry, since for a small compromise in CV, the theoretical ion path width is less than at 2:1, as discussed in Section 4.15.2.

4.17 Waveforms for Various K_h/K Behaviors

Thus far, the only ions to be considered in the discussion are small negative ions which exhibit an increase in K_h/K with increasing field strength (Figure 4.09 (b)), such as a type A ion in Figure 4.02. For this type of ion, an applied waveform which generates a high negative field and a low positive field (which satisfies Equation 4.58) causes the ion to have a net motion away from the lower plate to which the field was applied, as illustrated in Figure 4.09 (a). If the ion was type B or C, this applied waveform would have caused the ion to drift into the lower plate, due to a lower mobility at high negative fields. Note that a type B ion may be transmitted with this waveform at low values of applied field. Using this waveform (under high voltage conditions), only type A negative ions can be successfully focused and transmitted using a positive CV applied to the lower plate. The ion trajectory modeling used earlier does suggest that a type C ion might be transmitted at a high negative CV value, although only a single initial ion position can be balanced at a particular CV value. Furthermore, modeling suggests that very small changes in the magnitude of the applied CV (less than 0.01 V) can cause destabilization

of the ion trajectory. With the addition of random motions, there is little chance of transmission of a negative type C ion under these conditions. In fact, to properly transmit an anion of type C, the opposite waveform symmetry must be applied, which generates a low negative field, and a high positive field of shorter duration. Under these conditions, the type C anion would have a net drift towards the upper plate and be balanced with a positive CV applied to the lower plate. For these reasons, the two different waveform symmetries produce different spectra and are referred to as the N1 and N2 waveforms, as illustrated in Figure 4.23. The N1 waveform has a high negative DV and is used for type A anions, and the N2 waveform has a high positive DV and is used for type C anions [18]. Not surprisingly, a similar situation exists for positive ions. A waveform with the N2 symmetry combined with a negative CV applied to the lower plate is used for type A cations, and this mode is referred to as the P1 mode. Similarly, a waveform with N1 symmetry combined with a negative CV is used for type C cations, and is called the P2 mode. Again, each operational mode is distinct in the type of ion K_h/K behavior that it transmits. So, the FAIMS is operated in N1, P1, N2, or P2 mode, depending on the ion polarity and K_h/K behavior desired, and all modes produce different CV spectra [18, 31, 37]. Furthermore, due to the waveforms used in these modes, the waveforms are referred to as the N1-P2 waveform and the P1-N2 waveform [18].

(a)



(b)

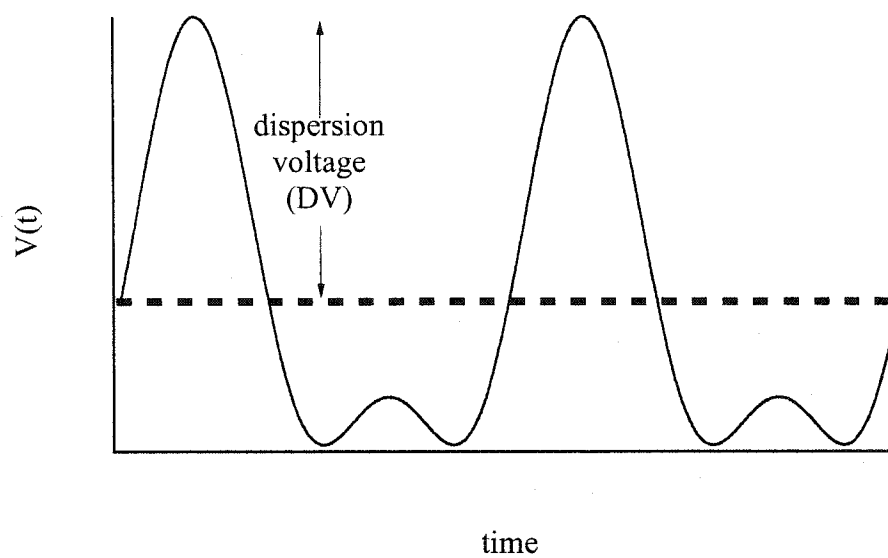


Figure 4.23 Waveforms used in FAIMS; (a) the N1-P2 waveform; (b) the P1-N2 waveform.

4.18 References

1. Eiceman, G. A.; Karpas, Z. *Ion Mobility Spectrometry*; CRC Press: Boca Raton, FL, 1994.
2. Mason, E. A.; McDaniel, E. W. *Transport Properties of Ions in Gases*; John Wiley & Sons, Inc., 1988.
3. Loboda, A. V. "Ion mobility spectrometer incorporating an ion guide in combination with an MS device"; *Canadian Intellectual Property Office* **2001**. Canada. Canadian Patent No. 2,364,676.
4. Srebalus, C. A.; Li, J.; Marshall, W. S.; Clemmer, D. E. "Gas-phase separations of electrosprayed peptide libraries"; *Anal. Chem.* **1999**, 3918-3927.
5. Srebalus-Barnes, C. A.; Clemmer, D. E. "Assessment of purity and screening of peptide libraries by nested ion mobility - TOFMS: Identification of RNase s-protein binders"; *Anal. Chem.* **2001**, 73, 424-433.
6. Srebalus-Barnes, C. A.; Hilderbrand, A. E.; Valentine, S. J.; Clemmer, D. E. "Resolving isomeric peptide mixtures: A combined HPLC / ion mobility - TOFMS analysis of a 4000-component combinatorial library"; *Anal. Chem.* **2002**, 74, 26-36.
7. Stone, E.; Gillig, K. J.; Ruotolo, B.; Fuhrer, K.; Gonin, M.; Schults, A.; Russell, D. H. "Surface-induced dissociation on a MALDI - ion mobility - orthogonal time-of-flight mass spectrometer: Sequencing peptides from an "in solution" protein digest"; *Anal. Chem.* **2001**, 73, 2233-2238.
8. Valentine, S. J.; Kulchania, M.; Srebalus-Barnes, C. A.; Clemmer, D. "Multidimensional separations of complex peptide mixtures: A combined high-performance liquid chromatography / ion mobility / time-of-flight spectrometry approach"; *Int. J. Mass Spectrom.* **2001**, 212 (1-3), 97-109.
9. Hoaglund-Hyzer, C. S.; Lee, Y. J.; Counterman, A. E.; Clemmer, D. E. "Coupling ion mobility separations, collisional activation techniques, and multiple stages of MS for analysis of complex peptide mixtures"; *Anal. Chem.* **2002**, 74, 992-1006.

10. Buryakov, I. A.; Krylov, E. V.; Nazarov, E. G.; Rasulev, U. K. "A new method of separation of multi-atomic ions by mobility at atmospheric pressure using a high-frequency amplitude-asymmetric strong electric field"; *Int. J. Mass Spectrom. Ion Proc.* **1993**, 128, 143-148.
11. Avakov, A. S.; Buryakov, I. A.; Krylov, E. V.; Nazarov, E. G.; Rasulev, U. K.; Soldatov, V. P. "Proceedings of the Eighth All-Union Conference"; *Physics of Low-Temperature Plasmas.*, , 1997.
12. Buryakov, I. A.; Krylov, E. V.; Soldatov, V. P. "Inventor's Certificate (USSR) No. 1485808 [in Russian], G01 No. 27/62"; *Byull. Izobret.* **1989**. USSR. No. 1485808.
13. Buryakov, I. A.; Krylov, E. V.; Makas', A. L.; Nazarov, E. G.; Pervukhin, V. V.; Rasulev, U. K. "Separation of ions according to mobility in a strong AC electric field"; *Sov. Tech. Phys. Lett.* **1991**, 17, 446-447.
14. Gorshkov, M. P. "Inventors Certificate (USSR) No. 966583"; *Byull. Izobret.* **1982**. USSR. No. 966583.
15. Carnahan, B. L.; Tarassov, A. S. "Ion Mobility Spectrometer"; **1995**, Mine Safety Appliances Company, Pittsburgh, Pa. United States. Patent No. 5 420 424.
16. Carnahan, B.; Day, S.; Kouznetsov, V.; Matyjaszczyk, M.; Tarassov, A. "Proceedings of the 41st Annual ISA Analysis Division Symposium"; *41st Annual ISA Analysis Division Symposium.*, Framingham, MA, April 21-24, 1996.
17. Riegner, D.; Harden, C.; Carnahan, B.; Day, S. "Proceedings of the 45th ASMS Conference on Mass Spectrometry and Allied Topics"; Palm Springs, FL, 1-5 June, 1997.
18. Purves, R. W.; Day, S.; Pipich, C. W.; Matyjaszczyk, M. S.; Guevremont, R. "Mass spectrometric characterization of a high-field asymmetric waveform ion mobility spectrometer"; *Rev. Sci. Instrum.* **1998**, 69, 4094-4105.
19. Barnett, D. A.; Guevremont, R.; Purves, R. W. "Determination of parts-per-trillion levels of chlorate, bromate, and iodate by electrospray ionization/high-field asymmetric waveform ion mobility spectrometry/mass spectrometry"; *Appl. Spectrosc.* **1999**, 53, 1367-1374.

20. Barnett, D. A.; Ells, B.; Purves, R. W.; Guevremont, R. "Separation of leucine and isoleucine by electrospray ionization-high field asymmetric waveform ion mobility spectrometry-mass spectrometry"; *J. Am. Soc. Mass Spectrom.* **1999**, 10, 1279-1284.
21. Barnett, D. A.; Ells, B.; Guevremont, R.; Purves, R. W.; Viehland, L. A. "Evaluation of carrier gases for use in high-field asymmetric waveform ion mobility spectrometry"; *J. Am. Soc. Mass Spectrom.* **2000**, 11, 1125-1133.
22. Barnett, D. A.; Purves, R. W.; Guevremont, R. "Isotope separation using high-field asymmetric waveform ion mobility spectrometry"; *Nuc. Instrum. Meth. Phys. Res. A* **2000**, 450, 179-185.
23. Barnett, D. A.; Purves, R. W.; Ells, B.; Guevremont, R. "Separation of *o*-, *m*- and *p*-phthalic acids by high-field asymmetric waveform ion mobility spectrometry (FAIMS) using mixed carrier gases"; *J. Mass Spectrom.* **2000**, 35, 976-980.
24. Ells, B.; Barnett, D. A.; Froese, K.; Purves, R. W.; Hrudey, S.; Guevremont, R. "Detection of chlorinated and brominated byproducts of drinking water disinfection using electrospray ionization-high-field asymmetric waveform ion mobility spectrometry-mass spectrometry"; *Anal. Chem.* **1999**, 71, 4747-4752.
25. Ells, B.; Barnett, D. A.; Purves, R. W.; Guevremont, R. "Detection of nine chlorinated and brominated haloacetic acids at part-per-trillion levels using ESI-FAIMS-MS"; *Anal. Chem.* **2000**, 72, 4555-4559.
26. Ells, B.; Froese, K.; Hrudey, S. E.; Purves, R. W.; Guevremont, R.; Barnett, D. A. "Detection of microcystins using electrospray ionization high-field asymmetric waveform ion mobility mass spectrometry / mass spectrometry"; *Rapid Commun. Mass Spectrom.* **2000**, 14, 1538-1542.
27. Ells, B.; Barnett, D. A.; Purves, R. W.; Guevremont, R. "Trace level determination of perchlorate in water matrices and human urine using ESI-FAIMS-MS"; *J. Environ. Monit.* **2000**, 2, 393-397.
28. Guevremont, R.; Siu, K. W. M.; Wang, J.; Ding, L. "Combined ion mobility / time-of-flight mass spectrometry study of electrospray-generated ions"; *Anal. Chem.* **1997**, 69, 3959-3965.

29. Guevremont, R.; Purves, R. W. "Atmospheric pressure ion focusing in a high-field asymmetric waveform ion mobility spectrometer"; *Rev. Sci. Instrum.* **1999**, *70*, 1370-1383.
30. Guevremont, R.; Purves, R. W.; Barnett, D. A.; Ding, L. "Ion trapping at atmospheric pressure (760 Torr) and room temperature with a high-field asymmetric waveform ion mobility spectrometer"; *Int. J. Mass Spectrom.* **1999**, *193*, 45-56.
31. Guevremont, R.; Purves, R. W. "High field asymmetric waveform ion mobility spectrometry-mass spectrometry: An investigation of leucine enkephalin ions produced by electrospray ionization"; *J. Am. Soc. Mass Spectrom.* **1999**, *10*, 492-501.
32. Guevremont, R.; Barnett, D. A.; Purves, R. W.; Vandermeij, J. "Analysis of a tryptic digest of pig hemoglobin using ESI-FAIMS-MS"; *Anal. Chem.* **2000**, *72*, 4577-4584.
33. Guevremont, R.; Barnett, D. A.; Purves, R. W.; Viehland, L. A. "Calculation of ion mobilities from electrospray ionization high-field asymmetric waveform ion mobility spectrometry mass spectrometry"; *J. Chem. Phys.* **2001**, *114*, 10270-10277.
34. Guevremont, R.; Ding, L.; Ells, B.; Barnett, D. A.; Purves, R. W. "Atmospheric pressure ion trapping in a tandem FAIMS-FAIMS coupled to a TOFMS: Studies with electrospray generated Gramicidin S ions"; *J. Am. Soc. Mass Spectrom.* **2001**, *12*, 1320-1330.
35. Handy, R.; Barnett, D. A.; Purves, R. W.; Horlick, G.; Guevremont, R. "Determination of nanomolar levels of perchlorate in water by ESI-FAIMS-MS"; *J. Anal. At. Spectrom.* **2000**, *15*, 907-911.
36. McCooeye, M. A.; Ells, B.; Barnett, D. A.; Purves, R. W.; Guevremont, R. "Quantitation of morphine and codeine in human urine using high-field asymmetric waveform ion mobility spectrometry (FAIMS) with mass spectrometric detection"; *J. Anal. Tox.* **2001**, *25*, 81-87.

37. Purves, R. W.; Guevremont, R. "Electrospray ionization high-field asymmetric waveform ion mobility spectrometry-mass spectrometry"; *Anal. Chem.* **1999**, *71*, 2346-2357.
38. Purves, R. W.; Barnett, D. A.; Guevremont, R. "Separation of protein conformers using electrospray-high-field asymmetric waveform ion mobility spectrometry-mass spectrometry"; *Int. J. Mass Spectrom.* **2000**, *197*, 163-177.
39. Purves, R. W.; Barnett, D. A.; Ells, B.; Guevremont, R. "Investigation of bovine ubiquitin conformers separated by high-field asymmetric waveform ion mobility spectrometry: Cross section measurements using energy-loss experiments with a triple quadrupole mass spectrometer"; *J. Am. Soc. Mass Spectrom.* **2000**, *11*, 738-745.
40. Purves, R. W.; Barnett, D. A.; Guevremont, R. "Separation of protein conformers using electrospray-high field asymmetric waveform ion mobility spectrometry-mass spectrometry"; *Int. J. Mass Spectrom.* **2000**, *197*, 163-167.
41. Purves, R. W.; Barnett, D. A.; Ells, B.; Guevremont, R. "Gas phase conformers of the $[M+2H]^{2+}$ of bradykinin investigated by combining high-field asymmetric waveform ion mobility spectrometry, hydrogen / deuterium exchange, and energy loss measurements"; *Rapid Comm. Mass Spectrom.* **2001**, *15*, 1453-1456.
42. Purves, R. W.; Barnett, D. A.; Ells, B.; Guevremont, R. "Elongated conformers of charge states +11 to +15 of bovine ubiquitin studied using ESI-FAIMS-MS"; *J. Am. Soc. Mass Spectrom.* **2001**, *12*, 894-901.
43. Guevremont, R.; Purves, R.; Barnett, D. A. "Method for separation of isomers and different conformations of ions in gaseous phase"; *Canadian Intellectual Property Office* **1999**. Canada. Canadian Patent No. 2,339,553.
44. Guevremont, R.; Purves, R. "Apparatus and method for desolvating and focussing ions for introduction into a mass spectrometer"; *Canadian Intellectual Property Office* **1999**. Canada. Canadian Patent No. 2,339,552.
45. Guevremont, R.; Purves, R.; Barnett, D. A. "Method for separation and enrichment of isotopes in gaseous phase"; *Canadian Intellectual Property Office* **1999**. Canada. Canadian Patent No. 2,339,549.

46. Guevremont, R.; Purves, R. "Apparatus and method for atmospheric pressure 3-dimensional ion trapping"; *Canadian Intellectual Property Office* **1999**. Canada. Canadian Patent No. 2,260,572.
47. Krylov, E. V. "A method of reducing diffusion losses in a drift spectrometer"; *Tech. Phys.* **1999**, 44, 113-116.
48. Spangler, G. E. "Fundamental considerations for the application of miniature ion mobility spectrometry to field analytical applications"; *Field Anal. Chem. Tech.* **2000**, 4, 255-267.
49. Spangler, G. E.; Miller, R. A. "Application of mobility theory to the interpretation of data generated by linear and RF excited ion mobility spectrometers"; *Int. J. Mass Spectrom.* **2002**, 214, 95-104.
50. Viehland, L. A.; Guevremont, R.; Purves, R. W.; Barnett, D. A. "Comparison of high-field ion mobility obtained from drift tubes and a FAIMS apparatus"; *Int. J. Mass Spectrom.* **2000**, 197, 123-130.
51. Weidner, R. T.; Sells, R. L. *Elementary Classical Physics*, Second ed.; Allyn and Bacon, Inc.: Boston, MA, 1973.
52. Krylov, E. V. "Pulses of special shapes formed on a capacitive load"; *Instrum. Exp. Tech.* **1997**, 40, 628-631.
53. Sohn, H.; Steinhanses, J. "Use of ion mobility for the preliminary evaluation of hazardous military waste sites - opportunities and limitations"; *Int. J. Ion Mob. Spectrom.* **1998**, 1, 1-14.

Chapter 5

Determination of Nanomolar Levels of Perchlorate in Water by ESI-FAIMS-MS^{1,2}

¹ A version of this chapter has been published. Russell Handy, David A. Barnett, Randy W. Purves, Gary Horlick, Roger Guevremont, *J. Anal. At. Spectrom.*, **2000**, *15*, 907-911.

² Paper featured in “Analytical Currents”; *Anal. Chem.*, **2000**, *21*, 680A.

5.1 Introduction

5.1.1 Concentric Cylinder FAIMS Prototype

A continuous flow technique for the separation of gas-phase ions at atmospheric pressure and room temperature, referred to as high-field asymmetric waveform ion mobility spectrometry (FAIMS), has been described [1-3]. This FAIMS apparatus was based upon a concentric cylinder design as patented by Carnahan and Tarrasov, and was manufactured by Mine Safety Appliances Co. [4]. This prototype was designed to couple a FAIMS with a corona discharge ionization source to a mass spectrometer, in an effort to characterize the peaks observed with the electrometer detection instrument. This prototype was modified by Guevremont, where the corona source was replaced by an electrospray ionization source.

As described in Chapter 4, the FAIMS separates ions by taking advantage of the dependence of gas-phase ion mobility on applied electric field, E . At low electric fields, ion mobility, K , is independent of field strength, whereas at high fields (e.g., $E > 10^4$ V/cm) ion mobility is a function of E and may be denoted as K_h . If two ions have different values of K_h/K at a set electric field, the FAIMS may be able to separate these two ions based on the difference in these values.

The FAIMS analyzer region, illustrated in Figure 5.01, consists of two concentric cylinders; the outer cylinder is kept at a constant dc potential while an asymmetric waveform is applied to the inner cylinder. The waveform, $V(t)$, is composed of a brief high-voltage component, and a longer low-voltage component of opposite polarity. The integrated voltage-time product of one complete cycle of the waveform is equal to zero. The magnitude of the high-voltage component is referred to as the dispersion voltage (DV). Consider an ion (e.g., perchlorate) that is transported by a gas stream between the two cylinders, as illustrated in Figure 5.01. If the high-field portion of $V(t)$ is sufficiently large, such that $K_h > K$, the distance traveled by the ion during the high-field portion is greater than the distance traveled during the low-field portion of $V(t)$. The ion, therefore,

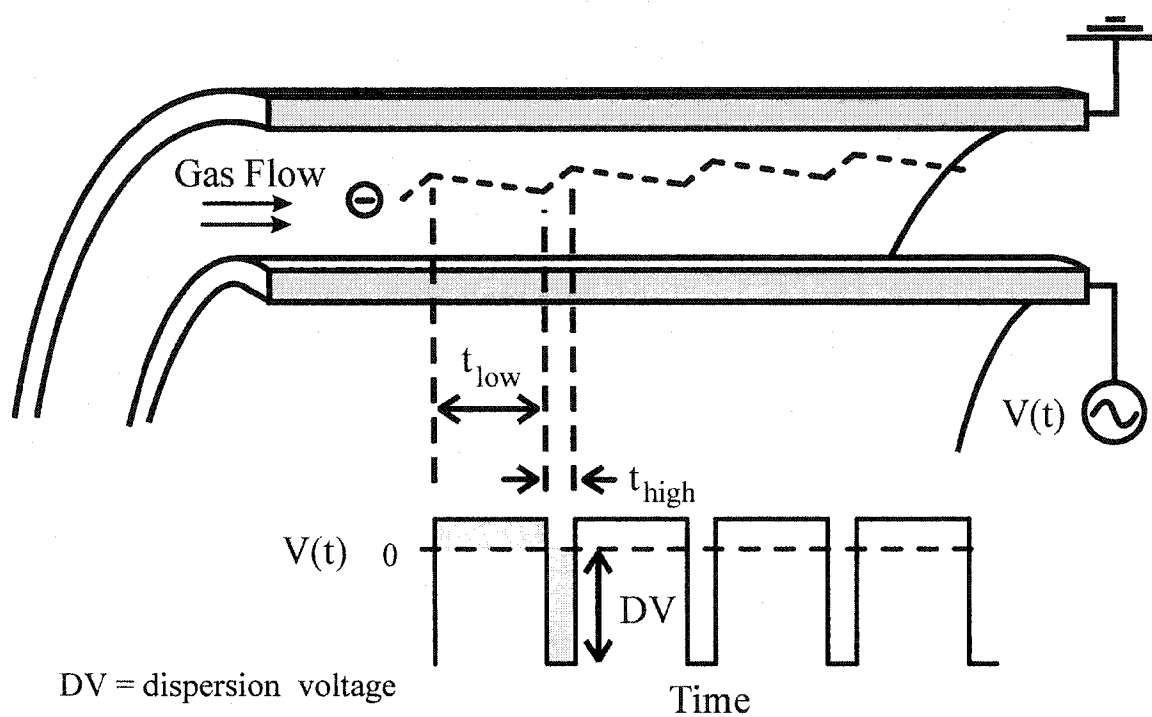


Figure 5.01 An illustration of ion motion between the concentric cylinders of the FAIMS analyzer during the application of an asymmetric waveform shown as $V(t)$; the ion is transported horizontally by a gas flow (distance not to scale).

experiences a net displacement from its original position during each cycle of $V(t)$, and begins to move toward the outer cylinder, as illustrated by the dashed line in Figure 5.01.

To “compensate” for the drift of this ion toward the outer cylinder, a constant dc voltage is applied to the inner cylinder. This dc voltage, referred to as the compensation voltage (CV), enables the ion to pass between the cylinders with no net drift toward either cylinder. If two ions (e.g., perchlorate and bisulphate) respond differently to the applied electric field (i.e., their ratios of K_h to K are not identical), the CV values necessary to prevent their drift will differ, allowing selective transmission of one ion over the other. To analyze a mixture of ions, the CV may be scanned to transmit each of the components of a mixture in turn, resulting in a CV spectrum.

Several applications of ESI-FAIMS-MS have recently been reported [5-10]. In this study, the advantages of using FAIMS to separate ESI-generated perchlorate ions from sulphate, phosphate, and other isobaric interferences, coupled with the selectivity and sensitivity of MS detection are demonstrated.

5.1.2 Analysis of Perchlorate

Production and handling of perchlorate salts, related to its use as a solid oxidant in missiles, rockets, and fireworks, have led to significant levels of perchlorate in the environment [11]. Elevated levels of perchlorate in drinking water have led to growing concerns regarding its toxicity. Perchlorate is a competitive inhibitor for iodide uptake in the human thyroid. Thus the potential exists for the disruption of thyroid hormone production and homeostasis, possibly causing abnormal metabolism, growth, and development [11]. Due to the lack of sufficient toxicological data, perchlorate has been added to the U.S. EPA’s Drinking Water Contaminant Candidate List (CCL). In 1997, the California Department of Health Services (CA DHS) established a provisional action level for perchlorate in drinking water of 18 parts-per-billion (ppb) [11].

Only one method, based on ion chromatography (IC), has gained acceptance for trace analysis of perchlorate. The detection limits are about 0.3-0.7 ppb or about 3-7 nM, with a reporting limit of about 4 ppb [12, 13]. This method relies on non-specific detection (i.e., matching of sample peak retention time with a standard peak), and the sample throughput is low due to analysis times on the order of ten minutes per sample. Other methods for measuring perchlorate with comparable detection limits are required to validate the IC method and to confirm results for difficult matrices. ESI-MS methods for perchlorate analysis have been reported with detection limits of about 50 nM [14]. However, this work was done in the absence of interfering matrix ions such as sulphate and phosphate. Recently, a method based on ESI-MS analysis of stable association complexes of perchlorate with organic cations has been developed and achieves method detection limits of about 1 nM [15].

5.2 Experimental

A schematic of the ESI-FAIMS-MS instrument used in this study is shown in Figure 5.02. A detailed description of this apparatus has been given previously [1, 3]. The inner cylinders had an inner diameter of 12 mm and an outer diameter of 14 mm. The short inner cylinder was about 30 mm in length, and the longer inner cylinder was about 90 mm in length. The outer cylinder has an inner diameter of 18 mm, and outer diameter of 20 mm, and a length of about 125 mm. The electrospray needle was placed inside the FAIMS apparatus, positioned within the short inner cylinder. Negative ions were produced with the electrospray needle biased at -2100 V, giving an electrospray current of about 40 nA. The DV of the asymmetric waveform applied to the long inner cylinder was varied between 0 and -3300 V, and the frequency of the asymmetric waveform was 210 kHz. Since the spacing between the cylinders was 0.2 cm, the values of DV correspond to electric fields of roughly 0 to -16,500 V/cm. The CV, which was also applied to the long inner cylinder of the FAIMS analyzer, could be scanned over specified voltage ranges, or set to a specific value to transmit selected ions. Note that slight differences in tuning the asymmetric waveform might cause day-to-day variations in the CV [16].

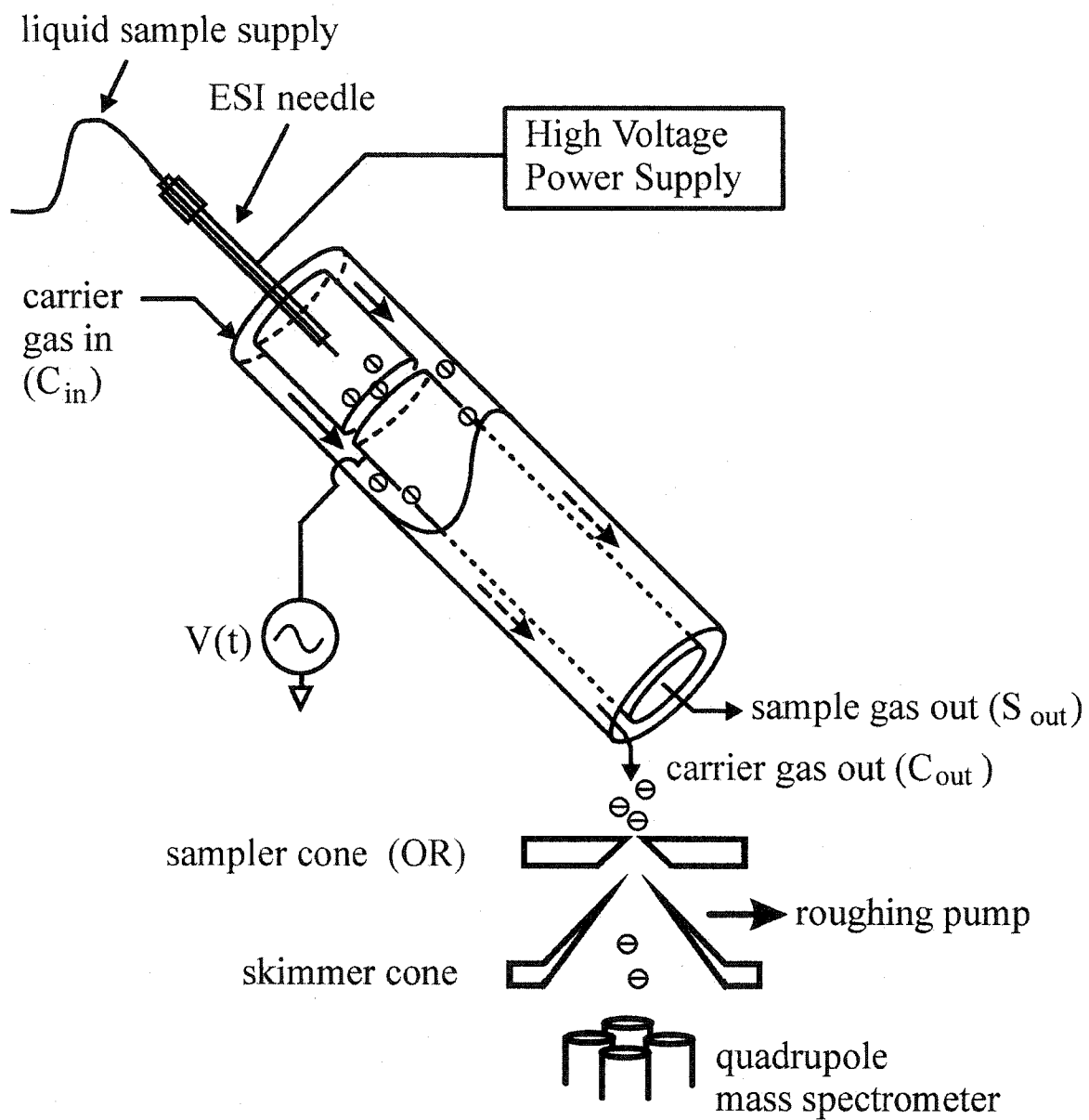


Figure 5.02 Schematic of the ESI-FAIMS-MS instrument.

With appropriate DV and CV values, ions were transmitted through the FAIMS analyzer and transferred through a 260 μm orifice to the vacuum chamber of a mass spectrometer (PE SCIEX API 300 triple quadrupole). The MS orifice was electrically insulated from the FAIMS and a separate voltage (V_{OR}) of -39 V was applied to it. An offset voltage (V_{F}), of -49 V was applied to the entire FAIMS unit to enhance the sensitivity of the FAIMS-MS interface. These values of V_{F} and V_{OR} were optimized for transmission of perchlorate at DV = -3300V. The skimmer cone was held at ground potential and the small ring electrode normally located behind the orifice of the API 300 was not incorporated into this design, likely resulting in some loss of sensitivity for low mass ions such as perchlorate. Compressed air was introduced into the carrier gas inlet (C_{in}) at a flow rate of 5 L/min. Gas exited through the carrier gas outlet (C_{out}) at 4 L/min and through the sample gas out port (S_{out}) at 1 L/min, such that $C_{\text{in}} = C_{\text{out}} + S_{\text{out}}$. Previous studies have demonstrated that these different gas flows need to be tuned for signal intensity, stability, and peak separation [2]. The pressure inside the FAIMS analyzer, which was measured with a MKS Baratron Type 170M-6B pressure meter (MKS Instruments Inc, Burlington, Mass), was kept at approximately 785 torr.

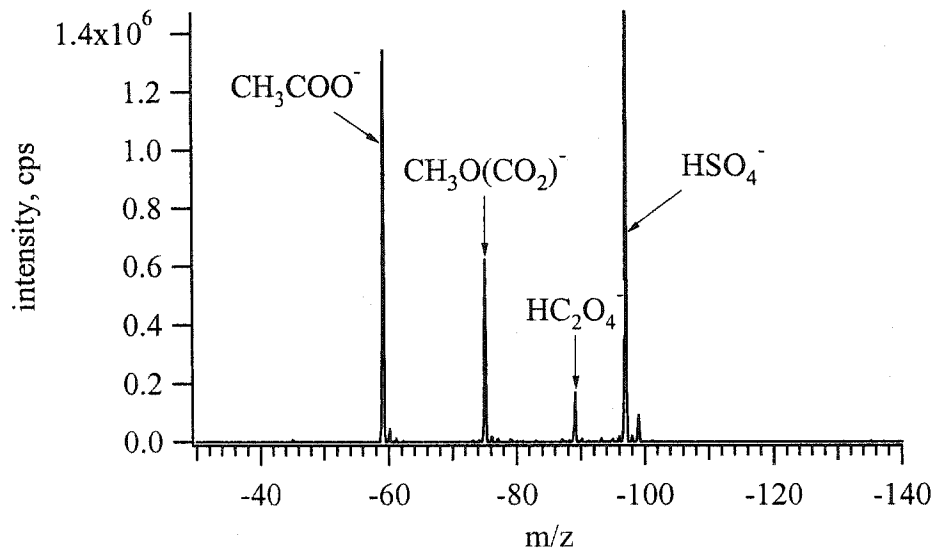
Potassium perchlorate, potassium dihydrogen orthophosphate (J.T. Baker Chemical Co., Phillipsberg, NJ), and potassium sulphate (Mallinkrodt, Montreal, QC) were used to prepare standard solutions in 9:1 methanol/water (v/v) containing 0.2mM ammonium acetate (Anachemia, Montreal, QC). Glass-distilled HPLC grade methanol (Anachemia, Montreal, QC) was used as received.

5.3 Results and Discussion

5.3.1 ESI-MS

An ESI-MS spectrum of 10 μM sulphate with 0.2 mM ammonium acetate in 9:1 methanol/water (v/v) is shown in Figure 5.03 (a). Intense peaks, including acetate (m/z - 59) and oxalate (m/z -89) are present. In ESI-MS, the sulphate appears as the bisulphate

(a)



(b)

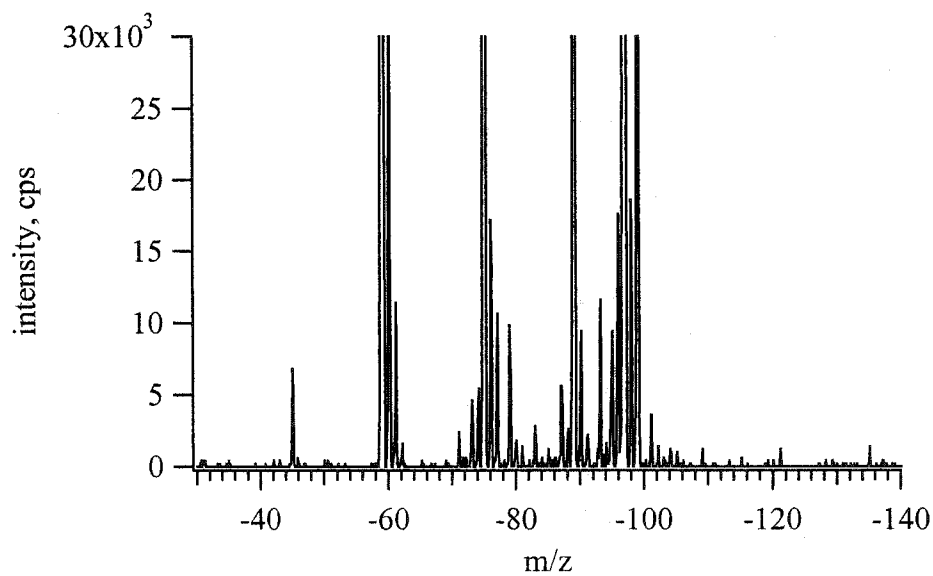


Figure 5.03 (a) Mass spectrum of 10 μM sulphate in 0.2 mM ammonium acetate (9:1 methanol/water (v/v)) acquired by conventional ESI-MS on an API 300 triple-quadrupole mass spectrometer; (b) expanded view of the spectrum shown in (a).

ion, HSO_4^- , with the major isotope at m/z -97 [17]. The isotopes of sulphur and oxygen contribute to peaks at m/z -99 and -101. Figure 5.03 (b) is a magnified view of Figure 5.03 (a), which illustrates the complex nature of the ESI-MS background. Since ESI is generally regarded as a non-selective ionization technique, many solution and gas phase species (known and unknown) appear in the low mass region, contributing to the background interference.

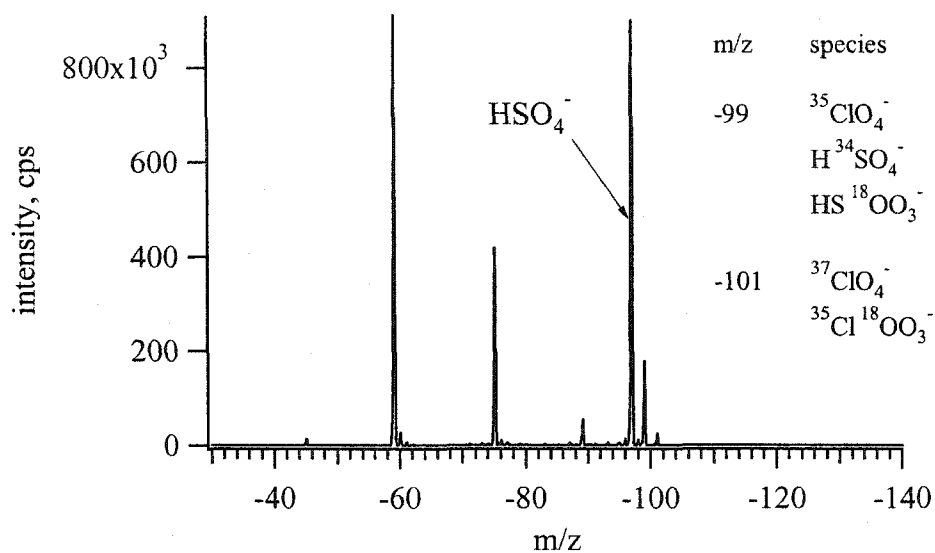
ESI of a perchlorate solution yields intact perchlorate anions, i.e., peaks at m/z -99 and -101 are observed in the mass spectrum. The presence of sulphate in solution can interfere with trace-level determination of perchlorate, due to the sulphate isotopes at m/z -99 and -101. Since sulphate is a common ion in groundwater and drinking water and an impurity in many types of chemicals, the direct analysis of perchlorate is limited with ESI-MS. Other ions, such as phosphate, can also interfere with perchlorate analysis. Phosphate can be observed as H_2PO_4^- (m/z -97) in ESI-MS with a minor isotope (due to ^{18}O) at m/z -99. For simplicity, the phosphate interference will not be examined in detail.

Figure 5.04 (a) is an ESI-MS spectrum similar to Figure 5.03 (a) except that $1\ \mu\text{M}$ perchlorate was added to the solution. Figure 5.04 (b) is an expanded view of the baseline, having the same absolute scale as Figure 5.03 (b). The peak at m/z -99 cannot be used for low level perchlorate quantitation, largely due to the isotope of sulphate. At m/z -101, there is far less contribution from sulphate isotopes, however the chemical background limits reliable identification and quantitation of ClO_4^- .

5.3.2 ESI-FAIMS-MS

Ions are separated in FAIMS based on their differences in high vs. low field mobilities (i.e., K_h/K). The effect of increasing E/N (where E is the electric field, and N is the number density of the carrier gas) on K_h/K for perchlorate and sulphate using compressed air as the drift gas is shown in Figure 5.05 (a) and for phosphate and sulphate in Figure 5.05 (b). These experimentally determined curves correspond to dispersion voltages varying from 0 to -3300 V. The curves were determined by first linearizing

(a)



(b)

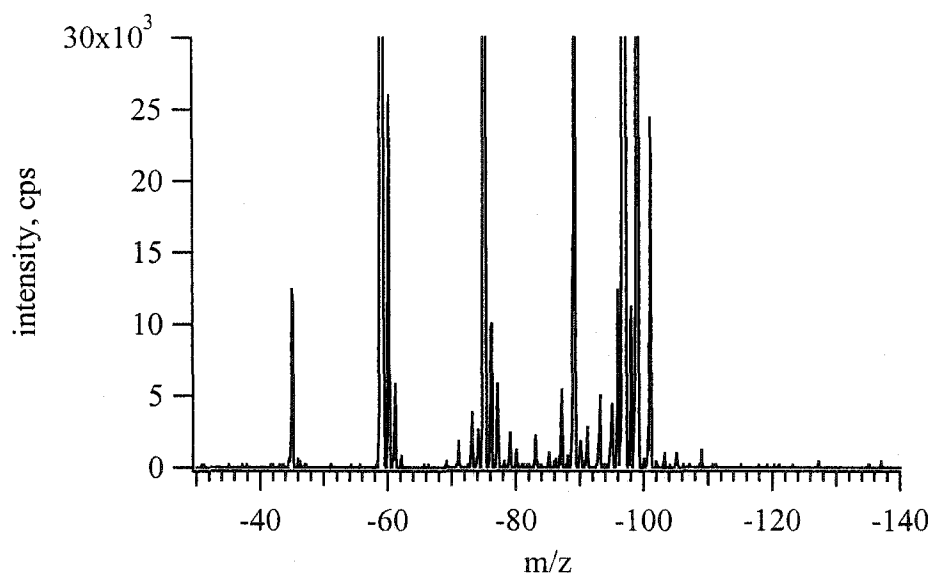
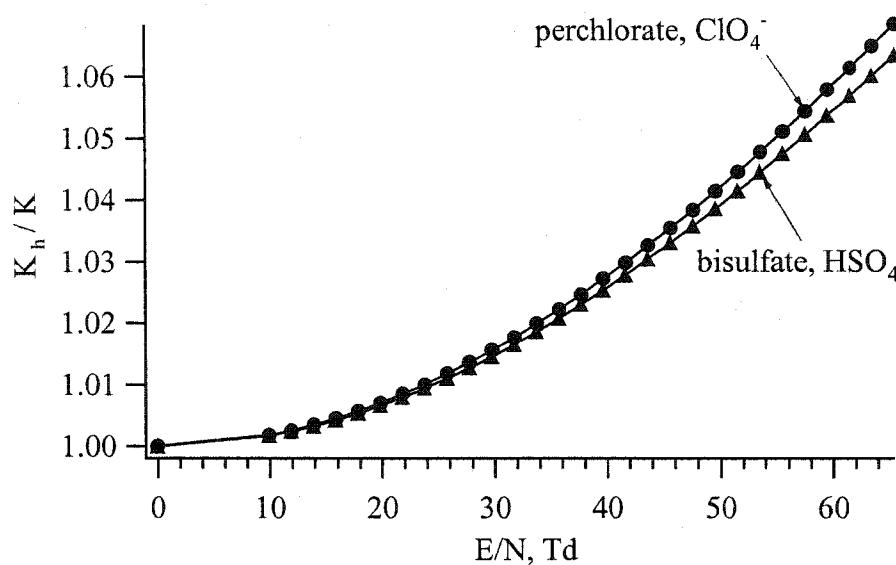


Figure 5.04 (a) Mass spectrum of 1 μM perchlorate and 10 μM sulphate in 0.2 mM ammonium acetate (9:1 methanol/water (v/v)) acquired by conventional ESI-MS on an API 300 triple-quadrupole mass spectrometer; (b) expanded view of the spectrum shown in (a).

(a)



(b)

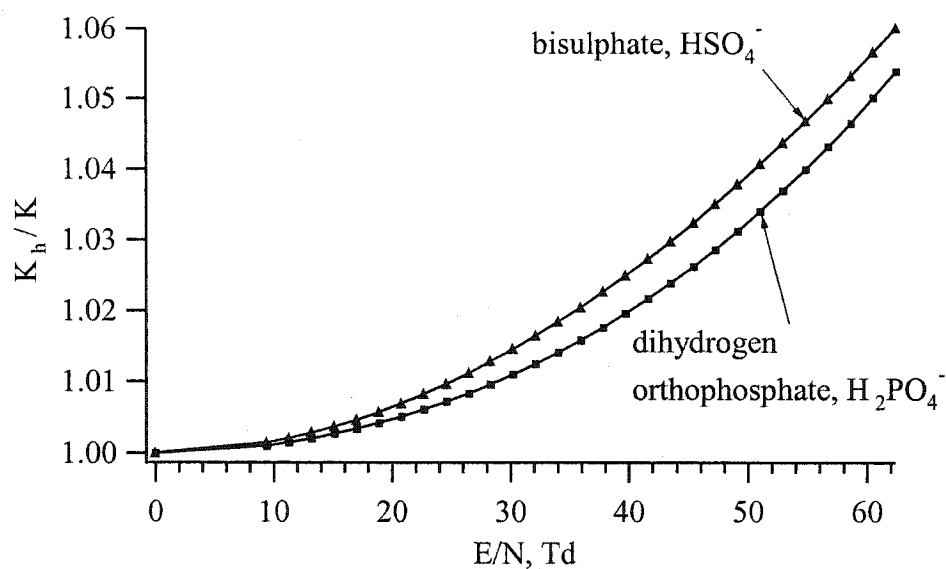


Figure 5.05 Measured dependence of ion mobility (expressed as K_h/K) in air for (a) perchlorate and bisulfate and (b) dihydrogen orthophosphate and bisulfate as a function of electric field strength within the FAIMS analyser (expressed as E/N , where N represents the gas number density).

Equation 5.01, shown below, to determine the values of the high-field mobility parameters (α and β) as described in reference 16,

$$(CV) + \alpha \left(\frac{(DV)^3}{9d^2} + \frac{15(CV)(DV)^2}{18d^2} + \frac{(CV)^3}{d^2} \right) + \beta \left(\frac{55(DV)^5}{486d^4} \right) = 0 \quad 5.01$$

where the compensation voltage is (CV) and the dispersion voltage is (DV), and the distance (d) between the inner and outer cylinders was 0.2 cm. From Equation 5.01, the obtained values of α and β have units of cm^2/V^2 and cm^4/V^4 , respectively. The determined gas number density ($N = 2.522 \times 10^{19}$ molecules/ cm^3) was used to convert α and β to units of $1/\text{Td}^2$ and $1/\text{Td}^4$, respectively, where $\text{Td} = 10^{-17} \text{ V}\cdot\text{cm}^2$. These new values of α and β were used to calculate K_h/K for each DV tested, according to the following equation:

$$\frac{K_h}{K} = 1 + \alpha \left(\frac{E}{N} \right)^2 + \beta \left(\frac{E}{N} \right)^4 \quad 5.02$$

Derivations of the equations describing the high-field behaviour in a FAIMS device have been given elsewhere [16]. Figure 5.05 (a) shows that for bisulphate and perchlorate ions, the difference in K_h/K continues to increase with increasing E/N to the maximum value tested ($\sim 65 \text{ Td}$). In the case of bisulphate and dihydrogen orthophosphate, the difference in K_h/K is largest at E/N of about 52 Td . The difference in the dependence of K_h/K with E/N for these ions allows their gas-phase separation at atmospheric pressure. Monitoring the FAIMS pressure was necessary to make a reasonably accurate determination of the gas number density within the FAIMS, and allowed the FAIMS to be set to a reproducible value of E/N . The variation of the observed ion CV as a function of the FAIMS pressure is shown in Figure 5.06 for bisulphate and dihydrogen orthophosphate ions. The DV was held constant at $DV = -3300 \text{ V}$, and the pressure was changed while maintaining the same gas flow rates. As the pressure was increased, the gas number density also increased, lowering the effective E/N and changing the ion's K_h/K behaviour. At lower E/N , the K_h/K is also lower, and the ions require less compensation voltage for transmission. Over the range of pressures tested, the CVs for bisulphate were observed to vary from 22.1 V at

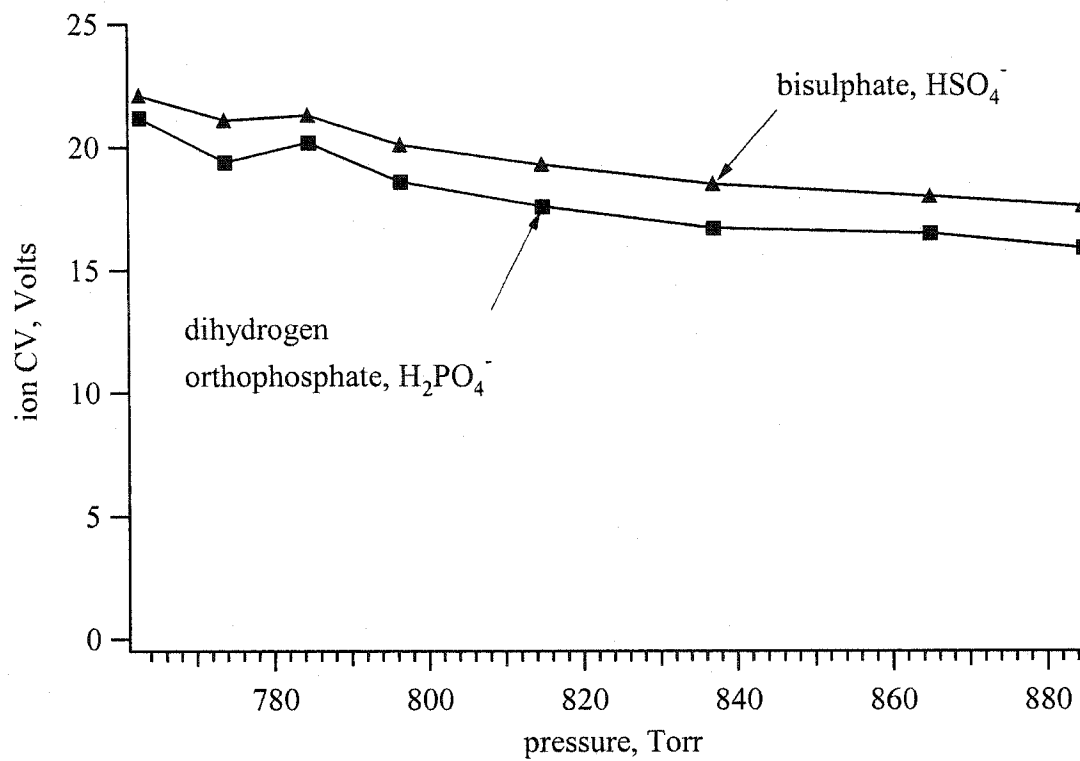


Figure 5.06 Variation of observed ion compensation voltage scan peak as a function of pressure within the FAIMS analyzer for bisulphate and dihydrogen orthophosphate in air drift gas at $DV = -3300$ V.

763 Torr to 17.6 V at 885 Torr. Similarly, the CVs for dihydrogen orthophosphate were observed to vary from 21.2 V at 763 Torr to 15.9 V at 885 Torr.

The ability of FAIMS to separate and focus perchlorate and bisulphate ions is demonstrated in Figure 5.07. In each trace of Figure 5.07, the voltage of the asymmetric waveform was set, and mass-selected CV spectra were acquired at m/z -97, -99, and -101 while the CV was scanned from -1 to +29 V. The trace for m/z -97 represents the major m/z of HSO_4^- , while the traces for m/z -99 and -101 represent minor m/z of HSO_4^- and the two major m/z of ClO_4^- . The dwell time and number of scans were kept constant for each spectrum. At $DV = 0$ V (trace (i)), the ions all appear at a compensation voltage near 0 V. The mass-selected CV spectra acquired at $DV = -1600$ V are shown in trace (ii). The transmitted ions have experienced small, field induced, increases in their mobility at this DV and therefore appear in the spectrum at CV values greater than zero. As the DV was made more negative, the species were transmitted at more positive CV values as shown in traces (iii)-(v). These shifts to more positive CV values are accompanied by increases in the measured ion intensity, a consequence of two-dimensional focusing within the FAIMS analyzer [9]. At $DV = -3300$ V, trace (v), the perchlorate ion (at m/z -99), has experienced an increase in sensitivity of about three orders of magnitude compared with the trace at $DV = 0$ V. At $DV = -3300$ V, bisulphate (m/z -97) appears at a CV value of 21.9 V, and perchlorate (m/z -99) is transmitted at a CV of 23.6 V. This DV (-3300 V), which is the highest voltage that could be applied with this FAIMS apparatus, provides the largest separation of these peaks.

To illustrate the improvement in the mass spectral background achieved using FAIMS, a mass spectrum was acquired by tuning the FAIMS to $DV = -3300$ V and $CV = 23.6$ V. This mass spectrum, shown in Figures 5.08 (a) and 5.08 (b), was acquired for a solution of 10 μM sulphate and 1 μM perchlorate in 0.2 mM ammonium acetate. In Figure 5.08 (b), the vertical axis has been expanded to the same number of absolute counts as was done previously for Figure 5.04 (b). A comparison of these expanded figures shows that the filtering action of the FAIMS analyser has significantly reduced the chemical background. Since the signal intensity at this DV is comparable to conventional ESI-MS,

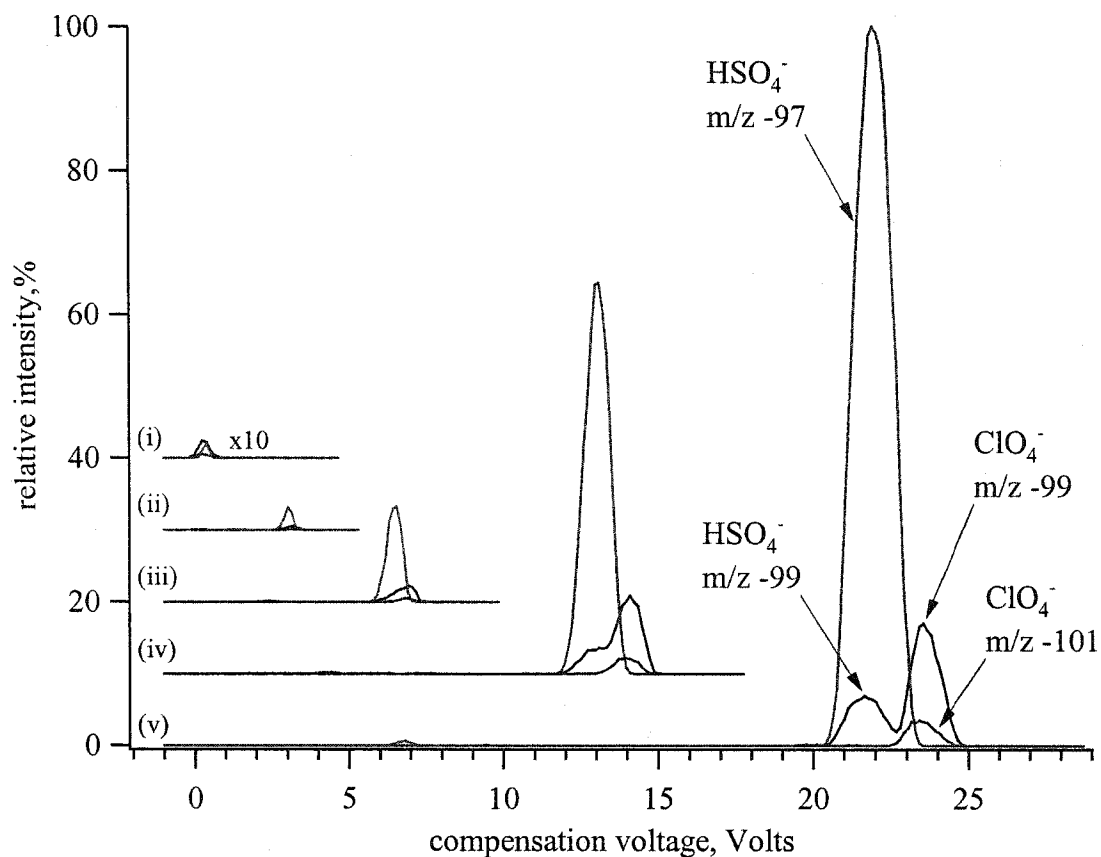
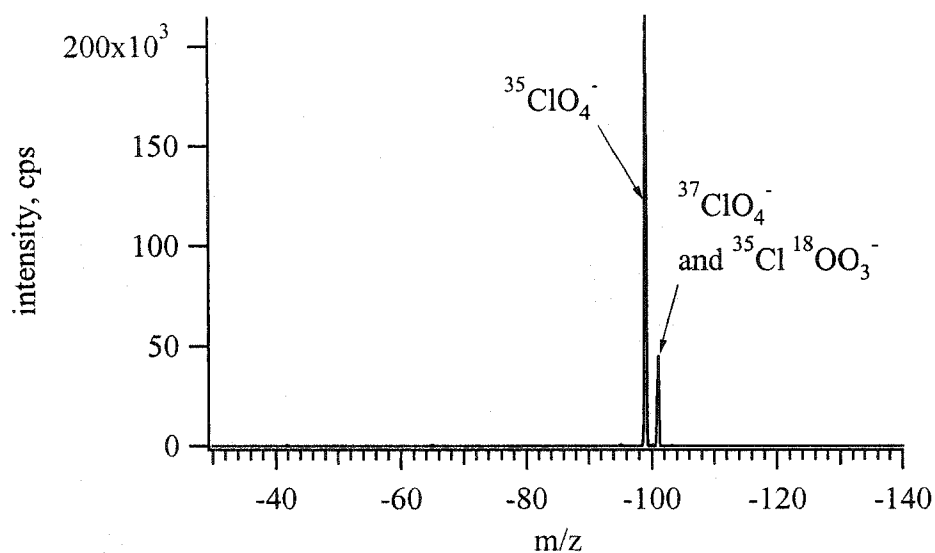


Figure 5.07 Mass-selected CV spectra (m/z -97, -99, and -101; CV = -1 V to 29 V; DV = -3300 V) of 1 μM perchlorate and 10 μM sulphate in 0.2 mM ammonium acetate (9:1 methanol/water (v/v)). (i) DV = 0 V, shown magnified 10x for clarity; (ii) DV = -1600 V; (iii) DV = -2100 V; (iv) DV = -2700 V; (v) DV = -3300 V.

(a)



(b)

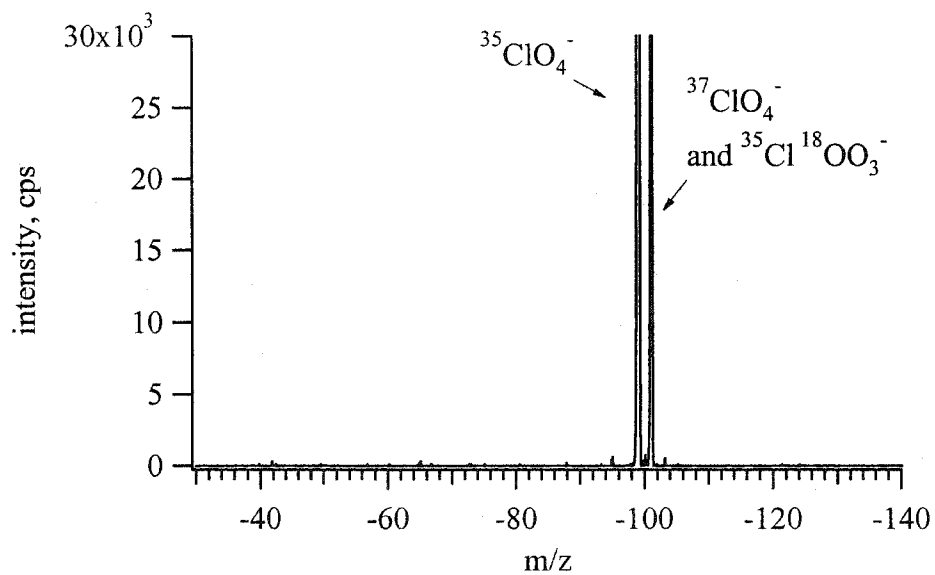


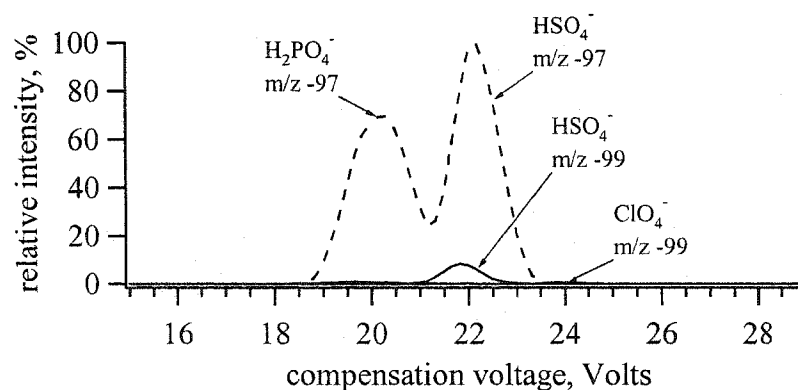
Figure 5.08 (a) Mass spectrum of $1\mu\text{M}$ perchlorate $10\mu\text{M}$ sulphate in 0.2 mM ammonium acetate (9:1 methanol/water (v/v)) at $\text{DV} = -3300\text{ V}$ and $\text{CV} = 23.6\text{ V}$; (b) expanded view of the spectra in (a).

significant improvements in the signal-to-background (S/B) are achieved using the FAIMS interface. Comparing the ESI-MS signals observed for a 10 μM sulphate “blank” solution and a solution containing 1 μM perchlorate and 10 μM sulphate, the S/B for perchlorate was 2.0 and 6.6 for m/z -99 and -101, respectively. An analysis of the same solutions using ESI-FAIMS-MS ($DV = -3300$ V and $CV = 23.6$ V) results in S/B at m/z -99 and -101 of 72, 000 and 15, 000, respectively. This dramatic improvement in S/B allows for low perchlorate detection limits in the presence of sulphate, and has been achieved without complicated sample preparation procedures or tandem mass spectrometry (MS/MS).

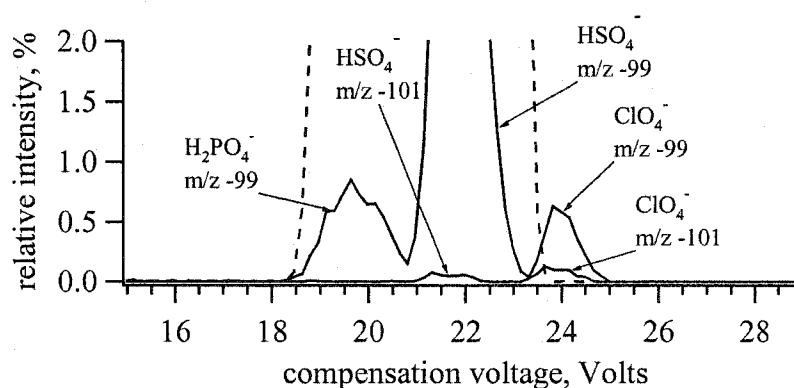
The ability of FAIMS to separate perchlorate and bisulphate is not compromised as the sulphate concentration is increased or as the perchlorate concentration is decreased. This ability is demonstrated in Figures 5.09 (a) and 5.09 (b), which show mass-selected CV spectra of 0.1 μM perchlorate in the presence of 50 μM sulphate and 50 μM phosphate. This represents a 10-fold decrease in the perchlorate concentration, a 5-fold increase in the sulphate concentration, and the addition of phosphate, compared with the test solution used in Figures 5.07 and 5.08. The expanded view illustrates the potential interference on the perchlorate analysis due to dihydrogen orthophosphate at m/z -99 and due to bisulphate at m/z -99 and -101. The figure shows that these interferents can be readily separated from the perchlorate signal. Consequently, this unique ability of FAIMS allows for the monitoring of perchlorate at a specific CV, over a wide range of sulphate and phosphate concentrations. The mass spectrum at $CV = 24.2$ V (Figure 5.09 (c)) shows the signal for the perchlorate ion (0.1 μM) with minimum background ion intensity.

A standard response curve for perchlorate in the presence of 10 μM sulphate (with 0.2 mM ammonium acetate in 9:1 methanol/water (v/v) as solvent) was established. The sample was continuously electrosprayed into the FAIMS analyzer and perchlorate (m/z -99) was monitored at $DV = -3300$ V and $CV = 24.2$ V. The dwell time was 300 msec and 30 integrations were averaged for each measurement. The concentration range of perchlorate analyzed was 0.01 μM to 1 μM . Figure 5.10 shows the resulting curve, which was linear over this range ($y = 9450[\text{ClO}_4^-] + 1.4$, $r^2 = 0.999$). The detection limit for perchlorate in 9:1 methanol/water with 0.2 mM ammonium acetate and 10 μM sulphate

(a)



(b)



(c)

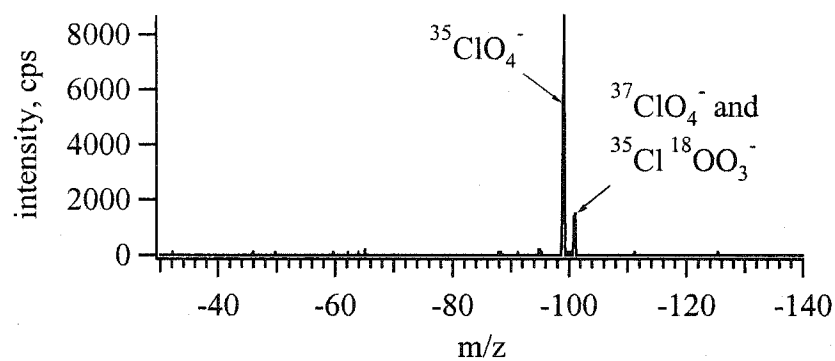


Figure 5.09 (a) Mass-selected CV spectra (m/z -97, -99, and -101; CV = 15 to 29 V; DV = -3300 V) of 0.1 μM perchlorate, 50 μM sulphate, and 50 μM phosphate in 0.2 mM ammonium acetate (9:1 methanol/water (v/v)); (b) expanded view of (a) with m/z -97 shown as a dashed line for clarity; (c) mass spectrum of the same solution at CV = 24.2 V.

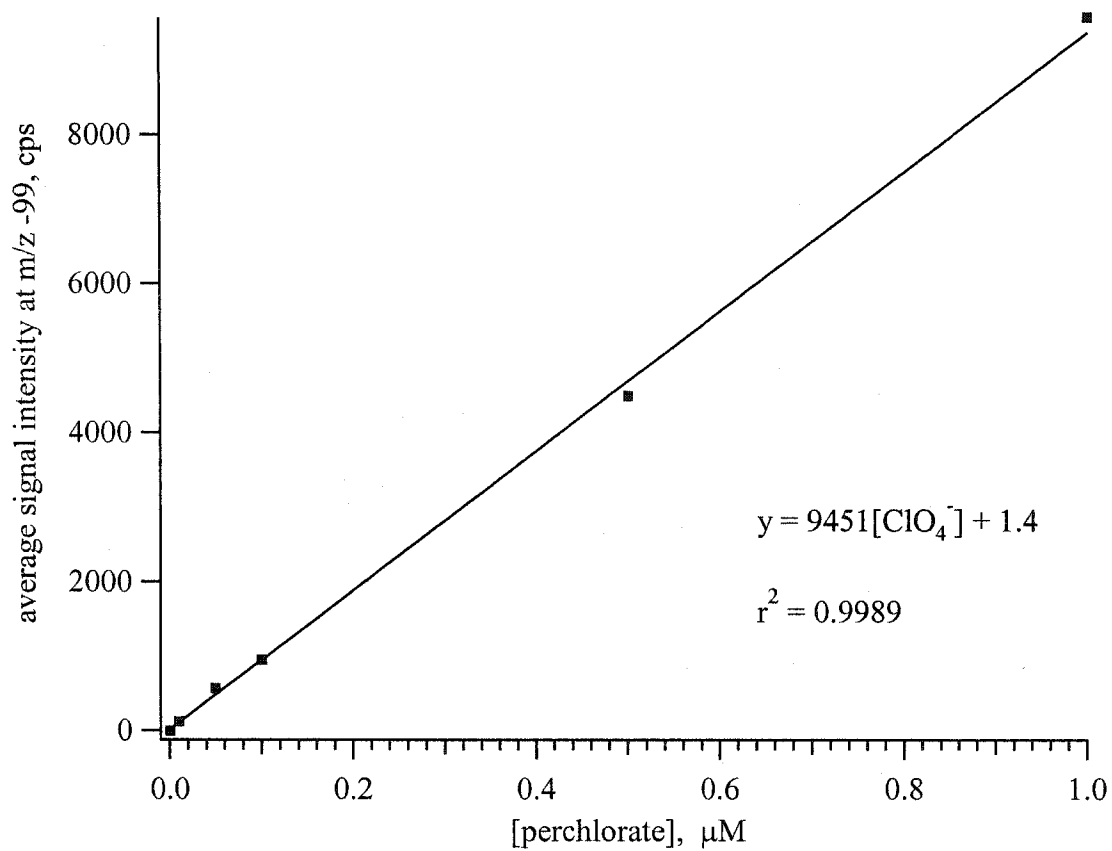


Figure 5.10 Signal intensity at m/z -99 (DV = -3300 V, CV = 24.2 V) as a function of perchlorate concentration (with 10 μM sulphate and 0.2 mM ammonium acetate in 9:1 methanol/water).

was determined to be 1 nM (~0.1 ppb), roughly 20 times below the provisional drinking water limit of 18 ppb [11]. This value was calculated based on 3 times the standard deviation of the blank (10 μ M sulphate in 0.2mM ammonium acetate in 9:1 methanol/water (v/v)).

5.4 Conclusions

The differences in K_{H}/K of perchlorate, sulphate and phosphate ions allows FAIMS to separate them in the gas phase at atmospheric pressure prior to their introduction into a mass spectrometer. The separating or filtering action of FAIMS allows for dramatic reduction in the background, and the focusing action of FAIMS provides signal intensity that is comparable to ESI-MS. Consequently, ESI-FAIMS-MS significantly improves the detection limit of perchlorate when compared with ESI-MS.

Relatively high concentrations of sulphate and phosphate were shown not to compromise the separation of perchlorate from these potentially interfering ions. Thus, even in the presence of variable amounts of sulphate and phosphate in the matrix, the FAIMS voltages can be tuned to continuously transmit perchlorate without interference. These characteristics make ESI-FAIMS-MS a powerful tool for the determination of perchlorate in aqueous samples.

More recently, a perchlorate analysis was performed using a different FAIMS prototype [18]. Improvements to the ESI-MS coupling, the waveform frequency, the DV amplitude, and drift gas composition, have led to significantly better detection limits (~20 times lower) in a variety of matrices.

5.5 References

1. Guevremont, R.; Purves, R. W. "Atmospheric pressure ion focusing in a high-field asymmetric waveform ion mobility spectrometer"; *Rev. Sci. Instrum.* **1999**, *70*, 1370-1383.
2. Purves, R. W.; Day, S.; Pipich, C. W.; Matyjaszczyk, M. S.; Guevremont, R. "Mass spectrometric characterization of a high-field asymmetric waveform ion mobility spectrometer"; *Rev. Sci. Instrum.* **1998**, *69*, 4094-4105.
3. Purves, R. W.; Guevremont, R. "Electrospray ionization high-field asymmetric waveform ion mobility spectrometry-mass spectrometry"; *Anal. Chem.* **1999**, *71*, 2346-2357.
4. Carnahan, B. L.; Tarassov, A. S. "Ion Mobility Spectrometer"; **1995**, Mine Safety Appliances Company, Pittsburgh, Pa. United States. Patent No. 5 420 424.
5. Purves, R. W.; Barnett, D. A.; Guevremont, R. "Separation of protein conformers using electrospray-high-field asymmetric waveform ion mobility spectrometry-mass spectrometry"; *Int. J. Mass Spectrom.* **2000**, *197*, 163-177.
6. Guevremont, R.; Purves, R. W. "High field asymmetric waveform ion mobility spectrometry-mass spectrometry: An investigation of leucine enkephalin ions produced by electrospray ionization"; *J. Am. Soc. Mass Spectrom.* **1999**, *10*, 492-501.
7. Ells, B.; Barnett, D. A.; Froese, K.; Purves, R. W.; Hrudey, S.; Guevremont, R. "Detection of chlorinated and brominated byproducts of drinking water disinfection using electrospray ionization-high-field asymmetric waveform ion mobility spectrometry-mass spectrometry"; *Anal. Chem.* **1999**, *71*, 4747-4752.
8. Barnett, D. A.; Guevremont, R.; Purves, R. W. "Determination of parts-per-trillion levels of chlorate, bromate, and iodate by electrospray ionization/high-field asymmetric waveform ion mobility spectrometry/mass spectrometry"; *Appl. Spectrosc.* **1999**, *53*, 1367-1374.
9. Barnett, D. A.; Ells, B.; Purves, R. W.; Guevremont, R. "Separation of leucine and isoleucine by electrospray ionization-high field asymmetric waveform ion

- mobility spectrometry-mass spectrometry"; *J. Am. Soc. Mass Spectrom.* **1999**, 10, 1279-1284.
10. Barnett, D. A.; Purves, R. W.; Guevremont, R. "Isotope separation using high-field asymmetric waveform ion mobility spectrometry"; *Nuc. Instrum. Meth. Phys. Res. A* **2000**, 450, 179-185.
 11. U.S.E.P.A. "Perchlorate Environmental Contamination: Toxicological Review and Risk Characterization Based on Emerging Information, Review Draft"; Document No. NCEA-1-503; US Environmental Protection Agency, Washington, DC. **1998**.
 12. Jackson, P. E.; Laikhtman, M.; Rohrer, J. S. "Determination of trace level perchlorate in drinking water and ground water by ion chromatography"; *J. Chromatogr. A* **1999**, 850, 131-135.
 13. CDHS. "Determination of Perchlorate by Ion Chromatography"; California Department of Health Services, Sanitation & Radiation Laboratories Branch, CA. **1997**.
 14. Barnett, D. A.; Horlick, G. "Quantitative electrospray mass spectrometry of halides and halogenic anions"; *J. Anal. At. Spectrom.* **1997**, 12, 497-501.
 15. Magnuson, M. L.; Urbansky, E. T.; Kelty, C. A. "Determination of perchlorate at trace levels in drinking water by ion-pair extraction with electrospray ionization mass spectrometry"; *Anal. Chem.* **2000**, 72, 25-29.
 16. Viehland, L. A.; Guevremont, R.; Purves, R. W.; Barnett, D. A. "Comparison of high-field ion mobility obtained from drift tubes and a FAIMS apparatus"; *Int. J. Mass Spectrom.* **2000**, 197, 123-130.
 17. Stewart, I. I.; Barnett, D. A.; Horlick, G. "Investigations into sulfur speciation by electrospray mass spectrometry"; *J. Anal. Atom. Spec.* **1996**, 11, 877-886.
 18. Ells, B.; Barnett, D. A.; Purves, R. W.; Guevremont, R. "Trace level determination of perchlorate in water matrices and human urine using ESI-FAIMS-MS"; *J. Environ. Monit.* **2000**, 2, 393-397.

Chapter 6

Experimental Characterization of a Dome FAIMS Prototype Using Small Anions

6.1 Introduction

In Chapter 4, some of the theoretical considerations for high-field asymmetric waveform ion mobility spectrometry (FAIMS) were discussed. FAIMS separates ions in the gas phase at atmospheric pressure based on the difference in the ion mobility, K , under conditions of high and low electric fields. The magnitude of the high (K_h) and low field mobility (K), may be expressed as the ratio K_h/K . Ions exhibiting different K_h/K ratios in response to an asymmetric field at radio frequency (RF) will require different compensation voltages (CVs) to balance their trajectories through the FAIMS apparatus. The FAIMS can act as a tunable bandpass filter, and the CV can be scanned to sequentially transmit different ions to a mass spectrometer (MS). The resultant data can be represented as mass-selected compensation voltage (CV) spectrum, where the signal intensity at a particular mass/charge (m/z) is plotted as a function of the applied CV, as hypothetically illustrated in Figure 6.01. In this example, ions A_1 and A_2 have the same m/z , but different K_h/K ratios under the test conditions. Ion A_1 has a greater K_h/K than A_2 , and requires a greater CV for transmission from the FAIMS to the MS. As such, ion A_1 can be continuously transmitted to the MS by setting the CV to the appropriate value, without the potential interference from ion A_2 .

In the development of FAIMS, different electrode configurations have been used in attempts to improve the performance of the interface. As discussed in Chapter 4, three main electrode configurations for FAIMS have been reported. These three interfaces are illustrated in Figure 6.02. The first interface designed was the parallel plate interface (Figure 6.02 (a)) [1, 2], which was later followed by the concentric cylinder interface (Figure 6.02 (b)) [3-6]. In Chapter 5, a concentric cylinder FAIMS interface was combined with electrospray ionization mass spectrometry (ESI-MS) as an ESI-FAIMS-MS prototype. This same ESI-FAIMS-MS prototype has been used in a variety of applications [7-17]. As discussed in Chapter 4, curved FAIMS electrode surfaces (such as those based on concentric cylinders and spheres), theoretically provide gains in the ion throughput, due to what has been described as an ion focusing mechanism [5, 6]. A modification to the concentric cylinder prototype is the dome prototype, as designed by

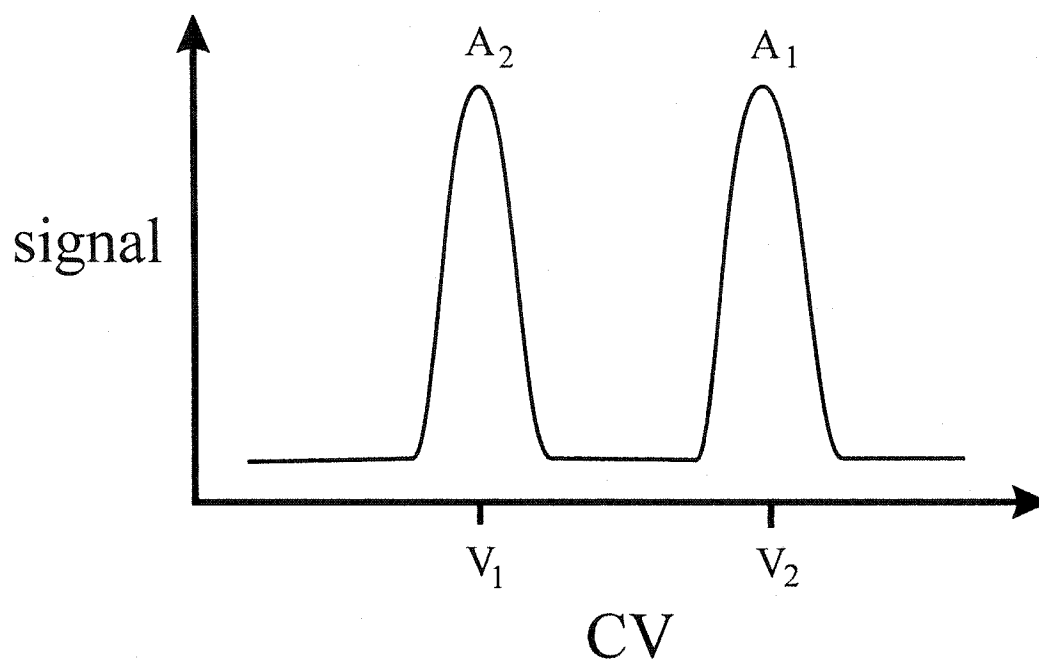


Figure 6.01 A hypothetical mass-selected compensation voltage (CV) spectrum of ions A_1 and A_2 . Signal intensity at a single mass/charge is plotted as a function of the applied compensation voltage (CV).

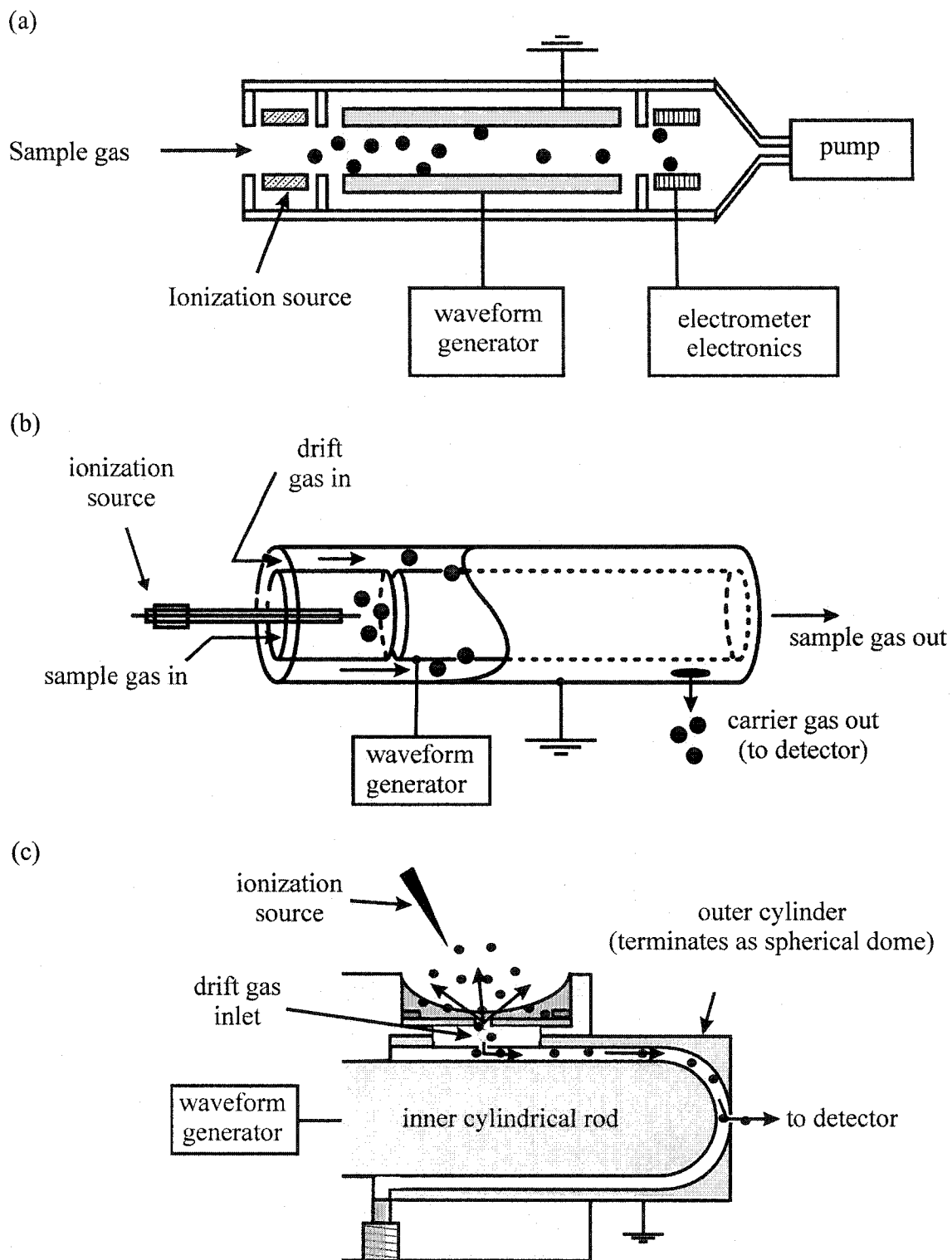


Figure 6.02 FAIMS electrode geometries. (a) parallel plates, (b) concentric cylinders, (c) concentric cylinders terminating as a spherical dome.

Guevremont and Purves (Figure 6.02 (c)) [6]. The first theoretical description of this design was presented as an ion trajectory modeling demonstration. A more detailed illustration of this geometry is presented in Figure 6.03. This interface consists of an inner cylindrical rod and an outer cylinder, which both terminate as a spherical dome. This design was patented [18, 19] and a dome prototype interface has been used in several of the FAIMS-based measurements to date [7, 11, 14, 18-29].

Although the dome interface has been used in a variety of work, no detailed descriptions of how this interface must be tuned have been reported. While this interface can be described using some of the same theoretical considerations as with a concentric cylinder interface, there are significant differences between the configurations and the tuning of these two interfaces. The dome FAIMS interface used in this work has several major changes compared to the concentric cylinder interface used in Chapter 5. The most obvious difference is that the dome FAIMS incorporates both concentric cylinder and concentric sphere electrode geometries. In this interface, ions that have a balanced trajectory are swept to the top of the dome by the flow of the drift gas. In the concentric cylinder interface, ions are swept by the drift gas to the end of the cylinders, with ions at all points of the radius. This difference makes the dome interface more efficient than a concentric cylinder interface for transmitting ions to the mass spectrometer sampling orifice, since all the ions are moved to the same final location with a dome interface.

Another significant change is the coupling of the FAIMS to the MS. With the old interface, the orifice plate was secured to the FAIMS housing. This required extra parts, and required that the vacuum be broken if the FAIMS was to be removed for cleanup or adjustments. With the new interface, the FAIMS can be easily removed or re-attached. Another difference is with the sampling of ions into the FAIMS. The external ESI source (Figure 6.02 (c)) used with the dome prototype makes for much easier coupling, and greatly reduces the possibility of contamination that can occur when using an internal ESI source (Figure 6.02 (b)). The gas flows used are also different. With the dome interface, only a single gas source, the curtain gas, is used. The gas flow within the dome FAIMS interface is determined by the rate of gas flow into the MS orifice. Unlike the concentric

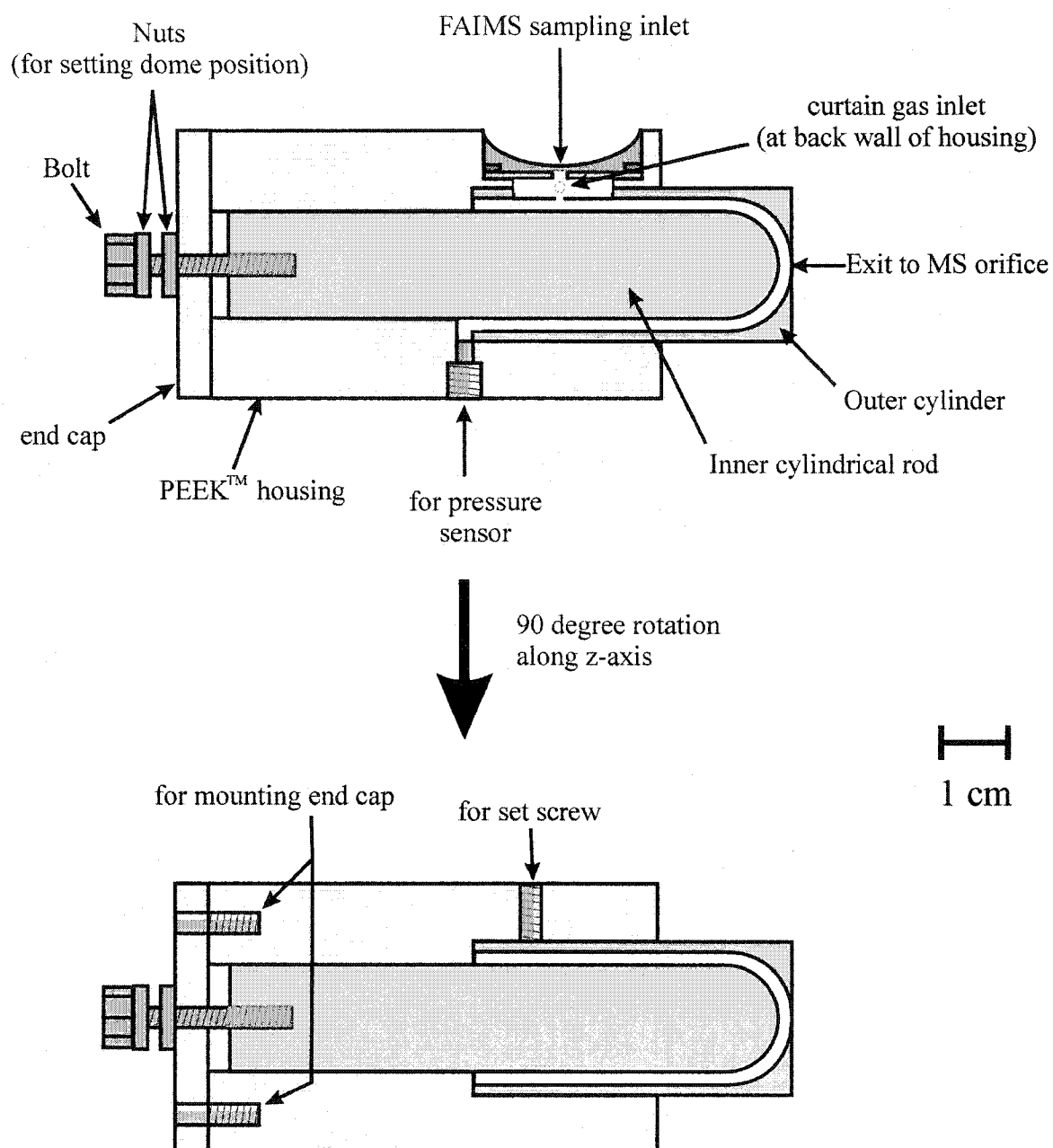


Figure 6.03 Longitudinal cross-sections of a FAIMS dome interface prototype.

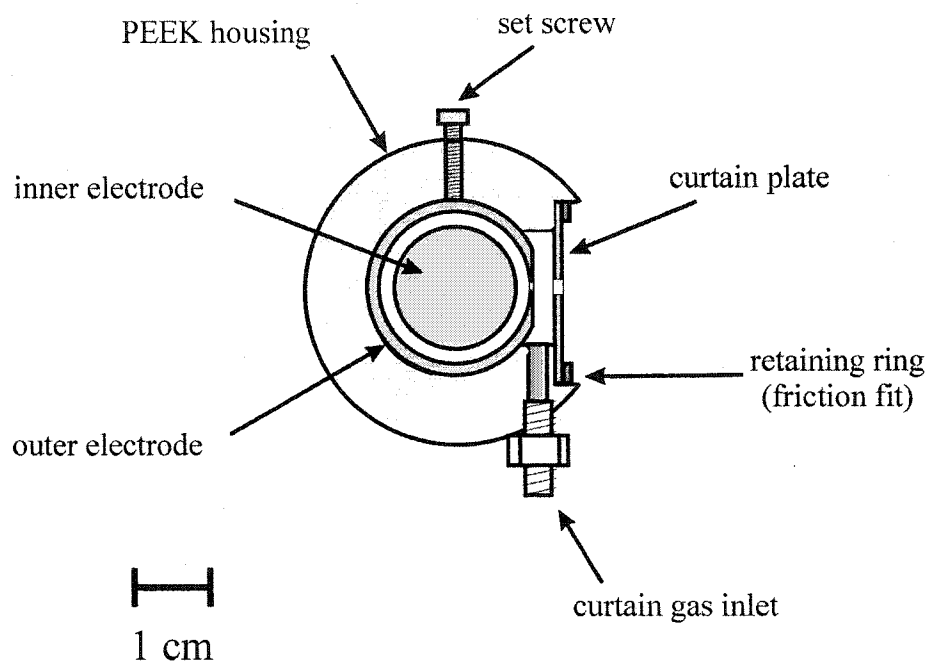
cylinder interface, which requires the setting of up to four different gas flows, the dome interface requires that only the curtain gas flow rate is set, making this system much easier to set up and operate. Improvements to the waveform generator have also been made. With the generator used in this study, higher dispersion voltages (DV) are available. The maximum DV is about 3500 V under either polarity, as compared to 3300 with the older interface. Other similar prototypes have utilized DVs up to 4400 V [20]. Also, the frequency of the waveform is 750 kHz, compared to 210 kHz for the older system. As discussed in Chapter 4, theory predicts that the higher frequency should allow for some gains in ion transmission.

This chapter will discuss some of the experimental parameters that must be tuned or controlled in a FAIMS experiment when using a dome interface. Where possible, a brief experimental characterization is related to the theoretical considerations discussed in Chapter 4. The effects of the curtain gas flow rate, the waveform symmetry, and the setting of the dome position were studied through their effects on the observed CV, the mass-selected CV peak width, and signal intensity of some selected small anions.

6.2 Experimental

6.2.1 FAIMS Dome Interface

The work presented in the following sections was done using a dome interface as designed by R. Guevremont (NRC), and manufactured by Sciex (Concord, ON, Canada). Measurements of the interface were taken using a set of calipers (Helius Kanon) with 1/20 mm (0.005 cm) resolution, so all reported measurements are assumed to be accurate to ± 0.005 cm. Longitudinal and radial cross sections of the interface are presented in Figures 6.03 and 6.04, and external views of the FAIMS are presented in Figures 6.05 and 6.06. When the top of the dome of the inner cylindrical rod electrode is positioned 0.198 cm from the top of the outer cylinder electrode, the spacing at all points along the curvature is 0.198 cm. The spacing at all points along the cylinder region is constant at



radial cross section at the sampling orifice

Figure 6.04 Radial cross section at the sampling inlet of the dome FAIMS prototype.

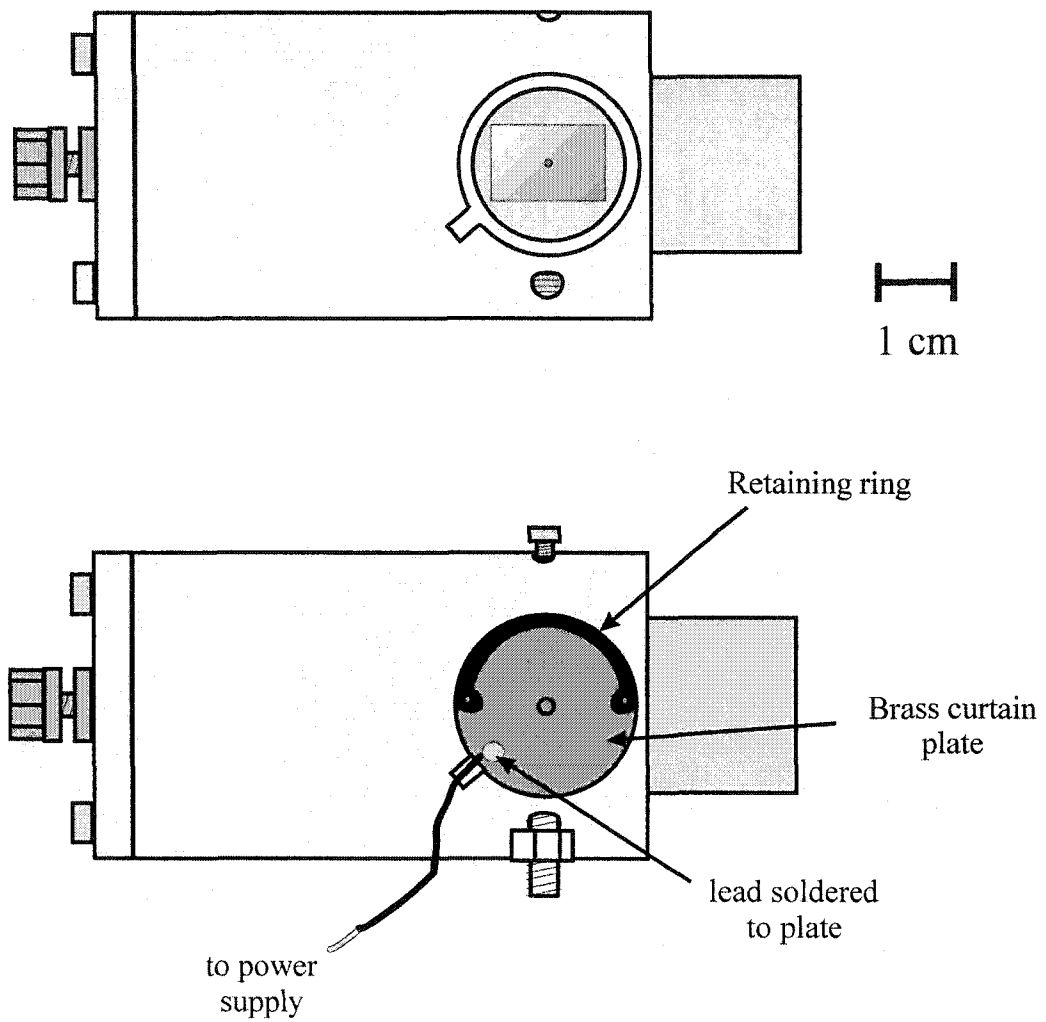


Figure 6.05 External side view of the dome FAIMS prototype.

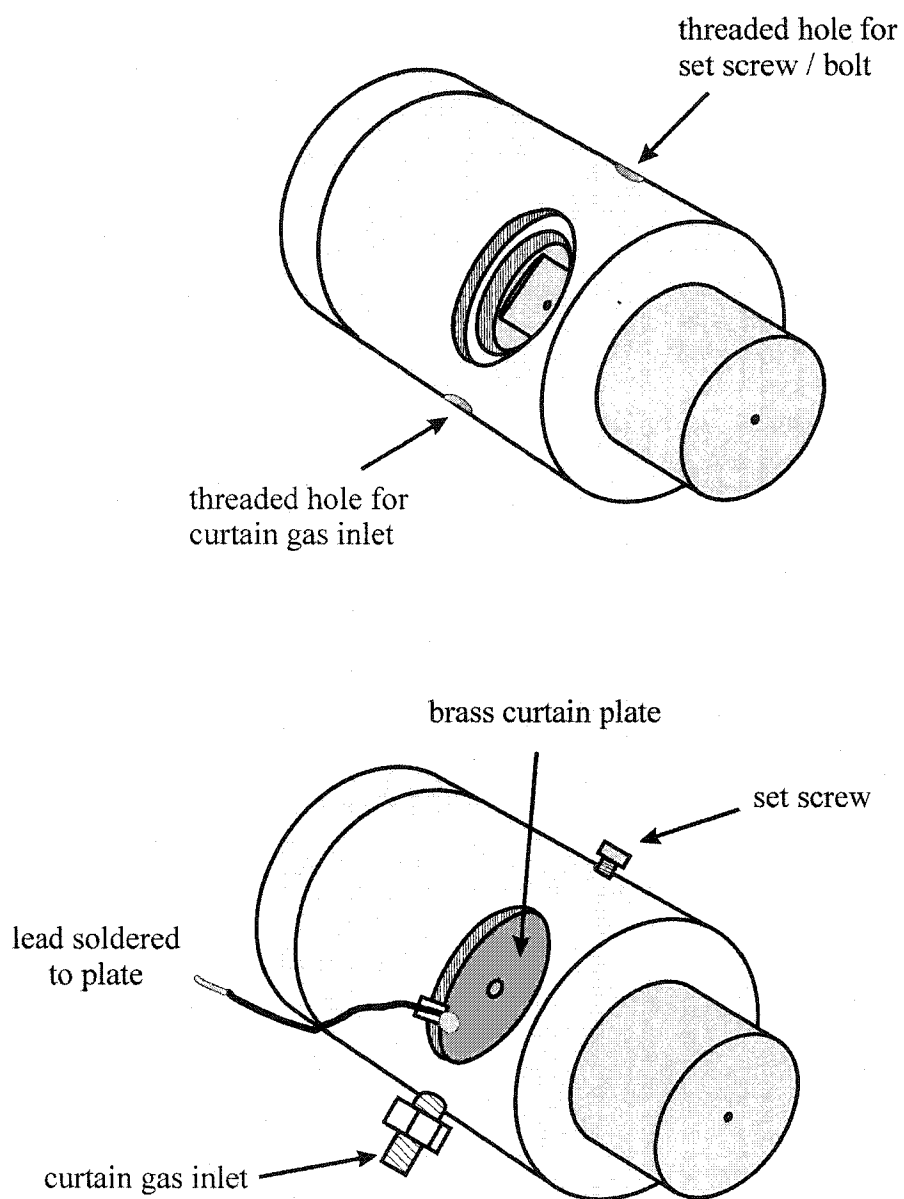


Figure 6.06 External side view of the dome FAIMS prototype.

0.198 cm, regardless of the dome position. The position of the inner electrode can be adjusted by positioning the nuts a set number of turns along the inner electrode bolt (Figure 6.03). The bolt is screwed into the end of the inner cylinder, but is free to slide through the end cap. The positioning of the nuts along the bolt determines the depth that the bolt is allowed to slide, stopping at the end cap. This adjusts the electrode spacing at the top of the dome, while allowing the cylinder regions to be maintained at a constant spacing of 0.198 cm.

For the dome spacing tests, the dome position was changed by turning the set nut by 1/12 of a turn increments, resulting in what calculates to be increments (or decrements) of about 0.006(6) cm. Since the nut had 6 sides, it was only reasonable to set increments of 1/12 of a turn from an initial position of zero turns. Since the distance per turn spacing was not adjustable and the number of turns of the nut was used to set the spacing, the dome was set according to the turns of the nut, as opposed to a specific spacing distance. In order to change the spacing of the dome, it was required that the waveform be turned off, since the set nut resides on the bolt attached directly to the inner cylinder, and cannot be touched without first turning off the waveform. So, after each re-positioning of the dome, the waveform was turned back on, and re-tuned to near-identical symmetry. The generator was not turned off for more than a few seconds in an attempt to maintain the operating temperature of the generator. Unless otherwise specified, the position of the dome was set for a spacing of 0.232 cm ($2\frac{1}{2}$ turns).

6.2.2 Waveform Generator

The waveform generator used for the following studies was built by Sciex, and is basically two quadrupole power supplies set to different frequencies and amplitudes, with both signals combined to form the final waveform. Each of the two supplies generates a sine wave. One wave has a frequency of 1500 kHz, and the other has a frequency of 750 kHz. The 1500 kHz sine wave has an amplitude that is 1/2 the amplitude of the 750 kHz wave, as illustrated in Figure 6.07 (a). As previously described in Chapter 4, the waveform required for small anions is the N1-P2 waveform, and the actual waveform

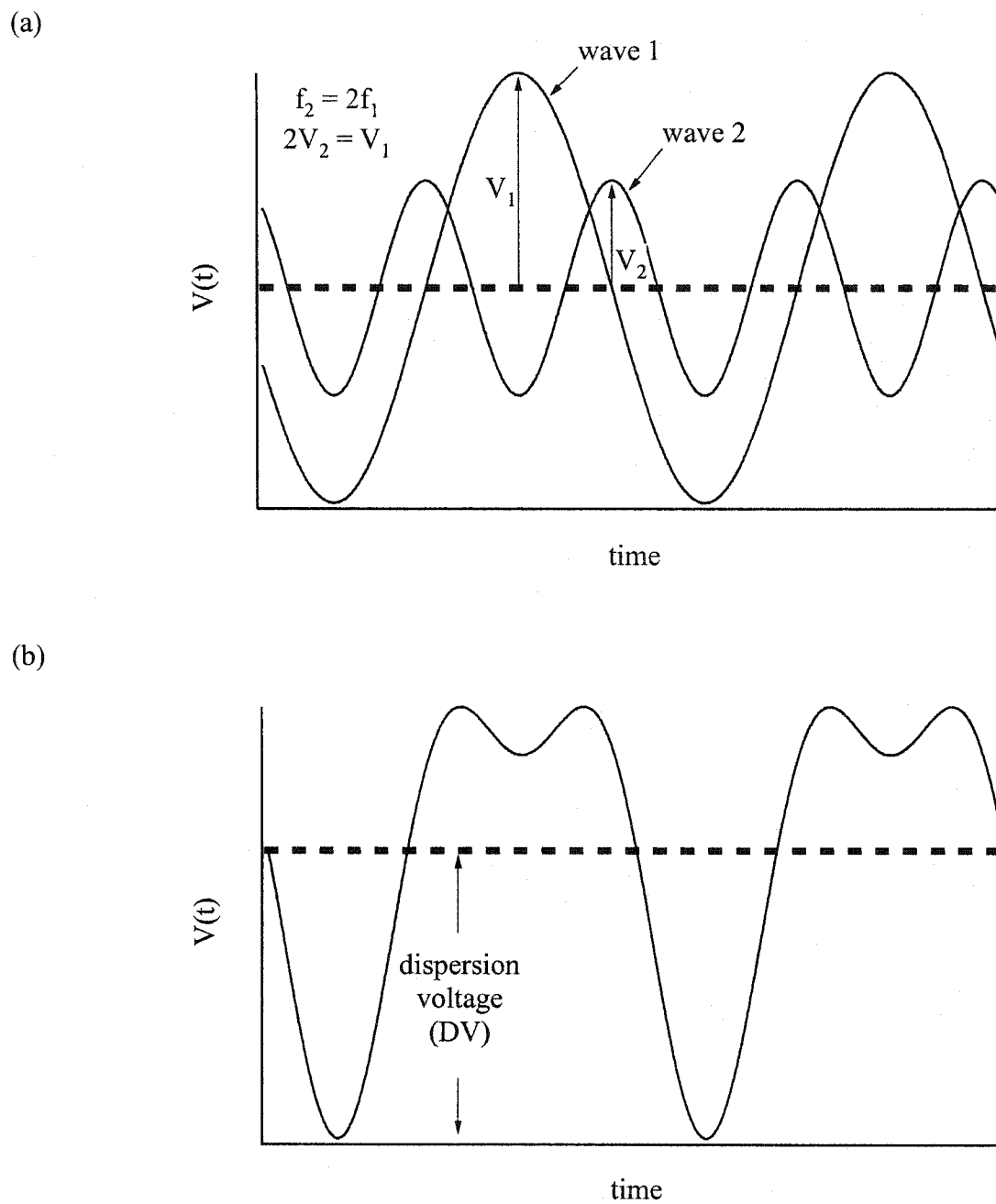


Figure 6.07 (a) Two composite sine waves that are combined to form (b) the asymmetric waveform for FAIMS operation.

used is illustrated in Figure 6.07 (b). The high:low voltage symmetry of this waveform is roughly 2:1. The high voltage peak (the negative polarity peak in this waveform) is called the dispersion voltage, DV. The generator has adjustments for the frequency, phase, and amplitudes of both sine waves. These adjustments are of critical importance, since changes in temperature (resistance) and capacitance can alter the form of the output wave, in both DV amplitude and waveform symmetry. For example, changing the dome position will alter the capacitance of the FAIMS interface, and tuning of the waveform may be required. Also, changes in the waveform seem to occur as the result of changes in the temperature of the generator. As a result, the stability of the output waveform is best when the generator has been running for about an hour to allow for thermal stabilization. It should also be noted that the generator tends to run hotter at higher DV settings than at lower ones, and the waveform needs to be re-tuned to proper symmetry when the DV is changed. If the DV is changed during an experiment, care must be taken to ensure the waveform is still in proper symmetry, and a slow drift of the waveform may be observed.

The waveform generator was powered using an external power supply (GW Laboratory Power Supply Model GPC-3030D Dual Tracking with 5V Fixed). The frequency of the asymmetric waveform was 750 kHz, and the symmetry and voltages were measured using a LeCroy 9310M Dual 300 MHz Oscilloscope (100 Ms/s, 50 kpts/ch). For all of the experiments, the DV was set to -3300 V. The CV was scanned in steps of 0.2 V over the desired voltage range.

6.2.3 Mass Spectrometry

The MS used for the dome interface studies was an API-150EX from MDS-Sciex (Concord, Ontario, Canada), and is a single quadrupole instrument with a mass range of 30 - 3000 m/z. The interface of this instrument has a sampling orifice plate and skimmer cone configuration, as illustrated in Figure 6.08. A bias may be applied to the orifice plate (OR) to generate collision-induced dissociation (CID) of the ions at the initial sampling.

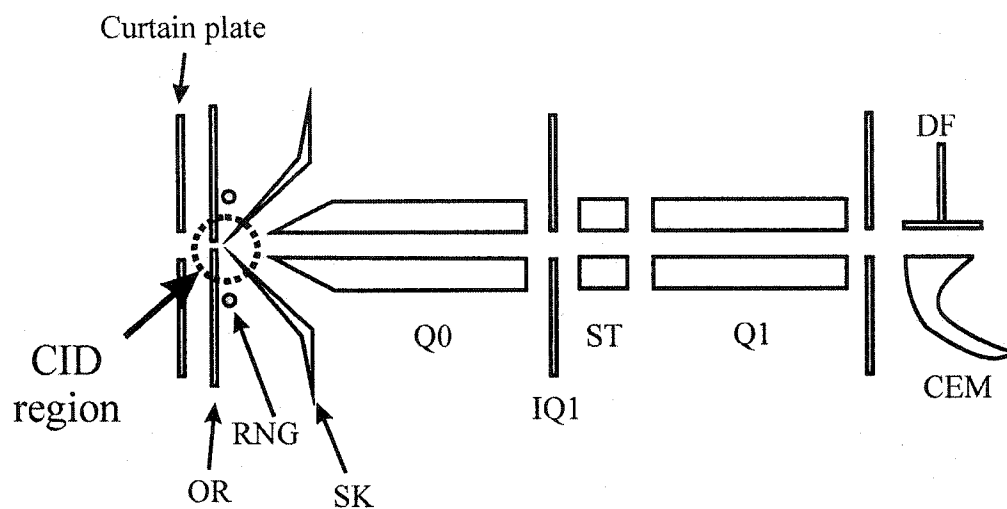


Figure 6.08 Ion optics schematic of the PE-Sciex API-150EX mass spectrometer with the collision-induced dissociation (CID) region highlighted. OR = orifice plate, RNG = ring electrode, SK = skimmer, Q0 = RF-only focusing quadrupole, IQ1 = intermediate quadrupole 1, ST = stubbies (quadrupole), Q1 = mass selection quadrupole, DF = deflector, CEM = channel electron multiplier detector.

6.2.4 ESI Source

The ESI source was an in-house laboratory design, and consisted of a fused silica capillary (180 μm OD, 50 μm ID) of about 45 cm length, with one end extending from a stainless steel capillary sheath (0.018" O.D., 0.009" I.D.), to which a voltage was applied (as described in Chapter 1). The tip was placed about 0.5 cm away from the curtain plate of the FAIMS, and was at an angle of about 45°. An in-house built floating digital ammeter with nanoampere sensitivity was placed in-line with the power supply and the tip. Both the magnitude and stability of the electrospray current was used to fine-tune the electrospray conditions. To generate negative ions, the MS ionspray power supply was used to bias the tip to a voltage of about -3 kV, drawing a current of about 50 nA during stable ESI operation. From the other end of the capillary, the sample solution was delivered at about 50 $\mu\text{L/hr}$ using a Cole-Parmer 74900 Series syringe pump.

6.2.5 ESI-FAIMS-MS Coupling

Coupling of the FAIMS to this system was fairly straightforward. First, the ion source and curtain plate were removed (a single unit), and the interlocks were defeated in order to operate without this source attached. Also, the curtain gas supply was cut off, but valve pressure was maintained to keep the interlocks active. To the outer face of the orifice plate of the spectrometer, two holes were drilled, and a mounting ring was attached, as illustrated in Figure 6.09. The inner diameter of the mounting ring was designed to match the outer diameter of the outer FAIMS electrode. Once the mounting ring was in place, the FAIMS was simply pushed into this hole. No further securing of the FAIMS to the MS was used. The thickness of the mounting ring was designed to let the flat face of the FAIMS outer electrode to be placed flush against the flat orifice of the MS. The contact between the outer FAIMS cylinder and the MS sampling orifice means that both of these parts will be biased to the same potential. An external power supply (Xantrex XT-120-0.5 Regulated DC Power Supply) was used to set this voltage, instead of using the MS power supply to do so, as illustrated in Figure 6.10. In this configuration, the orifice was manually set to a constant voltage. For experiments

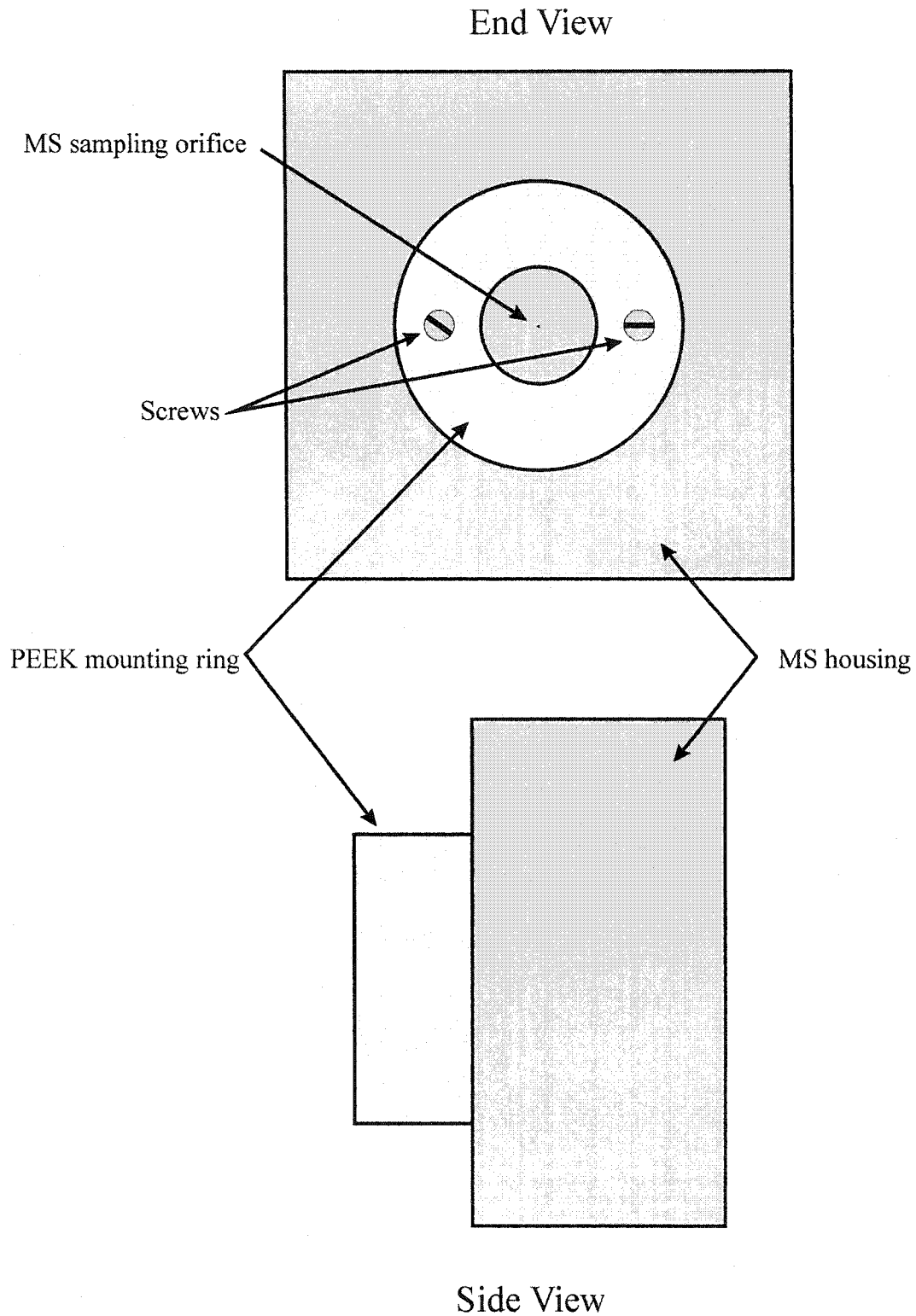


Figure 6.09 Face of API-150EX MS sampling orifice with mounting ring attached.

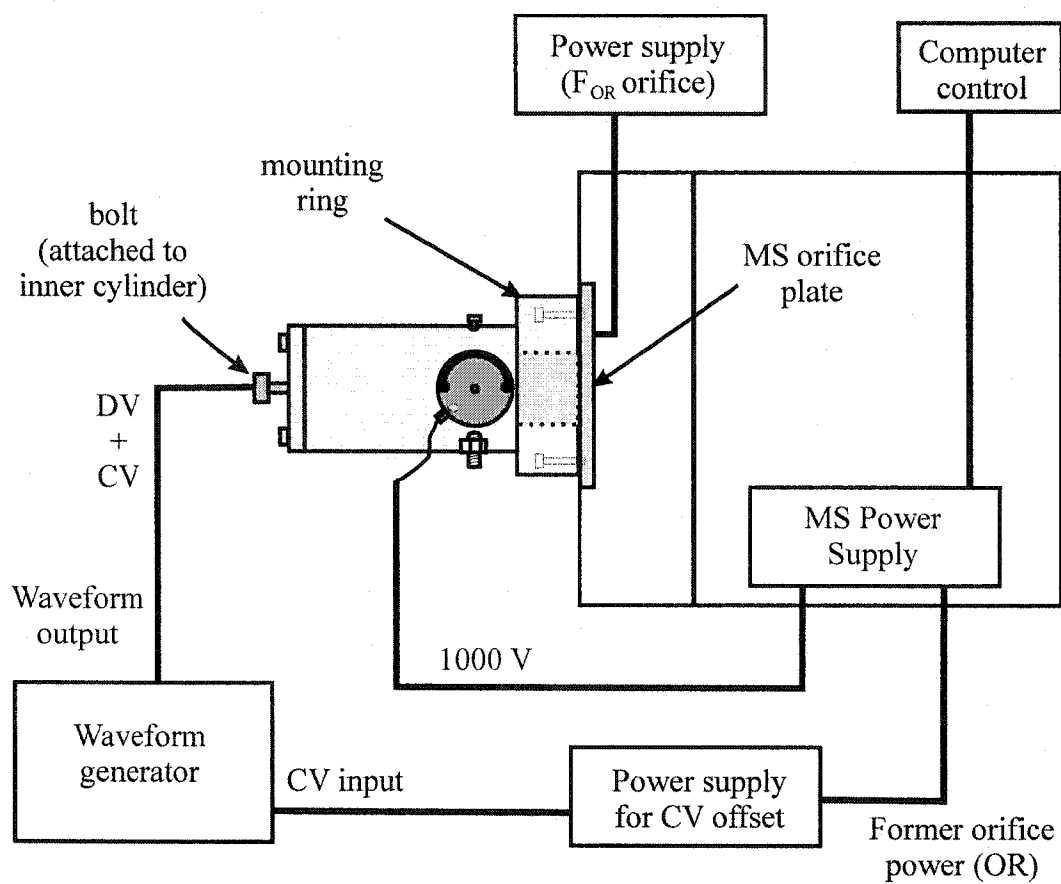


Figure 6.10 Electrical connections for the FAIMS-MS interface.

described in this Chapter, the MS orifice plate and the outer FAIMS electrode were biased to 0 V ($F_{OR} = 0$ V). Since the skimmer is grounded, there is no potential difference between the orifice plate and the skimmer, so no additional CID is introduced to the ions as they are sampled into the MS. The MS power connection (formerly for the orifice) was re-routed to the waveform generator to act as the compensation voltage power supply. By routing the former orifice (OR) power connection to the CV input of the waveform generator, the CV could be scanned by using the existing computer software. By putting an additional power supply (Xantrex XT-120-0.5 Regulated DC Power Supply) in series with the MS and the generator CV input, an additional voltage offset could be added. Since the software only allows the computer-set voltage polarity to match the polarity of the MS scan, this offset is necessary when opposite CV polarity is required. Since the MS was scanning for negative ions, it would only allow voltage settings of negative polarity. So, the waveform generator CV was offset by 80 V ($CV_{off} = 80V$), and scanning the MS voltage (formerly the OR supply) from -80 to 0 V allowed the net applied CV to be scanned from 0 to 80 V. Both the DV and the CV were combined in the final waveform, and this was applied to the inner cylinder through the bolt at one end of the FAIMS interface. Also, a -1kV bias was applied to the FAIMS curtain plate using the MS power supply.

Input ion flow during a FAIMS experiment using the dome prototype is illustrated in Figure 6.11. The curtain gas is introduced to the FAIMS between the curtain plate and the sampling orifice in the wall of the outer cylinder. The electrospray (ES) generated ions move towards the sampling orifice of the FAIMS electrostatically, and undergo typical droplet fissions and desolvation during the trip to the orifice. The bulk of the curtain gas exits the FAIMS through the curtain plate orifice and assists in the desolvation of the ES-generated ions. The remainder of the curtain gas comprises the drift gas for the FAIMS experiment. Since the MS orifice is constantly sampling gas (at about 0.56 L/min for this system), gas is drawn from the curtain gas inlet region and into the FAIMS analyzer region. So, as ions enter the FAIMS analyzer region, they are transported by the gas towards the MS orifice. As described earlier in Chapter 4, if the

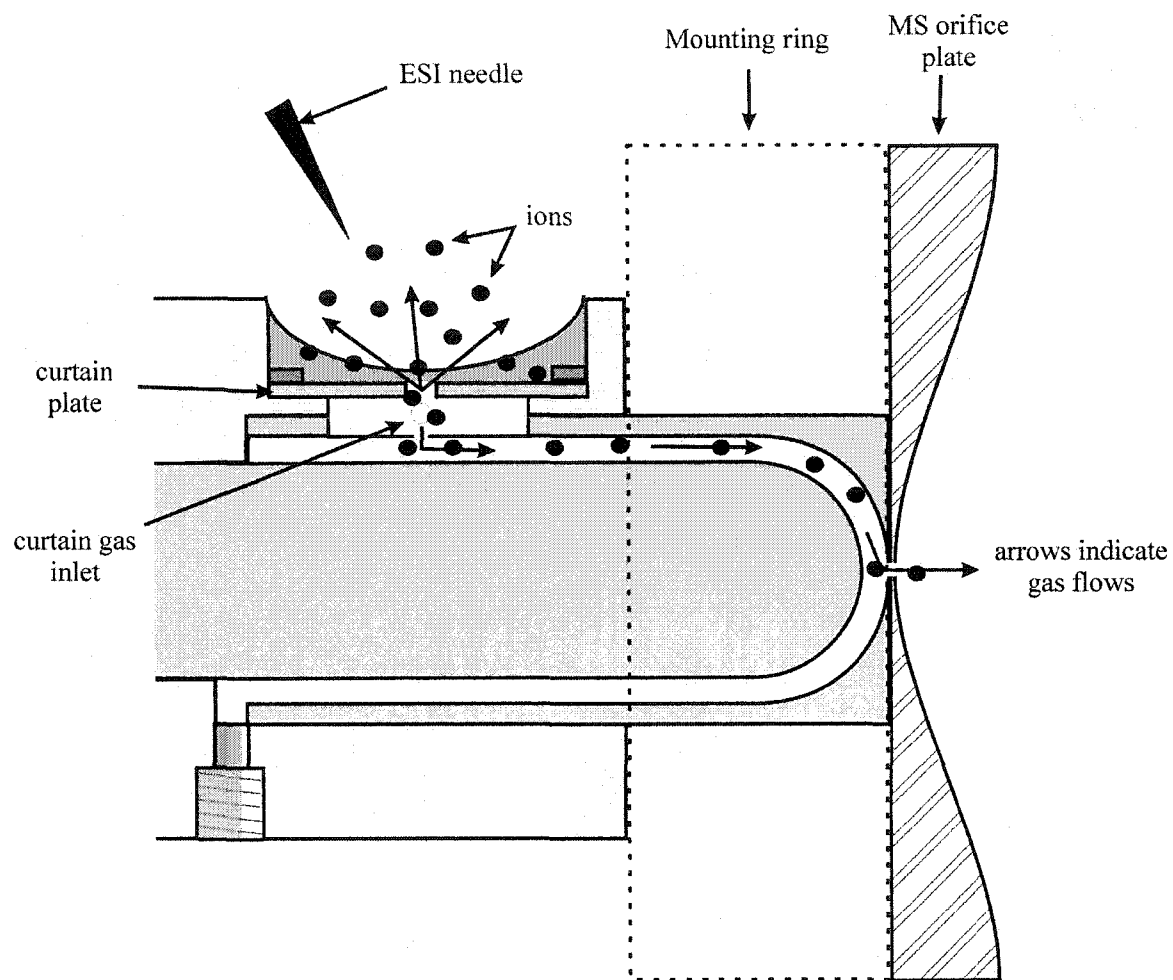


Figure 6.11 Ion sampling during an ESI-FAIMS-MS experiment.

combination of DV and CV are appropriate, the ion will not strike a wall and will be successfully transported by the gas flow to the MS orifice.

A Gilmont Instruments rotamer (0 – 5 SLPM Air) was used to set the N₂ curtain gas flow rate. Previous tests demonstrated that this meter's calibration was adequate for measuring N₂. Downstream of the flow meter, gas purifiers consisting of a combination of activated charcoal and a molecular sieve were used. Unless otherwise specified, the flow of the curtain gas was 2.0 L/min.

6.2.6 Reagents

Stock solutions were prepared from the appropriate reagent grade salt in 18 MΩ de-ionized water, then diluted in HPLC grade methanol to make the final test solutions. All test solutions were a matrix of approximately 5% water and 95% methanol, with 0.4 mM ammonium acetate as an electrospray stabilizer.

6.3 Results and Discussion

To demonstrate the effects of curtain gas flow rate and waveform symmetry, the effects of these parameters on the mass-selected compensation voltage spectra from several ESI-FAIMS-MS experiments were studied. A test solution containing 0.1 μM KClO₄ was used. In ESI-MS, perchlorate is observed as ClO₄⁻, and sulfate is observed as the bisulfate ion, HSO₄⁻. Although sulfate was not specifically added to the test solution, it was present at significant levels as a contaminant. The bisulfate ion has a major peak at m/z 97, but also has a significant peak at m/z 99, which is also the m/z of the major mass for ClO₄⁻. Mass-selected CV spectra were acquired for masses corresponding to the major masses of the ions ClO₄⁻ (m/z 99 and 101) and HSO₄⁻ (m/z 97) under the specified conditions of variable flow rate or variable waveform symmetry. After the mass-selected CV spectra were acquired, the peak CV, intensity, and the peak width (as 10% of its height) was determined for each ion. The traces for m/z 97 and 99 were used for HSO₄⁻

and ClO_4^- , respectively, for the mentioned measurements. An example of mass-selected CV spectra for these ions is presented in Figure 6.12, at a N_2 gas flow rate of 2.0 L/min. As described in Chapter 5, the presence of bisulfate can be a significant interference in the determination of perchlorate, largely due to HSO_4^- at m/z 99 interfering with the determination of ClO_4^- at this m/z . However, the FAIMS can separate these ions in the gas phase prior to the introduction to the MS, as the mass-selected CV spectrum in Figure 6.12 illustrates. The ClO_4^- is transmitted at $\text{CV} = 23.5$ V and the HSO_4^- is observed at $\text{CV} = 21.6$ V. If the CV is set to $\text{CV} = 23.5$ V, the FAIMS will continuously transmit ClO_4^- to the MS, filtering out and removing the potential interference from HSO_4^- .

These ions were selected for the gas flow rate and waveform symmetry studies due to their closely matched CVs when using N_2 carrier gas. Variations in the gas flow rate and the waveform symmetry for these ions should suggest the relative importance of these factors for the separation of ions with similar K_h/K behaviors, such as perchlorate and bisulfate.

6.3.1 Effects of Curtain Gas Flow Rate

The effects of gas flow rate on intensity, CV, and peak width are illustrated in Figures 6.13 (a), (b), and (c), respectively. As mentioned previously, the curtain gas plays two major roles. One is to desolvate the ions for sampling, and the other is to act as the drift gas for the FAIMS separation. At low gas flow rates (< 1 L/min), the observed intensity fluctuates, and is nearly zero at 0.3 L/min (Figure 6.13 (a)). This very low value is likely due, in part, to inefficient desolvation of the electrosprayed ions. Note that the flow through the MS orifice is estimated at about 0.56 L/min (specifications in instrument manual), so curtain gas flow rates near this value likely represent settings at which atmospheric gases are being sampled into the FAIMS. This may account for the large increase in CV observed at very low flow rates for these ions (Figure 6.13 (b)), since a different drift gas composition may alter the observed CV [29]. Obviously, gas flows greater than 0.56 L/min need to be used. The intensity is fairly consistent through flow rates of about 1.4 L/min to about 2.6 L/min, then decreases at flow rates in excess of

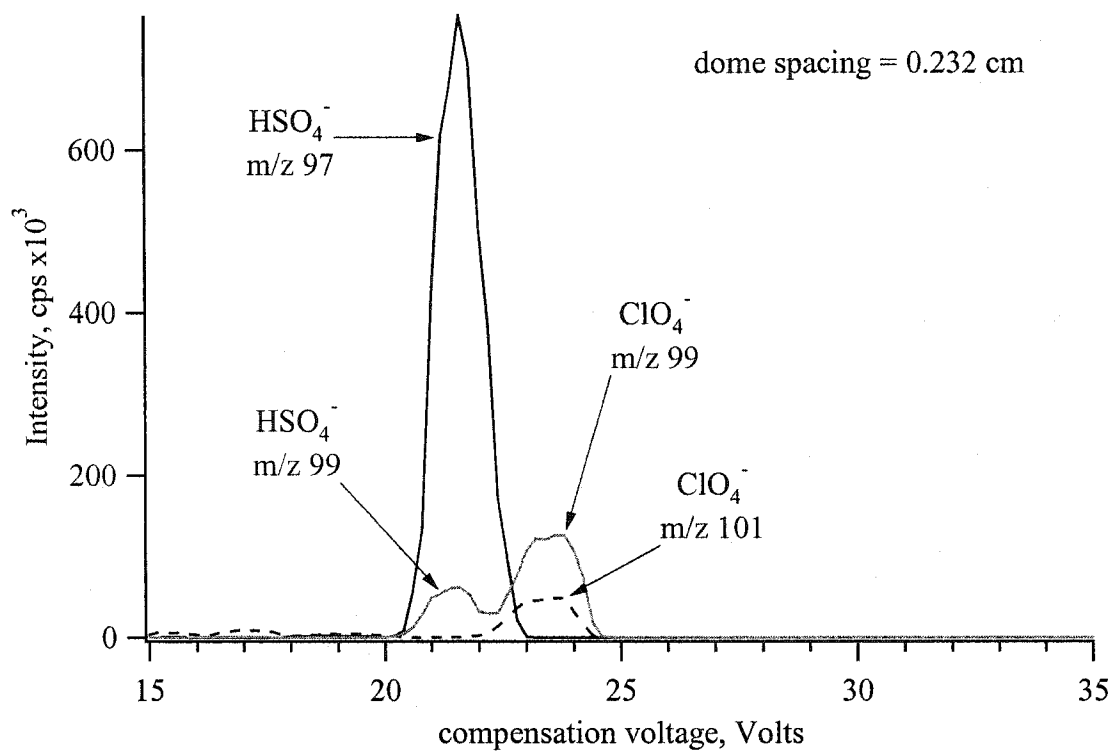


Figure 6.12 Superimposed mass-selected CV spectra of bisulfate and perchlorate from an ESI-FAIMS-MS experiment, monitored at m/z 97, 99, and 101. Sample solution was 0.1 mM KClO_4 , with 0.4 mM ammonium acetate in 95% methanol (5% water). Sulphate is present as a solution contaminant. Curtain gas = 2.0 L/min, DV = -3300 V. Dome spacing = 0.232 cm.

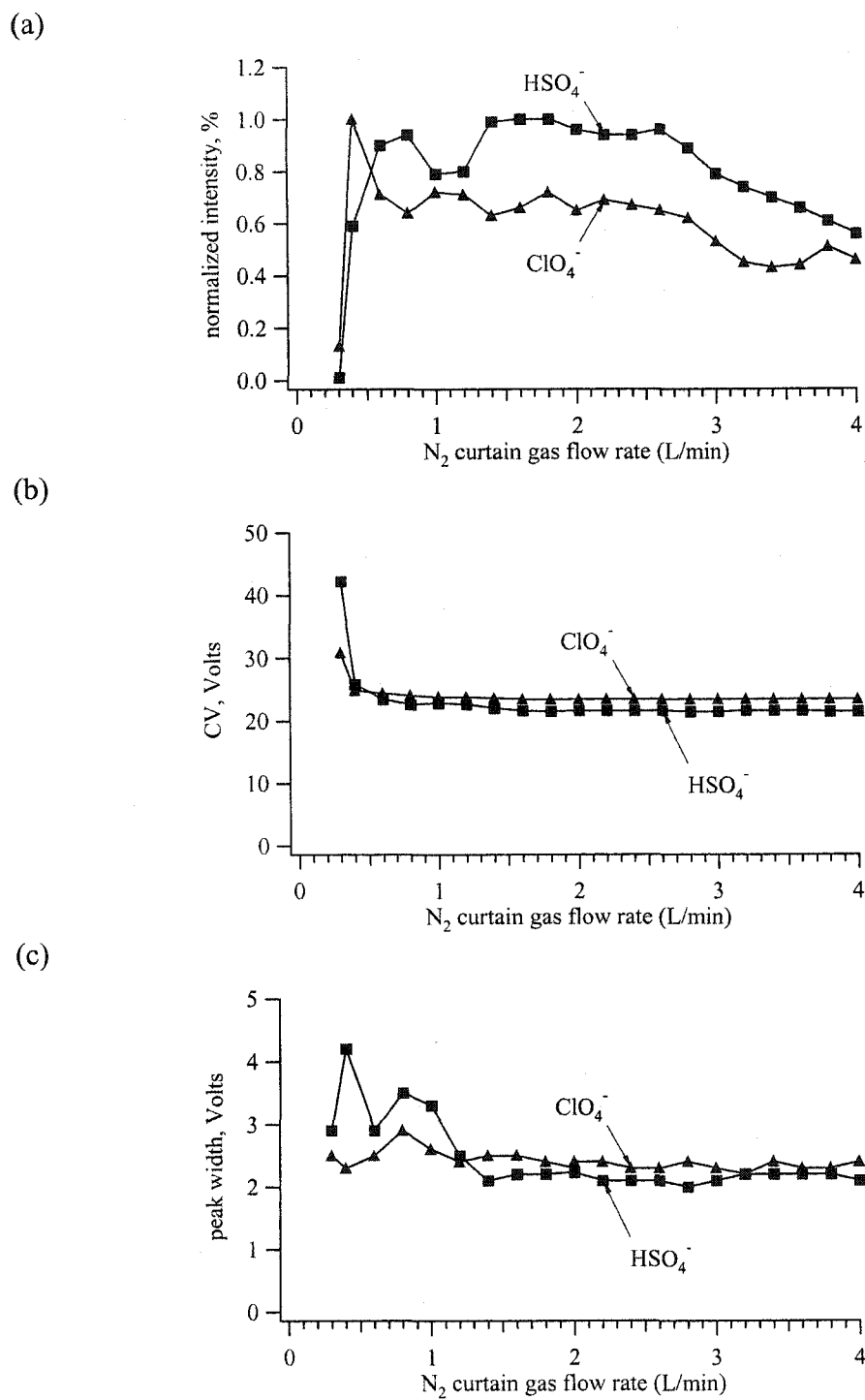


Figure 6.13 Effect of N₂ curtain gas flow rate on (a) normalized signal intensity, (b) peak CV, and (c) peak width for the ions perchlorate (ClO₄⁻) and bisulfate (HSO₄⁻).

2.6 L/min. This decrease is likely due to the large flow rate of gas exiting the curtain plate orifice, which likely reduces the efficiency of ion sampling.

Looking at Figure 6.13 (b), there is a slight increase in CV separation with increasing flow rate, with the CV separation being relatively constant at curtain gas flow rates greater than about 2 L/min. Also, the CVs of each ion remain relatively unchanged with curtain gas flow rate. The similarity of the CVs for a particular ion suggests that the atmospheric pressure gas-phase species is the same for all flow rates. In other words, the relative degree of desolvation or declustering is assumed to be consistent at all flow rates (ignoring very low values). So, differences in the observed CV might be due to differences within the FAIMS itself. Assuming the gas composition to be consistent, differences in the CV may be accounted for by slight changes in the pressure within the FAIMS, since the K_h/K is determined by the E/N . Unfortunately, this interface was not equipped with a pressure sensor. As discussed in Chapter 5, previous studies with the concentric cylinder interface demonstrate that pressure changes within the analyzer can result in CV shifts.

Figure 6.13 (c) shows that the peak width remains essentially constant at about 2.5 volts for all flow rates greater than about 1.2 L/min. Again, the possibility of atmospheric gases entering the FAIMS may be responsible for the observed peak widths at very low flows, or may also be due to the difficulty in measuring the width at low intensity.

Overall, it seems that a flow rate greater than about 1.6 L/min is required to give the narrowest peak widths, with near-optimal peak separation and intensity. In fact, it seems that any flow rate greater than 1.6 L/min can be effectively used, with some compromise in signal intensity at flow rates greater than 2.6 L/min. As long as the flow rate exceeds that required by the MS and the amount necessary for effective desolvation, the flow rate used has minor effects on the observed spectra for these ions. It should be noted that the flow rate for optimum separation and signal intensity may vary for different ions and different gas types, so should be optimized for the test conditions.

Some recent work suggests that the use of a high flow rate (~ 6 L/min) is required to separate some carbohydrate linkage isomers [30].

6.3.2 Effects of Waveform Symmetry

The effects of waveform symmetry were studied as the effects of two different adjustments: 1) the relative amplitude of one sine wave to the other, and 2) the phase of the two sine waves that combine to make the waveform. The waveforms were adjusted using the waveform generator, and the output waveform was measured using the oscilloscope. In all cases, the DV amplitude was adjusted to be constant at -3300 V. After the waveforms were set and measured, a CV window was scanned while monitoring m/z 97, 99, and 101.

For the amplitude variations, only the 1500 kHz sine wave amplitude (i.e., the lower voltage) was adjusted independently. After measuring the output waveform, Excel modeling was used to estimate what the amplitude ratio of the sine waves would be to produce a similar waveform. The theoretical ratio of the two sine wave amplitudes, expressed as “high/low” represents the ratio of the peak voltage of the high voltage and low voltage composite sine wave. For a perfect waveform, the amplitude ratio would be high/low = 2.0. From this, plots of normalized intensity, CV, and peak width (at 10% peak height) as a function of the amplitude ratio are presented as Figures 6.14 (a), (b), and (c), respectively. Adjustments of the waveform to values other than high/low = 2.0 ratio produce minor effects on signal intensity, as the data in Figure 6.14 (a) illustrate. With the exception of the HSO_4^- intensity at a high/low = 1.94, a general trend of slightly decreasing signal intensity with increasing high/low ratio was observed. It should be noted that the ES stability will have some influence here, so scatter around the points should be expected. The sudden dip in the intensity of the HSO_4^- signal intensity at high/low = 1.94 is likely related to an ESI instability, as opposed to a FAIMS effect. The high/low ratio was shown to have little effect on the peak CV (Figure 6.14 (b)). For all the amplitude ratios tested, the peaks for a particular ion were found to be within 1 V of each other. Also, the difference in CV between the two ions remains constant, even

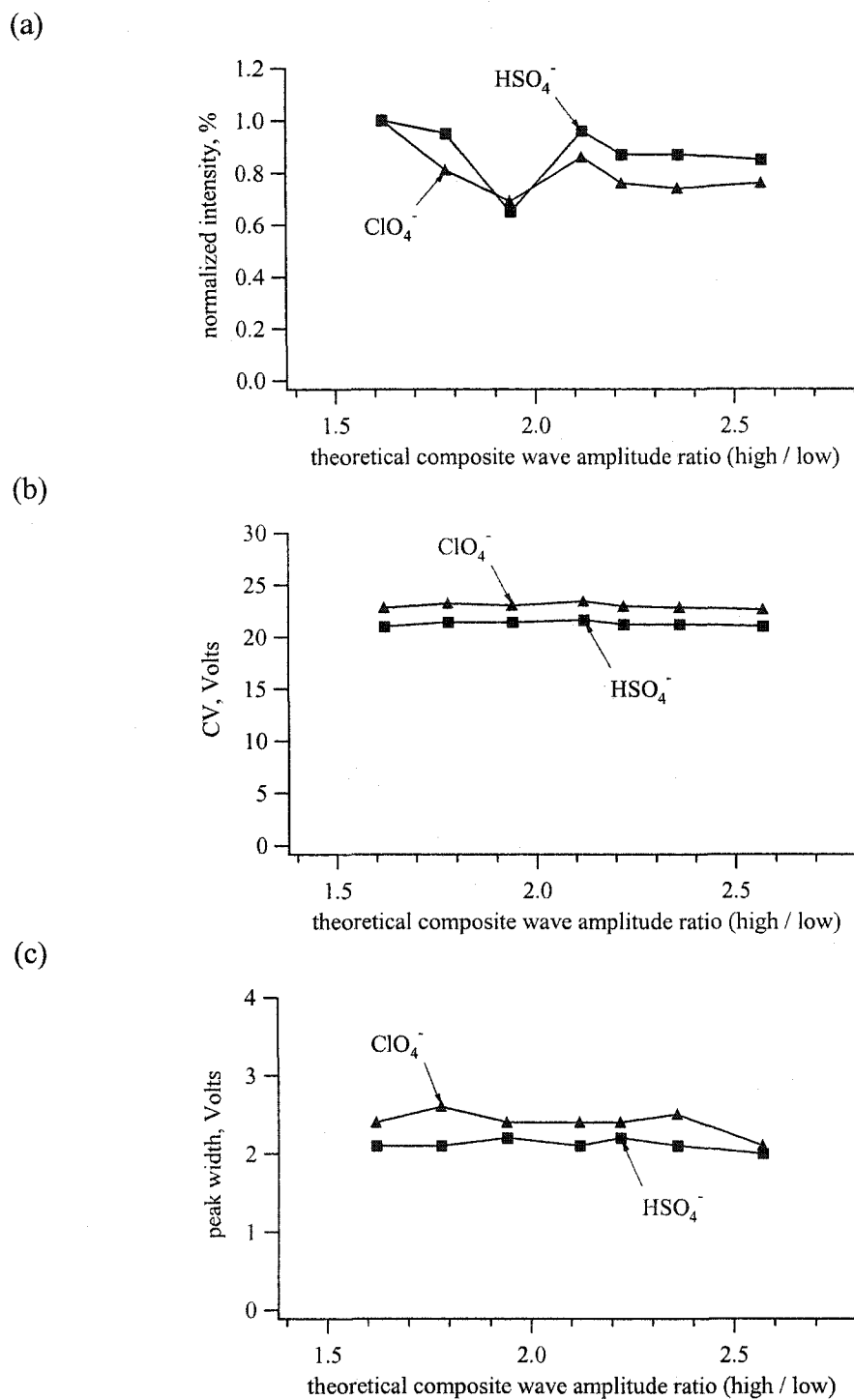


Figure 6.14 Effect of altering the theoretical composite sine wave amplitudes (high/low) on (a) normalized signal intensity, (b) peak CV, and (c) peak width for the ions perchlorate (ClO_4^-) and bisulfate (HSO_4^-).

though each individual ion's CV may have changed. The data in Figure 6.14 (c) show that the amplitude ratio had only minor effects on the mass-selected CV peak width, staying consistent at about 2 – 2.5 V. So, provided that the DV stays constant, slight variations in the relative sine wave amplitudes do not generate serious problems for the observed spectra. Provided the waveform is stable, it seems likely that a range of sine wave amplitude ratios can be effective.

The effect of varying the phase of the composite sine waves was also studied. The relative phase was expressed as the ratio of the peaks A and B, as illustrated in Figure 6.15. The range of ratios tested ($|A/B| = 1.98$ to 1.37) represent phase angles, ϕ , from $\sim 90^\circ$ (ideal waveform) to about 133° , as suggested by Excel modeling. As before, the phase of the waveform was adjusted, while maintaining the DV amplitude. These amplitude adjustments likely also alter the relative amplitude of the composite sine waves. However, the previous results indicated that this should have only a minor effect on intensity, CV, and peak width. The data in Figure 6.16 (a) illustrate the effect that phase has on the observed ion intensity. As the phase is increased from 90° , the observed intensity drops to about 50% at $\sim 133^\circ$. As the phase is varied from $\sim 90^\circ$ to $\sim 133^\circ$ ($|A/B| = 1.98$ to 1.37), the CVs of both ions were observed to decrease, and the relative CV separation was also decreased, as the data in Figure 6.16 (b) indicate. For perchlorate, the CV was observed to shift from about 24 V at phase = 90° , to about 18 V at phase = $\sim 133^\circ$. In this instance, the phase of 90° seems to produce the highest CVs and the maximum separation for these two ions. Ion trajectory modeling from Chapter 4 suggests that an ion's CV is maximized for a waveform with a 2:1 ratio of $t_{\text{low}}:t_{\text{high}}$, which is approximately what the ideal waveform represents. By altering the phase, the symmetry of the waveform is compromised. The positive polarity "low" field is increased, as the result of the increase in the peak voltage at point B (Figure 6.15). In this case, the ion is likely to travel farther during the positive portion of the waveform, and the net drift per cycle will be less. The end result is that less compensation will be required to balance the ion trajectory, and the observed ion CV will decrease. The loss in signal intensity as the phase is adjusted from $\sim 90^\circ$ to $\sim 133^\circ$ may be due to a decrease in ion focusing strength that normally accompanies shifts to lower CVs [6, 10].

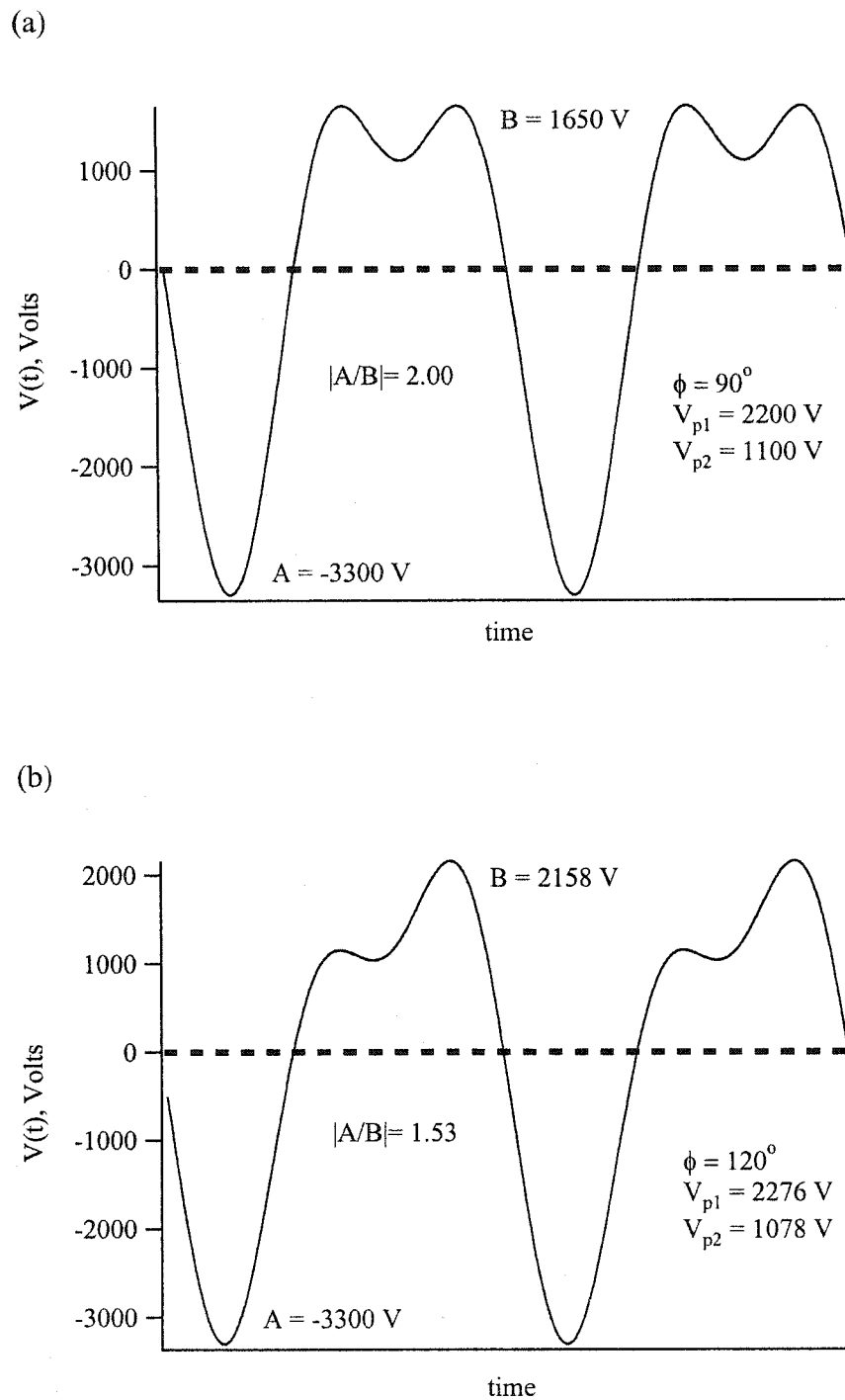


Figure 6.15 Examples of waveform symmetry for phases angles of (a) 90° and (b) 120° . V_{p1} and V_{p2} refer to the peak voltages of the composite sine waves.

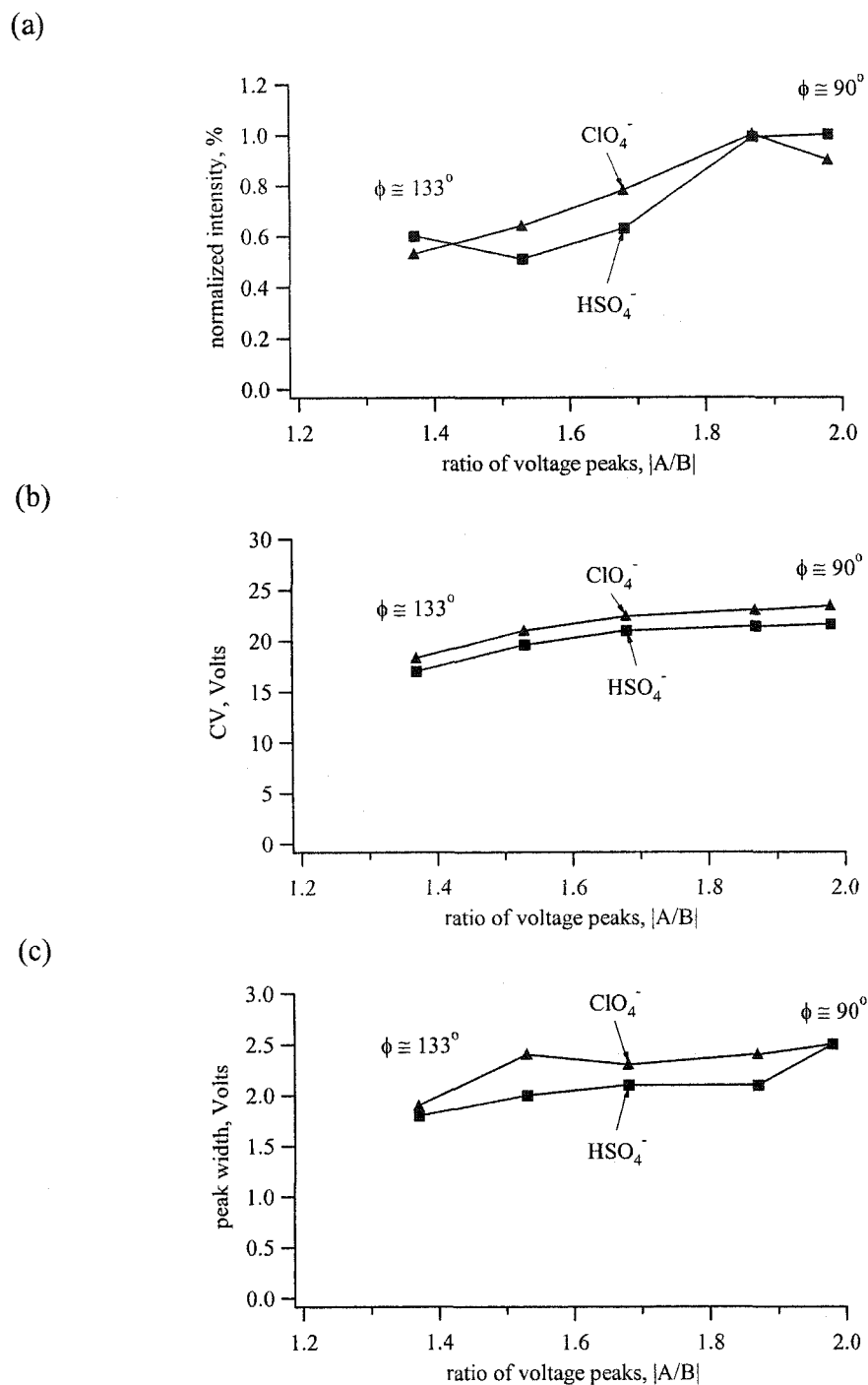


Figure 6.16 Effect of altering the phase of the composite sine waves on (a) normalized signal intensity, (b) peak CV, and (c) peak width for the ions perchlorate (ClO_4^-) and bisulfate (HSO_4^-). The symmetry of the resulting asymmetric waveform is represented as the ratio of the negative (A) and positive peak (B) voltage, expressed as $|A/B|$.

The effect of the composite sine wave phase on the observed width of the peaks is minor, as the data in Figure 6.16 (c) shows. At $\phi = \sim 90^\circ$, the peak widths are greatest, with slightly narrower peaks at $\phi = \sim 133^\circ$. These minor changes in the peak widths are likely related to the decrease in the observed CV [6, 10]. A more detailed explanation of the relationship between the observed CV and peak width will be discussed in Section 6.3.4.

The results indicate that the phase of the two sine waves seems to be more important than the ratio of their amplitudes. While optimum performance is achieved at ideal waveform symmetry, the system can still operate at a non-optimal one. However, operating at a non-optimal setting can result in a considerable compromise in the ion intensity and magnitude of the CV. The reduced CV of the ions can result in a change in the separation ability, potentially resulting in more ion species being transmitted at a particular CV. Also, this emphasizes that any changes to the waveform that occur throughout the course of a measurement or experiment can have serious adverse results. In other words, the stability of the waveform is critical, whereas the actual symmetry is less important. In fact, several different waveform symmetries can be used for such an apparatus, as outlined by Krylov [31].

6.3.3 Effect of Dome Spacing on CV

For the dome spacing studies, data were collected for two different test solutions. One solution contained 0.1 μM KClO_4 , 1 μM Na_2SeO_4 and 1 μM KI , and the second solution contained KCl , KBr , and KI , each at a concentration of 1 μM . Previous studies indicated that the halides were observed in the ESI-MS spectrum as the bare ion, X^- [32]. Perchlorate was also observed as the bare ion, ClO_4^- ; however, selenate was observed in the ESI-MS spectrum as biselenate, HSeO_4^- [33, 34]. Mass-selected CV spectra were acquired for masses corresponding to a major mass of each anion; m/z 35 (Cl^-), 79 (Br^-), 127 (I^-), 99 (ClO_4^-), and 145 (HSeO_4^-). Mass-selected CV spectra were collected at each dome setting at a $\text{DV} = -3300$ V. After all the dome spacings were tested, the DV was set to -2300 V, and mass-selected CV spectra were collected for the same dome settings.

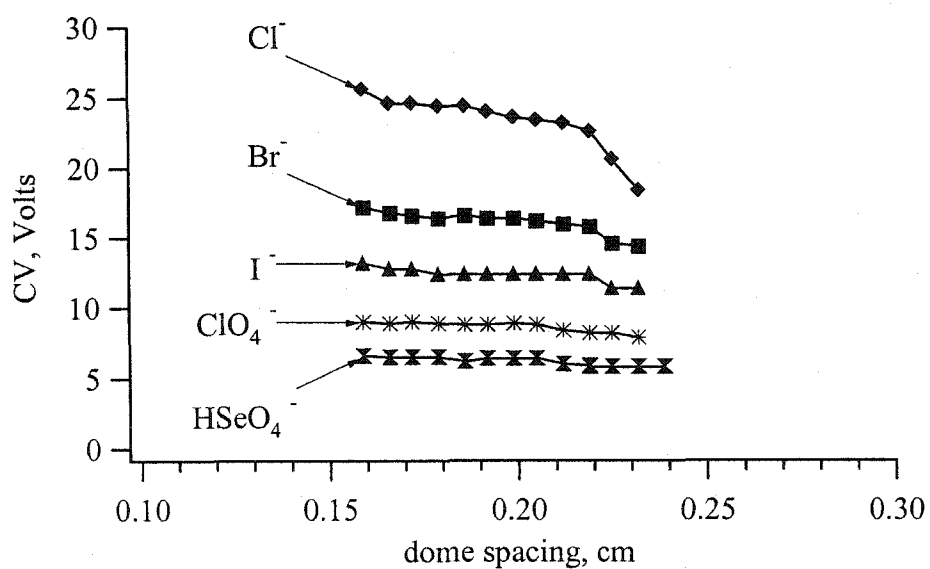
From the mass-selected CV spectra, the peak CV, peak intensity, and the peak width (as 10% of its height) was determined for each ion.

The peak CV of each ion was plotted as a function of the dome spacing. The data in Figure 6.17 illustrate the effect of dome position on the observed ion CV for the ions Cl^- , Br^- , I^- , ClO_4^- , and HSeO_4^- at (a) $\text{DV} = -2300 \text{ V}$ and (b) $\text{DV} = -3300 \text{ V}$. Both sets of data illustrate that the mass-selected CV peak of the ion decreases with increasing dome spacing. As the spacing is increased, the strength of the field at the dome is expected to decrease relative to the cylinder region (where the fields remain unchanged). The decrease in field strength means that the magnitude of K_h for these ions will be decreased (as will the K_h/K ratio), and so these ions will experience less net drift per cycle and require less CV in the dome region. Also, the rate of CV change with dome position was greater for ions with greater CV, which is likely related to the non-linear relationship of K_h/K with E/N . Ions that appear at higher CV tend to have mobility curves with a greater rate of change in K_h/K with increasing E/N , and hence show greater CV shifts with changes in the dome spacing. This trend holds true at both DV values tested, since the mobility curves for these ions likely show a significant non-linear rate of change under both DV settings. Overall, for these ions, higher CVs are required when narrower dome spacing is used.

6.3.4 Effects of DV and Dome Spacing on Mass-Selected CV Peak Width and Intensity

To illustrate the effect of dome position on the observed mass-selected CV peak width and intensity, these three variables were plotted on a single graph for each ion. The data at both $\text{DV} = -2300 \text{ V}$ and -3300 V are included on each plot, and the intensity for each ion was normalized to the maximum observed intensity at either DV setting. The data for Cl^- , Br^- , I^- , ClO_4^- , and HSeO_4^- are presented in Figures 6.18 to 6.22, respectively.

(a)



(b)

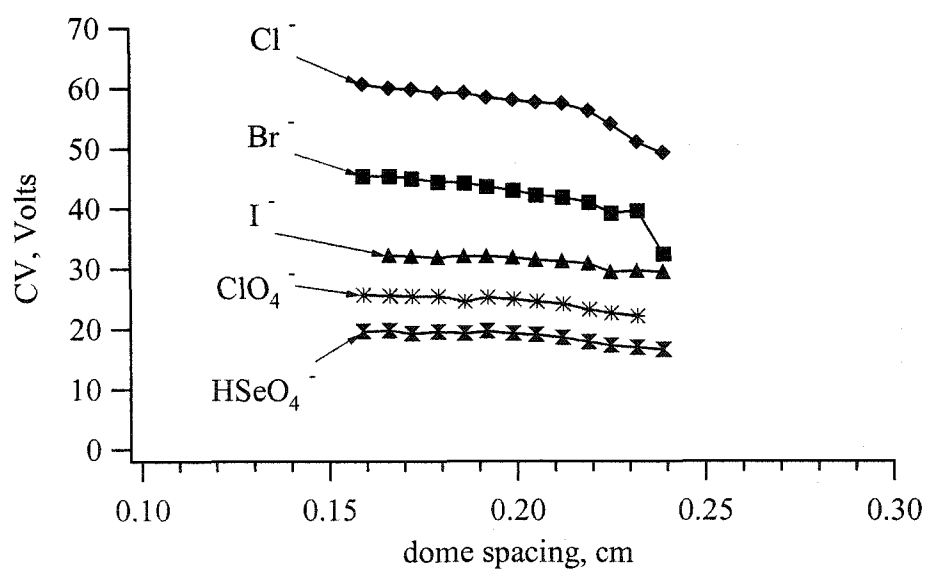


Figure 6.17 Observed peak CV as a function of the dome spacing. (a) DV = -2300 V; (b) DV = -3300 V.

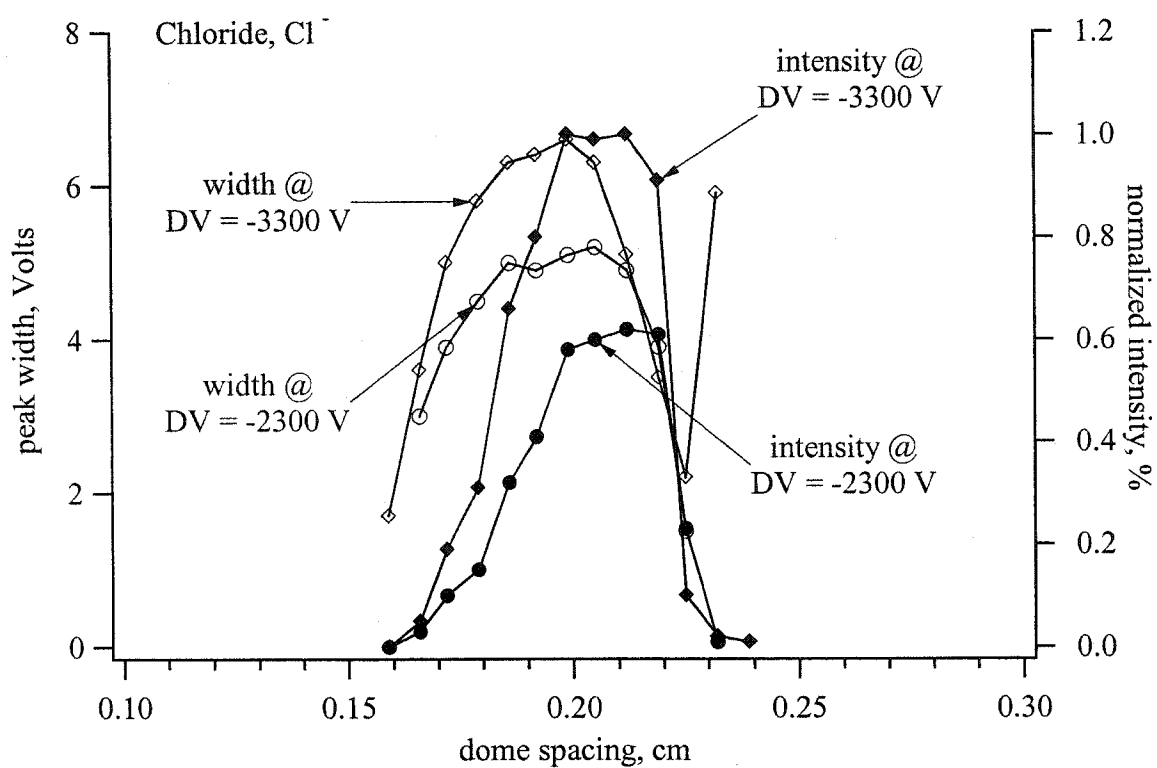


Figure 6.18 Variation of peak width and normalized intensity with dome spacing for the chloride ion (Cl^-) at DV = -2300 V and -3300 V.

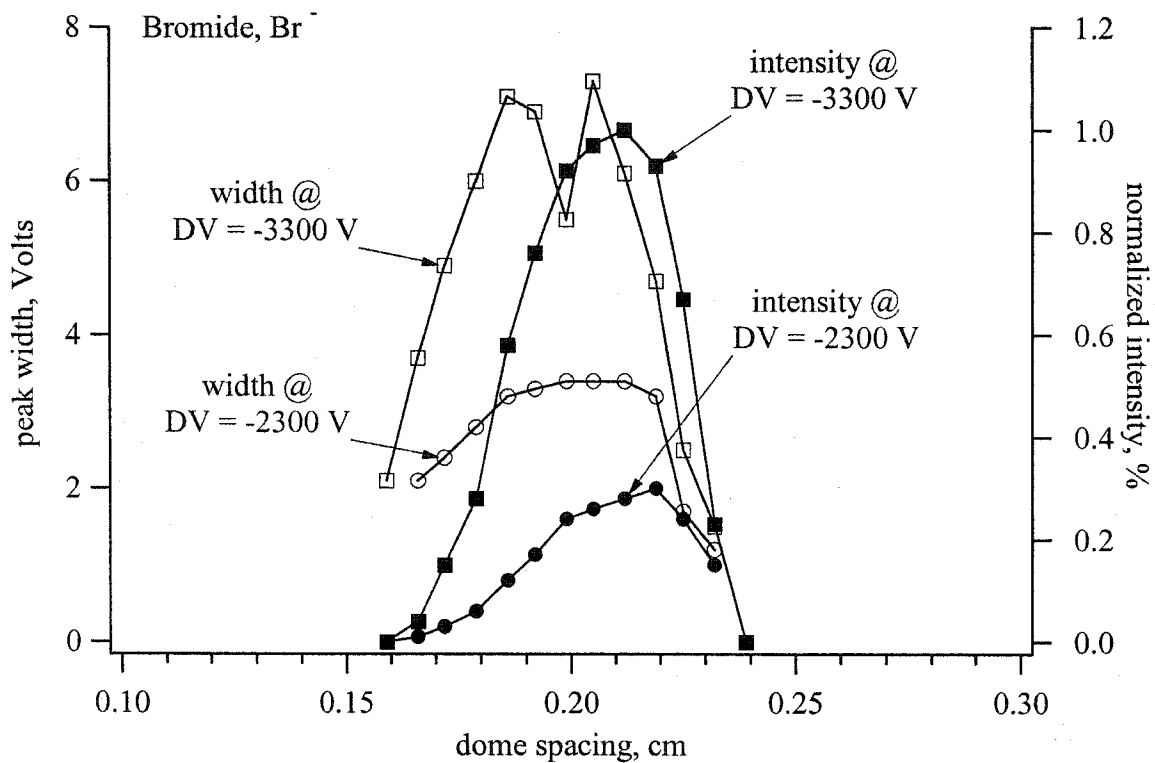


Figure 6.19 Variation of peak width and normalized intensity with dome spacing for the bromide ion (Br^-) at $\text{DV} = -2300 \text{ V}$ and -3300 V .

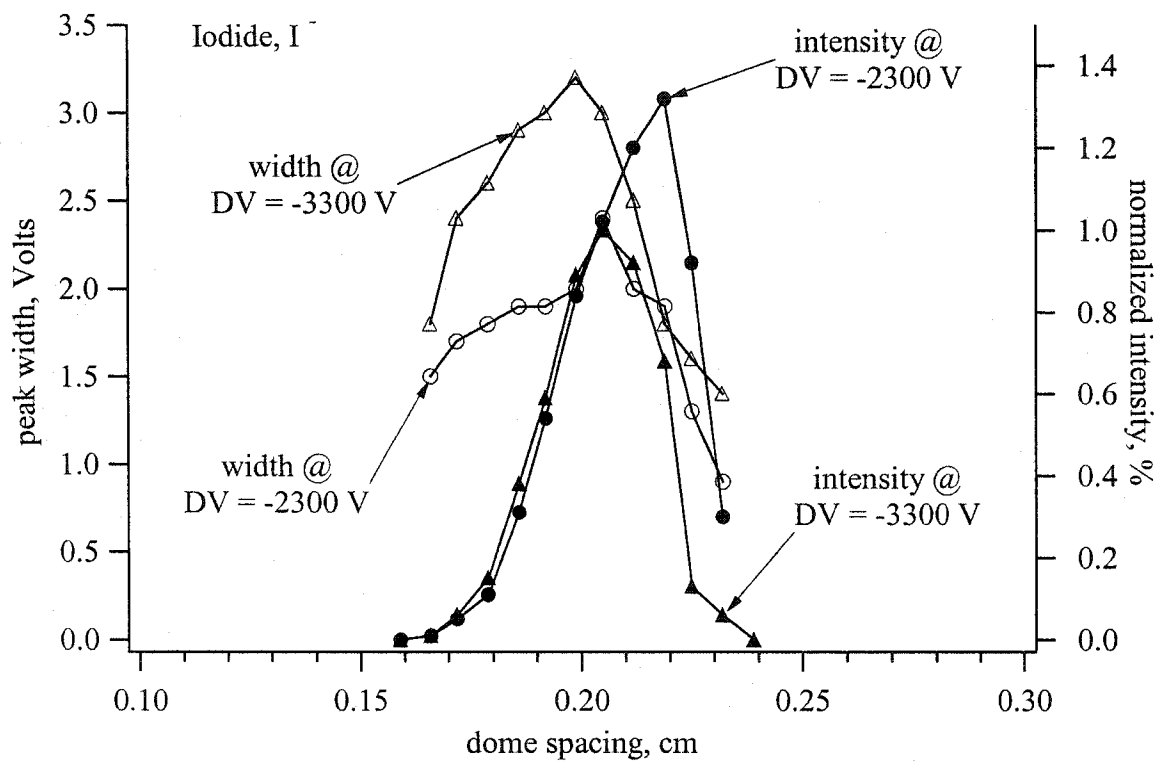


Figure 6.20 Variation of peak width and normalized intensity with dome spacing for the iodide ion (I^-) at DV = -2300 V and -3300 V.

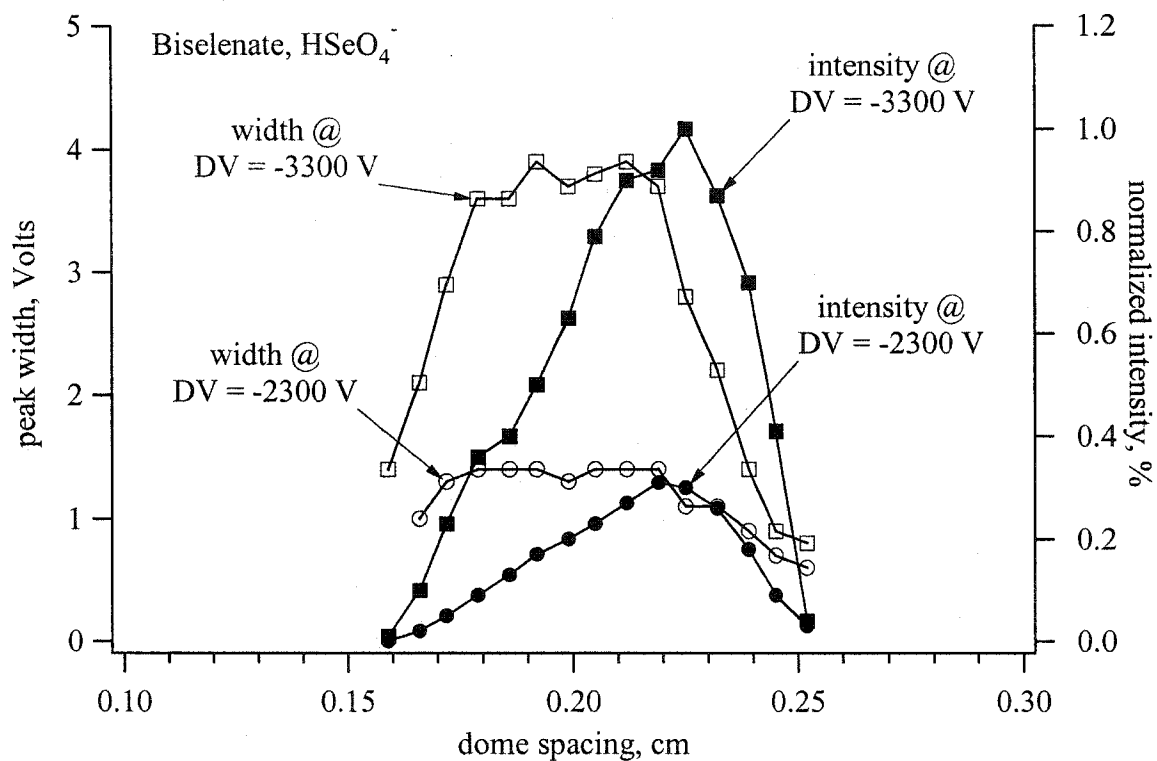


Figure 6.21 Variation of peak width and normalized intensity with dome spacing for the biselenate ion (HSeO_4^-) at DV = -2300 V and -3300 V.

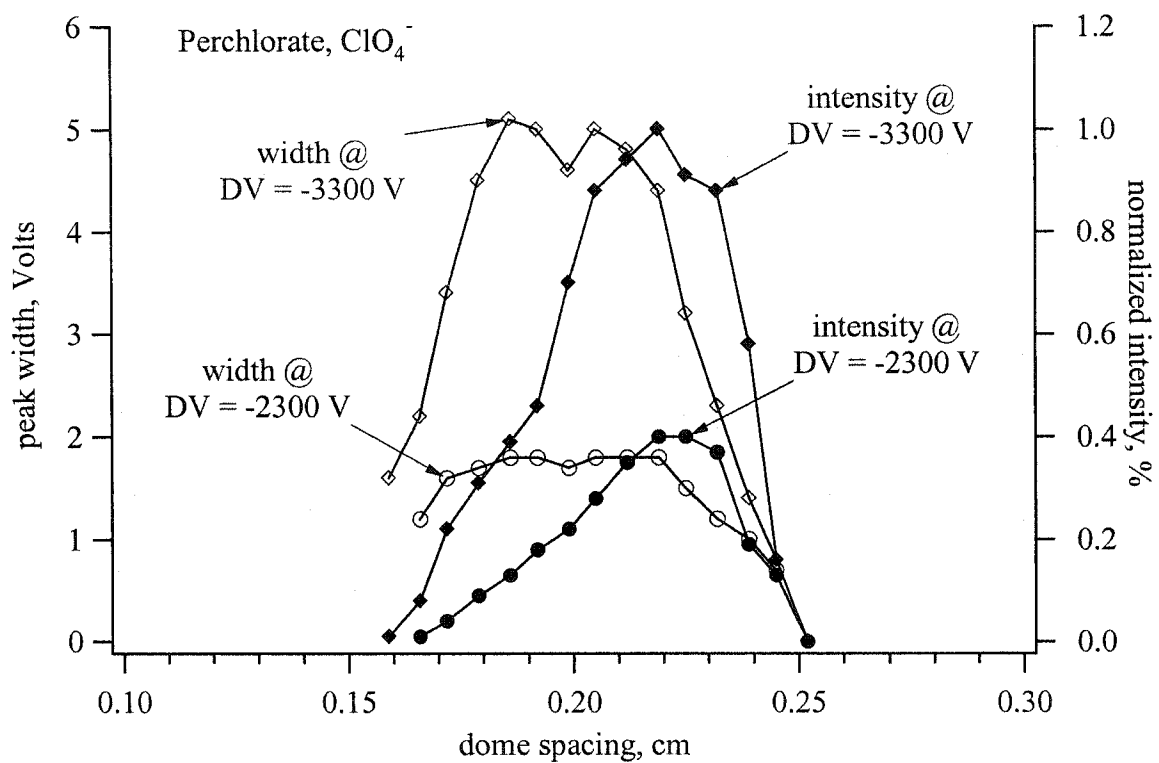


Figure 6.22 Variation of peak width and normalized intensity with dome spacing for the perchlorate ion (ClO_4^-) at DV = -2300 V and -3300 V.

The general effects of DV on the observed peak width and signal intensity with this interface are similar to that observed for the concentric cylinder interface [6, 10]. As briefly discussed Chapter 5, as the DV is increased, the signal intensity, the CV, and the CV peak width increase for small ions under these test conditions. For most of the small ions investigated, the increased DV led to an increased ion focusing effect, and an increased K_h/K , which generated higher CVs and wider mass-selected CV peak widths. An exception to this trend was observed for Γ . In the case of Γ , this ion was better transmitted (i.e., higher intensity signal) at DV = -2300 V than at DV = -3300 V (Figure 6.19). Some other factors must be preventing the effective transmission of this ion at DV = -3300 V. A possible explanation is that another ion present at relatively high concentrations in the FAIMS analyzer has a similar K_h/K behavior under these test conditions, and space-charge effects cause Γ to be lost to the walls of the FAIMS. Examination of the mass spectrum at the CV for Γ transmission at DV = -3300 V shows an intense signal at m/z 61, which may be HCO_3^- (present as a matrix contamination). At DV = -2300 V, the intense peak at m/z 61 is not observed at the same CV as Γ , and the Γ intensity is greater. Similar effects were observed for Cs^+ and Na^+ in positive mode operation, as discussed in Chapter 9.

Before investigating the effects of the dome position on the mass-selected CV peak width, some theoretical considerations for the peak width should be discussed. Simply put, the mass-selected CV peak width is the voltage range that will allow successful transmission of an ion through the FAIMS. First, consider the simpler case of concentric cylinders. As the CV is scanned, the ion trajectory is moved from near one electrode to near the other electrode. As the ion trajectory moves sufficiently away from either electrode, ions do not strike a wall and are successfully transmitted through the apparatus. At some point near the middle of the annular space, the ion transmission is the greatest, since the likelihood of random motions causing the ion to strike an electrode is minimized at this point (where the distance an ion must travel to strike an electrode is maximized). The minimum distance that an ion can approach a wall is highly dependent on the K_h/K of the ion. The greater that K_h/K deviates from 1, the greater the net distance traveled during each waveform cycle, and the ion focusing occurs more rapidly. Due to

the enhanced focusing effects, ions with higher K_h/K can be transmitted through the analyzer with ion trajectories that more closely approach one of the electrodes. As a result, ions with greater K_h/K should exhibit wider mass-selected CV peak widths. This general trend has been observed previously [6, 10]. This simplified explanation likely does not account for the peak widths of more complex ions, where the shape and folding of the ion may become a significant factor. Also, it has been suggested that dynamic chemical transformations or gas-phase association reactions may be partly responsible for wide CV peaks [23]. However, this simplified explanation suggests that any parameters that might enhance the degree of ion focusing for an ion should increase its mass-selected CV width. Such factors include increasing the DV, reducing the diameters of the FAIMS electrodes, altering the gas type to increase the ion's K_h/K , and changing the spacing between the electrodes (i.e., increasing the fields in the annular space).

Similar considerations can be discussed for a concentric sphere (dome) electrode geometry. Different ions will have different minimum distances that they can approach an electrode before having a high probability of hitting the surface. As discussed in Chapter 4, concentric sphere electrode geometry generates a steeper non-linear field gradient with radial position in the annular space, as compared to concentric cylinders of the same radii. As a result, the tendency for ion focusing is greater within a concentric sphere (dome) interface. Theoretically, this should allow all ions to more closely approach either electrode surface than was possible with concentric cylinders (for the same test conditions). A simple ion trajectory modeling simulation, similar to that used in Chapter 4, is illustrated in Figure 6.23. This simplified ion modeling suggests that for a dome FAIMS apparatus, if the dome spacing is equal to the cylinder spacing, the cylinder region determines the maximum CV window that will transmit ions. This is due to the different dependence of the variation of field strength with radial position between the cylinder and dome geometries. As a result, when the dome spacing is equal to the cylinder region, any ions that are transmitted through the cylinder region should be successfully transported through the dome region as well. Also, when the dome spacing is equal to the cylinder region, the widest possible CV transmission window for an ion should be observed, and the mass-selected CV peak width will be at a maximum. When

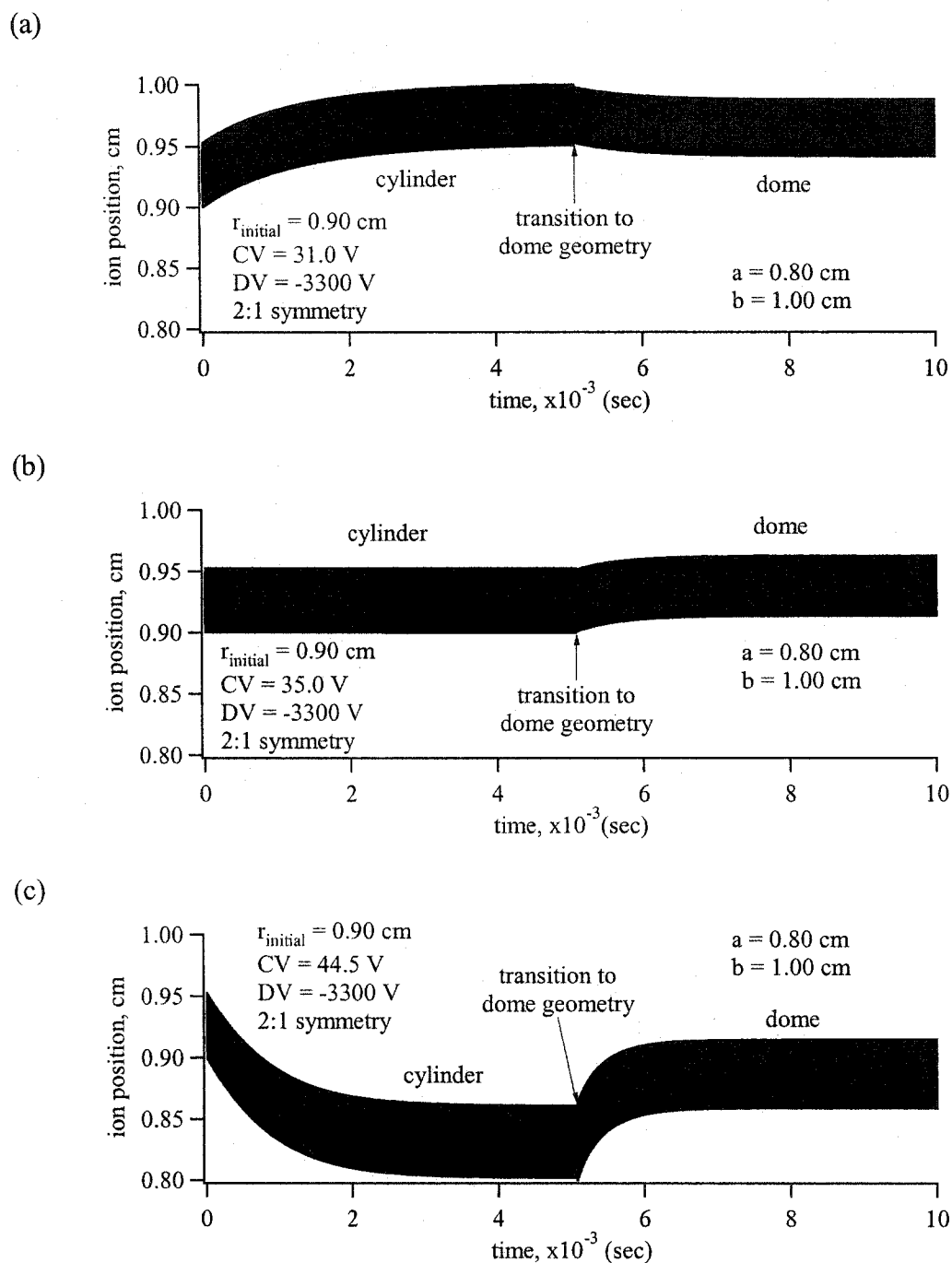


Figure 6.23 Calculated trajectory of a type A “perchlorate-like” ion in a FAIMS with both concentric cylinder and concentric dome geometry. Cylinder and dome regions have dimensions $a = 0.8$ cm, $b = 1.0$ cm. Square wave approximation, $f = 210$ kHz, 2:1 $t_{\text{low}}:t_{\text{high}}$, $DV = -3300$ V. X-axis (time) represents residence time in the analyzer region. Limits of the y-axis represent the surface of the electrodes. First half of modeling for concentric cylinder geometry, second half for concentric sphere geometry. (a) $CV = 31.0$ V, (b) $CV = 35.0$ V, (c) $CV = 44.5$ V.

the spacing of the dome is changed, the fields within the dome region are altered, whereas the fields in the cylinder region remain constant. For a set DV, the CV that will optimally transmit ions through the cylinders will not change, and the maximum CV transmission window will not change for the cylinder region. The altering of the fields within the dome region will have some adverse effects on the transmission of ions. As the spacing is widened, the ion trajectory balance point moves towards the inner dome, as discussed in Chapter 4. As the spacing is narrowed, the ion trajectory balance point will tend to be shifted towards the outer dome electrode. The more that the dome spacing is altered from the cylinder spacing, the greater the displacement of the ion trajectory towards one of the electrodes. As before, as the ion trajectory begins to move too close to the electrode surface, the ions are lost. The end result is that ions are transmitted through a narrower range of CVs, and the observed effect is that the mass-selected CV peak widths are reduced.

These types of effects were observed for all of the ions tested (Figures 6.18 – 6.22). All mass-selected CV peak widths were maximized when the dome spacing was roughly equivalent to the cylinder spacing of 0.198 cm. As the dome spacing was increased or decreased, the CV transmission window was decreased, as shown by the decrease in the mass-selected CV peak width. For all the ions, the mass-selected CV peak width was greater at DV = -3300V than at DV = -2300 V, due to the increase in K_t/K and increased focusing effects. As a general trend, ions that appear at a higher CV (Figure 6.17) exhibit greater peak widths than lower CV ions (Figures 6.18 – 6.22). For example, Cl^- (CV = ~60 V) exhibits a peak width of about 7 V at DV = -3300 V (Figure 6.18), whereas HSeO_4^- (CV = 20 V) has a peak width of about 4 V under the same test conditions (Figure 6.22). (Note that the peak width readings at the extremes of the dome positioning may be inaccurate due to the poor signal intensities at these dome settings.) Again, I^- is the notable exception. This ion exhibits narrower mass-selected CV peak widths than either HSeO_4^- or ClO_4^- , even though I^- is transmitted at a higher CV than these ions. Likely, the interference noted earlier for the transmission of this ion is responsible.

The importance of controlling the peak width is fairly straightforward. Since the main function of the FAIMS is to separate ions, wider peak widths may lead to a compromised separation of ions. Not surprisingly, adjusting the dome position to control the mass-selected CV peak width also leads to changes in the signal intensity. The behavior of the signal intensity as a function of the dome position was similar for all the ions tested, at both DV settings (Figures 6.18 to 6.22). The ion transmission (i.e., intensity) is dependent on the spacing of the dome, with different ions requiring different spacing for optimal transmission. At both DV settings, all ions tested were observed to exhibit intensity maximums at a dome spacing wider than the cylinder spacing of 0.198 cm. Note that the spacing of 0.198 cm was not tested, due to limitations imposed by the method of setting the dome position. Intuitively, it might be expected that the maximum signal intensity should be observed at a dome spacing that is equal to the cylinder spacing. The observation of maximum intensity at a different dome position suggests that other factors must be considered. As discussed earlier, for a dome spacing equal to the cylinder region, as the ion enters the dome region, its trajectory balance point is shifted towards the outer dome electrode (Figure 6.23). This occurs as a consequence of the different radial field dependence between concentric spheres and cylinders. By displacing the balance point away from the middle of the annular space, it is likely that relatively more ions are lost to the outer wall of the FAIMS via random motions, even though the field-induced path will still transmit ions. By increasing the dome spacing, the trajectory balance point can be returned to the middle of the annular space. This likely accounts for the observation of maximum signal intensity at a dome spacing greater than the cylinder spacing.

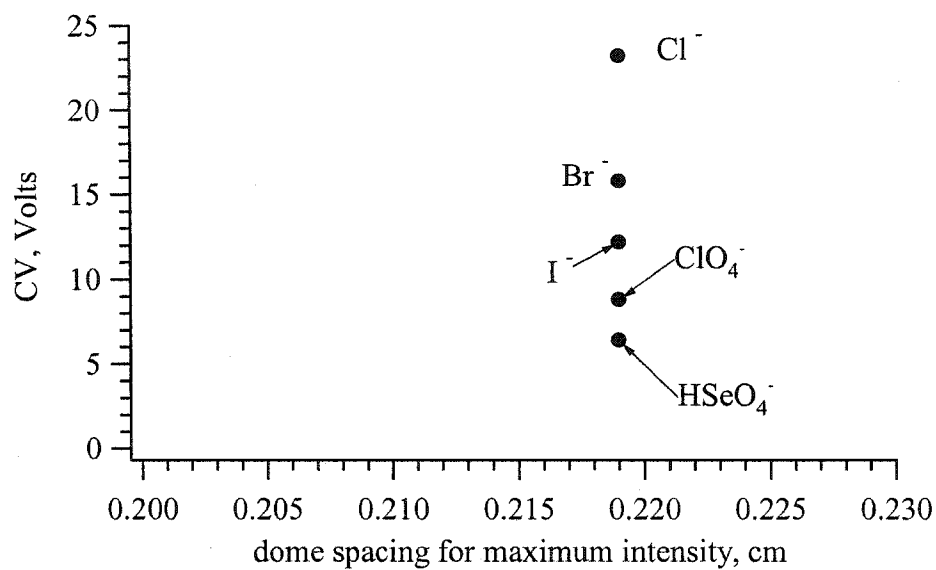
Another possible reason that the dome spacing and the ion trajectory balance point need to be changed may be the result of the movement of the carrier gas through the analyzer region. During the cylinder region of the analyzer, the gas flows in a direction parallel to the cylinder axis, and favorably transports the ions towards the dome region. As the gas enters the dome region, it is possible that the momentum of the gas tends to push ions along the axis of the cylinders, towards the outer dome electrode. By moving the dome electrodes farther apart, the balance point is shifted nearer the inner dome

electrode, with the net result that more ions would be prevented from striking the outer dome electrode. Ions with greater K_h/K and hence, CV, will travel further during each cycle of the waveform and be more rapidly focused than ions with a lower K_h/K . So, ions that exhibit a high K_h/K (i.e., high CV) would tend to require less compensation for gas momentum in the dome curvature. These high K_h/K ions would require less spacing at the dome for momentum compensation than would lower K_h/K ions.

If the observed ion CV is plotted as a function of the dome spacing required for maximum ion transmission (Figure 6.24), some interesting trends are observed. Figure 6.24 (a) is a plot of the ion data at $DV = -2300$ V, and Figure 6.24 (b) is the data at $DV = -3300$ V. At the lower DV, all the ions exhibit a CV less than 25 V, and the transmission of all ions is maximized at a dome spacing of 0.219 cm. At the higher DV, the dome spacing for optimum transmission varies with the type of ion, with higher K_h/K (higher CV) ions exhibiting optimal intensity at a narrower dome spacing. The exception of Γ to the seemingly linear trend in Figure 6.24 (b) is likely related to problems with the transmission of this ion at $DV = -3300$ V. However, the behavior of HSeO_4^- is also unusual. At $DV = -3300$ V, the HSeO_4^- exhibits maximum signal intensity at a wider dome setting (0.225 cm) than at $DV = -2300$ V (0.219 cm). This is unexpected, since the trajectory correction (or compensation for gas momentum) at $DV = -3300$ V should be greater than (or equal to) that required at $DV = -2300$ V. However, at 0.225 cm, the signal intensity for HSeO_4^- was only 4% less than at 0.219 cm. Considering the possible ESI stability, this difference may not be significant enough to claim that the 0.219 cm setting was significantly better. The intensity values for ClO_4^- are almost identical at both of these dome settings, so both of these lower CV ions may be considered optimally transmitted near 0.219 cm. More importantly, the data in Figure 6.24 (a) suggests that low CV ions may be optimally transmitted at a single dome spacing, whereas for higher CV ions (Figure 6.24 (b)), the dome spacing needs to be tuned for the ion of interest.

The implications for tuning the dome position in this FAIMS interface are very important. The important relationship between the peak width and signal intensity for these ions with respect to the dome spacing is that the maximum ion signals are observed

(a)



(b)

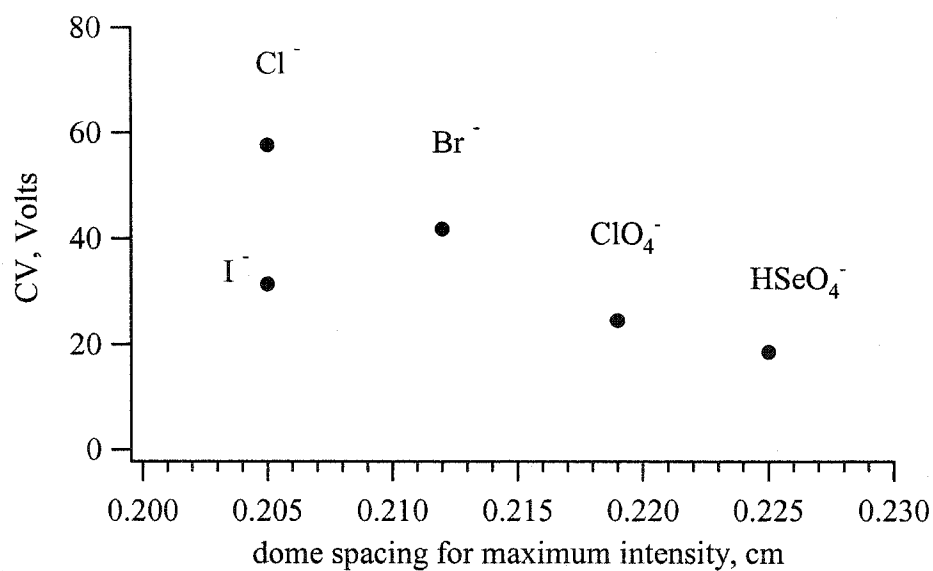


Figure 6.24 Observed ion CV at the dome position required for maximum signal intensity. (a) $DV = -2300$ V; (b) $DV = -3300$ V.

at a dome spacing greater than 0.219 cm, whereas the peak width maximums are observed near 0.198 cm. Generally, the narrower the mass-selected CV peaks, the more likely that an ion will be separated from other species in the gas phase prior to introduction to the MS. As such, narrower peak widths are desirable. The data (Figures 6.18 – 6.22) demonstrate that at a dome spacing narrower than 0.198 cm, the signal intensity may be too low to be useful, whereas at a wider spacing, the intensity is still reasonable. So, increasing the dome spacing greater than 0.198 cm is the only option that will provide narrower peaks with acceptable signal intensity. Generally, the dome position is set to achieve a compromise between peak width and signal intensity, whichever is of greater importance. An example of how the dome spacing can affect the resultant spectra is illustrated in Figure 6.25. These data are similar to those presented in Figure 6.12. Figure 6.25 (a) is the superimposed mass-selected CV spectra of the perchlorate and bisulphate ions at a dome spacing of 0.199 cm, which is (approximately) the spacing for the maximum peak width for the perchlorate ion. Similarly, Figure 6.25 (b) is the mass-selected CV spectrum at a dome spacing of 0.219 cm, which is the spacing for the maximum transmission of the perchlorate ion through the FAIMS. Figure 6.25 (c) is an "optimized" dome setting of 0.232 cm. Under these test conditions, the perchlorate and bisulphate ions are adequately separated, while maintaining ion signal intensity. The other dome settings would not be appropriate, since the m/z 99 signal due to bisulphate is not adequately separated from the perchlorate ion at m/z 99.

6.4 Conclusions

This relatively brief characterization for some small anions has highlighted some important considerations for using a dome FAIMS interface. The curtain gas flow rate must be greater than about 1.6 L/min to avoid problems, presumably related to inadequate desolvation and sampling of atmospheric gasses into the FAIMS analyzer region. Adding a pressure sensor may provide insight into the possible factors altered by increasing the curtain gas flow rate, and allow accurate E/N curves to be collected.

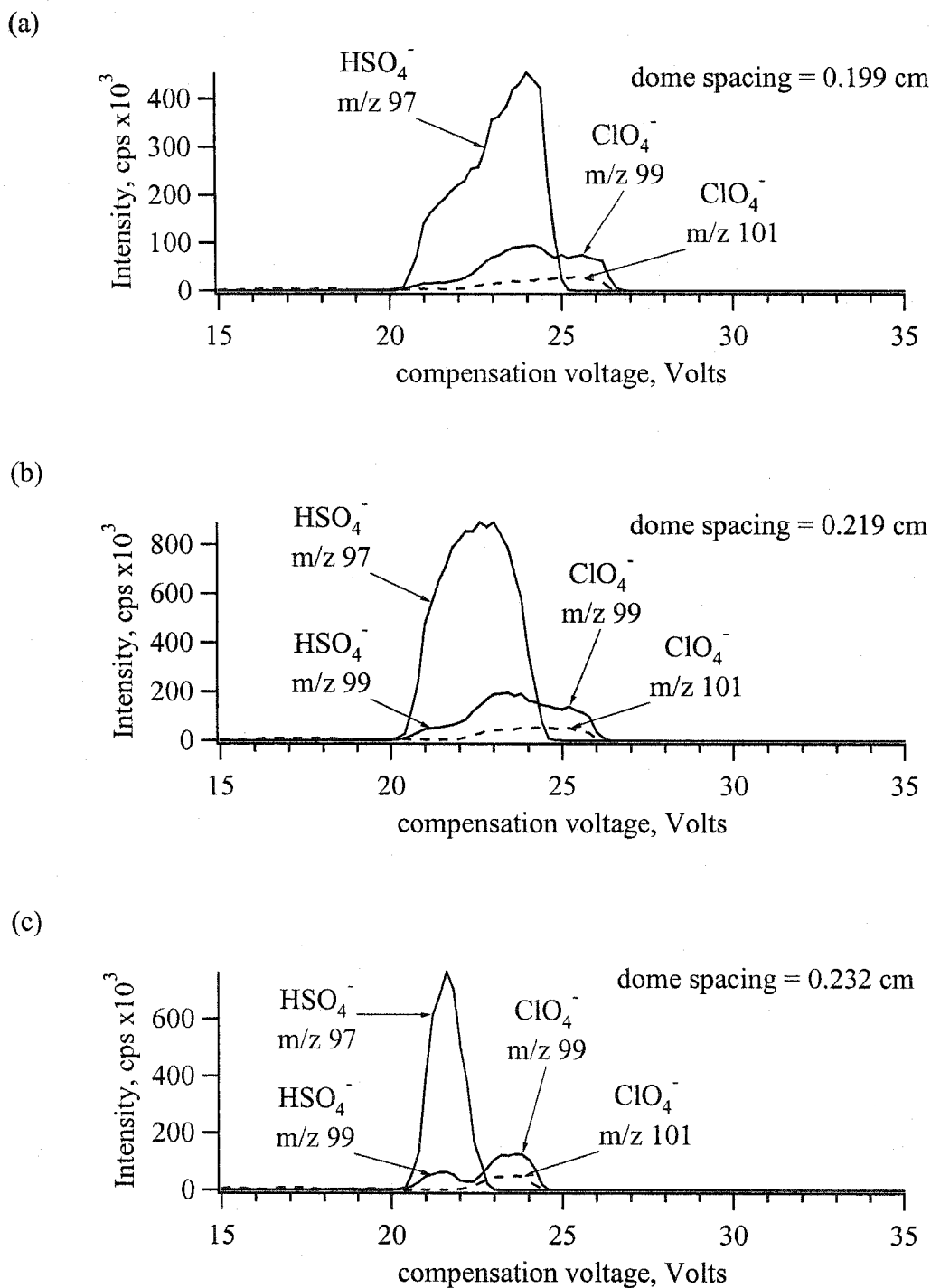


Figure 6.25 Observed variations in mass-selected CV spectra of bisulfate and perchlorate with the annular spacing at the dome region. Dome spacing of (a) 0.199 cm, (b) 0.219 cm, and (c) 0.232 cm. Solution and sampling conditions as in Figure 6.12, with noted exceptions.

It was demonstrated that the symmetry of the waveform was not critical to FAIMS operation, but significantly improved performance was achieved with the correct waveform. The tests did highlight that the stability of the waveform (especially the phase of the composite waves) for the duration of the experiment was very important for obtaining reproducible results. The position of the dome was shown to have a significant effect on the peak width and intensity, with a less influential role on an ion's CV. For the ions tested, the ions exhibiting a higher CV tended to require a wider dome spacing for optimal signal intensity. Also, the results highlighted the need to optimize the dome position for the desired peak width and intensity for the ion of interest. The observed results seem to be adequately explained using simple ion trajectory modeling; however, further work should be done to further refine these explanations for a wider range of ion species and mobility types.

6.5 References

1. Buryakov, I. A.; Krylov, E. V.; Soldatov, V. P. "Inventor's Certificate (USSR) No. 1485808 [in Russian], G01 No. 27/62"; *Byull. Izobret.* **1989**, USSR. No. 1485808.
2. Buryakov, I. A.; Krylov, E. V.; Makas', A. L.; Nazarov, E. G.; Pervukhin, V. V.; Rasulev, U. K. "Separation of ions according to mobility in a strong AC electric field"; *Sov. Tech. Phys. Lett.* **1991**, 17, 446-447.
3. Carnahan, B. L.; Tarassov, A. S. "Ion Mobility Spectrometer"; **1995**, Mine Safety Appliances Company, Pittsburgh, Pa. United States. Patent No. 5 420 424.
4. Carnahan, B.; Day, S.; Kouznetsov, V.; Matyjaszczyk, M.; Tarassov, A. "Proceedings of the 41st Annual ISA Analysis Division Symposium"; *41st Annual ISA Analysis Division Symposium.*, Framingham, MA, April 21-24, 1996.
5. Krylov, E. V. "A method of reducing diffusion losses in a drift spectrometer"; *Tech. Phys.* **1999**, 44, 113-116.
6. Guevremont, R.; Purves, R. W. "Atmospheric pressure ion focusing in a high-field asymmetric waveform ion mobility spectrometer"; *Rev. Sci. Instrum.* **1999**, 70, 1370-1383.
7. Purves, R. W.; Barnett, D. A.; Ells, B.; Guevremont, R. "Investigation of bovine ubiquitin conformers separated by high-field asymmetric waveform ion mobility spectrometry: Cross section measurements using energy-loss experiments with a triple quadrupole mass spectrometer"; *J. Am. Soc. Mass Spectrom.* **2000**, 11, 738-745.
8. Purves, R. W.; Barnett, D. A.; Guevremont, R. "Separation of protein conformers using electrospray-high-field asymmetric waveform ion mobility spectrometry-mass spectrometry"; *Int. J. Mass Spectrom.* **2000**, 197, 163-177.
9. Purves, R. W.; Guevremont, R. "Electrospray ionization high-field asymmetric waveform ion mobility spectrometry-mass spectrometry"; *Anal. Chem.* **1999**, 71, 2346-2357.

10. Purves, R. W.; Day, S.; Pipich, C. W.; Matyjaszczyk, M. S.; Guevremont, R. "Mass spectrometric characterization of a high-field asymmetric waveform ion mobility spectrometer"; *Rev. Sci. Instrum.* **1998**, 69, 4094-4105.
11. McCooeye, M. A.; Ells, B.; Barnett, D. A.; Purves, R. W.; Guevremont, R. "Quantitation of morphine and codeine in human urine using high-field asymmetric waveform ion mobility spectrometry (FAIMS) with mass spectrometric detection"; *J. Anal. Tox.* **2001**, 25, 81-87.
12. Guevremont, R.; Purves, R. W. "High field asymmetric waveform ion mobility spectrometry-mass spectrometry: An investigation of leucine enkephalin ions produced by electrospray ionization"; *J. Am. Soc. Mass Spectrom.* **1999**, 10, 492-501.
13. Ells, B.; Barnett, D. A.; Froese, K.; Purves, R. W.; Hrudey, S.; Guevremont, R. "Detection of chlorinated and brominated byproducts of drinking water disinfection using electrospray ionization-high-field asymmetric waveform ion mobility spectrometry-mass spectrometry"; *Anal. Chem.* **1999**, 71, 4747-4752.
14. Ells, B.; Barnett, D. A.; Purves, R. W.; Guevremont, R. "Detection of nine chlorinated and brominated haloacetic acids at part-per-trillion levels using ESI-FAIMS-MS"; *Anal. Chem.* **2000**, 72, 4555-4559.
15. Barnett, D. A.; Guevremont, R.; Purves, R. W. "Determination of parts-per-trillion levels of chlorate, bromate, and iodate by electrospray ionization/high-field asymmetric waveform ion mobility spectrometry/mass spectrometry"; *Appl. Spectrosc.* **1999**, 53, 1367-1374.
16. Barnett, D. A.; Ells, B.; Purves, R. W.; Guevremont, R. "Separation of leucine and isoleucine by electrospray ionization-high field asymmetric waveform ion mobility spectrometry-mass spectrometry"; *J. Am. Soc. Mass Spectrom.* **1999**, 10, 1279-1284.
17. Barnett, D. A.; Purves, R. W.; Guevremont, R. "Isotope separation using high-field asymmetric waveform ion mobility spectrometry"; *Nuc. Instrum. Meth. Phys. Res. A* **2000**, 450, 179-185.

18. Guevremont, R.; Purves, R. "Apparatus and method for atmospheric pressure 3-dimensional ion trapping"; *Canadian Intellectual Property Office* 1999. Canada. Canadian Patent No. 2,339,548.
19. Guevremont, R.; Purves, R. "Apparatus and method for desolvating and focussing ions for introduction into a mass spectrometer"; *Canadian Intellectual Property Office* 1999. Canada. Canadian Patent No. 2,339,552.
20. Purves, R. W.; Barnett, D. A.; Ells, B.; Guevremont, R. "Elongated conformers of charge states +11 to +15 of bovine ubiquitin studied using ESI-FAIMS-MS"; *J. Am. Soc. Mass Spectrom.* **2001**, 12, 894-901.
21. Purves, R. W.; Barnett, D. A.; Ells, B.; Guevremont, R. "Gas phase conformers of the $[M+2H]^{2+}$ of bradykinin investigated by combining high-field asymmetric waveform ion mobility spectrometry, hydrogen / deuterium exchange, and energy loss measurements"; *Rapid Comm. Mass Spectrom.* **2001**, 15, 1453-1456.
22. Guevremont, R.; Ding, L.; Ells, B.; Barnett, D. A.; Purves, R. W. "Atmospheric pressure ion trapping in a tandem FAIMS-FAIMS coupled to a TOFMS: Studies with electrospray generated Gramicidin S ions"; *J. Am. Soc. Mass Spectrom.* **2001**, 12, 1320-1330.
23. Guevremont, R.; Barnett, D. A.; Purves, R. W.; Vandermeij, J. "Analysis of a tryptic digest of pig hemoglobin using ESI-FAIMS-MS"; *Anal. Chem.* **2000**, 72, 4577-4584.
24. Guevremont, R.; Purves, R. W.; Barnett, D. A.; Ding, L. "Ion trapping at atmospheric pressure (760 Torr) and room temperature with a high-field asymmetric waveform ion mobility spectrometer"; *Int. J. Mass Spectrom.* **1999**, 193, 45-56.
25. Ells, B.; Barnett, D. A.; Purves, R. W.; Guevremont, R. "Trace level determination of perchlorate in water matrices and human urine using ESI-FAIMS-MS"; *J. Environ. Monit.* **2000**, 2, 393-397.
26. Ells, B.; Froese, K.; Hruday, S. E.; Purves, R. W.; Guevremont, R.; Barnett, D. A. "Detection of microcystins using electrospray ionization high-field asymmetric waveform ion mobility mass spectrometry / mass spectrometry"; *Rapid Commun. Mass Spectrom.* **2000**, 14, 1538-1542.

27. Barnett, D. A.; Ding, L.; Ells, B.; Purves, R. W.; Guevremont, R. "Tandem mass spectra of tryptic peptides at signal-to-background ratios approaching unity using electrospray ionization high-field asymmetric waveform ion mobility spectrometry / hybrid quadrupole time-of-flight mass spectrometry"; *Rapid Comm. Mass Spectrom.* **2002**, 16, 676-680.
28. Barnett, D. A.; Purves, R. W.; Ells, B.; Guevremont, R. "Separation of *o*-, *m*- and *p*-phthalic acids by high-field asymmetric waveform ion mobility spectrometry (FAIMS) using mixed carrier gases"; *J. Mass Spectrom.* **2000**, 35, 976-980.
29. Barnett, D. A.; Ells, B.; Guevremont, R.; Purves, R. W.; Viehland, L. A. "Evaluation of carrier gases for use in high-field asymmetric waveform ion mobility spectrometry"; *J. Am. Soc. Mass Spectrom.* **2000**, 11, 1125-1133.
30. Gabryelski, W.; Froese, K.; Hrudey, S. E.; Purves, R.; Guevremont, R. "Rapid and sensitive differentiation of anomers, linkage and position isomers of disaccharides using high-field asymmetric waveform ion mobility spectrometry (FAIMS)."; *49th ASMS Conference on Mass Spectrometry and Allied Topics.*, Chicago, Illinois, May 27-31, 2001.
31. Krylov, E. V. "Pulses of special shapes formed on a capacitive load"; *Instrum. Exp. Tech.* **1997**, 40, 628-631.
32. Barnett, D. A.; Horlick, G. "Quantitative electrospray mass spectrometry of halides and halogenic anions"; *J. Anal. At. Spectrom.* **1997**, 12, 497-501.
33. Barnett, D. A. Ph. D. Thesis, University of Alberta, Edmonton, Alberta, 1999.
34. Corr, J. J.; Anacleto, J. F. "Analysis of inorganic species by capillary electrophoresis - mass spectrometry and ion exchange chromatography - mass spectrometry using an ion spray source"; *Anal. Chem.* **1996**, 68, 2155-2163.

Chapter 7

FAIMS Dome Prototype: Investigations with Aqueous Sampling

7.1 Introduction

Elemental analysis techniques, such as those based on the inductively coupled plasma (ICP) and flame sources, have made trace level determinations of many of the elements possible in a variety of sample matrices. Today, trace element analysis has reached a relative degree of maturity, and atomic absorption, ICP-atomic emission spectroscopy (AES), and ICP-mass spectrometry (MS) instrumentation is common in a wide variety of commercial laboratories. However, as the evidence for distribution of the elements in a system (e.g., the environment) accumulates, it becomes apparent that simply understanding the elemental composition does not provide the complete picture. In other words, the chemical form of an element is very important. For example, inorganic forms of arsenic are highly toxic, whereas many of the organic forms exhibit much lower toxicity [1, 2]. Similar situations result in regards to how beneficial the presence of an element can be. At low concentrations, selenium is an essential nutrient, whereas at higher doses, it becomes toxic, and the degree of toxicity varies with the chemical species [1].

With the need for determining the chemical form or chemical species of an element, a variety of analytical techniques have been developed to achieve this goal. These determinations have been termed “elemental speciation” [1], and are generally carried out utilizing some combination of chromatography with an elemental analysis technique. In most methodologies, the different chemical species are separated by chromatographic means, such as ion chromatography (IC), high-pressure liquid chromatography (HPLC), or capillary electrophoresis (CE). Often, these separations are combined with element-specific detection, such as atomic absorbance, ICP-AES, or ICP-MS. These “hard” ionization sources break the chemical species down into its constituent atoms, allowing for element-specific detection. The information provided by these hyphenated systems is a chromatogram, where the response due to each element monitored is plotted as a function of elution time. By comparing this information to the retention time of known standards, the quantity of these chemical species in a sample can be determined. While using elemental analysis techniques generally provides superior

detection limits, the disadvantage is that information regarding the actual chemical form is lost. As a result, when peaks in the chromatogram are observed at a retention time other than those of the available standards, the species must be identified by other means.

Another type of detection for these separations is the use of electrospray ionization mass spectrometry (ESI-MS). Electrospray ionization is a relatively “soft” means of ionization, where the chemical form of an ion in solution is preserved during its promotion to the gas-phase. As a result, when using ESI-MS as the detection method, additional information about the elemental composition and structure of the actual chemical species can be determined. Unfortunately, this information can come at the expense of higher detection limits, due, in part, to the complex chemical background that may be present in an ESI-MS spectrum. Also, this method is limited to (generally) species that are pre-existing in the solution as ions, and ions with greater surface activity are usually observed to dominate in the mass spectrum [3-5]. Another disadvantage is the difficulty associated with electrospraying purely aqueous matrices, due to the high surface tension of water. As a result, the sample is generally diluted with volatile solvent to make the ESI process more reliable and easier to use.

As described in Chapter 2, an in-house designed ESI source allowed for the use of purely aqueous solvents. Initial studies demonstrated that the signal intensities and stability for the ions tested were comparable to that for a methanol solvent. Such an interface may be useful for speciation analysis, especially where concerns regarding the stability of the analyte in organic solvent are an issue. However, being able to electrospray purely aqueous solvents will not resolve issues regarding the complex spectral background typically observed with ESI-MS. Recently, a technique called high-field asymmetric waveform ion mobility spectrometry (FAIMS) has been developed [6-20]. By combining FAIMS with ESI-MS, several studies have shown that this technique can provide superior detection limits, largely as a result of its ability to dramatically simplify the spectral background [21-37].

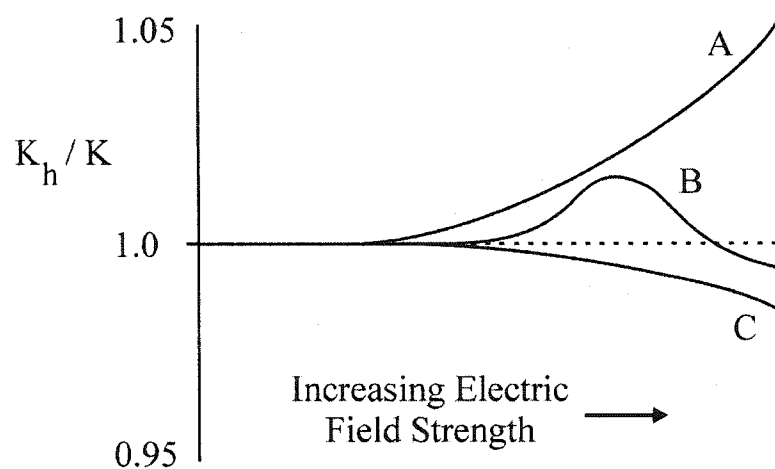
The development FAIMS in the 1980s was based on an ion's changing mobility at atmospheric pressure with high applied field [7, 38]. Under the influence of a low applied field ($E < \sim 200$ V/cm), an ion's mobility is essentially constant, whereas, at higher applied fields, the mobility varies as a function of the field magnitude [39]. Expressing the change in mobility as a ratio of high-field mobility (K_h) to low-field mobility (K), K_h/K , an ion's experimental behavior can be classified as three general types, as shown in Figure 7.01 (a). As the applied field strength increases, an ion's mobility can either increase (type A), decrease (type C), or show a more complex behavior (type B) [19]. Also, ions with similar mobility behavior (i.e., two type A ions) may have a different dependence of their K_h/K in response to a high-applied field, as hypothetically illustrated in Figure 7.01 (b).

The simplest FAIMS apparatus, similar to that described by Buryakov, *et al* [8, 9], is illustrated in Figure 7.02. This FAIMS is composed of two parallel metal plates separated by ~ 0.5 cm, and the ions are introduced between the plates via a flow of a carrier gas. The upper plate is grounded, and to the lower plate an asymmetric waveform is applied. The hypothetical square waveform shown is composed of a low voltage component of long duration, and a high-voltage component of short duration, with an approximate voltage magnitude of 2:1 high:low. The high-voltage peak of short duration is referred to as the dispersion voltage, DV. When the waveform is applied to the lower plate, alternating high and low fields are generated within the plate gap. In this example, a high negative field of short duration follows a low positive field of longer duration. Owing to the symmetry of the waveform, the voltage (V) \cdot time (t) products of the positive and negative portions of each cycle are of equal magnitude and opposite sign, and Equation 7.01 applies.

$$V_{\text{low}}t_{\text{low}} = -V_{\text{high}}t_{\text{high}} \quad 7.01$$

Owing to the uniform fields generated within parallel plates, the field (E) \cdot time (t) products are also equal and opposite (Equation 7.02).

(a)



(b)

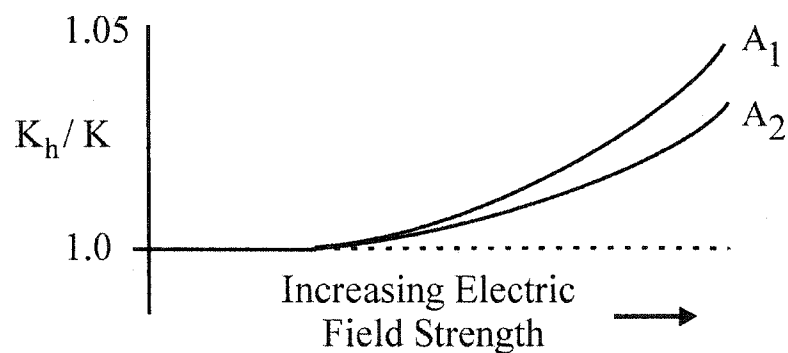


Figure 7.01 Ion mobility behavior (K_h/K) in response to increasing applied electric field strength. K_h = high field mobility. K = low field mobility. (a) General mobility behaviors; type A = increasing mobility with increasing applied field. Type B = complex mobility dependence with applied field; initially increasing, then decreasing with higher applied field. Type C = decreasing mobility with increasing applied field; (b) Two different hypothetical ions with type A mobility, A_1 and A_2 .

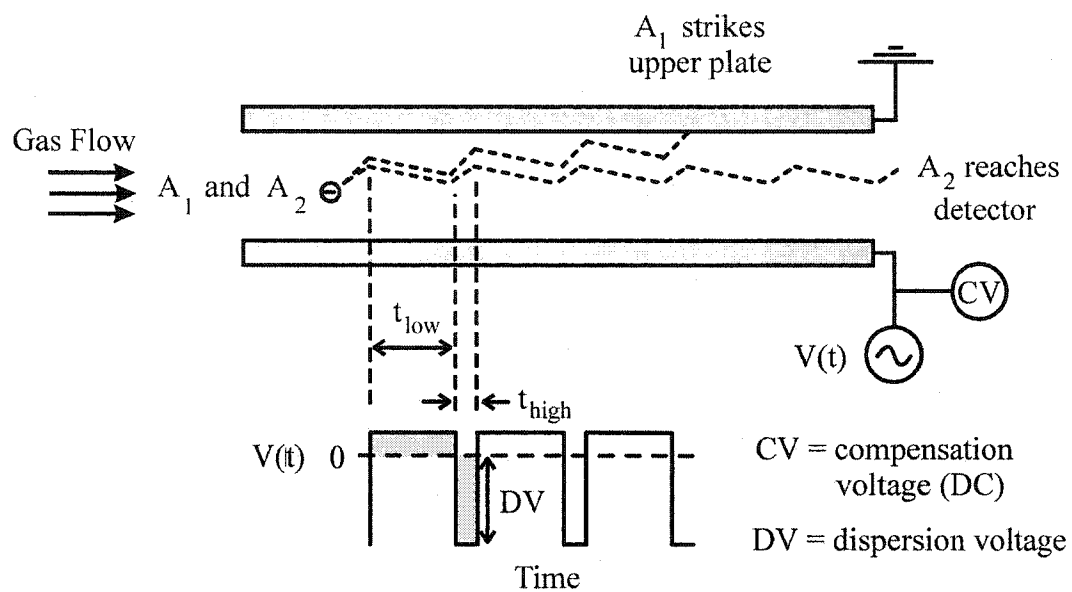


Figure 7.02 Schematic diagram of a parallel plate FAIMS analyzer region, with the application of an asymmetric waveform to the lower plate. DC potential (i.e., the compensation voltage, CV) set to transmit the A_2 ion.

$$E_{\text{low}}t_{\text{low}} = -E_{\text{high}}t_{\text{high}} \quad 7.02$$

The velocity of an ion due to an applied field (v_{drift}) can be described using Equation 7.03.

$$v_{\text{drift}} = KE \quad 7.03$$

Also, using d (distance) = vt , the Equations 7.04 and 7.05 can be derived.

$$d_{\text{low}} = KE_{\text{low}}t_{\text{low}} \quad 7.04$$

$$d_{\text{high}} = K_{\text{h}}E_{\text{high}}t_{\text{high}} \quad 7.05$$

Since the field · time products are equal, any differences in magnitude of the distance traveled will be proportional to the ion mobility ratio within the applied fields. This can be further expressed as Equation 7.06.

$$d_{\text{high}} / d_{\text{low}} = K_{\text{h}} / K \quad 7.06$$

Note that the relation $d_{\text{high}}/d_{\text{low}}$ depends on the magnitude of the applied fields, since $K_{\text{h}} = f(E_{\text{high}})$. Consider two different negative ions, A_1 and A_2 , which are located between the two plates, and have mobilities as described by the curves in Figure 7.01 (b). Since A_1 has a K_{h}/K greater than A_2 at the same applied field, the $d_{\text{high}}/d_{\text{low}}$ for A_1 will be greater, in accordance with Equation 7.06. Since the applied DV is negative, a negative type A ion will move towards the upper plate when the DV is applied, and towards the lower plate during the low-field positive portion of the waveform. So, for every cycle of the waveform, A_1 will have a greater net displacement to the upper plate than A_2 . In the absence of any other applied fields, both ions would eventually strike the upper plate. However, if a small direct current (dc) potential of polarity opposite to the ion's net charge is applied (in this case a positive voltage will be applied for a negative ion), a balance condition may result, and the ion experiences no net drift towards either plate.

This dc potential is called the compensation voltage (CV). In the example in Figure 7.02, the DV and CV are set to balance the drift of the A_2 ion, so A_1 strikes the upper plate and A_2 is transported by the carrier gas to the detector at the other side. The applied CV may be scanned, sequentially transmitting ions with different K_h/K ratios, or the CV may be held at a particular value to continuously transmit a particular bandpass of ions. If the applied CV is scanned, the FAIMS sequentially transmits ions with different K_h/K ratios, generating a spectrum (signal vs. applied CV), where the applied CV determines the bandpass of K_h/K ions that reaches the detector (at a given DV amplitude). A hypothetical illustration of a CV spectrum is presented in Figure 7.03. The lower K_h/K ion (i.e., A_2) is transmitted to the detector at a lower CV = V_1 , and the higher K_h/K ion (i.e., A_1) is transmitted at the higher CV = V_2 .

Since FAIMS separates ions based on their difference in K_h/K , factors affecting the mobility of the ion are important for tuning a separation. In particular, previous work has demonstrated that changing the drift gas composition is an effective way to control the separation of ions within the FAIMS [26, 28, 29, 33, 40]. The curves in Figure 7.04 illustrate how the K_h/K of an ion may be affected by using a different drift gas composition. In this hypothetical example, the same ion exhibits variable K_h/K behavior in drift gas types X, Y, and Z. The K_h/K response is a type A behavior in gases X and Y, but exhibits type C behavior in gas Z. These types of changes in mobility with varying drift gas composition within the FAIMS have been described, even with monatomic ions [40].

Since the initial description of parallel plate FAIMS, two different electrode geometry variants have been described, both of which are based on the use of concentric cylinder electrodes [10, 12, 14, 19, 20]. Early in the development of the concentric cylinder FAIMS prototype, concerns regarding water in the drift gas were discussed [12, 19]. Specifically, water was observed to have significant effects on the sensitivity of the system. A likely reason for this is related to the ability of the FAIMS to filter out ions that do not have a balanced trajectory under the applied field conditions. If the gas-phase ion normally has a mobility like the ion A_1 in Figure 7.01 (b), the balance of DV and CV

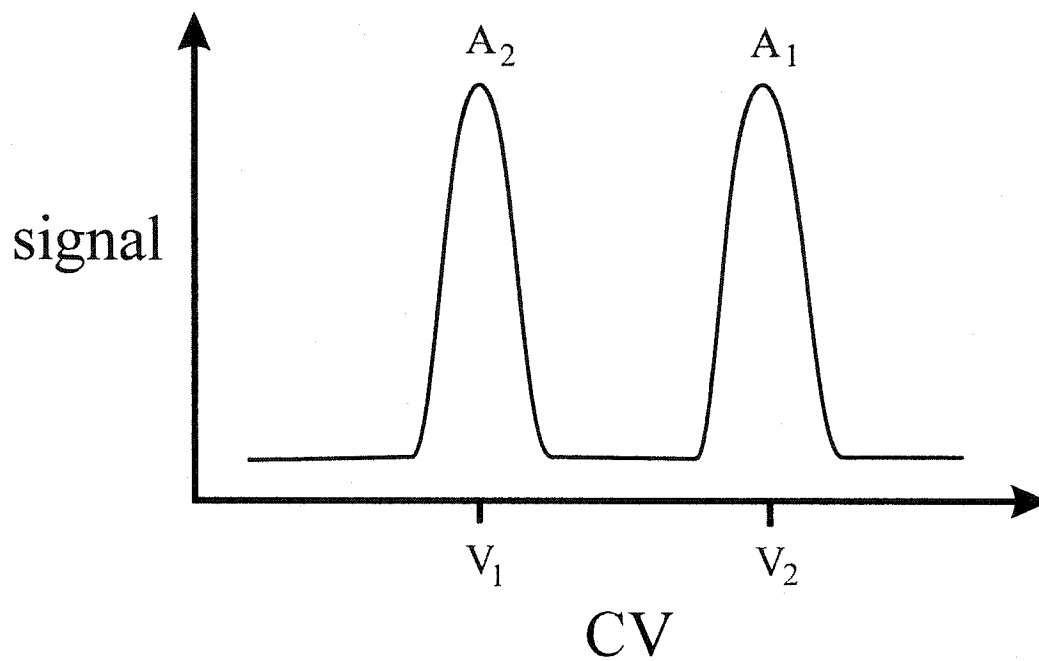


Figure 7.03 Hypothetical CV spectrum of negative ions A_1 and A_2 using the N1-P2 waveform, with hypothetical K_h/K mobility as illustrated in Figure 7.01 (b).

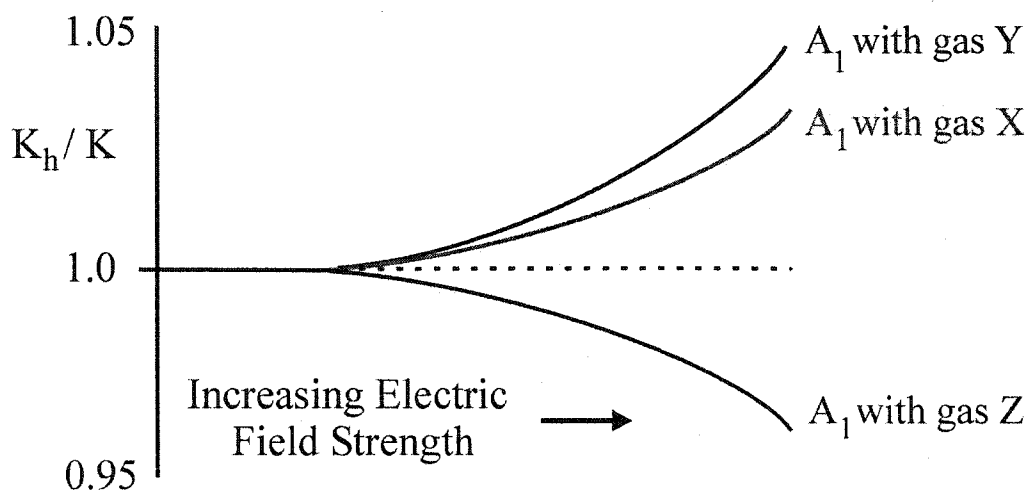


Figure 7.04 Theoretical variation of ion mobility in response to increasing electric field strength. The same ion, A₁, in three different drift gas compositions, X, Y and Z.

to transmit this ion will be different than for ion A_2 . If water in the drift gas forms an adduct with the analyte ion in the FAIMS analyzer region, it is conceivable that the mobility of this new species may be more like the A_2 K_h/K behavior. Since the settings of DV and CV to transmit A_1 and A_2 are different, an alteration in the gas-phase species during a FAIMS experiment may result in the ion being filtered out. So, it is important that the gas-phase ion has a stable K_h/K behavior in response to the applied fields within the FAIMS.

Owing to these concerns regarding water, it was unclear whether or not our in-house designed aqueous ESI source could be applied to an ESI-FAIMS-MS experiment. To test this configuration, the in-house designed ESI source was used to electrospray purely aqueous samples into the FAIMS-MS interface, and the results were compared to the performance of a typical ESI source using methanol solvent. The performance was studied in negative ion mode using some negatively charged arsenic and selenium compounds. A detailed speciation of the gas-phase species of selenite and arsenite was done, and highlights how this interface may offer a significant improvement for elemental speciation, as compared to ESI-MS alone.

7.2 Experimental

7.2.1 ESI-FAIMS-MS

The work presented in the following sections was done using a dome interface as designed by Guevremont, and manufactured by Sciex (Concord, ON, Canada) [13, 15, 16]. A detailed description of this interface is found in Chapter 4. The MS used was an API-150EX from MDS-Sciex (Concord, Ontario, Canada), and is a single quadrupole instrument with a mass range of 30 - 3000 m/z. Ions sampled into the MS could be declustered or fragmented by collision-induced dissociation (CID) in the MS interface region by applying a potential difference between the orifice (OR) and the skimmer (SK). Coupling of the FAIMS to this system was fairly straightforward. First, the normal

electrospray (ES) ion source and curtain plate were removed (a single unit), and the interlocks were defeated in order to operate without this source attached. Also, the curtain gas supply was cut off, but valve pressure was maintained to keep the interlocks active. Two holes were drilled into the orifice plate of the spectrometer, and a mounting ring was attached. The inner diameter of the mounting ring was designed to match the outer diameter of the outer FAIMS electrode. Once the mounting ring was in place, the FAIMS was simply pushed into this hole, as illustrated in Figure 7.05. No further securing of the FAIMS to the MS was used. The thickness of the mounting ring was designed to let the flat face of the FAIMS outer electrode to be placed flush against the flat orifice of the MS. The contact between the outer FAIMS cylinder and the MS sampling orifice (OR) means that both of these parts will be biased to the same potential. An external power supply (Xantrex XT-120-0.5 Regulated DC Power Supply) was used to set this voltage, instead of using the MS power supply to do so. In this configuration, the outer FAIMS electrode and the orifice were manually set to a constant voltage (F_{OR}). For experiments described in this chapter, the MS orifice plate and the outer FAIMS electrode were biased to 0 V ($F_{OR} = 0$ V), unless otherwise noted. Under these sampling conditions, there was no potential difference between the sampling orifice and the skimmer, and the relative degree of declustering and fragmentation of ions in the MS interface was minimized. The MS power connection (formerly for the orifice) was re-routed to the waveform generator to act as the compensation voltage power supply. By routing the former orifice power connection to the CV input of the waveform generator, the CV could be scanned by using the existing computer software. By putting an additional power supply (Xantrex XT-120-0.5 Regulated DC Power Supply) in series with the MS and the generator CV input, an additional voltage offset could be added. Since the software only allows the computer-set voltage polarity to match the polarity of the MS scan, this offset becomes necessary when opposite CV polarity was required. Both the DV and the CV were combined in the final waveform, and this was applied to the inner cylinder through a bolt at one end of the FAIMS interface. Under negative mode operation, the MS would only allow voltage settings of negative polarity. For example, the waveform generator CV was offset by 80 V ($CV_{off} = 80$ V), and scanning the MS voltage (formerly the OR supply) from -80 to 0 V allowed the net applied CV to be

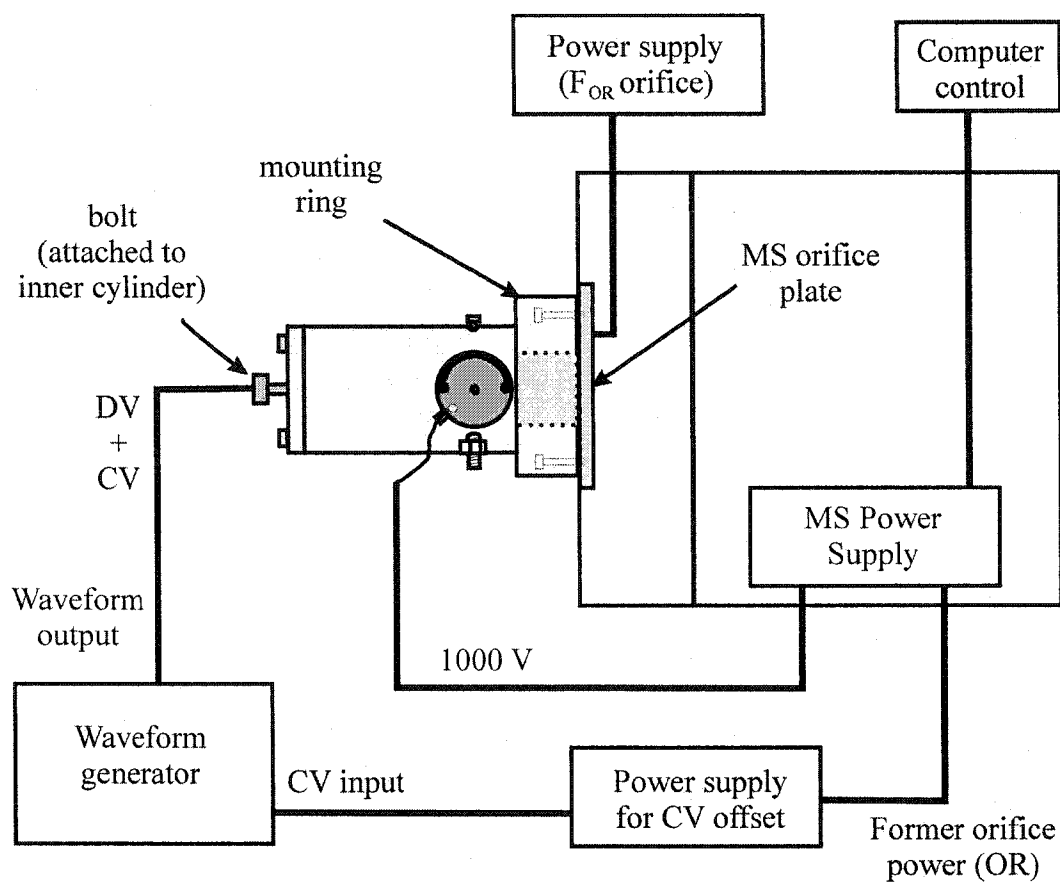


Figure 7.05 Electrical connections for the FAIMS-MS interface.

scanned from 0 to 80 V. Also, a -1kV bias was applied to the FAIMS curtain plate using the MS power supply.

A pair of rotamers (Gilmont Instruments, 0 – 5 SLPM Air) were used to set the curtain gas flow rate. Previous tests were done to calibrate these meters for N₂, CO₂, and Ar. Downstream of the flow meter, gas purifiers consisting of a combination of activated charcoal and a molecular sieve were used. Unless otherwise specified, the flow of the curtain gas was 2.0 L/min.

Figure 7.06 illustrates how an ion may be sampled during a FAIMS experiment using the dome prototype. The curtain gas was introduced to the FAIMS between the curtain plate and the sampling orifice in the wall of the outer cylinder. The ESI generated ions are moved towards the sampling orifice of the FAIMS by the potential difference, and undergo typical droplet fissions and desolvation during the trip to the orifice. The bulk of the curtain gas exits the FAIMS through the curtain plate orifice and assists in the desolvation of the ESI-generated ions. The remainder of the curtain gas comprises the drift gas for the FAIMS experiment. Since the MS orifice is constantly sampling gas (at about 0.56 L/min for this system), gas is drawn from the curtain gas inlet region and into the FAIMS analyzer region. So, as ions enter the FAIMS analyzer region, they are transported by the gas towards the MS orifice. If the combination of DV and CV are appropriate, the ion will not strike a wall and will be successfully transported by the gas flow to the MS orifice. Note that for these tests, the pressure port was closed off, and there was no gas flow through this opening.

7.2.2 Asymmetric Waveform

The waveform generator used for the following studies was built by Sciex, and a more detailed description can be found in Chapter 4. The waveform generator was powered using an external power supply (GW Laboratory Power Supply Model GPC-3030D Dual Tracking with 5V Fixed). The frequency of the asymmetric waveform was 750 kHz, and the symmetry and voltages were measured using a LeCroy 9310M Dual

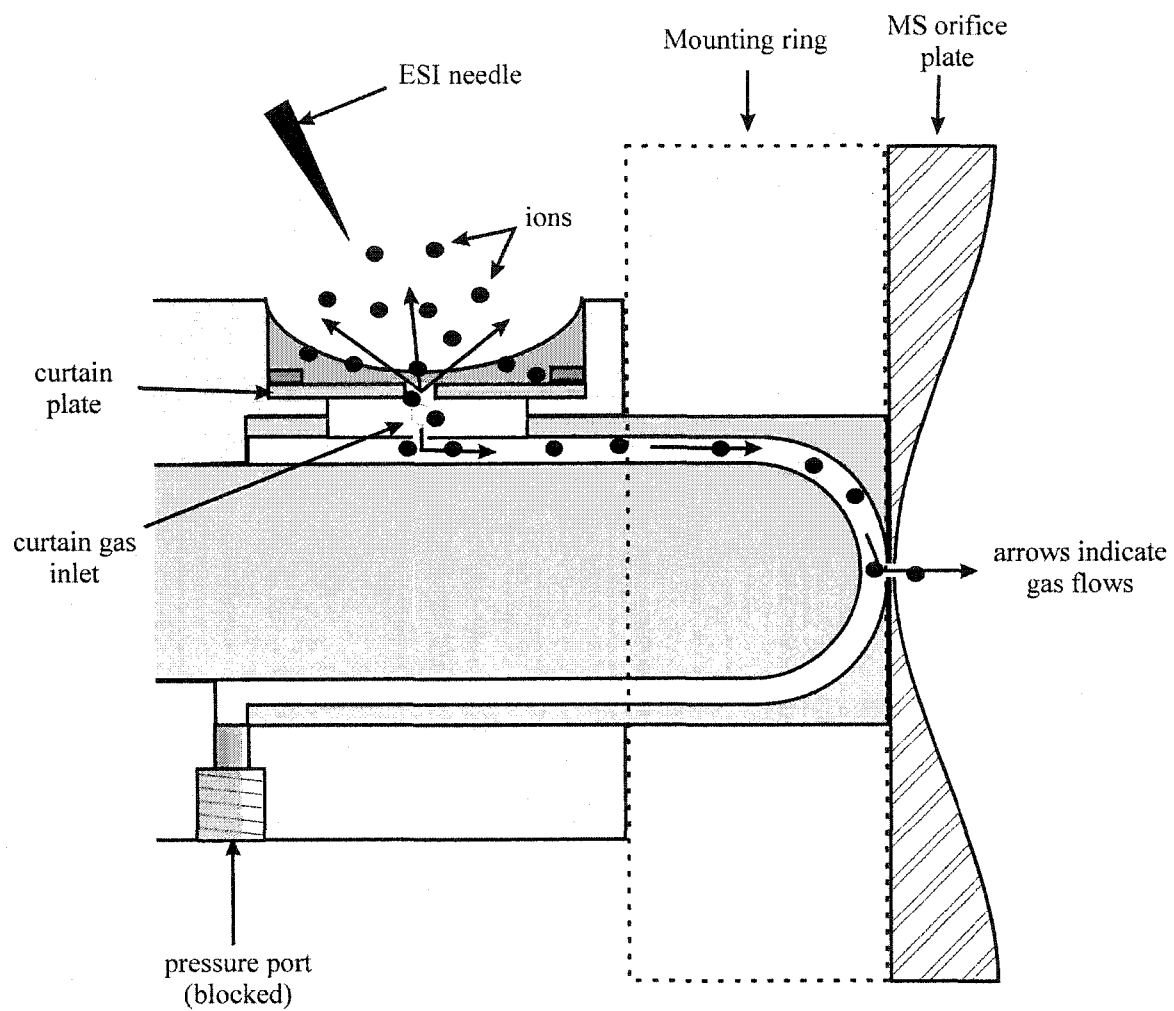


Figure 7.06 Cross-section of an ESI-FAIMS-MS interface.

300 MHz Oscilloscope (100 Ms/s, 50 kpts/ch). Unless otherwise specified, the magnitude of the DV was set to -3.5 kV. The CV was scanned using the MS software (i.e., the OR voltage), and was scanned in steps of 0.2 V over the desired voltage range (unless otherwise specified). The asymmetric waveform that was used for this study is a combination of two sine waves. One wave had a frequency of 1500 kHz, and the other a frequency of 750 kHz, with the 1500 kHz sine wave having an amplitude that was 1/2 the amplitude of the 750 kHz wave, as illustrated in Figure 7.07 (a). If these two sine waves are phase-shifted by 90° , the combination of these waves produces the waveform used for this FAIMS study. The waveform required for small anions, called the N1-P2 waveform [19], is illustrated in Figure 7.07 (b). The amplitude of the high voltage peak is referred to as the dispersion voltage (DV).

7.2.3 ESI Sources

The ESI sources used in this study were designed in-house. For the methanol solvent studies, the ESI source consisted of a fused silica capillary (150 μm OD, 50 μm ID) of about 45 cm length, with one end extending from a stainless steel capillary sheath (0.018" OD, 0.009" ID), as illustrated in Figure 7.08 (a). The extension of the FSC tip from the tip of the metal capillary was adjusted to provide a stable ESI operation. The tip was placed about 1 cm away from the curtain plate of the FAIMS, and was at an angle of about 45° . An in-house built floating digital ammeter with nanoampere sensitivity was placed in-line with the power supply and the tip. Both the magnitude and stability of the electrospray current was used to fine-tune the electrospray conditions. To generate ions, a power supply was used to bias the metal capillary to a voltage of about -3 kV in negative ion mode, drawing a current of about 50 nA during stable ESI operation. From the other end of the capillary, the sample solution was delivered at about 50 $\mu\text{L/hr}$ using a Cole-Parmer 74900 Series syringe pump and a Hamilton 250 μL syringe.

The electrospray interface used for purely aqueous sample matrices is shown in Figure 7.08 (b). A syringe pump and a 250 μL syringe with a stainless steel needle were used to deliver solution through a fused silica capillary with approximate dimensions of

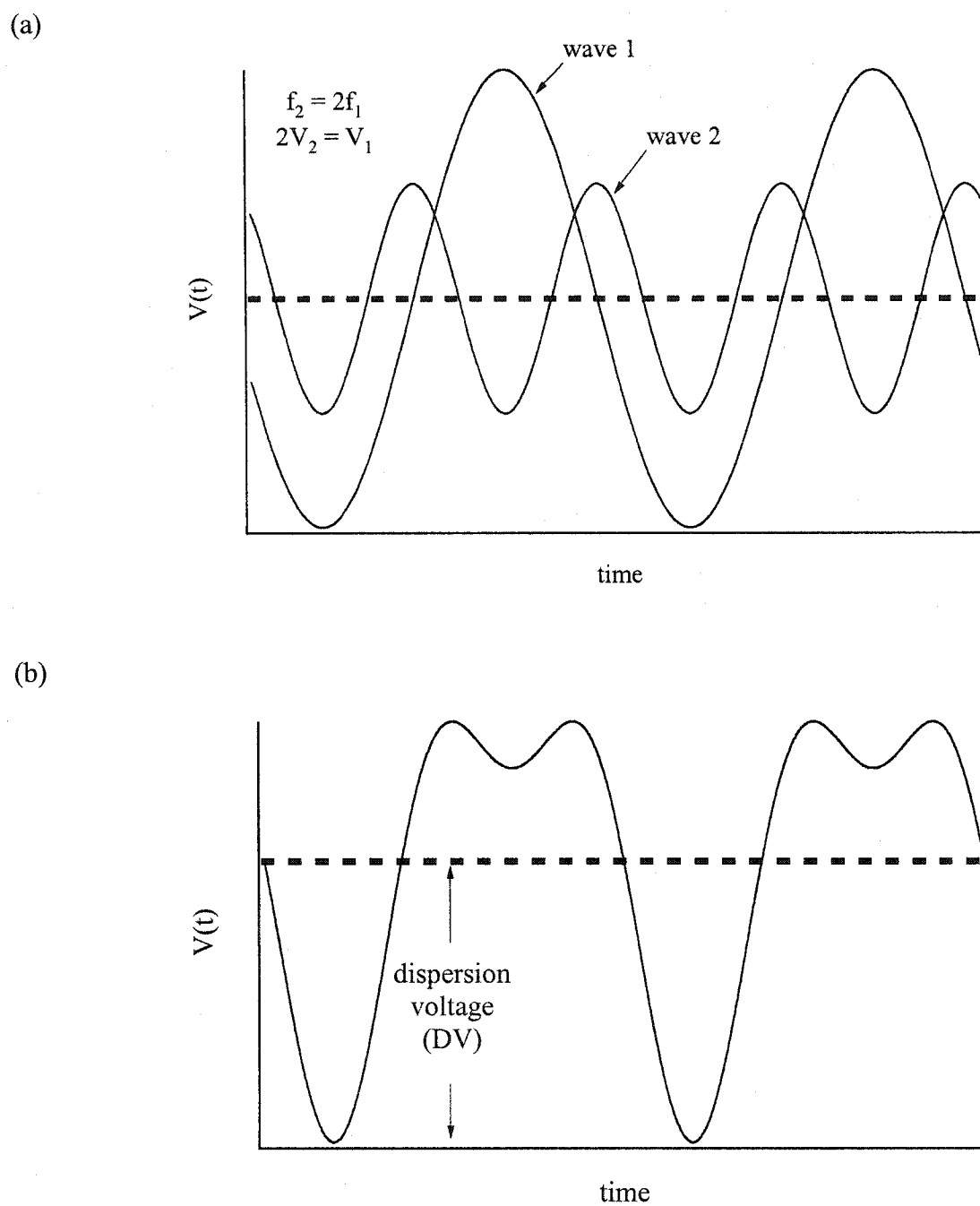


Figure 7.07 (a) Two composite sine waves that are combined to form (b) the N1-P2 asymmetric waveform for FAIMS operation.

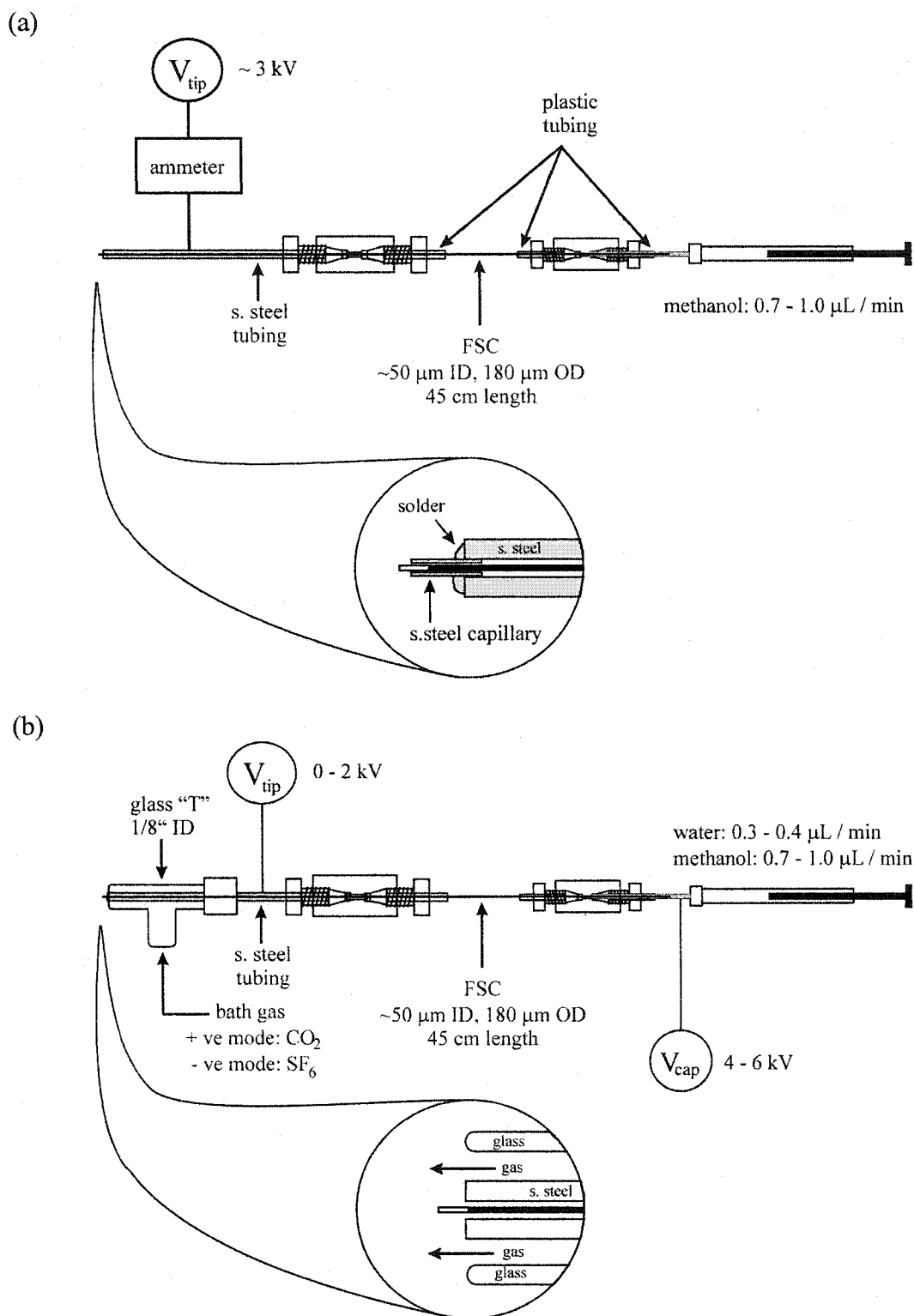


Figure 7.08 Two ESI interfaces; (a) typical interface for methanolic solvents, (b) interface for ESI of purely aqueous solvents.

50 μm ID, 180 μm OD, and 45 cm in length. The fused silica capillary was a continuous piece that began from inside the syringe needle and terminated as the ES tip. The polyimide coating was removed from the tip to remove any rough edges due to the coating, and the fused silica capillary was positioned to extend about 2 mm from the stainless steel support tubing. The only electrical contact with the solution was at the syringe. An ammeter with nanoampere sensitivity was added in series with the power supply and the needle contact in order to monitor the current. A second voltage applied to the stainless steel tubing near the tip enhanced sensitivity and stability. Glass tubing (1/8" ID) surrounded the stainless steel support and delivered a bath gas to enshroud the electrospray tip. Using this system, purely aqueous matrices could be reliably electrosprayed, without the help of pneumatic nebulization. For aqueous ESI operation in negative mode, typical parameters were about 18 $\mu\text{L/hr}$ solution flow rate, -4 to -6 kV at the syringe needle, and -1 kV at the tip support. The bath gas used was sulfur hexafluoride, SF_6 , at a flow rate of ~ 0.8 L/min.

7.2.4 Reagents

Standard solutions were prepared from the appropriate salt at a concentration of 0.01 M in 18 M Ω de-ionized water. Samples were prepared from dilutions of these standard solutions in the appropriate solvent, either methanol or de-ionized water. HPLC grade methanol (Fisher) was used as received. Reagent grade salts of Na_2SeO_4 , $\text{Na}_2\text{SeO}_3 \cdot 5\text{H}_2\text{O}$, $\text{Na}_2\text{HAsO}_4 \cdot 7\text{H}_2\text{O}$, and NaAsO_2 were used. Seleno-DL-methionine (Sigma) was prepared at a stock concentration of 1 mM in de-ionized water. Standard solutions were stored at 4 $^\circ\text{C}$, and the sample dilutions were made fresh as required.

7.3 Results and Discussion

Due to its ion-filtering action, FAIMS can provide mass spectra with very low levels of background ions in the low-mass region when using mild MS sampling conditions [27, 29-37]. The combination of mild MS sampling conditions, low spectral

background, and the potential for separation of different gas-phase species (especially with changing the drift gas composition) makes the FAIMS an excellent tool for evaluating the performance of an aqueous ESI system.

7.3.1 Performance Characteristics of the Aqueous ESI Source

To demonstrate the performance of both the classic ESI source and the aqueous ESI source, solutions with two different solvent compositions were prepared. One solution was purely aqueous, and the other was 95% methanol (5% water). Sodium selenate (Na_2SeO_4) stock solution was diluted to a final concentration of $1\ \mu\text{M}$ in the appropriate solvent, with $0.4\ \text{mM}$ ammonium acetate as an electrospray stabilizer. Previous studies [41] have demonstrated that selenate is observed as the biselenate ion (HSeO_4^-) and acetate as CH_3COO^- in ESI-MS spectra. Masses 145 and 143, corresponding to two of the major masses of HSeO_4^- were monitored, along with $m/z\ 59$, for the acetate ion, CH_3COO^- . The DV was set to $-3.5\ \text{kV}$, and the CV was scanned from 0 to 50 V as the mentioned masses were monitored in peak hopping mode to generate mass-selected compensation voltage (CV) spectra. CV spectra were acquired for each of the solutions using drift gas compositions of N_2 , $\sim 10\%$ Ar (balance N_2), $\sim 5\%$ CO_2 (balance N_2), and $\sim 10\%$ CO_2 (balance N_2). As an example, superimposed mass-selected CV spectra in N_2 drift gas of selenate and acetate in 100% aqueous solvent are presented in Figure 7.09 (a). The biselenate was transmitted to the MS at a $\text{CV} = 21.6\ \text{V}$, and the acetate at a $\text{CV} = 36.8\ \text{V}$. Clearly, the biselenate can be separated from the acetate ion in the gas phase and atmospheric pressure, prior to introduction to the MS. By setting the CV to a constant value of $21.6\ \text{V}$, the HSeO_4^- ion is continuously transmitted to the MS, while the acetate ion is filtered out and is not sampled by the MS. The MS spectrum at $\text{CV} = 21.6\ \text{V}$ is shown in Figure 7.09 (b), and the Se isotope pattern of the HSeO_4^- is clearly observed. The CV of the major Se species (HSeO_4^-) was determined in each drift gas composition, and the data are presented in Table 7.01. As the drift gas was varied, the observed CV was similar with either water or methanol solvent. Note that the step size of the CV scan was $0.2\ \text{V}$, and the observed peak CVs were within $0.2\ \text{V}$ in either solvent for a particular drift gas composition. The similarities of the CVs for a particular

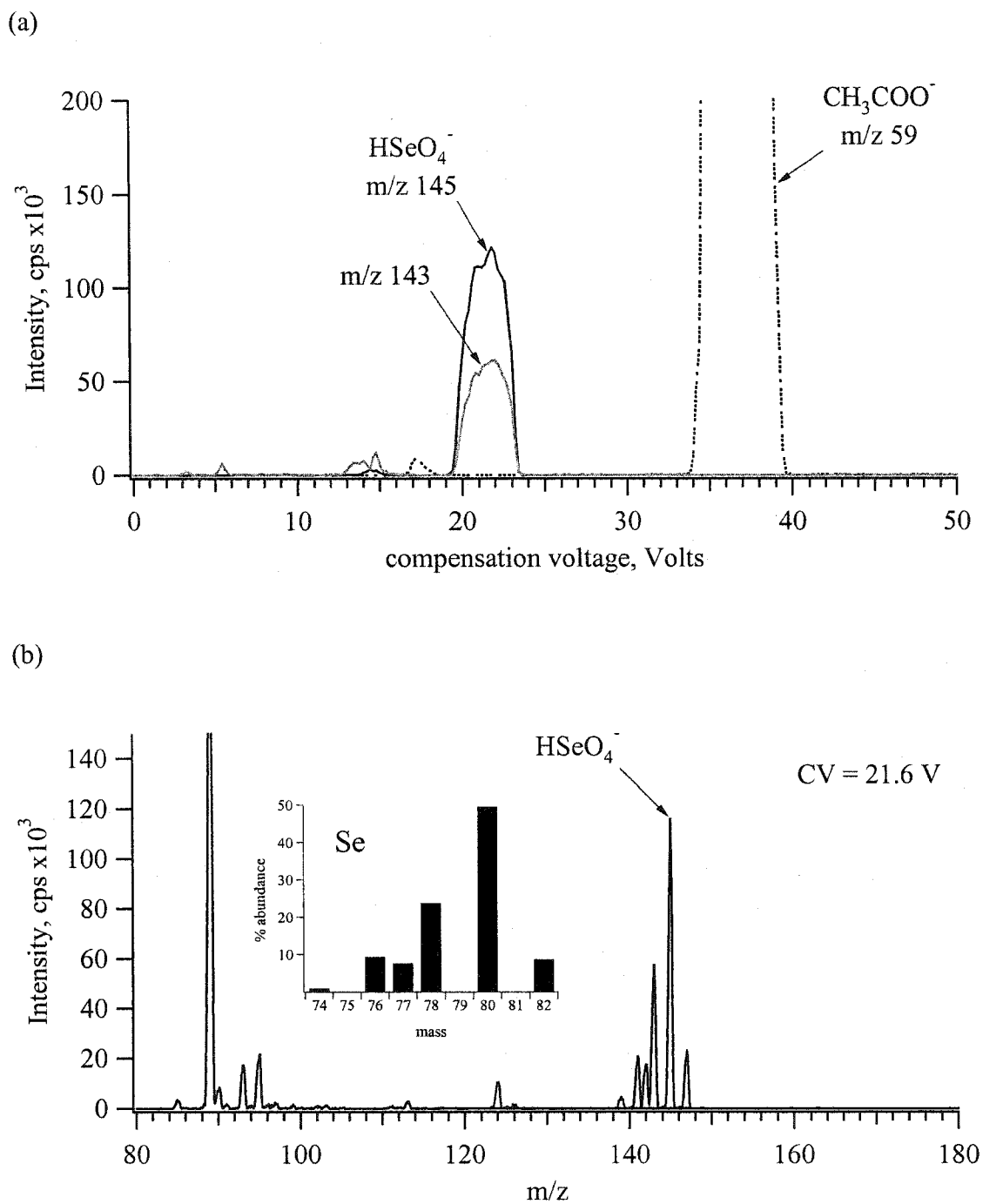


Figure 7.09 (a) Superimposed mass-selected CV spectra (m/z 59, 143, and 145) in N_2 drift gas of a solution containing Na_2SeO_4 at $1 \mu\text{M}$ with 0.4 mM ammonium acetate in 100 % water solvent. $\text{DV} = -3.5 \text{ kV}$, $\text{F}_{\text{OR}} = 0 \text{ V}$; (b) Mass spectrum of the same solution at $\text{CV} = 21.6 \text{ V}$.

Sample Solvent	Observed Ion CV @ m/z 145 in Various Drift Gases (Volts)			
	N ₂	10% Ar, 90% N ₂	5% CO ₂ , 95% N ₂	10% CO ₂ , 90% N ₂
Water	21.6	22.6	24.2	26.4
95% Methanol	21.8	22.4	24.4	26.4

Table 7.01 Observed CV (at DV = -3.5 kV) for the HSeO₄⁻ ion in various drift gases with different sample solvents.

drift gas composition suggest that the major atmospheric pressure gas-phase species (within the FAIMS) is the same with either solvent. While this data is not really conclusive (it is possible that different species may have the same CV), the lack of any variation in CV difference with varied drift gas composition strongly suggests that these are indeed the same.

To check the stability of these signals in N₂ drift gas, the CV was set to a constant value (21.6 V for water, 21.8 V for 95% methanol), and the signals at m/z 143 and 145 were monitored for 300 replicate readings, using a 100 msec dwell time and a 50 msec pause time. The intensity and stability results at each mass are presented in Table 7.02 for both solvent systems. The signal intensity when using the 100% aqueous solvent was about 50% of the methanolic solvent, although the signal stability was about the same in either solvent, at about 3% RSD. So, while the signal stability of each system was similar, there is some sacrifice in signal intensity with the water system. The very different physical configurations and different orientations of the tip near the FAIMS sampling orifice may have some effects. Since the aqueous ESI sprayer requires a bath gas for normal operation, the tip had to be positioned further away from the FAIMS orifice, to prevent the curtain gas from diluting the bath gas. Other possibilities for the lower signal intensity with the aqueous interface are that the ionization efficiency of the aqueous system may not be as good as with methanol, and perhaps some differences are observed due to filtering out of solvated species that lose their solvation during FAIMS operation.

7.3.2 Speciation of Selenite in Methanol Solvent

With the selenate work just presented, the performance of the aqueous ESI source was demonstrated to have comparable stability as compared to a classic ESI source using a methanolic solvent, with some compromise in signal intensity. However, certain analytical situations may arise in which an aqueous solvent may be advantageous, making the compromise in signal intensity an acceptable loss. One such possibility is when the ion originally present in the aqueous matrix reacts with the added organic

Sample Solvent	Average Intensity @ masses 145 / 143 (cps)	% RSD @ masses 145 / 143
Water	115,000 / 57,700	2.82 / 3.01
95 % Methanol	230,000 / 114,000	3.08 / 3.23

Table 7.02 Average signal intensity and stability for the HSeO_4^- ion in ESI-FAIMS-MS. DV = -3.5 kV, $F_{\text{OR}} = 0\text{V}$, N_2 drift gas.

solvent. This can make determination of the solution species complicated, unless the identity and chemistry of the original species is already known. An example of this kind of situation is the determination of the selenite ion, SeO_3^{2-} [41].

Previous measurements by ESI-MS have shown that when Na_2SeO_3 is diluted in methanolic solvent a complex mass spectrum is observed containing several selenium species, with the major species being the seleno-ester ion, $\text{SeO}_2(\text{OCH}_3)^-$ [41]. It is possible to clarify the composition of this solution utilizing ESI-FAIMS-MS. Based on the previous ESI-MS work, several different masses were monitored in an attempt to observe selected species in the mass-selected CV spectrum. The CV was then set to acquire mass spectra of the individual peaks in the mass-selected CV spectrum. For the more intense CV peaks, only single MS scans were acquired, whereas either 5 or 10 scans were acquired and averaged for the lower intensity peaks. The observed mass-selected CV spectra (N_2 drift gas) at certain selected masses (m/z 128 (SeO_3^-), 129 (HSeO_3^-), 143 ($\text{SeO}_2(\text{OCH}_3)^-$), 147 (?), 158, and 171 (unknown Se species) are shown in Figure 7.10. These masses were selected based on prior ESI-MS and ESI-FAIMS-MS work. The spectrum in Figure 7.10 (a) shows the major species, $\text{SeO}_2(\text{OCH}_3)^-$ with a peak intensity at a CV of 23.2 V, and an unknown species at m/z 147 with a peak CV of 22.4 V. Figure 7.10 (b) shows the same CV spectrum with several different m/z displayed. The different CVs of the Se species (indicated by arrows in the mass-selected CV spectra) demonstrate that these are different gas-phase species within the FAIMS, as opposed to species generated by CID in the MS interface. Mass spectra at several different CV values were acquired. Points in the mass-selected CV scan where Se species were identified are shown in Figure 7.10. Note that mass spectra were collected for all the peaks observed in the resultant mass-selected CV spectra, and a Se isotope pattern was only observed at a few values of CV. Also, the mass-selected CV scans were acquired for several different m/z (not shown), corresponding to several different proposed Se species, and those peaks were also examined for a Se isotope in the mass spectrum.

The mass spectra of the Se species identified are presented in Figures 7.11 – 7.14. Figure 7.11 is the mass spectrum of the major species, $\text{SeO}_2(\text{OCH}_3)^-$. Figure 7.11 (a) is the spectrum at the CV peak maximum for the m/z 147 peak, $\text{CV} = 23.2$ V, and a species partially obscuring the Se isotope of $\text{SeO}_2(\text{OCH}_3)^-$ is observed. By sampling at a slightly higher CV value, $\text{CV} = 24.2$ V, the major species can be observed without overlap, as shown by the spectrum in Figure 7.11 (b). In the mass-selected CV spectra, peaks identified as HSeO_3^- and SeO_3^- are partially separated under these test conditions (Figure 7.10 (b)). The CV can be set such that the mass-selected CV peak can be continuously sampled without interference from the adjacent peak. Figure 7.12 (a) shows the mass spectrum at $\text{CV} = 25.8$ V, and Figure 7.12 (b) the mass spectrum at $\text{CV} = 29.4$ V. In each case, the mass spectra were acquired at a CV other than the peak transmission of the species. The HSeO_3^- spectrum (Figure 7.12 (a)) is also free from $\text{SeO}_2(\text{OCH}_3)^-$, which also partially overlaps the mass-selected CV trace for HSeO_3^- . This is a good example of how the FAIMS can be tuned to transmit one ion while filtering out the other, even though the CV peaks do not appear to be well separated. In other words, full mass-selected CV peak separation is not required in order to get selective transmission to the mass spectrometer, and the selected species can be transmitted to the MS in a continuous fashion.

Mass spectra of the other species indicated in the CV spectrum are presented in Figures 7.13 and 7.14. In all of these spectra, 10 scans were averaged. This was done to counteract the random fluctuations of the ESI source so that the isotope pattern of the Se species could be distinguished at low intensity. A Se species at m/z 158, tentatively identified as $\text{SeO}(\text{OCH}_3)_2^-$ (Figure 7.13 (a)), was observed with an average intensity of about 3500 cps at the major isotope. Even with such a low intensity signal, the isotopic pattern of Se is clearly visible. A signal of similar intensity was observed for a Se species at m/z 171 tentatively identified as $\text{SeO}_2(\text{OOCCH}_3)^-$, with an average signal intensity of about 1500 cps (Figure 7.13 (b)). Selenium species with even lower signals were observed, as presented in Figure 7.14. These species were not part of the original mass-selected CV scans, but were found when examining the numerous peaks of the mass-selected CV scans at other m/z . At $\text{CV} = 8.8$ V, a Se species at m/z 201 was observed

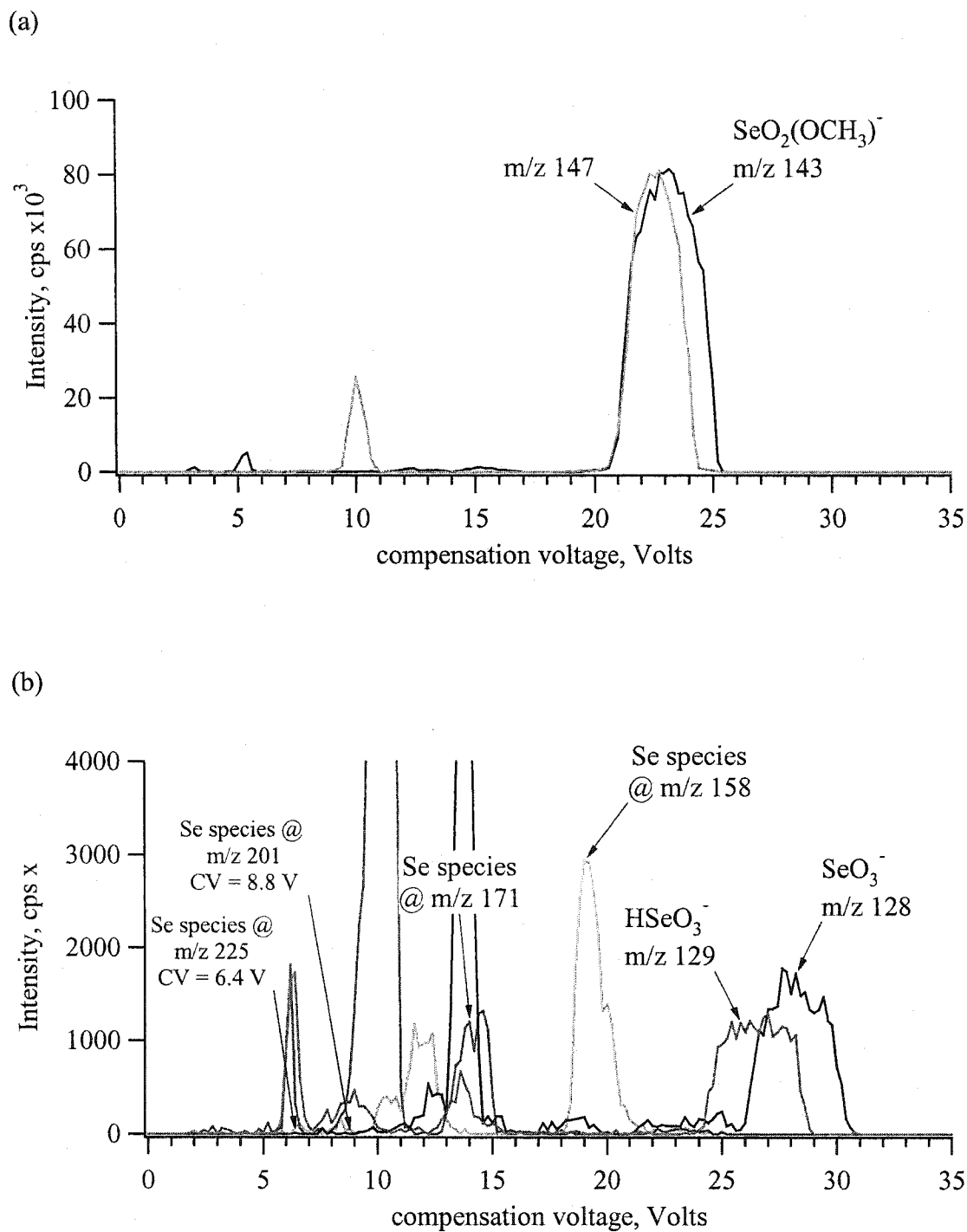


Figure 7.10 Superimposed mass-selected CV spectra in N_2 drift gas of a solution containing $1 \mu M Na_2SeO_3$ with $0.4 mM$ ammonium acetate in 95% methanol, 5% water. (a) m/z 143 and 147; (b) m/z 128, 129, 158, and 171. Se species at m/z 201 and 225 identified (traces not shown).

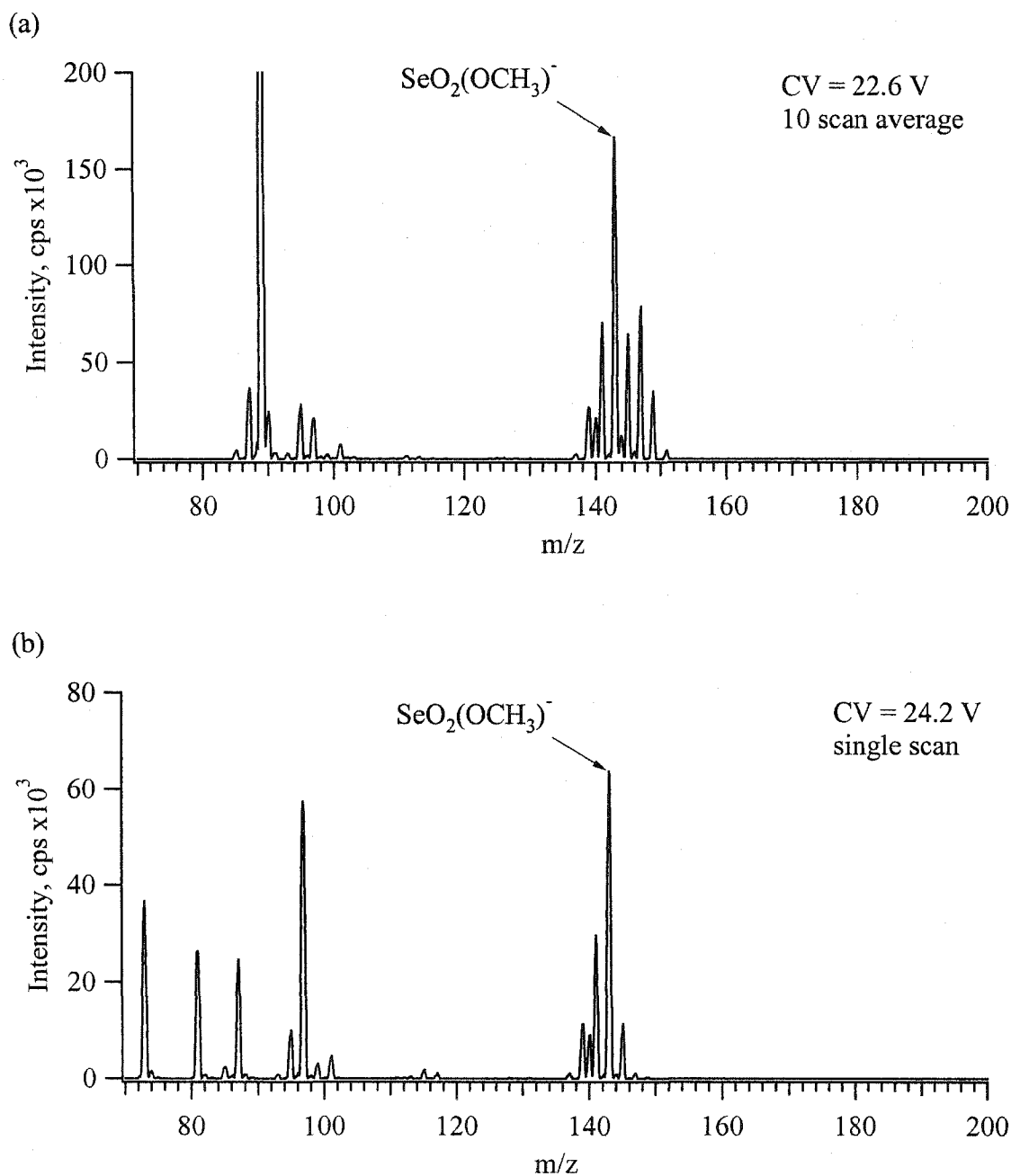


Figure 7.11 Mass spectra of selenium species found in the mass-selected CV spectra in Figure 7.10. $DV = -3.5$ kV, $F_{\text{OR}} = 0$ V, N_2 drift gas. Test solution was $1 \mu\text{M}$ Na_2SeO_3 with 0.4 mM ammonium acetate in 95% methanol, 5% water. (a) CV set to the m/z 143 peak in the CV spectrum, CV = 22.6; (b) CV set to transmit the high CV side of the same peak, CV = 24.2 V.

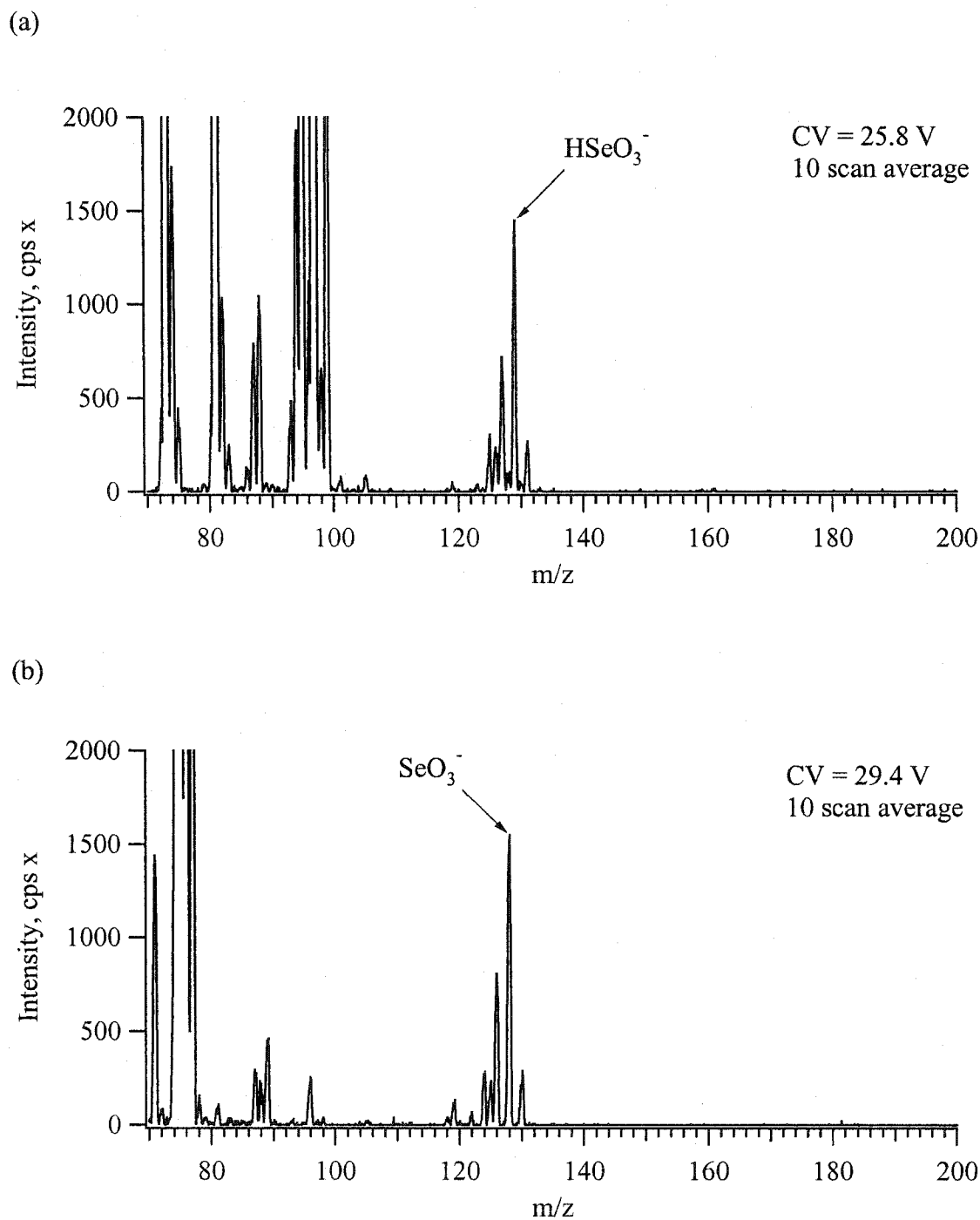
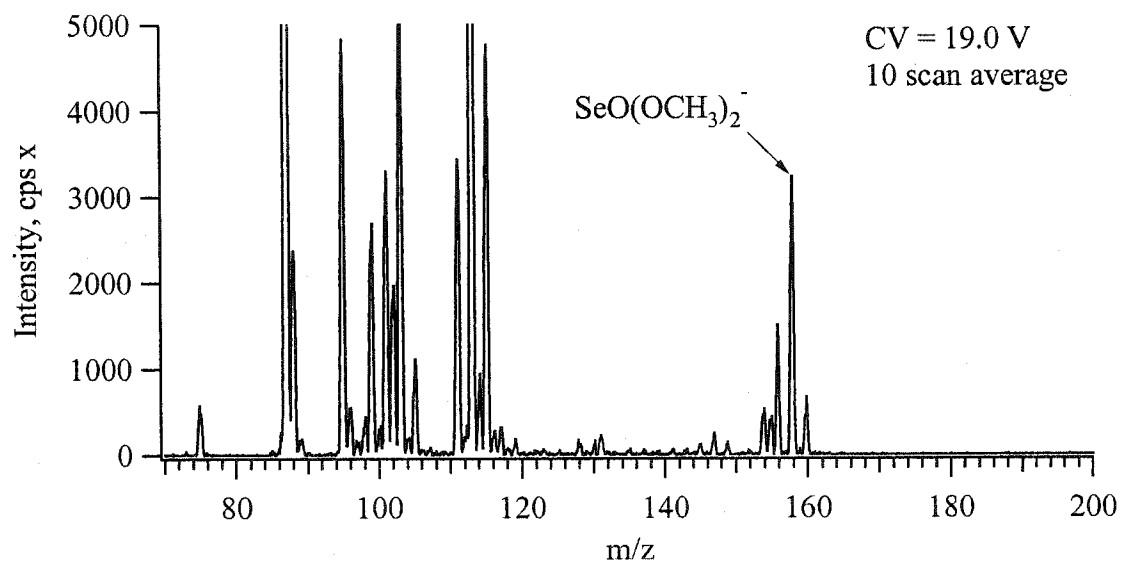


Figure 7.12 Mass spectra of selenium species found in the mass-selected CV spectra in Figure 7.10. $DV = -3.5$ kV, $F_{OR} = 0$ V, N_2 drift gas. Test solution was 1 μM Na_2SeO_3 with 0.4 mM ammonium acetate in 95% methanol, 5% water. (a) $CV = 25.8$ V; (b) $CV = 29.4$ V.

(a)



(b)

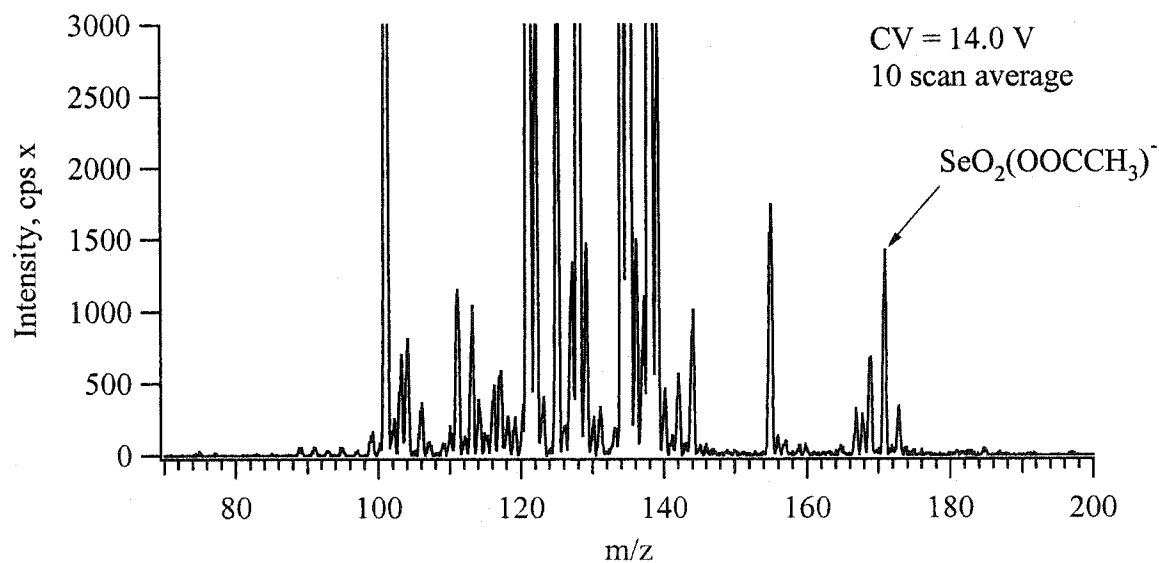


Figure 7.13 Mass spectra of selenium species found in the mass-selected CV spectra in Figure 7.10. $DV = -3.5$ kV, $F_{OR} = 0$ V, N_2 drift gas. Test solution was $1 \mu\text{M}$ Na_2SeO_3 with 0.4 mM ammonium acetate in 95% methanol, 5% water. (a) CV = 19.0 V; (b) CV = 14.0 V.

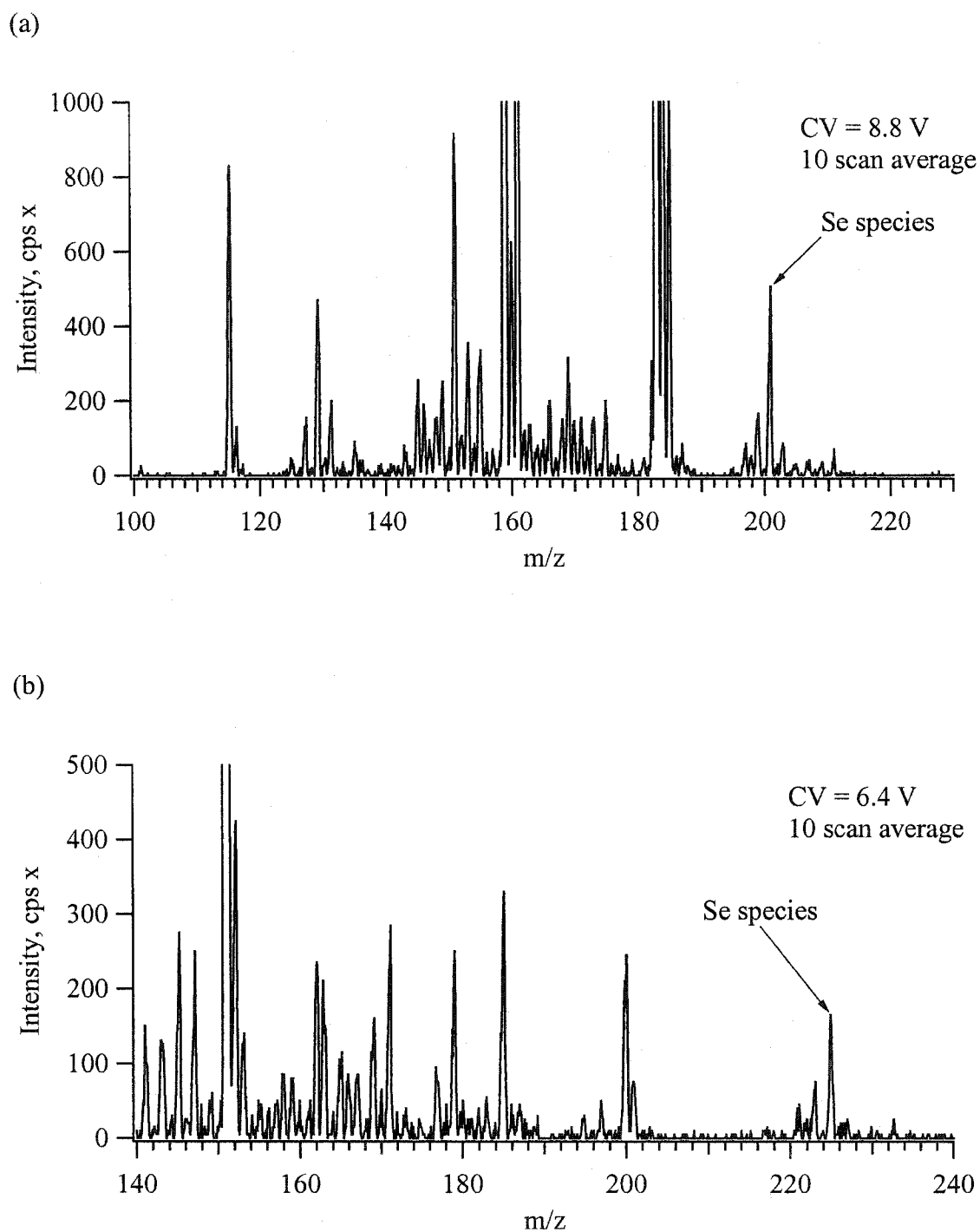


Figure 7.14 Mass spectra of selenium species found in the mass-selected CV spectra in Figure 7.10. DV = -3.5 kV, $F_{OR} = 0$ V, N_2 drift gas. Test solution was 1 μ M Na_2SeO_3 with 0.4 mM ammonium acetate in 95% methanol, 5% water. (a) CV = 8.8 V; (b) CV = 6.4 V.

(Figure 7.14 (a)). At CV = 6.4 V, what appears to be a Se species was observed at m/z 225 (Figure 7.14 (b)). In each case, although the MS spectrum was not free from background ions, the spectral window of the Se species was clean enough to allow the observation of a Se isotope pattern. The Se species at m/z 201 may be $\text{SeO}_2(\text{HC}_2\text{O}_4)^-$, and the species at m/z 225 may be $\text{SeO}_2(\text{OOCCH}_3)(\text{H}_2\text{O})_3^-$. The oxalate anion (HC_2O_4^- , m/z 89) is commonly observed in ESI-MS with methanolic solvent, presumably a product of electrolysis [41]. Without MS/MS or a more accurate mass determination, identifying these Se species is difficult.

As described earlier, the drift gas composition can be adjusted to tune the ions observed at a particular CV. With N_2 drift gas, it was observed that the major species $\text{SeO}_2(\text{OCH}_3)^-$ was transmitted with another species with an isotope at m/z 147, which resulted in spectral overlap with the isotopes of $\text{SeO}_2(\text{OCH}_3)^-$. With the addition of CO_2 to the drift gas (~10% CO_2 , 90% N_2), the species $\text{SeO}_2(\text{OCH}_3)^-$ is transmitted without this interference, as shown in the mass-selected CV spectra presented in Figure 7.15. As before with the N_2 drift gas, several m/z were monitored in the mass-selected CV scans using the 10% CO_2 drift gas, and mass spectra were acquired. No additional Se species were found. However, it is possible that the background ions present may be obscuring the observation of other low intensity Se species.

One significant difference between the drift gas compositions is that the intensity of the unknown species at m/z 147 is much lower with CO_2 in the drift gas (Figure 7.15 (a)). The identity of this species is unclear. The mass spectra of the m/z 147 peak in both drift gas compositions are presented in Figure 7.16. The spectrum in CO_2 drift gas is presented in Figure 7.16 (a), and shows a spectral pattern similar to the Se isotope pattern. The spectrum in N_2 drift gas (Figure 7.16 (b)) was calculated by subtracting a normalized version of spectrum Figure 7.11 (b) from a normalized version of Figure 7.11 (a). In the resulting spectrum, the "missing" peak at m/z 143 may be due to the over correction at this mass (the major m/z of $\text{SeO}_2(\text{OCH}_3)^-$). From the combination of the data in both drift gases, this species appears to contain Se, possibly $\text{HSeO}_3^-(\text{H}_2\text{O})$. However, due to the high abundance of the isotope at m/z 149 in both spectra, this

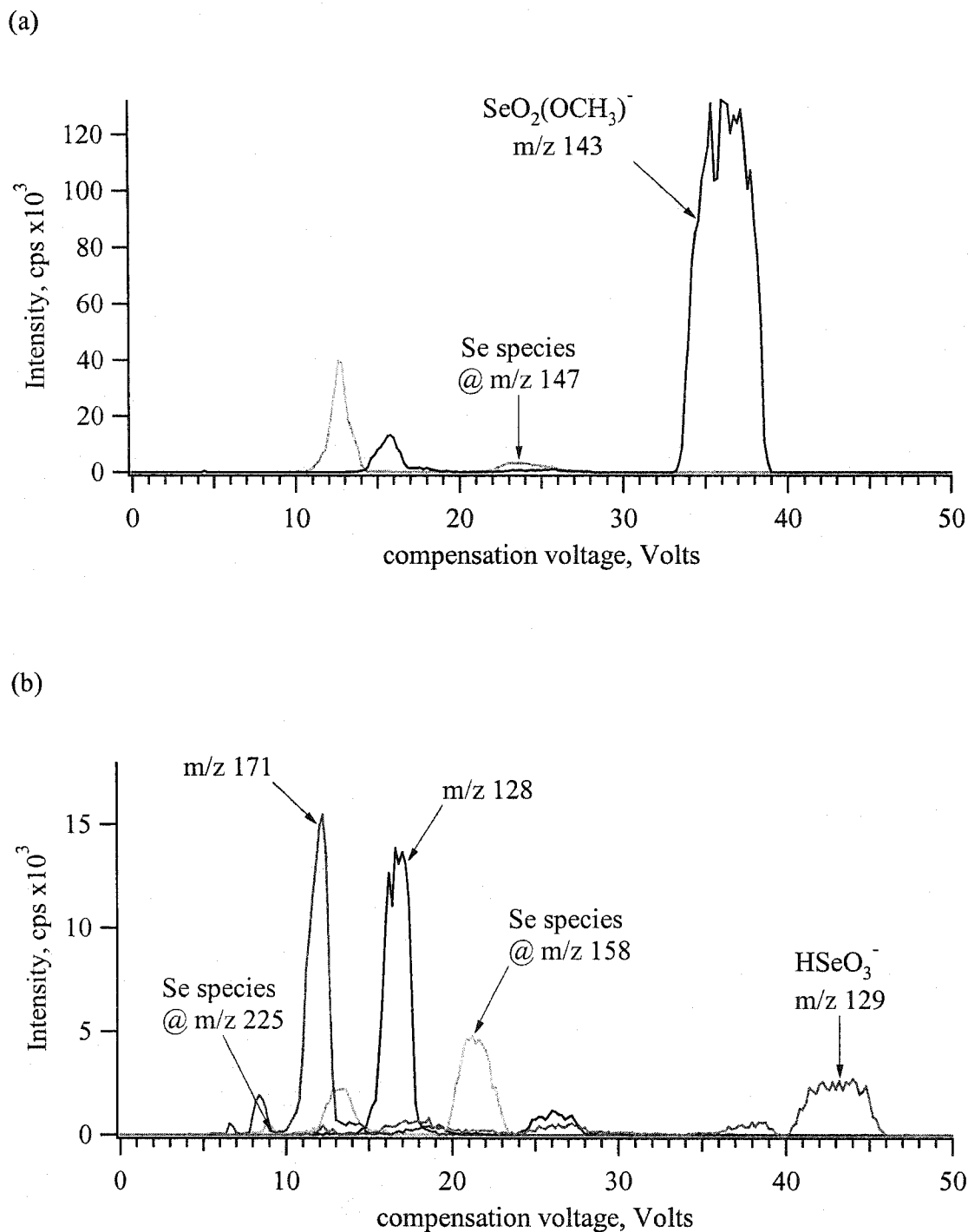


Figure 7.15 Mass-selected CV spectrum in ~10% CO₂, 90% N₂ drift gas of a solution containing 1 μ M Na₂SeO₃ with 0.4 mM ammonium acetate in 95% methanol, 5% water. (a) m/z 143 and 147; (b) m/z 128, 129, 158, and 171. Se species at m/z 225 identified (trace not shown).

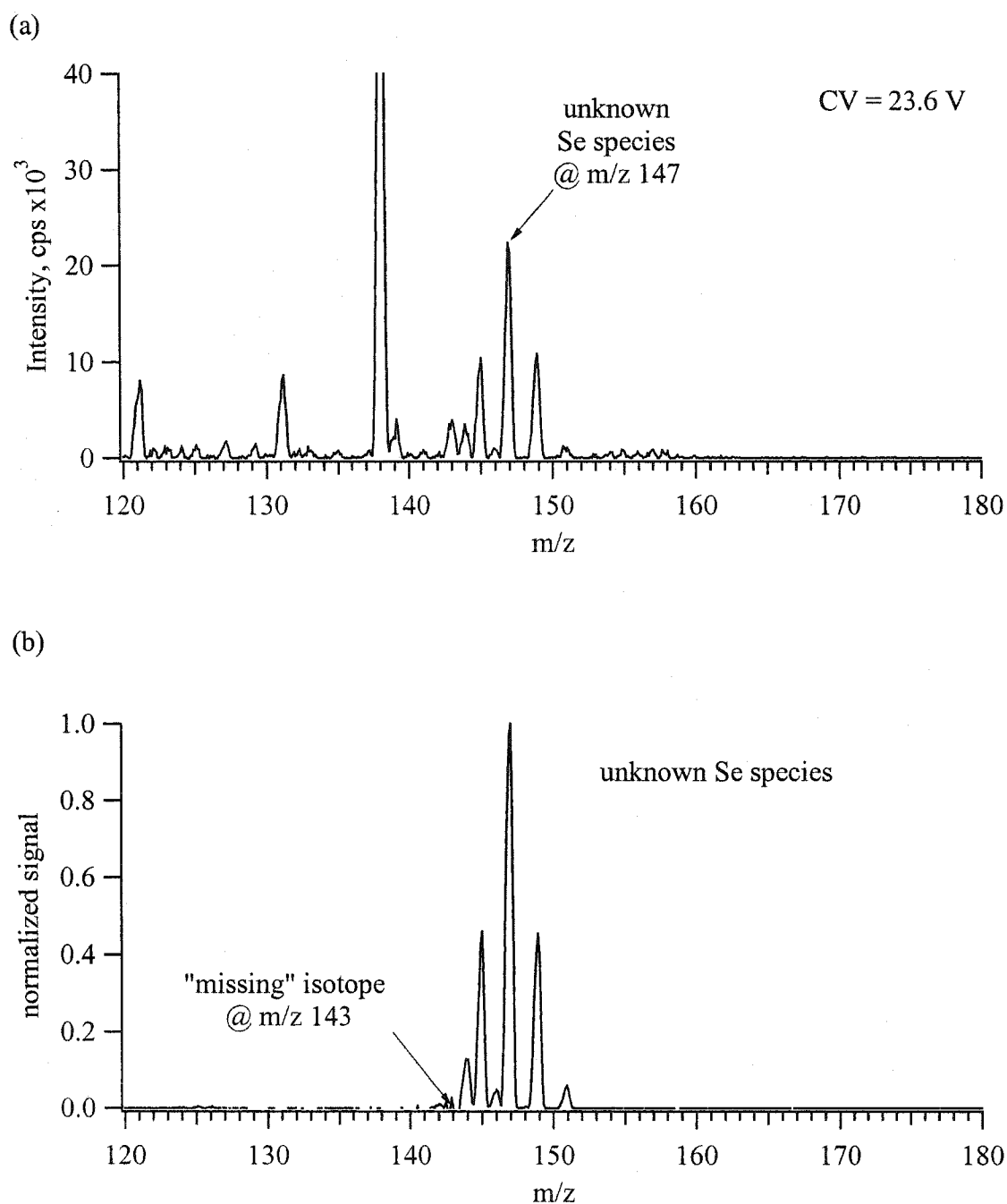


Figure 7.16 Mass spectra of the unknown m/z 147 mass-selected CV peak for $1 \mu\text{M}$ Na_2SeO_3 in 95% methanol solvent with 0.4 mM NH_4OAc . (a) $\sim 10\%$ CO_2 drift gas; (b) N_2 drift gas. The N_2 drift gas spectrum has been reconstructed by subtraction of spectra in Figure 7.11.

species may contain Cl. If Cl is present, the possibilities become very limited. A possible species may be SeO_2Cl^- or $\text{SeOCH}_3^-(\text{HCl})$. Neither of these species has been observed in prior ESI-MS work, and their formation seems unlikely.

Another significant difference between the mass-selected CV spectra in each drift gas is the higher levels of SeO_3^- observed in the N_2 drift gas spectra. In previous ESI-MS studies with selenite, under low CID conditions, the only observed species was $\text{SeO}_2(\text{OCH}_3)^-$ [41]. Under higher CID conditions, species such as SeO_3^- , NaSeO_3^- , and SeO_2^- were also observed. In the mass-selected CV data presented, neither NaSeO_3^- or SeO_2^- was observed. However, the presence of SeO_3^- seems to suggest that the FAIMS sampling is not as mild as previously thought. During the initial sampling into the FAIMS analyzer region, ions are immediately subjected to the alternating high and low fields. If the ion (or cluster) is vulnerable to CID or gas-phase charge transfer, it may be possible to alter the ion species during FAIMS sampling. As described earlier, if an ion undergoes a change in species during its travel through the FAIMS, it may be filtered out if the K_h/K of the new ion is not similar to the original ion. However, if the species changes very early in the FAIMS sampling, the product ions may be transmitted, even if the K_h/K is different. Simple ion modeling, such as that used in Chapter 4, suggests that filtering out of an ion could take as little as 0.001 sec (~ 750 cycles at 750 kHz), or many more cycles (i.e., several thousand cycles) for ions with more closely matched K_h/K behaviors. Since the FAIMS requires many cycles of the waveform to filter out ions with differing K_h/K , if fragment ions form prior to any significant ion filtering, these ions may be transmitted. In the case of SeO_3^- , it seems that this may account for its observation under, presumably, mild sampling conditions. When the same solution is acquired with CO_2 in the drift gas, SeO_3^- is not observed in the mass-selected CV spectrum. Previous reports using CO_2 in the FAIMS drift gas have indicated that CO_2 has the effect of preventing fragmentation of ions as they are sampled into the MS interface [33]. Here, the presence of CO_2 seems to prevent the generation of SeO_3^- via CID in the FAIMS interface.

Assuming the CO_2 is responsible for the prevention of fragmentation in the FAIMS interface, some inferences can be made regarding the Se species in the mass-selected CV spectrum. The Se species that were not observed in the CO_2 drift gas spectrum include the species at m/z 171 and 201, and the m/z 147 species was significantly reduced. This suggests that these species may have been generated via CID reactions in the FAIMS sampling interface with N_2 drift gas. This evidence is not conclusive, since it is conceivable that these species may have opposite K_{H}/K behavior with CO_2 , or CID with this drift gas composition may neutralize the charge on these species. Also, these low intensity species simply may not have been detected.

7.3.3 Speciation of Selenite in Purely Aqueous Solvent

When the same salt, Na_2SeO_3 , was dissolved and diluted in de-ionized water to a final concentration of 1 μM with 0.4 mM ammonium acetate, fewer species were observed by ESI-MS (as briefly discussed in Chapter 2). As with the methanol studies, several different possible Se species were considered, and the mass-selected CV spectra at these masses were acquired. After collecting mass spectra at all of the mass-selected CV peaks, some Se species were identified, and the CV spectra of these species are shown in Figure 7.17. In Figure 7.17 (a), the mass-selected CV at selected masses (m/z 128 (SeO_3^-), 129 (HSeO_3^-), 143 (HSeO_4^-), and 147) are shown. The mass-selected CV at m/z 158, 171, and 201 are shown in Figure 7.17 (b). A total of five different gas-phase Se species were identified, including HSeO_4^- . The major species, HSeO_3^- , was transmitted through the FAIMS to the MS at a $\text{CV} = 27.2$ V. An overlapping SeO_3^- species was observed, with a peak at a $\text{CV} = 29.0$ V. As with the methanolic solvent, Se species at m/z 171 and 201 were observed, and the mass spectra of these species are presented in Figure 7.18 (a) and (b), respectively. In this case, only 5 scans were averaged, and adequate isotope patterns were obtained for these low intensity species. The presence of the Se species at m/z 201 is unexpected, if the proposed species is correct ($\text{SeO}_2(\text{HC}_2\text{O}_4)^-$), since oxalate is believed to be present due the electrolysis of methanol. As with methanol, SeO_3^- (m/z 128) and the Se species at m/z 171 are observed with N_2 drift gas, however, the species at m/z 225 was not. The absence of the m/z 225

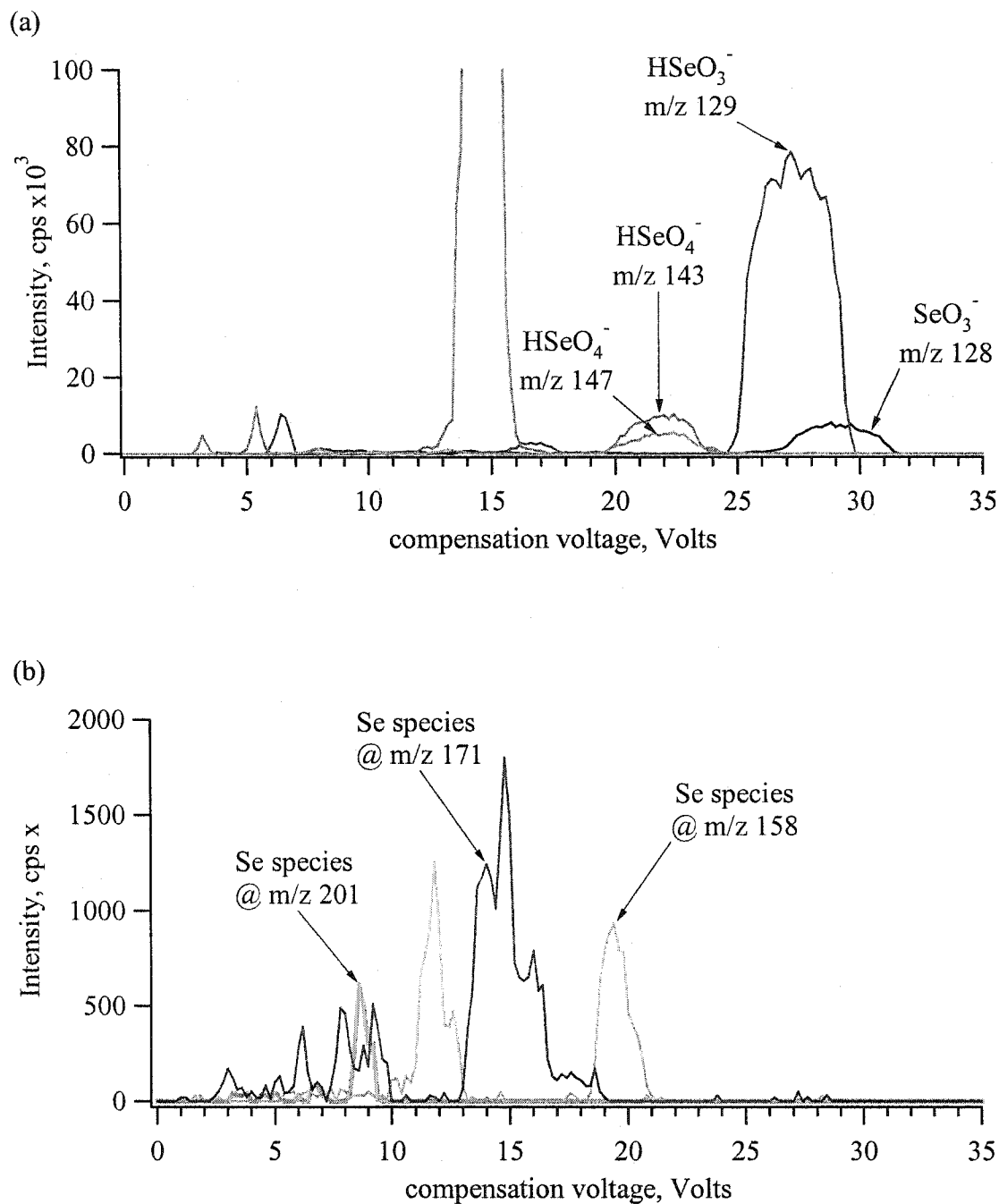


Figure 7.17 Superimposed mass-selected CV spectra in N_2 drift gas of a solution containing Na_2SeO_3 at $1 \mu\text{M}$ with 0.4 mM ammonium acetate in 100% water solvent. $\text{DV} = -3.5 \text{ kV}$, $\text{F}_{\text{OR}} = 0 \text{ V}$. (a) m/z 128, 129, 143, 147; (b) m/z 158, 171, 201.

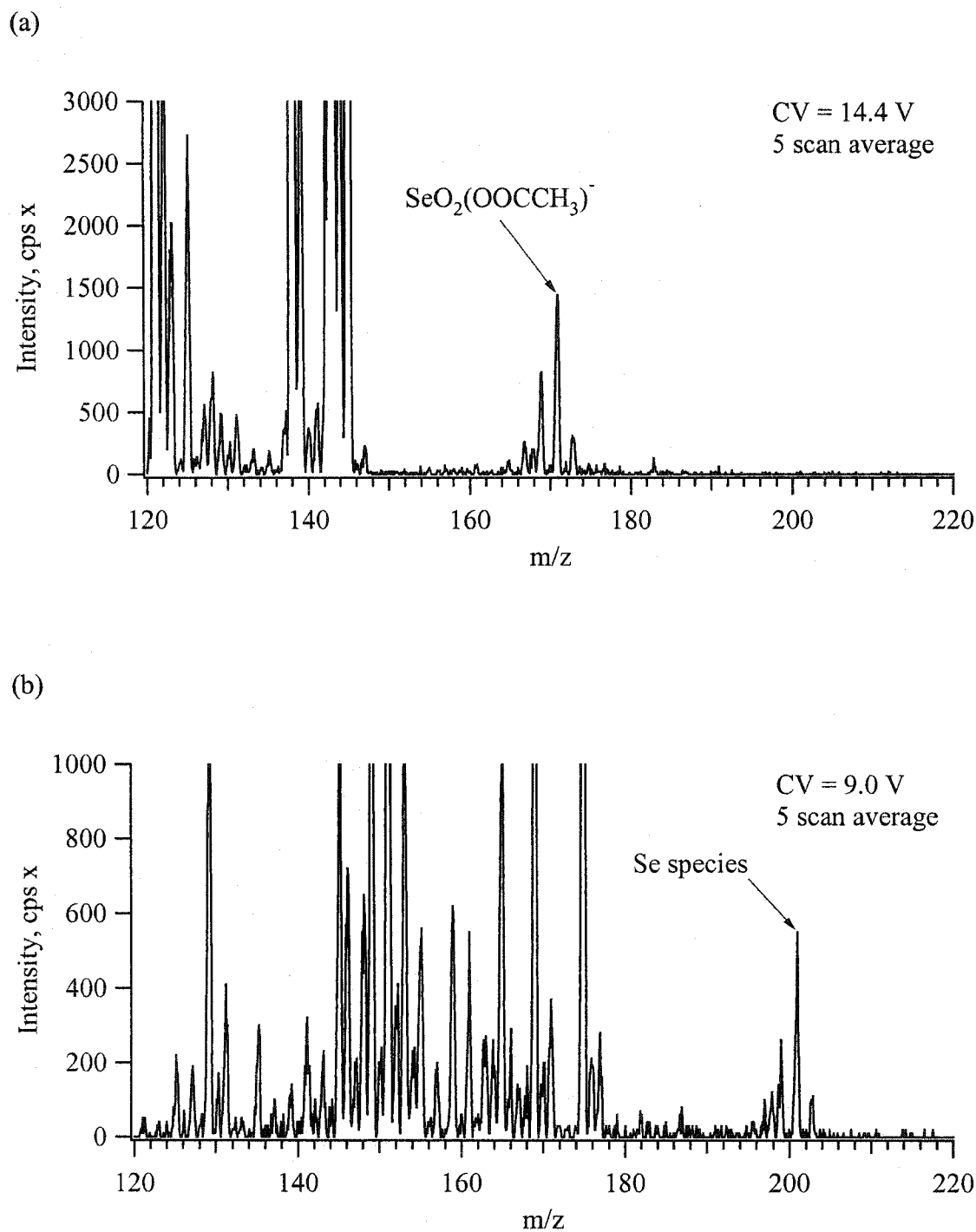


Figure 7.18 Mass spectra of from the CV spectrum in Figure 7.17 of a solution of 1 μM Na_2SeO_3 with 0.4 mM ammonium acetate in 100% water solvent. $\text{DV} = -3.5$ kV, $\text{F}_{\text{OR}} = 0$ V, N_2 drift gas. (a) CV = 14.4 V; (b) CV = 9.0 V.

species may be related to the solvent differences, or just to the inability to detect a low signal intensity.

Some significant differences between the aqueous and methanolic samples are observed. In this CV spectrum (Figure 7.17), the m/z 147 peak is due to HSeO_4^- , and the m/z 147 Se species observed with methanol was not observed with the water solvent. As noted earlier, the m/z 147 Se species observed with methanol may be generated in the FAIMS sampling interface. The absence of this species with water solvent and N_2 drift gas suggests that either water prevents the formation of this species, or that methanol is involved in the production of the species. The absence of detectable HSeO_4^- with the methanolic solvent suggests that it was not a contaminant or oxidation product originally present in the stock Na_2SeO_3 solution. The aqueous studies were done 1 day after the methanol studies using the same aqueous stock. Possibly, the HSeO_3^- was oxidized by another species (e.g., dissolved O_2) in solution to produce HSeO_4^- . Another possibility is that the sample delivery system was contaminated with low levels of HSeO_4^- . However, separate tests performed on other days showed evidence of HSeO_4^- present at similar levels. This suggests that the presence of HSeO_4^- is due to the oxidation of selenite. The absence of significant HSeO_4^- with methanol solvent suggests that methanol plays a role in preventing the presumed oxidation of selenite in solution. Possibly, the oxidizer preferentially reacts with methanol, leaving the selenite unaltered.

The mass-selected CV of the same selenite solution using ~10% CO_2 , 90% N_2 drift gas are presented in Figure 7.19. As with the methanol solvent, the Se species with m/z 171 was not observed, while the m/z 158 and 201 species were observed with CO_2 in the drift gas. Again, it is likely that the CO_2 prevents the formation of the m/z 171 species in the FAIMS interface.

7.3.4 Speciation of Selenite in a Solvent Mixture

If Na_2SeO_3 is first dissolved into de-ionized water, then diluted into a mixture of 1:1 methanol:water, a mixture of species is observed. The mass-selected CV spectra of

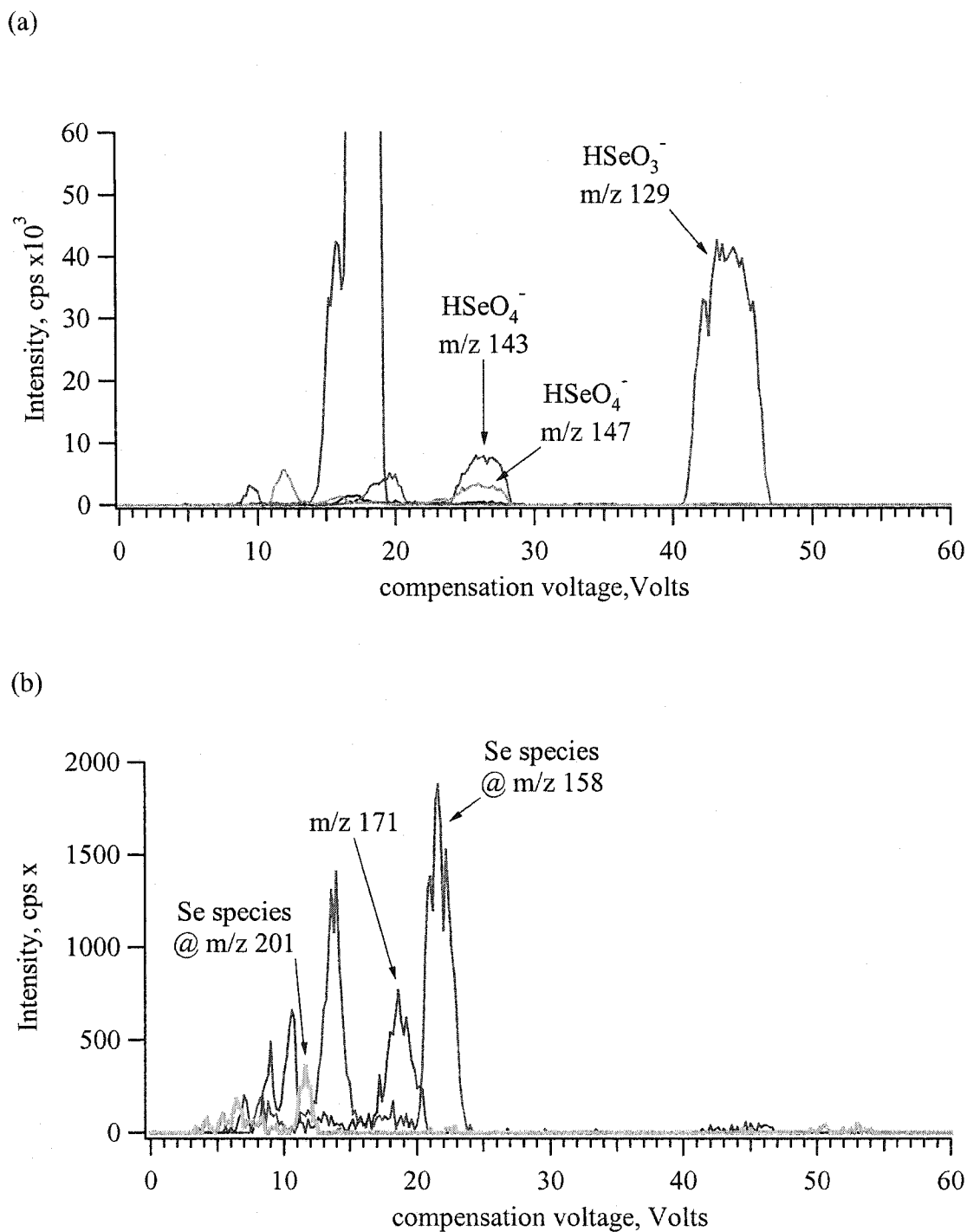
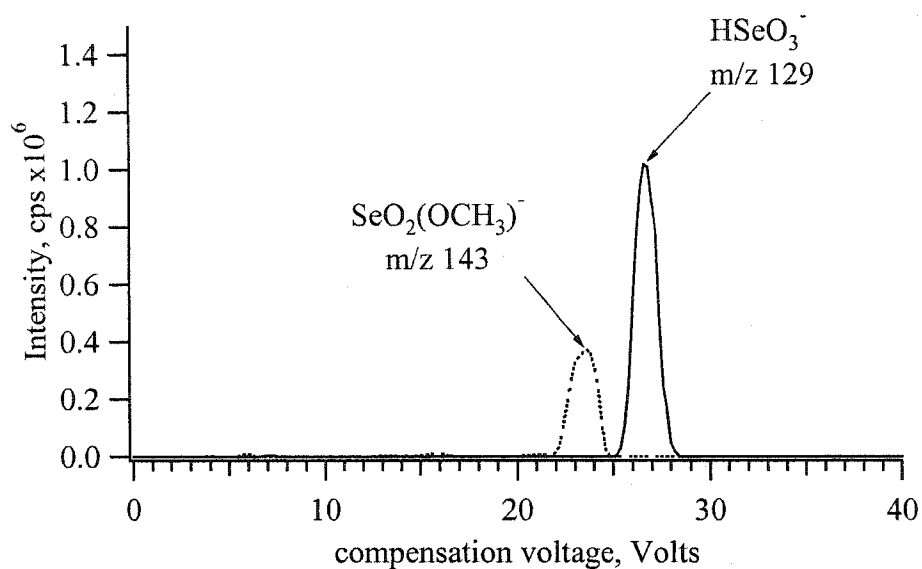


Figure 7.19 Superimposed mass-selected CV spectra in $\sim 10\%$ CO_2 , 90% N_2 drift gas of a solution containing Na_2SeO_3 at $1\ \mu\text{M}$ with $0.4\ \text{mM}$ ammonium acetate in 100% water solvent. $\text{DV} = -3.5\ \text{kV}$, $\text{F}_{\text{OR}} = 0\ \text{V}$. (a) m/z 128, 129, 143, 147; (b) m/z 158, 171, 201.

the major species at m/z 129 and 143 are shown in Figure 7.20. With this solvent composition, the need for SF_6 at the tip was significantly reduced, and could actually be turned off. The sample flow rate was $30 \mu\text{L/hr}$, and the ESI voltage conditions were similar to those used for the aqueous studies. In Figure 7.20 (a), the Na_2SeO_3 was added at a concentration of $10 \mu\text{M}$, and in Figure 7.20 (b) it is at a concentration of $1 \mu\text{M}$. Both of these solutions were prepared using an aqueous stock solution, which was then diluted into the solvent mixture. Also, the time between solution preparation and analysis was comparable for both the studies with 95% methanol and with 1:1 methanol:water. The ion HSeO_3^- was observed at about a 2:1 ratio with the $\text{SeO}_2(\text{OCH}_3)^-$ product. The data presented in the previous section demonstrated that both the seleno-ester (methanol solvent) and HSeO_3^- (water solvent) had similar signal intensity for equal concentrations of Na_2SeO_3 added. The mass-selected CV spectra demonstrate that the presence of the water in the solution serves to prevent the selenite from reacting with the methanol solvent, with the HSeO_3^- favored over the $\text{SeO}_2(\text{OCH}_3)^-$ in roughly a 2:1 ratio. The formation of HSeO_3^- over the $\text{SeO}_2(\text{OCH}_3)^-$ may be due to the water ligands being preferential to methanol for insulating the charge of $\text{SeO}_3^{2-}(\text{aq})$. Since water is the preferred ligand, methanol is less likely to react with the selenite. The similar ratio of products at $1 \mu\text{M}$ and $10 \mu\text{M}$ demonstrates that there does not seem to be any strong concentration dependence. Whether or not this is a true representation of the species in solution is unclear, especially in consideration of the apparent FAIMS sampling artifacts described earlier for selenite.

After 1 day, spectra of the same two solutions were acquired under the same operating conditions, and the CV spectra are presented in Figure 7.21. The CV spectra indicate that the observed ratio of HSeO_3^- to $\text{SeO}_2(\text{OCH}_3)^-$ has changed, with about twice as much $\text{SeO}_2(\text{OCH}_3)^-$ observed as compared to HSeO_3^- . The intensity of the seleno-ester product is about the same as last day, and the HSeO_3^- intensity was observed to decrease. Without internal standards and the ability to account for the Se mass balance (i.e., total Se analysis), it is difficult to say what might be happening here. In both Figure 7.19 and 7.20, there is a very low intensity signal at $\text{CV} = \sim 21 \text{ V}$ for the m/z 143 trace due to HSeO_4^- . The missing HSeO_3^- did not convert to HSeO_4^- , since the signal intensity at the

(a)



(b)

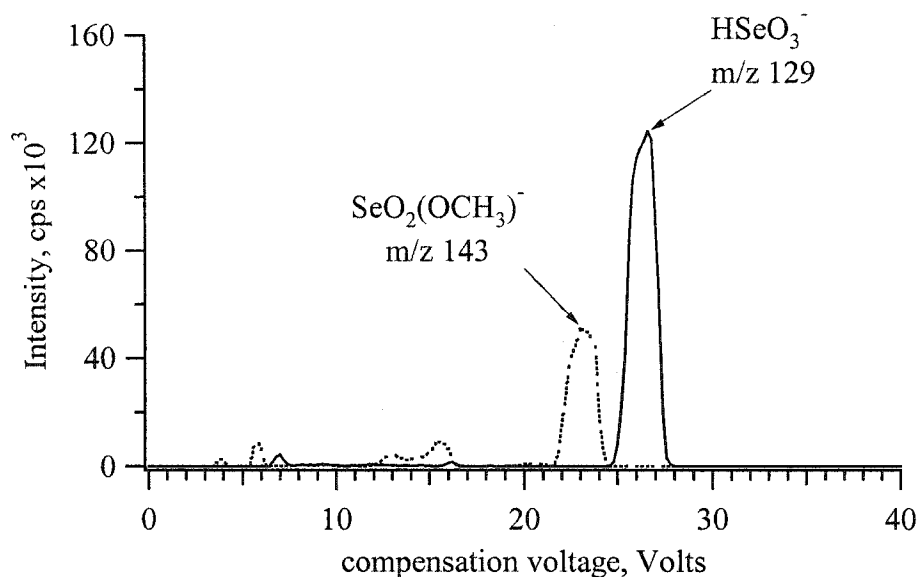


Figure 7.20 Superimposed mass-selected CV spectra (m/z 129 and 143) for a solution of Na₂SeO₃ diluted in a solvent mixture of 1:1 methanol:water, with 0.4 mM KOH. Drift gas ~10% Ar, 90% N₂, DV = -3.5 kV, F_{OR} = 0 V. (a) original [Na₂SeO₃] = 10 μM; (b) original [Na₂SeO₃] = 1 μM.

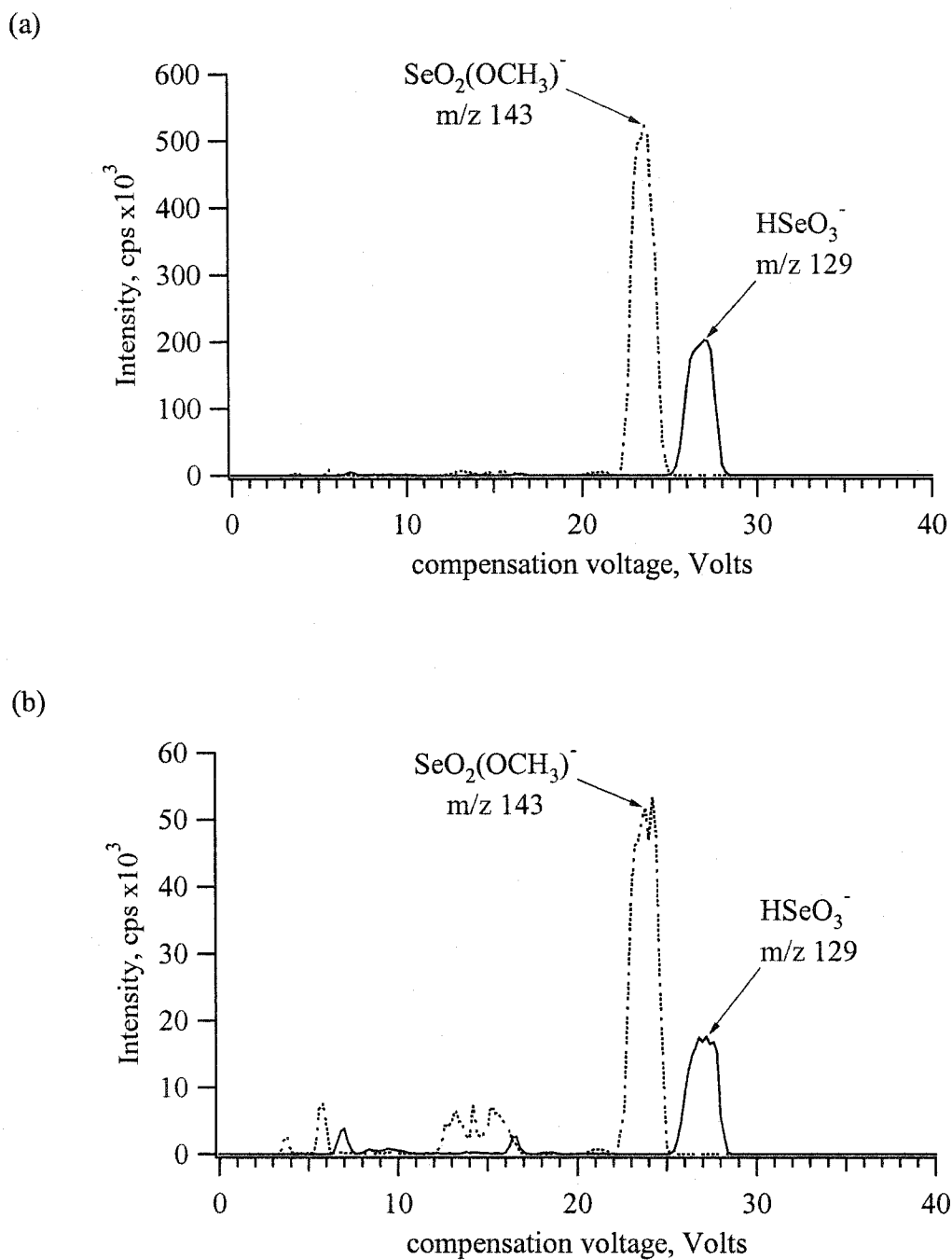


Figure 7.21 Superimposed mass-selected CV spectra (m/z 129 and 143) for the same solution of Na_2SeO_3 from Figure 7.17 after 1 day at room temperature. The Na_2SeO_3 was diluted in a solvent mixture of 1:1 methanol : water, with 0.4 mM KOH. Drift gas $\sim 10\%$ Ar, 90% N_2 , $DV = -3.5$ kV, $F_{\text{OR}} = 0$ V. (a) original $[\text{Na}_2\text{SeO}_3] = 10 \mu\text{M}$; (b) original $[\text{Na}_2\text{SeO}_3] = 1 \mu\text{M}$.

CV = ~21 V peak did not change proportionally. Possibly, HSeO_3^- is not stable in this solution at room temperature. Possibilities include adsorption of the species to the walls of the container, or reaction to form another product, possibly a neutral one that cannot be observed by ESI-MS.

7.3.5 Speciation of Arsenate

The mass-selected CV spectrum of a solution of 1 μM Na_2AsO_4 with 0.4 mM KOH in 100% aqueous solvent using ~10% CO_2 , 90% N_2 drift gas are presented in Figure 7.22 (a). Several different m/z were monitored during the CV scan, but only m/z 141 is presented in the mass-selected CV spectrum. As with the selenate, only one major species was confirmed, in this case the ion H_2AsO_4^- at a CV of 31.2 V (at DV = -3.5 kV, $F_{\text{OR}} = 0$ V). Similar results were obtained for arsenate in 95% methanol solvent (data not shown). The mass spectrum at CV = 31.2 V is presented in Figure 7.21 (b). In addition to a peak at m/z 141 for H_2AsO_4^- , another intense peak at m/z 105 is present. This species may be a CO_2 adduct, $\text{HCO}_3(\text{CO}_2)^-$. Again, without the aid of MS/MS or more accurate mass determination, species assignments can be difficult. The other peaks present in the mass-selected CV spectrum represent potential interferences to arsenate determination that the FAIMS has successfully resolved. This is especially important considering the relatively intense m/z 141 peak at CV = 16.4 V. This species was also observed in the mass-selected CV scans of a blank solution. The mass spectra of what was believed to be the same species in the blank is presented in Figure 7.23. The DV in these tests was -3.3 kV, and the sample was in 100% aqueous solvent. The mass spectrum in the N_2 drift gas (Figure 7.23 (a)) and ~ 10% CO_2 drift gas (Figure 7.23 (b)) look very similar. The isotopes suggest the presence of S, Si, C, or O. A possible species assignment may be $\text{HSO}_4^-(\text{CO}_2)$.

7.3.6 Speciation of Arsenite - Preliminary Results

Due to sensitivity problems with arsenite in this work, and due to the difficulty in identifying species without MS/MS and/or accurate mass determination, these results

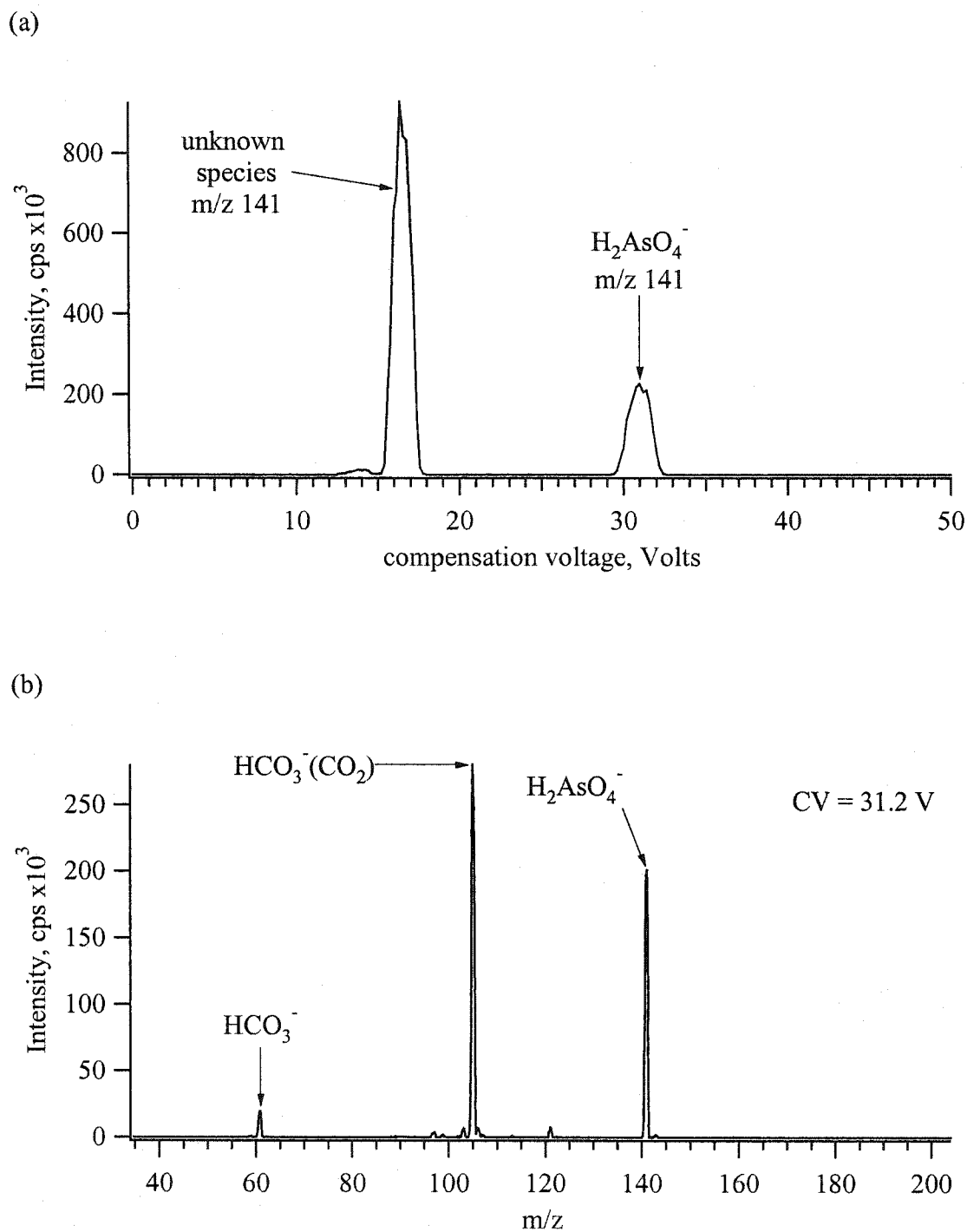


Figure 7.22 (a) Mass-selected CV spectrum (m/z 141) in $\sim 10\%$ CO_2 , 90% N_2 drift gas of a sample containing $1 \mu\text{M}$ NaH_2AsO_4 and 0.4 mM KOH in 100% water solvent. $\text{DV} = -3.5 \text{ kV}$, $\text{F}_{\text{OR}} = 0 \text{ V}$; (b) Mass spectrum at $\text{CV} = 31.2 \text{ V}$.

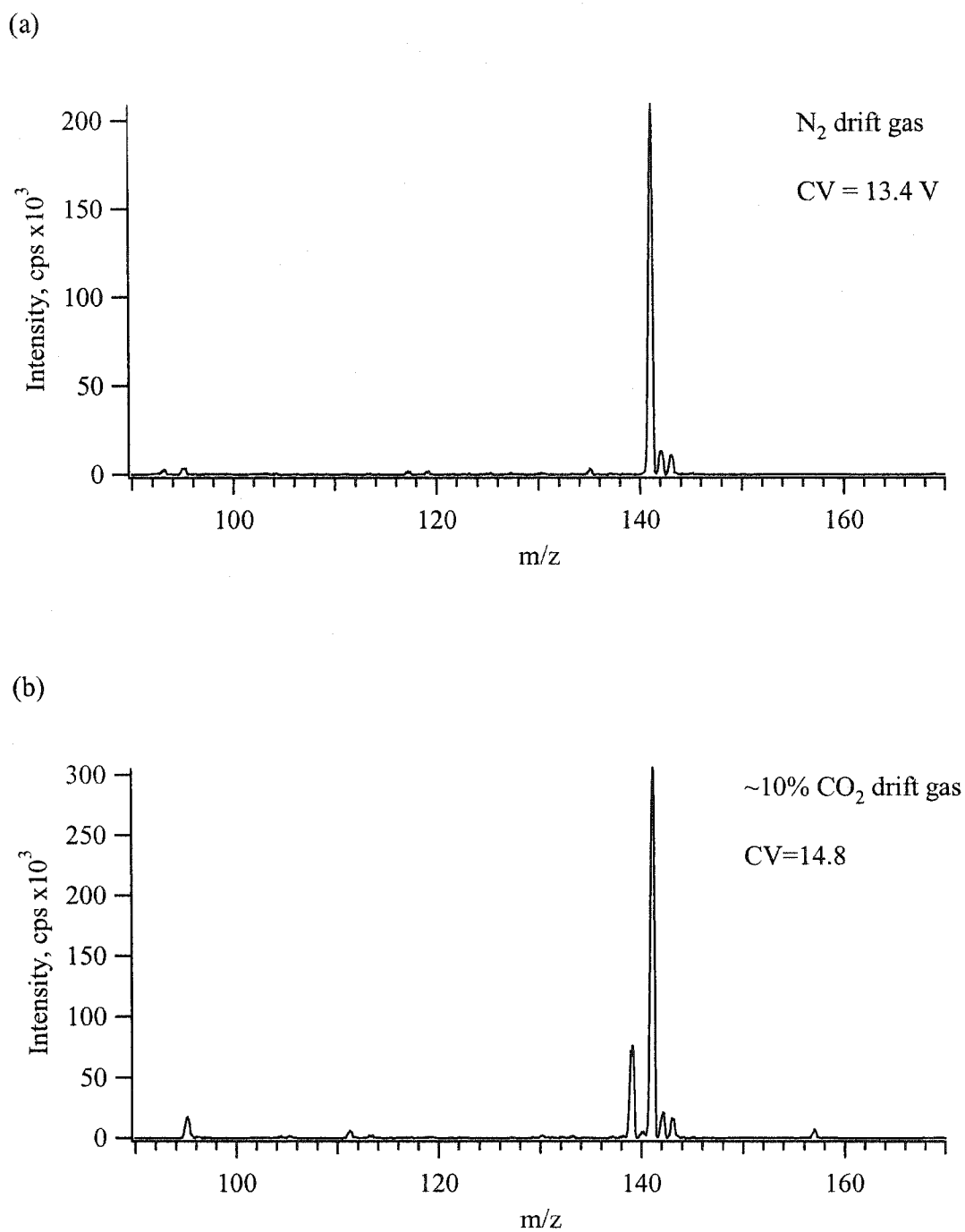
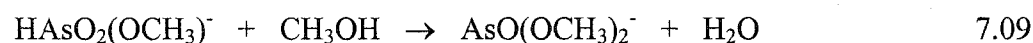
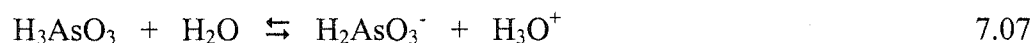


Figure 7.23 Mass spectra of the unknown m/z 141 peak in a blank solution of 0.4 mM KOH in 100% aqueous solvent. (a) N_2 drift gas, (b) ~10% CO_2 , 90% N_2 drift gas. DV = -3.3 kV, F_{OR} = 0 V.

represent preliminary work. While some As species were tentatively identified, the confidence of these assignments was improved with the examination of the CID products of these species, where possible.

Like selenite, arsenite is observed as a reaction product when methanol is present. Based on some previous ESI-FAIMS-MS work, selected m/z were monitored during the mass-selected CV scans with a drift gas composition of ~10% Ar, 90% N₂. The sample was 0.1 mM NaAsO₂ in 95% methanol and 5% water, with 0.4 mM KOH. The mass-selected CV spectrum (m/z 125, 139, and 153) is shown in Figure 7.24. A lower DV of 3.1 kV was used, as it seemed to produce better signal intensity for the observed species. Three major CV peaks were tentatively identified as HAsO₂(OCH₃)⁻ (m/z 139) at CV = 26.4 V, AsO(OCH₃)₂⁻ (m/z 153) at CV = 22.8 V, and H₂AsO₃⁻ (m/z 125) at CV = 18.2 V. The added NaAsO₂ apparently reacts with water to form H₃AsO₃ [42], which then reacts with the methanol solvent, as proposed in Equations 7.07 to 7.09.



The mass spectrum of the major species at CV = 22.8 V is presented in Figure 7.25. The major ion observed was AsO(OCH₃)₂⁻, with minor peaks for water and CO₂ adducts. The presence of CO₂ is attributed to low levels of CO₂ being released from a filter cartridge being used to filter the Ar before entering the FAIMS. This filter was previously used for CO₂, and tests have demonstrated that CO₂ is retained by the filter, and slowly bleeds off. This may also be influencing the observed CV of these ions. In Figure 7.26, the mass spectra of the other two peaks are presented. The species at CV = 18.2 V (Figure 7.26 (a)) was tentatively assigned as H₂AsO₃⁻, with minor peaks for H₂AsO₃(H₂O)⁻ and H₂AsO₃(CO₂)⁻. At CV = 26.4 V (Figure 7.26 (b)), the observed species was assigned as HAsO₂(OCH₃)⁻ with a minor adduct, HAsO₂(OCH₃)(CO₂)⁻.

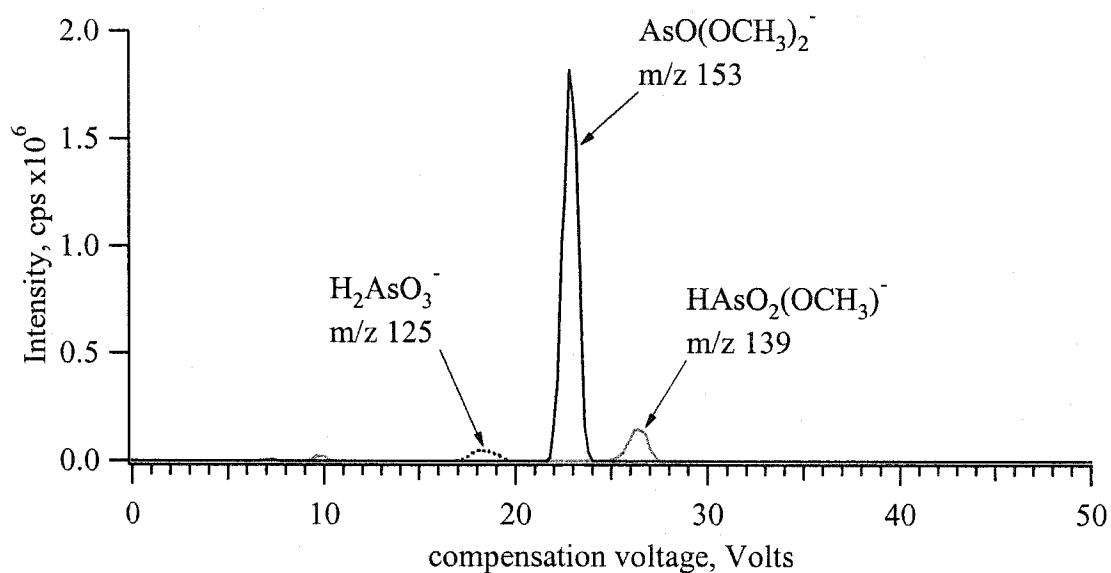


Figure 7.24 Superimposed mass-selected CV spectra (m/z 125, 139, and 153) of 0.1 mM NaAsO₂ with 0.4 mM KOH in 95% methanol, 5% water. Drift gas ~10% Ar, 90% N₂. DV = -3.1 kV, F_{OR} = 0 V.

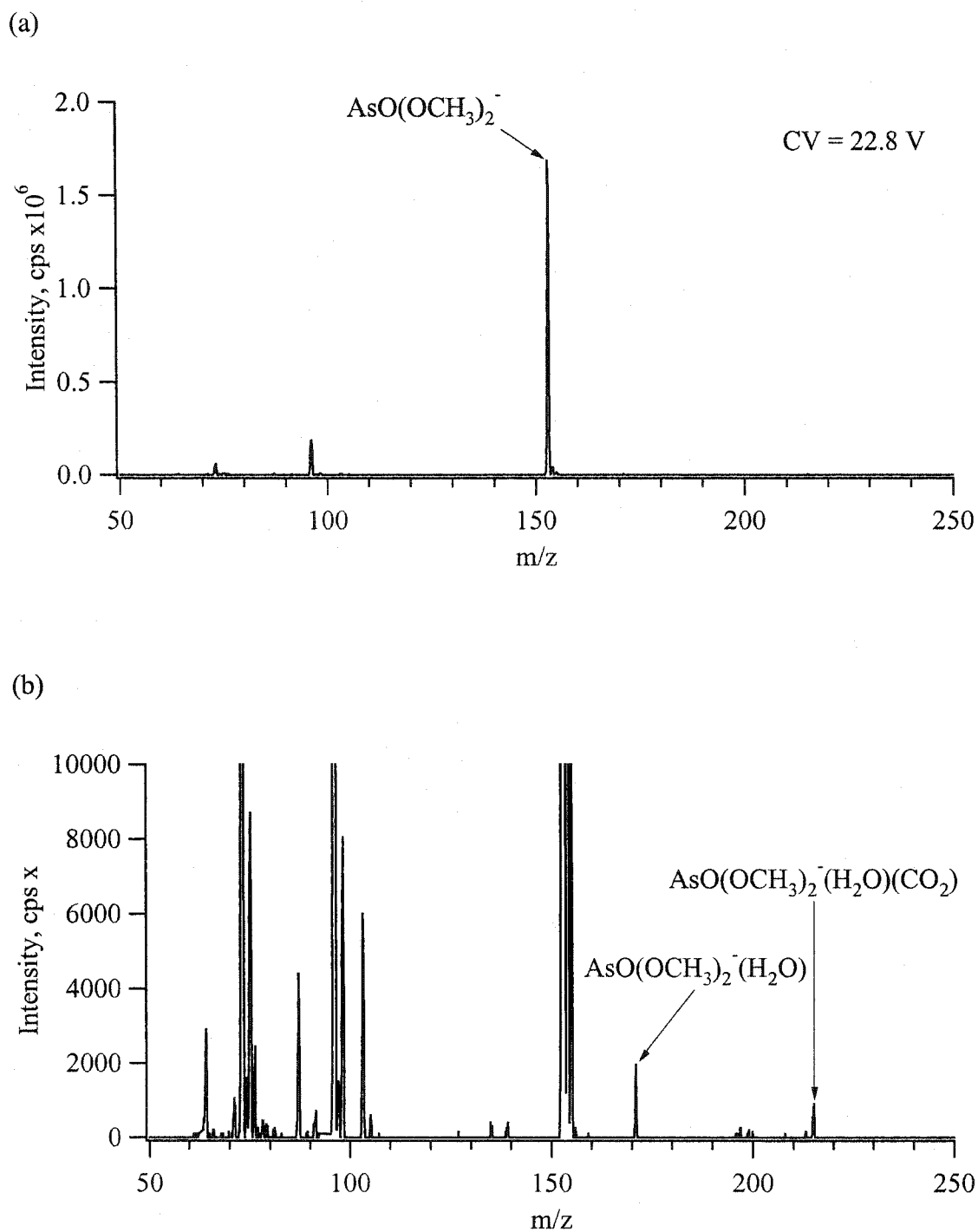


Figure 7.25 (a) Mass spectra at CV = 22.8 V with 0.1 mM NaAsO₂ with 0.4 mM KOH in 95% methanol, 5% water. Drift gas ~10% Ar, 90% N₂. DV = -3.1 kV, F_{OR} = 0 V; (b) expanded view of the spectrum in (a).

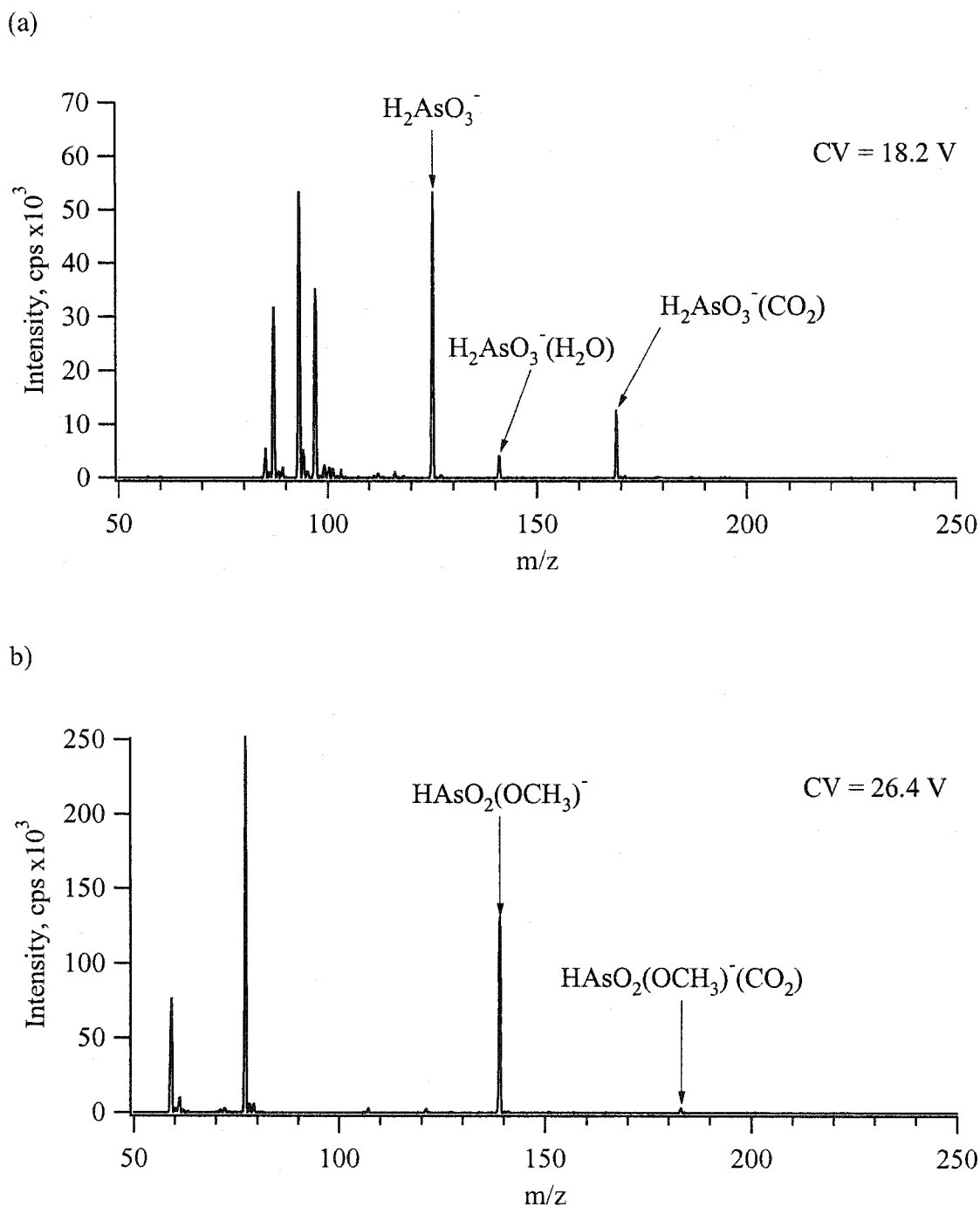


Figure 7.26 Mass spectra for 0.1 mM NaAsO_2 with 0.4 mM KOH in 95% methanol, 5% water. Drift gas $\sim 10\%$ Ar, 90% N_2 . DV = -3.1 kV, $F_{\text{OR}} = 0$ V; (a) CV = 18.2 V; (b) CV = 26.4 V.

To get additional confidence in these peak assignments, the concentration of added NaAsO_2 was varied, and the mass-selected CV peak intensity increased accordingly. To this point, all of the mass spectra acquired were done using no potential difference between the MS orifice and the skimmer ($F_{\text{OR}} = 0 \text{ V}$), minimizing declustering and fragmentation of the ions. By applying a potential to the outer FAIMS electrode and the MS orifice (F_{OR}), CID of the ions was generated at the MS interface. The mass-selected CV spectra (m/z 75 (As^-), 91 (AsO^-), 107 (AsO_2^-), 123 (AsO_3^-), 125 (H_2AsO_3^-), 139 ($\text{HAsO}_2(\text{OCH}_3)^-$), and 153 ($\text{AsO}(\text{OCH}_3)_2^-$)) of the same solution at $F_{\text{OR}} = -50 \text{ V}$ and $F_{\text{OR}} = -120 \text{ V}$ are presented in Figures 7.27 (a) and (b), respectively. Since only slight changes are made to the FAIMS operating conditions by changing the F_{OR} , it can be easily assumed that each species being transmitted by the FAIMS is the same at each F_{OR} setting. By changing the F_{OR} , the only change that occurs in the FAIMS operation is that the species are transmitted at lower CV values as the F_{OR} is increased. For the ion $\text{AsO}(\text{OCH}_3)_2^-$, the peak shifts from CV = 22.8 V at $F_{\text{OR}} = 0 \text{ V}$, to CV = 21.2 V at $F_{\text{OR}} = -50 \text{ V}$, and to CV = 20.2 V at $F_{\text{OR}} = -120 \text{ V}$. This is the result of the slight alteration in the fields within the FAIMS with the application of a bias to the outer electrode. By applying a negative voltage to the outer electrode (i.e., the F_{OR}), the CV required to produce a balance condition is reduced and the ion is transmitted at a lower CV. The major differences in the observed species in the mass-selected CV spectra are due to the fragmentation of the ions in the MS interface. At $F_{\text{OR}} = -70 \text{ V}$, the species formerly observed as $\text{AsO}(\text{OCH}_3)_2^-$ (CV = 21.2 V) is fragmented to form m/z 123 (AsO_3^-) and m/z 91 (AsO^-), with only a small contribution from m/z 107 (AsO_2^-). The two other candidate species in the mass-selected CV spectra ($\text{HAsO}_2(\text{OCH}_3)^-$ (CV = 25.6 V) and H_2AsO_3^- (CV = 17.4 V)) are both fragmented to m/z 107 (AsO_2^-).

At the higher $F_{\text{OR}} = -120 \text{ V}$, even further fragmentation is evident (Figure 7.27 (b)). The species $\text{AsO}(\text{OCH}_3)_2^-$ (CV = 20.2 V) has been fragmented to mostly m/z 91 (AsO^-), with minor peaks at m/z 107 (AsO_2^-) and m/z 75 (As^-). The species H_2AsO_3^- (CV = 16.8 V) and $\text{HAsO}_2(\text{OCH}_3)^-$ (CV = 24.8 V) are observed to have a small proportion of fragments at m/z 91 (AsO^-), but are still mostly m/z 107 (AsO_2^-). The intensity of the fragment species suggest that for the species $\text{HAsO}_2(\text{OCH}_3)^-$ and H_2AsO_3^- , the

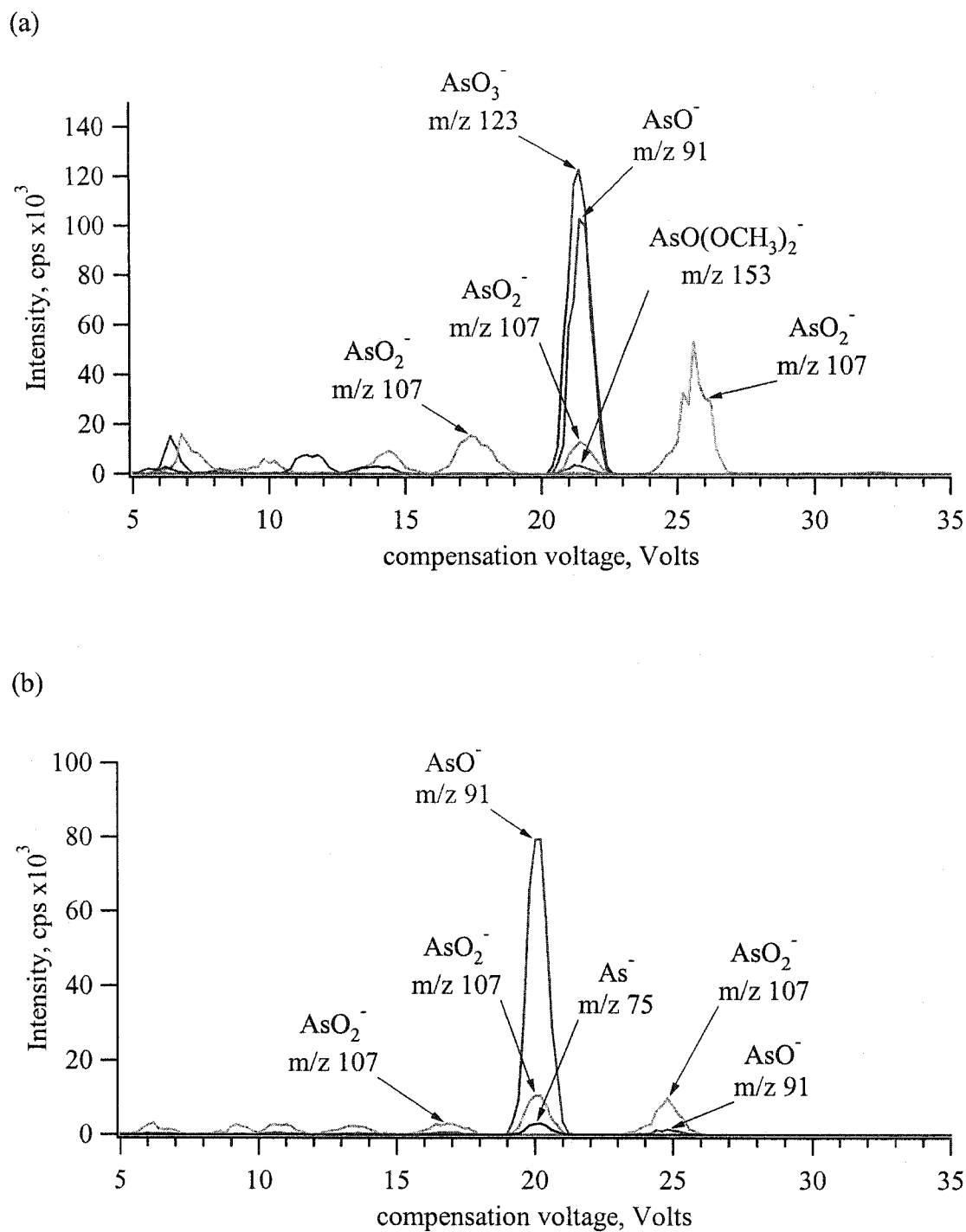
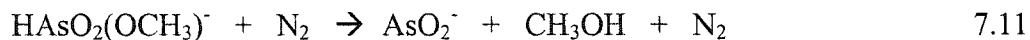
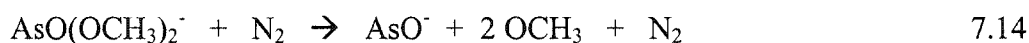
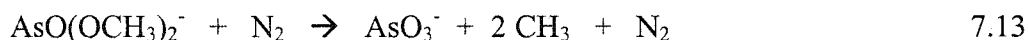


Figure 7.27 Superimposed mass-selected CV spectra (m/z 75, 91, 107, 123, 125, 139, and 153) in $\sim 10\%$ CO_2 , 90% N_2 drift gas of a sample containing 0.1 mM NaAsO_2 and 0.4 mM KOH in 100% water solvent. $\text{DV} = -3.3$ kV; (a) $F_{\text{OR}} = -70$ V; (b) $F_{\text{OR}} = -120$ V.

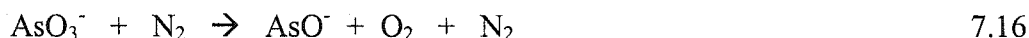
fragmentation to form AsO_2^- seems relatively easy, but further fragmentation to AsO^- is difficult. The CID reactions for these species are suggested in Equations 7.10 to 7.12.

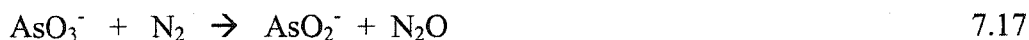


The production of AsO_2^- and an uncharged leaving group is the first step in the CID of these species (Equations 7.10 and 7.11), followed by fragmentation to AsO^- . The low AsO^- signals observed indicate that this fragment requires more energy to be produced from the respective parent ion. In contrast, the ion $\text{AsO}(\text{OCH}_3)_2^-$ produces relatively intense fragment signals for m/z 123 (AsO_3^-) and m/z 91 (AsO^-), but not for m/z 107 (AsO_2^-). Due to the apparent high CID energy required to fragment AsO_2^- to AsO^- , the AsO^- is likely not a fragment of AsO_2^- at this F_{OR} setting. The intense AsO^- and AsO_3^- fragments in the presence of a low intensity AsO_2^- fragment at low energy suggests that AsO^- forms without an AsO_2^- intermediate, as proposed in Equations 7.13 to 7.15.



These reactions suggest that the $\text{AsO}(\text{OCH}_3)_2^-$ can fragment to form one of two products, either AsO_3^- or AsO^- . Alternatively AsO_3^- may be the only product, which fragments to form AsO^- and AsO_2^- , with AsO^- being the preferred fragment, as suggested in Equations 7.16 and 7.17.





In any case, the fragmentation of $\text{AsO}(\text{OCH}_3)_2^-$ to AsO^- occurs at much lower energy, allowing the formation of As^- at CID energies where the other species only produce AsO^- .

As with the methanol solvent studies, when water was used as the solvent for an arsenite sample, the intensity of potential As species was relatively low. In solution, H_3AsO_3 has a $\text{pK}_{\text{a}1}$ of about 9.4 [42]. With such a high solution pK_{a} , perhaps it has a high gas-phase proton affinity, and readily removes a proton from another species (i.e., the solvent) to become uncharged and undetectable. Or, perhaps the gas-phase species is not very stable at high DV within the FAIMS. The mass-selected CV spectra of 0.1 mM NaAsO_2 in 100% water solvent with 0.4 mM KOH in ~10% CO_2 , 90% N_2 drift gas are shown in Figure 7.28 (a). A major peak at m/z 125, H_2AsO_3^- , was observed at a CV = 17.0 V. Another peak at CV = 28.9 V, due to H_2AsO_4^- is also observed. This is similar to the studies with selenite, where low levels of selenate were observed. Another species with m/z 141 is also observed (as with previous studies of arsenate, possibly HSO_4^- (CO_2)) at a CV = 15.0 V. The mass spectrum of the major peak at CV = 17.0 V is shown in Figure 7.28 (b). An intense peak at m/z 125 (H_2AsO_3^-) is observed, as well as an intense species at m/z 169. This species has been assigned as $\text{H}_2\text{AsO}_3(\text{CO}_2)^-$. The intensity of this adduct is considerably larger than observed for the other As and Se species studied, and indicates that CO_2 readily forms adducts with H_2AsO_3^- .

7.3.7 Sensitivity and Detection Limits of the Technique

So far, this work has dealt with the ability of ESI-FAIMS-MS to detect various species at a signal intensity that would be very difficult to detect by ESI-MS alone. One important consideration is what detection limits this technique can offer, since this will ultimately determine the success of the technique for a particular sample matrix.

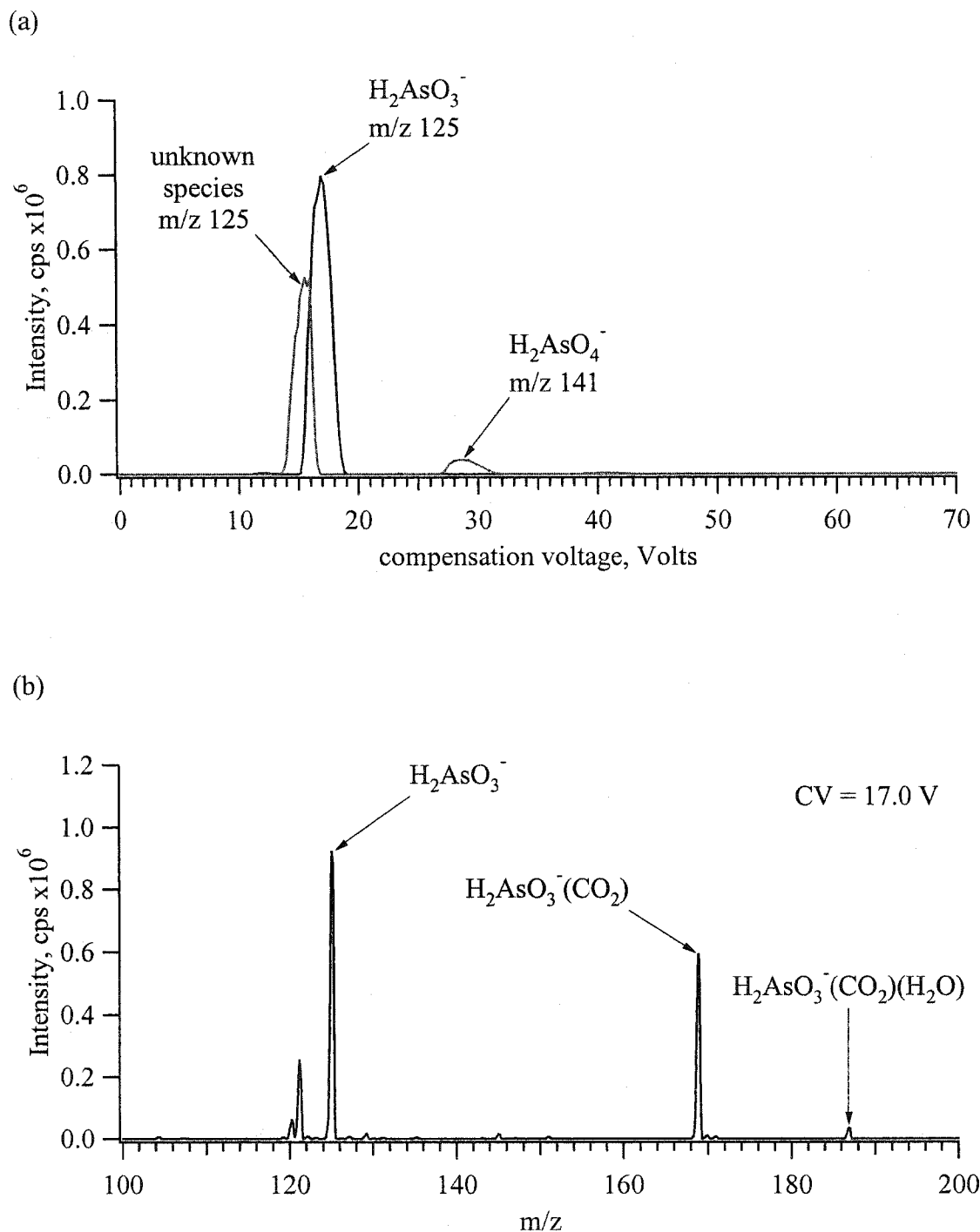


Figure 7.28 (a) Superimposed mass-selected CV spectra (m/z 125 and 141) in $\sim 10\%$ CO_2 , 90% N_2 drift gas of a sample containing 0.1 mM NaAsO_2 and 0.4 mM KOH in 100% water solvent. $\text{DV} = -3.3 \text{ kV}$, $\text{F}_{\text{OR}} = 0 \text{ V}$; (b) Mass spectrum at $\text{CV} = 17.0 \text{ V}$.

This section deals with the detection limits that can be achieved for these major species in laboratory standards.

With N_2 as the drift gas, the seleno-ester ($SeO_2(OCH_3)^-$), selenate and the arsenate ion have closely matched CVs. Separation of $HSeO_4^-$ from $H_2AsO_4^-$ is important for accurate determination of $H_2AsO_4^-$, due to the m/z 141 of $HSeO_4^-$. By adding CO_2 to the mixture, the CVs are changed to achieve better peak resolution. Using CO_2 , these test conditions could also be used for methanolic studies, since $H_2AsO_4^-$ is separated from both $SeO_2(OCH_3)^-$ and $HSeO_4^-$ (data not shown), both of which have potentially interfering isotopes. Standard analytical curves for selenate, selenite, arsenate, and selenomethionine were established. A curve for arsenite was not done, since the signal intensity as compared to the other species suggests that these sampling conditions were not optimal for the determination of arsenite. Further investigation into arsenite analysis with this system is required. A mixture of Na_2SeO_3 , Na_2SeO_4 , selenomethionine, and NaH_2AsO_4 was prepared in 100% water solvent. A series of standards was prepared at 0.05, 0.1, 0.5, and 1 μM concentration, with 0.4 mM KOH as a background ion. Each standard was continuously infused and electrosprayed into the FAIMS interface. The DV was set at -3.5 kV, and the drift gas composition was ~5% CO_2 , 95% N_2 . Some F_{OR} voltage was added to slightly increase the signal intensity, and was set to $F_{OR} = -10$ V. As an example of the observed CV scans, the mixture of ions at 0.1 μM is presented in Figure 7.29. The mass-selected CV traces (m/z 129, 141, 145, and 196) represent the major masses of the ions of interest. The signals of $HSeO_4^-$, $HSeO_3^-$, and $H_2AsO_4^-$ are clearly separated and have similar intensity. The intense peaks between CV 13 and 22 V (approx.) represent ions with masses identical to some of species of interest. Failure to separate these ions would severely compromise detection of the analyte ions at this concentration. The selenomethionine peak (CV = 6.8 V), has a much lower intensity for an equivalent concentration. Some intensity bias is present here, due to the optimization of the dome position for the selenate ion and due to lower peak heights that generally accompany ions at lower CVs [12, 14, 19, 20]. The spectra (single scans) of these species are presented in Figures 7.30 and 7.31. Even at this low concentration, the

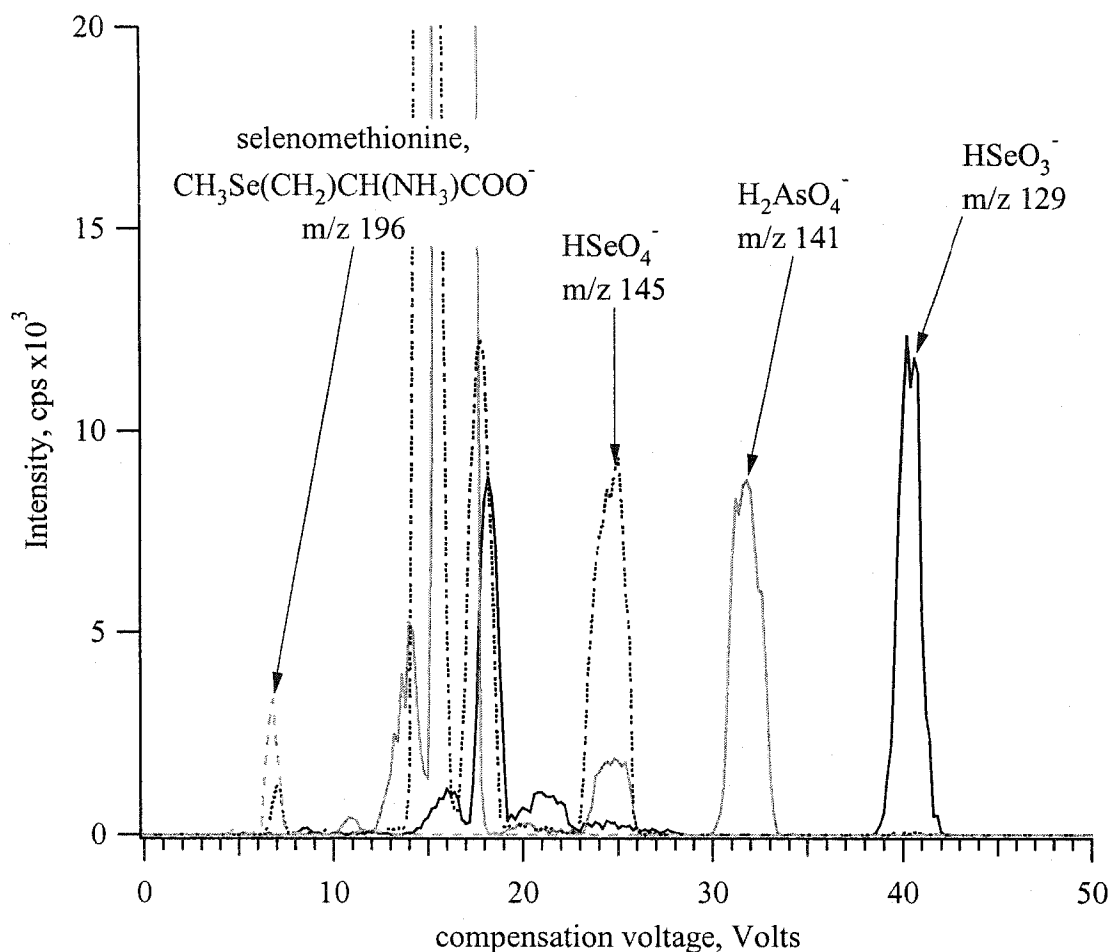


Figure 7.29 Superimposed mass-selected CV spectra (m/z 129, 141, 145, and 196) in $\sim 5\%$ CO₂, 95% N₂ drift gas of a mixture of Na₂SeO₄, Na₂SeO₃, NaH₂AsO₄, and selenomethionine each at a concentration of 0.1 μ M in 100% water solvent with 0.4 mM KOH as an electrospray stabilizer. DV = -3.5 kV, F_{OR} = -10 V.

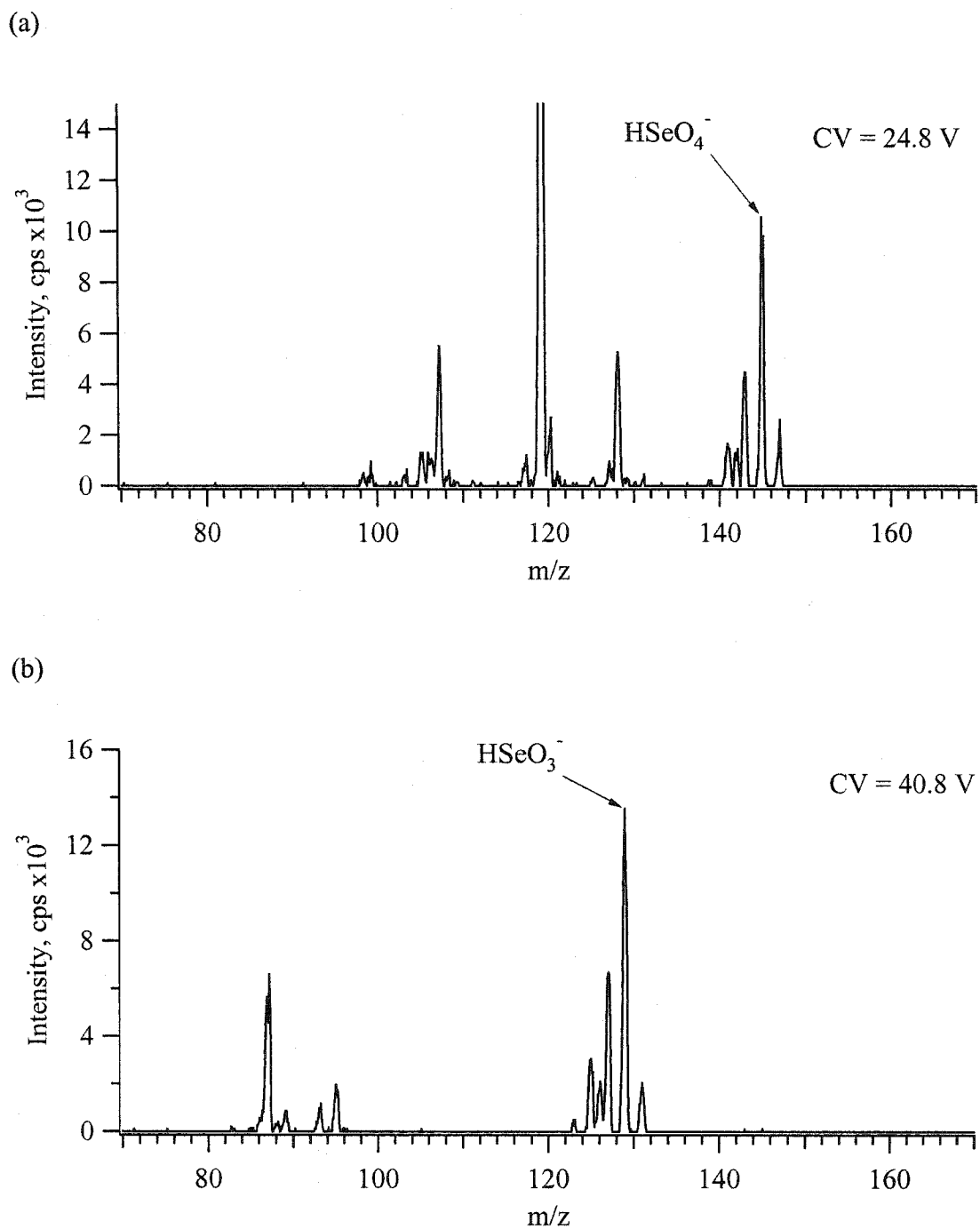


Figure 7.30 Mass spectra from a solution containing Na_2SeO_3 , Na_2SeO_4 , NaH_2AsO_4 , and selenomethionine, each at $0.1 \mu\text{M}$, with 0.4 mM KOH in 100% water solvent. Conditions as in Figure 7.29; $\text{DV} = -3.5 \text{ kV}$, $F_{\text{OR}} = -10 \text{ V}$, drift gas $\sim 5\% \text{ CO}_2$, $95\% \text{ N}_2$. (a) $\text{CV} = 24.8 \text{ V}$; (b) $\text{CV} = 40.8 \text{ V}$.

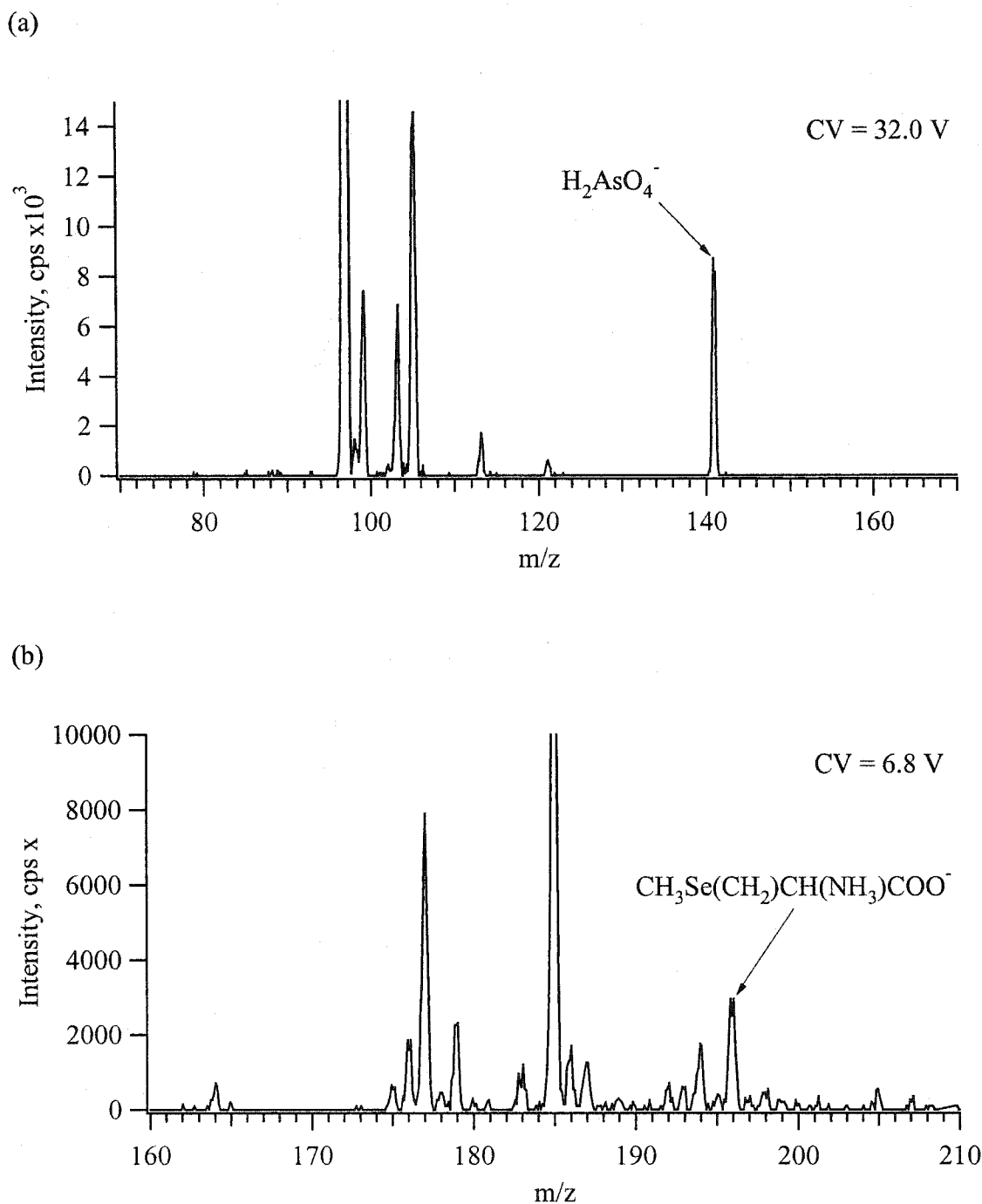


Figure 7.31 Mass spectra from a solution containing Na_2SeO_3 , Na_2SeO_4 , NaH_2AsO_4 , and selenomethionine, each at $0.1 \mu\text{M}$, with 0.4 mM KOH in 100% water solvent. Conditions as in Figure 7.29; $\text{DV} = -3.5 \text{ kV}$, $\text{FOR} = -10 \text{ V}$, drift gas $\sim 5\% \text{ CO}_2$, $95\% \text{ N}_2$. (a) $\text{CV} = 32.0 \text{ V}$; (b) $\text{CV} = 6.8 \text{ V}$.

spectra are relatively free of ions in the mass range of the species, with the exception of selenomethionine.

Setting the CV to the appropriate value, 60 replicate readings were measured for each of the major species for each standard solution. Each mass-selected CV peak was monitored in peak hopping mode for the major m/z of each species (m/z 129, 141, 145, and 196), taking about one minute per CV peak. From these results, the average intensity and the standard deviation were determined, and standard curves were plotted. Blank data were acquired at a CV voltage corresponding to each analyte CV peak while sampling a matrix of 0.4 mM KOH. The data were blank - corrected, and the plots were forced through zero to correct any minor bias in the y-intercept. The equations of the curves are presented in Table 7.03. For each ion, the curves were linear ($R^2 > 0.998$) over the concentration range. Using the blank data, detection limits based on 3 times the standard deviation (3σ) were determined. The detection limits were ~ 0.9 nM (at m/z 129) for HSeO_3^- , ~ 3 nM (at m/z 141) for H_2AsO_4^- , ~ 7 nM (at m/z 196) for selenomethionine, and ~ 0.3 nM (at m/z 145) for HSeO_4^- . The R^2 of the calibration curves suggests that this calibration is linear, but does not indicate how well that it might be applied for accurate quantitation. To get a better idea of the true linear range of these data, the measured signal intensity was divided by the concentration, and plotted as a function of the $\log(\text{concentration})$. Figure 7.32 is the plot for HSeO_4^- at m/z 145, and is very similar to the plots for the other ions tested. The line R_c , indicates the line of constant response, and the dashed lines indicate 5% tolerance on each side of this line. Standards from 1 nM to 10 μM were measured, and only a narrow range of concentrations demonstrated consistent response, as indicated by the values within the 5% tolerance. This indicates that the response is linear only between 0.05 μM and 1 μM . Also, the curve indicates that at low concentration, the signal response would indicate concentrations higher than actually present in solution. With these limited data, it is unclear whether this represents a problem inherent to the system (i.e., problems with the aqueous ESI source), or if the low concentration determinations for all of the ions tested are simply contaminated. This highlights the need for using some sort of internal standard to improve the accuracy of

Ion	m/z	Equation of Line*	$3\sigma_{\text{blank}}$ (cps)	Detection Limit (nM)
HSeO ₃ ⁻	129	$y = 1.28 \times 10^5 [X] \quad R^2 = 0.999$	112	0.88
	127	$y = 6.74 \times 10^4 [X] \quad R^2 = 0.998$	56	0.83
HSeO ₄ ⁻	145	$y = 9.09 \times 10^4 [X] \quad R^2 = 1.00$	22	0.24
	143	$y = 4.21 \times 10^4 [X] \quad R^2 = 1.00$	21	0.50
H ₂ AsO ₄ ⁻	141	$y = 8.62 \times 10^4 [X] \quad R^2 = 0.999$	266	3.1
CH ₃ Se(CH ₂)CH(NH ₃)COO ⁻	196	$y = 2.93 \times 10^4 [X] \quad R^2 = 1.00$	196	6.7
	194	$y = 1.38 \times 10^4 [X] \quad R^2 = 1.00$	156	11

* [X] is the solution ion concentration in μM ; y is the resultant intensity in cps.

Table 7.03 Figures of merit for the measurement of selected ions by ESI-FAIMS-MS in 100% water solution.

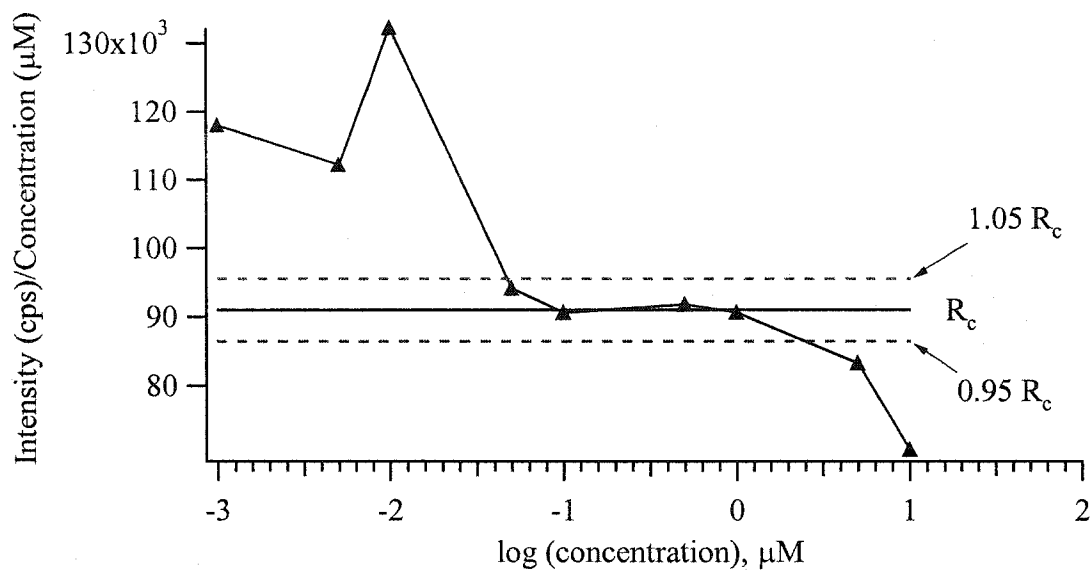


Figure 7.32 Linear range of HSeO_4^- at m/z 145. Intensity (cps) / concentration (μM) as a function of $\log(\text{concentration})$. R_c is the line of constant response. Linear range of response is within $0.95 R_c$ and $1.05 R_c$.

the quantitation, especially at the low end. However, using an internal standard with FAIMS would likely be difficult, due to the variation in signal intensity as a function of CV and the possibility of ion repulsion effects within the FAIMS itself for ions with an overlapping CV window. Standard addition techniques may be more successful; however, the response must linear under the concentration range of interest.

7.3.8 Comment on ESI-FAIMS-MS as a Tool for Speciation

The ability of FAIMS to separate species with similar or identical m/z while maintaining good signal intensity is critical to this study. In fact, peaks in the mass-selected CV spectra at CVs other than those identified as analyte-specific species represent isobaric interferences that would have interfered with the observation of these species by ESI-MS alone. Without this ion-filtering mechanism, these low-intensity ions would have surely been missed due to spectral overlap interferences. Classic chromatography in-line with the ESI-MS may have helped to further reduce the spectral background, provided that the background ions observed in the mass spectrum are due to solution ions that could be separated from the analyte-specific species. Other techniques such as MS/MS can often be employed to reduce the spectral background; however, typically only a single m/z is selected, so the resultant spectra would not display a correct isotopic ratio. Also, species with the same m/z as the target species will complicate the interpretation of the resultant spectrum. In the case of the Se species, the CV spectra displayed several peaks at a variety of CVs that were investigated for the presence of a Se isotopic pattern. Without this pattern, identification would be very difficult with this mass spectrometer.

It is unclear here whether or not the species observed represent solution species or are generated in the gas phase. In order to clarify this, putting a classical solution-based separation in front of the ESI may help. However, the FAIMS is a relatively slow scanning interface, so for an on-line analysis to occur, the chromatography peak widths would have to be fairly wide, and the MS would likely have to be a faster scanning instrument (e.g., TOF). One estimate of the time required for scanning a CV range of

~15V (in 0.2 V steps) with TOF detection (1000 amu window) is ~ 3 minutes per CV scan [28]. Obviously, 3 minutes per data point for on-line chromatography would be unacceptable, and this type of "full CV scan" operation would be applicable only for continuous infusion experiments. If the FAIMS could be scanned over a smaller CV window, and if the MS scan times could be reduced, some applications of this on-line configuration may be possible (i.e., target analysis). However, fractionation of the chromatographic peaks combined with continuous infusion of a sample to the ESI source would be much better when a range of CVs are to be examined (i.e., for novel species identification).

7.4 Conclusions

It was demonstrated that the application of an ESI source capable of electrospraying purely aqueous matrices could be used with the FAIMS. The performance of the source demonstrated similar signal stability to a classic ESI source when using methanol. Also, the gas-phase species that survived transmission through the FAIMS seemed to be the same, although the signal intensities observed with the aqueous ESI interface were lower than with the classic interface using methanol.

The combination of ion filtering and the ability of FAIMS to separate gas-phase ions allowed for the identification of several different species in the gas phase. Without the FAIMS, this information would not be available, since the observed ions may have been attributed to species generated by CID in the MS interface. However, concerns were raised that some ions may fragment during FAIMS sampling, which may either result in these ions getting filtered out or generating unexpected fragment ions in the mass-selected CV spectrum. The addition of CO₂ to the drift gas prevented the observation of some species, presumably due to the prevention of ion fragmentation in the FAIMS sampling interface.

The ion filtering mechanism can (in some cases) reduce the level of background ions in the spectral region of interest, which can allow for detection of very low intensity species, as demonstrated in the selenite studies. Some ions were demonstrated to have low detection limits, although some concerns regarding the linearity of an external calibration without an internal standard were raised. In any case, the potential for a low spectral background combined with good signal intensity, should make this technique a significant advance for ESI-MS studies, especially when trying to identify novel species.

7.5 References

1. Caruso, J.; Sutton, K.; Ackley, K. *Elemental Speciation: New Approaches for Trace Element Analysis*; Elsevier: New York, 2000.
2. Caroli, S.; la Torre, F.; Petrucci, F.; Violante, N. In *Element Speciation in Bioorganic Chemistry*; Caroli, S., Ed.; John Wiley & Sons, Inc.: Toronto, 1996; Vol. 135, pp 445-463.
3. Cech, N. B.; Enke, C. G. "Relating electrospray ionization response to nonpolar character of small peptides"; *Anal. Chem.* **2000**, *72*, 2717-2723.
4. Rundlett, K. L.; Armstrong, D. W. "Mechanism of signal suppression by anionic surfactants in capillary electrophoresis-electrospray ionization mass spectrometry"; *Anal. Chem.* **1996**, *68*, 3493-3497.
5. Tang, K.; Smith, R. D. "Physical / chemical separations in the break-up of highly charged droplets from electrosprays"; *J. Am. Soc. Mass Spectrom.* **2001**, *12*, 343-347.
6. Avakov, A. S.; Buryakov, I. A.; Krylov, E. V.; Nazarov, E. G.; Rasulev, U. K.; Soldatov, V. P. "Proceedings of the Eighth All-Union Conference"; *Physics of Low-Temperature Plasmas.*, , 1997.
7. Buryakov, I. A.; Krylov, E. V.; Soldatov, V. P. "Inventor's Certificate (USSR) No. 1485808 [in Russian], G01 No. 27/62"; *Byull. Izobret.* **1989**. USSR. No. 1485808.
8. Buryakov, I. A.; Krylov, E. V.; Makas', A. L.; Nazarov, E. G.; Pervukhin, V. V.; Rasulev, U. K. "Separation of ions according to mobility in a strong AC electric field"; *Sov. Tech. Phys. Lett.* **1991**, *17*, 446-447.
9. Buryakov, I. A.; Krylov, E. V.; Nazarov, E. G.; Rasulev, U. K. "A new method of separation of multi-atomic ions by mobility at atmospheric pressure using a high-frequency amplitude-asymmetric strong electric field"; *Int. J. Mass Spectrom. Ion Proc.* **1993**, *128*, 143-148.
10. Carnahan, B. L.; Tarassov, A. S. "Ion Mobility Spectrometer"; **1995**, Mine Safety Appliances Company, Pittsburgh, Pa. United States. Patent No. 5 420 424.

11. Carnahan, B.; Day, S.; Kouznetsov, V.; Matyjaszczyk, M.; Tarassov, A. "Proceedings of the 41st Annual ISA Analysis Division Symposium"; *41st Annual ISA Analysis Division Symposium.*, Framingham, MA, April 21-24, 1996.
12. Guevremont, R.; Purves, R. W. "Atmospheric pressure ion focusing in a high-field asymmetric waveform ion mobility spectrometer"; *Rev. Sci. Instrum.* **1999**, *70*, 1370-1383.
13. Guevremont, R.; Purves, R. W.; Barnett, D. A.; Ding, L. "Ion trapping at atmospheric pressure (760 Torr) and room temperature with a high-field asymmetric waveform ion mobility spectrometer"; *Int. J. Mass Spectrom.* **1999**, *193*, 45-56.
14. Guevremont, R.; Purves, R. W. "High field asymmetric waveform ion mobility spectrometry-mass spectrometry: An investigation of leucine enkephalin ions produced by electrospray ionization"; *J. Am. Soc. Mass Spectrom.* **1999**, *10*, 492-501.
15. Guevremont, R.; Purves, R. "Apparatus and method for atmospheric pressure 3-dimensional ion trapping"; *Canadian Intellectual Property Office* **1999**. Canada. Canadian Patent No. 2,339,548.
16. Guevremont, R.; Purves, R. "Apparatus and method for desolvating and focussing ions for introduction into a mass spectrometer"; *Canadian Intellectual Property Office* **1999**. Canada. Canadian Patent No. 2,273,322.
17. Guevremont, R.; Purves, R.; Barnett, D. A. "Method for separation and enrichment of isotopes in gaseous phase"; *Canadian Intellectual Property Office* **1999**. Canada. Canadian Patent No. 2,339,549.
18. Guevremont, R.; Purves, R.; Barnett, D. A. "Method for separation of isomers and different conformations of ions in gaseous phase"; *Canadian Intellectual Property Office* **1999**. Canada. Canadian Patent No. 2,339,553.
19. Purves, R. W.; Day, S.; Pipich, C. W.; Matyjaszczyk, M. S.; Guevremont, R. "Mass spectrometric characterization of a high-field asymmetric waveform ion mobility spectrometer"; *Rev. Sci. Instrum.* **1998**, *69*, 4094-4105.

20. Purves, R. W.; Guevremont, R. "Electrospray ionization high-field asymmetric waveform ion mobility spectrometry-mass spectrometry"; *Anal. Chem.* **1999**, *71*, 2346-2357.
21. Purves, R. W.; Barnett, D. A.; Ells, B.; Guevremont, R. "Elongated conformers of charge states +11 to +15 of bovine ubiquitin studied using ESI-FAIMS-MS"; *J. Am. Soc. Mass Spectrom.* **2001**, *12*, 894-901.
22. Purves, R. W.; Barnett, D. A.; Ells, B.; Guevremont, R. "Gas phase conformers of the $[M+2H]^{2+}$ of bradykinin investigated by combining high-field asymmetric waveform ion mobility spectrometry, hydrogen / deuterium exchange, and energy loss measurements"; *Rapid Comm. Mass Spectrom.* **2001**, *15*, 1453-1456.
23. Purves, R. W.; Barnett, D. A.; Guevremont, R. "Separation of protein conformers using electrospray-high field asymmetric waveform ion mobility spectrometry-mass spectrometry"; *Int. J. Mass Spectrom.* **2000**, *197*, 163-167.
24. Purves, R. W.; Barnett, D. A.; Ells, B.; Guevremont, R. "Investigation of bovine ubiquitin conformers separated by high-field asymmetric waveform ion mobility spectrometry: Cross section measurements using energy-loss experiments with a triple quadrupole mass spectrometer"; *J. Am. Soc. Mass Spectrom.* **2000**, *11*, 738-745.
25. Purves, R. W.; Barnett, D. A.; Guevremont, R. "Separation of protein conformers using electrospray-high-field asymmetric waveform ion mobility spectrometry-mass spectrometry"; *Int. J. Mass Spectrom.* **2000**, *197*, 163-177.
26. McCooeye, M. A.; Ells, B.; Barnett, D. A.; Purves, R. W.; Guevremont, R. "Quantitation of morphine and codeine in human urine using high-field asymmetric waveform ion mobility spectrometry (FAIMS) with mass spectrometric detection"; *J. Anal. Tox.* **2001**, *25*, 81-87.
27. Handy, R.; Barnett, D. A.; Purves, R. W.; Horlick, G.; Guevremont, R. "Determination of nanomolar levels of perchlorate in water by ESI-FAIMS-MS"; *J. Anal. At. Spectrom.* **2000**, *15*, 907-911.
28. Guevremont, R.; Barnett, D. A.; Purves, R. W.; Vandermeij, J. "Analysis of a tryptic digest of pig hemoglobin using ESI-FAIMS-MS"; *Anal. Chem.* **2000**, *72*, 4577-4584.

29. Ells, B.; Barnett, D. A.; Purves, R. W.; Guevremont, R. "Trace level determination of perchlorate in water matrices and human urine using ESI-FAIMS-MS"; *J. Environ. Monit.* **2000**, *2*, 393-397.
30. Ells, B.; Froese, K.; Hrudey, S. E.; Purves, R. W.; Guevremont, R.; Barnett, D. A. "Detection of microcystins using electrospray ionization high-field asymmetric waveform ion mobility mass spectrometry / mass spectrometry"; *Rapid Commun. Mass Spectrom.* **2000**, *14*, 1538-1542.
31. Ells, B.; Barnett, D. A.; Purves, R. W.; Guevremont, R. "Detection of nine chlorinated and brominated haloacetic acids at part-per-trillion levels using ESI-FAIMS-MS"; *Anal. Chem.* **2000**, *72*, 4555-4559.
32. Ells, B.; Barnett, D. A.; Froese, K.; Purves, R. W.; Hrudey, S.; Guevremont, R. "Detection of chlorinated and brominated byproducts of drinking water disinfection using electrospray ionization-high-field asymmetric waveform ion mobility spectrometry-mass spectrometry"; *Anal. Chem.* **1999**, *71*, 4747-4752.
33. Barnett, D. A.; Purves, R. W.; Ells, B.; Guevremont, R. "Separation of *o*-, *m*- and *p*-phthalic acids by high-field asymmetric waveform ion mobility spectrometry (FAIMS) using mixed carrier gases"; *J. Mass Spectrom.* **2000**, *35*, 976-980.
34. Barnett, D. A.; Purves, R. W.; Guevremont, R. "Isotope separation using high-field asymmetric waveform ion mobility spectrometry"; *Nuc. Instrum. Meth. Phys. Res. A* **2000**, *450*, 179-185.
35. Barnett, D. A.; Ells, B.; Purves, R. W.; Guevremont, R. "Separation of leucine and isoleucine by electrospray ionization-high field asymmetric waveform ion mobility spectrometry-mass spectrometry"; *J. Am. Soc. Mass Spectrom.* **1999**, *10*, 1279-1284.
36. Barnett, D. A.; Guevremont, R.; Purves, R. W. "Determination of parts-per-trillion levels of chlorate, bromate, and iodate by electrospray ionization/high-field asymmetric waveform ion mobility spectrometry/mass spectrometry"; *Appl. Spectrosc.* **1999**, *53*, 1367-1374.
37. Barnett, D. A.; Horlick, G. "Quantitative electrospray mass spectrometry of halides and halogenic anions"; *J. Anal. At. Spectrom.* **1997**, *12*, 497-501.

38. Gorshkov, M. P. "Inventors Certificate (USSR) No. 966583"; *Byull. Izobret.* **1982**. USSR. No. 966583.
39. Mason, E. A.; McDaniel, E. W. *Transport Properties of Ions in Gases*; John Wiley & Sons, Inc., 1988.
40. Barnett, D. A.; Ells, B.; Guevremont, R.; Purves, R. W.; Viehland, L. A. "Evaluation of carrier gases for use in high-field asymmetric waveform ion mobility spectrometry"; *J. Am. Soc. Mass Spectrom.* **2000**, 11, 1125-1133.
41. Barnett, D. A. Ph. D. Thesis, University of Alberta, Edmonton, Alberta, 1999.
42. Gailer, J.; Madden, S.; Cullen, W. J.; Denton, M. B. "The separation of dimethylarsinic acid, methylarsonous acid, methylarsonic acid, arsenate and dimethylarsinous acid on the Hamilton PRP-X100 anion-exchange column"; *Appl. Organometal. Chem.* **1999**, 13, 837-843.

Chapter 8

Low CID Sampling Conditions in the MS Interface Using ESI-FAIMS-MS

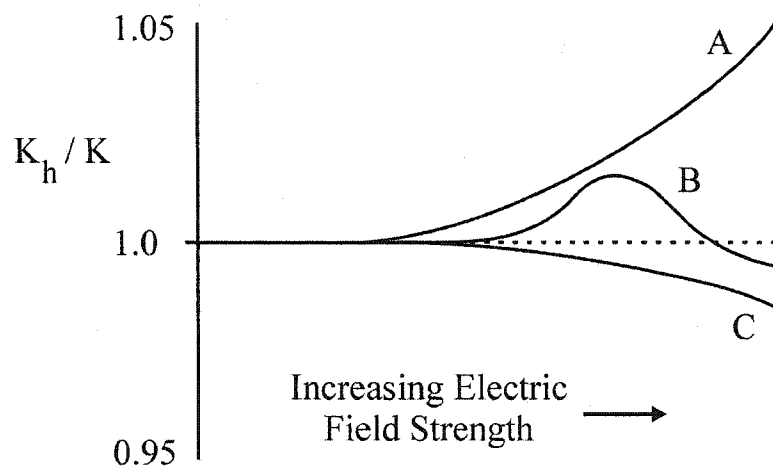
8.1 Introduction

Recently, a technique called high-field asymmetric waveform ion mobility spectrometry (FAIMS) has been developed [1-15]. The development of FAIMS in the 1980s was based on an ion's changing mobility at atmospheric pressure with high applied field [2, 13]. Under the influence of a low applied field ($E < \sim 200$ V/cm), an ion's mobility is essentially constant, whereas at higher applied fields, the mobility varies as a function of the field magnitude [16]. Expressing the change in mobility as a ratio of high-field mobility (K_h) to low-field mobility (K), K_h/K , an ion's experimental behavior can be classified as three general types, as shown in Figure 8.01 (a). As the applied field strength increases, an ion's mobility can either increase (type A), decrease (type C), or show a more complex behavior (type B) [15]. Also, ions with similar mobility behavior (i.e., two type A ions) may have a different dependence of their K_h/K in response to a high applied field, as hypothetically illustrated in Figure 8.01 (b).

Since the FAIMS separates ions based on their difference in K_h/K , factors affecting the mobility of the ion are important for tuning a separation. In particular, previous work has demonstrated that changing the drift gas composition is an effective way to control the separation of ions within the FAIMS [17-21]. The curves in Figure 8.02 illustrate how the K_h/K of an ion may be affected by using a different drift gas composition. In this hypothetical example, the same ion exhibits variable K_h/K behavior in drift gas types X, Y, and Z. The K_h/K response is a type A behavior in gases X and Y, but exhibits type C behavior in gas Z. These types of changes in mobility with varying drift gas composition have been described, even with monatomic ions [17].

One drift gas that seems particularly interesting is CO_2 . Applications using CO_2 in the drift gas have demonstrated that small amounts of CO_2 added to the drift gas can cause significant changes in the observed CV of an ion [18]. In addition to using CO_2 to optimize the separation of ions, a closer study of the effect of CO_2 on the K_h/K of selected ions was investigated. Evidence of gas-phase complexes of Cs^+ and CO_2 was noted, and further studies demonstrated that mixtures of N_2 and CO_2

(a)



(b)

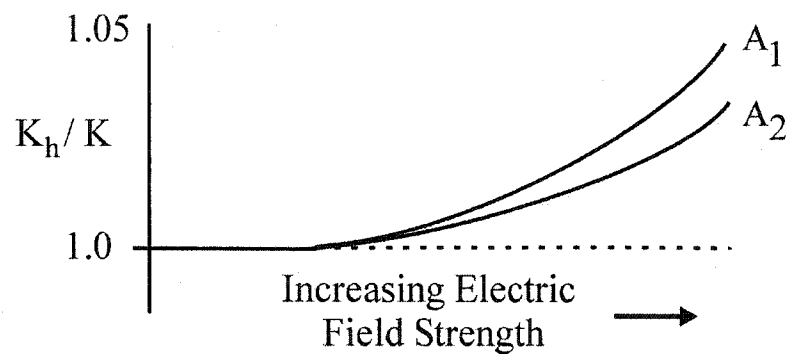


Figure 8.01 Ion mobility behavior (K_h/K) in response to increasing applied electric field strength. K_h = high field mobility. K = low field mobility. (a) General mobility behaviors; type A = increasing mobility with increasing applied field. Type B = complex mobility dependence with applied field; initially increasing, then decreasing with higher applied field. Type C = decreasing mobility with increasing applied field; (b) Two different hypothetical ions with type A mobility, A_1 and A_2 .

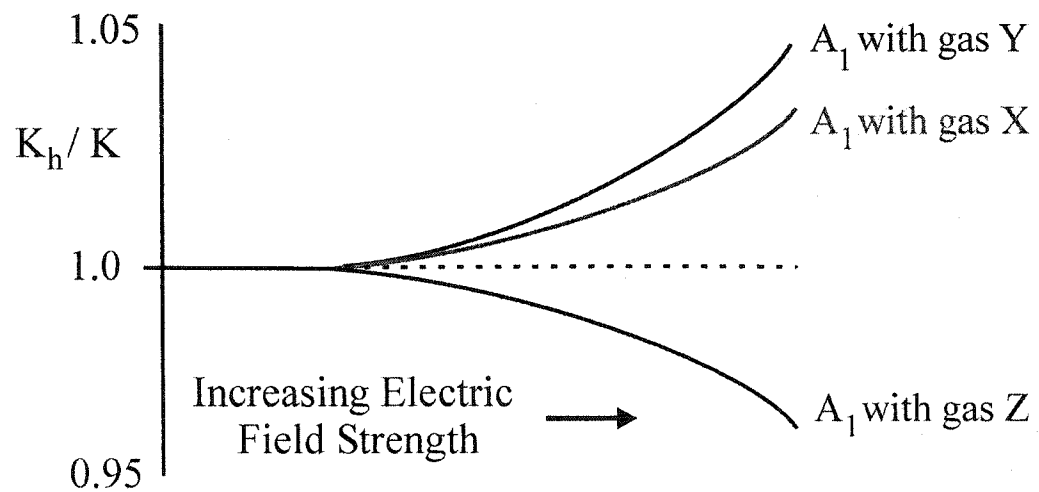


Figure 8.02 Theoretical variation of ion mobility in response to increasing electric field strength. The same ion, A_1 , in three different drift gas compositions, X, Y and Z.

could cause CV shifts that were greater than could be observed in either pure gas [17, 18]. Another interesting effect of CO₂ was that it was observed to prevent the fragmentation of certain ions during sampling into the mass spectrometer [18].

This previous work was the impetus to do some preliminary studies on how the addition of CO₂ might affect the observed mass spectra, especially in regards to adducts. If CO₂ does form adducts in the FAIMS, the addition of CO₂ may result in some adducts that may be observed in the mass spectrum. A demonstration of the spectral quality when using low energy CID sampling conditions in the MS interface is presented. Using these low energy CID sampling conditions, basic studies were done to examine the effects of a N₂ and a CO₂/N₂ drift gas mixture on the mass spectra for some Group I cations and some of the halides. The effects of the CO₂ were then examined for selected anions, including arsenite and hypochlorite.

8.2 Experimental

8.2.1 ESI-FAIMS-MS

The work presented in the following sections was done using a dome FAIMS interface, as designed by Guevremont, and manufactured by Sciex (Concord, ON, Canada) [8-10]. A detailed description of this interface is found in Chapter 4. The MS used was an API-150EX from MDS-Sciex (Concord, Ontario, Canada), and is a single quadrupole instrument with a mass range of 30 - 3000 m/z. Ions sampled into the MS could be declustered or fragmented by collision-induced dissociation (CID) in the MS interface region by applying a potential difference between the orifice (OR) and the skimmer (SK). As illustrated in Figure 8.03, the commercial ion source and curtain plate were removed from the MS, and the FAIMS was mounted to the MS orifice plate. The thickness of the mounting ring was designed to let the flat face of the FAIMS outer electrode to be placed flush against the flat orifice of the MS. The contact between the outer FAIMS cylinder and the MS sampling orifice (OR) means that both of these parts

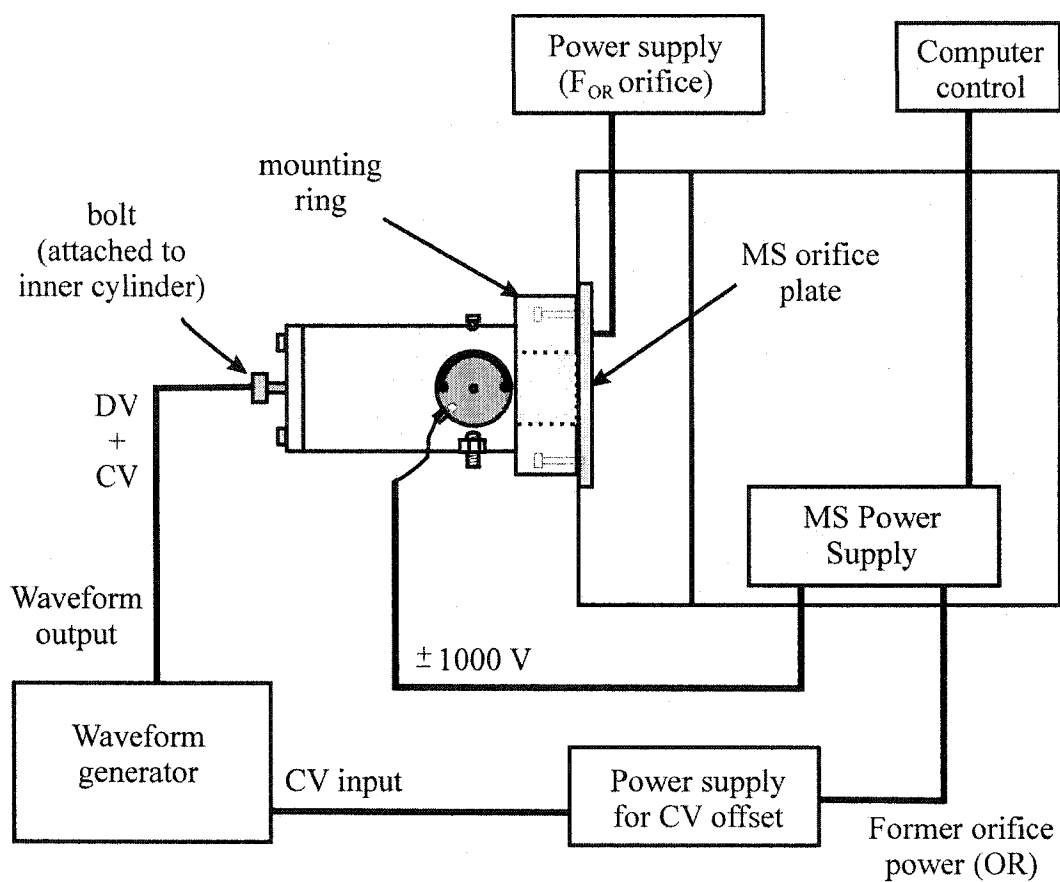


Figure 8.03 Electrical connections for the FAIMS-MS interface.

will be biased to the same potential. An external power supply (Xantrex XT-120-0.5 Regulated DC Power Supply) was used to set this voltage, instead of using the MS power supply to do so. In this configuration, the outer FAIMS electrode and the orifice were manually set to a constant voltage (F_{OR}). For experiments described in this work, the MS orifice plate and the outer FAIMS electrode were biased to 0 V ($F_{OR} = 0$ V), unless otherwise noted. Under these sampling conditions, there was no potential difference between the sampling orifice and the skimmer, and the relative degree of declustering and fragmentation of ions in the MS interface was minimized.

This FAIMS incorporates a waveform generator powered using an external power supply (GW Laboratory Power Supply Model GPC-3030D Dual Tracking with 5V Fixed). The asymmetric waveform that was synthesized is shown in Figure 8.04. The frequency of the waveform was 750 kHz, and the voltage symmetry of the waveform was roughly 2:1 high:low. The amplitude of the waveform is characterized by the amplitude of the high voltage peak, called the dispersion voltage (DV). For small, positive ions, the DV polarity was positive (Figure 8.04 (a), P1-N2 waveform). For small, negative ions, the N1-P2 waveform was used (Figure 8.04 (b)), which has a negative DV polarity. Unless otherwise specified, the waveform DV was maintained at 3.5 kV (of suitable polarity). The symmetry and voltages of the waveform were measured using a LeCroy 9310M Dual 300 MHz Oscilloscope (100 Ms/s, 50 kpts/ch). As illustrated in Figure 8.03, this waveform was applied to the inner cylinder electrode of the FAIMS.

To balance an ion's trajectory through the FAIMS in response to the applied DV, a DC potential called the compensation voltage (CV) was applied to the inner cylinder of the FAIMS (Figure 8.03). The MS power connection (formerly for the orifice) was re-routed to the waveform generator to act as the CV power supply. By routing the former orifice power connection to the CV input of the waveform generator, the CV could be scanned by using the existing computer software. By putting an additional power supply (Xantrex XT-120-0.5 Regulated DC Power Supply) in series with the MS and the generator CV input, a voltage offset could be added. Since the software only

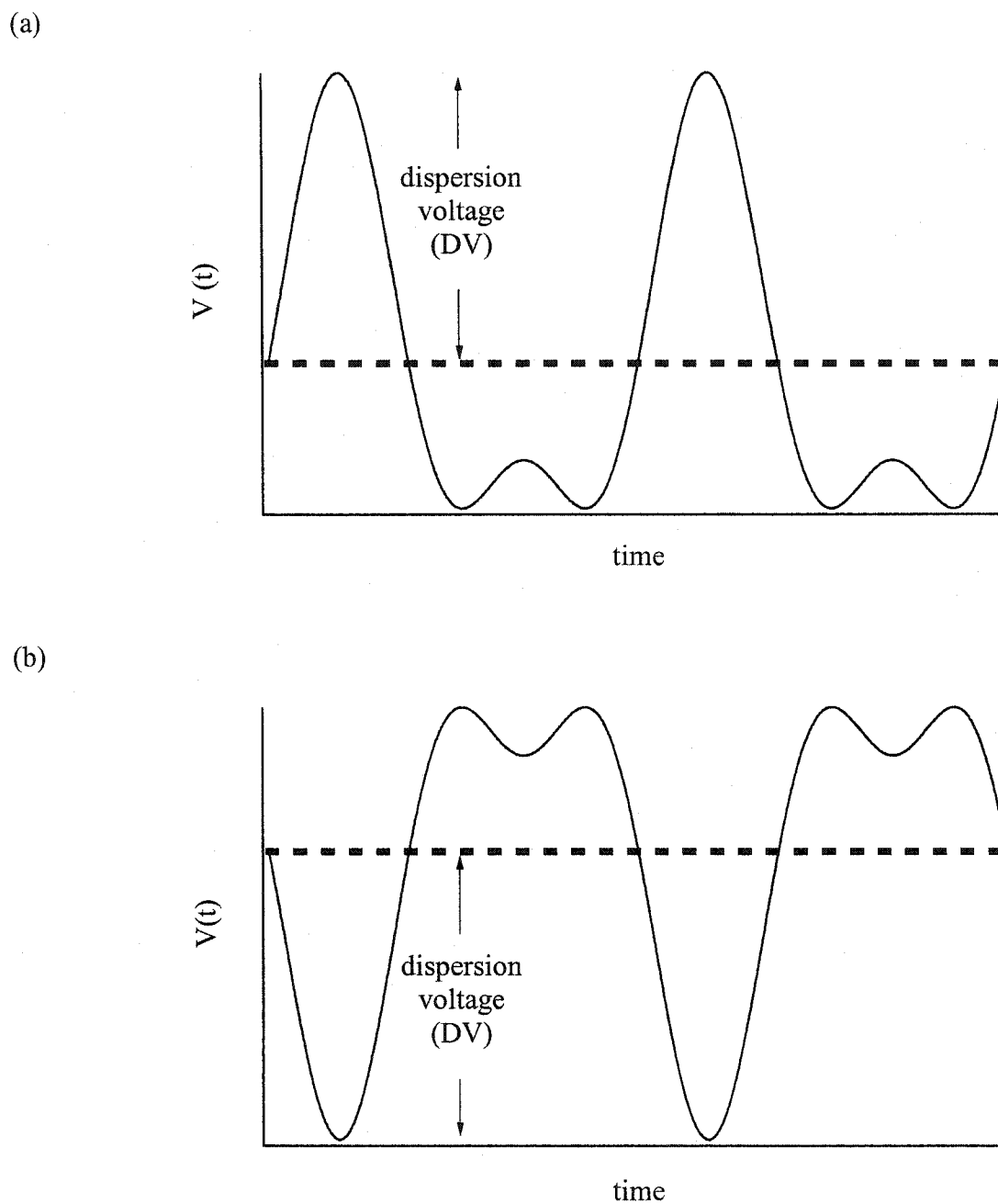


Figure 8.04 The asymmetric waveforms used in FAIMS; (a) the P1-N2 waveform, (b) the N1-P2 asymmetric waveform.

allows the computer-set voltage polarity to match the polarity of the MS scan, this offset becomes necessary when opposite CV polarity was required.

A pair of rotamers (Gilmont Instruments, 0 – 5 SLPM Air) were used to set the curtain gas flow rate. Previous tests were done to calibrate these meters for N₂ and CO₂. Downstream of the flow meter, gas purifiers consisting of a combination of activated charcoal and a molecular sieve were used. Unless otherwise specified, the flow of the curtain gas was 2.0 L/min.

Figure 8.05 illustrates how an ion may be sampled during a FAIMS experiment using the dome prototype. The curtain gas was introduced to the FAIMS between the curtain plate and the sampling orifice in the wall of the outer cylinder. The ESI generated ions are moved towards the sampling orifice of the FAIMS by the potential difference, and undergo typical droplet fissions and desolvation during the trip to the orifice. The bulk of the curtain gas exits the FAIMS through the curtain plate orifice and assists in the desolvation of the ESI-generated ions. The remainder of the curtain gas comprises the drift gas for the FAIMS experiment. Since the MS orifice is constantly sampling gas (at about 0.56 L/min for this system), gas is drawn from the curtain gas inlet region and into the FAIMS analyzer region. So, as ions enter the FAIMS analyzer region, they are transported by the gas towards the MS orifice. If the combination of DV and CV are appropriate, the ion will not strike a wall and will be successfully transported by the gas flow to the MS orifice. Note that for these tests, the pressure port was closed off, and there was no gas flow through this opening.

8.2.2 ESI Sources

The ESI sources used in this study were in-house designed interfaces. For the methanol solvent studies, the ESI source consisted of a fused silica capillary (150 μm OD, 50 μm ID) of about 45 cm length, with one end extending from a stainless steel capillary sheath (0.018" OD, 0.009" ID), as illustrated in Figure 8.06 (a). The extension of the FSC tip from the tip of the metal capillary was adjusted to provide a stable ESI

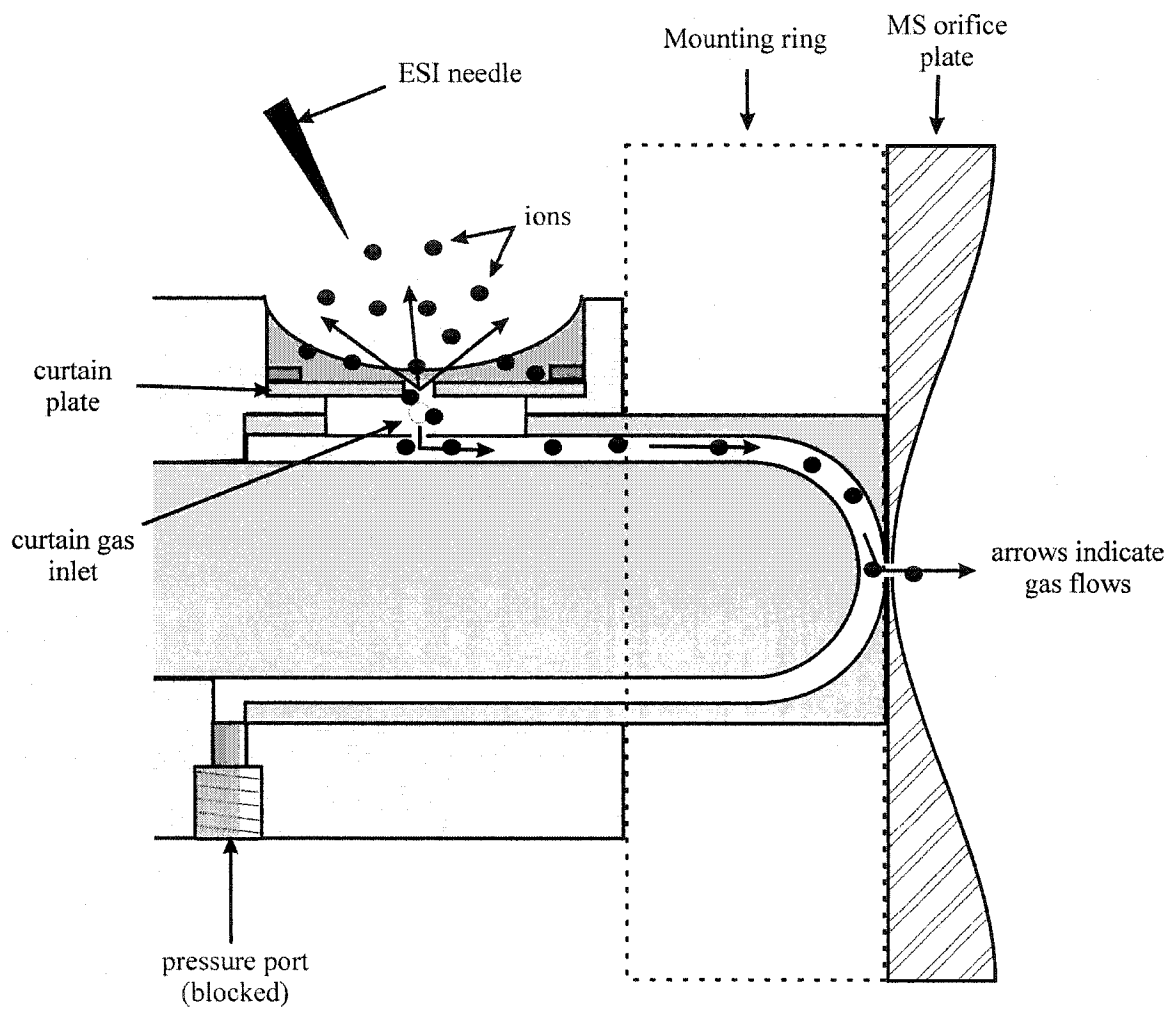


Figure 8.05 Cross-section of an ESI-FAIMS-MS interface.

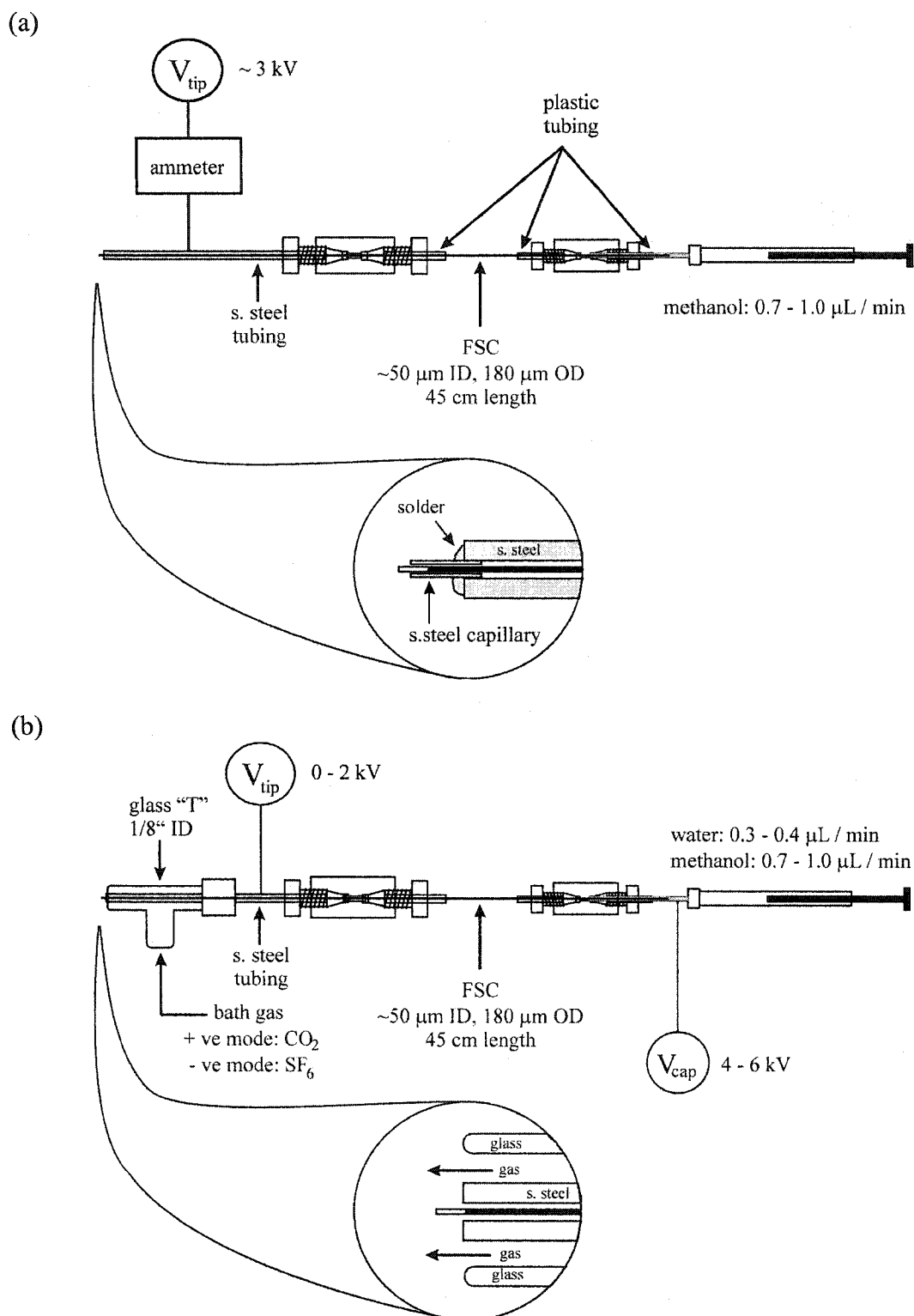


Figure 8.06 Two ESI interfaces; (a) typical interface for methanolic solvents, (b) interface for ESI of purely aqueous solvents.

operation. The tip was placed about 1 cm away from the curtain plate of the FAIMS, and was at an angle of about 45° . An in-house built floating digital ammeter with nanoampere sensitivity was placed in-line with the power supply and the tip. Both the magnitude and stability of the electrospray current was used to fine-tune the electrospray conditions. To generate ions, a power supply was used to bias the metal capillary to a voltage of about 3 kV in positive ion mode or about -3 kV in negative ion mode, drawing a current of about 50 nA during stable ESI operation. From the other end of the capillary, the sample solution was delivered at about 0.83 $\mu\text{L}/\text{min}$ using a Cole-Parmer 74900 Series syringe pump and a Hamilton 250 μL syringe.

The electrospray interface used for purely aqueous sample matrices is shown in Figure 8.06 (b). A syringe pump and a 250 μL syringe with a stainless steel needle were used to deliver solution through a fused silica capillary with approximate dimensions of 50 μm ID, 150 μm OD, and 45 cm in length. The fused silica capillary was a continuous piece that began from inside the syringe needle and terminated as the ES tip. The polyimide coating was removed from the tip to remove any rough edges due to the coating, and the fused silica capillary was positioned to extend about 2 mm from the stainless steel support tubing. The only electrical contact with the solution was at the syringe needle. An ammeter with nanoampere sensitivity was added in series with the power supply and the needle contact in order to monitor the current. A second voltage applied to the stainless steel tubing near the tip enhanced sensitivity and stability. Glass tubing (1/8" ID) surrounded the stainless steel support and delivered a bath gas to enshroud the electrospray tip. Using this system, purely aqueous matrices could be reliably electrosprayed, without the help of pneumatic nebulization. For aqueous ESI operation in negative mode, typical parameters were about 0.30 $\mu\text{L}/\text{min}$ solution flow rate, -4 to -6 kV at the syringe needle, and -1 kV at the tip support. The bath gas used was sulfur hexafluoride, SF_6 , at a flow rate of ~ 0.8 L/min.

8.2.3 Reagents

Standard solutions were prepared from the appropriate salt at a concentration of

0.01 M in 18 M Ω de-ionized water. Samples were prepared from dilutions of these standard solutions in the appropriate solvent. HPLC grade methanol (Fisher) was used as received. The metal solutions were prepared from CP (certified pure) grade chloride salts. The halide and hydroxide stocks were prepared from CP grade potassium salts. Reagent grade salt of NaAsO₂ was used. Seleno-DL-methionine (Sigma) was prepared at a stock concentration of 1 mM in de-ionized water. Commercial bleach (5% NaOCl) was used as a source of NaOCl_(aq), and was simply diluted as required. Standard solutions were stored at 4 °C, and the sample dilutions were made fresh as required.

8.3 Results and Discussion

8.3.1 Low CID Sampling for Simple Anions and Cations

Since FAIMS effectively behaves as an atmospheric pressure ion filter, very mild MS interface sampling conditions can be used. The orifice and the skimmer can be biased to zero volts, since many of the background ions and ion clusters may be filtered out by the FAIMS. By doing so, there is no potential difference between the orifice and skimmer, so no additional collision-induced dissociation (CID) is introduced to the ions as they are sampled into the mass spectrometer.

Mass-selected compensation voltage (CV) spectra of a mixture of KCl, RbCl, and CsCl at a concentration of 10 μ M in methanol with 0.4 mM ammonium acetate in N₂ drift gas is presented in Figure 8.07 (a). The dispersion voltage (DV) was set to 3.5 kV, and the FAIMS-orifice voltage (F_{OR}) was set to 0 V. Masses 133, 87, 85, 59, 41, and 39 were monitored in peak hopping mode as the compensation voltage was scanned. Similarly, Figure 8.07 (b) is the mass-selected CV spectra (*m/z* 35, 37, 79, 81, and 127) of a mixture of KCl, KBr, and KI at 10 μ M in methanol with 0.4 mM ammonium acetate in N₂ drift gas. For both the cations and the anions, the major unsolvated species were separated in the gas phase at atmospheric pressure prior to MS sampling. The CV peaks

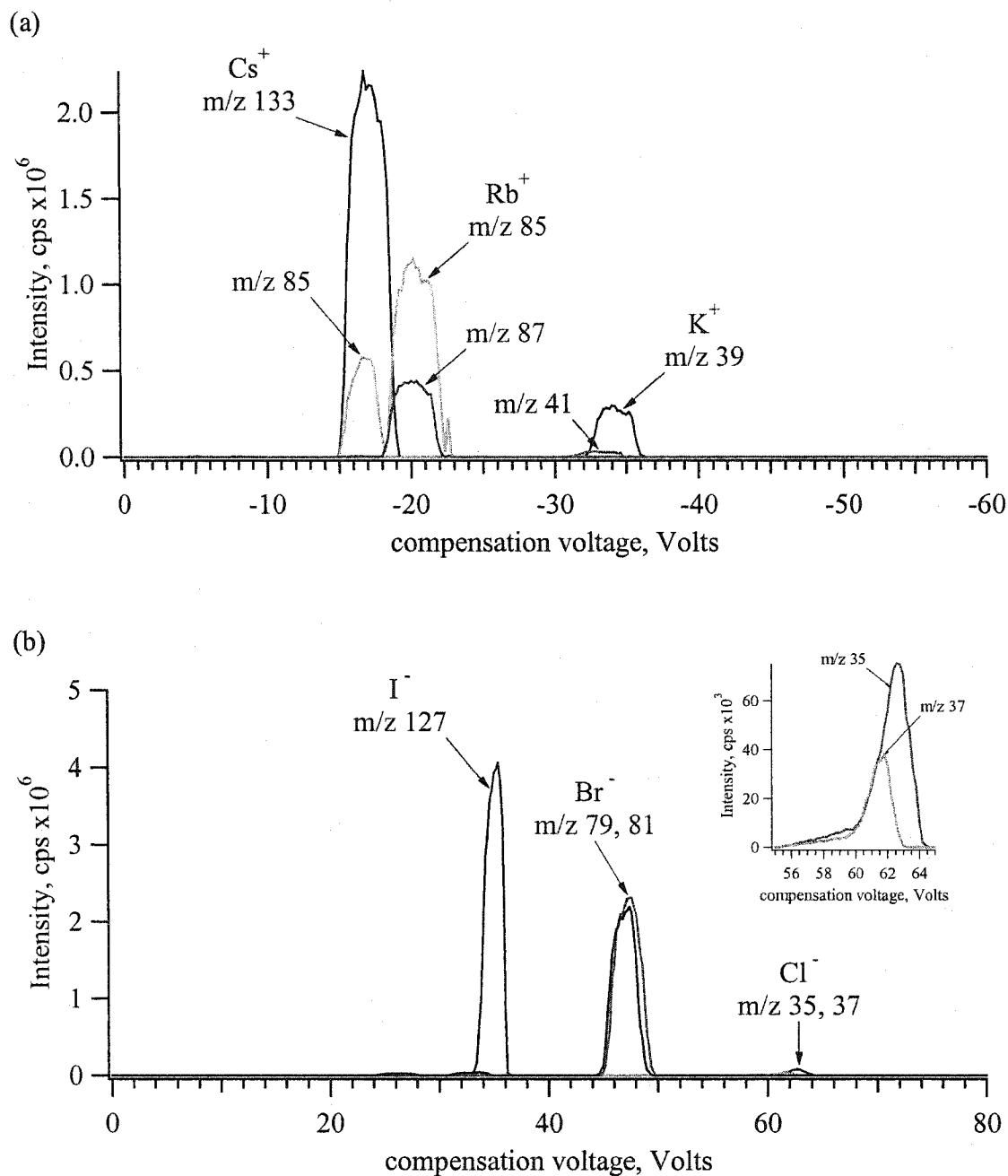


Figure 8.07 Superimposed mass-selected CV spectra. (a) (m/z 39, 41, 59, 85, 87, and 133) in N_2 drift gas of a mixture of KCl , RbCl , and CsCl at $10 \mu\text{M}$ in methanol with 0.4 mM ammonium acetate. $\text{DV} = 3.5 \text{ kV}$, $\text{F}_{\text{OR}} = 0 \text{ V}$; (b) (m/z 35, 37, 79, 81, and 127) in N_2 drift gas of a mixture of KCl , KBr , and KI at $10 \mu\text{M}$ in methanol with 0.4 mM ammonium acetate. $\text{DV} = -3.5 \text{ kV}$, $\text{F}_{\text{OR}} = 0 \text{ V}$.

for Cs^+ and Rb^+ show slight overlap, and an unknown species with m/z 85 appears at the same CV as Cs^+ . However, this m/z 85 species was separated from the $^{85}\text{Rb}^+$.

The CV was set to transmit the mass-selected CV peak maximum of each of the major peaks observed in the mass-selected CV spectrum, and mass spectra were acquired. Figures 8.08 (a), (b), and (c) are the mass spectra for Cs^+ (CV = -17.0V), Rb^+ (CV = -20.4V), and K^+ (CV = -34.2 V), respectively. At each of these CVs, the major species observed is the bare metal ion, M^+ , with a minor contribution from $\text{M}^+(\text{H}_2\text{O})$. No adducts with higher numbers of water ligands were observed in these spectra. Figures 8.09 (a), (b), and (c) are the mass spectra for I^- (CV = 35.4 V), Br^- (CV = 47.2 V), and Cl^- (CV = 62.8 V), respectively. At each of these CVs, the major species observed is the bare anion, X^- , with a minor contribution from $\text{X}^-(\text{H}_2\text{O})$. No adducts with higher numbers of water ligands were observed in these spectra. The relative levels of water adducts were less with the anions than the cations. The poor isotopic pattern for the Cl^- is due to the partial separation of the Cl^- isotopes under these conditions; the m/z 35 and m/z 37 peaks appear at slightly different CVs (62.8 V and 61.8 V, respectively). Since the mass-selected CV peak was sampled at the m/z 35 peak, an isotope bias is observed. Isotope separation has been reported previously with FAIMS [22], and is generally only significant for ions with a high relative mass difference and high K_h/K mobility that require high CVs.

Previous results for both of these groupings of anions and cations with typical ESI-MS using N_2 curtain gas demonstrated that these species are observed with numerous solvated clusters under mild CID conditions [23-25]. Different masses corresponding to the solvated ions were scanned in the CV spectra in separate experiments, but evidence of solvated species was only found at the same CV as the bare ion. This suggests that the peaks observed in the mass-selected CV spectra represent the only analyte-specific species that are transmitted through the FAIMS under these test conditions. Perhaps the solvated clusters that are observed in typical ESI-MS are not stable within the FAIMS analyzer, and are filtered out. Under the influence of the high applied fields, an ion in the FAIMS experiences a high number of collisions. A term called the "effective

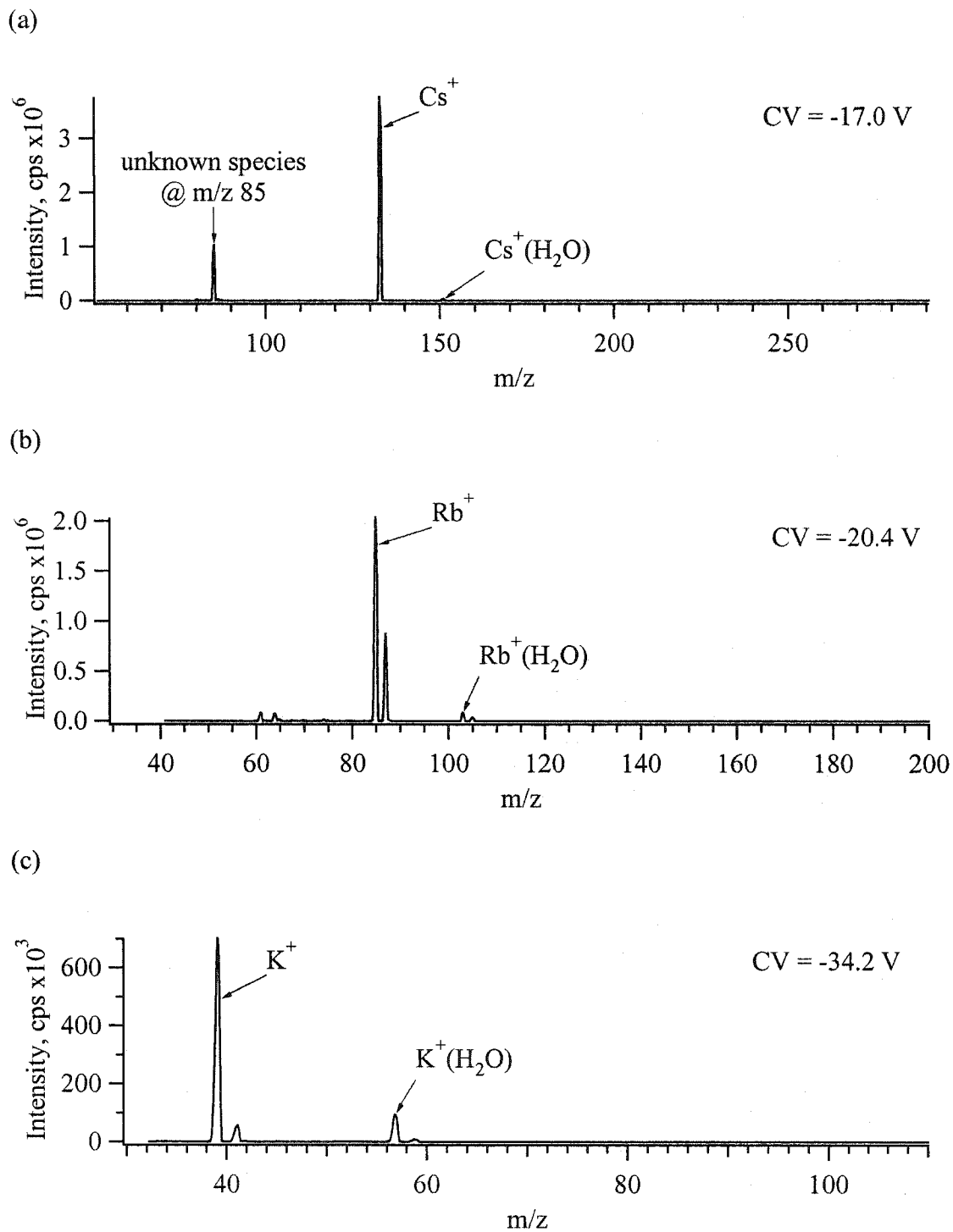


Figure 8.08 Mass spectra of (a) Cs^+ , (b) Rb^+ , and (c) K^+ in N_2 drift gas. Conditions as in Figure 8.07 (a). CVs set as indicated in Figures.

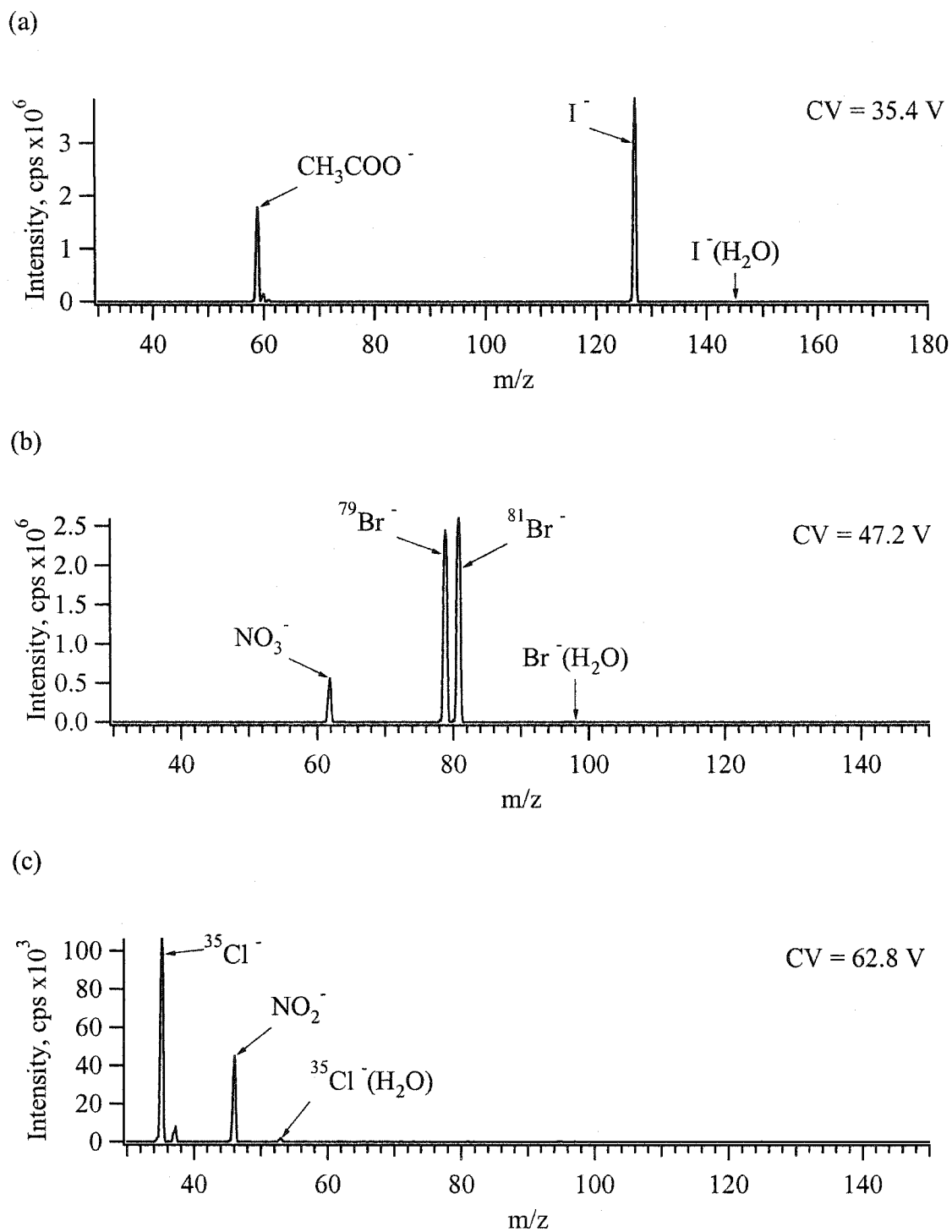


Figure 8.09 Mass spectra of (a) I^- , (b) Br^- , and (c) Cl^- in N_2 drift gas. Conditions as in Figure 8.07 (b). CVs set as indicated in Figures.

temperature”, T_{eff} , has been used to describe the effect that these collisions have on an ion in the FAIMS [17]. Under similar sampling conditions, the effective temperature for a Cs^+ ion has been estimated at 1000 K [17]. It is likely that these collisions may remove any solvent associated with an ion. If this significantly changes the K_h/K of the ion cluster, it may be filtered out during sampling, and would not be transmitted to the MS. Alternatively, as suggested in Chapter 7, the solvated ions may have their solvent removed early in the FAIMS sampling (due to the high T_{eff}), and the bare ion may be transmitted successfully. Considering the high effective temperature just described, the most likely explanation for the observation of water clusters in the FAIMS-MS mass spectra is due to low levels of water in the drift gas that condense with the ion as it is sampled into the MS.

8.3.2 Solvent and Gas Adducts Observed with CO_2 in the Drift Gas

Mass-selected CV spectra of the same solutions of cations and anions were acquired using CO_2/N_2 drift gas mixture. Figure 8.10 (a) is the mass-selected CV spectra (m/z 39, 41, 59, 85, 87, and 133) for the cation mixture at $\text{DV} = 3.5$ kV, $F_{\text{OR}} = 0\text{V}$, using $\sim 15\%$ CO_2 , 85% N_2 drift gas. Figure 8.10 (b) is the mass-selected CV (m/z 35, 37, 79, 81, and 127) for the halide mixture at $\text{DV} = -3.5$ kV, $F_{\text{OR}} = 0\text{V}$, using $\sim 10\%$ CO_2 , 90% N_2 drift gas. In both cases, the CV of the major species have shifted to higher values, indicating an increase in their K_h/K with the addition of the CO_2 . More importantly, is that the relative changes in K_h/K for each ion are different. In Figure 8.10 (a), the unknown species at m/z 85 is now well-separated from both the Cs^+ and the Rb^+ peaks. These types of changes are the basis for using different drift gas mixtures, since the drift gas can often be tuned to alter the ions that are transmitted at a particular DV and CV, allowing selective tuning of the bandpass. This can become important if isobaric interferences for a particular target analyte are identified, since it may be possible to tune the drift gas to separate these species. One major difference in the cation spectrum is the appearance of species with m/z 41 and 59 that appear at the same CV as the Cs^+ . This species was identified as a solvated Na^+ ion, which was not observed with only nitrogen in the drift gas. The Na^+ is present in the sample as a contaminant ion in the sample

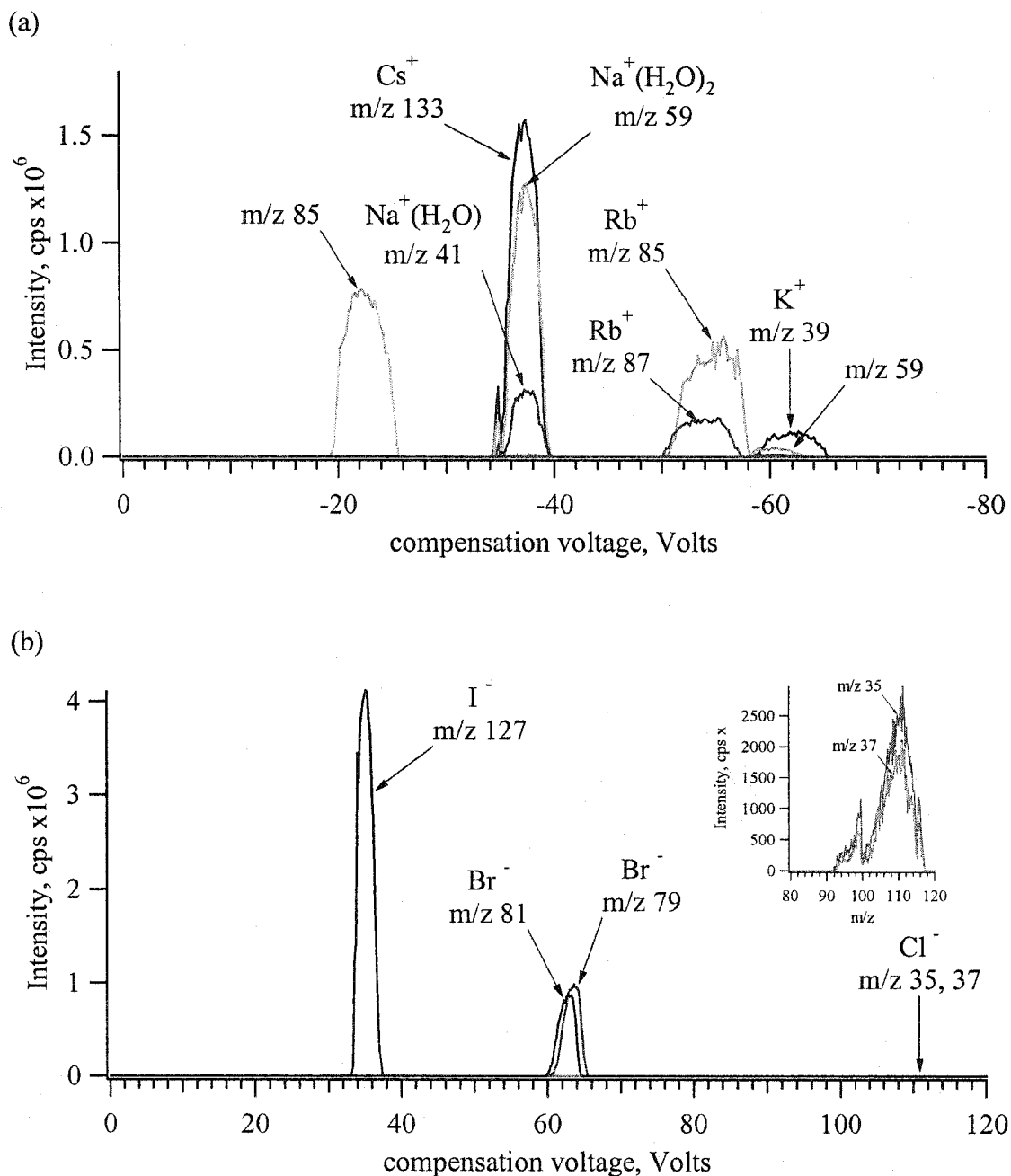


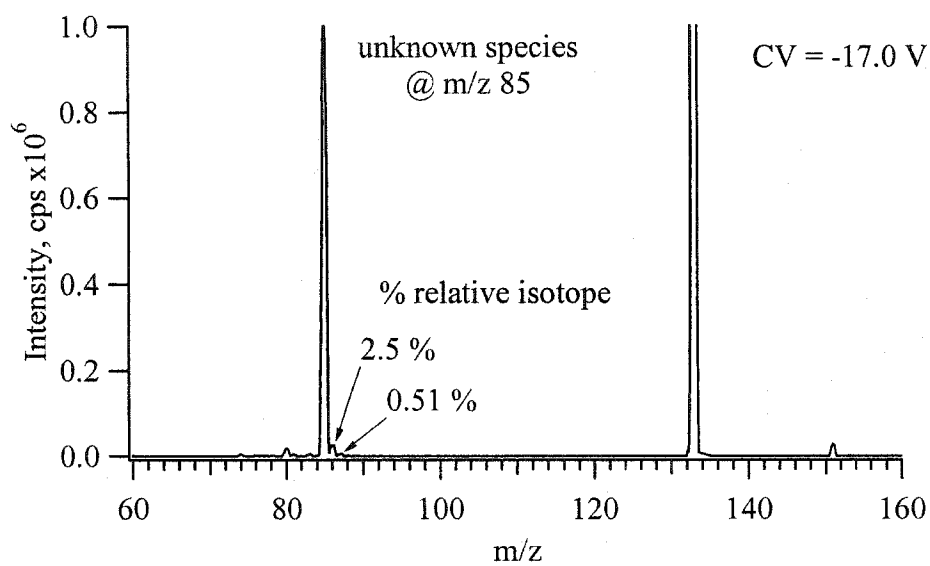
Figure 8.10 Superimposed mass-selected CV spectra. (a) (m/z 39, 41, 59, 85, 87, and 133) in $\sim 15\%$ CO_2 , 85% N_2 drift gas of a mixture of KCl , RbCl , and CsCl at $10 \mu\text{M}$ in methanol with 0.4 mM ammonium acetate. $\text{DV} = 3.5 \text{ kV}$, $F_{\text{OR}} = 0 \text{ V}$; (b) (m/z 35, 37, 79, 81, and 127) in $\sim 10\%$ CO_2 , 90% N_2 drift gas of a mixture of KCl , KBr , and KI at $10 \mu\text{M}$ in methanol with 0.4 mM ammonium acetate. $\text{DV} = -3.5 \text{ kV}$, $F_{\text{OR}} = 0 \text{ V}$.

matrix. Note that the bare Na^+ ion could not be observed with this mass spectrometer, due to a low mass cutoff of m/z 30.

A closer examination of the mass spectrum of the unknown m/z 85 species is shown in Figure 8.11. This is the same spectrum as Figure 8.08 (a), with the axes expanded to get a more detailed look at the m/z 85 species spectrum. The isotopes are present in the relative percentages indicated in the Figure. Based on these isotopes and knowledge of the solution composition, the elements present in the sample can be limited to H, C, N, O, and Na. Based on these limitations, this ion might be $\text{Na}^+(\text{H}_2\text{O})(\text{CO}_2)$ or $\text{Na}^+(\text{H}_2\text{CO}_3)$. As discussed in Chapter 7, a significant level of HCO_3^- is observed as a background ion in negative mode, so the presence of significant levels of carbonate and dissolved CO_2 are expected.

The mass spectra of the cations were also obtained with the CO_2/N_2 drift gas, and the data are presented in Figure 8.12 (a), (b), and (c) for Cs^+ , Rb^+ , and K^+ , respectively. The major difference in these spectra as compared to the nitrogen spectra is the increased levels of solvated metal species. For K^+ and Rb^+ , the $\text{M}^+(\text{H}_2\text{O})$ species was the dominant observed species and ions with 2 water ligands are observed. As noted earlier, a solvated Na^+ species, $\text{Na}^+(\text{H}_2\text{O})_2$, with m/z 59 was observed at the same CV as the Cs^+ , and various solvated forms of Na^+ are observed in the mass spectrum. The relative levels of water adducts follows the trend $\text{Na}^+ > \text{K}^+ > \text{Rb}^+ > \text{Cs}^+$, which corresponds with the “hardness” of the charges. This has been reported previously in the determination of the free energy of transfer from solution to the gas phase [26]. In addition to solvent adducts, CO_2 gas adducts were observed with all of the cations, including Na^+ . The wide variety of species observed under these test conditions may be explained under a few different scenarios. If the gas-phase species that is transmitted through the FAIMS is solvated, perhaps the CO_2 prevents removal of these ligands during the CID process in the MS interface. Another possibility is that the ion is transported through the FAIMS as an unsolvated ion, and simply picks up water or gas to form an adduct during the rapid cooling that occurs as the ion is sampled into the vacuum of the MS. In this case, the CO_2 added to the drift gas may contribute additional water into the gas stream, increasing

(a)



(b)

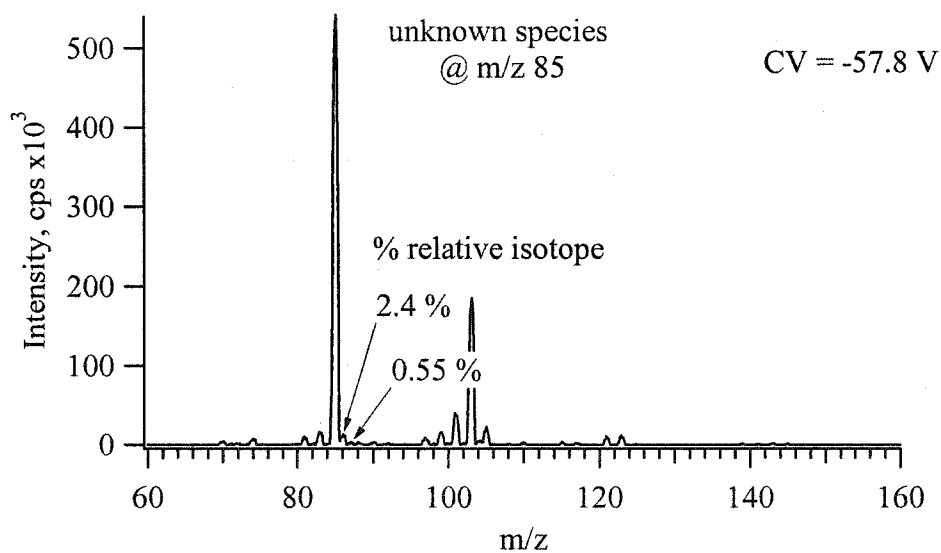


Figure 8.11 Mass spectra of the unknown m/z 85 mass-selected CV peak with (a) N_2 drift gas and (b) $\sim 15\%$ CO_2 , 85% N_2 drift gas.

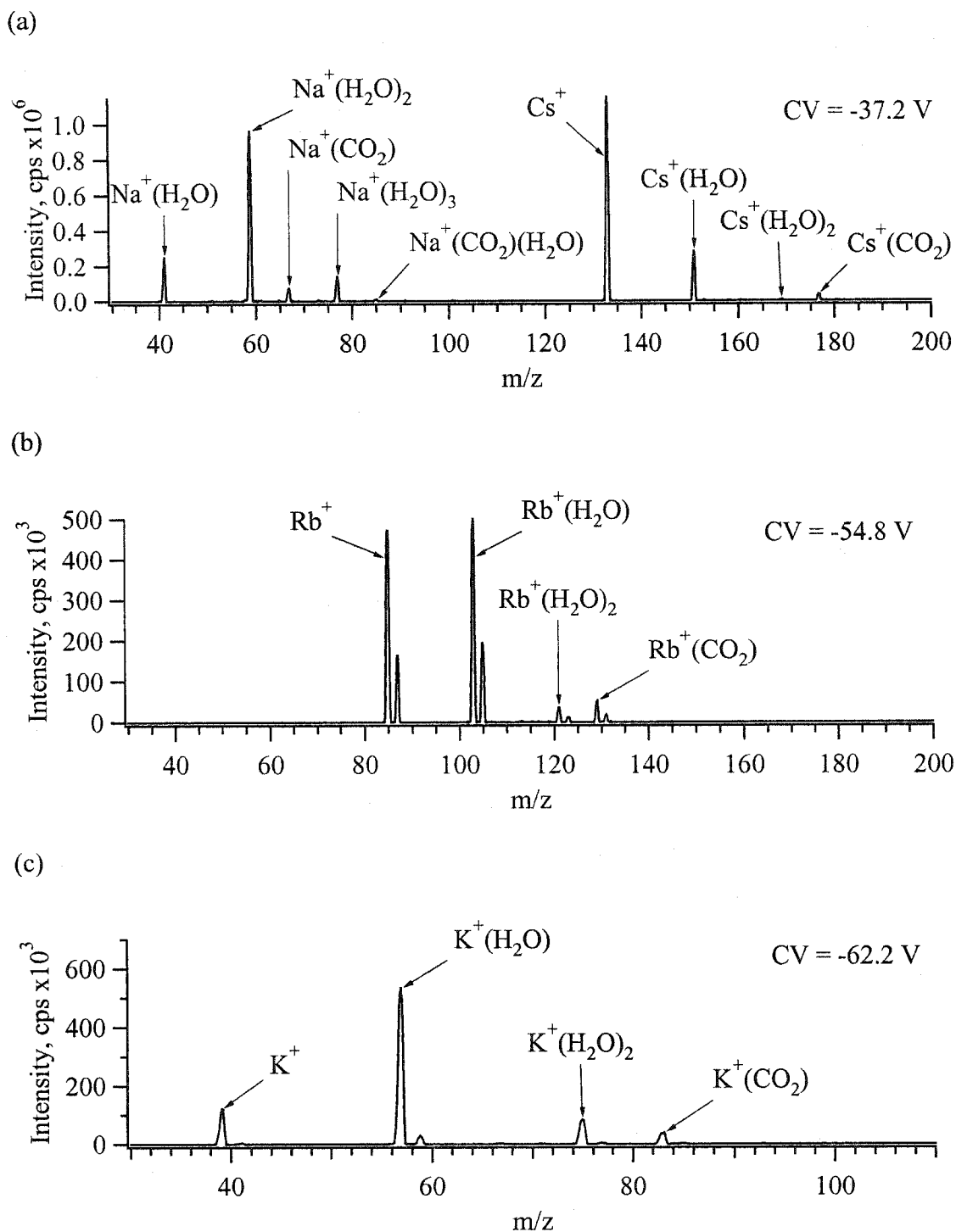


Figure 8.12 Mass spectra of (a) Cs^+ , (b) Rb^+ , and (c) K^+ in $\sim 15\%$ CO_2 , 85% N_2 drift gas. Conditions as in Figure 8.11 (b). CVs set as indicated in Figures.

the likelihood of a water adduct forming, or may simply prevent CID removal of the water adducts that form. Previous work suggests that a Cs^+ ion is unsolvated in a FAIMS experiment [27]. The presence of low intensity CO_2 adducts demonstrates how this gas is much more likely to form adducts than nitrogen. As discussed earlier, previous work in other labs has demonstrated that CO_2 may form adducts with ions in the gas phase at atmospheric pressure [17].

Species assignment of some of these low intensity peaks is made possible due to the very low intensity of background ions under these test conditions. Figure 8.13 is the mass spectra from the CO_2/N_2 drift gas study in Figure 8.12, with the intensity axis expanded to show the spectral background. The spectra demonstrate that very few peaks are observed other than the major species described earlier. The absence of an intense spectral background allows identification of very low intensity species that could not be otherwise identified. Some very low intensity species observed were $M+28$ and $M+32$ for all the cations. The identity of these species is unknown. While these masses match for N_2 and O_2 , it seems unlikely that these gases would form adducts, due to the absence of any dipole. Other possibilities may be things such as CO (28 Da) and CH_3OH (32 Da), or some other impurities present in the drift gas.

The mass spectra of the halide anions were also obtained with the CO_2/N_2 drift gas, and the data are presented in Figure 8.14 (a), (b), and (c) for I^- , Br^- , and Cl^- , respectively. The mass spectra of these species showed some increase in the intensity of the water adduct and the presence of a CO_2 adduct; however, at much lower levels than were observed for the cations. While the levels of CO_2 used in the drift gas for the anions is lower, the lower levels of adducts is not due to less CO_2 . Tests done with the cations using the same levels of CO_2 in the drift gas exhibited only slightly lower relative levels of adducts (data not shown).

As was done earlier for the N_2 drift gas, mass-selected CV spectra were acquired in CO_2/N_2 drift gas mixtures, monitoring masses corresponding to solvated forms of these ions. Again, only species with the same CV as the bare ion were observed. Based on

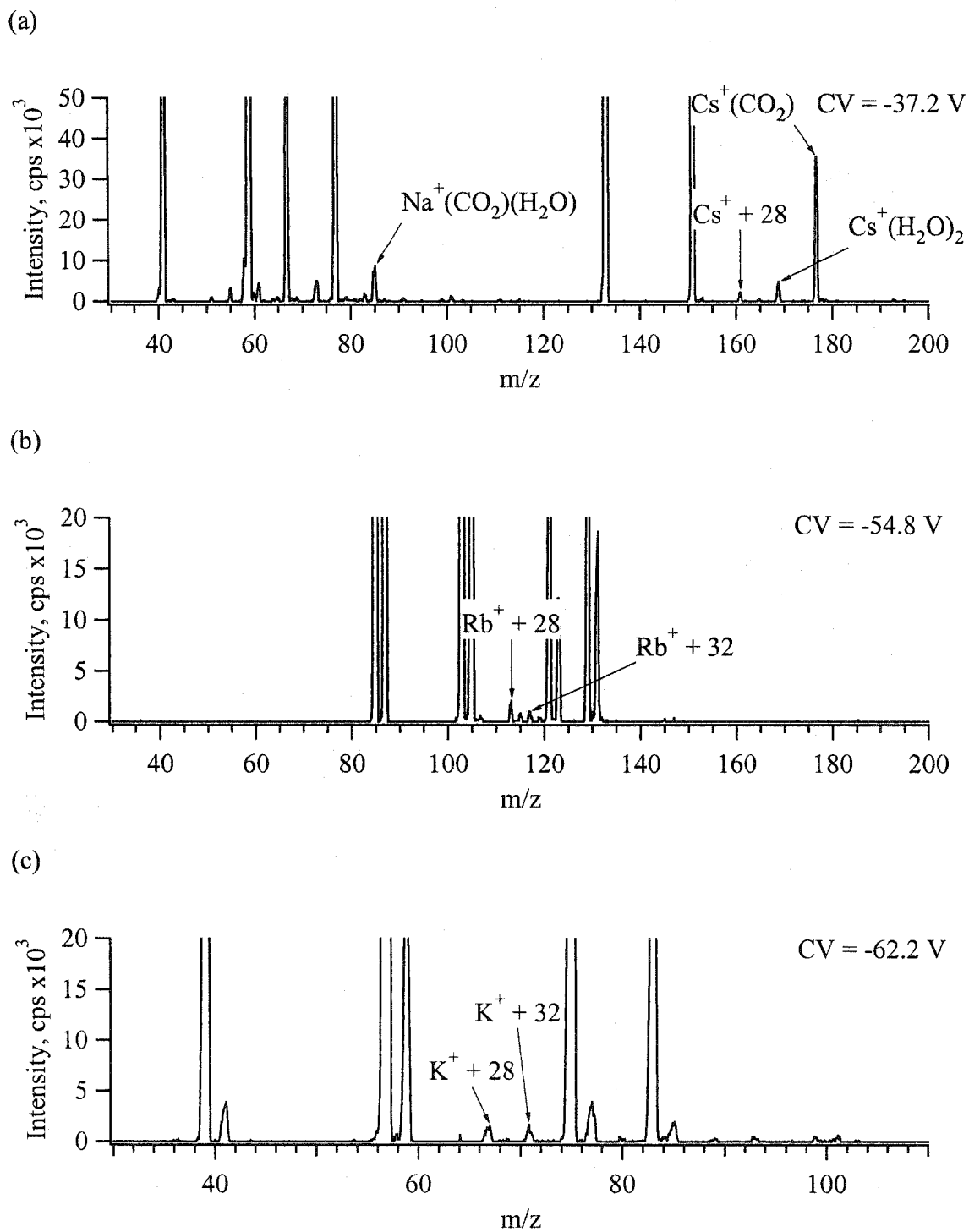


Figure 8.13 Expanded view of the mass spectra in Figure 8.12. Mass spectra of (a) Cs^+ , (b) Rb^+ , and (c) K^+ in $\sim 15\%$ CO_2 , 85% N_2 drift gas.

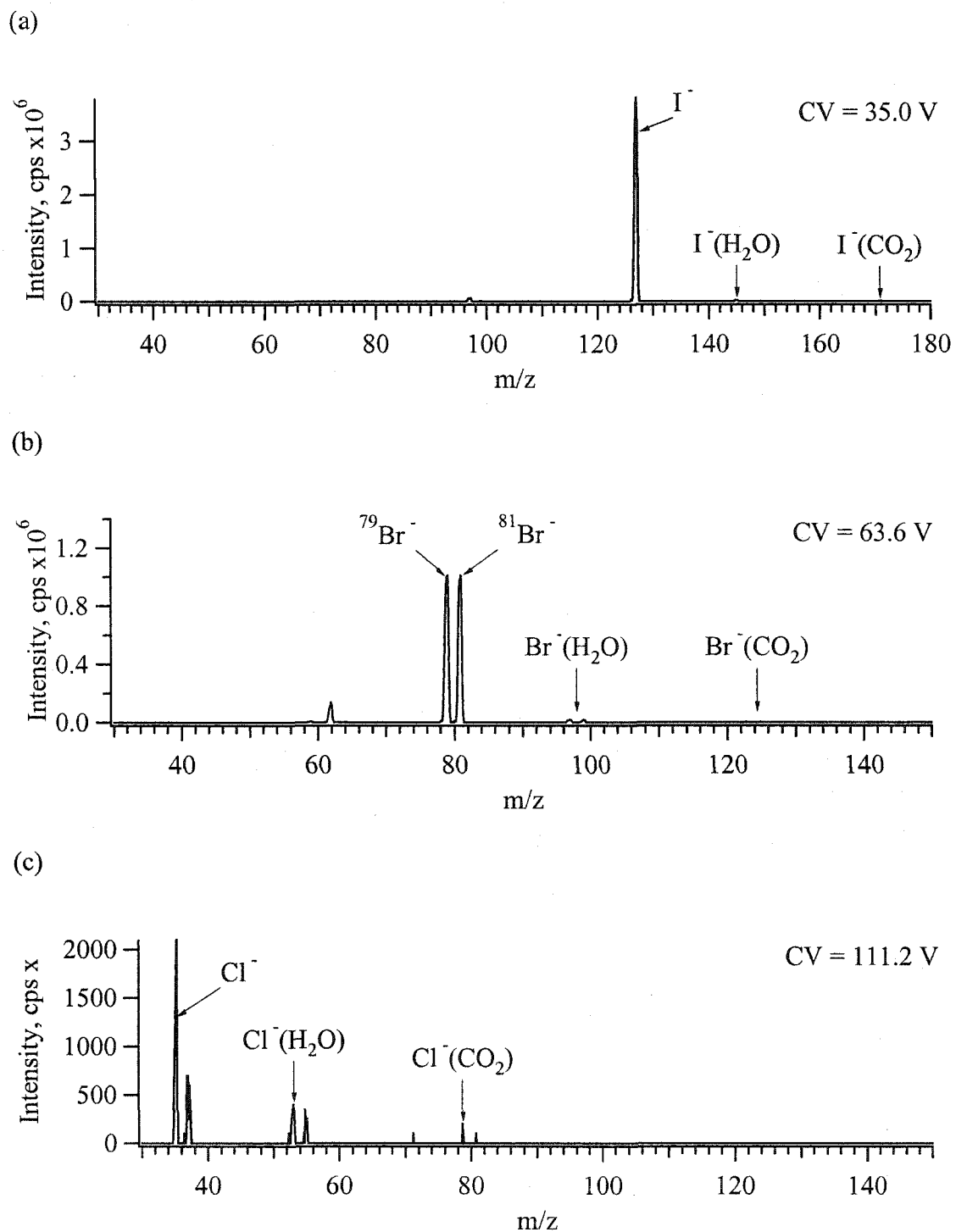


Figure 8.14 Mass spectra of (a) I^- , (b) Br^- , and (c) Cl^- in $\sim 10\%$ CO_2 , 90% N_2 drift gas. Conditions as in Figure 8.11 (b). CVs set as indicated in Figures.

the data acquired for these types of small ions, is it reasonable to expect that if a solvated ion was a stable species in the FAIMS that it would appear at a different CV than the bare ion. In these experiments, no variations were observed between the CV of the solvated and unsolvated forms, even with variation of the drift gas composition. Combining these observations with the high effective temperature in the FAIMS described earlier, it seems very likely that most ions are not solvated as they travel through the FAIMS. So, the observation of such a wide variety of solvated and gas adduct species based on a single M^+ or X^- , strongly suggests that these adducts form in the MS interface. A possible exception may be for Na^+ , where two different gas-phase species have been proposed. In either case, the addition of CO_2 increases the relative abundance of the solvated ion in the mass spectrum, although the actual role of the CO_2 here is unclear. If the CO_2 used has high levels of water and other impurities present, then more water adducts might be expected.

8.3.3 Collision-Induced Dissociation (CID) with CO_2

The effects of CO_2 in the drift gas are apparent in both the changes to an ion's CV and due to the increased potential for solvent and gas adducts. However, use of CO_2 to prevent the fragmentation of certain species has been reported [18]. To demonstrate this, selenomethionine ($CH_3Se(CH_2)CH(NH_3)COOH$) was selected as a species easily fragmented by MS sampling. In this experiment, the orifice was maintained at 0 volts and the MS ring voltage (RNG) was set to -100 V. The data presented to this point have used a ring voltage of 40 V (of suitable polarity). A solution of 10 μM selenomethionine with 0.4 mM KOH in methanol was electrosprayed into the FAIMS-MS interface. When using nitrogen as the drift gas and a RNG = -100 V, a large amount of fragmentation of the selenomethionine to $SeCH_3^-$ at m/z 95 is observed, as shown in Figure 8.15 (a). With the addition of CO_2 to the drift gas (~10% CO_2 , 90% N_2), the amount of fragmentation was observed to be almost non-existent with RNG = -100 V, as the data in Figure 8.15 (b) demonstrate. With N_2 , the relative amount of fragmentation (relative to m/z 196) was 20%, as compared to 0.46% with the CO_2/N_2 mixture, about 40 times less relative fragmentation. Also, much more intense signals were observed with the CO_2/N_2 mixture,

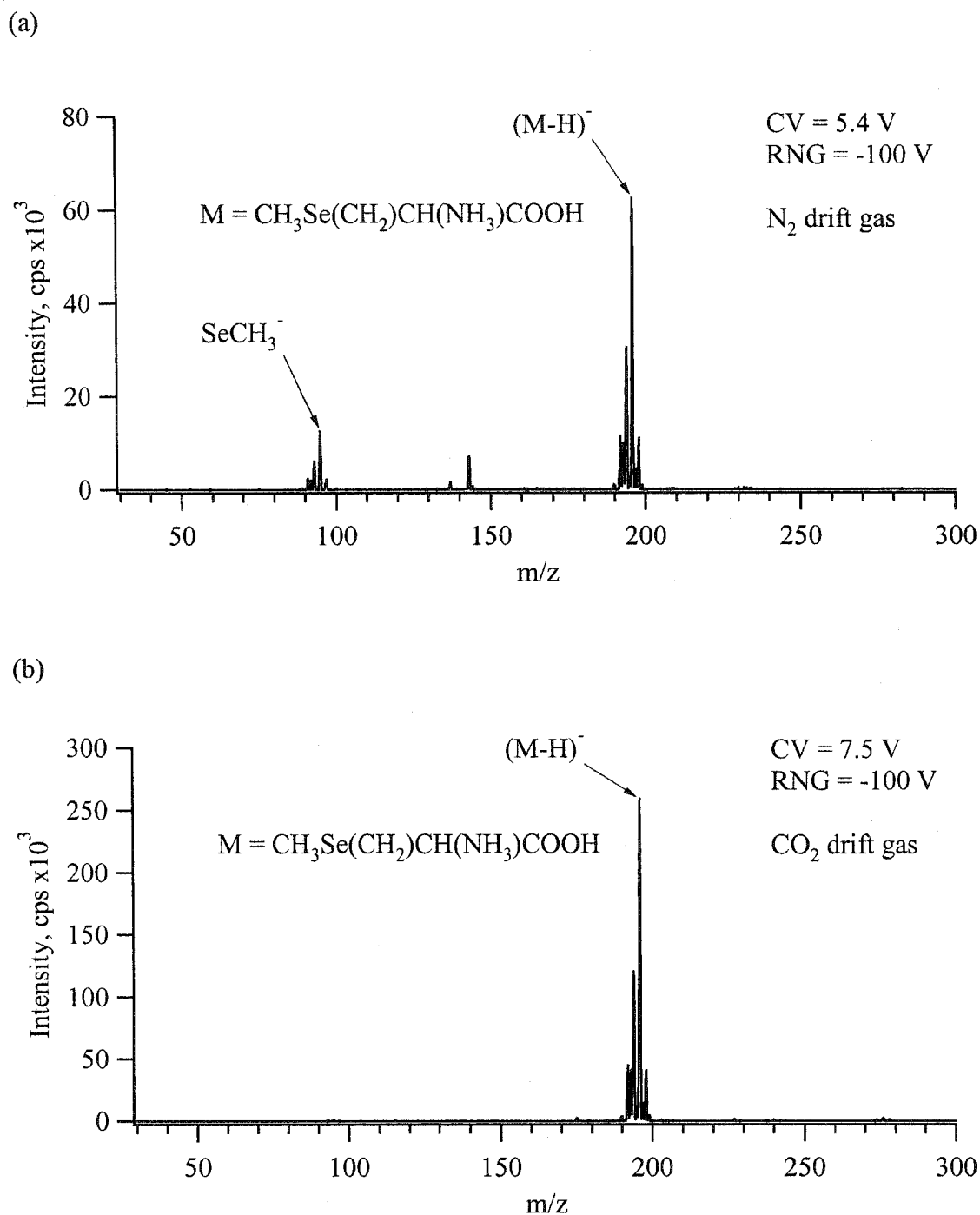


Figure 8.15 Mass spectra of a solution containing selenomethionine at $10 \mu\text{M}$ and 0.4 mM KOH in methanol using (a) N_2 drift gas and (b) $\sim 10\% \text{ CO}_2$, $90\% \text{ N}_2$ drift gas. $\text{DV} = -3.5 \text{ kV}$, $\text{F}_{\text{OR}} = 0 \text{ V}$, $\text{CV} = 5.4 \text{ V}$, $\text{RNG} = -100 \text{ V}$.

with 259,000 cps observed at m/z 196, as compared to only 62,500 cps when using N_2 .

These data demonstrate that CO_2 may be used to reduce fragmentation, allowing some tuning of the MS sampling conditions to maximize the ion intensity, which would not be possible when only nitrogen was present in the CID region. The protection effect of the CO_2 may be related to its adduct-forming characteristics. It is possible that CO_2 does not provide a good target for CID, or prevents fragmentation by forming adducts. The CO_2 would be expected to have more vibrational modes than N_2 , and would likely absorb more energy in a collision with an ion. As a result, the amount of internal energy imparted to the ion would be less, reducing fragmentation. As mentioned previously, this may also explain the higher relative water adducts observed in the mass spectrum.

In some cases, significantly elevated levels of CO_2 adducts may be observed. In the case of chlorite and hypochlorite, the addition of CO_2 can dramatically alter both the mass-selected CV and the observed mass spectrum.

8.3.4 Arsenite in Water Solvent using CO_2 in the Drift Gas

The mass-selected CV spectra of 0.1 mM $NaAsO_2$ in 100% water solvent with 0.4 mM KOH are shown in Figure 8.16 (a). The DV is -3.3 kV, the $F_{OR} = 0$ V, and the drift gas is ~10% CO_2 , 90% N_2 . A major peak at m/z 125, $H_2AsO_3^-$, was observed at a CV = 17.0 V. Another peak at CV = 28.9 V, due to $H_2AsO_4^-$ (m/z 141) is also observed. The intense species at m/z 141 at a CV of about 15 V is a contaminant ion (possibly $HSO_4^-(CO_2)$). The presence of arsenate has been attributed to oxidation of the arsenite in solution. Figure 8.16 (b) is the mass spectrum of the major peak at CV = 17.0 V. An intense peak at m/z 125 ($H_2AsO_3^-$) is observed, as well as an intense species at m/z 169. This species has been assigned as $H_2AsO_3(CO_2)^-$. The intensity of this adduct is considerably larger than observed for the other As and Se species studied (Chapter 7), and indicates that CO_2 readily forms an adduct with $H_2AsO_3^-$.

8.3.5 Speciation of Hypochlorite in Water Solvent using CO₂ in the Drift Gas

Mass-selected CV spectra (m/z 51, 67, 83, 95, and 99) are presented in Figure 8.17 (a) for N₂ drift gas and (b) for ~10% CO₂, 90% N₂ drift gas for the same solution containing 1 μ M KClO₄, 10 μ M KClO₂, and ~ 0.1 mM NaOCl in 100% water solvent with 0.4 mM KOH. In N₂ curtain gas, three major species were observed at the masses monitored. ClO₄⁻ was observed at a CV = 24.2 V, ClO₃⁻ at CV = 28.8 V, and ClO₂⁻ at CV = 37.0 V. Very low signals were observed at CV = 53.2 V for Cl⁻ (not shown). With N₂ curtain gas, several different possible solvated and gas adducts of ClO⁻ were monitored in the mass-selected CV scans, however, no species corresponding to ClO⁻ could be found. The presence of ClO₃⁻ in the mass-selected CV scans is due to its presence as a decomposition product of ClO⁻ in the bleach solution used [28]. Previous ESI-MS work using N₂ curtain gas (Chapter 2) has demonstrated that a bare ClO⁻ species can be observed. The absence of this species indicates that it may either be unstable in the FAIMS, or it may have a type C mobility (i.e., $K_h/K < 1$) under these test conditions.

The mass-selected CV spectra in Figure 8.17 (b) shows three intense species, including ClO₄⁻ at CV = 25.4 V, ClO₃⁻ at CV = 37.2 V, and a species identified as ClO⁻(CO₂) at CV = 32.4 V. This CO₂ adduct was the only species that was identified as ClO⁻. Surprisingly, no species corresponding to ClO₂⁻ could be found under these test conditions, among a wide variety of possible species that were examined in the mass-selected CV scans. Again, the absence of this species indicates that it may either be unstable in the FAIMS, or it may have a type C mobility (i.e., $K_h/K < 1$) under these test conditions. This demonstrates how changing the drift gas can change both the observed CV of an ion, as well as the species that are observed.

The strength of the ClO⁻(CO₂) interaction is indicated by the data presented in Figure 8.18. Figure 8.18 (a) shows the spectrum acquired with F_{OR} = -20 V. The signal at m/z 51 (ClO⁻) is only 0.54% of the signal at m/z 95 (ClO⁻(CO₂)). When the F_{OR} was increased to -80 V, more than half of the ClO⁻(CO₂) has been fragmented to ClO⁻. By comparison, the ClO₃⁻ signal was measured at F_{OR} = -80 V, and the fragmentation to

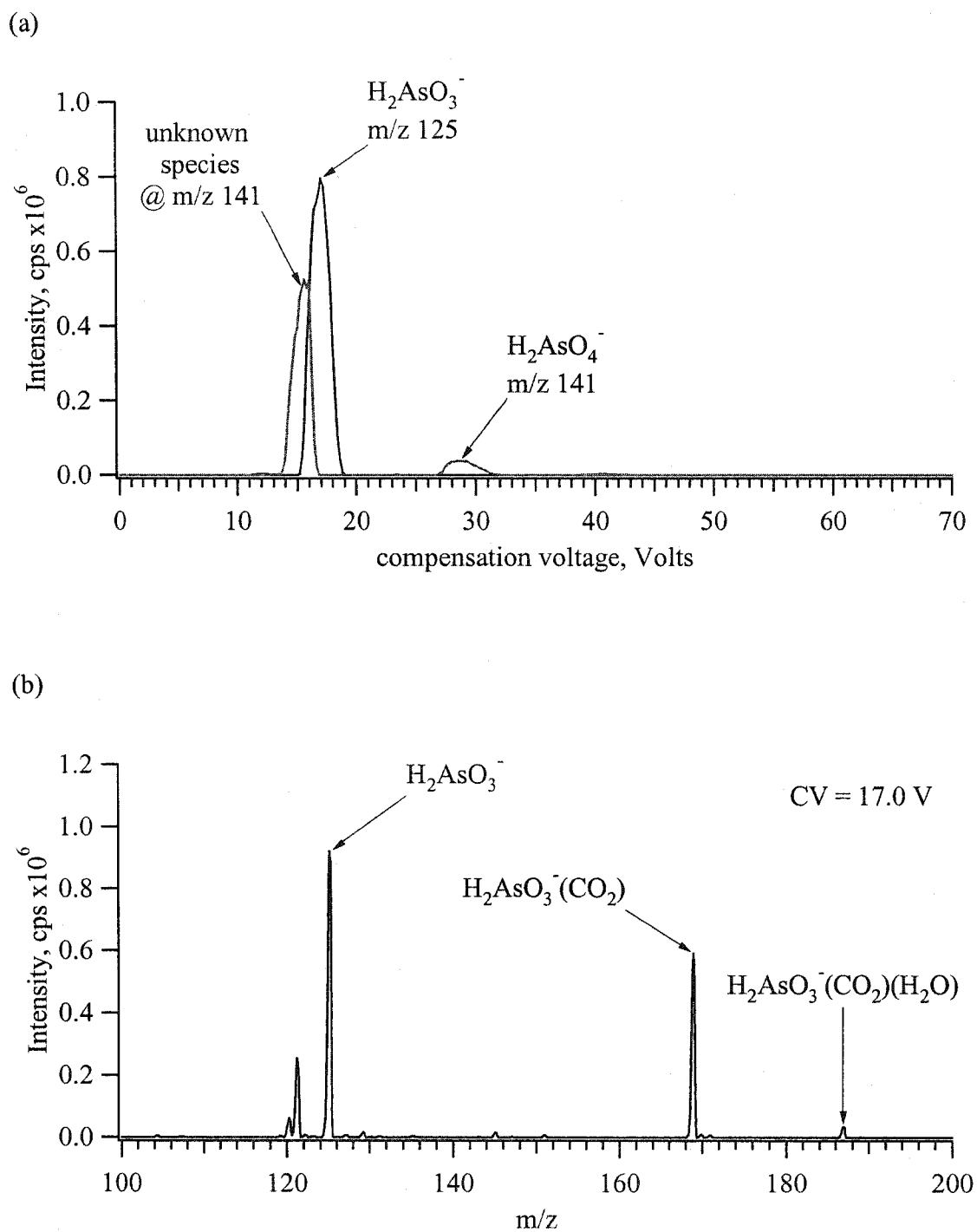


Figure 8.16 (a) Superimposed mass-selected CV spectra (m/z 125 and 141) in ~10% CO_2 , 90% N_2 drift gas of a sample containing 0.1 mM NaAsO_2 and 0.4 mM KOH in 100% water solvent. $\text{DV} = -3.3$ kV, $\text{F}_{\text{OR}} = 0$ V; (b) Mass spectrum at $\text{CV} = 17.0$ V.

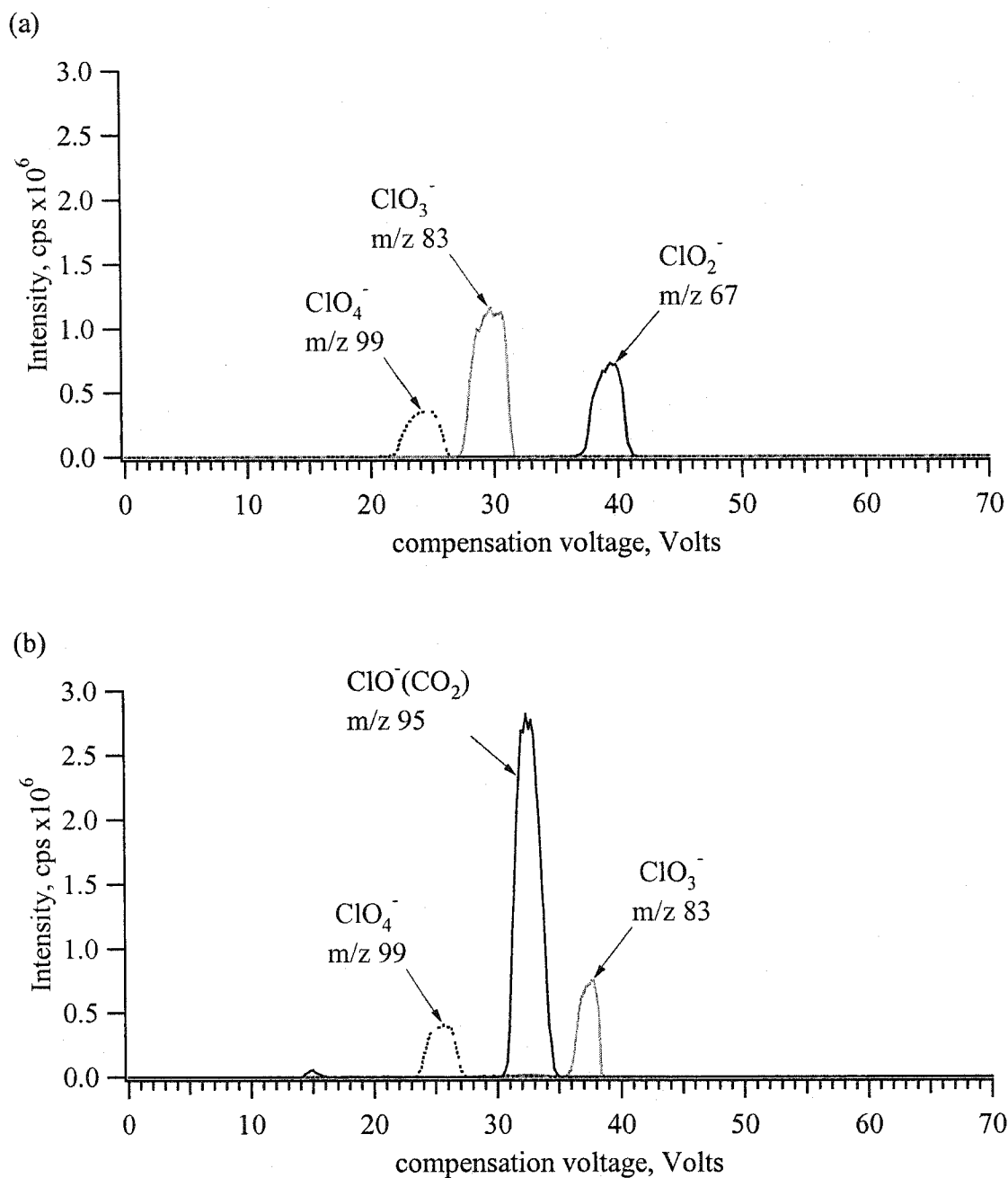


Figure 8.17 Superimposed mass-selected CV spectra (m/z 51, 67, 83, 95, and 99) in (a) N_2 drift gas and (b) $\sim 10\%$ CO_2 , 90% N_2 drift gas for the same solution containing $1 \mu M$ $KClO_4$, $10 \mu M$ $KClO_2$, and ~ 0.1 mM $NaOCl$ in 100% water solvent with 0.4 mM KOH . $DV = -3.3$ kV, $F_{OR} = 0$ V. Trace for m/z 51 present but not visible.

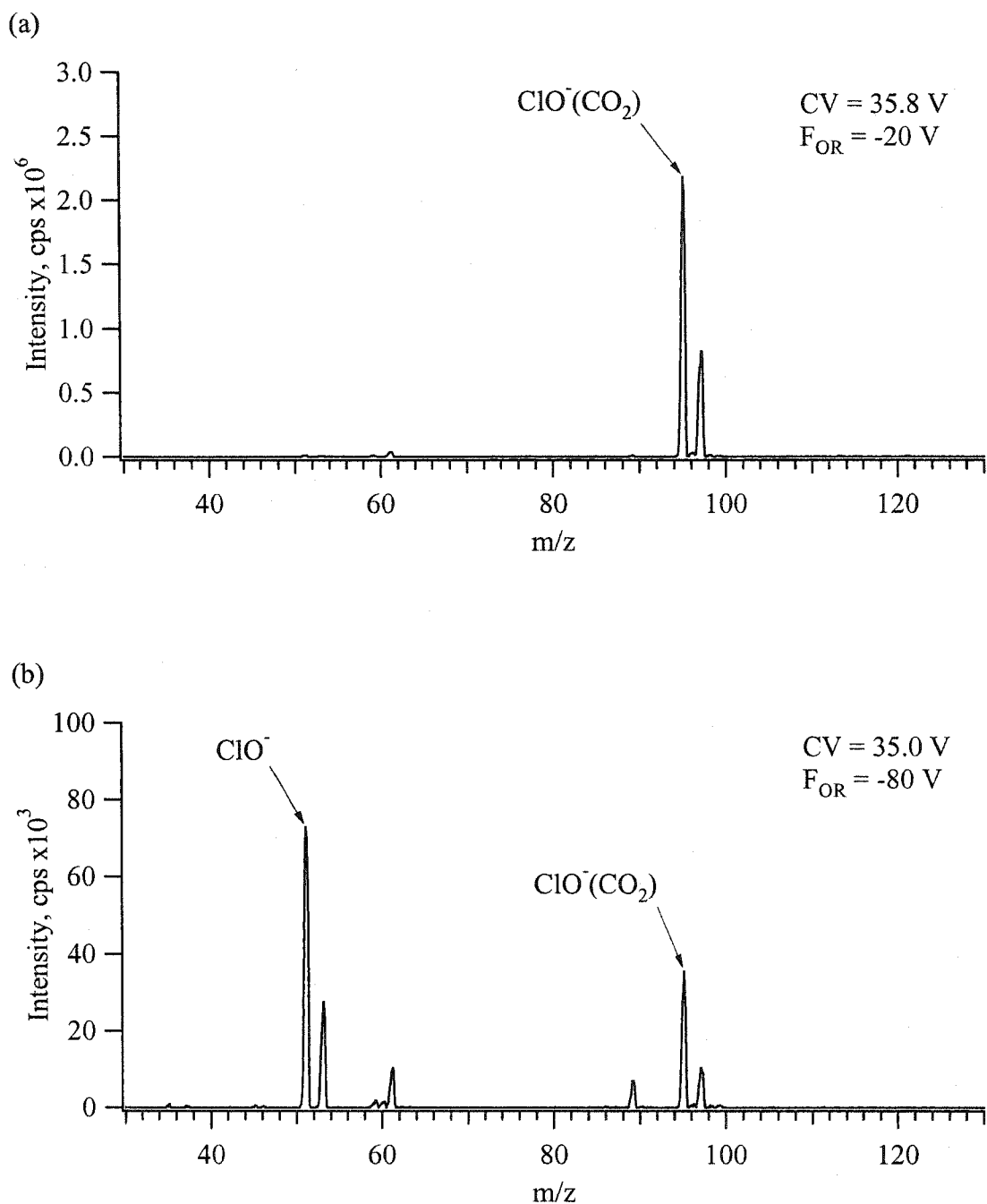


Figure 8.18 Mass spectra of a hypochlorite species observed when using ~10% CO_2 , 90% N_2 drift gas at different orifice voltages, (a) F_{OR} = -20 V, (b) F_{OR} = -80 V. DV = -3.5 kV. Solution used was a commercial bleach sample diluted to give a $[\text{ClO}^-]$ of ~0.1 mM in 100% water solvent with 0.4 mM KOH.

ClO_2^- (m/z 67) was determined to be 1.6% relative to the ClO_3^- (m/z 83). So, while the $\text{ClO}^-(\text{CO}_2)$ is less resistant to CID than breaking a Cl-O bond in ClO_3^- , this does demonstrate that the $\text{ClO}^-(\text{CO}_2)$ species is relatively stable.

8.4 Conclusions

Due to the ion filtering mechanism, very mild MS interface conditions can be applied, while still dramatically reducing the levels of observed background ions. Concerns regarding the filtering out of unstable species, especially solvated ones, were indicated. In the case when the FAIMS is unable to separate interfering ions, changing the composition of the drift gas can allow for differential separation of the gas-phase ions.

The addition of CO_2 was observed to prevent fragmentation of selenomethionine, as well as form adducts at very low intensity for many of the ions examined. In the case of water adducts, it seems that CO_2 prevents the removal of water ligands that may form an adduct as the ions are sampled into the mass spectrometer. Also, in the presence of CO_2 , gas adducts were observed that were not observed with N_2 alone.

In most cases, the addition of CO_2 to the drift gas will not complicate the observed spectrum or adversely affect the ability to detect species. Exceptions to this were demonstrated for arsenite, chlorite, and hypochlorite. In these select cases, the addition of CO_2 can alter the observed species, by forming intense CO_2 species in the mass spectrum. In the case of ClO^- and ClO_2^- , dramatic changes were observed. These examples highlight that caution should be exercised when doing speciation studies with FAIMS, since the absence of an ion in the mass-selected CV spectra may not accurately reflect the sample composition. Furthermore, ions observed in an ESI-MS spectrum may not survive FAIMS sampling, especially ions which may not be stable to the high number of collisions during FAIMS sampling.

8.5 References

1. Avakov, A. S.; Buryakov, I. A.; Krylov, E. V.; Nazarov, E. G.; Rasulev, U. K.; Soldatov, V. P. "Proceedings of the Eighth All-Union Conference"; *Physics of Low-Temperature Plasmas.*, , 1997.
2. Buryakov, I. A.; Krylov, E. V.; Soldatov, V. P. "Inventor's Certificate (USSR) No. 1485808 [in Russian], G01 No. 27/62"; *Byull. Izobret.* **1989**. USSR. No. 1485808.
3. Buryakov, I. A.; Krylov, E. V.; Makas', A. L.; Nazarov, E. G.; Pervukhin, V. V.; Rasulev, U. K. "Separation of ions according to mobility in a strong AC electric field"; *Sov. Tech. Phys. Lett.* **1991**, 17, 446-447.
4. Buryakov, I. A.; Krylov, E. V.; Nazarov, E. G.; Rasulev, U. K. "A new method of separation of multi-atomic ions by mobility at atmospheric pressure using a high-frequency amplitude-asymmetric strong electric field"; *Int. J. Mass Spectrom. Ion Proc.* **1993**, 128, 143-148.
5. Carnahan, B. L.; Tarassov, A. S. "Ion Mobility Spectrometer"; **1995**, Mine Safety Appliances Company, Pittsburgh, Pa. United States. Patent No. 5 420 424.
6. Carnahan, B.; Day, S.; Kouznetsov, V.; Matyjaszczyk, M.; Tarassov, A. "Proceedings of the 41st Annual ISA Analysis Division Symposium"; *41st Annual ISA Analysis Division Symposium.*, Framingham, MA, April 21-24, 1996.
7. Guevremont, R.; Purves, R. W. "Atmospheric pressure ion focusing in a high-field asymmetric waveform ion mobility spectrometer"; *Rev. Sci. Instrum.* **1999**, 70, 1370-1383.
8. Guevremont, R.; Purves, R. W.; Barnett, D. A.; Ding, L. "Ion trapping at atmospheric pressure (760 Torr) and room temperature with a high-field asymmetric waveform ion mobility spectrometer"; *Int. J. Mass Spectrom.* **1999**, 193, 45-56.
9. Guevremont, R.; Purves, R. "Apparatus and method for atmospheric pressure 3-dimensional ion trapping"; *Canadian Intellectual Property Office* **1999**. Canada. Canadian Patent No. 2,260,572.

10. Guevremont, R.; Purves, R. "Apparatus and method for desolvating and focussing ions for introduction into a mass spectrometer"; *Canadian Intellectual Property Office* **1999**. Canada. Canadian Patent No. 2,273,322.
11. Guevremont, R.; Purves, R.; Barnett, D. A. "Method for separation and enrichment of isotopes in gaseous phase"; *Canadian Intellectual Property Office* **1999**. Canada. Canadian Patent No. 2,339,549.
12. Guevremont, R.; Purves, R.; Barnett, D. A. "Method for separation of isomers and different conformations of ions in gaseous phase"; *Canadian Intellectual Property Office* **1999**. Canada. Canadian Patent No. 2,339,553.
13. Gorshkov, M. P. "Inventors Certificate (USSR) No. 966583"; *Byull. Izobret.* **1982**. USSR. No. 966583.
14. Purves, R. W.; Guevremont, R. "Electrospray ionization high-field asymmetric waveform ion mobility spectrometry-mass spectrometry"; *Anal. Chem.* **1999**, *71*, 2346-2357.
15. Purves, R. W.; Day, S.; Pipich, C. W.; Matyjaszczyk, M. S.; Guevremont, R. "Mass spectrometric characterization of a high-field asymmetric waveform ion mobility spectrometer"; *Rev. Sci. Instrum.* **1998**, *69*, 4094-4105.
16. Mason, E. A.; McDaniel, E. W. *Transport Properties of Ions in Gases*; John Wiley & Sons, Inc., 1988.
17. Barnett, D. A.; Ells, B.; Guevremont, R.; Purves, R. W.; Viehland, L. A. "Evaluation of carrier gases for use in high-field asymmetric waveform ion mobility spectrometry"; *J. Am. Soc. Mass Spectrom.* **2000**, *11*, 1125-1133.
18. Barnett, D. A.; Purves, R. W.; Ells, B.; Guevremont, R. "Separation of *o*-, *m*- and *p*-phthalic acids by high-field asymmetric waveform ion mobility spectrometry (FAIMS) using mixed carrier gases"; *J. Mass Spectrom.* **2000**, *35*, 976-980.
19. Ells, B.; Barnett, D. A.; Purves, R. W.; Guevremont, R. "Trace level determination of perchlorate in water matrices and human urine using ESI-FAIMS-MS"; *J. Environ. Monit.* **2000**, *2*, 393-397.
20. Guevremont, R.; Barnett, D. A.; Purves, R. W.; Vandermeij, J. "Analysis of a tryptic digest of pig hemoglobin using ESI-FAIMS-MS"; *Anal. Chem.* **2000**, *72*, 4577-4584.

21. McCooeye, M. A.; Ells, B.; Barnett, D. A.; Purves, R. W.; Guevremont, R. "Quantitation of morphine and codeine in human urine using high-field asymmetric waveform ion mobility spectrometry (FAIMS) with mass spectrometric detection"; *J. Anal. Tox.* **2001**, 25, 81-87.
22. Barnett, D. A.; Purves, R. W.; Guevremont, R. "Isotope separation using high-field asymmetric waveform ion mobility spectrometry"; *Nuc. Instrum. Meth. Phys. Res. A* **2000**, 450, 179-185.
23. Barnett, D. A.; Horlick, G. "Quantitative electrospray mass spectrometry of halides and halogenic anions"; *J. Anal. At. Spectrom.* **1997**, 12, 497-501.
24. Agnes, G. R.; Horlick, G. "Electrospray mass spectrometry as a technique for elemental analysis: Preliminary results"; *Appl. Spectros.* **1992**, 46, 401-406.
25. Agnes, G. R.; Horlick, G. "Effect of operating parameters on analyte signals in elemental electrospray mass spectrometry"; *Appl. Spectros.* **1995**, 49, 324-334.
26. Kebarle, P.; Tang, L. "From ions in solution to ions in the gas phase"; *Anal. Chem.* **1993**, 65, 972A-986A.
27. Spangler, G. E.; Miller, R. A. "Application of mobility theory to the interpretation of data generated by linear and RF excited ion mobility spectrometers"; *Int. J. Mass Spectrom.* **2002**, 214, 95-104.
28. U.S.E.P.A. In *EPA Guidance Manual: Alternative Disinfectants and Oxidants*, 1999, pp 1-54.

Chapter 9

Conclusions and Future Work

9.1 Summary

The success of electrospray mass ionization spectrometry (ESI-MS) as a common application is largely due to the ability of the electrospray (ES) process to gently promote solution ions to the gas phase, maintaining the integrity of the ion in the process. From the point of view of elemental speciation applications, ESI-MS allows the determination of the chemical species present in solution, as opposed to just the elemental composition. However, the application of this technique does not come without its disadvantages. The ES process itself is not particularly robust, and the electrospray of liquids with a high surface tension tends to be difficult. Also, the spectra can be quite complex, due to the wide range of ionic species that can be present in solution, as well as the wide variety of charged species that can form in the gas phase. This generates what is commonly referred to as the "chemical background", and is especially prevalent at lower masses. As a result, the detection limits that ESI-MS can provide are sometimes compromised.

When this work was started in 1998, ES sources using fused silica tips were just beginning to find common application. Early results suggested that a fused silica interface could be capable of electrospraying purely aqueous solvents. The general lack of aqueous solvent ES-MS in the literature suggested that the use of aqueous solvents was avoided, due to the difficulty in tuning a stable ES while maintaining signal intensity. It was hoped that a more reliable way of electrospraying purely aqueous solvents could be developed and applied to ESI-MS speciation studies.

An ES interface was developed and was used to electrospray purely aqueous solvent. In Chapter 2, the signal intensity and stability with aqueous solvents was demonstrated as comparable to using methanolic solvent. Also, the intensity of the chemical background with either solvent was similar, indicating that there was no significant compromise with using purely aqueous solvent for the analytes tested. Examples of how the observed species may be changed were presented for selenite, sulfite, and hypochlorite. While the operation in positive mode was both easy and effective, the operation in negative mode was less so.

In Chapter 3, this aqueous ES source was further investigated and compared to methanolic solvent for the analysis of the lanthanides. It was demonstrated that the water solvent preserved the M^{2+} charge state much better than using methanol. Again, the signal intensity and spectral backgrounds using either methanol or water were comparable. With the modification of the MS interface, very high potential differences could be used, which allowed for high-energy collision-induced dissociation (CID). This high-energy CID was demonstrated as effective for breaking metal-oxide bonds without severely affecting the observed lanthanide ion intensity. As a result, the "metal ion mode" of operation was significantly improved, as compared to previous work, and the resultant lanthanide spectra resembled that for ICP-MS.

The late 1990s also marked the emergence of high-field asymmetric waveform ion mobility spectrometry (FAIMS). With the combination of FAIMS with ESI-MS, it was demonstrated that the addition of FAIMS could dramatically reduce the intensity of the chemical background, while maintaining signal intensity. Furthermore, the possibility of separating ions with the same m/z was demonstrated. This led to significant improvements in the detection of many species using ESI-FAIMS-MS as compared to ESI-MS alone.

Simple ion trajectory modeling was developed, and the factors influencing the performance of the FAIMS were discussed from a theoretical standpoint. A parallel plate FAIMS was demonstrated to have a resolving power that is partly dependent on the residence time within the analyzer. However, a FAIMS based on concentric cylinders or concentric spheres has the advantage of an ion focusing mechanism, which serves to reduce losses of ions to the walls of the FAIMS. As a result, higher ion transmission efficiency is possible with an interface based on either concentric cylinders or spheres. Analyzers with a smaller radius have the effect of increasing the strength of the ion focusing, which should reduce ion losses. For a FAIMS based on concentric spheres with the same radii as a comparable concentric cylinder FAIMS, the spheres were shown to have stronger ion focusing effect as a consequence of the geometry. Higher waveform

frequency was theoretically demonstrated to improve ion transmission through the analyzer by reducing the ion path width. This reduces the minimum distance that an ion can approach the wall of the analyzer (ignoring diffusion and ion repulsion), further reducing ion losses. A waveform with a high:low voltage symmetry ratio of 2:1 was demonstrated to produce the highest ion CVs, however, waveforms with a greater high:low ratio were shown to theoretically produce narrower path widths. It was suggested that, for simple ions (i.e., ignoring the effects of molecular folding and related shape effects), the observed mass-selected CV peak width was the combination of the adverse effects of diffusion and the strength of the ion focusing. Ions with higher K_h/K mobilities will be more effectively focused, and have greater peak widths due to reduced diffusional losses. These ions also exhibit greater CVs, hence the general observation of greater peak width with greater ion CV. Changing the FAIMS geometry may lead to enhanced focusing and ion transmission, however, this may come at the expense of the mass-selected CV peak width, which may compromise the separation of ions.

In Chapter 5, analysis of perchlorate was investigated using the first reported ESI-FAIMS-MS prototype. It was demonstrated that perchlorate could be separated from sulfate and phosphate (which are typical interferents for the analysis of perchlorate by ESI-MS) in the gas phase at atmospheric pressure. Due to the FAIMS ion filtering, the chemical background was dramatically reduced, and the ion focusing maintained the signal intensity. As a result, significant improvements in the signal to background ratio for the determination of perchlorate were demonstrated. This led to the achievement of environmentally relevant detection limits, which could not be achieved by ESI-MS alone.

Using a dome FAIMS prototype interface, some basic investigations of this interface were done in Chapter 6. The spacing at the dome was demonstrated to have significant effects on both the intensity and mass-selected CV peak widths. As such, the dome position needs to be optimized for peak width and intensity for the CV range of interest. The maximum intensity and maximum mass-selected CV peak width tend to optimize at different settings, so the dome position needs to be optimized to achieve a reasonable compromise between mass-selected CV peak width and intensity. The

stability of the waveform was shown to be critical for operation; however, the actual symmetry was not very important, provided that it was a stable one. Slight changes to the waveform through the course of an experiment can potentially cause significant changes in the observed ion CV.

Using different drift gases in FAIMS has been previously demonstrated as an effective means of controlling a separation. Also, the use of CO₂ in the drift gas has also previously been shown to prevent fragmentation of ions. In this work, CO₂ was shown to prevent fragmentation of different species, and formed what appeared to be stable associations with hypochlorite and arsenite. Due to the filtering action of FAIMS, the MS interface can be successfully operated with no potential difference between the sampling plate and the skimmer. Using this mild MS interface sampling conditions, it was shown that low levels of gas adducts could be observed, which likely form as the ions are sampled into vacuum. These adducts would have surely been impossible to identify without the reduction in the spectral background. With the ESI-FAIMS-MS system, very mild MS interface sampling conditions could be used. However, it was shown that selenite may be fragmented during the sampling of ions into the FAIMS itself. The addition of CO₂ into the drift gas seemed to prevent this type of fragmentation from occurring.

The aqueous sprayer interface was successfully coupled to the FAIMS. The performance of the system was demonstrated to be very similar to using methanol solvent when in positive mode. However, in negative mode, the signals were observed with slightly lower intensity. Response curves for some arsenic and selenium species in purely aqueous matrix were established, and suggest low nanomolar detection limits are possible for these species in water matrix. However, some concerns were raised in regards to linearity at the low end of the response curve. Nevertheless, ESI-FAIMS-MS offers a significant improvement for the detection of these species.

The variety of species observed, for presumably single analyte solutions, raises the issue of possible artifacts introduced by the ESI source. These potential artifacts

include the alteration of the actual solution species to other species and ionization bias as the result of surface activity and gas-phase acidity. In order to reduce these concerns, any speciation work done with ESI-MS should be accompanied by a classic chromatographic separation, where a difference in the retention time should confirm the presence of multiple solution species. From the data presented in Chapters 7 and 8, concerns regarding the potential loss of species in the FAIMS should be addressed. It is possible that some weak interactions may not survive the FAIMS transmission, and thus not be observed in any of the operating modes. Considering these potential limitations of the FAIMS and possible artifacts introduced by the ESI, interpretation of the resultant spectra should be done cautiously. In any case, the incorporation of FAIMS represents a significant improvement for any analysis where ESI-MS would typically be used.

9.2 Future Work

9.2.1 Negative Mode ES with Aqueous Solvents

Due to the expense and environmental effects of sulfur hexafluoride (SF_6), an alternate means of electrospraying in negative mode still needs to be developed. Since the use of SF_6 is being phased out for use in conventional high-voltage applications, such as in electrical transformers, the search for a new gas to prevent discharge is underway [1]. Possibly, a different gas or mixture of gases for preventing discharge will be developed. Variations on the nanospray interface may also provide some additional advantages, or at least reduce the volume of gas required to maintain stable, intense signals.

9.2.2 Matrix Effects in ESI-FAIMS-MS

In the investigation of some of the basic behavior of simple cations in ESI-FAIMS-MS (Chapter 8), it was found that when ~15% CO_2 , 85% N_2 was used as the drift gas, Cs^+ and Na^+ could be transmitted at the same combination of DV and CV. In similar

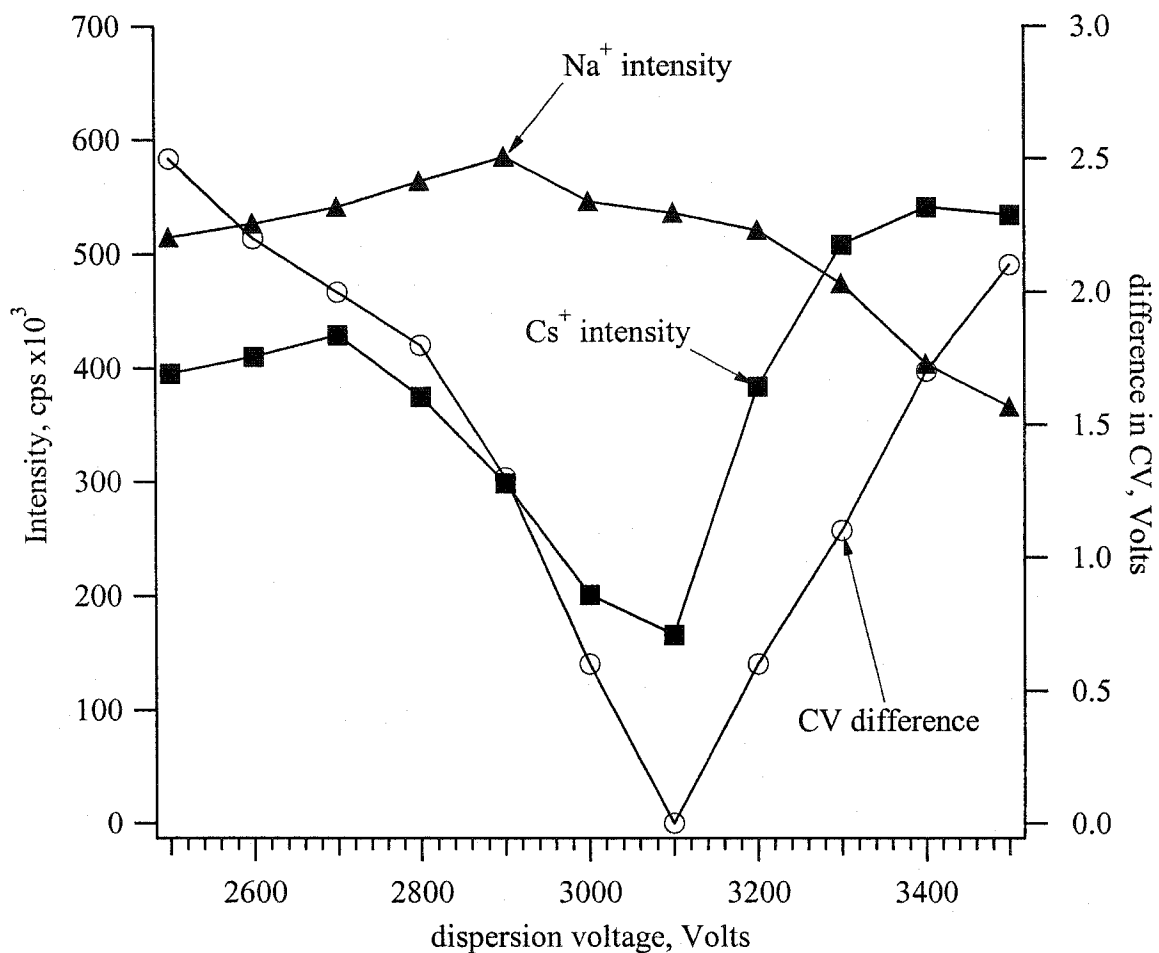


Figure 9.01 Observed signal intensity of Na⁺(H₂O) at m/z 41 and Cs⁺ at m/z 133 as a function of applied DV. Second axis represents the difference in CV of Na⁺(H₂O) and Cs⁺ as a function of DV. Sample was 0.01 mM CsCl, RbCl, and KCl with 0.4 mM ammonium acetate in 100% water matrix. Drift gas ~ 15% CO₂, 85% N₂. F_{OR} = 0 V.

tests (with conditions as in Chapter 8), if the background levels of Na^+ were significant, matrix effects in the FAIMS were observed. The DV was changed, and the CV was scanned at each DV setting. From the mass-selected CV scans, the intensity of the signals and the difference in the CV of each peak were determined. Figure 9.01 is a plot of the signal intensity of $\text{Na}^+(\text{H}_2\text{O})$ and Cs^+ monitored as a function of the applied DV, and also includes a plot of the difference in observed CV as a function of DV. As the DV was increased, the $\text{Na}^+(\text{H}_2\text{O})$ CV peak was observed to shift to higher CVs at a rate of change greater than the Cs^+ peak. As a result, the Na^+ was observed to overlap with the Cs^+ peak at $\text{DV} = -3300 \text{ V}$ (i.e., a difference in CV = 0 V). As the $\text{Na}^+(\text{H}_2\text{O})$ peak began to overlap with the Cs^+ peak, a significant drop in the intensity of the Cs^+ signal was observed. Similar results were observed in Chapter 5, with the matrix ion HCO_3^- decreasing the observed intensity of I^- at high DVs. These results seem to indicate that the presence of a high concentration of ions in the gas phase can affect the transmission of ions present at lower levels. This may occur through charge-repulsion interaction within the FAIMS. These types of interactions could lead to significant matrix effects when complex matrices are being analyzed, and requires further study to quantify the levels and types of ions that cause the most significant effects.

9.2.3 Multiply Charged Cations

The cations presented in earlier chapters were limited to the alkali metals. The omission of multiply-charged cations was not an oversight. Figure 9.02 is the mass-selected CV spectra of BaCl_2 (Figure 9.02 (a)) and LaCl_3 (Figure 9.02 (b)) in purely aqueous matrix (conditions as specified in the Figure caption). As with other studies, masses corresponding to the major isotopes of these ions were monitored, looking for species known to exist in the mass spectrum under these test conditions. Unlike the simple cations, these ions were found at a large range of CV values, suggesting that several different gas-phase species for these ions are transmitted through the FAIMS. Mass spectra were acquired at several different CVs, and in each case, the evidence of each cation was found. Two mass spectra from the LaCl_3 work are presented in Figure 9.03, and demonstrate that different types of La species were observed at the different

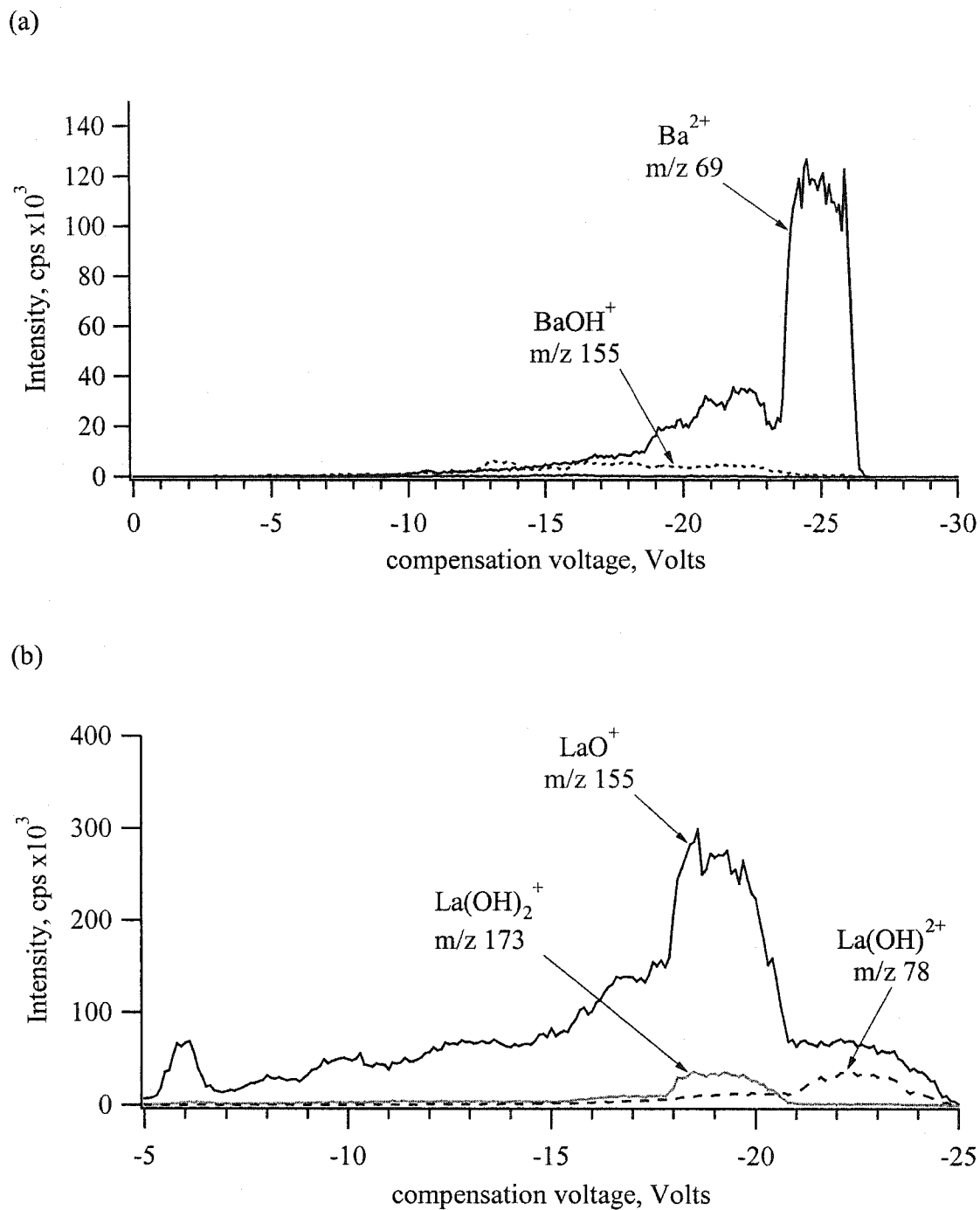


Figure 9.02 Superimposed mass-selected CV spectra in N_2 drift gas of (a) 0.1 mM BaCl_2 with 0.4 mM ammonium acetate in water matrix and (b) 0.1 mM LaCl_3 with 0.4 mM ammonium chloride in water matrix. $\text{DV} = 3.5$ kV, $F_{\text{OR}} = 65$ V.

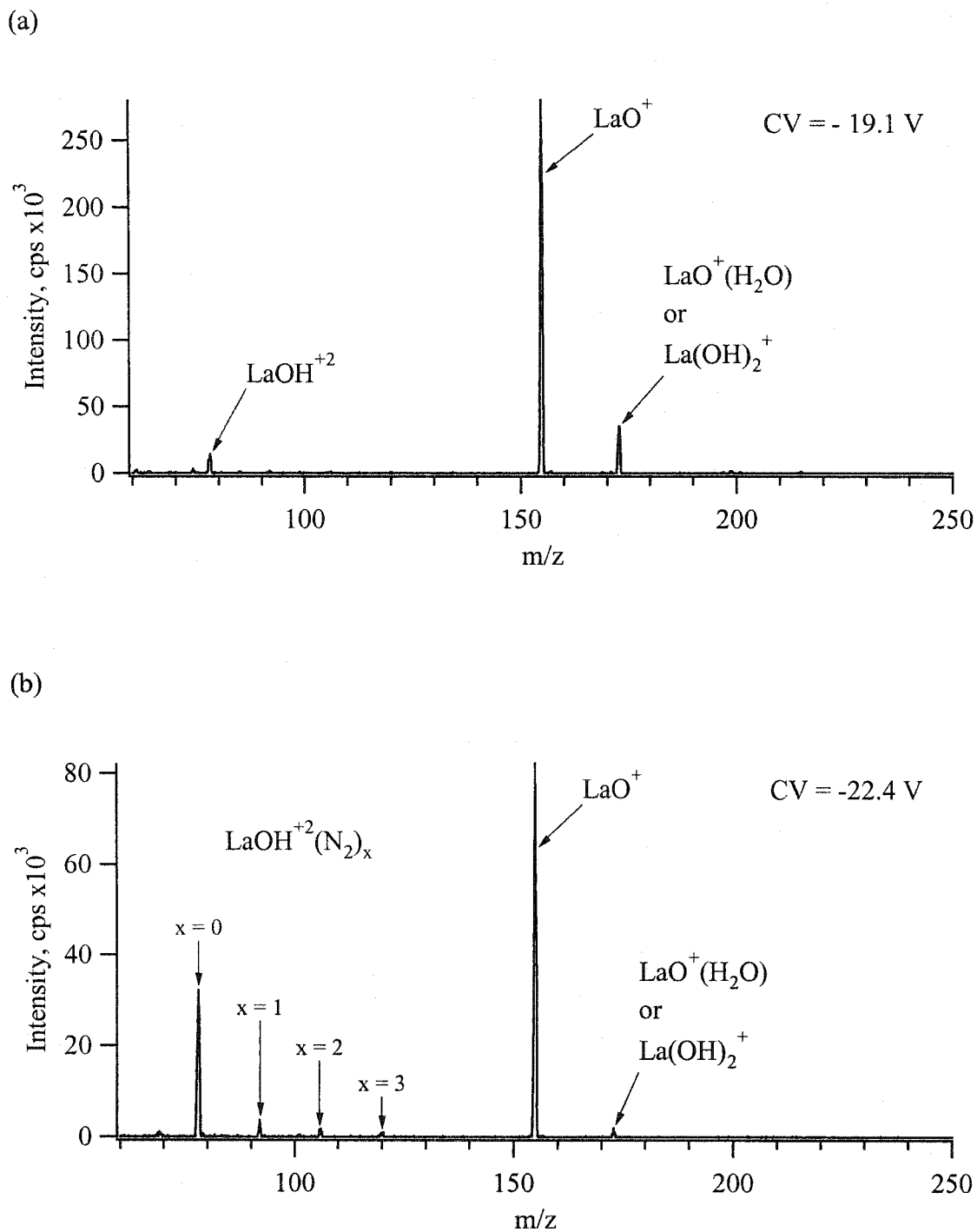


Figure 9.03 Mass spectra in N₂ drift gas of 0.1 mM LaCl₃ with 0.4 mM ammonium chloride in water matrix. DV = 3.5 kV, F_{OR} = 65 V. (a) CV = -19.1 V; (b) CV = -22.4 V.

CVs. Also, the relatively poor signal intensity of both Ba and La with these tests suggests that transmission through the FAIMS is poor. If these ions do not rapidly reach a stable gas-phase species in the FAIMS, they may be filtered out, as described in earlier chapters. The identity of these different gas-phase species should be determined, and possibly the FAIMS interface should be modified to induce better or more tunable declustering prior to sampling the ions into the RF fields.

9.2.4 Modifications to the FAIMS Interface

As described in Chapter 5, a FAIMS apparatus with smaller dimensions can theoretically lead to significant gains in the degree of ion focusing. While this type of interface may be advantageous for ion transmission, it may produce wider mass-selected CV peak widths as the result of reduced losses to the walls of the FAIMS. Recent work with a tandem FAIMS apparatus utilized a larger FAIMS for ion separation, followed by a smaller FAIMS for ion transmission and trapping [2].

Changes to the waveform generator are also required. The stability of the waveform leaves much to be desired, as does the maximum attainable DV. A more rapid switching between waveform polarities would also facilitate scanning between the various modes, such as quickly changing from P1 to P2 mode operation. Also, tuning of the system would be easier if the dome position could be tuned while the waveform was operational. This would require a different means of attachment of the high voltage RF line to the inner cylinder. This connection should be shielded, so that the experimenter cannot inadvertently touch this kind of dangerous high-voltage connection.

Another likely avenue of investigation is how ions are sampled into the FAIMS. Currently, ions must be sampled at right angles to the eventual direction of gas and ion flow within the analyzer. If the ions could be sampled into the analyzer region such that the orifice was aligned with the mid-point of the analyzer spacing, perhaps some minor enhancements in the sampling of ions could be realized.

9.2.5 FAIMS – Drift Tube IMS Coupling

The use of FAIMS as an orthogonal separation for drift tube IMS should also be investigated. Since the separation of ions within the FAIMS is different than with drift tube IMS, increased reliability in the IMS spectra may be possible. Using the ion filtering of FAIMS, it is possible that ions known to interfere with detection in drift tube IMS applications may be filtered out, increasing the detection confidence by reducing the appearance of false-positive signals. This could represent some significant advantages for field testing using IMS, such as biological and chemical detection. However, this would require that the waveform generator be miniaturized and the power requirements reduced. As suggested by Krylov [3], some different waveform generator variants may be able to fulfill this requirement with further development.

9.2.6 Alternate Ion Sources with FAIMS-MS

While ESI has become one of the most common types of ionization sources for mass spectrometry, some other types of ionization sources should be explored. The limitation here is that the ionization source must be able to operate at (or near) atmospheric pressure. One interesting coupling might be with atmospheric pressure matrix assisted laser desorption ionization (AP-MALDI) [4]. The filtering action of the FAIMS may serve to remove many of the matrix ions that are generated, and may reduce the non-specific background observed at low levels with MALDI sources [5, 6]. Also, the incorporation of a FAIMS interface would likely improve the sampling of ions into the MS orifice, since the FAIMS is well-suited for sampling ions at atmospheric pressure, due to its ion-focusing effects. This may also introduce the added benefit of separating the analyte ion from background ions of the same mass prior to introduction to the MS, which may improve the signal to noise and enhance detection limits.

9.3 References

1. Fitzpatrick, G.J.; Olthoff, J.K.; Powell, R.M., National Institute for Standards and Technology. "Measurement support fo the U.S. electric-power industry in the era oderegulation with focus on electrical masurements for transmission and distrubution"; **1997**.
2. Guevremont, R.; Ding, L.; Ells, B.; Barnett, D.A.; Purves, R.W. "Atmospheric pressure ion trapping in a tandem FAIMS-FAIMS coupled to a TOFMS: Studies with electrospray generated Gramicidin S ions"; *J. Am. Soc. Mass Spectrom.* **2001**, *12*, 1320-1330.
3. Krylov, E.V. "Pulses of special shapes formed on a capacitive load"; *Instrum. Exp. Tech.* **1997**, *40*, 628-631.
4. Laiko, V.V.; Baldwin, M.A.; Burlingame, A.L. "Atmospheric pressure matrix-assisted laser desorption/ionization mass spectrometry"; *Anal. Chem.* **2000**, *72*, 652-657.
5. Keller, B.O.; Li, L. "Detection of 25,000 molecules of Substance P by MALDI-TOF mass spectrometry and investigations into the fundamental limits of detection in MALDI"; *J. Am. Soc. Mass Spectrom.* **2001**, *12*, 1055-1063.
6. Keller, B.O.; Li, L. "Discerning matrix-cluster peaks in matrix-assisted laser desorption / ionization time-of-flight mass spectra of dilute peptide mixtures"; *J. Am. Soc. Mass Spectrom.* **2000**, *11*, 88-93.